Modelling the behaviour of granular material on the surface of asteroids and under different gravity conditions (e.g., Mars, the Moon)

Thesis

Modelling the behaviour of granular material on the surface of asteroids and under different gravity conditions (e.g., Mars, the Moon)

Naomi Murdoch

MPhys. Astrophysics

Planetary and Space Sciences Research Institute
The Open University, U.K.

in a cotutelle arrangement with

The Côte d'Azur Observatory
The University of Nice Sophia Antipolis, France

A thesis submitted for the degree of
Doctor of Philosophy

December 2011

PAGINATED BLANK PAGES ARE SCANNED AS FOUND IN ORIGINAL THESIS

NO INFORMATION IS MISSING

NOTIFICATION OF REDACTION

THESIS TITLE:
Modelling the behaviour of granular material on the surface of asteroids and under gravity conditions (e.g., Mars, the Moon).

AUTHOR:
Naomi Murdoch

YEAR:
2011

CLASSMARK:
523.44 MUR

The following pages/sections have been redacted from this thesis:

Page No.	Item/section redacted
4	Photograph/Image
5	Photograph/Image
7	Photograph/Image
8	Photograph/Image
9	Photograph/Image
10	Photograph/Image
11	Photograph/Image
12	Photograph/Image
13	Photograph/Image
31	Photograph/Image
36	Photograph/Image
37	Photograph/Image
134	Photograph/Image
139	Photograph/Image
146	Photograph/Image
314	Photograph/Image
316	Photograph/Image
327	Photograph/Image
332	Photograph/Image
335	Photograph/Image
-	SUPPLEMENTARY MATERIAL CD

This thesis is dedicated to my grandparents: Anna Olive Elizabeth Murdoch, Kenneth Lyle Stewart Murdoch, Eileen Margaret Anderson and Keith Arthur Anderson.

"Qui donc peut calculer le trajet d'une molécule? que savons-nous si des créations de mondes ne sont point déterminées par des chutes de grains de sable?"

"Who could ever calculate the path of a molecule? How do we know that the creations of worlds are not determined by falling grains of sand?"

Victor Hugo, Les Miserables

Acknowledgements

First I would like to express my gratitude to Dr. Simon F. Green and Dr. Patrick Michel who have guided me through this Ph.D. thesis as an excellent supervisory team. Simon and Patrick have both helped me to develop the skills to become a researcher and to develop the important skills of scientific communication. I am indebted and thankful to them both for agreeing to supervise an unconventional thesis that involved numerical and experimental work, two scientific fields and several institutions. I also wish to thank them for having helped me to secure the funding that made this Ph.D. possible and for having supported and encouraged me as I pursued interests and opportunities that took me around the world during the course of my Ph.D..

This Ph.D. thesis was the first formal collaboration between The Open Unversity and the University of Nice Sophia Antipolis, and The Open University's very first 'co-tutelle' Ph.D. thesis, I thank everyone involved in overcoming the difficulties of establishing formal collaborations at an institutional level, which I hope will benefit others in future. I would equally like to express my gratitude to Thales Alenia Space who agreed to co-finance this thesis and for their willingness to fund scientific research without direct commercial gain.

I would like to thank Dr. Iain Gilmour, Prof. Iwan Williams, Dr. Stephen Lewis, Prof. Alexandre Chemenda, Dr. Olivier Pouliquen and Prof. Marcello Fulchignoni for accepting to be part of my jury panel. I am pleased and honoured that you all accepted to examine this thesis.

There are several people, without whom, the experimental part of this thesis would not have been possible. First, I would like to express my sincere thanks to Dr. Ben Rozitis from The Open University for the very important role he played in proposing, designing, constructing and flying the AstEx experiment. Although not directly involved in the data analysis Ben was also willing to provide help whenever it was needed. I thank Thomas-Louis de Lophem for providing engineering advice, for producing the experiment engineering designs and for being a wonderful zero-gravity photographer. I thank Prof. Wolfgang Losert of the University of Maryland for his help during the AstEx design phase and for his assistance with the AstEx data analysis. I would also like to thank Chris Hall, Damian Flack and, particularly, Kevin Dewar from the Planetary and Space Sciences Research Institute workshop for helping to design and construct the experimental hardware. Lastly, with regards to the experimental work, I thank the ESA Education office for giving the AstEx Team the opportunity to be part of the 51st ESA microgravity research campaign through the 'Fly your Thesis' programme. I acknowledge also the financial contributions to the AstEx experiment from The Open University and the Royal Astronomical Society.

With regards to the numerical part of this thesis I thank Prof. Derek C. Richardson of the University of Maryland for giving me access to the numerical code `pkdgrav` and for making the

necessary modifications to the code for this thesis. I thank Derek also for always responding to my questions in a timely and pertinent manner. I thank Dr. Kevin J. Walsh, currently at the Southwest Research Institute in Boulder, Colorado for all of his advice, particularly during the first half of my Ph.D., which certainly made my life easier. I extend thanks to Dr. Kerstin Nordstrom, from the University of Maryland, who stepped in at the last minute and saved the day with the analysis of collective motion in the numerical simulations. I also thank Prof. Wolfgang Losert for making the collaboration between his experimental group and our numerical group possible.

As a Young Scientist member of an International Space Science Institute International Team, I express my thanks to all of the team members for their educational presentations and stimulating discussions during our meetings in Bern, Switzerland. I would also like to thank the ESA Education office for giving me the opportunity to present some of my work at the 60th International Astronautical Congress in Daejon, South Korea in 2009, which I attended as an ESA sponsored student. Further results from this thesis were presented at the 2010 EPSC conference in Rome and the 2011 joint EPSC-DPS conference in Nantes with the financial assistance from the Europlanet Support Committee. I also express my gratitude to the organisers and participants of the memorable 2011 NASA Astrobiology Winter School in Hawai'i, during which I learnt an incredible amount as a result of exposure to academic research in different fields and also met potential future collaborators.

It has been an immense pleasure to be part of the Planetology Group (Laboratoire Cassiopée) at the Observatoire de la Côte d'Azur and part of the Planetary and Space Sciences Research Institute at The Open University. My colleagues and friends in both places have contributed immensely to my personal and professional life during my Ph.D.. I also deeply appreciate the encouragement and help my colleagues in Nice have given me to improve my french over the last three years. I thank the members, coaches and supporters of the OCA female rugby team for all of the good times we have had. I thank Khaled along with Nadia and Karima for providing the wonderful food and atmosphere at the OCA restaurant. I also thank the Riviera Rugby Club for having welcomed me into their training sessions, which often provided much needed stress relief. I am also extremely thankful for the dedication of my friends in Nice and Cannes who have gone out of their way to help me study granular materials on the beaches and the ski slopes of the Côte d'Azur.

Lastly, I would like to thank my family for their love and encouragement. For my parents, Julie Murdoch and Stewart Murdoch, who have always supported and helped me in all my pursuits. For my sisters, Dr. Mhairi Murdoch and Nina Murdoch, for having always believed in their little big sister. For Aurélien Dupuis who has been with me throughout this Ph.D. offering words of encouragement, advice and an ever ready, extremely patient, listening ear. Thank you.

Naomi Murdoch

Abstract

This thesis, at the interface between the scientific disciplines of planetary science and granular physics, has two key components, both of which intend to increase our understanding of granular dynamics in varying gravitational conditions. The dynamics of granular materials are involved in the evolution of solid planets and small bodies in our Solar System, whose surfaces are generally covered with regolith. Understanding granular dynamics is also critical for the design and/or operations of landers, sampling devices and rovers to be included in space missions.

The first component of this thesis is the validation of the hard-sphere discrete element method implementation in the N-body code `pkdgrav` to model the dynamics of granular material. By direct comparison with results from laboratory experiments, it is demonstrated that the hard-sphere discrete element method implementation in `pkdgrav` is valid for modelling granular material in dilute regimes and is capable of reproducing the complex dynamical behaviour of a specific dense system as well. The second component is focussed on the AstEx parabolic flight experiment. This experiment, with the aim of characterising the response of granular material to rotational shear forces in a microgravity environment, was designed, constructed, flown and the data were analysed as part of this thesis. It was found that the effect of constant shearing on a granular material in a direction perpendicular to the gravity field is not strongly influenced by gravity. The AstEx experiment has demonstrated, for the first time, that the efficiency of granular convection may decrease in the presence of a weak gravitational field, similar to that on the surface of small bodies. The first measurements of transient weakening of granular material after shear reversal in microgravity are also reported. Results suggest that the force contact network may be weaker in microgravity, although the influence of any change in the contact network is felt by the granular material over much larger distances. This may have important implications for our interpretation of asteroid surfaces.

Continued advancement of our understanding of granular materials in varying gravitational conditions requires futher experiments and the development of the soft-sphere discrete element method implementation in `pkdgrav` in order to model the granular regimes that are inaccessbile to the hard-sphere implementation.

Contents

Chapter 1

Granular material and the Solar System

1.1 An introduction to the Solar System

The history of our Solar System started 4.6 billion years ago when a dense cloud of interstellar gas and dust collapsed under its own gravity and formed the primitive solar nebula, at the centre of which, was the Sun. Within this nebula there existed a protoplanetary disk from which the planets formed. Planetary formation is a complex process involving three distinct stages. The first stage involves the growth from micron-sized dust particles to kilometre-sized objects called planetesimals. Initially, the micron-sized dust particles are thought to form fluffly agglomerates which can reach centimetre sizes (e.g., Blum & Wurm, 2000; Wurm & Blum, 1998). However, as the dust aggregates increase in size the average collision velocity increases above the threshold level for direct sticking due to van der Waals forces. Despite the many hypotheses proposed and dust collision experiments performed in recent years (see review by Blum & Wurm, 2008) it is still not fully understood how further growth occurs. The second stage of planetary formation involves the accretion of planetesimals due to mutual gravitational interactions to form planetary embryos (lunar to Mars-sized objects) and, finally, the third stage is when the planets are formed by high-velocity collisions between planetary embryos. The terrestrial planets and giant planets are formed in the inner and outer parts of the Solar System, respectively. Some of the primordial objects that never coalesced into a planet still exist today in the form of small-bodies and they contain the clues to the origins of the Solar System. It has also been proposed that the complex organic molecules, which may be capable of triggering pre-biotic synthesis, and water could have been delivered to Earth by primitive small bodies (e.g., Walsh *et al.*, 2011). In addition, such small bodies continue to shape planetary surfaces throughout the Solar System via

collisions.

Several different populations of small bodies currently exist in the Solar System. A schematic is shown of the inner Solar System in Fig. 1.1. The main belt of asteroids, residing between Mars and Jupiter, is the dominant small body population in the inner Solar System containing a total mass of ~5% the mass of the Moon (Asphaug, 2009). The small bodies which have perihelion[1] distances of less than or equal to 1.3 AU[2] are called near-Earth objects (NEOs). The NEO population is composed of near-Earth asteroids (NEAs) and also some comets.

The compositional definition of a comet is an ice-rich body as opposed to the rocky and metallic asteroids. Specifically, comets are capable of developing a coma if they come close to the Sun (Asphaug, 2009). In fact, comets have highly eccentric orbits and, as such, only a small fraction of their orbital period is spent in the inner Solar System; most of the time comets reside in the outer Solar System. Interestingly, recent observations have also revealed water ice in the spectra of a number of the asteroids of the outer main belt; these objects, some of which exhibit comae, have been given the name main-belt comets (MBCs) (Hsieh & Jewitt, 2006).

Comets with periods greater than 200 years are called long-period comets, while those with periods less than 200 years are categorised as short-period comets. The short period comets can be further divided into the Jupiter family (periods less than 20 years) and Halley family (periods between 20 and 200 years). Long-period comets are thought to originate from the Oort cloud. This cloud of small bodies, located at ~50,000 AU from the Sun, was hypothesised by J. Oort in 1950 but has never been detected. Short-period comets are expected to originate from the Kuiper belt (a flattened ring beyond the orbit of Neptune but within 50 AU). The presence of the Kuiper belt was proposed by K. E. Edgeworth in 1943 and G. P. Kuiper in 1951 and the first detection of a Kuiper belt object took place in 1992 (Jewitt & Luu, 1993). Kuiper belt objects (KBOs) are part of a larger class of icy bodies called the Trans-Neptunian Objects (TNOs), which is the name given to all small bodies which orbit the Sun at a distance greater than the orbit of Neptune (i.e., >30 AU).

Returning to the inner Solar System there is a population of asteroids that follow essentially the same orbit as Jupiter, but lead or trail the planet by an angular distance of 60 degrees; these are called Jupiter's Trojans. Another population, the Hilda group, exist in the 3:2 mean motion resonance with Jupiter[3] and their aphelia are found either opposite Jupiter or 60 degrees ahead of, or behind Jupiter.

Throughout the history of the Solar System all of these populations of small bodies have been involved in, and continue to be involved in, collisions with each other and with larger planetary bodies. The cumulative effect of such collisions and impacts is the presence of granular material

[1]The perihelion of an orbit is the closest point to the Sun. The furthest point is called aphelion.
[2]AU stands for an Astronomical Unit and refers to the mean Earth-Sun distance, which is $\sim 1.5 \times 10^{11}$ m.
[3]Being in a 3:2 mean motion resonance with Jupiter means that for every two orbits Jupiter makes around the Sun, the Hilda group bodies make three orbits.

(regolith), ranging in size from a few microns (dust) or few hundreds of microns (sand) to a few centimetres or metres (gravels, pebbles, boulders), on the surfaces of solid planets and small bodies of our Solar System. Although this superficial layer of regolith, which extends to variable depths, results mostly from impact processes via excavation, fragmentation and ejection of material, regolith may also be produced via other geological processes such as volcanic activity, erosion, transport as well as thermal fragmentation. As a result regolith is extremely common at the surface of all solid planetary bodies.

The dynamics of granular materials are, therefore, involved in planetary evolution and are also critical for the design and operations of landers, sampling devices and rovers.

1.2 The granular nature of asteroids

In this section we will first discuss the evidence from ground based observations and space missions that indicates that regolith is dominant on the surface of asteroids. Then we will discuss the evidence that indicates that asteroids may not only have granular material at their surface, but some may, in fact, be entirely granular in nature.

1.2.1 Direct observations of asteroid surfaces

To date there have been three space missions sent to characterise an asteroid in detail: the NASA near-Earth asteroid rendez-vous (NEAR) mission which arrived at the near-Earth asteroid (433) Eros in 2000 (Cheng *et al.*, 1997), the JAXA Hayabusa sample return mission which arrived at the near-Earth asteroid (25143) Itokawa in 2005, and the NASA Dawn mission to the main-belt asteroids (4) Vesta and (1) Ceres, which arrived at Vesta, the first of the two targets, in 2011 (Russell *et al.*, 2007). There have also been other missions which have flown past asteroids. For example, the ESA Rosetta mission, whose primary target is Comet 67P/Churyumov-Gerasimenko, flew by asteroid (21) Lutetia in 2010. The NEAR spacecraft flew by asteroid (253) Mathilde in 1997 before reaching Eros and the Galileo spacecraft flew by asteroids (951) Gaspra and (243) Ida in 1991 and 1993, respectively, on its way to Jupiter. Figure 1.2 shows all asteroids that have been visited by spacecraft either during a flyby or during a rendez-vous mission.

The first two in-situ observations of asteroids (those of Eros and Itokawa) greatly increased our knowledge of asteroid surface properties whilst highlighting the complexities and variations in the surface environments. Before the NEAR and Hayabusa space missions most scientists assumed that the smallest asteroids were all monolithic rocks with a bare surface, although, there had been a few articles suggesting a possible alternative internal structure (e.g., Michel *et al.*, 2001). Calculations had

Figure 1.1: **Inner Solar System diagrams showing the positions of asteroids and comets** - The positions of all numbered asteroids and comets on 1/10/2008 plotted (a) from above the ecliptic plane (the plane containing the Earths orbit) and (b) from the edge of the ecliptic plane. The orbits and positions of Mercury, Venus, Earth, Mars, and Jupiter are shown; the Trojan, main-belt, and near-Earth asteroid populations are evident. Asteroids are yellow dots and comets are sunward-pointing wedges. Images taken from Asphaug (2009) but produced by P. Chodas (NASA/JPL).

Figure 1.2: **Asteroids visited by spacecraft** - This composite image shows the comparative sizes of nine asteroids visited by a spacecraft. The largest asteroid, Vesta, is ~530 km in diameter. The smallest asteroid, Itokawa, is only a few hundred metres in diameter. Image credit: NASA/JPL-Caltech/JAXA/ESA.

been performed of ejecta velocity assuming that asteroids experience impacts in the main asteroid belt. Given the low gravitational acceleration on the surface of an asteroid, it was thought that regolith formation would not be possible; even if small fragments of rock were created during the impact process nothing would be retained on the surface. However during these two space missions NEAR revealed a substantial regolith covering Eros (Robinson *et al.*, 2002), and Hayabusa revealed Itokawa to be a rubble pile asteroid essentially made of regolith throughout (Fujiwara *et al.*, 2006).

In addition to finding each of these bodies to be regolith-covered, there is strong evidence that this regolith is very complex and active. In fact, it was due to the NEAR observations of Eros that the local gravity was first understood to be of importance to asteroid surface processes (Robinson *et al.*, 2002). This was further emphasised when the first images were received from the Hayabusa probe. Compared to Eros, Itokawa was found, astonishingly, to have entirely different structural and surface properties despite their similar taxonomic class. The reason for these different properties is not clearly understood, but perhaps this shouldn't have been surprising; because of their size (mass) difference, if gravity is the discriminator, then Itokawa is expected to be as different from Eros, geologically, as Eros is from the Moon (Asphaug, 2009).

We will now discuss, in detail, the in-situ observations of some asteroids.

1.2.1.1 Asteroid (433) Eros

Eros is the second largest near-Earth asteroid with a mean diameter of ~17 km and a bulk density of ~2.67 g cm^{-3} (Yeomans *et al.*, 2000). Its pickle-like shape (Fig. 1.3) suggests that Eros is a body with strength. From the data obtained during the NEAR mission it has been possible to calculate the gravitational slopes (the angle between the local gravitational field and the normal to the surface) over the surface of the asteroid (Fig. 1.4). The gravitational slope varies over the surface of the asteroid; in some locations there is no slope at all, and in other locations (such as the walls of craters) slopes exist of 30-40 degrees (Zuber *et al.*, 2000). However, all of these slopes are consistent with surfaces of loose granular material. Indeed, the regolith of Eros consists of fine dust with an estimated depth between 10 to 100 metres (Veverka *et al.*, 2000).

The surface of Eros is heavily cratered and has a high abundance of boulders (Veverka *et al.*, 2001b). However, despite the large number of craters, there is a deficiency of small (m-sized) craters compared to the expected extrapolations from larger crater sizes or from what is observed on the Moon (Veverka *et al.*, 2001b). There is, in fact, a larger abundance of boulders than small craters (Chapman *et al.*, 2002). It has been suggested that impact-induced seismic shaking, which causes the regolith to move, may erase small crater features and thus explain their paucity compared to predictions of dynamical models of projectile populations (e.g., Michel *et al.*, 2009; Richardson *et al.*, 2004). This

Figure 1.3: **Asteroid (433) Eros** - Global image of Eros. Image taken by the NASA NEAR spacecraft in 2000. Image credit: NASA.

Figure 1.4: **Slopes of asteroid (433) Eros** - The shape model of Eros is shaded in degrees of slope between the surface normal and the vector of gravitational acceleration in the rotating frame of reference. The crater rims and a few other areas have local slopes of 30° - 40°, whereas non-cratered areas are relatively "flat" (Zuber *et al.*, 2000). Figure taken from Asphaug (2009) but reproduced from Asphaug *et al.* (2002).

will be discussed in greater detail in Section 1.3.2. Some of the boulders appear in clusters on the surface. This may indicate that they are formed from secondary ejecta or that they are small pieces of a larger thermally broken boulder.

The older craters are, in general, shallower than the fresher craters (Robinson *et al.*, 2002). In fact, many of the topographic lows are filled with smooth, flat deposits of fine granular material (Cheng *et al.*, 2002; Robinson *et al.*, 2001; Veverka *et al.*, 2001b). These features, referred to as "ponds" are characterised by smooth, level surfaces that are sharply delineated; they are found prefentially at low latitudes and in the bottoms of small (<1 km) craters. Some examples of such ponds are shown in Fig. 1.5. Several mechanisms have been proposed to explain the formation of these dust ponds including seismic shaking (Cheng *et al.*, 2002), electrostatic levitation and transport of fine grains (Lee, 1996; Robinson *et al.*, 2002) as well as thermal erosion of boulders (Dombard *et al.*, 2007).

Figure 1.5: **Dust ponds on (433) Eros.** - Images taken by the NASA NEAR spacecraft in 2000. Image credit: NASA.

There are also ~10 to 100 m-wide scarps[1] on the surface of Eros. They are supported in the walls of long, linear fractures, some extending for kilometres and mostly running in parallel (Prockter *et al.*, 2002). It has been suggested that these fractures are evidence of competent rock below the regolith - they result from stresses from large events, which have refocussed and caused fracture far from the crater (Asphaug *et al.*, 1996; Fujiwara & Asada, 1983), or that they are due to thermal stresses (Dombard & Freed, 2002) and body stresses induced by changes in spin. However, Asphaug (2009) suggests that these fractures are perhaps faults in a granular matrix and are, therefore, evidence for a fractured granular interior.

[1] A scarp is a steep cliff which can be produced by faulting or erosion processes.

Downslope regolith movement has also been observed on Eros and granular flows have been reported to form both 'debris aprons' and 'talus cones'[1] (Robinson *et al.*, 2002; Thomas *et al.*, 2002; Veverka *et al.*, 2001a) as demonstrated in Fig. 1.6. In these images, especially Fig. 1.6 A, the brighter surfaces imply freshly exposed material that has not yet been subjected to space weathering (the time-dependent modification of an asteroid's reflectance spectrum due to impingement by micrometeoroids and solar wind particles; Chapman, 2004).

Figure 1.6: **Indications of downslope regolith motion on (433) Eros** - (A) Bright steaks of freshly exposed material on a large crater wall, as the darker material moves downslope; (B) talus cones and debris avalanches emanating from a steep scarp; (C) a debris apron extending into a highly eroded crater from a rise at the top of the image, and a thick layer of regolith gently encroaching into the same crater from the bottom of the image; and (D) the collection of regolith (and scattered boulders) in topographic lows, several degraded (softened) craters, a few barely visible 'ghost' craters, and a general lack of small craters, particularly in the smooth areas on the right. Images taken by the NEAR spacecraft but this compiled figure is from Richardson *et al.* (2005).

[1]Talus cones and debris aprons both refer to accumulations of material that have been gravitationally transported away from topographic highs.

1.2.1.2 Asteroid (25143) Itokawa

One of the most remarkable features of the ~320 m near-Earth asteroid Itokawa is the global shape, which seems to consist of two parts: a small "head" and a large "body" (Fig. 1.7). These two parts have a sea otter-shape that seems to be separated by a constricted "neck" region (Demura *et al.*, 2006). The steep slope on the head side of the depression has landslide materials at the bottom. It is highly likely that Itokawa is composed of rubble held together by gravity instead of being a monolithic body. In fact, observations from the Hayabusa mission suggest that the core constituents of the asteroid Itokawa consist of boulders of the order of tens of metres and less (Fujiwara *et al.*, 2006). This type of asteroid, which is a gravitational aggregate, is referred to as a "rubble pile". The low bulk density of Itokawa (1.95 ± 0.14 g cm^{-3}) provides further evidence for the rubble pile interior structure (Abe *et al.*, 2006).

Figure 1.7: **Asteroid (25143) Itokawa** - The rubble pile structure is evident in this global image of the Itokawa. The images were taken by JAXA's Hayabusa spacecraft in 2005. Image credit: JAXA.

On Itokawa the regolith consists of gravel and pebbles larger than one millimetre with a depth that is probably not greater than one metre (Miyamoto *et al.*, 2007). The Muses Sea (Fig. 1.8) is an area densely filled with size-sorted regolith of similar brightness, mostly ranging from millimetre to centimetre scales. Also evident is a gradual decrease of both the average size of regolith particles and the spatial density of large rocks from the boundary with the rough terrain to the center of the Muses Sea. These rocks, tens of centimetres in size, often have rounded corners and have flat sides facing down. They also tend to collect together (Yano *et al.*, 2006). Smooth terrains cover roughly 20% of the total surface area of the rubble pile asteroid Itokawa. In these terrains there are small regolith particles whose grain-size distribution does not vary greatly (Yano *et al.*, 2006). However,

the granular material on the surface of Itokawa appears to be dominated by grains >1 mm in size.

The existence of large facets[1] and many boulders implies that Itokawa has experienced a number of large impacts (Fujiwara *et al.*, 2006). However, Itokawa has very few craters in general and absolutely no distinct craters <1 m in diameter (Fujiwara *et al.*, 2006; Saito *et al.*, 2006). This suggests that there is a mechanism erasing the craters.

Figure 1.8: **Surface of (25143) Itokawa** - Evidence of downslope movement can be seen in image A. The small white arrows in the Muses Sea region indicate the thin, boulder-rich layer similar to landslide deposits. B: The darker depressed region in Little Woomera, which is one of the largest facets, is surrounded by a brighter rim. (Inset) A high resolution image of the northern rim of Little Woomera. The images were taken by JAXAs Hayabusa spacecraft in 2005. Compiled image from Saito *et al.* (2006).

1.2.1.3 Asteroid (21) Lutetia

Asteriod Lutetia (Fig. 1.9 A), a main-belt asteroid with a diameter of ~100 km, has a complex geology, a very old surface and one of the highest asteroid densities measured so far (3.4 ± 0.3 g cm^{-3}). It has been suggested that Lutetia may have partially differentiated, forming a metallic core overlain by a primitive chondritic crust (Weiss *et al.*, 2011).

The surface of Lutetia is covered by an extensive (up to ~600 m; Sierks *et al.*, 2011) and uniform regolith cover, similar to that of the Moon (Coradini *et al.*, 2011). The thick layer of regolith in the north pole region is seen to flow in major landslides. Landslides have also been seen inside craters (Fig. 1.9 B). The linear features seen on the surface (Fig. 1.9 C,D) are similar in appearance to those on the martian moon Phobos, which are commonly interpreted as resulting from a large impact (Thomas *et al.*, 1979). As mentioned above, the existence of similar grooves on Eros has been

[1]The surface of Itokawa appears to have a polyhedral angular structure. Each face of the angular structure is called a facet (Demura *et al.*, 2006).

interpreted as evidence of competent rock below the regolith, although recent work has suggested that the interior may be more granular in nature (Asphaug, 2009). The pattern of grooves on Lutetia and the crater morphology indicate that Lutetia's interior has considerable strength and relatively low porosity (Sierks *et al.*, 2011). It is, therefore, likely that Lutetia is not a rubble pile and has survived the age of the Solar System with its primordial structure intact; i.e., it has not been disrupted by impacts (Sierks *et al.*, 2011).

Figure 1.9: **Surface features on Asteroid (21) Lutetia** - (A) Global image of Lutetia. (B) The central 21-km-diameter crater cluster. Arrows *a*, *b*, and *c* point to landslides. Landslides *a* and *b* appear to have buried the boulders that are pervasive within the crater. Landslide *b* may have exposed a rocky outcrop. Opposite *e* a similar possible outcrop is seen. The material at point *d* has a mottled appearance. (C) The boundary between the young terrain associated with the central crater cluster and the old terrain is extremely well defined in some places, as indicated by the arrow *a*. Arrows *b* and *c* highlight curvilinear features. (D) Arrows *c*, *d*, and *e* point to further curvilinear features on the surface of Lutetia. The curvilinear features cut the crater and its rim. Feature *c* cuts through the debris apron *b* of the crater *a*. This implies that these linear features are younger than the craters or result from an impact into an area with existing large-scale cracks and subsequent regolith movement. Images taken by ESA's Rosetta spacecraft in 2010. Compiled figure and corresponding text taken from Sierks *et al.* (2011).

1.2.1.4 Asteroid (4) Vesta

Vesta is the second most massive main-belt asteroid with an average diameter of ~530 km. Its roundness reveals that it is close to hydrostatic equilibrium. It is also one of the fastest rotators of the large asteroids with a period of 5.3 hours (Russell *et al.*, 2011). Vesta has complex features including lava flows, troughs, ridges, cliffs, hills and a large iron core. Figure 1.10 (a) shows an image of asteroid Vesta in which impact craters and grooves can be seen. One of the most dramatic discoveries on the surface of Vesta is an 18 km high mountain in the centre of a huge (460 km-wide) crater (Massey, 2011). This peak is the second highest in the Solar System (after Olympus Mons on Mars). There are also strong indications of regolith activity. For example, Fig. 1.10 (b) shows a possible landslide

Figure 1.10: **Surface features on Asteroid (4) Vesta** - (a) This global view of Vesta shows impact craters of various sizes and grooves parallel to the equator. (b) Near the image center is a very deep cliff running about 20 km from top to bottom. The topography of the scarp and its surroundings indicates that huge landslides may have occurred down this slope. The scarp's origin remains unknown, but parts of the cliff face itself must be quite old as several craters have appeared in it since it was created. The images were taken by NASA's Dawn spacecraft in 2011. Image Credit: NASA, JPL-Caltech, UCLA, MPS, DLR, IDA.

down the side of a cliff.

1.2.2 Thermal properties of asteroids

The optical brightness of an asteroid is proportional to its projected area and albedo[1] and can, therefore, give a rough indication of the asteroid's size. However, ground based measurements of thermal emission are a much better proxy for size and can be used to determine the size of an asteroid more accurately (Mueller, 2007). The thermal emission of an asteroid can, however, be significantly influenced by the thermal inertia, surface roughness, shape, and spin state, all of which are typically unknown (Mueller, 2007). This means that accurate determination of the size of an asteroid can sometimes be difficult, although, it also means that the thermal emission of an asteroid can provide a wealth of information.

It is possible to use observations performed in the thermal infrared to estimate the thermal inertia of a material, i.e., its resistance to temperature change, by means of a thermophysical model (e.g., Lebofsky *et al.*, 1986; Mueller, 2007; Rozitis & Green, 2011). The surface of an object with zero thermal inertia would be in instantaneous thermal equilibrium with external heat sources; the surface

[1]The amount of solar flux absorbed by an asteroid is proportional to (1 - A) where the bolometric Bond albedo A is defined as the ratio of reflected or scattered flux to incoming flux; scattering into all directions is considered. A is, therefore, restricted to lie between 0 and 1 (Mueller, 2007).

temperature on an asteroid with zero thermal inertia, in particular, would drop to zero immediately after sunset, hence no thermal emission would originate from the non-illuminated hemisphere (Mueller, 2007). The thermal inertia of an asteroid depends predominantly on regolith particle size and depth, degree of compaction, and exposure of solid rocks and boulders within the top few centimetres of the illuminated surface. It is used, therefore, to infer the presence or absence of loose material (i.e., regolith) on the surface of asteroids (Delbo *et al.*, 2007).

Recent observations suggest that most NEOs have lower thermal inertias than that of bare rock, but greater than the lunar regolith, indicating the presence of an insulating layer of granular material on their surface (Harris, 2005). From Fig. 1.11 we can see that all asteroids, even sub-kilometre ones, have been found to have a significant thermally-insulating surface layer (Delbo *et al.*, 2007). It can also be noted that larger asteroids seem to have a finer, or deeper[1], regolith than small ones.

However, we may still expect that very small fast-rotating asteroids would be regolith-free. Consider, for example, the small (<100 m-sized) NEA (54509) YORP. Observations of this asteroid, which has an ultra-fast rotation period of only 12 minutes, provided the first direct detection of the YORP[2] effect (Kaasalainen *et al.*, 2007; Lowry *et al.*, 2007; Taylor *et al.*, 2007). Due to the object's fast rotation, the surface gravity is overwhelmed by the centrifugal force on most of its surface, for any plausible density. Yet, evidence has been found to suggest that there may still be regolith covering the surface (Mueller, 2007)! This would imply that there must be some cohesion present at the surface of the asteroid.

Using a thermal model (e.g., Rozitis & Green, 2011), estimates can been made of the range of temperatures found at the surface of an asteroid at any moment in time. The minimum surface temperature, found near the poles, can be close to 0 K (assuming the poles are perpendicular to the orbital plane). The maximum surface temperature is around 400 K at similar distances from the Sun as the Earth and can increase up to 500-600 K if the asteroid gets as close to the Sun as Mercury (Rozitis, 2011). Asteroids, therefore, exhibit very large temperature variations across their surface.

To understand the surface and sub-surface temperature variations of asteroids over their lifetimes Michel & Delbo (2010) used a dynamical model of the near-Earth asteroid population to estimate the most likely source region and orbital history of four objects which are potential targets for asteroid sample return missions. Then, for each asteroid, the dynamical history was predicted and surface and sub-surface temperatures of these bodies were computed using a thermal model. Delbo & Michel (2011) have also performed a similar study to estimate the temperature history of (101955) 1999 RQ36 (the primary target of the mission OSIRIS-REx, selected in the program New Frontiers of NASA).

[1]From thermal inertia measurements it is not possible to discriminate between a thin layer of fine regolith and a deep layer of coarse regolith.

[2]See discussion on the YORP effect in Section 1.3.3.

Their results suggest that the surfaces of these asteroids have experienced temperatures greater than 400 K and at most 500 K with 50% probability. However, the temperature of sub-surface materials drops very rapidly with depth. This means that at a depth of only about 3-5 cm the material will have temperatures about 100 K below those at the surface.

These studies demonstrate that asteroids may be subjected to very large temperature variations across their surface and during their lifetimes. There is also a very strong decrease in temperature with sub-surface depth.

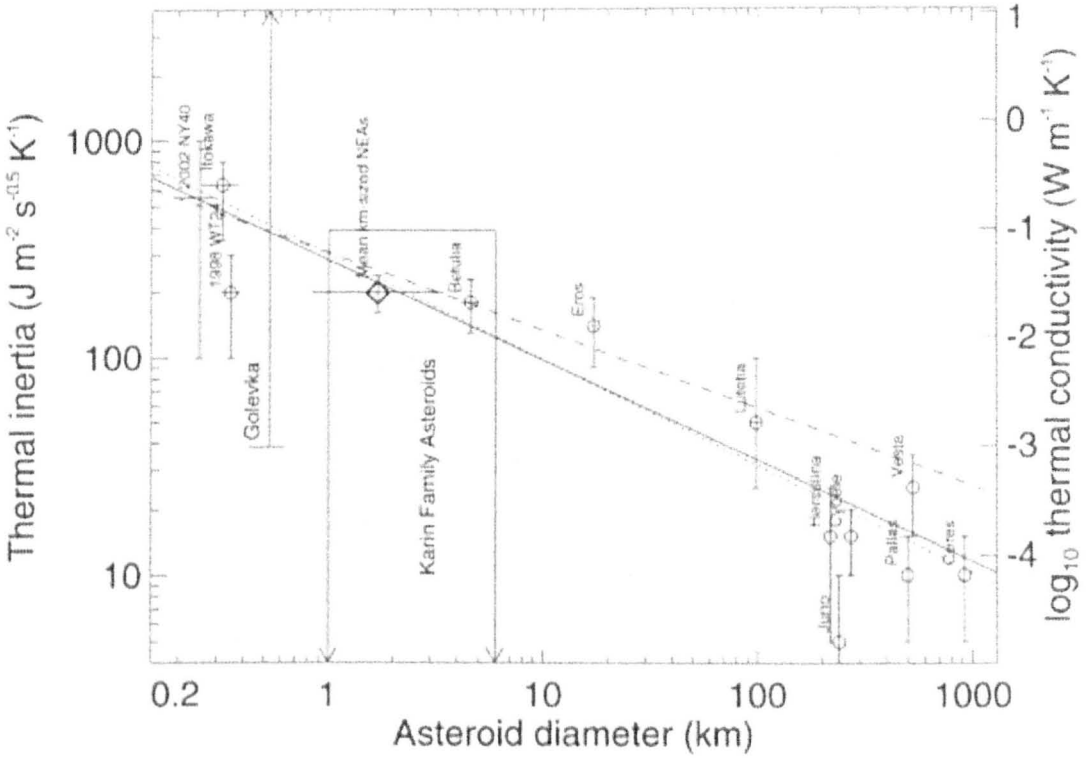

Figure 1.11: **Thermal inertia as a function of asteroid diameter** - Small open circles represent values from the literature derived by means of thermophysical models. The large open diamond is the result from the work of Delbo *et al.* (2007). The axis on the right-hand side gives the asteroid surface thermal conductivity assuming constant surface density of 2500 kg m^{-3} and specific heat capacity of 600 J kg^{-1} K^{-1}. The straight (continuous) line gives the best fit to the trend of increasing thermal inertia with decreasing asteroid diameter. The dotted and dashed lines give the best fit to this trend for main-belt asteroids and near-Earth asteroids only, respectively. Note that fine dust and bare rock have typical thermal inertia values of 30 and 2200 J m^{-2} K^{-1} s$^{-0.5}$, respectively. This figure is taken from Delbo *et al.* (2007).

1.2.3 Size and spin rate distributions

A model of the debiased orbital and absolute magnitude distribution of NEAs has been developed in the last decade (Bottke *et al.*, 2002a). From this model, the total NEA population is estimated to contain approximately 1200 objects with absolute magnitude[1] H<18 and approximately 30,000

[1]The absolute visual magnitude is defined as the visual magnitude (i.e., a measure of the apparent brightness) corrected to heliocentric and observer-centric distances of 1 AU and a solar phase angle of 0° (Bowell *et al.*, 1989).

objects with H<22 (a histogram of the current NEA absolute magnitude distribution is given in Fig. 1.12). It is usually assumed that objects with H = 18 and H = 22 have diameters of ~1 km and ~200 m respectively, although the exact relation depends on the albedo of the object. However, the model of NEO population (Bottke *et al.*, 2002a) is still not perfect as there seems to be an observed excess of high inclination NEOs compared with the model predictions (Michel, 2011). The comparison between the debiased orbital-magnitude distribution of NEAs with H<18 (Bottke *et al.*, 2002a) and the observed distribution of discovered objects suggests that most of the NEAs >1 km in size have now been discovered.

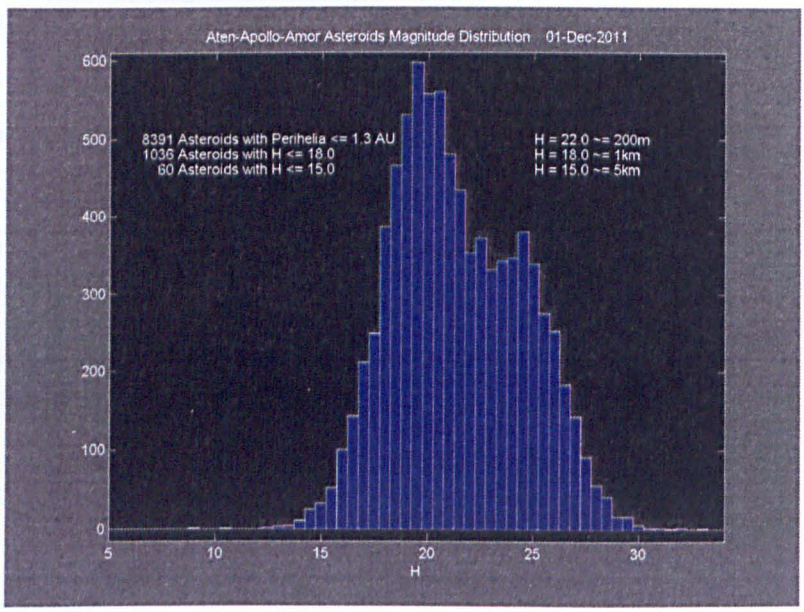

Figure 1.12: **Near Earth Asteroids absolute magnitude distribution** - The current distribution of NEA absolute magnitudes (from *The Near-Earth Asteroids Data Base*).

The spins of approximately 1500 asteroids are shown in Fig. 1.13 plotted versus the asteroid diameters. The spin periods of asteroids can cover a wide range of values, from several days to about a minute. Another interesting feature of this plot is that there are very distinct structures in the data related to the strength properties of the object. The period of about 2.1 hours was identified by Harris (1996) as the maximum spin a body can sustain without spinning off material from the longest axis. This is often referred to as the "spin barrier". More refined analyses have been performed (Holsapple, 2001, 2004) showing that a more typical spin limit before major shear failure for bodies having zero cohesive or tensile strength[1] is 2.6 hours. This spin barrier is shown by the broad horizontal red band in Fig. 1.13.

Until a few years ago, all known spins of asteroids with a size greater than a few kilometres were, to within error bars, below these limits. This observation led to the erroneous conclusion that all those

[1]The cohesive strength is the shear strength at zero confining pressure. This is usually assumed to be the same value as tensile strength.

bodies have a rubble-pile structure (Michel, 2011). An analysis of those spins using a comprehensive strength model approach demonstrated that the spin limits of larger bodies are constrained by their self-gravity, independently of their cohesive strength (Holsapple, 2007). This means that, in this gravity regime, even monolithic bodies may disrupt above the spin limit. The spin barrier is, therefore, not evidence that all those bodies must be rubble pile. Of course, the bodies may be rubble piles, but this observation alone is not conclusive evidence.

For bodies less than about 10 kilometres in diameter, the cohesive/tensile strength is sufficient to allow them to spin faster than pure gravitational binding would allow. Bodies with such spin rates are called *fast rotators* and are all in the strength regime. Figure 1.13 shows the line corresponding to the strength limit of these bodies[1]. As shown in the figure, the strength limit decreases with increasing size of the body. This is because the larger bodies are believed to have a greater number of cracks and faults that reduce their strength. Analytical estimates suggest that even small amounts of strength or cohesion in a rubble pile can render rapidly spinning small bodies stable against disruption (Holsapple, 2007).

This means, therefore, that, just as the spin barrier at large sizes does not necessarily imply that all large bodies are rubble piles (even though they may be), the fast spin rates of smaller bodies do not necessarily imply that all small bodies are fully monolithic.

1.2.4 Composition of asteroids

Asteroids can be separated into taxonomic classes based on their spectral properties at visible and near-infrared wavelengths. Broadly speaking, C-type refers to asteroids which are dark and probably rich in carbonaceous material (similar to carbonaceous chondritic meteorites), S-type refers to asteroids which are bright and probably rich in silicates i.e., rocky material (similar to stony meteorites or ordinary chondrites), D-type asteroids are expected to have organic-rich silicates but have no meteorite analog (except maybe the Tagish-Lake meteorite), and M-type asteroids are expected to be rich in metals (probably iron). There are many other smaller and sub-classes of asteroids that are found in the main asteroid belt and the near-Earth population. For full details on the taxonomic (spectral) classification of asteroids see DeMeo *et al.* (2009) and Bus *et al.* (2002).

Almost all asteroid types have been found in the near-Earth population, although, observations suggest that S-type asteroids dominate the inner asteroid belt and the sampled near-Earth object population. This is partially due to selection effects because S-type asteroids have higher albedos than C-types, making their discovery and observation more likely (Binzel *et al.*, 2002). Benedix *et al.*

[1]The curve which gives a good upper envelope for the current data over the range of asteroid sizes has a size-variable strength with $k = 2.25 \times 10^7 / r^{0.5}$ dynes cm^{-2} (where r is the radius of the object in cm). However, this curve implies that a cm-sized object would have a strength which is one order of magnitude less than expected. In otherwords, this is perhaps equivalent to having a cm-sized rocky object with the strength of ice.

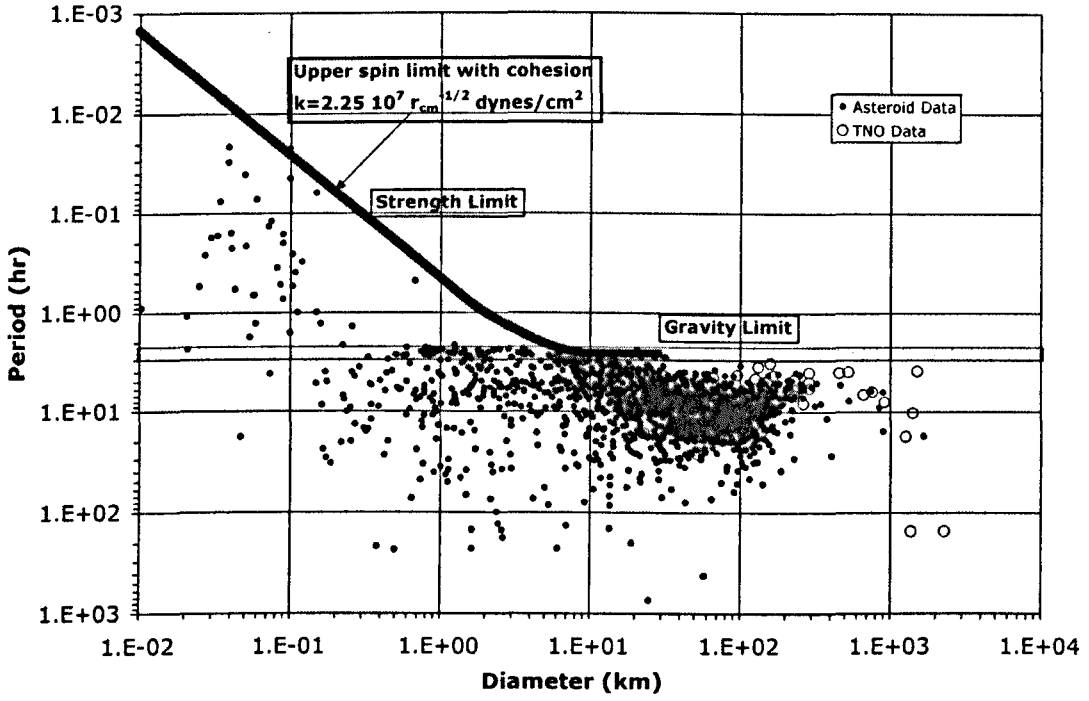

Figure 1.13: **The spin limits and data for small Solar System bodies.** - The dark sloped line assumes a size-dependent strength; it becomes asymptotic to the horizontal red band for materials without cohesion. On the left, the spin limit for cohesive bodies is determined by that cohesive/tensile strength and defines a strength regime. The horizontal asymptote on the right characterizes a gravity regime where the tensile/cohesive strength is of no consequence. The gravity regime values do depend on shape and friction angle, so average values have been assumed. The data in the upper left triangular region are the fast spinning near-Earth asteroids. Image taken from Holsapple & Michel (2008) and some data from the figure come from Holsapple (2007).

(1992), Lupishko & di Martino (1998) and Whiteley (2001) find that after debiasing the observations in the near-Earth object population, at any given size, there are relatively equal proportions of C- and S-type objects. However, C-type asteroids are predominant in the outer asteroid belt (closest to Jupiter), while S-type asteroids are predominant in the inner belt (closest to Mars) and the near-Earth population (Gradie & Tedesco, 1982; Mothe-Diniz *et al.*, 2003). Recently, Walsh *et al.* (2011) suggest that the significant compositional differences across the asteroid belt can be explained by considering the inward-then-outward migration of Jupiter. They propose that Jupiter first migrated inwards, then 'tacked' at 1.5 AU and migrated outward, owing to the presence of Saturn (for details see Walsh *et al.*, 2011). Due to the motion of Jupiter the small bodies were scattered throughout the whole Solar System; the asteroid belt was initially emptied but then repopulated. The inner-belt bodies originate from within 3.0 AU and the outer-belt bodies originate from between and beyond the giant planets, thus explaining the compositional differences of the two regions. D-type asteroids, found in the outer main belt, are thought to be the most primitive of asteroids (and thus a very interesting target for space missions). There is also some evidence suggesting that D-type asteroids found in the near-Earth population may be extinct comets (e.g., Abell *et al.*, 2005; Hicks *et al.*, 2000).

1.2.5 Density and porosity measurements

The only knowledge regarding the internal structure of asteroids comes from the bulk densities measured by spacecraft, either during fly-bys or during rendez-vous missions. These measurements indicate that dark-type bodies have a density that is lower than that of bright types. For instance, the NEAR space probe flew by the ~53 km-sized dark C-type asteroid Mathilde in 1997 and the bulk density of the asteroid was estimated to be ~1.3 g cm^{-3} (Veverka *et al.*, 1997; Yeomans *et al.*, 1997). However, the bulk density measured by the same space probe of the bright ~17 km-sized S-type asteroid Eros was estimated to be ~2.67 g cm^{-3} (Yeomans *et al.*, 2000), that of the sub-kilometre S-type asteroid Itokawa measured by the Hayabusa space probe is ~2 g cm^{-3} (Abe *et al.*, 2006) and that of the ~28 km-size asteroid Ida (also an S-type) measured by the Galileo space probe on its way to Jupiter is ~2.6 g cm^{-3} (Belton *et al.*, 1995). The ~100 km-sized asteroid Lutetia visited by Rosetta has one of the highest bulk densities measured so far at ~3.4 g cm^{-3} (Sierks *et al.*, 2011).

The amount of porosity in several asteroids has been inferred through the comparison of the asteroids' bulk density with that of their meteorite analogues (see Fig. 1.14 and Britt & Consolmagno, 2000; Britt *et al.*, 2002). As the bulk densities of the asteroids are much less than the meteorite analogues we can reasonably assume that asteroid internal structures must contain some degree of porosity. The typical range of porosities appears to be from 30% for S-type asteroids up to 50% and higher for C-type asteroids. However, the nature of this porosity is entirely unclear.

There are two types of porosity: microporosity and macroporosity. If an object has microporosity then it has pores that are sufficiently small that their distribution can be assumed uniform and isotropic over the relevant scales of the asteroid. A rock such as pumice contains this kind of porosity. Macroscopic porosity, on the other hand, is characterised by pores whose sizes are such that the medium can no longer be assumed to have homogeneous and isotropic characteristics over the scales of the object. It corresponds to large voids in an otherwise non-porous rock. While macroporosity may explain the difference in density between S-type asteroids and their meteorite analogues (ordinary chondrites), some fraction of microporosity may still be needed in addition to explain the lower bulk density of C-type asteroids (Michel, 2011).

Britt *et al.* (2002) suggest that asteroids with macroporosities of ~20% are probably heavily fractured, and asteroids with macroporosities of >30% are loosely consolidated rubble pile structures. However, we do not have any direct evidence of the kind of porosity that resides inside an asteroid, even the ones for which the density was estimated. The type of porosity of an asteroid has important implications for interpreting their evolutionary histories (we may expect to find huge voids inside an asteroid that was formed from collisional disruption and reaccumulation of major fragments; Michel *et al.*, 2001) and also for their continuing geological evolution (a microporous body may compact due to pore crushing during an impact whereas the voids in a macroporous rubble pile may protect the body causing more localised and less extensive damage; Jutzi *et al.*, 2008).

1.2.6 The asteroid surface environment

The effective gravity at the surface of an asteroid depends on the asteroid's rotation rate and the proximity to the equator. This is demonstrated in Fig. 1.15 from Scheeres *et al.* (2010). In this figure the net gravitational accelerations across the surface of 1999 KW4 Alpha, the primary body of the binary asteroid 1999 KW4, are shown taking into account the gravitational attraction of the asteroid and the inertial effects that arise due to the rotation of the small body. From this example we see that the surface acceleration can range over orders of magnitude, and thus the ambient gravitational environment for grains on the surface may have significant differences as one moves from polar to equatorial regions.

This is demonstrated further in Fig. 1.16 (also from Scheeres *et al.*, 2010), which shows the relation between asteroid radius, spin period and ambient gravity at the equator for asteroids spinning at less than their critical rotation period. There may be, therefore, extremely low values of ambient gravity at the surface of some asteroids.

In addition to the thermal variations (as discussed in Section 1.2.2), the surface of asteroids is subject to many non-gravitational forces. When the ambient surface gravity is very low these non-

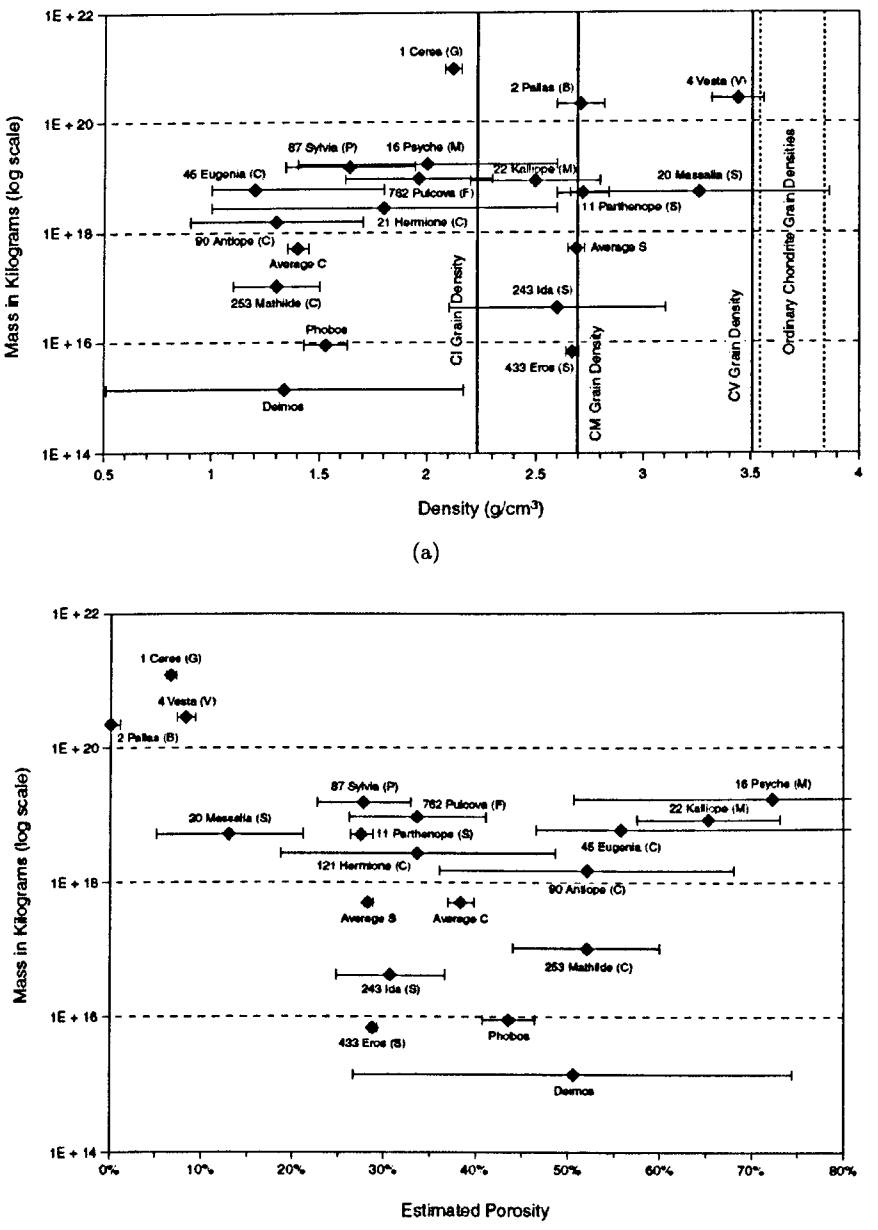

Figure 1.14: **Estimated asteroid bulk densities and porosities** - (a) Measured bulk densities of asteroids and the grain densities of common mereorites for comparison. (b) Estimated porosity of asteroids with measured bulk density. The bulk density of the asteroid is scaled by the grain density of its best meteoritic spectral analog to provide an estimate of the asteroid's total porosity. This includes the small-scale microporosity common in meteorites and the large-scale macroporosity that can affect the asteroid's structure. Also included in the plots are the asteroid-like moons of Mars, Phobos and Deimos, as well as estimates for the average C- and S-type asteroids. Figures taken from Britt *et al.* (2002).

gravitational forces may dominate regolith dynamics. One example of such a non-gravitational force is the electrostatic force that may occur on the surface of asteroids. It is known that objects in space charge to a floating potential determined by the balance between charging currents in the local plasma environment (Goertz, 1989; Whipple, 1981). The dominant currents are the flux of electrons and ions from the ambient plasma, the electrons created by secondary emission and the photoelectrons. The charging of a surface in space will proceed until the sum of the charging currents is zero and the object has reached an equilibrium floating potential (Sickafoose *et al.*, 2000). Such surface charging has been observed on the Moon with the nightside surface reaching potentials of up to -4.5 kV (Halekas *et al.*, 2009) and has been known to cause the lunar dust to levitate (Colwell *et al.*, 2007). It has been speculated that a similar mechanism may cause levitation and transport of grains on the surface of an asteroid (Colwell *et al.*, 2005; Hughes *et al.*, 2008; Lee, 1995). Solar radiation pressure is also known to influence small particles in the Solar System (Burns *et al.*, 1979). However, recent analytical comparisons of the known relevant forces that act on regolith at the surface of asteroids have shown that cohesive forces are more likely to significantly effect the mechanics and evolution of asteroid surfaces and interiors (Scheeres *et al.*, 2010).

Scheeres *et al.* (2010) find that, in the milli to micro-g range, g being the gravitational acceleration at the surface of the Earth, the cohesion between two particles due to van der Waals forces becomes comparable to, or greater than, the weight of a particle for particles of radius 1 cm up to 1 m in size and smaller. This indicates that regolith containing grains of millimetre to decimetre sizes on small bodies may undergo significantly different geophysical processes than similar sized particles in the terrestrial environment. In Table 1.1 (taken from Scheeres *et al.*, 2010) a list of grain sizes is given at which the ambient weight and the cohesive force are equal, as a function of different ambient accelerations. The fact that the role of cohesion becomes so important in these low-gravity environments may explain the observations that suggest that regolith is present at the surface of all asteroids, even the smallest and fastest rotating (as discussed in Section 1.2.2).

1.2.7 Binary systems

It is estimated that ~16% of NEAs larger than 200 metres in diameter may be binary systems (Margot *et al.*, 2002). The dynamics of binary systems are directly tied to the morphology of the material out of which the binary is formed. In other words, the internal structure and the surface geology determine the mass distribution of the bodies, which gives the mutual potential that drives the dynamics of the system. In return, the dynamics affect the internal structure and surface geology of the components (Bellerose *et al.*, 2008).

One example of the effect of dynamics on internal structure and surface geology in such systems

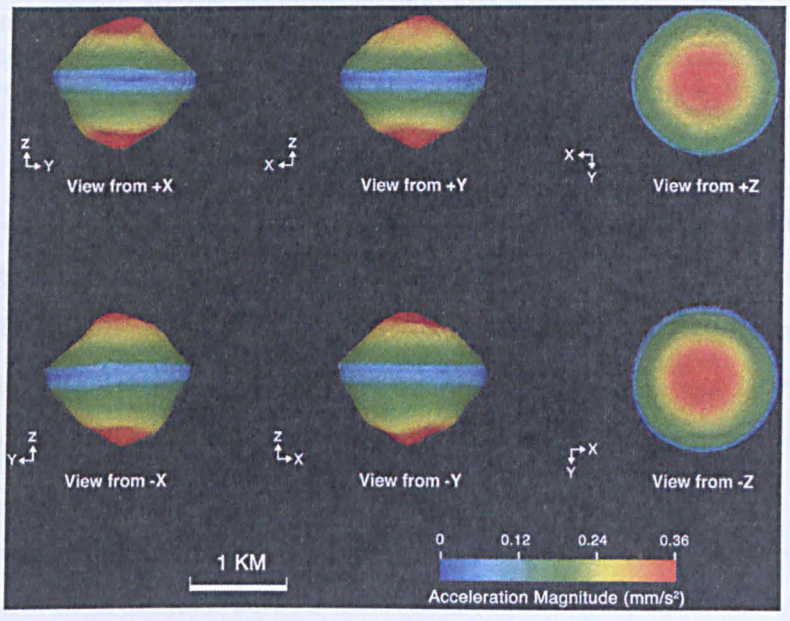

Figure 1.15: **Surface accelerations across the surface of the primary of the asteroid binary 1999 KW4** - Image taken from Scheeres *et al.* (2010)

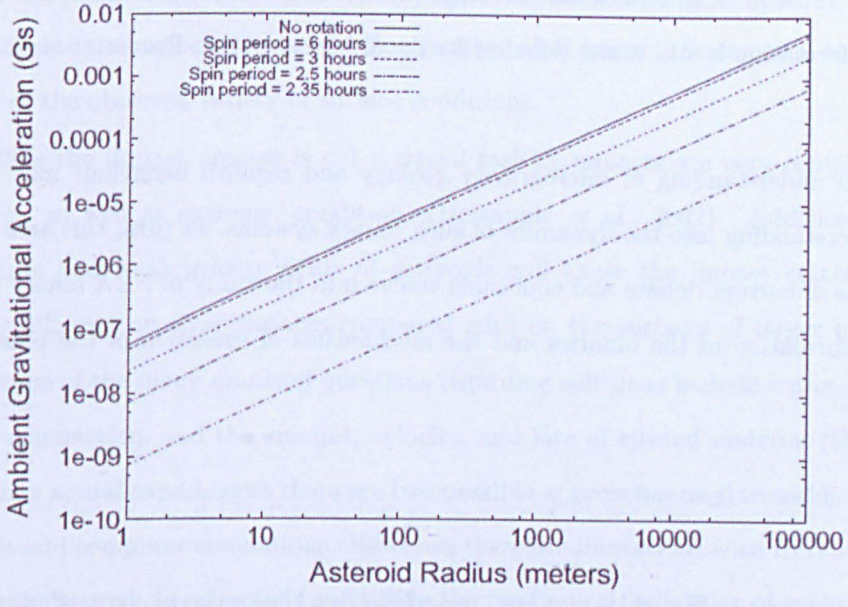

Figure 1.16: **Ambient gravity at the surface of a rotating asteroid** - Surface ambient gravity as a function of asteroid size and spin period, computed for a spherical asteroid with a bulk density of 2 g cm^{-3}. Image taken from Scheeres *et al.* (2010).

Table 1.1: Radius at which ambient weight and cohesive force are equal, along with nominal parent body sizes. These values assume lunar regolith properties and a cleanliness ratio of unity, which means the surfaces of particles are essentially separated by the diameter of their constituent mineral molecules. This is a reasonable assumption as, in space, there are closer effective distances between surfaces due to the lack of adsorbed molecules on the surface of materials (Perko *et al.*, 2001). Table and data from Scheeres *et al.* (2010).

Gravity (in units of g)	**Grain radius (m)**	**Analog body**
1	6.5×10^{-4}	Earth
0.1	2×10^{-3}	Moon
0.01	6.5×10^{-3}	(180 km)
0.001	2×10^{-2}	Eros (18^1 km)
0.0001	6.5×10^{-2}	Toutatis (1.8 km)
0.00001	2×10^{-1}	Itokawa (0.18^2 km)
0.000001	6.5×10^{-1}	(0.018 km)
0.0000001	2×10^{0}	KW4 equator

is landsliding and material motion on the primary due to its rapid rotation. Many binary NEA systems have a short primary rotation period, meaning the primary is spinning nearly at the critical rate at which the gravity force and the centrifugal force at points on its equator cancel out. It has actually been suggested that the secondary bodies may be formed by gradual mass-shedding from the equator and subsequent gravitational accretion (Walsh *et al.*, 2008). However, the mechanism of binary asteroid formation is still under debate (Bottke & Melosh, 1996; Pravec *et al.*, 2010; Scheeres, 2007).

An increased understanding of microgravity geology and regolith behaviour may allow greater insight and understanding into the dynamics of such binary systems. In turn, this area is relevant to two major topics of current debate and continued research in the study of NEA binary asteroids: the mechanisms of formation of the binaries and the mechanisms of evolution of the binaries following their formation.

1.3 Processes affecting the geological evolution of asteroids

There are many processes that influence the evolution of asteroids. In this section a short overview will be given of some of the processes that influence their geological evolution and are, therefore, closely linked to regolith dynamics and the surface processes occurring on small bodies.

1.3.1 Impacts and craters

Impact craters and regolith are the dominant landform on solid planetary bodies such as the Moon, Mars and Mercury, and also on small bodies such as Itokawa (~0.3 km), Eros (~17 km) and Lutetia (~100 km). Impact crater accumulation provides a way to determine the exposure age of a planetary surface (e.g., Ivanov, 2001). Impact crater morphologies and size-distribution may also be used to quantify surface erosion as the morphology of fresh craters is understood and smaller craters are removed first (Hartmann *et al.*, 1999). Despite the observations of different stages of crater degradation on the surfaces of asteroids, the Moon and Mars, the cratering process and subsequent crater modification processes on a planetary surface that consists of granular material are not fully understood. Improving our knowledge of these processes is, therefore, important for estimating the surface age of such bodies.

Comparing the many observations of impact-riddled bodies, two asteroids draw attention: Eros and Itokawa. Both of these asteroids have far fewer smaller craters than would be expected given their estimated age and the estimated impact flux in the main asteroid belt. Itokawa has very few craters in general and absolutely no distinct craters under 1 m diameter (Fujiwara *et al.*, 2006; Saito *et al.*, 2006). Similarly Eros, although having many craters greater than 100 m, has an apparent deficit of craters at smaller sizes (Richardson *et al.*, 2004; Veverka *et al.*, 2001b). It has been proposed that seismic shaking (see Section 1.3.2) may be at least partly responsible for the lack of small craters (Michel *et al.*, 2009; Richardson *et al.*, 2004), but a greater understanding of both the impact process itself and the events that affect asteroid surface geology after impacts is essential to gaining a true understanding of the observed variety of surface conditions.

Understanding the impact process is not a trivial task as impacts are very complex and involve a wide range of, as well as extreme, conditions (Holsapple *et al.*, 2002). Additionally, the small radii of curvature and weak gravity fields of asteroids will cause the impact cratering process to be significantly different on their surfaces compared with on the surfaces of larger planets (Cintala *et al.*, 1978). Some of the many unsolved questions regarding collisions include crater size, the shape, the amount of compaction, and the amount, velocity, and fate of ejected material (Holsapple *et al.*, 2002). Other than actual experiments there are two possible approaches used to tackle such problems: scaling methods and computer simulations. However, there are limitations with the current computer simulation techniques such as accurately modelling the mechanical behaviour of geological materials. This is considered to be more difficult than modelling the common metals and alloys used in structural applications (Holsapple *et al.*, 2002).

Despite the difficulties involved, continuum codes (see Section 1.7) are often used to model impacts at high-velocity. One group from Tokyo has also shown that a 3d Distinct Element Method code (see

more details of this method in Section 1.7) can successfully model the cratering process caused by low-velocity impacts into granular materials with no adhesion (Wada *et al.*, 2003). In a later paper the same group added a simple adhesion model into the code in order to investigate the influence of inter-particle adhesion (e.g., van der Waals forces) on the cratering process (Wada *et al.*, 2005). By varying the degree of adhesive force it was concluded that the cratering process in a regolith layer of an asteroid will be affected by adhesive forces even if the particle size is >1 mm.

1.3.2 Seismic shaking

Asteroids, particularly those with low inclination (Farinella & Davis, 1992), suffer frequent collisions with other small bodies which may produce a seismic shaking of the entire body. Richardson *et al.* (2005) suggest that impact-induced seismic shaking of an asteroid in the 1 to 100 km size range is a plausible mechanism for three reasons. First, the small volume of the asteroid keeps the concentration of seismic energy high even after the seismic energy injected by an impact has completely dispersed throughout the body (Cintala *et al.*, 1978). Second, the very low surface gravity of the asteroid permits small seismic accelerations to destabilise material resting on slopes (Cintala *et al.*, 1978). Third, S-type asteroids such as Eros, which are composed of silicate rock, reside in a vacuum and have an extremely low moisture content, should have very low seismic energy attenuation rates (Dainty *et al.*, 1974).

The first evidence for seismic shaking on an asteroid was presented by Thomas & Robinson (2005). They have shown that the formation of a relatively young crater (7.6 km in diameter) on asteroid Eros has resulted in the removal of other craters as large as 0.5 km over nearly 40% of the asteroid's surface. Burial by ejecta cannot explain the observed pattern of crater removal and, as the best correlation of crater coverage is with distance from the centre of the asteroid, they conclude that seismic shaking is the most probable mechanism.

This impact-induced seismic shaking may trigger global-scale granular processes in the dry, vacuum, microgravity environment (Miyamoto *et al.*, 2007) and is, therefore, an attractive mechanism to explain the destabilisation of regolith slopes and the avalanches or landsliding behaviour found on the surfaces of asteroids. Observations of asteroid Eros during the NEAR mission have shown lots of evidence of downslope movement of the regolith layer (see Section 1.2.1.1, Fig. 1.6). The location and morphology of gravel on Itokawa indicate that the small body has experienced considerable shaking (see Section 1.2.1.2, Fig. 1.8). As mentioned above, it has also been proposed that seismic shaking is a suitable mechanism to form ponds (Cheng *et al.*, 2002) as seen on Eros (see Section 1.2.1.1, Fig. 1.5), although other mechanisms for pond formation have also been suggested such as electrostatic levitation and transport of fine grains (Lee, 1996; Robinson *et al.*, 2002) and thermal erosion of boulders

(Dombard *et al.*, 2007).

The occurrence of many large boulders on the surface of the rubble pile asteroid Itokawa (Fig. 1.7) has been attibuted to the so-called "Brazil-nut effect" which may be activated by global shaking by non-disruptive collisions over long periods of time (Asphaug *et al.*, 2001). More information on the "Brazil-nut effect" and the segregation of granular materials can be found in Section 1.6.2.

1.3.3 Yarkovsky and YORP effects

For the last several decades, it has been generally assumed that collisions and gravitational forces were the primary mechanisms governing the evolution of asteroids (Bottke *et al.*, 2002b). However, around the year 1900 Ivan Osipovich Yarkovsky noted that the diurnal heating of a rotating object in space would cause it to experience a force that, whilst tiny, could lead to large effects in the orbits of small bodies. More explicitly, there can be an excess of thermal emission on one side of the asteroid which results in a net photon force pushing in the same direction as the orbital motion. This process, known an the Yarkovsky effect, causes the orbit of prograde asteroids to expand and the orbit of retrograde asteroids to shrink (Farinella & Vokrouhlicky, 1999; Rubincam, 2000).

Besides changing the heliocentric orbit, Yarkovsky forces can also produce torques that affect the spin rate and spin axis orientation of asteroids. Such an effect is known as the Yarkovsky-OKeefe-Radzievskii-Paddack effect, or YORP for short. Figure 1.17 (from Rozitis, 2011) shows a schematic of the Yarkovsky and YORP effects acting on an ideal spherical asteroid with non-zero surface thermal inertia, rotating in a prograde sense, and with two wedges attached to cause an asymmetry in the shape. As the wedges are at slightly different angles the thermal emission directions are slightly different and the photon torques do not cancel out. The YORP process depends, therefore, on the shape asymmetry.

The timescale of the YORP effect varies proportionally to the square of the asteroid's radius, such that bodies with smaller sizes spin up or spin down much more quickly than larger bodies. This is thought to be why there is an excess of fast and slow rotators among the small-asteroid population (Bottke *et al.*, 2006). The full effect this changing spin rate has upon the asteroid surface and structure is not yet well understood. Landsliding behaviour, shape changing and even mass shedding are some of the possible consequences of increased spin rate. It has also been proposed that rotational break-up due to YORP-increased spin rate could be responsible for the formation of small binary asteroids (Walsh *et al.*, 2008).

The Yarkovsky and YORP effects depend on an asteroid's shape, size, mass and moment of inertia, rotation state, its orbit around the Sun and the surface thermal properties (Rozitis, 2011). As mentioned in Section 1.2.2, the surface thermal properties are very closely linked to the regolith

properties. Therefore, a better understanding of the regolith properties on asteroid surfaces could help to make existing Yarkovsky and YORP models more accurate.

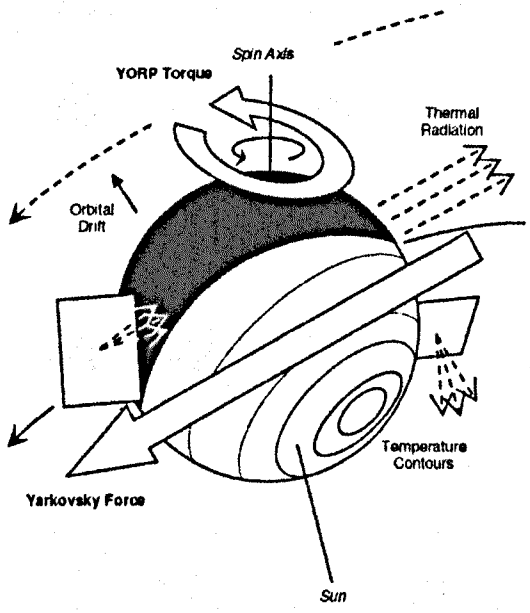

Figure 1.17: **Yarkovsky and YORP effects** - Schematic of the Yarkovsky and YORP effects on the orbit and spin properties of a small asteroid. Image from Rozitis (2011).

1.3.4 Tidal forces

Tidal shear occurs when a loosely consolidated rubble pile body is pulled apart into two or more components through shear in response to tidal forces during a close planetary fly-by. If the resulting fragments impact a planetary body, rather than escape into space, a crater chain can occur. Such a crater chain is defined as a regularly spaced row of three or more impact craters with similar sizes and apparently identical ages (Bottke & Melosh, 1996). This is the same type of phenomenon behind the break-up of Comet P/Shoemaker-Levy 9 into the famous "string of pearls" that plunged into Jupiter in July 1994. There are several other observations that support the occurrence of such events such as crater chains found on Jupiter's Galilean satellites (Melosh & Schenk, 1993; Schenk *et al.*, 1996), the Earth's moon (Melosh & Whitaker, 1993) and even possibly the Earth (Rampino & Volk, 1996). Further evidence of tidal shear are the observations of the Earth crossing asteroid (1620) Geographos whose strange elongated shape could only have been caused by tidal shear effects (Bottke *et al.*, 1999). Tidal shear has also been studied as a possible formation mechanism of NEA binaries (Richardson *et al.*, 1998; Walsh & Richardson, 2006; Walsh & Richardson, 2008). However, the binaries produced through tidal shear disruption mostly have a large separation and elongated primaries (Walsh & Richardson, 2006) and, as such, do not match the observed properties of small binaries. For example, radar observations of binary near-Earth asteroid (NEA) 1999KW4 show that the primary is oblate

with a pronounced equatorial belt (Ostro *et al.*, 2006). Owing to the quality of the observations, and the diagnostic 'top-like' shape of the primary, this system is a key constraint for binary formation models (Walsh *et al.*, 2008). In addition, binaries produced through tidal shear are more likely to be seperated during subsequent planetary fly-bys.

Apart from the global modification an asteroid may suffer due to tidal forces, it has also been proposed that tidal stress on the surface of asteroids during planetary encounters is strong enough to disturb and expose unweathered surface grains and is the most likely dominant short-term asteroid resurfacing process (Marchi *et al.*, 2006; Richardson *et al.*, 1998). Recent research has reinforced this theory by demonstrating that asteroids that have had a close encounter with the Earth have fresher surfaces (Binzel *et al.*, 2010). However, the resurfacing predicted to occur during these close encounters has never been modelled directly so the actual degree of resurfacing that can occur on an asteroid surface during a close planetary encounter is still unknown.

1.4 Granular material in the Solar System

So far we have specifically focussed on granular material on asteroids as the primary aim of this work is to understand the dynamics of regolith on the surface of these low-gravity bodies. However, granular material is ubiquitous in the Solar System and is involved in many different physical processes. Some examples are cratering (Fig. 1.18(a)) and debris flows on many other planetary surfaces. The Martian moons Phobos (~11 km) and Deimos (~6 km) are both irregularly shaped and have smooth surfaces with filled-in craters. Phobos has a heavily cratered surface which also shows linear grooves (Thomas *et al.*, 1979). The largest of Phobos' craters is ~10 km in diameter.

Venus' surface has ~900 impact craters ranging in diameter from ~3 km to a few hundred km (Lodders & Fegley Jr., 1998). There are no smaller craters due to atmospheric disruption of small impactors. The smallest impact craters are irregular in shape indicating that they were perhaps formed by many fragments rather than by one impactor. The crater ejecta patterns on Venus are also unlike those found on any other planetary surface in our Solar System. This is probably due to the dense atmosphere and prevailing winds (Lodders & Fegley Jr., 1998). Crater removal may also occur on Venus due to the continuing volcanic activity (e.g., Campbell, 1999).

The Moon is also highly cratered and covered with regolith extending to a depth of 32 m (Wilcox *et al.*, 2005). Recent observations from the NASA Messenger spacecraft of Mercury's regolith-covered surface have discovered two large (>250 km) basins which appear to have a fresh surface. The young age of these basins, whose floors are partially covered by smooth plains, was recently confirmed by an analysis of crater chronology (Marchi *et al.*, 2011).

Some of the longest landslides in the Solar System (up to 80 km) have been found on Iapetus (Singer *et al.*, 2009) - a fascinating moon of Saturn with an equatorial ridge which is up to 10-15 km tall and around 50 km wide (Fig. 1.18(b)). Figure 1.18(c) shows the snow-like appearance of the thick accumulations of very fine particles on the surface of another moon of Saturn, Enceladus (Massey, 2011).

Granular matter is also the constituent of one of the most recognisable features in the Solar System - the rings of Saturn (Fig. 1.18(d)). The rings consist of billions of individual particles of mostly water ice. They spread over hundreds of thousands of kilometres, yet they are extremely thin - perhaps only 10 metres thick. Recent work has suggested that many of Saturn's small moons may have been formed by the gravitational accumulation of these icy particles as the granular material of a ring spreads beyond the Roche limit (Charnoz *et al.*, 2010, 2011).

Several examples may be found in the current and future space agency programs for which understanding granular physics in varying gravitational environments will be essential. Surface features resulting from granular processes are or will be observed by various instruments in the frame of small body missions and missions to the Moon, Mercury, Mars, Venus and the Moons of Jupiter and Saturn. Whereas interpretation of morphological data from images and topography requires a better understanding of granular physics, several onboard instruments may be also sensitive to the physical properties of granular material (e.g., grain size, through thermal observations, visible or near-infrared spectroscopy). For some of these missions there are also instruments dedicated to characterising the regolith at grain size level (e.g., GIADA on ESA's Rosetta spacecraft and MicrOmega onboard the ESA/NASA ExoMars lander).

The Rosetta mission, devoted to in-situ characterization of a comet in 2014, already involves the interaction of an instrument (a lander) with the surface of the body. Deployment of landing vehicles on surfaces of loose granular material will also be required in the exploration of the Moon in the next two decades. Sample-return missions to small bodies and planets are underway or have been studied by at least three main space agencies: NASA, ESA, and JAXA. These missions (e.g., OSIRIS-REx (NASA), Hayabusa 2 (JAXA), MarcoPolo-R (ESA), Mars Sample Return (ESA/NASA)) will require the design of an efficient sampling device to collect material from the surface of either a small body or a planet (e.g., Mars) for in-situ analysis or return to Earth.

Understanding the response of granular media to a variety of stresses is important in the design of any device which will interact with a regolith covered planetary surface and is crucial for the design of a successful surface sampling tool, since the efficiency of collecting a sample from the surface of such bodies is highly dependent on the surface properties and on the response of the surface to the applied forces. Although constitutive equations linking stress and strain exist for granular interactions

Figure 1.18: **Granular material in the Solar System** - (a) A Martian crater with the ejecta sitting above the surrounding terrain to form raised platforms (this type of crater is called a pedestal crater). Image credit: NASA/JPL/ University of Arizona; (b) Equatorial ridge of Saturn's moon Iapetus. Some of the longest landslides in the Solar System have been found on Iapetus (Singer *et al.*, 2009). Image credit: NASA/JPL/SSI; (c) "Snow"-covered slopes of Saturn's moon Enceladus. The image shows the heavily fractured terrain which lies north of the edge of the active south polar region. The fainter dimples are older craters and fractures that appear to be covered by thick accumulations of very fine particles. Image credit: NASA/ Processing by Paul Schenk (Lunar and Planetary Institute, Houston); (d) Saturns rings. Image Credit: NASA/JPL/Space Science Institute.

on Earth (see Section 1.5.3) the inferred scaling to the gravitational and environmental conditions on other planetary bodies such as asteroids (as mentioned above and discussed in Scheeres *et al.*, 2010) is currently untested. Designing a suitable anchorage mechanism necessary to attach a lander to the surface or a sub-surface sampling mechanism also requires knowledge of how the regolith granular matter responds to various different external forces.

1.5 An introduction to granular materials

All the discussions above demonstrate the great importance of understanding the dynamics of granular matter for planetary science applications. On Earth we can observe granular materials involved in dramatic avalanches and rockslides, as well as active sand dunes moving across deserts. Industries

also handle several different types of granular materials. Some examples are tablets or powders in the pharmaceutical trades as well as agricultural products such as wheat, oats, rice and other cereals and sands in the construction industry.

Granular materials are unlike solids, in that they can conform to the shape of the vessel containing them, thereby exhibiting fluid-like characteristics. On the other hand, they cannot be considered a fluid, as they can be heaped (Gudhe *et al.*, 1994). Analysis of physical systems involving granular materials requires a clear understanding of their behaviour not only at the single particle level, but should also consider the solutions of multi-physics problems involving multi-scale phenomena (Antony *et al.*, 2004).

The study of granular dynamics is incredibly complex and constitutes an entire field of research by itself. In fact, in 1998 P. G. De Gennes, a French physicist and Nobel Prize laureate, said that, *"For physicists, granular matter is a new type of condensed matter; as fundamental as liquid, or solid; and showing in fact two states: one liquid-like, one solid-like. But, there is yet no consensus on the description of these two states. Granular matter, in 1998, is at the level of solid state physics in 1930."*.

In this section a short introduction will be given to granular materials and granular flows. Some granular processes, which may also be important for planetary science, are also discussed.

1.5.1 What is a granular material?

There are two different definitions of granular material. The first states that it is a material for which the relevant energy scale is the potential energy rather than the thermal energy i.e., particles in a granular material are massive enough for their potential energy to be orders of magnitude larger than their thermal energy (Schroter *et al.*, 2005). For example, a typical grain of sand of mass m, raised by its own diameter d, in the Earth's gravity g, will have potential energy mgd which is at least 10^{12} times the thermal energy k_BT at room temperature on Earth (Jaeger *et al.*, 1996). The second definition states that the forces necessary to deform the system are small compared to those necessary to break the grains (Staron, 2011).

Table 1.2 shows the classification of granular materials based on the size of the constituent particles as defined by Wentworth (1922). The size of the constituent particles is closely linked to the type of interactions between the particles. The term granular material is most often used to describe a material containing a large number of particles that interact with each other through dissipative contact forces (Jaeger *et al.*, 1996; Richard *et al.*, 2005). On Earth the approximate size at which dissipative contact interactions dominates is 100 μm. At grain sizes <100 μm humidity, van der Waals forces and even the presence of air will influence the particle interactions. However, we have seen that on the surface

Table 1.2: The Wentworth grain size chart classifies granular materials into groups based on the size of the constituent particles (from Wentworth, 1922).

Grain size	Classification
>256 mm	Boulder gravel
64 - 256 mm	Cobble gravel
4 - 64 mm	Pebble gravel
2 - 4 mm	Granule gravel
1 - 2 mm	Very coarse sand
1/2 - 1 mm	Coarse sand
1/4 - 1/2 mm	Medium sand
1/8 - 1/4 mm	Fine sand
1/16 - 1/8 mm	Very fine sand
1/256- 1/16 mm	Silt
<1/256 mm	Clay

of an asteroid forces such as cohesion (i.e., due to van der Waals forces) become as important as the weight of the particles for significantly larger grain sizes than on Earth. It may, therefore, be possible that gravel-like material on asteroids behaves like powders on Earth (see Section 1.2.6 and Scheeres *et al.*, 2010).

1.5.2 Why are granular materials interesting but difficult to model?

The first difficulty with granular materials is that there are several different length scales that are important from the very small scale contact between the particles to the large scale material and even structural scales (see schematic in Fig. 1.19). However, there is no clear scale separation between micro-, meso- and macro-scopic descriptions (Staron, 2011).

Figure 1.19: **Length scales in granular dynamics** - Schematic demonstrating the different length scales involved in the study of granular physics. Image credit: F. Radjai.

Secondly, although individual particles are solid, granular materials are thixotropic. This means that they exhibit solid-, liquid- and gas-like behaviour. This is demonstrated in Fig. 1.20 that shows the solid, liquid, and gas flow regimes obtained in an avalanche-like situation by pouring steel beads on a pile. In a solid-like state, such as a heap or pile, the material is said to be "quasi-static" as

the individual particles are in a stable mechanical equilibrium with their local neighbours. In the liquid-like and gas-like states the material is said to "flow". Dense flows, i.e., when in the liquid-like state, are dominated by many-body interactions and occur when particles have long-lived contacts with many neighbours. In rapid or dilute flows, i.e., when in the gas-like state, there are no enduring contacts and the collision time is much smaller than the time between collisions. Such dilute flows can be described with some success by kinetic theories for hard spheres that interact through uncorrelated and instantaneous binary collisions (Campbell, 1990; Delannay *et al.*, 2007; Goldhirsch, 2003).

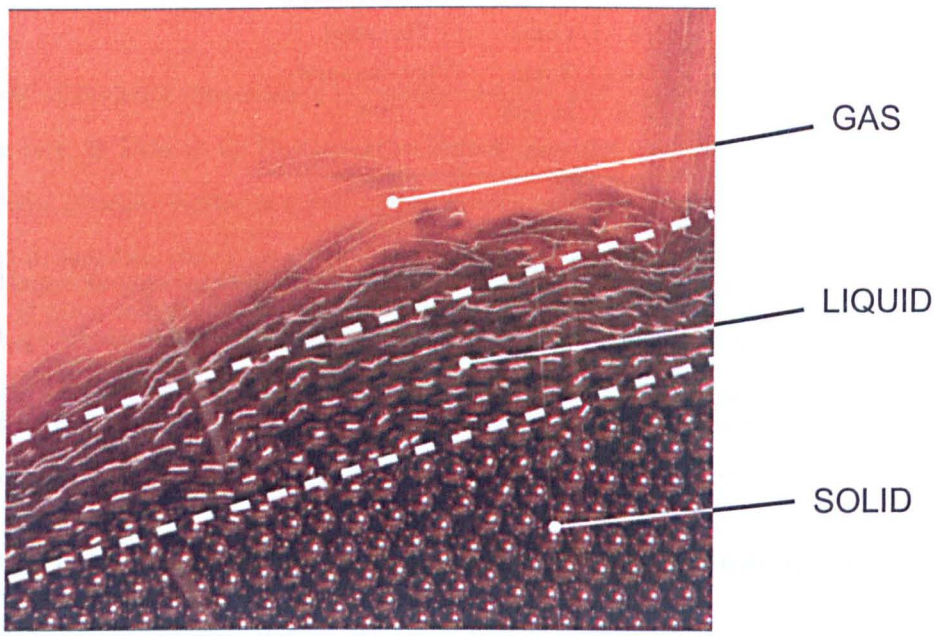

Figure 1.20: **Solid, liquid or gas?** - An illustration of the solid (bottom), liquid (middle), and gas (top) flow regimes obtained by pouring steel beads on a pile. Image from Forterre & Pouliquen (2008).

It should also be noted that in the low gravity regime of an asteroid (see Section 1.2.6) the potential energy of an individual grain is lower and thus the energy required to move past its neighbours is reduced. Assuming an individual grain in this regime has the same kinetic energy as on Earth, a flow, which on Earth would have been in the slow dense regime, may move to the faster more dilute regime on the surface of the asteroid. This implies that bodies with low surface gravity may be very sensitive to processes that appear irrelevant in the case of larger planetary bodies. For example, to seismic vibrations induced by small impacts that can occur throughout a small body (see Section 1.3.2). However, as discussed above, cohesive forces (due to van der Waals) become more important in low-gravity environments. Perhaps, therefore, on the surfaces of asteroids there may be an interesting competition between the increased particle motion due to the lower potential energy of particles and the enhanced importance of cohesion that will inhibit particle motion. It is even possible that the two competing factors compensate for each other resulting in granular flows that are similar to those on

Earth.

Another important aspect of granular materials that is difficult to model is related to the non-local effects. One example of such non-local effects is an experiment performed by Nichol *et al.* (2010) in which a granular medium of 1 mm beads is fluidised through localised stirring. A large heavy intruder (a stainless steel ball) is placed far from the main flow region and is seen to sink into the granular material (Fig. 1.21). This implies that the granular material is behaving like a liquid even in regions far from the main flow region (Nichol *et al.*, 2010).

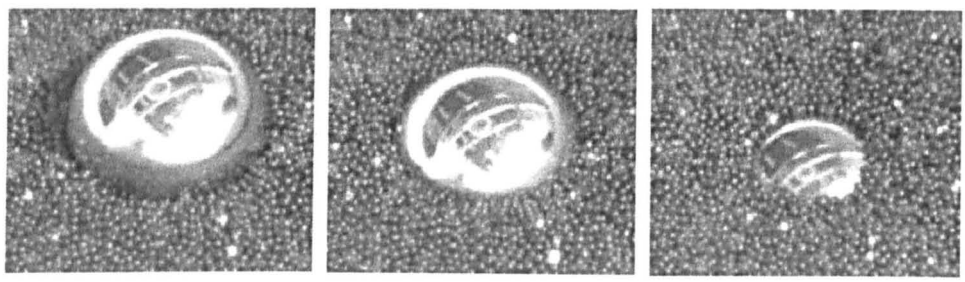

Figure 1.21: **Non-local effects in a granular material** - Snapshots of a stainless steel ball sinking into a stationary but fluidised granular material. Image from Nichol *et al.* (2010).

A further difficulty related to the contact interactions in a granular material is that flowing granular materials segregate according to particle properties (size, density, shape, and more). An example of such segregation in a bi-disperse granular medium (i.e., a granular material containing two particle sizes) is shown in Fig. 1.22 (from Gray & Hutter, 1997). In the tumbler there is a mixture of (white) sugar crystals and (dark) spherical iron powder with mean grain diameters of 0.5 mm and 0.34 mm, respectively. It is clear from the images that the white and the dark particles segregate. The phenomenon of segregation, which will be discussed in a little more detail in Section 1.6.2 below, is a continued source of frustration for industries and can be a costly problem for industries involved in, for example, pharmaceutical products, ceramics or agriculture (McCarthy, 2009). However, segregation may help us to explain several geological features observed on the surface of asteroids.

A final, but very important, property of granular materials is the non-linear transmission of force between particles via force chains. A force acting on a granular material is distributed through a complex force distribution network that depends on the positioning and packing of the individual particles. This grain network resists reorganisation when stressed and imposes a granular drag force when a solid object is pushed through the material (Costantino *et al.*, 2008). Figure 1.23 shows the force chains inside a quasi-static granular pile. The force chains are imaged using photoelastic ellipses which, when viewed though polarising filters, show the transmission of force between particles. The presence of force chains means that when a granular material is held in a tall cylindrical container, such as a silo, no height-dependent pressure head[1] occurs as it does with a normal fluid: the pressure

[1]Pressure head is a term used in fluid mechanics to represent the internal energy of a fluid due to the pressure

Figure 1.22: **Segregation of particles in a tumbler** - The large (white) and small (black) particles segregate in the tumbler. At low rotation rates intermittent avalanche release in a thin rotating disk filled with a granular mixture leads to the formation of stripes tangent to the free surface (a), which are then rotated and buried to form a Catherine wheel[4] effect (b). At faster rotation rates a quasi-steady flow develops (c) in which the free surface is fixed in space and there is a continuous distribution of particle sizes outside the central core (d). Image taken from Gray & Hutter (1997).

at the base of the container does not increase indefinitely as the height of the material inside is increased. Instead, for a sufficiently tall column, the pressure reaches a maximum value independent of height (Jaeger *et al.*, 1996). It is the force network between the grains and the static friction with the container walls which make this behaviour possible (Jansen, 1895). However, for a badly designed silo these force chains can also cause problems (Fig. 1.24).

Figure 1.23: **Force chains in a granular pile** - Photoelastic ellipses viewed through polarising filters. The ellipses manifest force chains (white) composed of weight-supporting particles. Removal of such particles poses the greatest danger for pile collapse. Image taken from Krim & Behringer (2009).

Figure 1.24: **Silo collapse** - Local jamming of grains inside this silo resulted in an uneven weight distribution, and eventually led to the collapse of this grain container. Image taken from: *http://behringer.phy.duke.edu/pages/research.php*

exerted on its container.

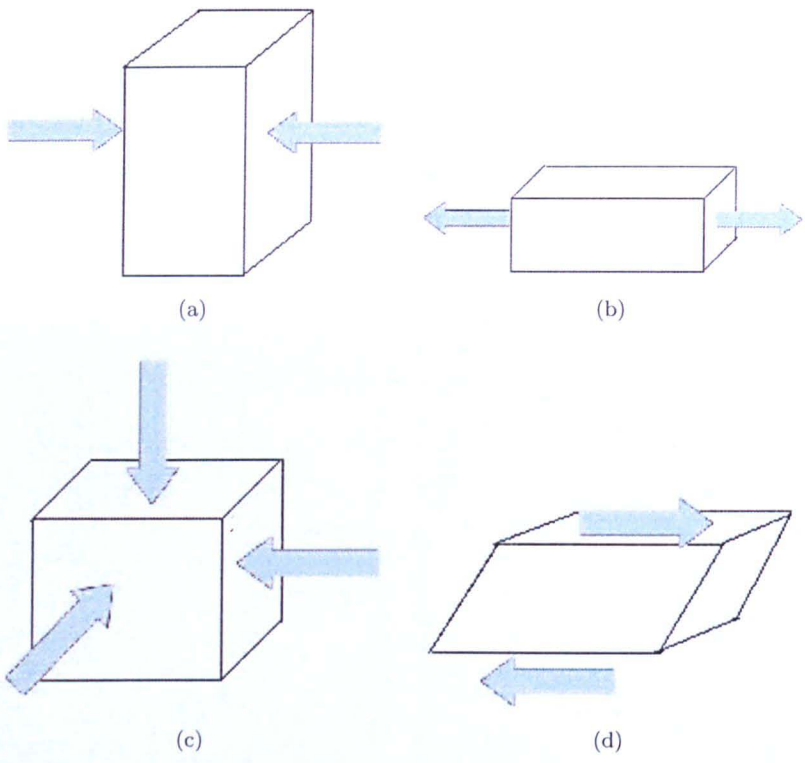

Figure 1.25: **Different types of stress** - Schematics explaining (a) uniaxial compressional stress, (b) uniaxial tensional stress, (c) confining stress and (d) shear stress.

1.5.3 Granular flows

To describe the steady flow properties of granular matter, the system is usually characterised by its packing density[1], granular temperature, and pressure (Toiya *et al.*, 2004). Unlike ordinary fluids, granular materials do not exhibit intrinsic thermal motion (Losert *et al.*, 2000). Instead, the concept of a *granular temperature* concept has been introduced by Ogawa *et al.* (1980): the mechanical energy of granular flow is first transformed into random particle motion and then dissipated into internal energy; the granular temperature is generally defined as the square of root-mean-square velocity fluctuations of particle motion in the flow.

Due to their highly dissipative nature granular materials only flow if a continuous energy input is provided. The energy can be provided in several ways, for example, by applying shear stress. Shear stress is a stress applied parallel to the material and results in translation. There are also different types of stress: compressional stress squeezes the material, tensional stress stretches the material and confining stress is an equal stress from all directions (Fig. 1.25).

Any external forces that are imposed onto a granular material are distributed via a complex force distribution network (see the granular pile under the force of gravity in Fig. 1.23). This force

[1]In granular physics the terms *packing density*, *packing fraction* and *volume fraction* are all interchangeable terms used to describe the fraction ϕ of a given volume filled by the granular material. The term *porosity*, which is used more commonly in the planetary science community, is equivalent to (1 - ϕ).

distribution network depends on the packing and positioning of the particles in the granular material. Granular materials and ordinary fluids, therefore, react differently to shear stresses. Fluids deform uniformly whilst granular materials develop shear bands (Mueth *et al.*, 2000). A shear band is a narrow zone of large relative particle motion bounded with essentially rigid regions. Almost all of the energy input into the granular system by shearing is dissipated by friction within this narrow region producing large velocity gradients (this will be discussed in more detail in Chapters 4 and 6). Shear bands mark areas of flow, material failure, and energy dissipation, and as such they are important in many geophysical processes.

Loosely packed granular material will compact during shear. However, densely packed granular material will dilate[1]. The concept of dilatency, first introduced by Reynolds (Reynolds, 1885), describes how a compacted granular material must expand in order to undergo shear. Dilatancy occurs because under applied normal stress the grains interlock and the material will only begin to deform at a particular yield point. The yield point is set by the applied normal stresses (Jaeger *et al.*, 1996). Once the yield point is reached grains will begin to slide past each other. To understand this concept we can think of a simple experiment involving a balloon filled with densely packed sand. If water is poured into the balloon and then the balloon is squeezed the water-level will descend and not rise. The reason for this is that the granular material (sand) has dilated creating larger voids for the water to fill. The same phenomenon occurs when wet sand dries around our feet when walking at the beach.

The effects of compaction and dilation mean that both loosely packed and tightly packed granular materials, when sheared over large enough strains, will eventually reach the same packing fraction and the same level of internal stress (see schematic in Fig. 1.26). However, the paths to get to the final state, or "critical" state, will differ (Brown & Richards, 1970; Schofield & Wroth, 1967; Wood, 1990). The critical state will depend on the type of interaction between the grains (Makse *et al.*, 2000). Granular materials, therefore, can exhibit plastic behaviour. This plasticity has also been demonstrated using numerical simulations (Radjai & Roux, 2004).

Granular flows have been studied, both experimentally and numerically, often using one of the experiment configurations shown in Fig. 1.27 is often used. These configurations can be divided in two families: flows confined between walls as in shear cells or silo and free surface flows such as flows down an inclined plane, flows in a rotating drum, or flows on a pile (GRD Midi, 2004).

Using experimental data from all of these different experiment configurations, Pouliquen *et al.* (2006) have proposed that dense, dry granular flows can be described by simple constitutive laws. This simple rheological[2] model depends on a single dimensionless number: the *inertial number*, I, given by:

[1]To dilate means to expand as a result of shaking or applied pressure (Kaye, 1997).
[2]Rheology is the study of deformation and flow of matter.

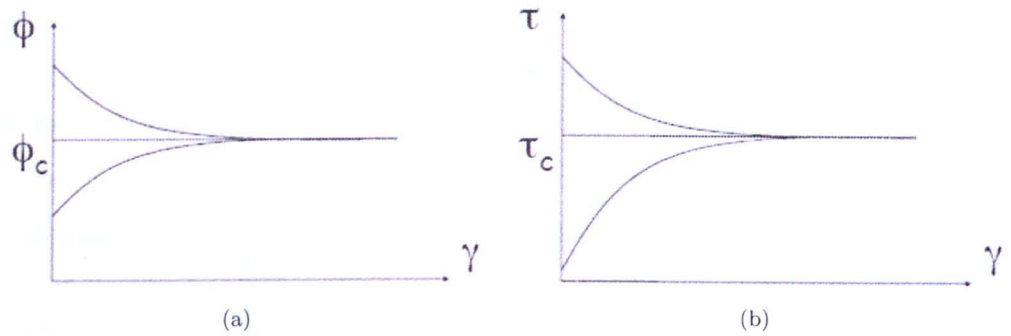

Figure 1.26: **The critical state of sheared granular materials** - The evolution of (a) packing fraction, ϕ, and (b) shear stress, τ, as initially compacted and initially loose granular materials are sheared. After large enough strains the granular materials lose the memory of their initial states and reach a state which only depends on the imposed strain, γ. This is the critical state. Figures taken from Pouliquen (2010).

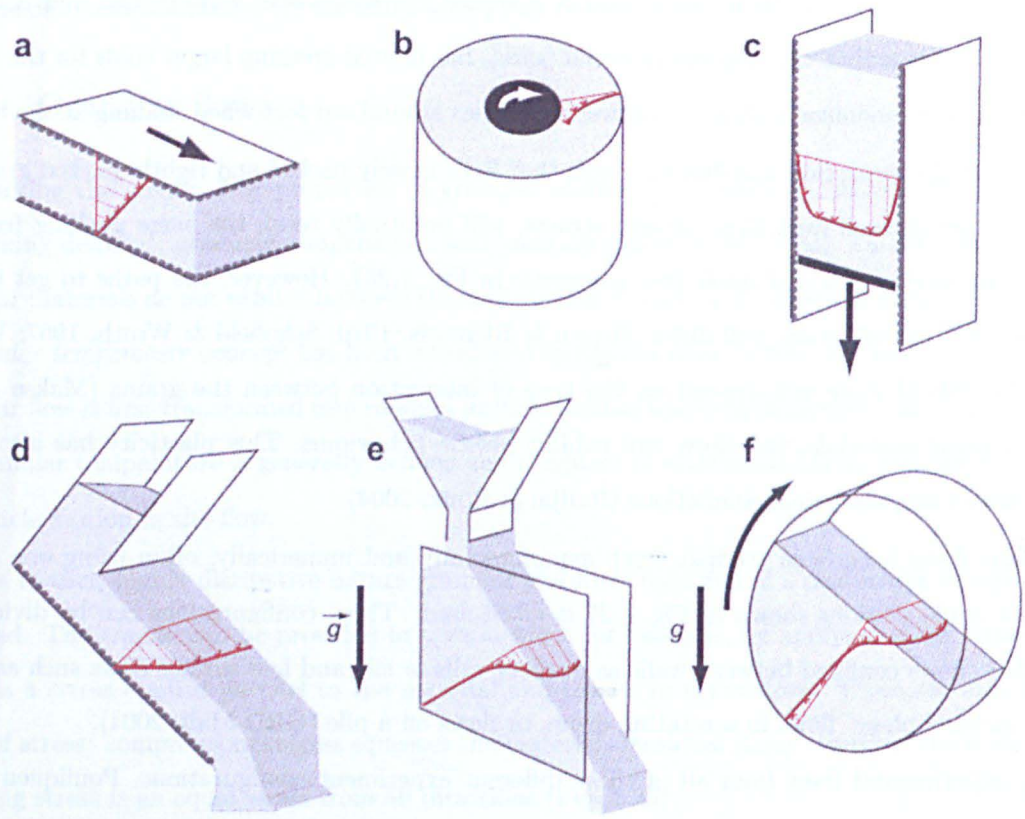

Figure 1.27: **Different granular flow configurations** - (a) plane shear, (b) Couette cell, (c) silo, (d) flows down an inclined plane, (e) flows on a pile, and (f) flows in a rotating drum. The red arrows represent the flow velocity of particles. Image taken from Forterre & Pouliquen (2008).

$$I = \frac{\dot{\gamma} d}{\sqrt{P/\rho_p}} \tag{1.1}$$

for a granular material made of particles with diameter d and density ρ_p, under a confining pressure, P, and being sheared at a given shear rate, $\dot{\gamma}$. The inertial number can be interpreted as the relationship between two different timescales of the granular flow: the timescale of mean deformation i.e., the time it takes for the beads to roll over each other ($\propto 1/\dot{\gamma}$) and the timescale of microscopic rearrangements i.e., the time it takes for a bead to fall into the gaps between other particles ($\propto d/\sqrt{P/\rho_p}$) (Forterre & Pouliquen, 2008).

The inertial number allows the different granular flow regimes to be classified (Pouliquen *et al.*, 2006). When the timescale for mean deformation is much longer than the timescale for rearrangements the inertial number tends towards zero and the flow is defined as quasi-static. Note that the quasi-static regime can be reached either by shearing slowly or by exerting a large confining pressure; the effects of the two processes are the same on a rigid granular system. In the quasi-static regime the contact network between the particles is at its strongest. At intermediate values of the inertial number (0.01 - 0.1) liquid-like flows are observed and then, as the inertial number tends towards one, the gas-like regime is reached in which binary collisions dominate and there is nearly no contact network. Such a gas-like regime can be reached either by having a large shear rate or by decreasing the confining pressure.

It has been shown (da Cruz *et al.*, 2005; GRD Midi, 2004; Iordanoff & Khonsari, 2004) that for rigid grains the shear stress, τ, is given by:

$$\tau = P\mu(I) \tag{1.2}$$

where the friction coefficient $\mu(I)$ is not necessarily a linear function of I but the shear stress varies linearly with confining pressure. Similarly, the volume fraction ϕ is given by:

$$\phi = \phi(I). \tag{1.3}$$

It has been demonstrated (da Cruz *et al.*, 2005; Forterre & Pouliquen, 2008) that the friction coefficient increases with shear rate (i.e., with I) and then eventually decreases when reaching the kinetic gas regime. The volume fraction decreases linearly over the range of inertial numbers investigated implying that the system expands as the shear rate increases (consistent with Reynold's dilatency principle for densely packed granular materials undergoing shear).

This rheological model has also been generalised to 3d (Jop *et al.*, 2006). In this *visco-plastic* model the shear stress varies linearly with the shear rate and depends on a pressure-dependent effective

viscosity (for details see Jop *et al.*, 2006). The visco-plastic approach successfully predicts the liquid regime of dry granular flows in all of the experiment geometries shown in Fig. 1.27. However, the existence of a shear band in the quasi-static limit is not captured by this simple rheology (Pouliquen *et al.*, 2006).

All of the experiments shown in Fig. 1.27 are performed in the presence of an external gravitational field and, thus, in the presence of a confining pressure. Although analytical expressions can be found to predict the properties of shear flow of granular material at constant volume (without a confining pressure) no such experiments have ever been done. There are two possible methods to investigate such constant volume flows: numerical simulations (e.g., Campbell, 2002) and microgravity experiments (see Chapter 4).

1.6 Granular processes of interest to planetary surfaces

Below we will discuss some granular processes which may be of direct interest to planetary surfaces. As the domain of granular physics is so vast there are probably many more processes which have not been discussed here but which may also be relevant to planetary surfaces and to planetary science in general.

1.6.1 Granular compaction

A granular material can explore many different packing configurations by supplying energy to the system via tapping[1](Knight *et al.*, 1995), gentle shaking, shearing (Toiya *et al.*, 2004) or thermal cycling (Slotterback *et al.*, 2008b). It has been shown that gentle tapping results in a gradual increase of packing fraction to a very dense final state. On the other hand, fast tapping results in a rapid increase in packing fraction to a looser final state (Ciamarra *et al.*, 2007). Thermal cycling can be applied by alternately heating and cooling the material and its container (Slotterback *et al.*, 2008b). All these methods cause the material to compact as the particles explore different packing geometries with higher packing fractions.

Divoux *et al.* (2009) have shown that temperature variations, even of a few degrees in amplitude, can lead to the compaction of a loose granular pile. They have also shown that the thermal conductivity of a granular pile can be influenced by tapping - the thermal conductivity of a loose sample will increase with the number of imposed thermal cycles as the granular material compacts. On the other hand, the thermal conductivity of a sample that has been tapped prior to thermal cycling only slightly fluctuates around a constant value.

[1]A "tap" is defined as an individual vertical acceleration applied momentarily to the system.

Thermal cycling effects are very likely to occur on asteroids (see Section 1.2.2) as they rotate and during their orbits. This is likely to result in a gradual compaction of the regolith material. In addition, the individual grains found on an asteroid surface may have different thermal expansion coefficients thus helping the process. However, as we have seen in Section 1.2.2, the large temperature variations are localised close to the surface of the asteroids. This means that the interiors of asteroids may not experience the same compaction due to thermal cyling.

On the other hand, a rubble pile asteroid may experience seismic shaking throughout the body due to micrometeorite impacts (see Section 1.3.2). This seismic shaking may cause the entire asteroid to compact if it is truly a granular aggregate. Through the effects of both thermal cycling and seismic shaking it may be possible that regolith material on, and inside, an asteroid is very compact. However, it is not clear how the process of granular compaction may differ in the low gravity environment of an asteroid.

1.6.2 Granular segregation

When granular materials are shaken the larger particles tend to move to the top. This resulting size segregation has been named the "Brazil-nut effect" (Rosato *et al.*, 1987). It has been suggested that global shaking by non-disruptive collisions can activate the Brazil-nut effect on asteroids. This may explain the presence of large boulders on the surface of asteroid Itokawa (Fig. 1.7 above and Asphaug *et al.*, 2001).

However, the mechanism driving such segregation is still under debate. It has been suggested that the upward movement of larger particles is caused by smaller particles avalanching (due to gravity) into the voids generated underneath large particles during the vibrations. An alternative mechanism proposed is that the small particles fall through the gaps between the large particles (Chowhan, 1995; Rosato *et al.*, 1987; Williams, 1976). However, other experimental results from Knight *et al.* (1993) have shown that vibration-induced size segregation in a vibrated cylindrical column arises from convective processes and not always from local rearrangements as previously thought. The resultant flow, taking the form of convective rolls, continuously transports grains (Fig. 1.28). The rise velocity is dependent upon the distance to the surface but not on the height (Knight *et al.*, 1993). The sense of the convection is dependent upon container shape, wall and interparticle friction and internal phase boundaries (Jaeger *et al.*, 1996), although, in a typical cylindrical or rectangular vessel the flow is upwards in the centre of the vessel with a thin downwards flow along the side walls (Knight *et al.*, 1993). To emphasise the argument that convection is indeed responsible for particle size segregation, Knight *et al.* (1993) also designed two different containers in which, during vibration, the large particles descend to the bottom rather than rise to the top (Fig. 1.29). In the first container one side has been

coated with rough sand and the particles close to this side descend to the bottom. In the second, conical-shaped, container the particles flow upwards along the walls and then downwards in the middle of the vessel due to convection. Shinbrot & Muzzio (1998) and Breu *et al.* (2003) also reported on experiments in which a large particle, depending on its density, could also sink to the bottom of the container.

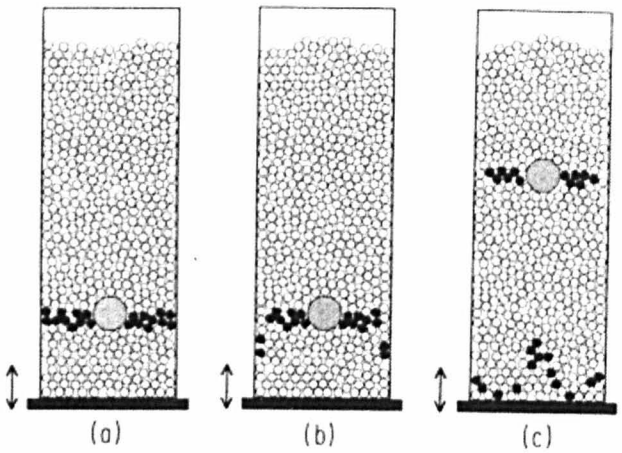

Figure 1.28: **Brazil-nut effect via granular convection** - A schematic diagram of experimental results from Knight *et al.* (1993). (a) The initial configuration. (b) Configuration after one or two taps - note the coloured beads against the wall begin to move downwards. (c) After more taps , both the large bead and the small coloured beads at the centre move up in the cylinder. The beads near the wall which have reached the bottom of the cylinder move inwards and start to rise. Image from Knight *et al.* (1993).

Segregation in a granular material occurs in almost all granular flows where the particles have different physical properties. Another example is the segregation of particles according to their size during an avalanche flow of a polydisperse granular material, with the smallest particles nearest the bottom and the largest particles on the top (Fig. 1.30). Since the small particles are concentrated at the bottom of the avalanche they are deposited first. The faster moving, large particles (the avalanche flow velocity is greatest at the surface) are transported to the front thus travelling furthest.

The dominant mechanism for such segregation in granular avalanches, provided the density-ratio and the size-ratio of the particles are not too large, is *kinetic sieving*. As the grains avalanche downslope, there are fluctuations in the void space and the smaller particles are more likely to fall, under gravity, into gaps that open up beneath them, because they are more likely to fit into the available space than the coarse grains. The fine particles, therefore, percolate towards the bottom of the flow, and force imbalances squeeze the large particles towards the surface (Gray & Chugunov, 2006). This is exactly the process that caused the segregation in the rotating tumbler mentioned above and shown in Fig. 1.22; the segregation takes place in a very thin dynamic layer close to the free surface, which can be described as a granular avalanche.

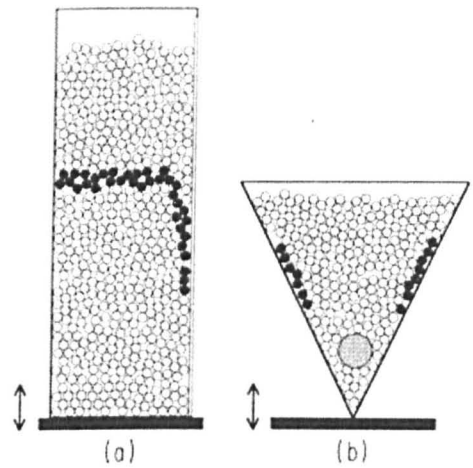

Figure 1.29: **Reverse Brazil-nut effect** - (a) The right side of the cylinder is coated with rough sand. The particles near the rough part of the wall move quickly towards the bottom of the cylinder -during tapping while the rest remain much less affected. (b) A conical configuration. The large bead follows the convection roll through the centre of the cone from its bottom, but then cannot follow the smaller coloured beads back up along the walls in the thin region of the convection roll. Image from Knight *et al.* (1993).

This type of segregation is, by its nature, gravity-driven (Gray & Chugunov, 2006). Although it is not certain that such segregation will occur in granular flows in the low-gravity environment of an asteroid, it does seem likely. Recall the images of asteroid Itokawa in Fig. 1.8 - there is evidence of a boulder-rich layer similar to segregated landslide deposits even on this tiny (~320 m) asteroid. Therefore, the possibility that segregation has occured on asteroid surfaces must be considered when interpreting the debris deposits of granular flows or when choosing potential sampling sites.

1.7 Numerical simulations of granular material

Improving our understanding of the dynamics of granular materials under a wide variety of conditions requires that both experimental and numerical work be performed and compared. Once numerical approaches have been validated by successful comparison with experiments, then they can cover a parameter space that is too wide for, or unreachable by, laboratory experiments.

Various numerical codes have been developed to study granular dynamics (Mehta, 2007). Some of these codes are purely hydrodynamic in the sense that the granular material is represented as a fluid or as a continuum (e.g., Elaskar *et al.*, 2000). In the case of solid-like granular behaviour, the continuum approach usually treats the material as elastic or elasto-plastic and models it with the finite element method or a mesh-free method (e.g., Elaskar *et al.*, 2000). Analytical and continuum approaches have also been used in modeling asteroid internal structures and shapes (Holsapple, 2001, 2004; Holsapple & Michel, 2006; Holsapple & Michel, 2008; Sharma *et al.*, 2006, 2009). In the case

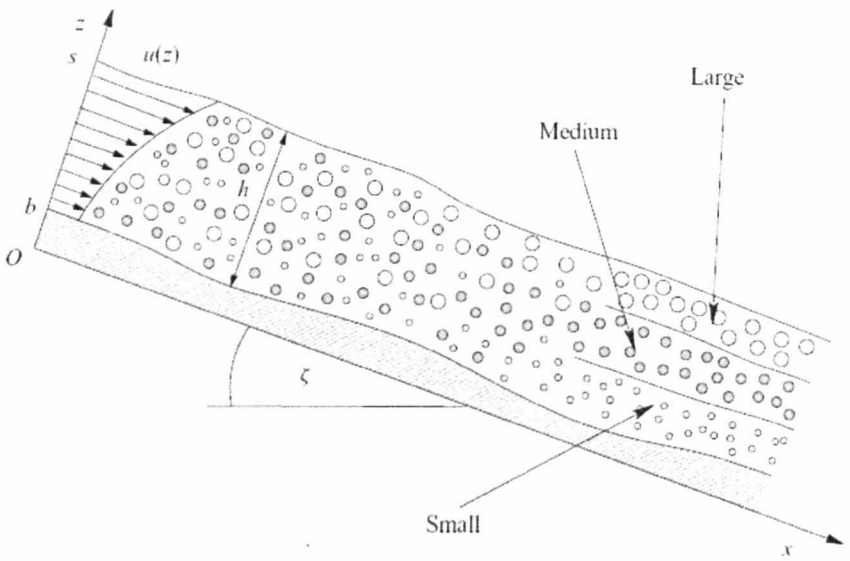

Figure 1.30: **Segregation of particles in an avalanche flow** - A schematic diagram of the particle-size segregation in an avalanche with three particle sizes. At the origin O the particles enter in a homogeneously mixed state, but as they avalanche down slope, the large grains gradually rise to the surface, the small ones percolate down to the base and the medium-sized grains are sandwiched in between. This creates three inversely graded layers sufficiently far downstream. The arrows on the left-hand side indicate the downstream velocity profile $u(z)$ through the avalanche. Image taken from Gray & Ancey (2011).

of liquid-like or gas-like granular flow, the continuum approach may treat the material as a fluid and use computational fluid dynamics. However, continuum models need constitutive laws which are difficult to find for granular matter. In addition, the homogenisation of the granular-scale physics is not necessarily appropriate and, in most cases, the discreteness of the particles and the forces between particles (and walls) need to be taken into account (Wada *et al.*, 2006). Therefore, limits of such homogenisation must be considered carefully before attempting to use a continuum approach.

Statistical approaches such as the Monte-Carlo method have also been employed to model granular dynamics (e.g., Kawasaki, 1986; Rosato *et al.*, 2009). Other codes, such as contact dynamics methods, soft- and hard-sphere codes have also been developed, all of which treat the granular material as interacting solid particles (e.g., Cleary & Sawley, 2002; Fraige *et al.*, 2008; Hong & McLennan, 1992; Huilin *et al.*, 2007; Kosinski & Hoffmann, 2009; Latham *et al.*, 2008; Szarf *et al.*, 2010). These three types of discrete particle codes are often referred to as Distinct Element Methods (DEM). In each of the three methods the dynamics in between particle collisions are found by integrating the equations of motion for each particle. The differences between the methods arise mostly in how the contacts are treated. Molecular Dynamics (MD) is a special case of DEM when the simulated particles do not have rotational degrees of freedom as it was designed to simulate molecules rather than particles. However, the terms DEM and MD are often used rather loosely due to their close relation.

In order to model short range interactions such as collisions and contacts between particles, the soft-particle method relates the interaction force between two discrete particles to the overlap of the particles that serves to represent the deformation at contact. In the hard-sphere method all particles are assumed to be perfectly rigid and the collisions are both binary and instantaneous. This means that an event-driven algorithm can be employed to resolve collisions by anticipating trajectory crossing, thus providing hard-sphere codes with a major time advantage in the resolution of a single collision compared to the soft-sphere method. In the contact dynamics method, the small length and timescales involved in the dynamics of granular media are neglected and their effects are absorbed into contact laws together with a non-smooth formulation of particle dynamics described at a larger scale than small elastic response times and displacements (Radjai & Richefeu, 2009).

1.7.1 Granular codes in planetary science

Granular dynamics is a field of intensive research with a range of industrial applications. A variety of laboratory experiments and numerical methods have been developed to study granular dynamics, but the applications of these experiments and numerical codes to problems related to the dynamics of granular materials in the framework of planetary science have only recently begun.

For example, Wada *et al.* (2006) studied the cratering process on granular materials both by impact experiments and numerical simulations using a soft-sphere numerical code. Sanchez *et al.* (2010) simulated the particles forming an asteroid by means of soft-sphere molecular dynamics. In this approach, particles forming the aggregate have short- and long-range interactions, for contact and gravitational forces respectively, which are taken into account using two types of potentials (for details see Sanchez *et al.*, 2010).

There have been several recent contributions focussing on rubble piles (defined as a special case of a gravitational aggregate in Richardson *et al.*, 2002) that have further highlighted the connection between granular physics and planetary science. Specifically, Walsh *et al.* (2008) performed hard-sphere numerical simulations to show that binary asteroids may be created by the slow spin-up of a rubble pile asteroid by means of the thermal YORP effect (see Section 1.3.3). The properties of asteroid binaries produced by their model match those currently observed in the small near-Earth and main-belt asteroid populations, including the binary 1999 KW4 observed by radar techniques (Fig. 1.31). Goldreich & Sari (2009) developed a quantitative theory for the effective dimensionless rigidity of a self-gravitating rubble pile and then used this theory to investigate the tidal evolution of rubble pile asteroids. Additionally, Sánchez & Scheeres (2011) simulated the mechanics of asteroid rubble piles using a self-gravitating soft-sphere model.

(a) (b)

Figure 1.31: **Comparison of binary asteroid radar images and numerical simulation outcomes** - (a) Radar model of binary Asteroid (66391) 1999 KW4 (Ostro *et al.*, 2006), (b) Simulation outcome of YORP spin-up model of binary asteroid formation (Walsh *et al.*, 2008).

1.7.2 Why use numerical code `pkdgrav`?

The numerical code `pkdgrav`, which started as a cosmology code written at the University of Washington, is a fully parallel N-body hard-sphere code that can both spatially adapt to large ranges in particle densities, and temporally adapt to large ranges in dynamical timescales (Stadel, 2001). The advantages of the N-body hard-sphere adaptation of `pkdgrav` over many other hard- and soft- sphere models include full support for parallel computation and a unique combination of the use of hierarchical tree methods to rapidly compute long-range inter-particle forces (namely gravity, when included) and to locate nearest neighbours and potential colliders.

In a complete N-body calculation a code will require $O(N^2)$ operations in order to fully and accurately calculate a gravitational potential acting on one particle. In order to reduce the number of operations and thus the computational timescales, a tree code works by assuming that the gravitational potential of distant particles can be well approximated by a low-order multipole expansion. It is only the gravitational potential of a particle's nearest neighbours that are calculated exactly. A tree structure is used to introduce these explicit approximations into the calculation of potential. A collection of particles is split into hierarchical groups which are then subdivided again and again - thus explaining the name; tree code. Finally, the method to evaluate the potential at a point reduces to a descent down through branches of the tree. Using such a hierarchical structure allows `pkdgrav` to follow extremely large dynamic ranges in densities at modest 'cost per force evaluation' (Richardson *et al.*, 2000). The use of a tree code, therefore, reduces the number of operations necessary to calculate the gravitational potential acting on one particle to $O(N \log N)$.

There are several different types of tree which can be used. Originally `pkdgrav` used a k-D tree (hence the name which stands for Parallel K-Dimensional tree GRAVity code). However, in the k-D tree the cells can be elongated causing errors in gravity calculations. `Pkdgrav` now uses a spatial binary tree with squeeze to avoid these errors. Figure 1.32 shows the difference in the cell sizes resulting from

these two trees.

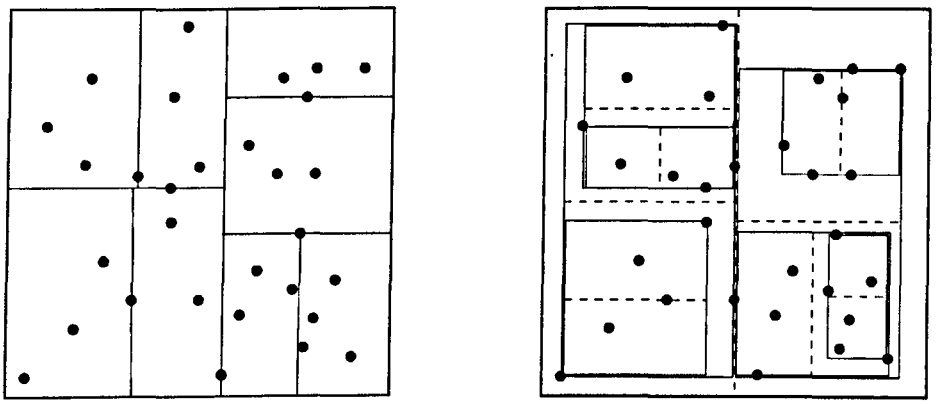

Figure 1.32: **Comparison of Computational Trees** - The cells used to separate the particles into hierarchial groups using a k-D Tree (left) and a Spatial Binary Tree with Squeeze (right). Image credit from Stadel (2001).

In addition, pkdgrav is an event-driven code, which means that collisions are determined prior to advancing particle positions, ensuring that no collisions are missed and that collision circumstances are computed exactly (in general, to within the accuracy of the integration), which is a particular advantage when particles are moving rapidly. Collisions are carried out in time order, properly accounting for repeated collisions between particles (and between particles and walls) during each step. Particles are treated as rigid spheres (so the collisions are instantaneous), with collision outcomes parameterised by coefficients of normal and tangential restitution. In addition to having a velocity vector, each particle also has a spin vector allowing particle rotation to be treated (if the tangential coefficient of restitution is <1). More details on the collision equations in pkdgrav will be provided in Chapter 2. There are also options available for particle bonding to make irregular shapes that are subject to rigid-body rotation and non-central/off-axis impacts (see Richardson *et al.*, 2009).

In pkdgrav the equations of motion are integrated using a Leapfrog integrator (Richardson *et al.*, 2000). This type of integration is equivalent to updating positions and velocities at interleaved time points (i.e., they 'leapfrog' over each other). This means that there are two types of steps: the *drift* step during which the velocities remain fixed and the positions are drifted forward, and the *kick* step during which the positions are held constant and the velocities are kicked according to the acceleration. For pkdgrav the Leapfrog integrator is normally used with the "KDK"combination of steps i.e., *kick* half a timestep, *drift* a full timestep, *kick* half a timestep (Richardson *et al.*, 2000). The Leapfrog integrator was chosen as it is time-reversible (i.e., one can integrate forward n steps, and then reverse the direction of integration and integrate backwards n steps to arrive at the same starting position, if the system is not chaotic) and as it is sympletic (energy is conserved).

Pkdgrav has already been used very successfully in numerous astrophysical applications. For

example, simulation of collisions of rubble pile asteroids (Leinhardt *et al.*, 2000), planetesimal dynamics including modelling oligarchic growth and illustrating the effect of Jovian resonances on the inner planet disk (Richardson *et al.*, 2000), reproduction of key features of binary minor planets (Richardson & Walsh, 2006), binary near-Earth asteroid formation via tidal disruptions and rotational break-up of rubble piles asteroids (Walsh & Richardson, 2006; Walsh & Richardson, 2008; Walsh *et al.*, 2008), the effect of fragmentation on terrestrial planet formation (Leinhardt & Richardson, 2005), catastrophic disruption of asteroids (Michel *et al.*, 2001; Michel *et al.*, 2003) and investigations of gravitational instability and clustering in a disk of planetesimals (Tanga *et al.*, 2004). However, before this Ph.D. thesis `pkdgrav` had never been used to model granular interactions on a laboratory scale. One of the main aims of this thesis is, therefore, to determine if this incredibly successful and efficient astrophysical code `pkdgrav` can be used to model granular material and thus regolith dynamics. Our long-term goal is to understand how scaling laws, different flow regimes, segregation, and so on change with gravity, and to apply this understanding to asteroid surfaces, without the need to simulate the surfaces in their entirety. Before we can simulate granular interactions on planetary bodies, the simulations must first be able to reproduce the dynamics of granular materials in more idealised conditions and match the results of existing laboratory experiments.

1.8 Scope of this thesis

This thesis has two key components, both of which aim to increase our understanding of granular dynamics in varying gravitational conditions. The first component is the validation of the hard-sphere discrete element method implementation in the N-body code `pkdgrav` to model the dynamics of granular material in varying gravitational environments. The validation will be performed by a direct comparison between the numerical simulations and the results of existing laboratory experiments. The second component is focussed on the AstEx parabolic flight experiment. The AstEx experiment, with the experimental aim to characterise the response of granular material to rotational shear forces in a microgravity environment, was designed, constructed, flown and the data were analysed as part of this thesis.

Chapter 2

Modifications to pkdgrav for this investigation

2.1 Summary of Chapter

In this chapter the method to simulate the dynamics of granular materials is presented, along with a few basic tests that show its ability to address different problems involving these dynamics. A more complete validation, by comparison with a well-documented laboratory experiment investigating collective particle behaviour on vibrating plates, is the subject of Chapter 3.

To simulate granular dynamics a new particle-based (discrete element) numerical method is used. The method employs the parallel N-body tree code `pkdgrav` to search for collisions and compute particle trajectories. Provided in this chapter are the details of how particle-particle collisions are treated. Particle confinement is achieved by combining arbitrary combinations of four defined wall primitives, namely infinite plane, finite disk, infinite cylinder, and finite cylinder. Various wall movements, including translation, oscillation, and rotation, are supported. For completeness full derivations of collision prediction and resolution equations are provided in the Supplementary Material (and in Richardson *et al.*, 2011) for all geometries and motions.

After the details of the numerical method are presented a short introduction to how the walls can be used and an overview of some techniques that were developed to facilitate their use is provided. Finally, a series of tumbler simulations is presented as one test of the numerical method.

The detailed modifications to the code reported below were presented in Richardson *et al.* (2011). I was responsible for testing and debugging the new implementations of `pkdgrav` as well as working on the tumbler application.

2.2 Why make modifications to pkdgrav?

The N-body code pkdgrav (Stadel, 2001) has previously been adapted for hard-body collisions (Richardson *et al.*, 2000, 2009). However, it has, until now, only ever been used for large (solar-system or larger) scale simulations (see Section 1.7.2 for details on previous studies performed with pkdgrav). In order to use pkdgrav for the specific purposes of granular material simulations, several modifications and additions had to be made to the code.

The advantages of the N-body hard sphere adaptation of pkdgrav over other many discrete element (DEM) approaches include full support for parallel computation and a unique combination of the use of hierarchical tree methods to rapidly compute long-range interparticle forces (namely gravity, when included) and to locate nearest neighbours and potential colliders. In addition, collisions are determined prior to advancing particle positions, ensuring that no collisions are missed and that collision circumstances are computed exactly (in general, to within the accuracy of the integration), which is a particular advantage when particles are moving rapidly. There are also options available for particle bonding to make irregular shapes that are subject to Eulers laws of rigid-body rotation with non-central impacts (see Richardson *et al.*, 2009).

In this chapter the focus is on the implementation of a wide range of boundary conditions ("walls") that can be used to represent the different geometries involved in experimental setups, but more generally provide the needed particle confinement and possible external forcings, such as induced vibrations, for small-scale investigations of regolith dynamics in varying gravitational environments (different surface slopes, etc.). The approach is designed to be general and flexible: any number of walls can be combined in arbitrary ways to match the desired configuration without any code adaptation, whereas many existing methods are tailored for a specific geometry. The long-term goal is to understand how scaling laws, different flow regimes, segregation, and so on change with gravity, and to apply this understanding to asteroid surfaces, without the need to simulate the surfaces in their entirety.

The full details of the numerical method are presented in Section 2.3, the software developed to set-up and launch simulations is discussed in Section 2.4 and the basic tests of the method are described in Section 2.5.

2.3 Numerical method

This section details the numerical method employed in the granular dynamics simulations. Pkdgrav, a parallel N-body tree code that has been adapted for hard-body collisions (Richardson *et al.*, 2000, 2009) is used. The general strategy of searching for and resolving collisions among particles, and

between particles and the "walls" of the simulated apparatus are discussed. The detailed derivations of the collision equations for the four wall "primitives" that have been developed so far, namely the infinite plane, finite disk, infinite cylinder, and finite cylinder are included in the Supplementary Material (and in Richardson *et al.*, 2011).

In `pkdgrav` collisions are predicted based on trajectory extrapolation at the beginning of each integration step. A second-order Leapfrog integrator is used: each step consists of "kicking" particle velocities by a half step (keeping particle positions fixed), "drifting" particle positions at constant velocity for a full step, recomputing accelerations due to gravity, then performing a final half-step velocity kick (for details see Richardson *et al.*, 2009).

Collision searches are performed during the drift step by examining the trajectories of enough neighbours of each particle to ensure no collisions are missed. There is no interparticle gravity for the granular dynamics experiments discussed in this chapter (only a configurable uniform gravity field) but this unique ability of `pkdgrav` is used in Chapter 3. In order to speed up neighbour searches a tree is used (as described in Section 1.7.2). Additionally, efficient parallelism reduces computation time for large simulations. Also, more complex gravity fields for which there is no analytical solution for particle motion can be easily integrated into the simulations. Such a capability will be very important, for example, when modelling granular material on the surface of an asteroid with an irregular gravitational field.

The relative position and velocity of two particles, with initial vector positions $\mathbf{r}_1$ and $\mathbf{r}_2$ and velocities $\mathbf{v}_1$ and $\mathbf{v}_2$, are $\boldsymbol{\rho} \equiv \mathbf{r}_2 - \mathbf{r}_1$ and $\boldsymbol{\nu} \equiv \mathbf{v}_2 - \mathbf{v}_1$, respectively (Fig. 2.1). The condition for two particles to collide after a time interval t (measured from the start of the drift step in this case) is

$$|\boldsymbol{\rho} + \boldsymbol{\nu} t| = s_1 + s_2, \tag{2.1}$$

where s_1 and s_2 are the radii of the particles (treated as perfect hard spheres). To collide, the particles must be approaching one another, so $\boldsymbol{\rho} \cdot \boldsymbol{\nu} < 0$. It is assumed that the particles are not initially touching or overlapping, i.e., it is required that $\rho > s_1 + s_2$, where $\rho \equiv |\boldsymbol{\rho}|$. Equation (2.1) can be solved for t by squaring both sides and applying the quadratic formula:[1]

$$t = \frac{-(\boldsymbol{\rho} \cdot \boldsymbol{\nu}) \pm \sqrt{(\boldsymbol{\rho} \cdot \boldsymbol{\nu})^2 - [\rho^2 - (s_1 + s_2)^2]\,\nu^2}}{\nu^2}, \tag{2.2}$$

where $\nu \equiv |\boldsymbol{\nu}|$ and the sign ambiguity is resolved by taking t to be the smallest positive value of any real roots. If t is between zero and the drift step time interval (i.e., the simulation timestep), the collision takes place during this integration step. Collisions are treated as instantaneous events with

[1] In practice, a version of the quadratic formula optimized to reduce round-off error is used in `pkdgrav`—see Press *et al.* (2007).

no flexing and a configurable amount of energy loss due to restitution (parameterised by the normal coefficient of restitution $0 \leq \varepsilon_n \leq 1$, where 0 means perfect sticking and 1 means perfect bouncing) and surface coupling (parameterised by the transverse coefficient of restitution $-1 \leq \varepsilon_t \leq 1$, where -1 means reversal of transverse motion on contact, 0 means complete damping of transverse motion, and 1 means no surface coupling). For completeness, the collision resolution equations for perfect spheres are:

$$\begin{aligned}
\mathbf{v}_1' &= \mathbf{v}_1 + \frac{m_2}{M}\left[(1+\varepsilon_n)\mathbf{u}_n + \frac{2}{7}(1-\varepsilon_t)\mathbf{u}_t\right], \\
\mathbf{v}_2' &= \mathbf{v}_2 - \frac{m_1}{M}\left[(1+\varepsilon_n)\mathbf{u}_n + \frac{2}{7}(1-\varepsilon_t)\mathbf{u}_t\right], \\
\boldsymbol{\omega}_1' &= \boldsymbol{\omega}_1 + \frac{2}{7}\frac{\mu(1-\varepsilon_t)}{I_1}(\mathbf{s}_1 \times \mathbf{u}), \\
\boldsymbol{\omega}_2' &= \boldsymbol{\omega}_2 - \frac{2}{7}\frac{\mu(1-\varepsilon_t)}{I_2}(\mathbf{s}_2 \times \mathbf{u}),
\end{aligned}$$

where the primes denote post-collision quantities, $M = m_1 + m_2$ is the sum of the particle masses, $\mathbf{u} = \boldsymbol{\nu} + (\boldsymbol{\sigma}_2 - \boldsymbol{\sigma}_1)$ is the total relative velocity at the contact point (with $\boldsymbol{\sigma}_i = \boldsymbol{\omega}_i \times \mathbf{s}_i$, $i = 1, 2$, where $\boldsymbol{\omega}_i$ is the spin vector of particle i, $\mathbf{s}_i = (-1)^{(i-1)} s_i \hat{\mathbf{n}}$, and $\hat{\mathbf{n}} = \boldsymbol{\rho}/\rho$), $\mathbf{u}_n = (\mathbf{u} \cdot \hat{\mathbf{n}})\hat{\mathbf{n}}$, $\mathbf{u}_t = \mathbf{u} - \mathbf{u}_n$, μ is the reduced mass $m_1 m_2 / M$, and $I_i = \frac{2}{5} m_i s_i^2$ is the moment of inertia of particle i; the factor of 2/7 results from using spheres (for details see Richardson *et al.*, 2009). These equations come from conservation of linear and angular momentum combined with the following statement of energy loss:

$$\mathbf{u}' = -\varepsilon_n \mathbf{u}_n + \varepsilon_t \mathbf{u}_t. \tag{2.3}$$

The approach for handling wall collisions is similar: first the time to collision is determined, then the collision is resolved. The collision condition is that the distance of the particle centre from the point of contact on the wall must equal the particle radius, i.e.,

$$|\mathbf{r}_{\text{impact}} - \mathbf{c}| = s, \tag{2.4}$$

where $\mathbf{c}$ is the vector position of the point of contact and the subscript i has been dropped.

For the derivations that follow, the convention has been adopted that the wall corresponds to $i = 1$ and the particle to $i = 2$; this minimises the number of minus signs in the equations. As $\mathbf{c}$ depends on the particular wall geometry, it is best to consider each geometry in turn and exploit any symmetries to determine more conveniently when (if at all) this contact condition is satisfied for a given particle and wall pair. Note that often a wall consists of a combination of more than one geometry (for example,

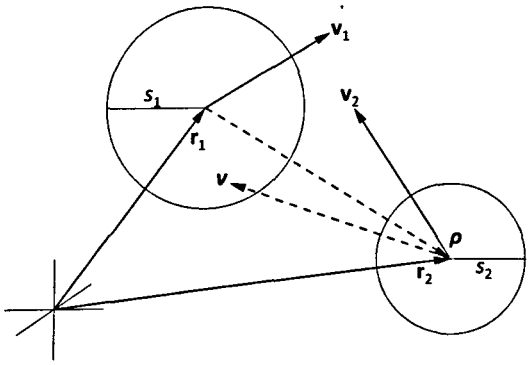

Figure 2.1: **Collision Prediction of Two Spheres** - Diagram illustrating the quantities used for predicting the collision of two spheres (see Eqs. (2.1)–(2.2)). Although the diagram depicts a collision in two dimensions, the derivations apply to the full three-dimensional case.

a finite disk is a round portion of a plane plus a surrounding ring, i.e., a cylinder of zero length) - the collision prediction routines for walls in pkdgrav return a list of possible collision times, one for each "face" (for the finite disk example, there are 3 faces: one flat side, the opposite flat side, and the perimeter ring), with the smallest positive time corresponding to the face that will be struck first.

In pkdgrav, after all neighbours of a given particle have been checked for possible collisions, every wall is checked also. Whatever body (whether particle or wall) that gives the shortest time to collision is taken to be the next collision event. That collision is resolved, collision times are updated depending on whether the collision that just happened changes future collision circumstances, and the next collision is carried out until all collisions during the current drift interval have been handled. Walls are treated as having infinite mass, so the restitution equations reduce to:

$$\mathbf{v}' = \mathbf{v} - (1+\varepsilon_n)\mathbf{u}_n - \frac{2}{7}(1-\varepsilon_t)\mathbf{u}_t, \tag{2.5}$$

$$\omega' = \omega - \frac{5}{7}s^{-2}(1-\varepsilon_t)\mathbf{s}\times\mathbf{u}, \tag{2.6}$$

where

$$\mathbf{u} = \mathbf{v} + \omega\times\mathbf{s} \tag{2.7}$$

(for a static wall), ε_n and ε_t are specific to the wall (see below), and $\mathbf{s} \equiv -s\hat{\mathbf{n}}$, with $\hat{\mathbf{n}}$ being the unit vector in direction $(\mathbf{r}+\mathbf{v}t)-\mathbf{c}$, i.e., from the point of contact (which depends on the wall geometry) to the particle centre. To account for any wall motion, $\mathbf{u}$ in Eq. (2.7) is adjusted as needed (see below).

The parameters of each wall type are specified by the user at run time via a simple text file. Information common to each wall that must be specified includes the origin (a vector reference point), orientation (a unit vector), normal coefficient of restitution, ε_n, and tangential coefficient of restitution, ε_t, for the wall (which override the particle values during a particle-wall collision), as well as colour and transparency (for drawing purposes). In addition, each geometry has a unique set of parameters particular to that geometry, e.g., radius in the case of the finite disk and cylinders, and length for the finite cylinder. Also, simple motions are supported for each geometry; e.g., a plane or disk can have translational and/or sinusoidal oscillatory motion, while a cylinder can rotate around its symmetry (orientation) axis. Oscillations are treated by updating the wall position in stepwise fashion, holding the velocity constant between timesteps. In `pkdgrav`, a single function is used to get the position and velocity of a particle relative to any (possibly moving) wall at a given time. Finally, a wall can be "sticky," meaning any particles that come into contact with it become rigidly held. Alternatively a wall can also be "absorbing," meaning any particles that come into contact with it are removed from the simulation. These latter options are encoded as special cases of the wall normal coefficient of restitution (0 indicating sticky, < 0 indicating absorbing). The sticky wall is particularly useful for creating a rough surface (see Section 2.5.1); the absorbing wall is helpful when particles are no longer needed, such as when they have moved beyond the flow regime of interest.

For a particle hitting another particle that is rigidly stuck to a wall, Eqs. (2.5) and (2.6) also apply when resolving the collision (the stuck particle is treated as having infinite mass), with $\hat{\mathbf{n}}$ pointing from the centre of the stuck particle to the centre of the free particle, and ε_n and ε_t being the usual particle values (i.e., not the values specific to the wall). Detection of collisions with stuck particles is handled by setting the stuck particles' velocities equal to the instantaneous velocities of their host walls at the start of the step. In the case of particles stuck on rotating cylinders, the component $\boldsymbol{\Omega} \times [(R \pm s)\hat{\mathbf{n}}]$ is added to the particle velocities, where $\boldsymbol{\Omega}$ is the cylinder's rotation vector and R is its radius, and in this case $\hat{\mathbf{n}}$ is the perpendicular from the cylinder rotation axis to the particle centre at the start of the step (the sign of s depends on whether the particle is on the outer [positive] or inner [negative] surface). The positions of particles stuck on moving/rotating walls are updated at the end of the drift step. Collisions with particles stuck on rotating cylinders can optionally be predicted to higher order using a quartic expression that accounts for the curvilinear motion (see Eq. (A.4) of Richardson *et al.*, 2009).

For resolving collisions with moving walls, and particles stuck to moving walls, each wall's instantaneous velocity at the start of the step is substracted from $\mathbf{u}$ in Eq. (2.7) before applying Eqs. (2.5) and (2.6). For cylinder rotation, with the rotation axis parallel to the symmetry axis of the cylinder, $\boldsymbol{\Omega} \times (R\hat{\mathbf{n}})$ is subtracted, where $\hat{\mathbf{n}}$ is as defined for those equations. For particles stuck to rotating walls,

the stuck particle itself is given an extra speed component (see above), which is taken into account when resolving the collision outcome.

The implementation details of the wall geometries in pkdgrav are given in the Supplementary Material (and in Richardson *et al.*, 2011).

2.4 Using the walls

2.4.1 Setting up simulations

Several functions and scripts were written, in the programming language Python, to facilitate the fast and efficient generation of the correct initial conditions using the wall boundary conditions. The different approaches developed to place particles into a 'container' are described briefly below and snap-shots of example runs are shown.

The first programs, with the goal of dropping many particles in a box, use a short user-generated parameter file to perform the complete simulation set up and then launch the simulations. The box is constructed using the infinite plane geometries now available in pkdgrav (see Section 2.3). Four infinite planes, two with normal vectors in the positive and negative x-directions and two with normal vectors in the positive and negative y-directions, form the sides of the box. One infinite plane with normal vector in the z-direction forms the base of the box. When using these programs to fill a box with particles all of the dimensions of the box are defined in the short parameter file. These dimensions are then automatically translated to pkdgrav input files. Several important parameters such as the timestep[1] for the simulation are also automatically calculated in the programs and subsequently added to automatically generated pkdgrav parameter files.

The particles can be created and dropped into a box in four different ways:

1. One particle can be created in the very middle of a box (Fig. 2.2).

2. A "rubble pile", or ball, of a specified number of particles can be created in the very middle of a box (Fig. 2.3).

3. A long line of particles can be dropped into the box (Fig. 2.4).

4. A column consisting of several layers of particles can be dropped into a box. In order to avoid simultaneous particle-wall collisions each particle has a fixed x and y coordinate but a range of z coordinates (within given limits). The particles are also given a very small random velocity in the x and y directions (Fig. 2.5).

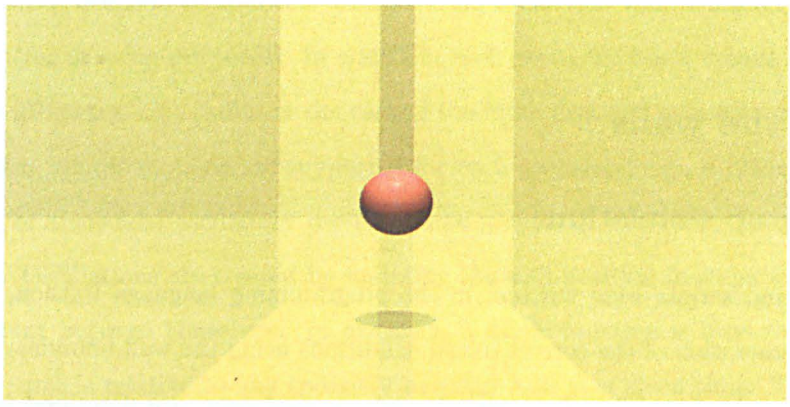

(a)

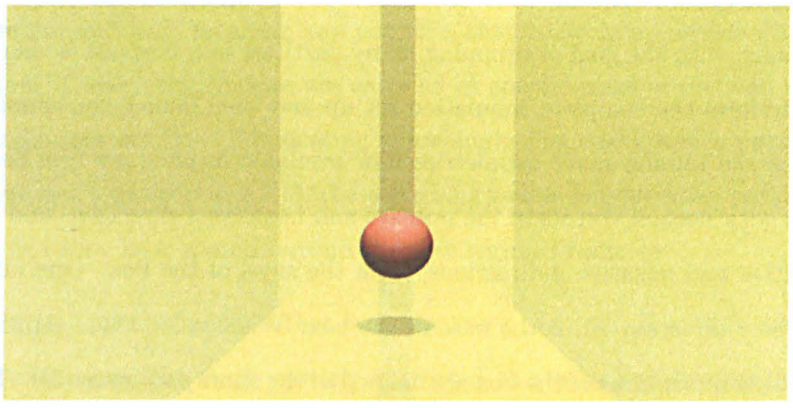

(b)

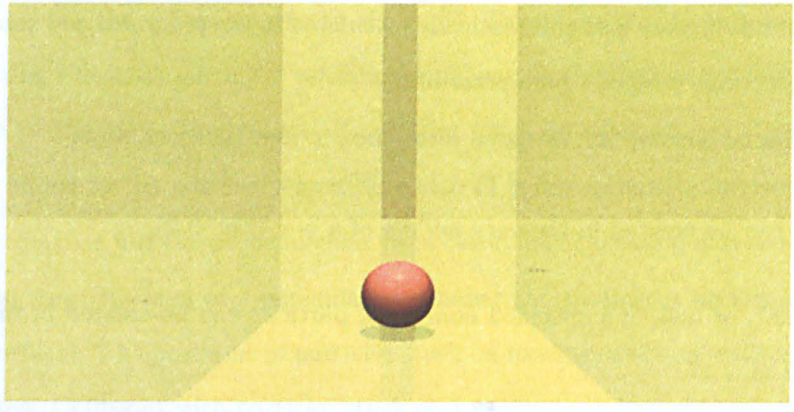

(c)

Figure 2.2: **One particle dropped into a box** - (a) Initial particle position (b) Particle position part-way through simulation (c) Particle position at end of simulation. Note: due to high coefficient of restitution the particle never comes to rest in this run.

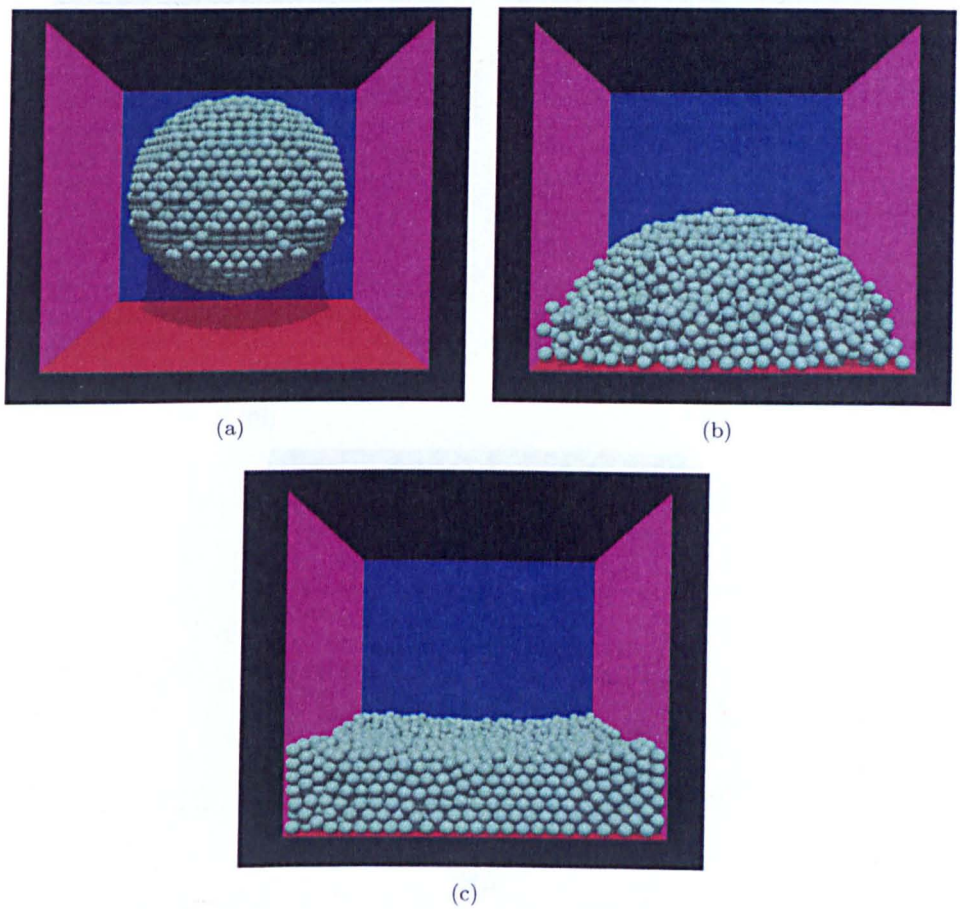

Figure 2.3: **A "rubble pile" dropped into a box** - 4331 particles are dropped into a box starting from a Rubble Pile configuration. (a) Initial particle positions (b) Particle positions part-way through simulation (c) Particle positions at end of simulation.

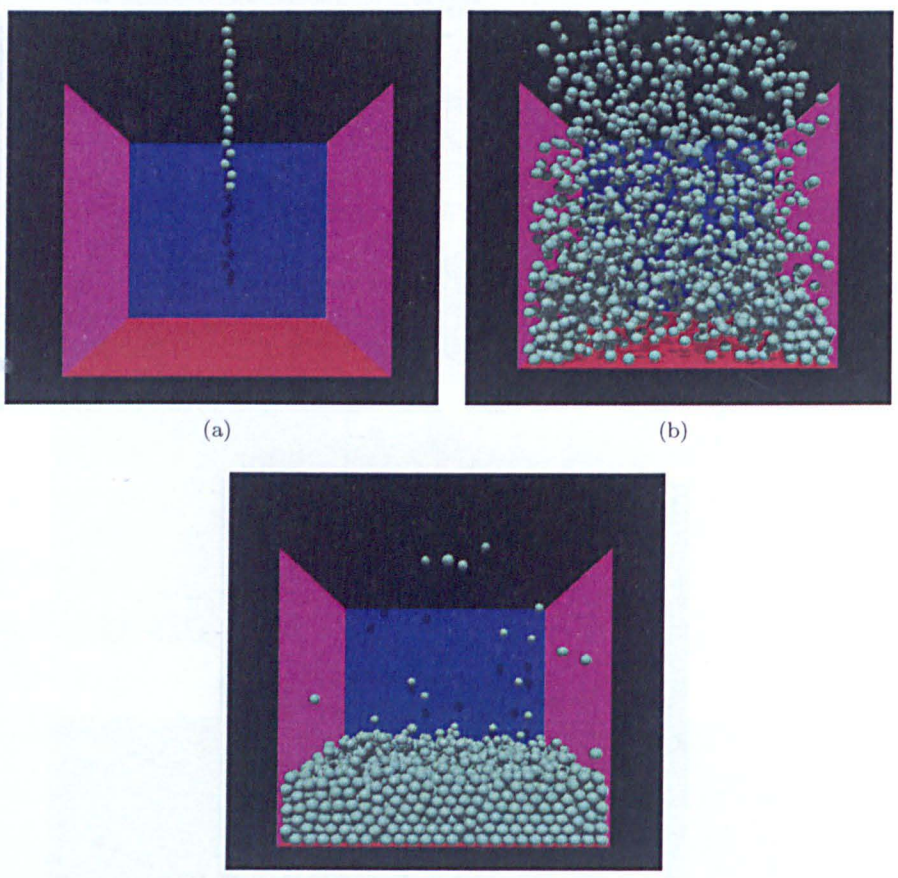

Figure 2.4: **A line of particles dropped into a box** - 4400 particles are dropped into a box starting from a vertical line configuration. (a) Initial positions of the particles in the field of view (b) Particle positions part-way through simulation (c) Particle positions at end of simulation. Note: due to the very high particle energies the particles do not all come to rest in this run.

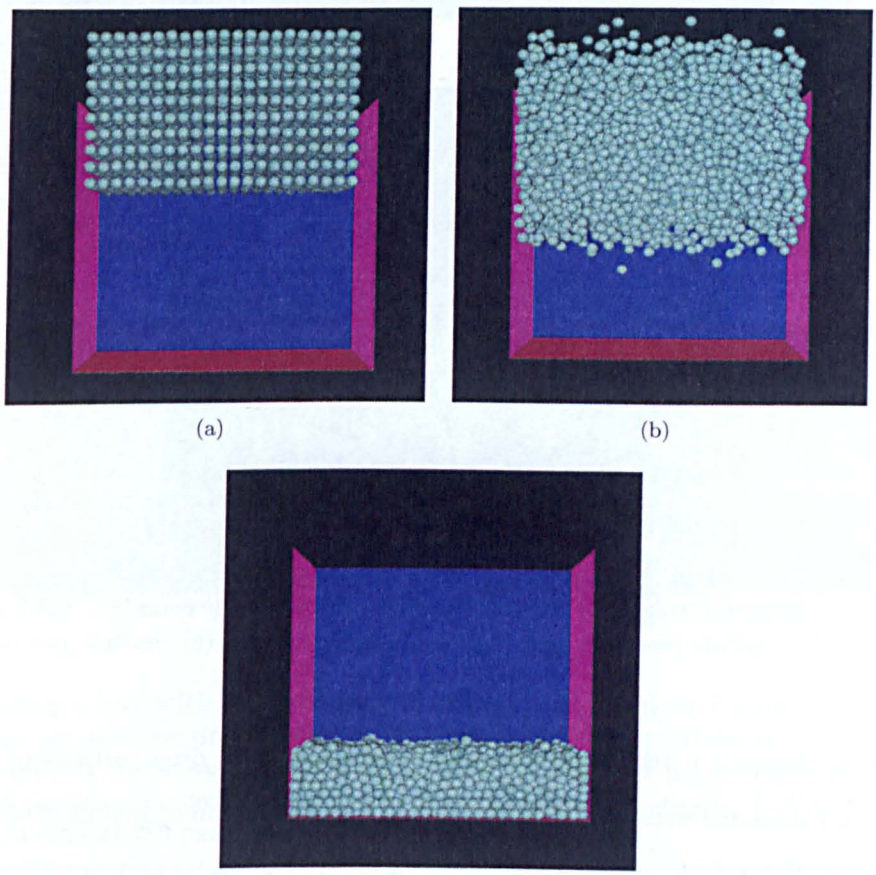

Figure 2.5: **A column of particles dropped into a box** - 4410 particles are dropped into a box starting from a layered configuration. All of the particles have some random velocities and the z-positions are also slightly randomized. (a) Initial positions of the particles in the field of view. (b) Particle positions part-way through simulation (c) Particle positions at end of simulation.

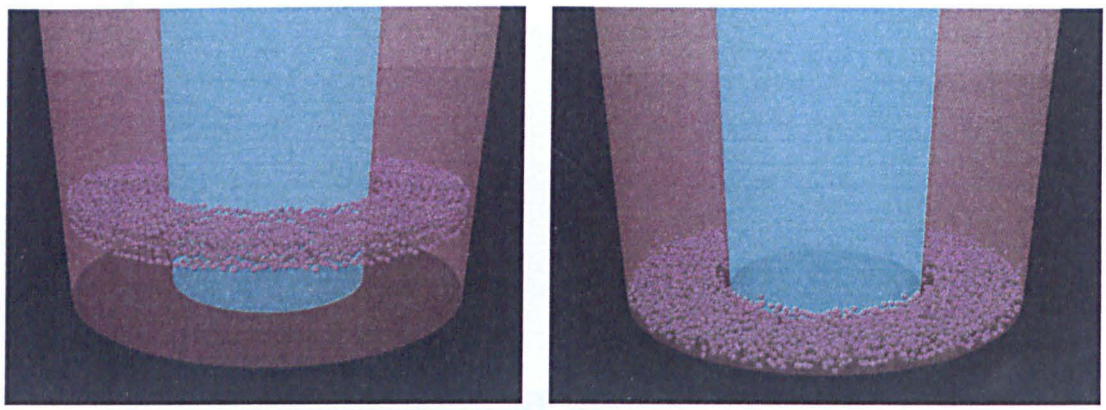

(a) (b)

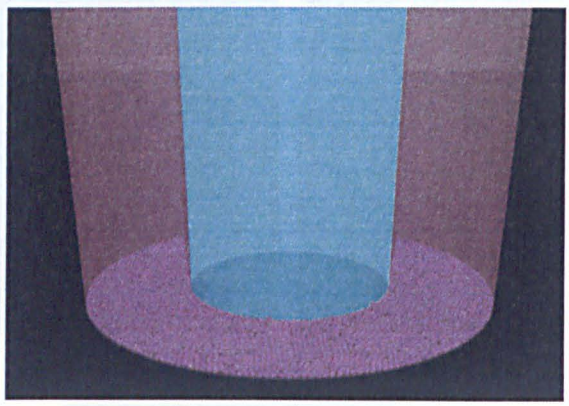

(c)

Figure 2.6: **A ring of particles dropped into the space between two cylinderical containers** - 4236 particles are dropped in rings into the gap between two concentric cylinders. (a) Initial positions of the particles. (b) Particle positions part-way through simulation (c) Particle positions at end of simulation.

In addition to dropping particles into a box it is also possible to drop particles into a container constructed with cylindrical walls. An example of this, where a column consisting of several layers of many rings of particles is dropped into a box, is shown in Fig. 2.6. Again particles initially have fixed x, y positions and z velocities but random z positions and x, y velocities.

It was decided that out of all of the possible methods for filling a container with particles the most realistic were methods 2 and 4. However, dropping very large numbers of particle into a box at any one time was found to be inefficient even in parallel mode. Therefore, if large numbers of particles were needed, the box was always filled by dropping several *blocks* of particles in stages into the box (each *block* consists of a small column of particles). In the user-generated parameter file the total number of particles to be dropped is specified. The user also specifies into how many *blocks* these particles should be divided. This process, once launched with the correct parameter files, is fully automatic. Each of the `pkdgrav` input files are automatically generated then the first block of

[1]The standard timestep chosen for dropping particles into a box is such that for a particle starting from rest and falling under gravity it would take approximately 30 timesteps for it to drop one particle diameter i.e., the timestep = $(1/30)\sqrt{2d/g}$ where d is the particle diameter and g the gravitational acceleration.

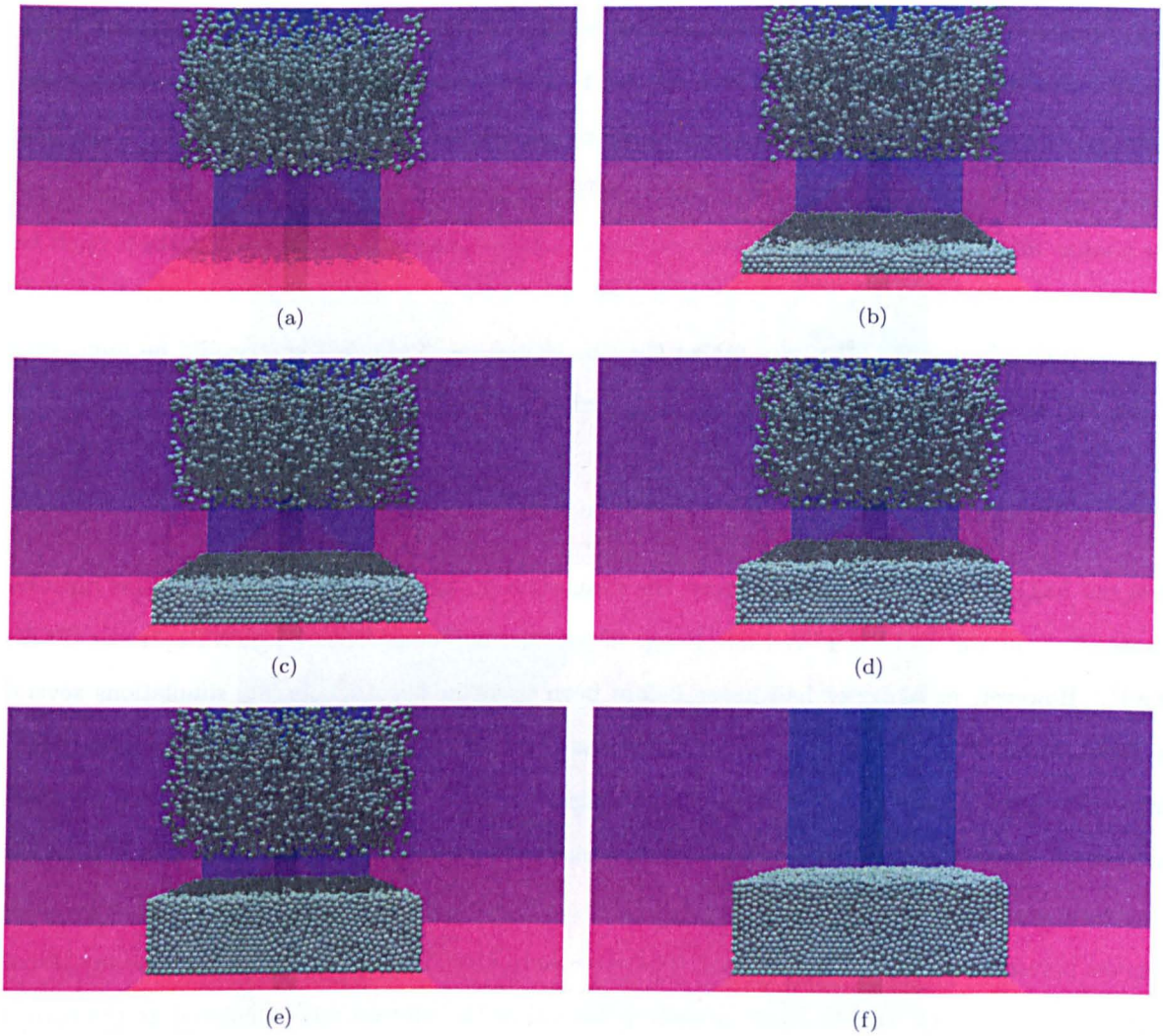

Figure 2.7: **Filling a box with discrete blocks of particles** - A block of particles in several layers is produced, the particles are dropped into a box, another block of particles is created and dropped into the box and this continues until the box contains the required number of particles. (a) - (e) Blocks of 6,250 particles are created and dropped into a box automatically (f) Filled box at end of simulation containing 31,250 particles.

particles is created and the simulation is launched. Then, after a set amount of time (defined by the user-generated parameter file) the simulation is paused. A second block of particles is added and the simulation is re-launched. This process continues until the user-specified number of particles are in the box (see example in Fig. 2.7).

2.4.2 Simulation issues

When running `pkdgrav` at small-scales for the first time subtle intricacies and difficulties were discovered. For example, due to the high particle densities in some test simulations both long-lasting contacts and frequent collisions were found to occur. In the original hard-sphere version of `pkdgrav` simultaneous collisions were not allowed because (1) if two or more particles all hit together at the

same time, the outcome is undetermined without solving for the force network; (2) it usually was a sign of a problem. This criterion has been relaxed to allow simultaneous collisions when using walls. However, the order in which simultaneous collisions are resolved is essentially random. Therefore, wherever possible the timestep should be made small enough so as to avoid "simultaneous" collisions. For similar reasons when creating several particles (e.g., to drop into a box) each particle must be given slightly different parameters (e.g., positions or velocities) so multiple particles do not collide with walls simultaneously. This also makes the simulations more physical as it would be impossible to drop all the particles from the same height exactly simultaneously.

2.4.3 Turning run outcomes into movies

Pkdgrav has an inbuilt function to convert the simulation output files into image files. This function creates files suitable to be rendered into image files using the Persistence of Vision Raytracer (POV-Ray)[1]. However, as pkdgrav had never before been used for such small-scale simulations several problems arose. POV-Ray uses floats (i.e., ~7 digits of precision) internally instead of doubles (which have ~15 digits of precision), so the dynamic range is limited: the range of scales in the file must not exceed about 1 million. For example, if the smallest detail to be discerned has size 1, then the maximum scale that can be visualised is $\sim 10^6$. To overcome this problem a "Scale Factor" was added into the parameter file which multiplies all length scales by that factor. This means that the ray-traced images and thus movies are actually scaled up but all of the physics was calculated at the correct scales.

2.5 Basic Tests

A suite of simple tests was developed during the coding stage to exercise each new feature/geometry as it was added. Examples include dropping particles into a cylinder bisected by an inclined plane (Fig. 2.8), "rolling" a perfectly balanced sphere on the inside edge of a vertical ring (Fig. 2.9), and bouncing hundreds of spheres on an oscillating disk inside a cylinder (Fig. 2.10). In this section a simple test designed to demonstrate the correct dynamical behaviour of the granular assembly is discussed in detail.

2.5.1 Tumbler

Brucks *et al.* (2007) carried out a series of laboratory experiments to measure the dynamic angle of repose β of glass beads in a rotating drum (tumbler) at various effective gravitational accelerations.

[1] http://www.povray.org/

(a)

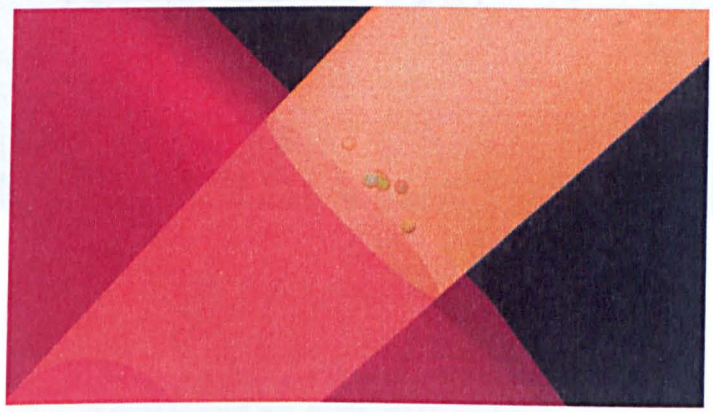

(b)

(c)

Figure 2.8: **Cylinder intersected by a plane** - Six particles are dropped into a cylinder bisected by an inclined plane. There is an external gravitational field acting in the downwards direction and thus the particles, as expected, come to rest in the place of lowest gravitational energy.

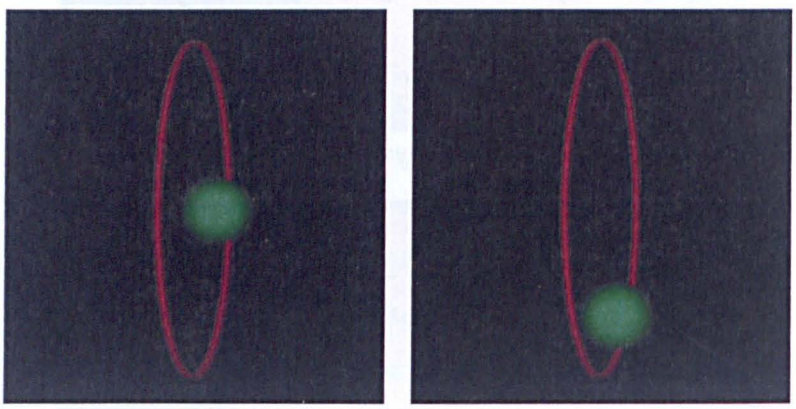

(a) (b)

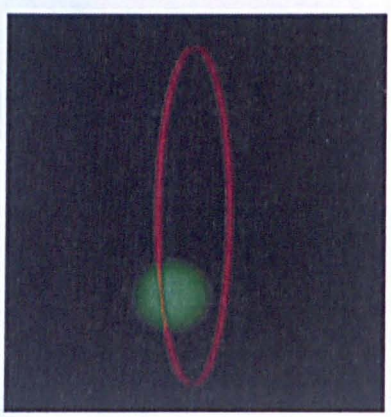

(c)

Figure 2.9: **Rolling on a ring** - A perfectly balanced sphere is "rolled" on the inside edge of a vertical ring.

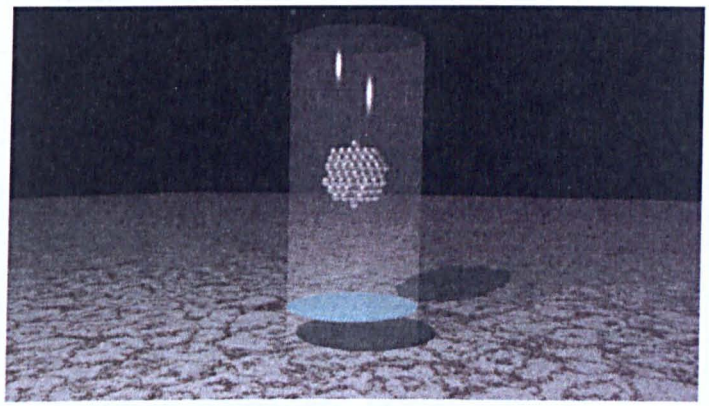

(a)

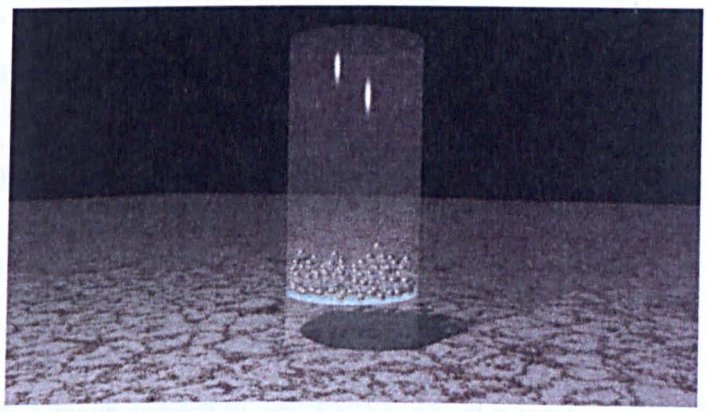

(b)

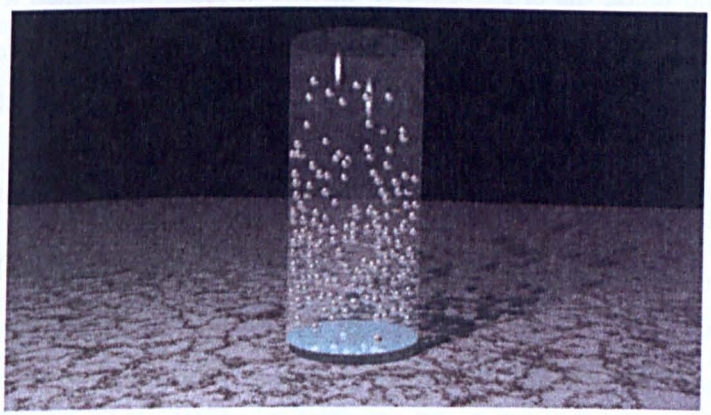

(c)

Figure 2.10: **Bouncing hundreds of particles** - 223 particles are dropped under an external gravitational field onto an oscillating disk inside a cylinder.

The beads had *diameter* (not radius) $d = 0.53 \pm 0.05$ mm and occupied ~50% of the volume of a tumbler of radius $R = 30$ mm and length $L = 5$ mm. A tumbler with $R = 45$ mm was also used, but our comparison is restricted to the smaller one for this test. The inner wall of the tumbler was lined with sandpaper to provide a rough surface. A centrifuge was used to provide effective gravitational accelerations between 1 and 25 g (where $g = 9.81$ m s^{-2}). The angular rotation speed of the tumbler Ω was varied to achieve a range of Froude numbers ("Fr") for the system, where Fr is defined as the ratio of centripetal to effective gravitational acceleration at the cylinder periphery[1]:

$$\mathrm{Fr} \equiv \frac{\Omega^2 R}{g_{\mathrm{eff}}}. \tag{2.8}$$

Figure 3 of Brucks *et al.* (2007) shows β as a function of Fr for various g_{eff} obtained in their experiment. Our aim for this test was to compare simulated results for $g_{\mathrm{eff}}/g = 1$ and $\mathrm{Fr} \geq 0.001$. Smaller Fr numbers are computationally challenging due to the limited motion of the particles (but the β curve is essentially flat for $\mathrm{Fr} \lesssim 0.01$ anyway). Different g_{eff}, particularly $g_{\mathrm{eff}}/g < 1$ (a regime Brucks *et al.* (2007) could not explore), will be the subject of future work.

The simulated experimental apparatus is constructed using an infinite horizontal cylinder of radius R (30 mm) cut into a short segment by two infinite vertical planes separated by a distance L (5 mm). For the purpose of this test, the planes were "frictionless" ($\varepsilon_n = \varepsilon_t = 1$). To keep the tests tractable, a fixed particle *radius* of $s = 0.53$ mm was used, i.e., twice the size of the glass beads used in the experiment (thereby providing nearly a factor of 10 savings in particle number, so the computational time of each run would be on the order of a day, instead of much more than a week). The initial conditions were prepared in stages (Figs. 2.11–2.13), alternately filling the "bottom" of the cylinder (i.e., by removing one plane and having gravity point down the length of the cylinder), closing and rotating the cylinder to allow particles to stick uniformly to the inner cylinder wall (to mimic the roughness provided by the sandpaper in the real experiment), refilling to get the desired volume fraction (about 50%), rotating some more, and then allowing the particles to settle. There were 6513 particles in total, of which 568 ended up stuck to the cylinder wall[2]. This starting condition was used for all the runs. For particle collisions, the normal coefficient of restitution $\varepsilon_n = 0.64$ (an estimate for glass beads derived by Heißelmann *et al.* (2009)) and the tangential coefficient of restitution $\varepsilon_t = 0.8$ (to provide some roughness; this value is poorly constrained).

As an aside, initially this experiment was conducted with surface coupling (i.e., $\varepsilon_t < 1$ for the cylinder) instead of sticky walls. Although, for sufficiently fast cylinder spin, the particles also start

[1] Occasionally the square root of the quantity on the right-hand-side of Eq. (2.8) is found in the literature, i.e., $\mathrm{Fr} = \Omega\sqrt{R/g}$; the expression in Eq. (2.8) is used to compare our results more easily with Brucks *et al.* (2007)

[2] In order to allow for the finite diameter of the stuck particles, the cylinder was actually $R + 2s = 31.06$ mm in radius.

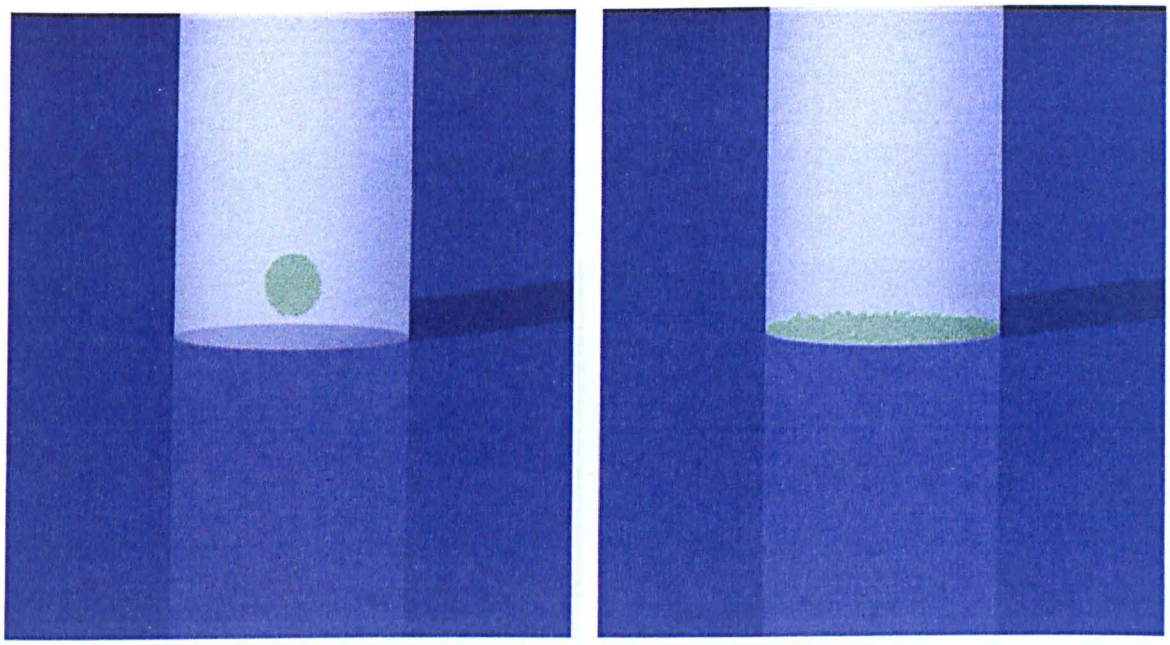

(a) (b)

Figure 2.11: **Stage 1 of tumbler preparation** - The bottom of the cylinder is filled by removing one plane and dropping a ball of particles into the cylinder. Gravity points downwards in the figure. (a) The initial configuration for this stage, before the particles are dropped. (b) The final configuration for this stage, with all the particels at the "bottom" of the cylinder.

to tumble in this setup, the particle spins quickly align with the cylinder spin (so that $\omega_i s \sim \Omega R$, within a factor of a few) and the particles settle to the bottom of the cylinder, sloshing around slightly. A rough surface instead provides a constant, somewhat random perturbation that ensures the tumbling behaviour persists among the loose particles.

Figure 2.14 shows ray-traced snapshots after achieving equilibrium for 8 different Froude numbers (0.001, 0.01, 0.05, 0.1, 0.3, 0.5, 1.0, and 1.5). For the sub-critical cases (Fr < 1), the total simulated run time was about 2.5 s, with a fixed timestep of about 5 μs. For Fr $= 1.0$ and 1.5, the run time was $\sim$0.5 s with a timestep of $\sim$1 μs (these latter cases achieve equilibrium faster, but the more rapid cylinder rotation dictated a smaller timestep). Also shown for the sub-critical cases is the estimated slope, which was measured by fitting straight lines to sample surface points over several snapshots and taking the average. Only particles to the left of centre were considered for these measurements, as particles tend to pile up on the right. As expected, for Fr $= 1.0$, it can be seen that centrifuging has begun; by Fr $= 1.5$, a thin layer of free particles persists along the inner surface of the upper-right quadrant of the cylinder. For Fr < 1, β depends on the rotation rate, with roughly the expected dependence from the experiments.

Figure 2.15 shows the measured values of β from the simulations (filled squares), with 1-σ uncertainty errorbars, along with data taken from Fig. 3 of Brucks *et al.* (2007) for the $R = 30$ mm tumbler. The experimental data show systematically larger dynamic slopes compared with the simulated data,

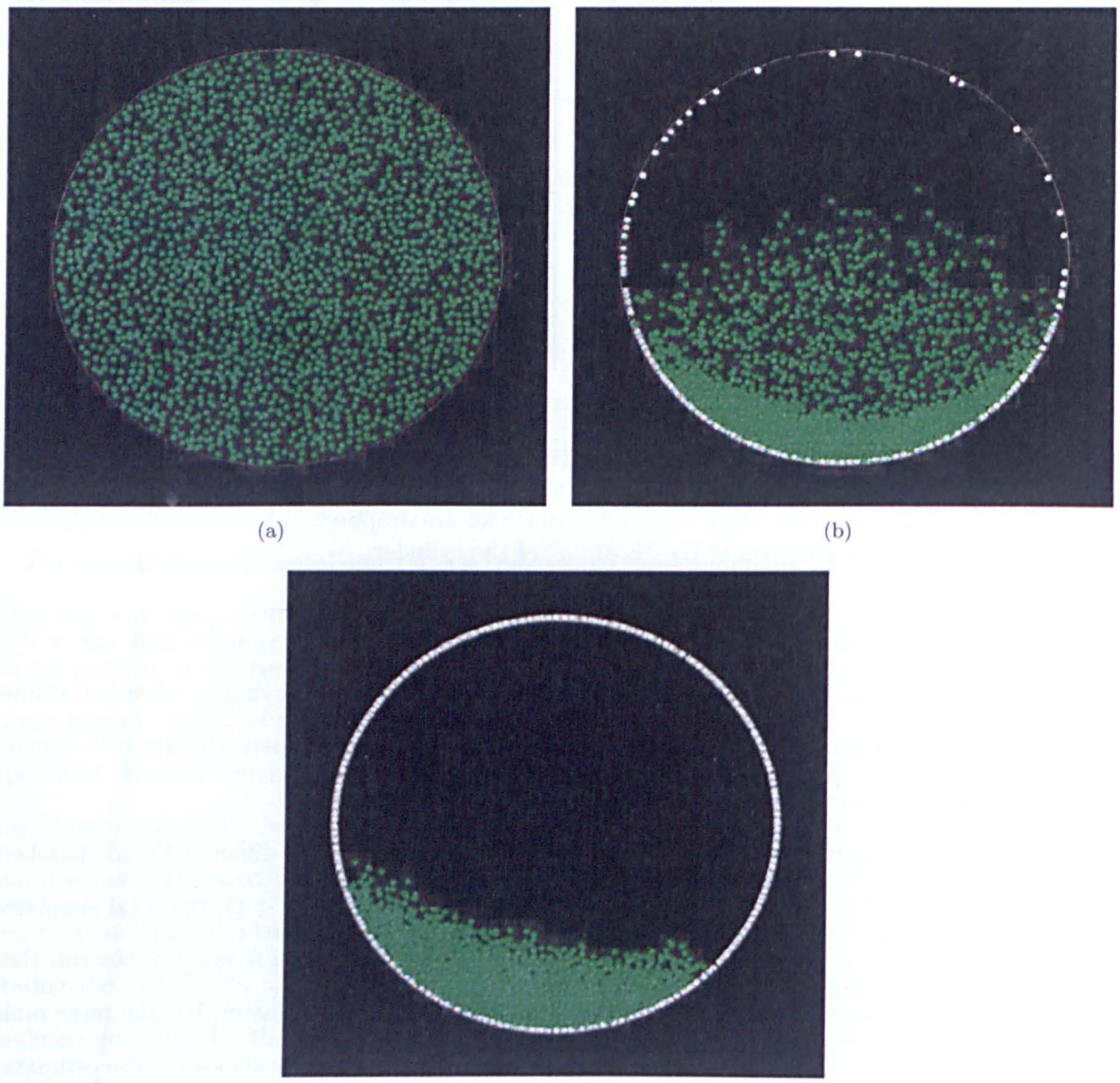

(a) (b)

(c)

Figure 2.12: **Stage 2 of tumbler preparation** - The cylinder is closed by introducing a plane behind the particles to confine them. Gravity points downwards in the figure. (a) The initial configuration for this stage which is also the final configuration from Stage 1 viewed from a different angle. (b) The cylinder is rotated to allow particles to stick uniformly to the inner cylinder wall (to mimic the roughness provided by the sandpaper in the real experiment). Once the particles are stuck to the wall they become white. (c) The particles are now stuck uniformly to the inner wall of the cylinder.

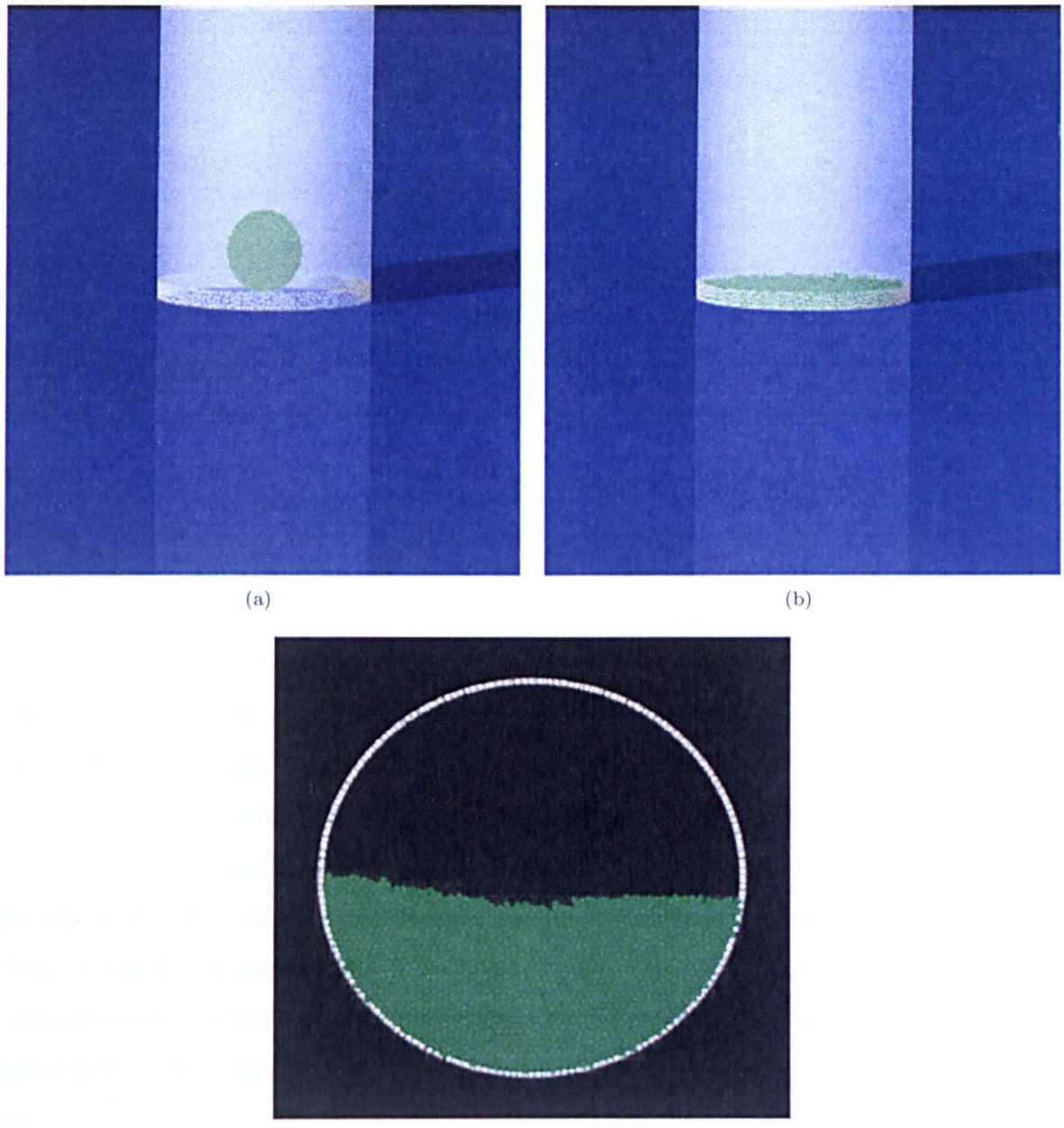

Figure 2.13: **Stage 3 of tumbler preparation** - To get the desired volume fraction (about 50%) another ball of particles is dropped into the cylinder. (a) The initial configuration for this stage - the inner wall of the cylinder is coated in (white) particles and a ball of (green) particles is ready to be dropped into the cylinder to fill it. Gravity points downwards in the figure. (b) The cylinder is rotated some more and gravity continues to point down the length of the cylinder. (c) The cylinder stops rotating. The viewing angle is changed and so is the direction of gravity (now perpendicular to the axis of the cylinder but still shown as downwards in the figure). The particles are allowed to settle into the bottom of the tumbler until the average particle velocity becomes less than a small theshold value.

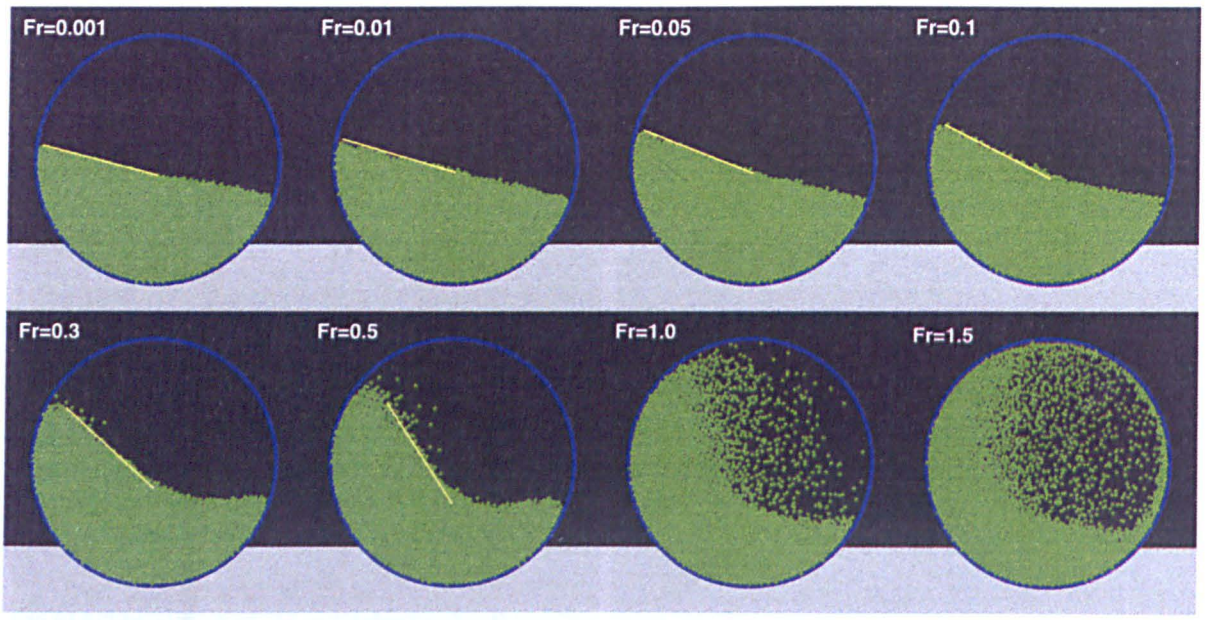

Figure 2.14: **Tumbler Snapshots** - Snapshots of the simulated tumbler experiments taken at the end of each run. The Froude number (Eq. (2.8)) is indicated. View size is about 7.5 cm across each frame. The view is down the cylinder axis, and rotation is in the clockwise rotation direction (at this viewing angle, the short cylinder itself cannot be seen). The blue particles along the inner surface of the cylinder are "glued" in place to provide roughness. Where shown, the yellow line indicates an estimate of the surface slope (Fig. 2.15).

but both follow a similar trend with Froude number. Additionally, the closer match to the experimental results at high Froude number suggests that our hard-sphere model is more suited to the dilute flow regimes of high Froude number rather than dense flow regimes of low Froude number.

However, it was considered possible that some of the discrepancy in slope may arise from the different R/s ratio for the data sets, namely about 110 for the experiment while only 57 for the simulations. Some simulations were performed increasing the R/s ratio of the simulations to match the experiments, which requires a factor of 8 more free particles (as well 4 times more stuck particles). The dynamic angle of repose does not change in these high resolution simulations with respect to the low resolution simulations.

A study by Taberlet *et al.* (2006) shows that the shape of the granular pile in these kinds of experiments depends on interactions with the end caps, with friction leading to "S" shapes and lack of friction leading to straighter slopes (as in our case). The baseline simulation used frictionless confining planes, whereas the flat walls in the experiment were comprised of a metal plate and a glass plate, both constrained to rotate with the cylinder, and neither of which were frictionless. Some studies were performed to test the dependency of the numerical simulation results on the parameters of the end caps, although in our simulations the end caps never rotate with the cylinder. Several simulations were performed varying the normal and tangential coefficients of restitution (ε_n and ε_t respectively) of the end caps with Fr kept constant at 0.3 (Fig. 2.16). In each plot there are four

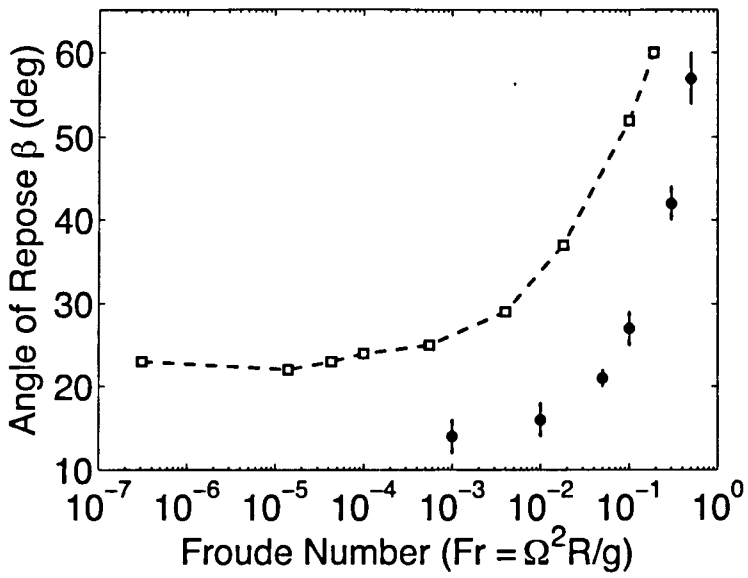

Figure 2.15: **Tumbler dynamic repose angle.** - Dynamic angle of repose as a function of Froude number for the simulated tumblers (filled squares) and from the experiments of Brucks et al. (2007; open squares connected with dashed line, from their Fig. 3). Errorbars for the simulated points are 1-σ uncertainties from averaging slope estimates over several snapshots. The simulated points are shifted down and to the right compared with the experiments. See main text for discussion.

different colours of particles with each colour belonging to a simulation with different parameters. For each simulation all of the particles' locations at the end of the simulation are plotted. The particle locations for the four different simulations are super-imposed to allow detection of any changes in the shape of the profile. In both of these plots there is no difference in the profile for the different colours. This implies that, in our simulations, varying the normal and tangential coefficients of restitution of the end caps of the tumbler does not appear to change the dynamic angle of repose, nor does it lead to an "S" shaped granular pile.

The adopted ϵ_n and ϵ_t values for the particles in the simulations are mostly educated guesses. It is possible that the values do not match those of the real particles exactly. A series of tests were performed to determine the influence of changing the particle ϵ_n and ϵ_t on the dynamic slope angle. As in the tests for the end caps, Fr was kept constant at 0.3. Varying the particle ϵ_n does not change the dynamic angle of repose of the particles but does increase the energy of the particles in the tumbler, as would be expected. As ϵ_n approaches 1.0 more particles follow free-fall trajectories within the tumbler. In the simulations of $\epsilon_n = 1.0$ there are large numbers of energetic particles at the bottom of the slope. This can be seen in Fig. 2.17 (a) in which the final particle locations for two different simulations are super-imposed. One simulation, represented by the red particles, has $\epsilon_n = 0.4$ and the second simulation, represented by the blue particles, $\epsilon_n = 1.0$.

The consequences of varying the values of ϵ_t of the particles can be seen in Fig. 2.17 (b) in which the red particles represent the final particle locations in a simulation in which the particles have $\epsilon_t =$

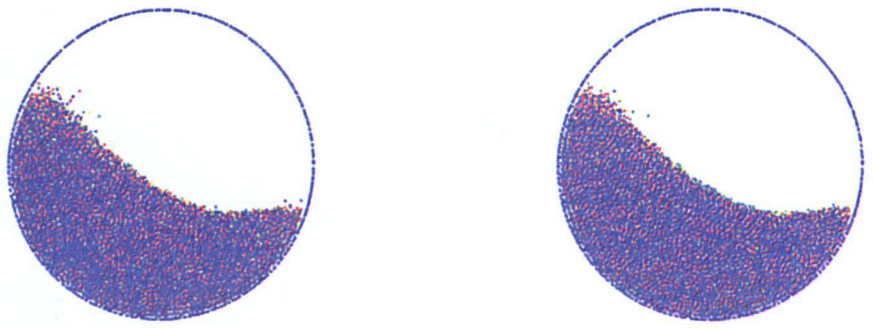

(a) (b)

Figure 2.16: **Tumbler with varying normal and tangential coefficients of restitution of end caps** - In each plot there are four different colours of particles with each colour belonging to a simulation with different parameters. For each simulation all of the particles' locations at the end of the simulation are plotted. The particle locations for the four different simulations are super-imposed to allow detection of any changes in the profile. Shown in (a) are the results of varying the end plane normal coefficient of restitution (ε_n). The colour code represents the value of ε_n used: green: $\varepsilon_n = 1.0$, yellow: $\varepsilon_n = 0.8$, red: $\varepsilon_n = 0.6$, blue: $\varepsilon_n = 0.4$. For all these simulations the tangential coefficient of restitution remains constant at 1.0. Shown in (b) are the results of varying the end plane tangential coefficient of restitution (ε_t). The colour code represents the value of ε_t used: green: $\varepsilon_t = 1.0$, yellow: $\varepsilon_t = 0.8$, red: $\varepsilon_t = 0.6$, blue: $\varepsilon_t = 0.4$. For all these simulations the normal coefficient of restitution remains constant at 1.0. In both of these plots there is no difference in the profile for the different colours.

0.4 and the blue particles represent the final particle locations in a simulation in which the particles have $\varepsilon_t = 1.0$. It can be seen that changing ε_t does not change the dynamic angle of repose of the particles but does cause the particles to dilate a little. The particles appear to accumulate more readily at the base of the slope in the simulation with $\varepsilon_t = 1.0$. This is because there is no tangential coupling between particles within the tumbler and the particles stuck to the walls and so it is more difficult for the particles to be pulled downwards following the tumbler motion.

It has been demonstrated that the dynamic angle of repose is not influenced by the coefficients of restitution of the end caps nor of the particles in the tumbler. However, there are other caveats to consider as well. The simulated particles are identical in size and are perfectly spherical; deviations from uniformity of the glass beads used in the experiments may increase the dynamic slopes. In the simulations, the cylinder rotation rate was imposed instantaneously at the start, which may have caused spurious bulking as the assemblage reacted to the sudden shear stress. It is possible that a better approach would have been to accelerate the tumbler gradually to the desired rotation rate. Again this has not been investigated in this thesis but would be an interesting future project. The dynamic angle of repose may also be affected by the initial packing fraction of the particles, which depends on the dominant interparticle forces. In the absence of interparticle friction, random close packing is expected, whereas with friction, random loose packing is a more likely starting condition

(a) (b)

Figure 2.17: **Tumbler with varying normal and tangential coefficients of restitution of particle** - In both figures the final particle locations for two different simulations are super-imposed to allow detection of any changes in the flow profile. Shown in (a) are the results of varying the normal coefficient of restitution (ε_n) of the particles. Red: $\varepsilon_n = 0.4$, blue: $\varepsilon_n = 1.0$. For both these simulations the tangential coefficient of restitution remains constant at 0.8. Shown in (b) are the results of varying the tangential coefficient of restitution (ε_t) of the particles. Red: $\varepsilon_t = 0.4$, blue: $\varepsilon_t = 1.0$. For both of these simulations the normal coefficient of restitution remains constant at 0.64.

(Makse *et al.*, 2000), and may lead to a different dynamic angle of repose. The effect of varying the interparticle friction (ε_t) on the particle profiles within the tumbler was explored in this chapter. However, in these simulations the initial particle positions of the baseline simulation were used and then ε_t was varied. The influence of varying ε_t on the initial particle packing and the subsequent consequences on the dynamic angle of repose were not explored here but could be part of a future investigation.

2.6 Chapter discussion

Our numerical approach, in the context of granular dynamics literature, can be characterised as hard-sphere DEM (see Chapter 1), which is particularly well-suited to simulating dilute granular flows (Mehta, 2007). In the dilute regime, soft- and hard-particle methods should give equivalent results, but so-called event-driven simulations, in which no computations are needed between collision events, are typically much faster (Luding, 2004). However, within dense granular flows in which many-body interactions dominate and particles have long-lived contacts with many neighbours, it is possible that the assumptions of the event-driven and hard-sphere DEM models fail (Delannay *et al.*, 2007).

In a rotating tumbler (see Section 2.5.1), there exists a region of long-lived contacts but also a faster-flowing layer. By varying the Froude number, it is possible to investigate many different regimes, from the fast-flowing regime with a large Froude number to the regime when the Froude number is low and most contacts are longer-lived. Thus the tumbler is an intermediate regime between dilute and dense flows, providing a convenient test of the range of applicability of our hard-sphere method.

Indeed, the tumbler has been studied in detail with many different numerical techniques; as described briefly here.

McCarthy & Ottino (1998); McCarthy *et al.* (1996, 2000) used a soft-sphere model to compare simulations of non-cohesive granular materials in a slowly-rotating drum to experimental data. In order to limit the number of particles necessary in the simulations they proposed a "hybrid" simulation technique. This method involves using a geometrical model to determine the bulk motion of the particles and then performing particle dynamics simulations on only the particles contained within and bordering the avalanching wedge. They found a favourable match between experiment and simulation, at low computational cost, but with the trade-off that the method is tailored to a very specific geometry.

Khakhar *et al.* (1997) used a similar technique to separate the granular material in the rotating drum into a "rapid flow region" and a "fixed bed." A continuum model in which averages are taken across the layer was used to analyse behaviour of the flowing layer. The motion of grains on the free surface of a granular mixture in a rotating drum was also investigated by Monetti *et al.* (2001) using Monte Carlo simulations of a two-dimensional lattice gas model. The model takes into account rotational frequency, frictional forces, and the gravitational field.

Soft-sphere methods have also repeatedly and successfully been used to describe granular material in a rotating drum (Dury & Ristow, 1999; Dury *et al.*, 1998; Pohlman *et al.*, 2006; Rapaport, 2002; Taberlet *et al.*, 2006). This has also been extended to two-dimensional simulations of irregular-shaped particles by Poschel & Buchholtz (1995).

Hard-sphere methods have not been commonly used for rotating drums. However, Gui & Fan (2009) did perform numerical simulations of motion of rigid spherical particles within a 2d tumbler with an inner wavelike surface. The rotation of the tumbler was simulated as a traveling sine wave around a circle.

The observed behaviour in our tumbler simulations shows that our code correctly models the transitions from global regimes with increasing Froude number. The differences between experiment and simulation are larger at lower Froude number and start to decrease at higher Froude number. This suggests that our hard-sphere model is more suited to the dilute flow regimes of high Froude number rather than dense flow regimes of low Froude number. Soft-sphere DEM is typically used for dense granular flows (Zhu *et al.*, 2007), as the detailed characterisation of interparticle contacts is more suitable for this regime. However, hard-sphere methods can approach experimental and soft-sphere simulation results for very low friction materials. For example, Pohlman *et al.* (2006) found an angle of repose of only 16.9°, for low friction ($\mu = 0.1$) chrome steel beads at a Froude number of 4.94×10^{-5}. This is within a few degrees of our expected results at this Froude number.

In summary, this numerical approach currently favours dilute or fluid flows over dense granular flows. Whether regolith in low-gravity environments, such as the surface of an asteroid, when reacting to external stresses, is more appropriately modeled as a dilute or dense granular flow is the subject of ongoing investigation. Regardless, numerical methods will play an important role in the study of these environments.

In Chapter 3 a stringent test of this numerical code will be performed through investigations of collective particle behaviour of granular material on vibrating plates.

Chapter 3

Particle dynamics in a shaken granular material

3.1 Summary of Chapter

In this chapter an in-depth validation exercise is performed of the numerical method used in this thesis. As a stringent test of the numerical code the complex collective ordering and motion of granular material is investigated and compared with laboratory experiments of a vibrated granular material.

First, the motivation for choosing such an experiment to use in the validation exercise is discussed and then the experiment that served as a reference basis for the numerical simulations of shaking motion is presented. Next, an explanation is given on how the numerical simulations were performed. Detailed discussions are provided about the different analysis techniques and approaches that can be applied for such a simulation and laboratory experiment and an in-depth discussion is included highlighting the difficulties in comparing experimental and simulation data. A detailed comparison (either qualitative or, where appropriate, quantitative) is performed with the laboratory experiment. Then the consequences of varying the external gravitational acceleration on string frequency and length are considered. This demonstrates the ability of the code to simulate the range of gravitational environments that can be encountered among the solid planetary bodies within our solar system. Indeed, in the reduced-gravity simulations both the gravitational conditions and the frequency of the vibrations roughly match the conditions on asteroids subjected to seismic shaking (Richardson *et al.*, 2004, 2005), though real regolith is likely to be much more heterogeneous and less ordered than in the idealised simulations. In this same section one of the unique advantages of the code `pkdgrav` is demonstrated: the ability to model inter-particle gravity. By varying the particle density it is possible

to examine what happens to the granular system when the gravitational forces between the particles become increasingly strong compared to the external gravitational acceleration. Finally, in the last section, the relevance of the results to planetary science are discussed.

The results in this chapter have been submitted for publication (Murdoch *et al.*, 2012a). All of the numerical simulations and the analysis of the simulation data were performed by myself with the sole exception of the strings analysis presented in Section 3.5.4 and Section 3.6; this was performed by K. Nordstrom (University of Maryland). The experimental analysis was also performed by myself, again with the exception of the strings analysis. I was not, however, responsible for performing the experiments or the experimental particle-tracking. The experimental data which I used for the analyses were the particle-tracking outputs provided to me by collaborators from the University of Maryland.

3.2 Why study particle dynamics in a shaken granular material?

Before we can simulate granular interactions on planetary bodies, the simulations must first be able to reproduce the dynamics of granular materials in more idealised conditions and the results of existing laboratory experiments. The experiment used as a reference basis of shaking motion (Berardi *et al.*, 2010) was chosen as it focuses on collective ordering and behaviour of particles. This collective motion will provide a more stringent test of the simulation than statistics of individual particle motion.

The experimental study was aimed at analysing the motion of dense configurations of bidisperse (i.e., two different particle sizes) particles under vertical shaking. In the dense arrangement of particles many of the larger particles formed hexagonal close-packed arrangements (the densest possible configuration of spheres in a plane). Such ordered regions, refered to as *grains*, are similar to crystalline grains in polycrystalline materials. These grains are surrounded by less densely packed, disordered regions that are named *grain boundaries*. It is in these grain boundary regions that most of the smaller particles can be found.

The particle dynamics in the grain boundary have been found to be similar in character to a super-cooled fluid with string-like collective motion. Rearrangements of particles are characterised as strings, if particles move towards each other's previous position as if they were beads moving along a string. The existence of this collective particle motion and the length and number of cooperatively moving clusters of particles (hereafter *granular strings*) can be determined (Aichele *et al.*, 2003; Donati *et al.*, 1998; Riggleman *et al.*, 2006; Zhang *et al.*, 2009). Such string-like collective motion of particles is a characteristic for systems close to jamming, such as dense suspensions of colloidal particles and in

glassy systems (Donati *et al.*, 1998; Weeks *et al.*, 2000). A glassy system describes a polymer below the glass transition temperature. The glass transition, something which only occurs in polymers, defines the temperature where a polymer goes from a hard, glass like state to a ductile rubber-like state. This type of transition can be witnessed by putting a rubber band (rubber-like state, very flexible) into a container of liquid nitrogen. When removed the rubber band is solid and inflexible: it is in the glassy state. While in the glassy state the rubber band can be shattered. However, if the rubber band is allowed to warm to room temperature it will again become flexible and rubbery (it has returned to the rubber-like state). Some common polymers such as hard plastics (e.g., polystyrene) have a glass transition temperature well above room temperature and are used in their glassy state. These materials are generally brittle. Other materials, such as rubber elastomers[1], are used above their glass transition temperature in a rubbery state, where they are soft and flexible.

Both the ordering and string-like dynamics are collective effects and can be used as more subtle measures to assess whether the simulations recover collective ordering and motion. However, both grain boundaries and granular strings also affect important materials properties. Strings highlight how the yielding of granular matter is similar to the plasticity of glasses; both exhibit similar string-like collective dynamics (Stevenson & Wolynes, 2010). The presence of granular strings indicates that a material is fragile. In glasses, fragility is generally defined as how quickly viscosity increases when the temperature of a material is lowered toward the glass transition temperature. In granular matter, strain may be considered as the equivalent of temperature (Liu & Nagel, 1998) and fragility is associated with sudden changes in strain with increasing stress. Granular materials are, by their nature, thought to be fragile and are, therefore, prone to sudden, avalanche-like failures (Riggleman *et al.*, 2006).

Measurements of string length offer one way to quantify this propensity for fragile behaviour - longer strings have been shown to indicate higher fragility (Dudowicz *et al.*, 2005). In contrast, short granular strings indicate a more ductile behaviour, where failure and granular rearrangements are more uniformly distributed in space and time. String-like dynamics within grain boundaries directly affect grain boundary mobility and, therefore, play an important role in the bulk mechanical properties of more ordered systems (increased grain boundary mobility implies increased ductility) (Zhang *et al.*, 2006).

Therefore, by simulating a laboratory experiment in which collective ordering and strings are present it is possible to assess the ability of the numerical code to capture collectively emerging structures and dynamics with a focus on those collective structures and dynamics that significantly affect the mechanical properties of the ensemble. While previous simulations have shown that strings

[1]An elastomer is a polymer with the property of viscoelasticity, generally having a notably low Young's modulus and a high yield strain compared with other materials

exist in elastic disordered systems (Dudowicz *et al.*, 2005) and in ordered systems with grain boundaries (Zhang *et al.*, 2006), the simulation of strings in a dissipative system in general, and in a vibrated lattice in particular, has not been previously carried out. This study is, therefore, the first direct comparison of the frequency and length of granular strings between experiment and simulation.

As well as being a stringent test of the numerical method and an example of an interesting physical phenomenon that is directly related to material properties, these experimental conditions may also be relevant to asteroid surfaces. As discussed in detail in Chapter 1, seismic shaking is expected to occur when small projectiles impact the surface of asteroids on which gravity is low enough that surface motion can be influenced over long distances by seismic wave propagation. As a result of the seismic shaking, the surface granular material can be subject to various kinds of motion, among them, downslope migration and degradation, or erasure, of small craters. Regolith motion resulting from seismic shaking of asteroids has been discussed in several papers, but without simulating explicitly the dynamics of the regolith. For instance, Richardson *et al.* (2005) investigated the global effects of seismic activity resulting from impacts on the surface morphology of fractured asteroids. They used a Newmark sliding-block analysis (Newmark, 1965), which can be applied in the regime where the regolith layer thickness is much smaller than the seismic wavelengths involved. In this case, the motion of a mobilised regolith layer is approximated by modelling the motion of a rigid block resting on an inclined plane (Fig. 3.1). Miyamoto *et al.* (2007) discussed regolith migration and sorting on the asteroid Itokawa by analysing regolith properties from images obtained by the Hayabusa probe and derived the possible regolith motion due to seismic shaking based on experiments performed on Earth.

Although real regolith is likely to be much more heterogeneous and less ordered than in the idealised simulations, varying the gravity between the numerical simulations can be used to show the sensitivity of an idealised granular system to variations in self-gravity and external gravitational acceleration. By perfoming varying gravity simulations it is possible to demonstrate the ability of the code `pkdgrav` to simulate the range of gravitational environments that can be encountered among the solid planetary bodies within our solar system.

In summary, investigating particle dynamics in a shaken granular material with the numerical code `pkdgrav` allows a rigorous test of our numerical method. In doing such a test we also perform the first direct comparison of collective motion in a granular system between experiment and simulation. In addition, grain boundaries and granular strings significantly affect the mechanical properties of materials and this may also be relevant to planetary surfaces, if such structures are found to be present on those surfaces.

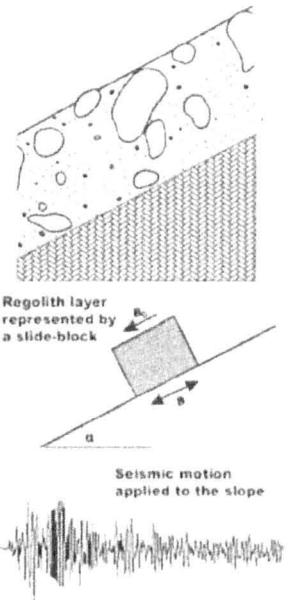

Figure 3.1: **A basic illustration of the Newmark slide-block model** - The regolith layer resting on a slope is represented by a rigid block resting on an inclined plane. Forces on the rigid block include surface gravity (static loading), seismic accelerations (dynamic loading, applied by the inclined plane), and frictional forces (both static and dynamic). Ballistic launching of the block (layer) is also permitted and tracked in this model. Figure from Richardson *et al.* (2005).

3.3 Shaking experiments

As briefly mentioned in Section 3.2, the experimental studies used as a reference in this investigation were aimed at analysing the motion of dense configurations of bidisperse particles under vertical shaking (Berardi *et al.*, 2010). The studies were carried out in a quasi-2d system (Fig. 3.2). The goal was to analyse how a system of large and small particles arranges into ordered and disordered regions, and to elucidate the dynamics, especially in the more mobile disordered regions. The observed structure and dynamics show strong similarities to grains and grain boundaries. The large particles arranged into hexagonally ordered grain-like regions and the small particles localised in grain boundaries. Additionally, the particle dynamics in the grain boundary demonstrate string-like collective motion. Both the ordering and string-like dynamics are collective effects. Berardi *et al.* (2010) demonstrate that the surface area occupied by grain boundaries and the length and number of the granular strings increase with increasing concentrations of small particles.

In the laboratory experiment steel spheres 3.0 mm in diameter (with the addition of 2.0 mm steel spheres, which take up from 3 to 10% of the covered surface area) were confined into a dense arrangement in a round container of 292 mm diameter with 0.1 mm separation between the large particles and a covering lid (Fig. 3.2 for a diagram of the experiment and Table 3.1 for exact experiment conditions). When the container was vibrated vertically (at a frequency of 125 Hz with a maximum acceleration of 4.5 g), the dense arrangement of particles moved in a way that is characteristic for

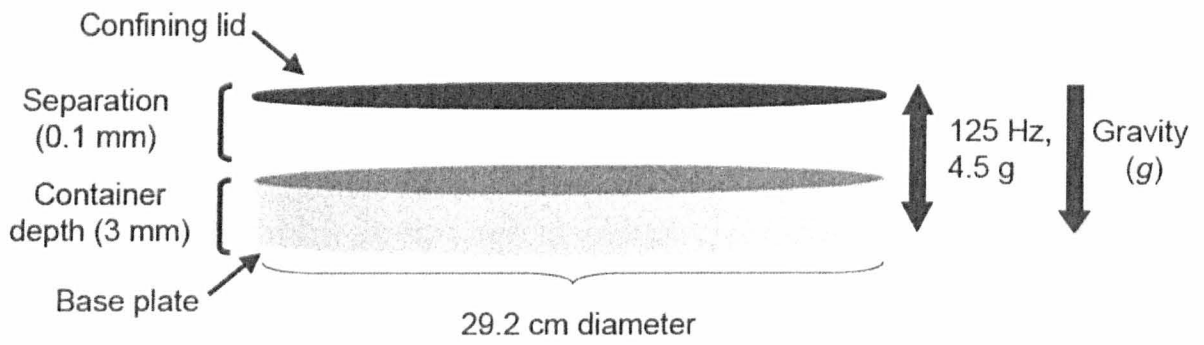

Figure 3.2: **Schematic of the shaking experiment** - Schematic of the experiment used in Berardi *et al.* (2010). The container depth is 3 mm and the separation between the top of the largest particles and the confining lid is 0.1 mm. The base plate, container and the confining lid vibrate together at a frequency of 125 Hz and with a maximum acceleration of 4.5 g. The system is referred to as quasi-2d as there is only one layer of particles in the container. Note: Figure not to scale.

Table 3.1: The experimental conditions. The entire experiment was 670 cm^2 in area, although during the analysis a test area of only 215 cm^2 was considered (see Section 3.5 for more details and discussion on the differences between experiment and simulations). An estimation was made of the worst-case error in the total number of particles in the entire experiment. From this worst-case error, the maximum possible uncertainties in total surface area, small particle area coverage and the total number of particles in the test area were calculated.

Small particle area coverage (% of total covered surface area)	Total surface area coverage (%)	Total number of particles in test area
3 ± 0.1	85 ± 0.21	2615 ± 20
5 ± 0.1	85 ± 0.21	2600 ± 20
7 ± 0.1	85 ± 0.21	2640 ± 20
10 ± 0.1	85 ± 0.21	2680 ± 20

systems close to jamming. Most significantly, many of the larger (3 mm) particles formed hexagonal close-packed arrangements (grains), similar to crystalline grains in polycrystalline materials. These grains are surrounded by less densely packed, disordered regions that are named grain boundaries. It is in these grain boundary regions that most of the smaller 2 mm particles can be found.

Particle motion was imaged with a high-speed, high-resolution camera. The pixel scale of the images is determined by choosing several large particles in a line from within a crystalised region. The distance between the centres of all of these particles can be combined with the known particle radius to calculate the pixel scale. In the case of the experiments of Berardi *et al.* (2010) a pixel scale of 0.264 mm per pixel was found. From the images, the position and the motion of large and small particles were determined using an adaptation of a subpixel-accuracy particle detection and tracking algorithm (Crocker & Grier, 1996). First, images were bandpass filtered to subtract the background. This yields well-separated bright peaks whose positions are found with subpixel-accuracy by peak-finding algorithms (for more information on the tracking procedures see Section 5.2.1). The peak-finding

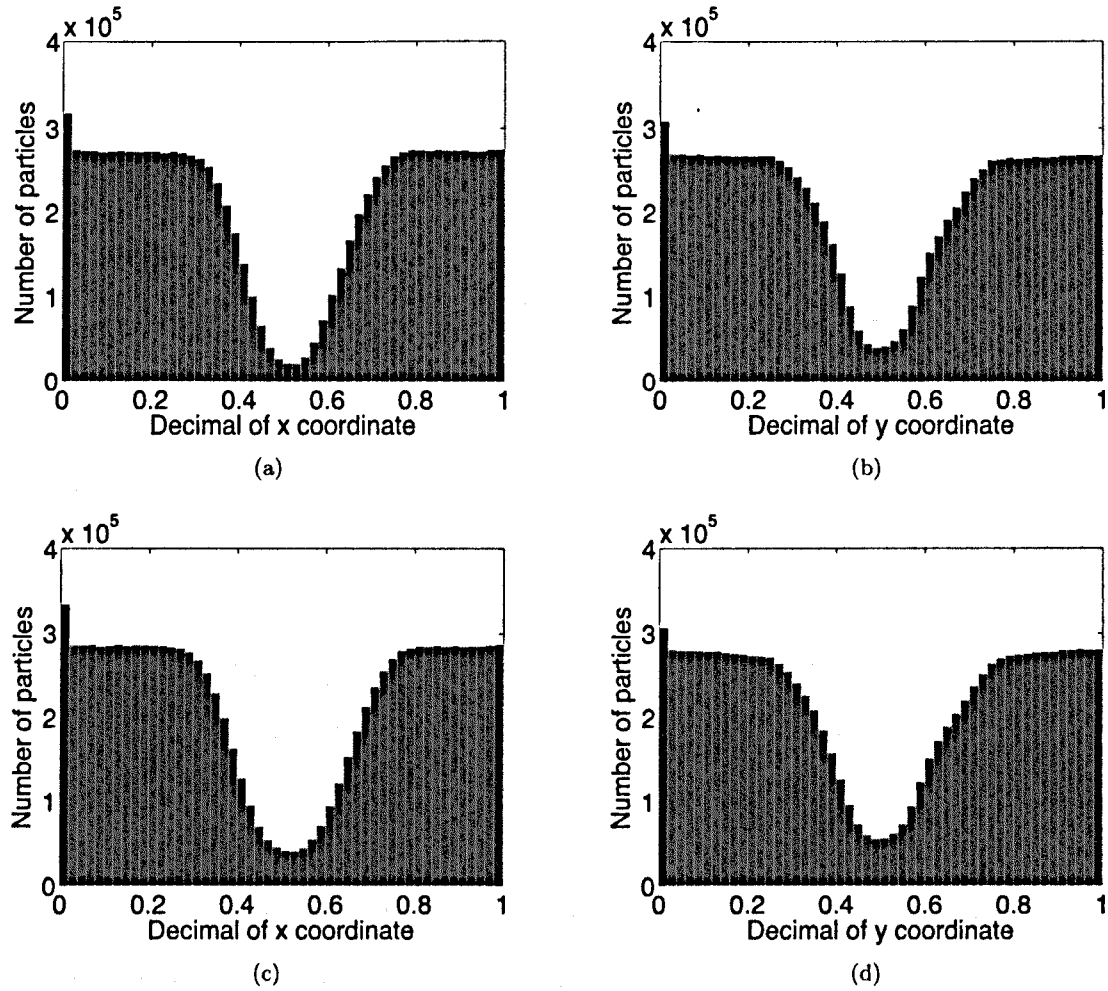

Figure 3.3: **Examples of pixel biasing in the shaking experiments** - Histograms of the fractional part of the particle position coordinate for the laboratory experiments at 3% small-particle concentration ((a) x coordinate and (b) y coordinate), and at 10% small-particle concentration ((c) x coordinate and (d) y coordinate). See Section 5.2.1 for a more detailed explanation.

algorithms are capable of locating particle positions with an accuracy of $\pm 1/10$ pixel (i.e., 0.026 mm in this case). However, it was discovered that during the experimental particle tracking there were some strong pixel biases present (Fig. 3.3). Unfortunately this means that the accuracy of the particle positions was reduced to $\pm 1/2$ pixel. Nevertheless this still gives an accuracy in the particle position of better than 0.132 mm (i.e., 1/15 of the small particle diameter).

To analyse motion, peaks (i.e., particles) are then tracked through image sequences with the requirement that particles move less than half a particle diameter between frames (preferably the particles move <1/10 of a particle diameter between frames). Comparison with the original image shows that more than 99% of all particles in each frame are detected with this algorithm. To estimate the quantity of small particles that may have been incorretly labelled as large particles the distribution of particle brightness for all of the particles detected in one experiment is considered (Fig. 3.4). As two peaks can be seen in the data this tells us that there are two distinct particle sizes. A tracked

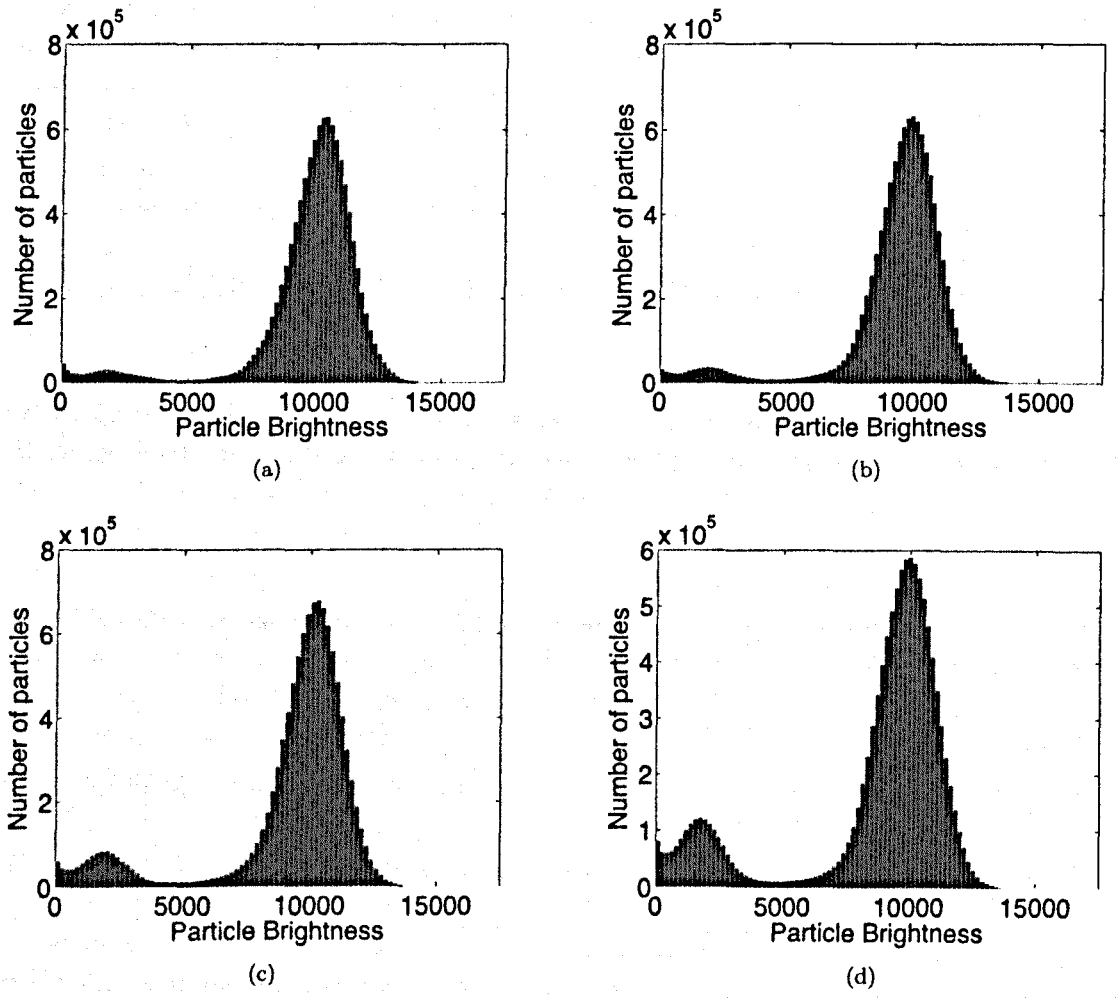

Figure 3.4: **Histogram of particle brightness in the shaking experiments** - Histograms are shown of the particle brightness for the laboratory experiments at (a) 3% small-particle concentration, (b) 5% small-particle concentration, (c) 7% small-particle concentration, (d) 10% small-particle concentration. As two peaks can be seen in the data this tells us there are two distinct particle sizes. As expected the size of the smaller peak increases with increasing small-particle concentration.

particle was labelled as large or small based on the average brightness of the peak. The particles at risk of being mislabelled are the particles with brightness between the two peaks. By calculating the number of particles found in this region of the histrogram, and assuming that all of the particles in this area are all either small or large, it can be estimated that a maximum of 3.8 $\pm$ 0.1% of small particles are mislabelled or 0.04 $\pm$ 0.01% of large particles are mislabelled. Therefore, we can state that the algorithm correctly labels more than 99.9% of large particles and more than 96.1% of small particles.

The diffusion coefficient, D, of a system of particles has units of length-squared over time. Thus, the characteristic timescale to diffuse over a distance L is L^2/D. The statistics of motion, therefore, provide a characteristic timescale when considering motion over characteristic length-scales of a particle radius. It possible to identity "mobile" particles based on their larger-than-expected displacement over this characteristic time interval. The method for identifying these mobile particles is discussed

in more detail in Section 3.5.4. One characteristic of such mobile particles in a system close to jamming is that they leave their "cage" of neighbours, i.e., they change neighbours. The local geometric arrangement also affects particle mobility - mobile particles preferentially appear in grain boundaries. Once mobile particles have been identified it is then possible to examine their behaviour to determine if they are exhibiting string-like collective motion (as introduced in Section 3.2 and discussed in detail later in Section 3.5.4).

3.4 Numerical simulation method

The area covered by the particles is calculated by projecting the spheres, as 2d circles, onto the plane of the bottom of the container. The surface area coverage is then the percentage of the total container surface area that is covered by the projected surface area of all of the particles. This definition is used instead of the usual "volume fraction" because the system is quasi-2d and not a full 3d system. Similarly, the small particle surface area coverage, or small-particle concentration, is defined as the percentage of total surface area covered by the small-particle additive. In the experiments (Berardi *et al.*, 2010) the surface area coverage studied was 85%.

The following method was used in the simulations to reach a similar total surface area coverage as in the experiments (Berardi *et al.*, 2010). First, a box of 120 mm × 120 mm is constructed using the infinite plane geometries now available in `pkdgrav` (see Chapter 2). Four infinite planes, two with normal vectors in the positive and negative x-directions and two with normal vectors in the positive and negative y-directions, form the sides of the box. One infinite plane with normal vector in the z-direction forms the base of the box.

The monolayer of particles at the bottom of the box is created in several steps. First, several layers of particles with radius (Rp) 1.5 mm are generated starting at a height of approximately 15 mm (10 Rp) above the base of the box (measured from the base of the box to the center of the particles in the bottom layer). The particles in each layer are evenly distributed in the x and y directions with a spacing of 4.5 mm (3 Rp) between the centers of the particles in each direction. The z position of each particle is randomly generated within the limits of $\pm 1/Rp$ from the mean layer height. This is to prevent all particles in each layer from impacting the base of the box simultaneously, which is unrealistic (it would be impossible in an experiment to drop all the particles from the same height exactly simultaneously). The number of particles generated depends on the desired final surface area coverage and small-particle concentration. Due to the fixed inter-particle spacing there are 625 particles in each generated, and dropped, full layer. However, in order to have the correct number of particles in the box, the last layer dropped into the container is often a partial layer. The particle

layers are formed one at a time by generating rows of particles from one side of the box to the other. All the particles are given a small initial velocity on the order of 1 mm s^{-1} in the x and y directions but not in the vertical z direction. Gravity (acceleration in the vertical z direction) is 1 g (where g = 9.8 m s^{-2}).

At the start of the simulation the generated layers of particles are allowed to fall into the box, under gravity (with no inter-particle gravity). The simulation runs until the mean vertical component of the particle translational velocity drops below a threshold of 0.1 mm s^{-1}, i.e., the particles continue to move around the bottom of the box but are no longer bouncing in a significant way. The timestep used for the dropping phase of the simulations is such that for a particle starting from rest and falling under gravity it would take approximately 30 timesteps for it to drop one particle diameter.

A fraction of large particles are then replaced with smaller ones (radius 1 mm). In these tests the small-particle concentration was a configurable parameter that was explored and thus the fraction of large particles replaced depends on the desired final small-particle concentration. As the total surface area coverage remains constant, the greater the desired final small-particle concentration, the greater the number of large particles that are replaced with smaller ones. The new particles have the same position and velocity coordinates as the particles they replace but the particle radius and particle mass are updated accordingly in order to maintain a constant particle density.

A sixth infinite plane is then introduced into the simulation to provide confinement in the vertical z direction (i.e., a lid is put onto the box). This infinite plane is placed parallel to the base of the box at a height of 0.1 mm above the top surface of the largest particles. This confinement allows the particles to move horizontally but prevents the particles from forming a second layer.

The four walls in the x and y directions are then moved inwards gradually with a speed of ~2 mm s^{-1} until the box reaches a size of 100 mm × 100 mm. During this movement the box remains centred on the origin. This was found to be an effective method of increasing the particle surface coverage while avoiding the problem of forming a second layer of particles. The particles are then allowed to settle in the box with all walls stationary until they reach a steady state with an equilibrated horizontal velocity. This horizontal velocity is small in magnitude but not zero due to the initial setup. This is in fact necessary to ensure that collisions occur between particles in the next (vibrating) phase. If this wasn't the case the particles would simply bounce up and down in place and never collide.

Finally, the base wall and confining lid are made to vibrate in phase. Just as in the real experiments (Derardi *et al.*, 2010), the maximum acceleration of the vibration is 4.5 g and the frequency is 125 Hz. The amplitude of the oscillations is thus 7.15 × 10^{-2} mm. During the vibrations the downward acceleration due to gravity remains constant at 9.8 m s^{-2} and there is no inter-particle gravity. For this phase of the simulations the timestep is reduced to resolve each particle-particle and particle-wall

collision. During the vibration phase a particle starting from rest and falling under gravity would take approximately 130 timesteps to drop one large-particle diameter.

Fig. 3.5 shows ray-traced images of an example simulation during the vibration phase. The six infinite planes (walls) are all made completely transparent in order to facilitate observation of the particles.

Chrome steel ball bearings that were very accurate in size and shape (i.e., spheres of 3.000 ± 0.025 mm and 2.000 ± 0.025 mm diameter with a shape deviating from spherical by no more than 10^{-3} mm in any direction) were used in the laboratory experiments and, therefore, in the simulations an exact bimodal size distribution is used (i.e., spherical particles of exactly 3.0 mm and 2.0 mm diameter). The particles in the simulations have a density slightly less than the density of the experiment ball bearings (7000 kg m^{-3} compared to 7900 kg m^{-3}). However, the particle accelerations resulting from the combination of shaking and gravity are independent of particle mass and thus density. A normal coefficient of restitution of 0.5 (where 1.0 would mean completely elastic collisions) and a tangential coefficient of restitution of 0.9 (where 1.0 would be completely smooth), are arbitrarily chosen for all the particles in the simulation, meaning there is some dissipation of energy. These are nominal values used as an example, although a larger parameter space is explored later in Section 3.5.5. For a full list of all of the differences between the experiment and the simulations see Section 3.5.

The walls also have their own configurable normal and tangential coefficients of restitution. The normal coefficient of restitution is set to 0.9 and the tangential coefficient of restitution is set to 0.9 for all of the walls in these simulations. Again these values are chosen arbitrarily and a larger parameter space is explored in Section 3.5.5.

Simulations are made with $3 - 10\%$ small-particle area coverage (for a total surface area of 100 cm^2). The simulated time of the vibration phase is ~40 seconds. The exact conditions of the runs are given in Table 3.2.

As described in Chapter 2, the collisions in our numerical method are always instantaneous and binary. In order for the assumption of binary collisions to be valid the average time between collisions must be longer than the average collision duration. The ratio between these two timescales can be estimated using the soft-sphere method (see Chapter 1) to model the collision. The characteristic collision time (T_{bc}) for a binary collision between two identical particles can be calculated using the following equation from Campbell (2002):

$$T_{bc} = \frac{\pi}{\sqrt{\frac{2k}{m} - \frac{D^2}{m^2}}} \tag{3.1}$$

In this equation k is the *stiffness* used to model the collision (in the normal direction), m is the

particle mass and D is given by:

$$D^2 = \frac{2mk}{(\frac{\pi}{ln\epsilon_n})^2 + 1} \tag{3.2}$$

where, ϵ_n is the coefficient of restitution of the particles (in the normal direction). The mean value that should be used for k can be estimated from:

$$k \approx \mu(\frac{V}{X})^2 \tag{3.3}$$

where, μ is the reduced mass of the system ($m/2$ for a collision with particles of identical mass), V is the mean particle speed and X is the amount of overlap that occurs during the collision. As steel is very hard, X is assumed to be 0.1% of the radius of the particle (this is a very conservative estimate as the actual value may be much smaller than this).

Using the mean particle speed and the coefficient of restitution from the baseline simulations with an overlap (X) of 0.1% of the radius, the binary collision time for a normal collision between two large particles is estimated to be 7.8×10^{-5} seconds and, between two small particles it is estimated to be 3.3×10^{-5} seconds. As most collisions will be off axis and/or between particles of two different sizes, the real collision times between particles are likely to be much shorter than this. Also, if the overlap (X) is smaller than 0.1% of the radius of the particle, then this will also decrease the collision duration.

The time between collisions during the vibration phase can be estimated by looking at the collisions in the simulations. Taking the baseline 10% small-particle concentration simulation as an example there are approximately 1.6 million particle - particle collisions occurring every second. Assuming every collision involves two particles and all 1352 particles have a similar collision frequency this gives an average time between collisions involving a given particle of approximately 4×10^{-4} seconds.

As the time between collisions (4×10^{-4} seconds) is at least an order of magnitude greater than the collision duration ($<8 \times 10^{-5}$ seconds) the assumption of binary collisions seems to be reasonable. This demonstrates that even at high densities binary collisions can dominate in excited granular systems and provides further support for the choice of numerical method.

3.5 Analysis and comparison with experiments

Before a detailed comparison is performed between the experimental and simulation results it is important to point out some clear differences between the numerical simulations and the original experiment of Berardi *et al.* (2010). Note that the experiment was performed well before the current

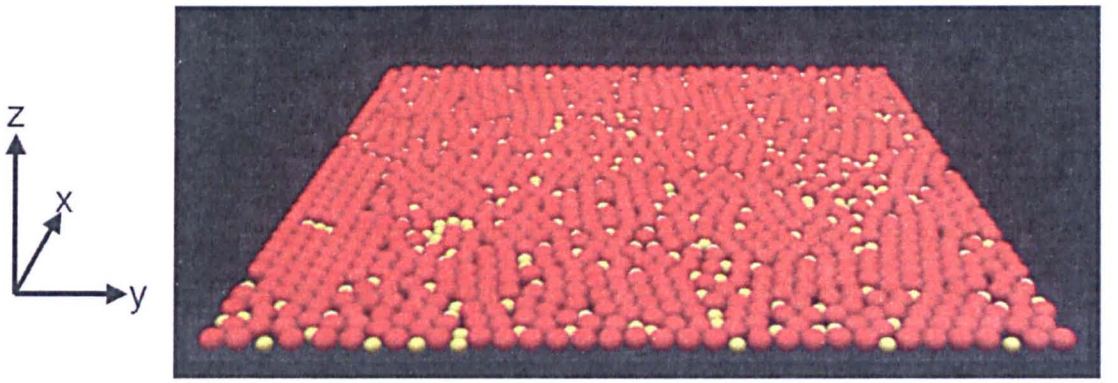

(a)

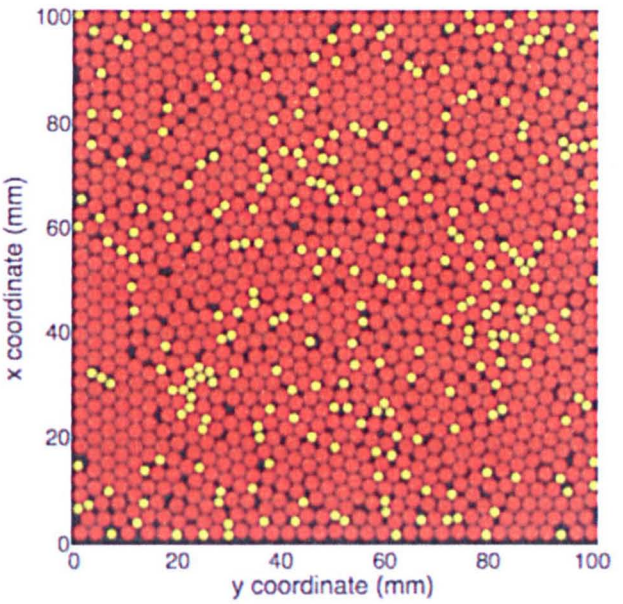

(b)

Figure 3.5: **Images of shaking simulations** - Ray-traced images of a simulation during the vibration phase as seen from (a) ~45° and (b) above. Particles are contained in a box of 100 mm × 100 mm. There is a confining lid in the z-direction 0.1 mm above the largest particles (Fig. 3.2). All walls are made transparent to facilitate observation. There are two sizes of particles: 1.5 mm radius (red) and 1 mm radius (yellow). The total surface area coverage is 83.63%. The 1 mm radius particles cover 8.50% of the entire container surface area (i.e., 8.50% of 100 mm^2), which is equivalent to 10.16% of the total covered surface area (i.e., 10.16% of 83.63 mm^2).

Table 3.2: The conditions of the numerical simulations. The normal coefficient of restitution of the particles is 0.5 (where 1.0 would mean completely elastic collisions) and the tangential coefficient of restitution is 0.9 (where 1.0 would be completely smooth).

Small particle area coverage (% of total covered surface area)	Total surface area coverage (%)	Total number of particles in test area
2.91	83.76	1247
4.84	83.85	1277
6.89	83.85	1307
10.16	83.63	1352

study was defined and, therefore, its set-up was not designed with the perspective of a comparison with simulations.

An extensive list of these differences is provided in Table 3.3 and here a few of the key differences between the experiment and simulations are highlighted. Firstly, and possibly most importantly, are the different boundary conditions. In the experiment a large circular container is used and a rectangular area (the "test-area") of particles in the center is imaged and subsequently analysed. However, in the numerical simulations a square container was used and the motions of all the particles in the container were analysed. The circular container was not adopted in the simulations due to the difficulties involved in increasing the particle packing density to the correct level (cylinders with radius changing in time are not currently supported in `pkdgrav`).

Also, in the experiments the particles were not homogeneously distributed, probably due to slight inhomogeneities in shaking amplitude across the plate. This caused particles, particularly the small ones, to move closer to the edges of the field of view rather than stay homogeneously distributed across the container as in the simulations. Another factor that may have contributed to the inhomogeneity of particle distribution in the experiments is that there is a small amount of horizontal movement associated with the vertical shaking whereas in the simulations the shaking axis is constrained exactly to the vertical direction. Unfortunately, we cannot currently implement more than one vibration mode per wall with `pkdgrav`.

Nevertheless, while there are some clear differences between the experiment and simulations, the overall dynamics of the experiment should be reproduced with the numerical simulations either qualitatively or, where appropriate, quantitatively.

3.5.1 Calculation of grains and grain boundaries

Densely packed granular systems are found to organise themselves into regions of crystallisation (grains) as well as regions of disorder (grain boundary (GB) regions) (Berardi *et al.*, 2010).

To determine the locations of grains and regions of disorder, the simulation data is analysed using exactly the same algorithm as used for the analysis of the experiments (Berardi *et al.*, 2010). This algorithm calculates the orientational order of the system by employing the bond orientational order parameter ψ_N for each particle. The local value of ψ_N is given by (Jaster, 1999; Reis *et al.*, 2006):

$$\psi_{N,i} = \frac{1}{N_i} \left| \sum_{j=1}^{N_i} e^{i6\Theta_{i,j}} \right| \tag{3.4}$$

where N_i is the number of nearest neighbours of particle i and Θ_{ij} is the angle between particles i and j and an arbitrary but fixed reference. In the analysis of the experimental and simulation data

Table 3.3: Detailed list of differences between experiments and simulations

PARAMETER	EXPERIMENT	SIMULATION
Total surface area	670.1 cm^2	100.0 cm^2
Surface area considered in analysis	214.6 cm^2	100.0 cm^2
Shape of container	Circular (292 mm diameter)	Square (100 mm × 100 mm)
Shape of area considered in analysis	Rectangular (169 mm × 127 mm)	Square (100 mm × 100 mm)
Shaking axis	In the z-direction with a small acceleration (<0.5%) in the horizontal (x-y) plane	In the z-direction
Particle sizes	Diameter tolerance of 0.0254 mm	Exactly 2.0 mm or 3.0 mm diameter
Particle density	7900 kg m^{-3}	7000 kg m^-3
Particle shapes	Uncertainty of 10^{-6} m	Exactly spherical
Small-particle concentration	Calculated by weight for the entire container	Calculated exactly
Movement of walls during shaking	Entire container shaken so all container walls shaken in phase	Top and bottom walls shake in phase, side walls are stationary
Bottom wall shape	Slightly convex	Exactly planar

the six nearest neighbours of each particle are considered therefore, in this case, $N = N_i = 6$. From this point forward the bond orientational parameter will, therefore, be referred to as ψ_6. As a value of 1 for ψ_6 implies hexagonal packing, deviations of ψ_6 from 1 can therefore be taken as a measure of disorder. The smaller the value of ψ_6, the less jammed the system and thus the greater the local disorder. This measure of disorder is then used to locate the grain boundary regions. As in the experiments a value of ψ_6 <0.7 is used to define the grain boundary regions. These regions of order and disorder are a consequence of the initial particle packing in the system and not a result of the shaking behaviour.

The packing arrangements of particles during the numerical simulations are found to correctly reproduce such regions of crystallisation and regions of disorder. This is demonstrated in Fig. 3.6 that compares the degree of local order (i.e., ψ_6) at the position of each particle for both the laboratory experiments and numerical simulations when the small-particle concentration is 3% and 10%. A region of 90 mm × 90 mm has been extracted from both the simulations and experiments to examine the ordering at the same scale. The dark blue colour signifies near-hexagonal particle packing with ψ_6 close to 1. Green and red colours correspond to more disordered packing with ψ_6 <0.7 (i.e., GB regions). In the crystallised regions the hexagonal lattice is almost defect-free.

It is clear that the simulations reproduce the experimentally observed collective ordering; regions of crystallisation and less ordered grain boundary regions. There are, however, some differences between

the experimental and simulation particle arrangements: in the experiments the crystallised regions are randomly oriented but in the simulations the crystals are all aligned.

On closer inspection it is also evident that most of the crystallised regions in the simulations are aligned from the beginning (Fig. 3.7 shows the initial particle locations in the 3% and 10% small-particle concentration simulations). Initially the shape of the boundaries was not considered to be important in such an investigation but it is possible that, given the rigid square boundary conditions in the simulations, the system is acting like one globally ordered single domain, which extends across the entire container. If this is the case, it could be likened to the investigations of Olafsen & Urbach (2005) who show that for spheres arranged in a hexagonal lattice at low accelerations the particle positions fluctuate continuously but no particle rearrangements are observed. As the amplitude of the acceleration is increased the spheres begin to explore all of the volume available to them and thus the density of topological defects increases dramatically. To investigate further the origin of the aligned crystals, the small-scale particle rearrangements as well as the effect of boundary conditions, further work must be done. This is not, however, in the scope of the current validation excercise.

To take a closer look at the particle dynamics, the particle rearrangements over time have been investigated. Plotted in Fig. 3.8 are the trajectories of the particles in the 10% small-particle concentration simulation over the duration of a simulation. The positions of all the particles are plotted every 1/125 seconds to form the super-imposed image. The particles and container are plotted to scale with the small particles in red and the large particles in blue. Regions of string-like cooperative behaviour can be seen on the left-hand side of the container but there is a surprising lack of overall particle rearrangement.

It has been experimentally observed that mean grain boundary area increases as a function of small-particle concentration and, therefore, the amount of crystallisation decreases with increasing small-particle concentration (Berardi *et al.*, 2010). The numerical simulations have also reproduced this result. This can be demonstrated by comparing the regions of crystallisation (grains) and grain boundary regions in the 3% small-particle concentration simulation in Fig. 3.6(b) to those of the 10% small-particle concentration simulation in Fig. 3.6(d). The total area of crystallisation has decreased in Fig. 3.6(d) while the grain boundary regions have greatly increased in size. This is demonstrated more clearly in Fig. 3.9 that shows the trend of increasing grain boundary area with increasing small-particle concentration in both the laboratory experiments and the numerical simulations. The grain boundary coverage is calculated many times over the duration of each simulation and experiment. The mean value is plotted along with the standard deviation of the mean. One difference that can be noted between the simulations and the laboratory experiment is that the fraction of the total area covered by grain boundaries is consistently greater in the simulations than in the laboratory

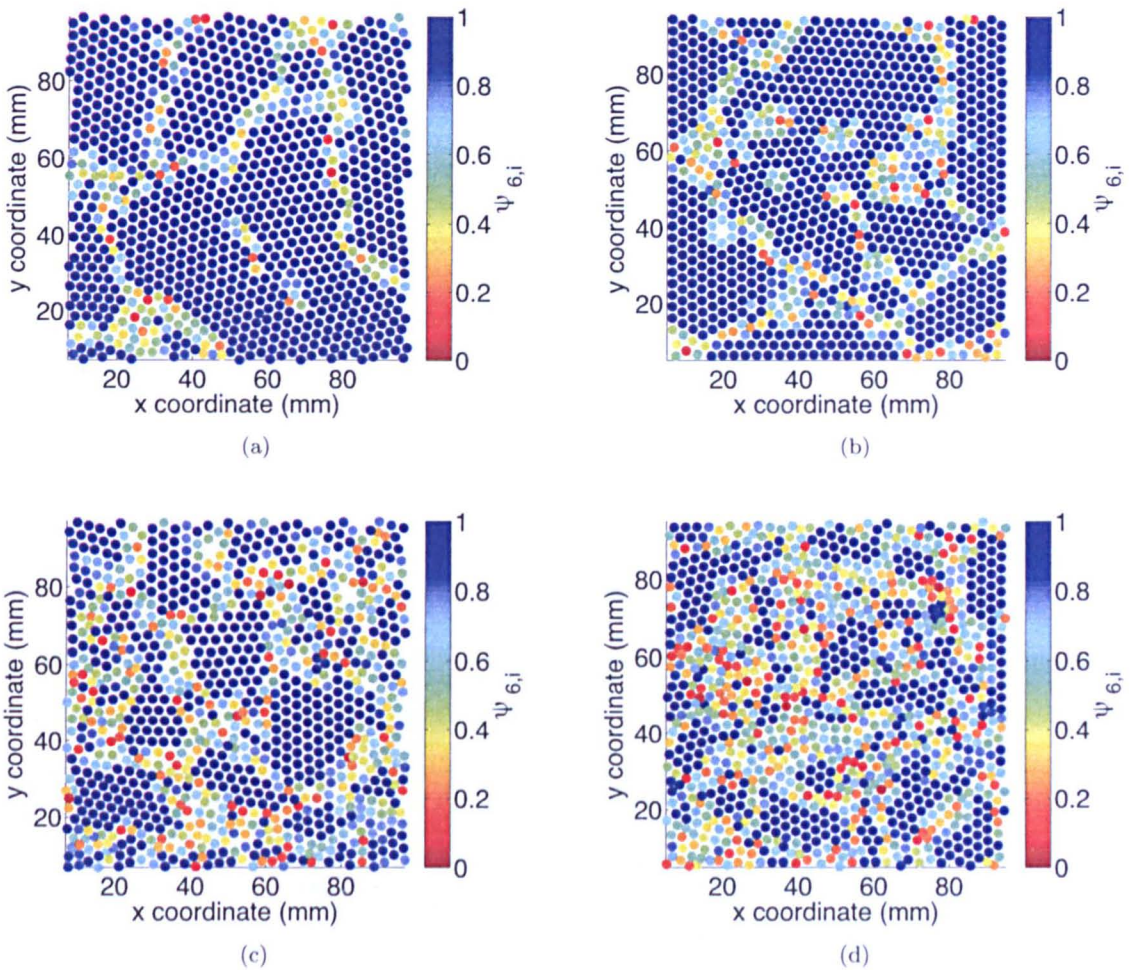

Figure 3.6: **Comparisons of collective ordering in experiments and simulations** - (a) 3% small-particle concentration experiment, (b) 3% small-particle concentration simulation, (c) 10% small-particle concentration experiment, (d) 10% small-particle concentration simulation. Grain Boundary (GB) regions determined using the algorithm of Berardi *et al.* (2010). The dark blue colour signifies near-hexagonal particle packing with ψ_6 close to 1. Green and red colours correspond to more disordered packing with ψ_6 <0.7 (i.e., GB regions). See Eq. (3.4) for the definition of ψ_6. Particles are not drawn to scale.

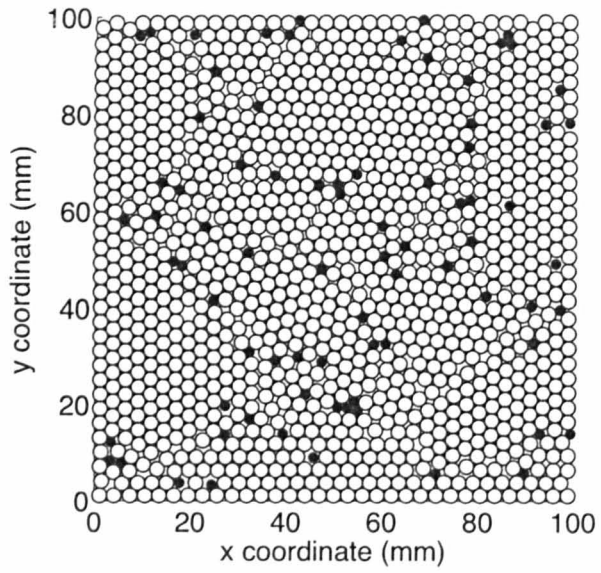

(a)

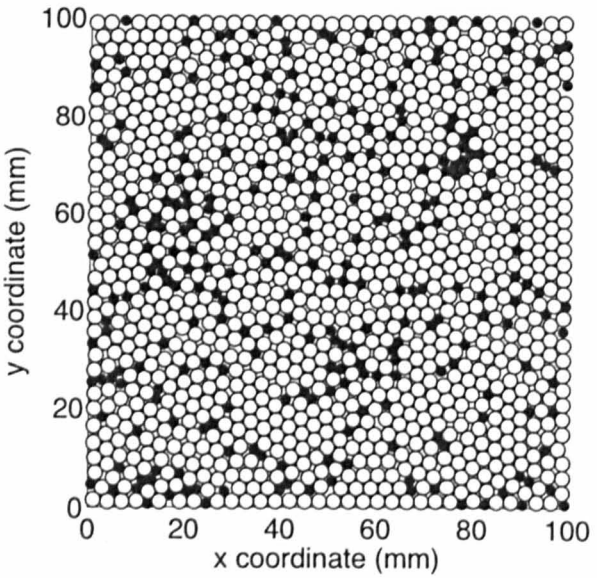

(b)

Figure 3.7: **Particle arrangement at the start of simulations.** - The locations of all particles at the start of the vibration phase of the numerical simulations when the small-particle concentration is (a) 3% and (b) 10%. Large (3 mm) particles are white, small (2 mm) particles are black. Figures are drawn to scale. In both figures regions of crystallisation can be seen.

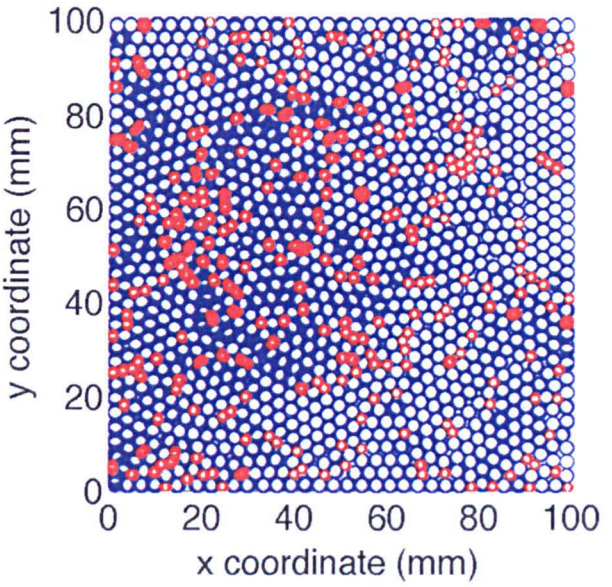

Figure 3.8: **Particle rearrangement during simulations.** - A super-imposed image of all the particle positions at every 1/125 seconds, plotted in this way in order to see the overall displacement of each particle. The particles and container are drawn to scale. Large (3 mm) particles are blue and small (2 mm) particles are red. The results shown are for a numerical simulation using 10% small-particle concentration.

experiments. The square boundary conditions may be partially responsible but the more probable explanation is that, as described above, in the laboratory experiments the particles (particularly the small ones) have a tendency to move to the edge of the container (due to off-axis shaking and the slight inhomogeneities in shaking amplitude across the container). This means that the experimental small-particle concentration in the test-area is probably not exactly the same as the small-particle concentration in the entire experimental container.

It was also found that, similar to the experiments, the total grain boundary area and grain boundary locations remain almost constant in the simulations throughout the duration of the shaking and the small particles are almost all localised in grain boundary regions (Fig. 3.10).

3.5.2 Particle velocities

In numerical simulations of granular material, instantaneous particle velocities are known at each simulation timestep thus giving a very accurate measure of the mean particle velocity at any moment in time. However, as will be explained below, since particles collide more frequently in a dense granular material than their position can be imaged, and since position measurements have inherent uncertainty, comparing the true velocity from simulations with particle velocities extracted from image sequences is not meaningful in a dense system (Xu *et al.*, 2004). Consequently, particle velocity cannot be used as a tool to directly compare the dynamics of a simulated granular ensemble to the dynamics of a

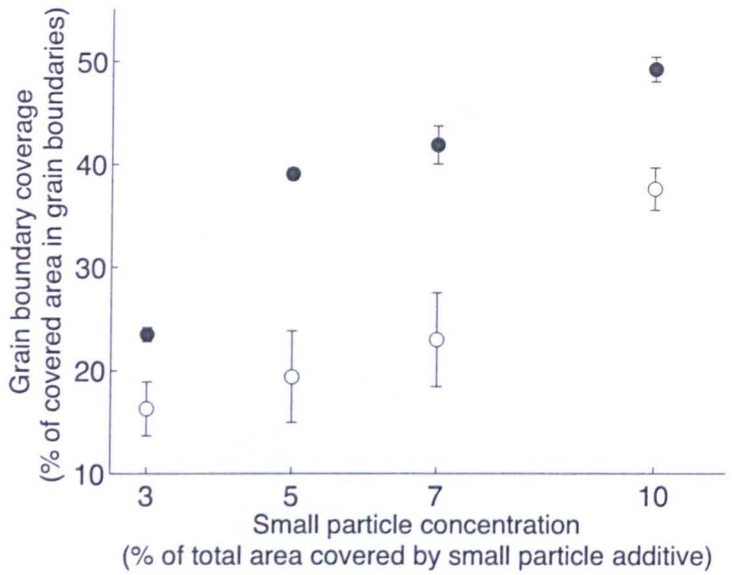

Figure 3.9: **Comparison of grain boundary area coverage in simulation and experiment** - The fraction of the covered surface area that is grain boundaries (i.e., ψ_6 <0.7) against small-particle concentration for the laboratory experiments (white, open circles) and the numerical simulations (black, filled circles). The grain boundary coverage is calculated every 0.08 seconds over the duration of the numerical simulation and the mean value is plotted along with the standard deviation of the mean. The experimental data is from Berardi *et al.* (2010). The quantitative differences between experimental and numerical simulation results are discussed in Section 3.5.1.

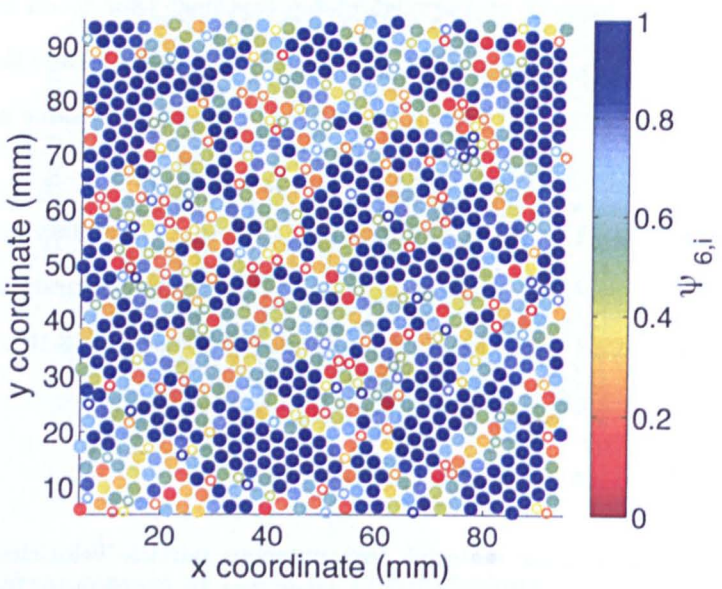

Figure 3.10: **Small particle location** - The degree of local order (i.e., packing density) at the position of each particle in a numerical simulation when the small-particle concentration is 10%. Grain Boundary (GB) regions are determined using the algorithm of Berardi *et al.* (2010). The dark blue colour signifies near-hexagonal particle packing with ψ_6 close to 1. Green and red colours correspond to more disordered packing with ψ_6 <0.7 (i.e., GB regions). See Eq. (3.4) for the definition of ψ_6. The small (2 mm) particles are all drawn with an open circle. The laboratory experiment results are not shown here, but in both the experiments and the numerical simulations the small particles are mostly located in grain boundaries.

laboratory experiment. Despite this, the relative particle speeds within a simulation or experiment can be used as a diagnostic to infer further details about the location and behaviour of specific particles. This is discussed in further detail at the end of this section.

To calculate experimental particle velocities as accurately as possible the particles are imaged at a high frame rate and the resulting particle velocities are calculated based on the particle positions in each consecutive image. However, the accuracy of the experimentally determined velocity will depend on the frame rate and resolution of the imaging, and the subsequent particle tracking. Further complications are introduced when we consider that even with very precise imaging and subsequent particle tracking there are inherently errors in any experiment. In order to extract meaningful information from the experimental data the positions of the particles must be smoothed over time. Without performing such smoothing the data would be dominated by noise. However, the more smoothing that is applied to the particle position data the more the resulting velocities are reduced.

To demonstrate the effect of smoothing, Fig. 3.11 shows the horizontal speed of one particle in a numerical simulation as a function of time over a period of 0.25 seconds. The three curves shown are for the same particle but calculated using three different methods of sampling and analysis; the first shows the instantaneous particle horizontal speed output directly from the numerical simulations, the second shows the horizontal particle speed calculated using the position coordinates of the particle sampled at 125 fps and finally the third shows the horizontal particle speed calculated using the position coordinates of the particle sampled at 125 frames per second (fps) and smoothed over 0.1 seconds (the technique used in the analysis of the experimental data; Berardi *et al.*, 2010). The horizontal particle speed was also calculated using the position coordinates of the particle sampled at 1250 fps but is not shown because it is very similar to the instantaneous particle speed but with a smaller magnitude. The values in Table 3.4 highlight even further how great the differences in the mean particle horizontal speed can be depending on the method of sampling and analysis.

In conclusion, as the experimental velocities can never be known exactly in a dense material where the collision rate between particles exceeds the imaging speed, or the distance between collisions is smaller than the imaging resolution, the instantaneous numerical simulation velocities can never be directly compared to experimental velocities. Even the comparison of velocities sampled at the same frame rate and analysed using the same method is unlikely to result in an accurate comparison due to inherent experimental and tracking uncertainties that do not exist in numerical simulations and that are hard to artificially introduce in simulations.

Possible alternative solutions to allow velocity comparisons could be considered; for example, if it was possible to accurately quantify the level of noise in the experiments then noise could be introduced to the simulation data. An alternative could be to use the experimental particle-tracking algorithm to

track the particle motion in the simulations i.e., ray-traced images of the simulation could be provided as input to the particle tracking algorithm. However, this approach is associated with new problems because the particle tracking algorithm is designed to track real three-dimensional spherical particles. New sources of error due to poor tracking accuracy are likely to be introduced. This is discussed in more detail in Chapter 5 and Appendix B.

Nevertheless, the relative particle velocities within a simulation or experiment can be used as a diagnostic to infer further details about the location and behaviour of specific particles. It was found, by investigating the mean particle velocities in the different regions, that there is a direct link between the particle velocity and the local ordering near the particle. The mean velocity of particles contained in the grain boundaries is much higher than the mean velocity of particles contained in the grains, as expected. Therefore, the velocity of a particle in such a dense shaken system will give an indication of whether it is trapped within a crystallised grain or found within a disordered grain boundary region.

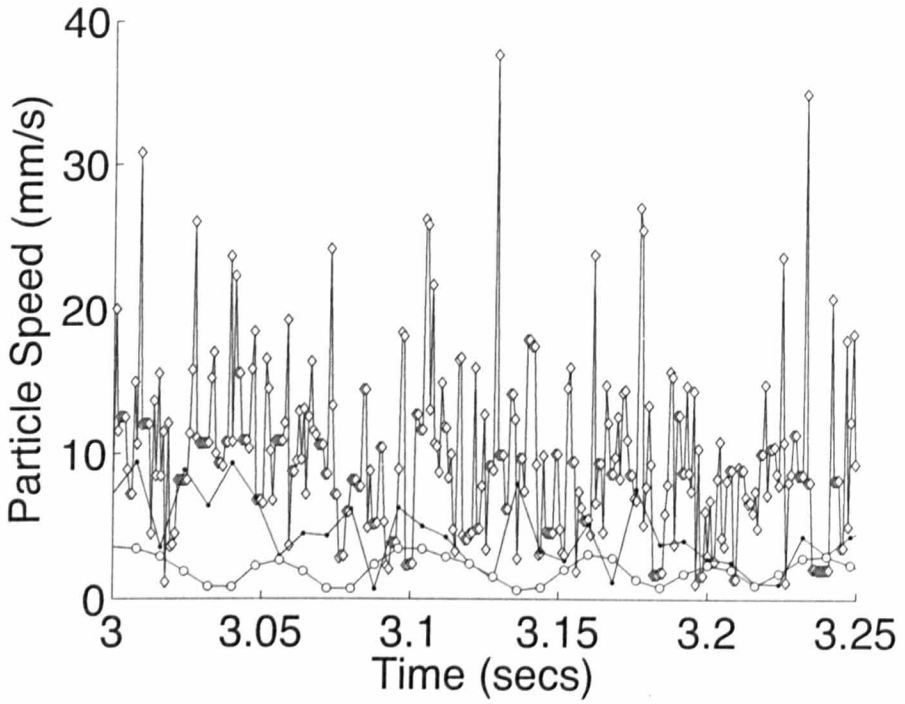

Figure 3.11: **Comparison of different methods of velocity calculation** - The speed of one particle in a numerical simulation over a period of 0.25 seconds, calculated using three different methods: Method A (white diamonds), Method C (black dots) and Method D (open white circles). See Table 3.4 and text for explanation of the methods.

3.5.3 Calculation of long-term particle displacements

Given the difficulties involved in calculating and comparing short-term particle motion (i.e., particle velocities) a logical step is to consider the long-term particle displacements. This is particularly appropriate for the dynamical system we are trying to model given that it is only at long timescales

Table 3.4: The mean speed of one particle in a numerical simulation during a period of 5 seconds is given for the same particle but calculated in four different ways. Method A calculates the mean horizontal particle speed from the numerical simulation instantaneous velocity outputs. Method B calculates the mean particle horizontal speed using the position coordinates of the particle sampled at 1250 fps. Method C calculates the mean particle horizontal speed using the position coordinates of the particle sampled at 125 fps. Finally, Method D calculates the mean particle horizontal spped using the position coordinates of the particle sampled at 125 fps and smoothed over 0.1 seconds. The error provided is the standard deviation of the mean speed.

Method	Mean horizontal particle speed (mm s^{-1})
A: Instantaneous speed	9.9 ± 5.7
B: 1250 fps sampling	8.5 ± 4.9
C: 125 fps sampling	4.4 ± 2.4
D: 125 fps sampling with smoothing	2.0 ± 1.1

that the complex, collaborative string-like motion should become apparent.

One method for investigating the long-term motion of particles is to consider the mean-squared displacement (MSD) profile of the system. MSD profiles are used in granular physics studies (e.g., Weeks *et al.*, 2000; Xu *et al.*, 2004) but are also extensively used in many different fields of research, for example, in studies of molecular and cell biology (e.g., Fritsch & Langowski, 2010; Mika & Poolman, 2011; Sahl *et al.*, 2010). An MSD plot indicates by what distance a particle has been displaced. The MSD is not the actual distance travelled by the particle (i.e., including all random vibrational motion) but rather the net motion in a given time (i.e., the displacement). Therefore, in the long-time limit the MSD measurements focus on larger distances, where the experimental uncertainties are relatively less important. We note that based on the accuracy of the experimental particle tracking, it can be assumed that once we get to displacements of one pixel or more the MSDs are real and not dominated by errors.

The MSD of a system of N particles is calculated using the following equation:

$$MSD(\tau) = \frac{1}{N}\sum_{i=1}^{N} |(r_i(t+\tau) - r_i(t))|^2 \tag{3.5}$$

where $r(t)$ is the position of particle i at time t, and τ is the time step between the two particle positions used to calculate the displacement.

The shape of the MSD of the shaken system is an indicator of whether the numerical simulations can successfully capture the experimentally observed complex long-term dynamics. There should be three distinct regions of the MSD profile if the dynamics are captured correctly. The MSD curve would be expected to rise initially because the particles exhibit diffusive motion as they wiggle around within the "cages" set up by their neighbours. On short timescales, the particles effectively do not

"notice" the cage and simply diffuse within the cage. On longer timescales, the cage confines their motion and therefore the average displacement cannot increase with increasing measurement time. This leads to a characteristic plateau in the MSD. For long enough times, if the system is not fully jammed, the particles will be able to break out of their cage and rearrange. This leads to a rise in the MSD curve back to a diffusive characteristic. Cage breaking involves larger-scale motion and slower dynamics that are more easily compared between experiment and simulations. Conceptually, the timescale of breaking out of the cage characterises how far from jamming the system is. For the experimental conditions, the cage breaking time was found to be on the order of tens of seconds.

The baseline simulation curve in Fig. 3.12 demonstrates that the particles in the numerical simulations of this shaken system are able to reproduce the predicted dynamical evolution (i.e., the predicted MSD profile). This is the first indicator that, even though a hard-sphere method that resolves only two-body interactions is being used, we are capable of reproducing complex long-term and large-scale collective particle dynamics. The obvious differences in the magnitudes of the experimental and simulation MSD plateau values are likely to be due to pixel noise in particle position detection in the experiments. The plateau of the experimental MSD profile in Fig. 3.12 is consistent with pixel noise (one pixel is equal to 0.264 mm, and thus an average change in apparent particle position of one pixel due to noise would lead to an MSD of order $[0.264\ \text{mm}]^2 = 0.07\ \text{mm}^2$). This means a direct quantitative comparison of the magnitudes of the experimental and simulation MSD plateaus would be unreliable.

Nevertheless, the MSD plots can still be used to qualitatively compare experiments and simulations by looking at the "cage-breaking" timescale. The cage-breaking timescale is defined as the time at which the MSD begins to rise again. This will tell us the timescale that is needed for the jammed particles to escape their cages. Considering the MSD of the baseline simulation in Fig. 3.12 and comparing it to the experimental MSD it can be seen that, even though the magnitudes are different, the simulations capture the correct dynamics of the system because the cage-breaking timescale and the slope of the two MSD curves are very similar.

As mentioned in Section 3.5, in the experiments the small particles have a slight tendency to segregate near the containers walls as a result of off-axis shaking. To verify that this does not influence the experimental MSD profiles in any way, the MSD profiles were recalculated considering only the large particles. Figure 3.13 shows the MSD profiles for all particles, as in Fig. 3.12, and also the MSD profiles for only the large particles. Apart from a small quantitative difference there is no change to the form of the MSD profiles. It can, therefore, be assumed that the slight segregation of small particles near the containers walls in the experiments does not affect the MSD profiles.

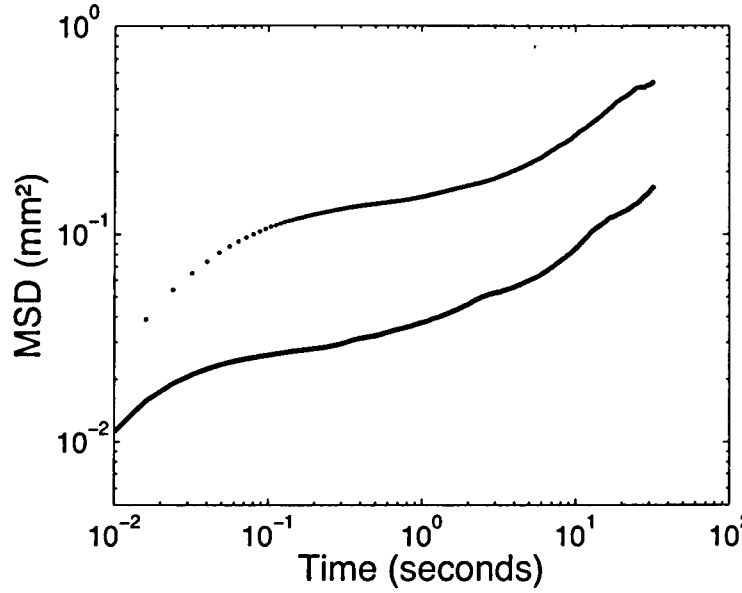

Figure 3.12: **Comparison of simulation and experiment MSD** - The mean-square displacement (MSD) curves for the laboratory experiment with 10% small-particle concentration (dotted line) and for the baseline numerical simulation also with 10% small-particle concentration (solid line). The shape of the MSD curve for the baseline simulation is very similar to the shape of the laboratory experiment MSD curve. The large magnitude discrepancy between experimental and simulation MSD curves is probably due to experimental measurement error (see Section 3.5.3).

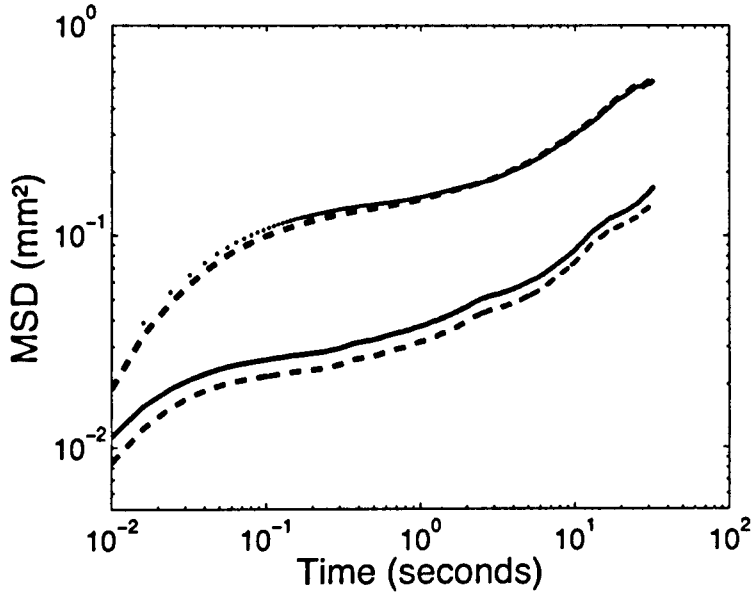

Figure 3.13: **Influence of small particle segregation on MSD profiles** - The mean-square displacement (MSD) curves are shown for the laboratory experiment with 10% small-particle concentration (dotted line) and the baseline numerical simulation (solid line) also with 10% small-particle concentration. The MSD profiles calculated using only the large particles are shown as the thick dashed lines.

3.5.4 Calculation of string-like collective motion

As previously mentioned in Section 3.5.1, the behaviour of caged motion means that a particle is always surrounded by the same neighbours. Jammed granular systems thus exhibit a characteristic timescale in which particles undergoing caged motion escape their cage (Aichele *et al.*, 2003; Donati *et al.*, 1998; Zhang *et al.*, 2009). This mean time to escape defines a timescale over which string-like motions should be observable. Likewise, as described in Section 3.5.3, the same sorts of ensembles also exhibit a characteristic mean-squared displacement profile: over short (<1 second) timescales motion is diffusive, over longer timescales (seconds) displacement is minimal and over long timescales (10s of seconds) displacement is once again diffusive. The characteristic length scale, as introduced in Section 3.3, is a function of this diffusivity and the characteristic time (provided by the statistics of motion). Particles whose displacement is greater than that characteristic length scale over the characteristic time are identified as mobile particles. Some of the mobile particles are seen experimentally to exhibit cooperative motion with a string-like appearance (granular strings).

The presence of mobile particles and cooperative string-like motion in the simulations were confirmed using the same algorithms as for the experiments of Berardi *et al.* (2010). The timescale associated with cage-breaking, t^*, is given by the location of the peak of the non-Gaussian parameter $\alpha_2(\tau)$. This non-Gaussian parameter, plotted in Fig. 3.14 for the baseline simulation with 10% small-particle concentration, is calculated using the following equation,

$$\alpha_2(\tau) = \frac{1}{2}\frac{MFD(\tau)}{[MSD(\tau)]^2} - 1 \tag{3.6}$$

where the MSD of a system of N particles is calculated using Eq. (3.5) and the mean displacement to the fourth power, MFD, is given by,

$$MFD(\tau) = \frac{1}{N}\sum_{i=1}^{N} |(r_i(t+\tau) - r_i(t))|^4 \tag{3.7}$$

where $r(t)$ is the position of particle i at time t, and τ is the time step between the two particle positions used to calculate the displacement.

Next, the van Hove correlation function of the system at t^* (i.e., $G(r, t^*)$) is calculated and compared to a purely diffusive system i.e., to particles undergoing random walk motion. The van Hove correlation function is a space-time correlation function which gives the probability of finding a particle at position r at time $t = t^*$, given that there was a particle at the origin at time $t = 0$ (Hopkins *et al.*, 2010). For a set of N particles with time-dependent position coordinates $r_i(t^*)$ the van Hove correlation function is defined as follows:

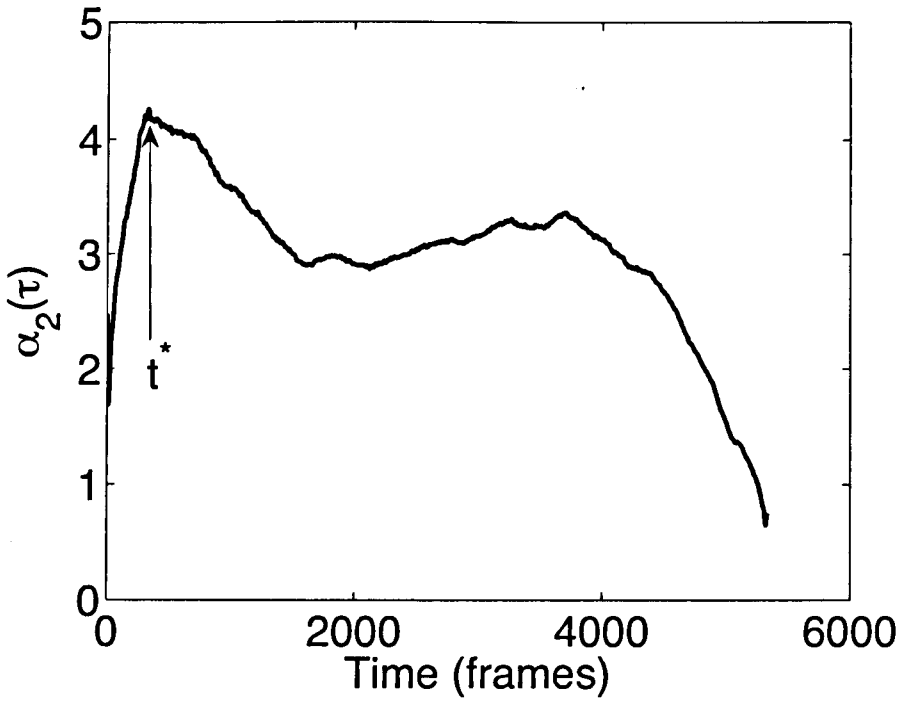

Figure 3.14: **The non-Gaussian parameter** - The non-Gaussian parameter $\alpha_2(\tau)$ as defined in Eq. (3.6) is plotted for the baseline simulation with 10% small-particle concentration. The peak of this curve gives the characteristic timescale associated with cage-breaking, t^*. For this example $t^* = 322$ frames.

$$G(r,t^*) = \frac{1}{N}\left\langle \sum_{i=1}^{N}\sum_{j=1}^{N} \delta(r + r_j(0) - r_i(t^*)) \right\rangle \tag{3.8}$$

where $\langle . \rangle$ represents an ensemble average and $\delta(.)$ is the three-dimensional Dirac delta function.

The van Hove correlation function $G(r,t^*)$ is plotted in Fig. 3.15 for the baseline simulation with 10% small-particle concentration (dashed line). This is compared to the profile that would be expected from a purely diffusive system i.e., for particles undergoing random walk motion (solid line). The intersection of these two curves gives a length-scale r^*, which is used to identify mobile particles: particles moving a distance greater than r^* in a time interval t^* are mobile.

From the mobile particles, the subset that are also members of strings are then determined. Consider two mobile particles i and j, at times t and $t + t^*$. If particle i at $t + t^*$ has moved into particle j's position at t (or vice versa) then the two particles are considered part of the same string. Of course, particle i will rarely occupy exactly particle j's original position, so a cut-off distance, Δ_c, is defined, which is how close particle i has to be to particle j's position. For historical reasons, this Δ_c is chosen to be 0.6 times a large particle diameter (Donati *et al.*, 1998). It should be noted that the absolute values of the average number of strings and string length are dependent on one's choice of the value of Δ_c. However, the overall *trend* in these parameters with respect to particle concentration

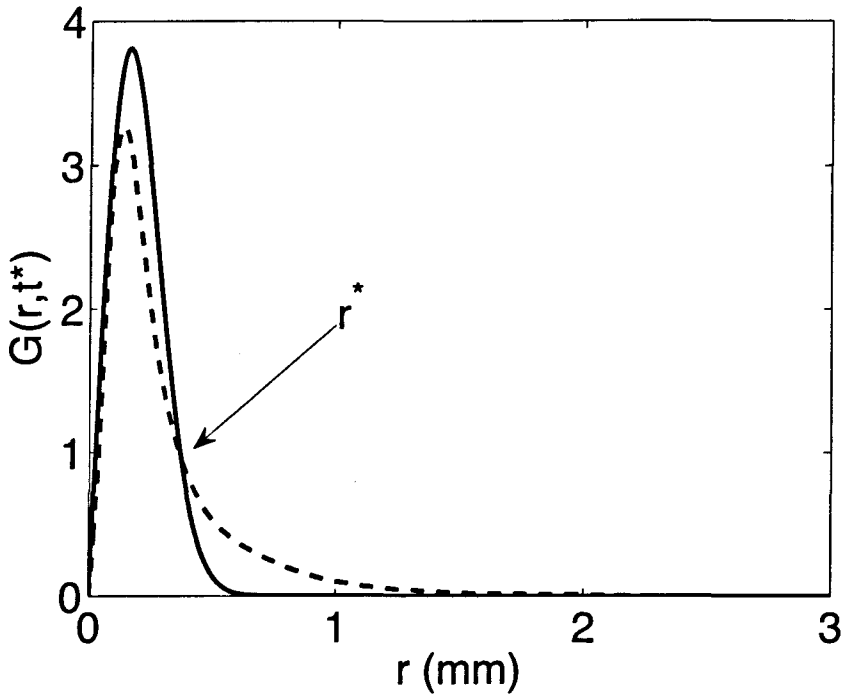

Figure 3.15: **The van Hove correlation function** - The van Hove correlation function $G(r, t^*)$ as defined in Eq. (3.8) is plotted for the baseline simulation with 10% small-particle concentration (dashed line). Also shown is the profile that would be expected from a purely diffusive system i.e., for a particle undergoing random walk motion (solid line). The intersection of these two curves gives a length-scale r^*, which is used to identify mobile particles. For this example $r^* = 0.37$ mm.

is insensitive to the exact choice of Δ_c.

As in the experiments, the granular strings were located in the grain boundary regions and not within the grains. The number of granular strings at a given time during the simulations and the average string length (in number of particles) were also analysed for each small-particle concentration (Figs. 3.16 and 3.17). It was experimentally observed that as the concentration of small particles is increased, the scale of the cooperative motion also increases, i.e., the number and size of the granular strings increase with increasing small-particle concentration (Berardi *et al.*, 2010). The numerical simulations reproduce the correct dependence on small-particle concentration, with both the number and length of granular strings increasing with small-particle concentration.

The experimental and simulated systems were not the same size and thus do not contain the same number of particles. In order to quantitatively compare the average number of granular strings detected per timestep, the number of strings detected is normalised by dividing by the surface area of the experiment or simulation. Figure 3.16 demonstrates that the normalised average number of granular strings detected in the numerical simulations does show the correct dependence on small-particle concentration, i.e., the larger the concentration of small particles, the more granular strings are detected. It must be noted that the magnitudes of the normalised values are not the same and the

gradient of the increase in collective motion with small-particle additive is not exactly the same in the numerical simulations and the experiments. This may be a result of the different boundary conditions, the differences in initial configurations of the grains or may be due to experimental uncertainties that are not taken into account here. However, it is clear that the simulations are behaving as expected, at least qualitatively.

A direct quantitative comparison investigating the average size of the granular strings in the system and how this depends on small-particle concentration can also be performed. It is demonstrated, in Fig. 3.17, that not only do the numerical simulation results show the correct dependence of granular string length on small-particle concentration but they also reproduce almost exactly the average size of the granular strings found in the experiments. This final test demonstrates clearly the capabilities of this adaptation of `pkdgrav` to accurately model the key features of the collective ordering and motion of a shaken granular material in a dense regime.

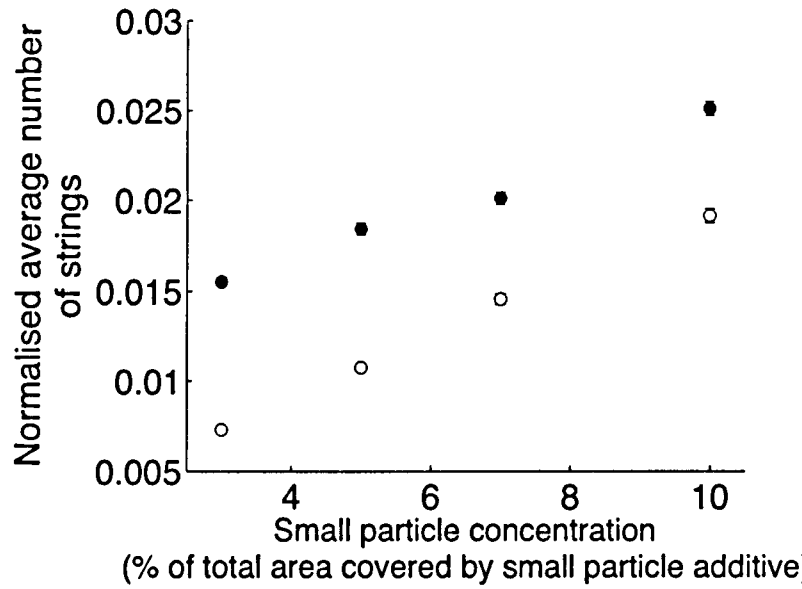

Figure 3.16: **Quantitative comparison of average string frequency** - Average number of granular strings normalised by the surface area considered for the analysis. The laboratory experiment (open circles) and the numerical simulations (solid circles) are plotted as a function of additive concentration, defined as the percentage of total area covered by the small particle additive. The error bars, which are sometimes smaller than the size of the markers, are the normalised standard error of the mean for one experiment at one small-particle concentration. As each experiment measures thousands of strings, it is expected to sample all configurations and so the standard error is reported and not the standard deviation. The experimental uncertainties are not taken into account here.

3.5.5 Sensitivity to simulation parameters

One of the clear advantages of numerical simulations over experiments is the ability to investigate a much wider parameter space, often including environmental conditions or material properties that are not easily investigated experimentally. Conversely, one of the key drawbacks of numerical simulations

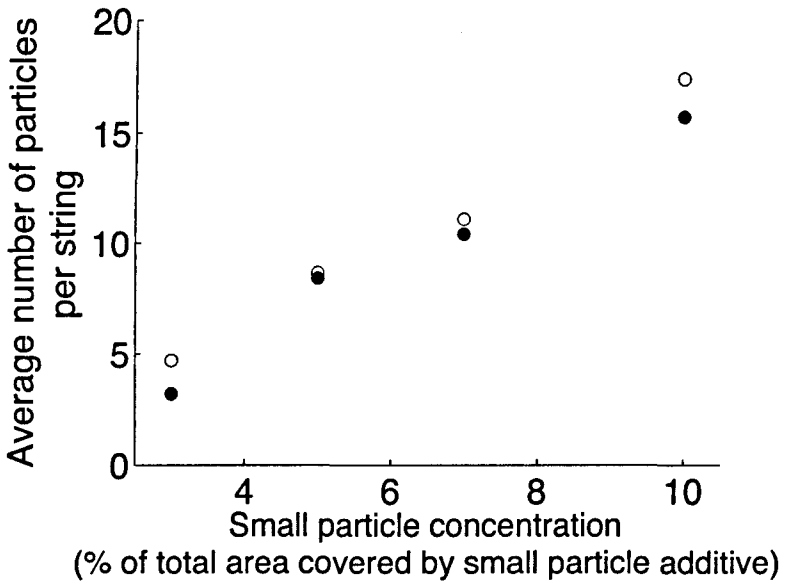

Figure 3.17: **Quantitative comparison of average string length** - Average granular string length in number of particles as a function of additive area coverage, defined as the percentage of total area covered by the small particle additive from the laboratory experiment (open circles) and the numerical simulations (solid circles). The error bars, which are smaller than the size of the markers, are the standard error of the mean for one experiment at one small-particle concentration. As each experiment measures thousands of strings, it is expected to sample all configurations and so the standard error is reported and not the standard deviation. The experimental uncertainties are not taken into account here.

is the capacity to "tune parameters" to sometimes unrealistic values in order to match the desired outcomes.

Here the results of several investigations performed into the sensitivity of the simulations to the internal parameters are presented. These investigations have two aims: firstly, to develop our understanding of how the simulation parameters influence the particle behaviour in such a system, and secondly, to allow us to conclude beyond any doubt that `pkdgrav` can accurately model the correct behaviour and physics of granular materials in a dense regime as a result of shaking and that the results are not random and are in fact closely related to the initial conditions.

Several investigations were performed varying the key internal parameters of the numerical simulations. Given the volume of tests performed, only the important results and trends will be discussed in detail; however, details of all the simulations performed can be found in Table 3.5.5. In each of these tests the simulation set-up was identical to the one described in Section 3.4. The surface area, total surface coverage and initial particle packing configurations were unchanged.

The first set of investigations focussed on the influence of changing the coefficients of restitution of the particles and the walls with particular attention paid to the resulting MSD profiles as a way of interpreting the system behaviour. As discussed in Chapter 2 there are two types of coefficient of restitution: the normal coefficient of restitution (where 1.0 would mean completely elastic collisions)

and the tangential coefficient of restitution (where 1.0 would apply to completely smooth surfaces). By changing these parameters a system can be produced where there is a varying degree of energy dissipation and coupling between particles and between particles and walls. It is noted that for large coefficients of restitution, particularly the normal coefficient of restitution of the particles, there is an increase in the MSD profile only at very long timescales and thus the particles, while losing less energy in each collision, need a longer time to break out of their local cage. Conversely, low coefficients of restitution result in particles breaking out of their cage rapidly (Fig. 3.18). From this it can be concluded that lower coefficients of restitution, i.e., lower particle velocities and more inter-particle and inter-wall coupling, are likely to result in more complex cooperative motion despite the fact that the low coefficients also reduce the overall energy of the system.

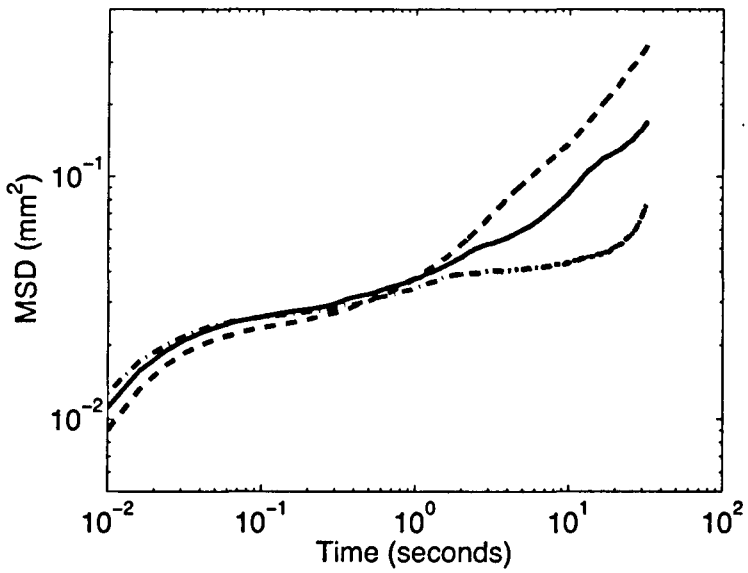

Figure 3.18: **MSD profile demonstrating sensitivity to coefficients of restitution** - The mean-square displacement (MSD) curve for the baseline numerical simulation with 10% small-particle concentration is shown (solid line). Also shown for comparison, and to demonstrate the sensitivity of the simulations to different parameters (see Section 3.5.5), are two extreme 10% small-particle concentration numerical simulation MSD profiles: case A in which the particles break out of their cage very early (dashed line) and case B where the particles remained jammed over much longer timescales (dashed - dotted line). The parameters for cases A and B are, respectively: normal coefficient of restitution of the particles = 0.1 and 0.9; tangential coefficient of restitution of the particles = 0.5 and 0.9; normal coefficient of restitution of the walls = 0.5 and 0.9; tangential coefficient of restitution of the walls = 0.5 and 0.9.

A separate investigation considered the effect of changing the simulation timestep on the system dynamics. The simulation timestep was changed so that for a large particle starting from rest and falling under Earth's gravity it would take 130, 217, 650, 1300 and 6500 timesteps to fall one particle diameter. The data output frequency was kept constant at 125 Hz. It was found that, although the mean particle velocities remain unchanged at all times during the simulations regardless of the timestep, a certain small variation in the MSD is noted (Fig. 3.19). However, the overall MSD profiles

are consistent and qualitatively similar. Additionally, there is no trend in the variations of the MSD profiles with decreasing timestep; as the simulation timestep decreases there is no convergence to a more accurate MSD profile. Therefore, it can be concluded that the variations in MSD profiles, caused by changing the timestep, are most probably random and, as long as the timestep is small enough, they are not critical.

The final investigation of the simulation parameters considered the impact of changing the simulation output frequency, or the rate at which the data is sampled, while keeping the timestep of the numerical simulations constant. As discussed in Section 3.5.2, the data sampling frequency can have a large influence in the measured velocities of the system. First the influence of sampling bias on particle position was considered. The simulation output frequency was varied (125 Hz, 250 Hz, 417 Hz, 625 Hz and 1250 Hz) and the mean particle position (in the vertical z-direction) was calculated and plotted for each output. Note that in order to have an output frequency of 1250 Hz the time step had to be decreased by an order of magnitude. Figures 3.20 and 3.21 show the influence of changing sampling (output) frequency on the results. There is a clear sampling bias at small output frequencies. Unsurprisingly this sampling bias also influenced the velocities of the particles. Figure 3.22 shows an example of this where the mean velocities (z-direction) of all particles are plotted over time during a shaking simulation for three different output frequencies (125 Hz, 625 Hz and 1250 Hz).

Any potential bias in the horizontal positions and velocities of the particles would be much harder to detect given that the particles are not confined to a small space, nor are they accelerated along these axes at a regular frequency. Therefore, to verify if this sampling bias was influencing the results, the MSD profile was calculated for each of the sampling frequencies. It was found that, despite the bias in the vertical positions and velocities, MSD profiles were largely unaffected by the changes in sampling frequency and thus are unlikely to be affected by sampling bias (Fig. 3.23).

However, it must also be noted that simulations are "perfect" in the sense that they do not contain inherent real-world characteristics. Therefore, these types of biases are much more evident than they would be in laboratory experiments. Nevertheless, as the sampling frequency can be chosen with much greater flexibility in numerical simulations, such simulations could be an invaluable tool to help experimentalists determine what level of sampling frequency is necessary to avoid any potential sampling biases.

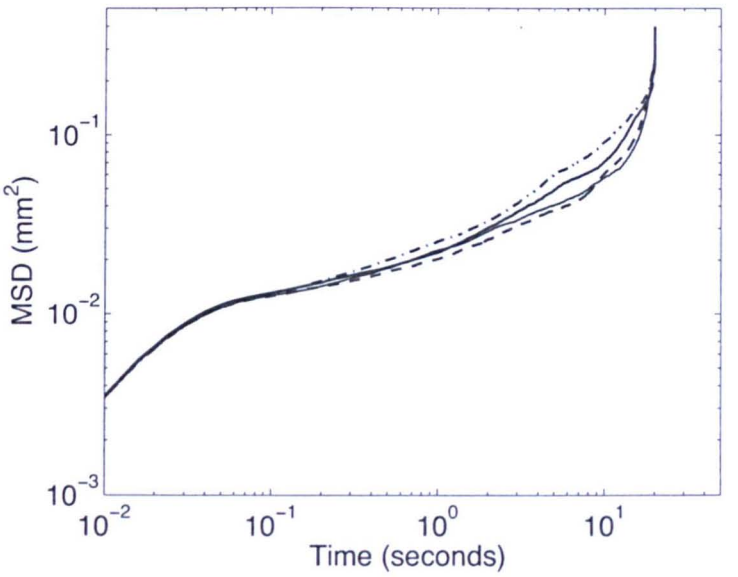

Figure 3.19: **MSD profile demonstrating simulation timestep** - The mean-square displacement (MSD) curves for numerical simulations with 10% small-particle concentration with varying simulation timesteps. The simulation timestep was changed so that for a large particle starting from rest and falling under Earths gravity it would take 130 (thick solid line), 217 (dashed-dotted line), 650 (dashed line) and 1300 (thin solid line) timesteps to fall one particle diameter. This gives simulation timesteps of 2.13 $\times 10^{-5}$, 1.28 $\times 10^{-5}$, 4.26 $\times 10^{-6}$ and 2.13 $\times 10^{-6}$ seconds, respectively. All MSD curves are calculated using particle coordinates output at 125 fps.

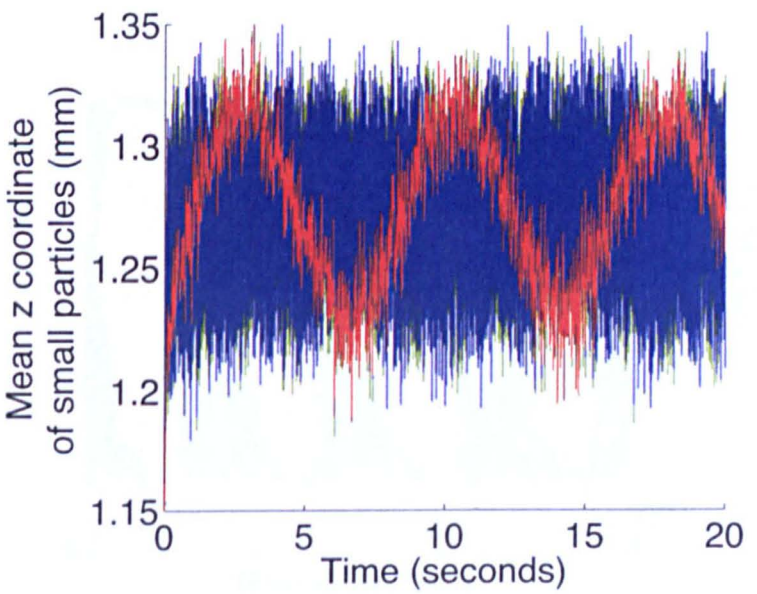

Figure 3.20: **Sampling bias in the z-position of small particles** - The variation in time of the mean small particle position (in the vertical z-direction) is shown for three different sampling frequencies: 1250 fps (green), 625 fps (blue) and 125 fps (red). There is a sampling bias when the sampling frequency is small. The base of the container vibrates between -0.07 mm $< z <$ 0.07 mm.

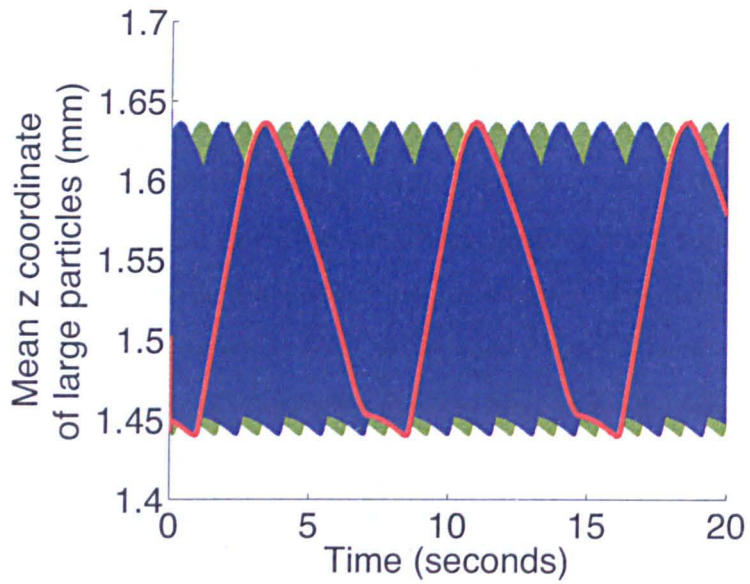

Figure 3.21: **Sampling bias in the z-position of large particles** - The variation in time of the mean large particle position (in the vertical z-direction) is shown for three different sampling frequencies: 1250 fps (green), 625 fps (blue) and 125 fps (red). There is a sampling bias when the sampling frequency is small. The base of the container vibrates between -0.07 mm $< z <$ 0.07 mm.

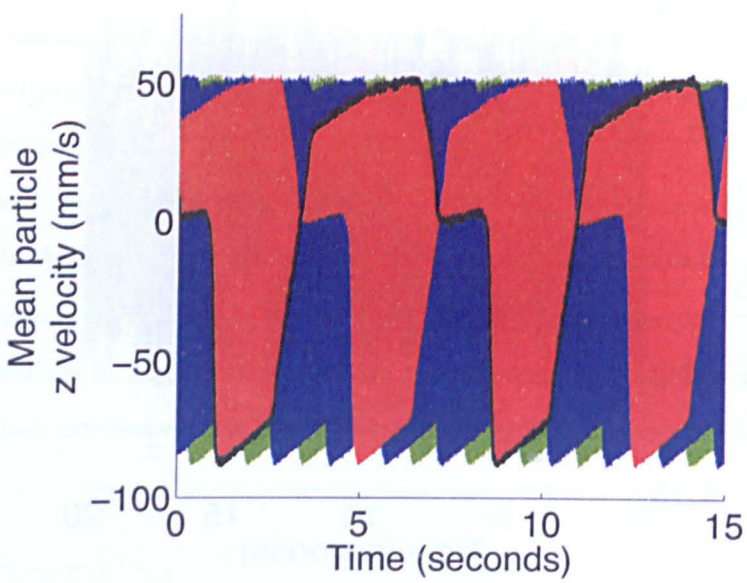

Figure 3.22: **Sampling bias in the z-velocity** - The variation in time of the mean particle velocity (in the vertical z-direction) is shown for three different sampling frequencies: 1250 fps (green), 625 fps (blue) and 125 fps (red). There is a sampling bias when the sampling frequency is small.

Table 3.5: List of all the different simulations performed over the course of this study. The parameters in bold are the baseline parameters used in this study. ε_n and ε_t are the normal and tangential coefficients of restitution, respectively.

Simulation timestep (number tsteps to fall $1d$)	ε_n **(particles)**	ε_t **(particles)**	ε_n **(walls)**	ε_t **(walls)**
130	0.1	0.1	0.1	0.1
130	0.5	0.5	0.5	0.5
130	0.9	0.9	0.9	0.9
130	0.5	0.1	0.1	0.1
130	0.9	0.1	0.1	0.1
130	0.1	0.5	0.5	0.5
130	1.0	0.5	0.5	0.5
130	0.1	0.9	0.9	0.9
130	0.5	0.9	0.9	0.9
130	0.1	0.5	0.1	0.1
130	0.1	0.9	0.1	0.1
130	0.5	0.1	0.5	0.5
130	0.5	1.0	0.5	0.5
130	0.9	0.1	0.9	0.9
130	0.9	0.5	0.9	0.9
130	0.1	0.1	0.5	0.1
130	0.1	0.1	0.9	0.1
130	0.5	0.5	0.1	0.5
130	0.5	0.5	1.0	0.5
130	0.9	0.9	0.1	0.9
130	0.9	0.9	0.5	0.9
130	0.1	0.1	0.1	0.5
130	0.1	0.1	0.1	0.9
130	0.5	0.5	0.5	0.1
130	0.5	0.5	0.5	1.0
130	0.9	0.9	0.9	0.1
130	0.9	0.9	0.9	0.5
130	0.4	0.4	0.6	0.6
130	0.3	0.9	0.7	0.95
130	0.3	0.6	0.5	0.5
130	0.4	0.8	0.3	0.95
130	0.8	0.9	0.6	0.95
217	0.8	0.9	0.6	0.95
650	0.8	0.9	0.6	0.95
1300	0.8	0.9	0.6	0.95
6500	0.8	0.9	0.6	0.95
130	0.4	0.4	0.6	0.6
130	0.3	0.9	0.7	0.95
130	0.3	0.6	0.5	0.5
130	0.4	0.8	0.3	0.95

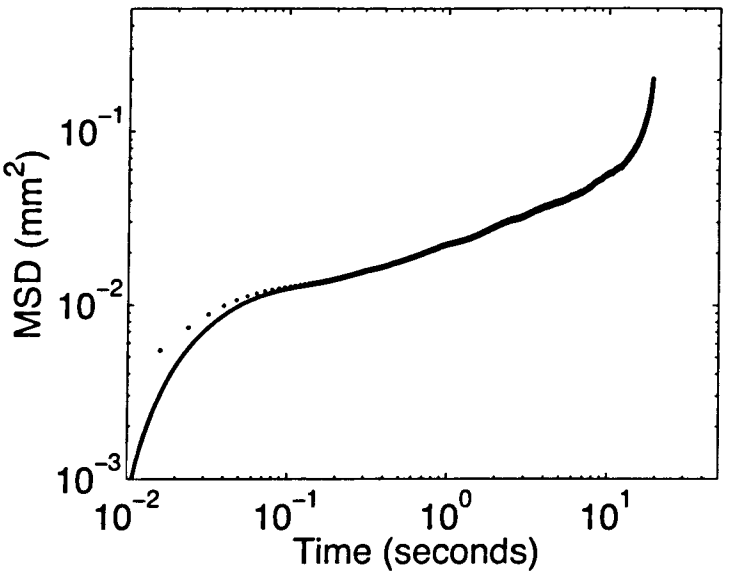

Figure 3.23: **MSD profile demonstrating sensitivity to sampling (output) frequency** - The mean-square displacement (MSD) curves for the numerical simulation with 10% small-particle concentration are shown calculated using particle coordinates output at 1250 fps (solid line) and 125 fps (dotted line).

3.6 Placing the simulations in a varying gravitational context

Finally, we apply our measure of collective dynamics and fragility - string length and number - to simulate conditions that are hard to replicate experimentally. First, we consider the consequences of varying the external gravity on string frequency and length. Next, we demonstrate one of the unique abilities of our code: the ability to model inter-particle gravity. By varying the particle density we examine what happens to our granular system when the gravitational forces between the particles become increasingly strong.

3.6.1 Varying the external gravitational acceleration

In this section, we consider the consequences of varying the external gravitational acceleration on string frequency and length. This demonstrates the ability of our code to simulate the range of gravitational environments that can be encountered among the solid planetary bodies within our solar system. The external gravity is varied from 0.01 - 10 g between numerical simulations. The particle density remains unchanged and the vibrational amplitude and frequency remain the same as in the experiments and baseline simulations. In addition, each simulation has an identical initial configuration (i.e., identical initial particle locations).

In the reduced-gravity simulations (when $g << 1$) the gravitational acceleration is of a magnitude

similar to that found on the surfaces of asteroids. In addition, the frequency of the vibrations roughly matches the conditions on asteroids subjected to seismic shaking (Richardson *et al.*, 2004, 2005). Although vibrations due to seismic shaking on an asteroid are not likely to act always in the same direction, string-like collective motion can still be expected in excited, heterogeneously sized and shaped regolith. However, grain boundaries would not be expected to occur in regolith. In the ordered and idealised system of equal sized spheres the grain boundaries are the heterogeneous regions where collective rearrangements take place. In glassy i.e., disordered systems, string-like motion is expected to occur everywhere. Nevertheless, these simulations have demonstrated that we have the capability of varying the external gravitational acceleration and have shown the sensitivity of the idealised system to such variations in the external gravitational acceleration.

It is found that the length and the frequency of strings decrease with increasing external gravitational acceleration (Fig. 3.24). This indicates that decreasing the external gravitational acceleration makes the granular ensemble more fragile when subjected to local excitation amplitudes. At the same time, cooler, less energetic systems appear to become less fragile.

3.6.2 Varying the inter-particle gravitational acceleration

In this section, one of the unique abilities of the code is demonstrated: the ability to model inter-particle gravity. By varying the particle density over several orders of magnitude it is possible to examine what happens to the granular system when the gravitational forces between the particles become increasingly strong. In this investigation the external gravitational field was removed (i.e., the system is in zero-gravity) and the vibrational amplitude and frequency remain the same as in the experiments and baseline simulations. Again, each simulation has an identical initial configuration (i.e., identical initial particle locations).

The measured resulting changes in string properties with varying particle density, and thus varying inter-particle gravity, are shown in Fig. 3.25. This system has a natural length-scale, which is the distance between particles at which the gravitational potential energy between two particles is equal to the mean particle kinetic energy. For each simulation we have determined this natural length-scale for both the large and the small particles. It is found that, for the largest particles (which are the most numerous), the natural length-scale is equal to one particle diameter for particles of density $\sim 1.5 \times 10^{13}$ kg m^{-3} (for the smaller particles, the density giving a natural length-scale of approximately one particle diameter is slightly larger). This indicates that, at the smaller densities that have been tested, the dynamics of the system are dominated by the kinetic energy of the particles and at the largest densities the gravitational potential energy may begin to play an important role in the dynamics of the system. The analysis and simulations indicate that the scale of the collective motion decreases in

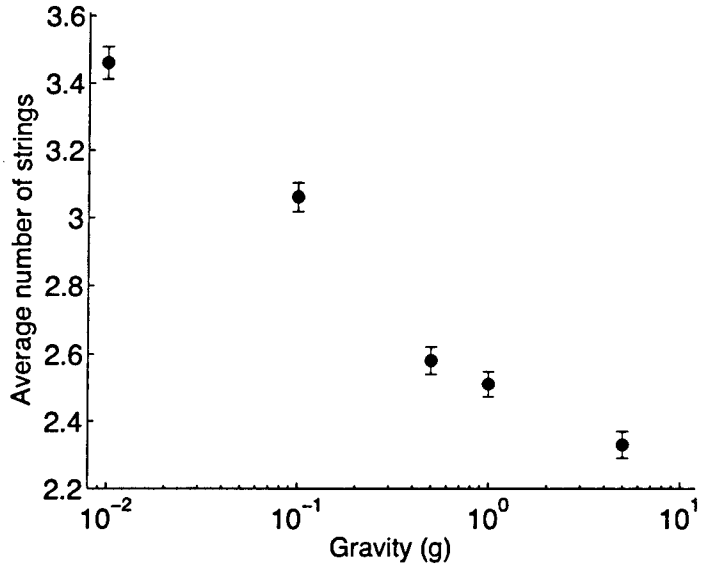

(a)

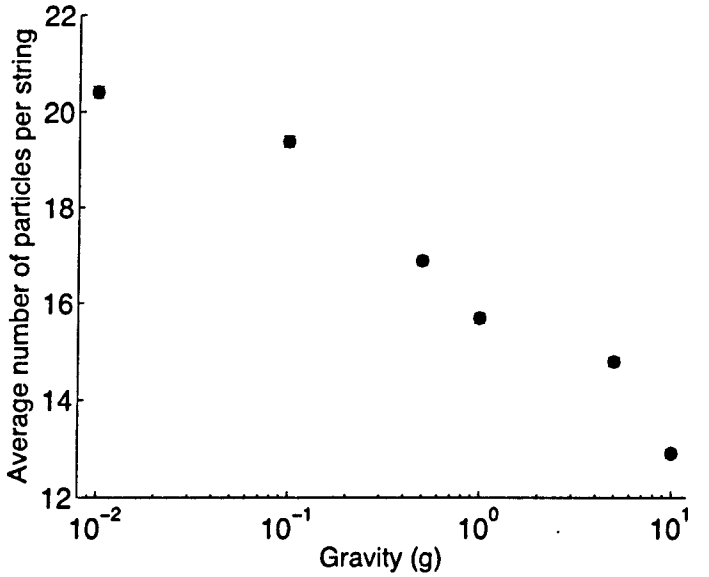

(b)

Figure 3.24: **Effect of varying external gravity on collective motion** - (a) Average number of granular strings and (b) average granular string length as a function of varying external gravity for simulations with 10% small-particle concentration. The errors bars, which are sometimes smaller than the markers, are the standard error of the mean for one simulation at one small-particle concentration. As each simulation is thousands of frames, it is expected to sample all configurations and so report the standard error and not the standard deviation.

the region where the gravitational potential energy between particles is of a comparable magnitude to the mean particle kinetic energy (Fig. 3.25). This may be because the inter-particle gravity is acting like an adhesive force between particles thus reducing the fragility of the system. A full study would be needed to confirm this, but this is outside the scope of this thesis.

It should be noted that the densities considered for this investigation are unrealistically large. However, the pair-wise gravitational attraction between two identical particles in contact, $F_g \propto \rho^2 r^4$, where ρ is the bulk density of the particles and r is the radius. Therefore, this study varying density is equivalent to a study where the radius of the particles of standard density of 10^3 kg m^{-3} is varied from $\sim$1 mm to $\sim$400 m. In future studies it may be useful to consider a full 3d system to investigate in more detail the role that self-gravity plays in affecting collective motion.

3.7 Chapter conclusions and discussion

The work in this chapter has demonstrated that the implementation of the hard-sphere discrete element method in the N-body code `pkdgrav` is capable of simulating the key features of the complex collective motion of a particular densely packed, driven granular system. While there are some clear differences in the experiment and simulations, the overall dynamics of the experiment have been reproduced either qualitatively or, where appropriate, quantitatively.

As a first test it was shown that the numerical simulations correctly reproduce the regions of crystallisation (grains) and regions of disorder (grain boundaries) found experimentally. The difficulties involved when trying to compare experiments and simulations quantitatively were discussed and it was concluded that, due to inherent experimental and tracking errors, particle velocities are not a meaningful variable to compare. This is particularly true in a dense material where the collision rate between particles exceeds the imaging speed, and the distance between collisions is smaller than the imaging resolution. It was suggested that mean-squared displacement (MSD) profiles are a more reliable means of comparison and have matched the experimental cage-breaking timescale (i.e., the timescale at which jammed particles may escape their cage of neighbours) and gradient of the subsequent rise of the MSD profile. As a final test the granular system was examined for mobile particles and string-like collective motion. In previous studies such string-like motion has been found to be a signature of fragility: an important material property that indicates how quickly a material softens under increasing external forcing. It was found that mobile particles are present and that the numerical simulations reproduce the key features of the experimentally observed string-like collective motion of such mobile particles even though the simulations are based on pairwise collisions only. Just as in the experiments, it was demonstrated that the scale and frequency of occurrence of the

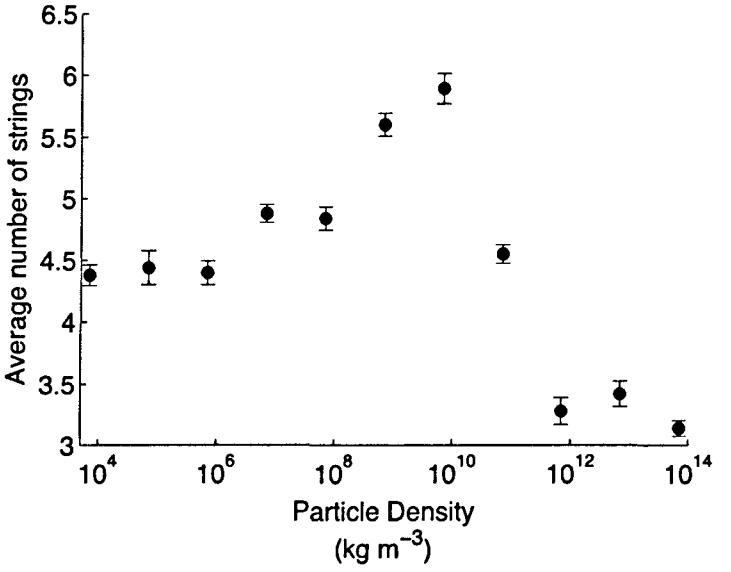

(a)

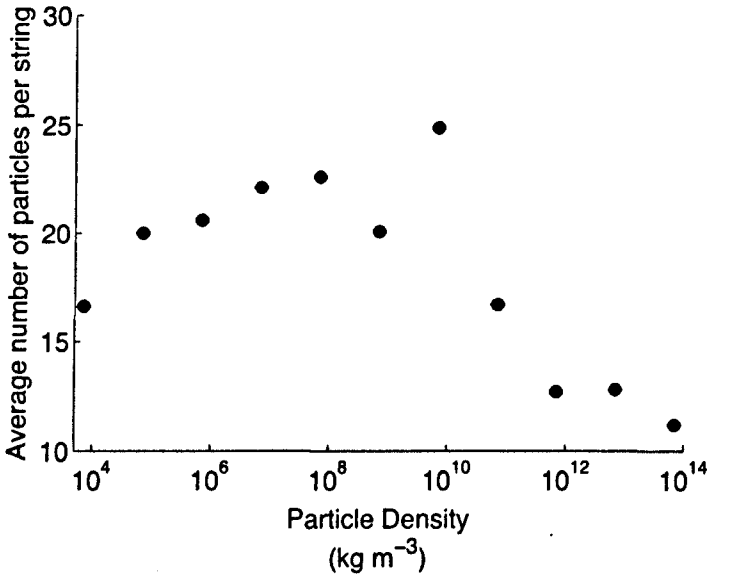

(b)

Figure 3.25: **Effect of varying self-gravity on collective motion** - (a) Average number of granular strings and (b) average granular string length as a function of varying particle density for simulations with 10% small-particle concentration and inter-particle gravity. The errors bars, which are sometimes smaller than the markers, are the standard error of the mean for one simulation at one small-particle concentration. As each simulation is thousands of frames, it is expected to sample all configurations and so report the standard error and not the standard deviation.

collective motion of the shaken granular system can be increased by the addition of small particles. The close match found between experimental and simulation results during a quantitative comparison of the average size of the granular strings is further validation of the numerical scheme. It was also successfully demonstrated that in this dense regime the behaviour and physics of the shaken granular matter predicted by the numerical simulations are not random and are closely related to the particle parameters and simulation initial conditions.

Based on the experience gained during this comparison it is suggested that, due to the complexity of experiment and simulation comparison, if a fundamental step is to perform validation tests of simulations, the experiments should be designed in collaboration with the modellers in advance. This gives the modellers a better understanding of the experiment but also allows the experiment to be designed in a way that is easier to model (e.g., with simple boundary conditions). However, it should always be taken into account that in experiments, particle positions are only sampled with uncertainty and in finite time intervals, and thus displacements on longer time intervals and over larger distances (e.g., MSD and granular strings) provide better comparison points. Numerical simulations can also be a very useful tool to help determine what parameters sensitively affect the behaviour of the experimental system. Once this is known, those parameters can be controlled and measured with particular care in the experiments.

As mentioned above and discussed in detail in Section 3.3, previous studies have shown that the presence of granular strings indicates that a material is fragile, i.e., prone to more sudden, avalanche-like failures. However, short granular strings indicate a more ductile behaviour. Flow of granular material has been inferred from observations of the asteroid Itokawa's surface taken by the Hayabusa spacecraft and from observations of the asteroid Lutetias surface taken by the Rosetta spacecraft (see Chapter 1 for details). As noted by Miyamoto *et al.* (2007) there are strong indications that gravels on Itokawa, based on their locations and morphological characteristics on the surface of Itokawa, were relocated after their accumulation/deposition, implying that the surface has been subject to global vibrations. These vibrations are likely to have triggered global-scale granular processes including landslide-like granular flows and particle sorting that result in the segregation of the fine gravels into areas of potential lows. However, from the existing observations, one cannot easily discriminate between gradual and abrupt changes on Itokawa's surface. From a strictly mechanical point of view, some differences may be expected between these two modes of migration. Simulations in conditions close to the asteroid environment are required to understand what these differences could be and which circumstances are necessary to lead to the observed characteristics. Such an understanding is crucial for interpreting observations of asteroid surfaces, and to derive the regolith properties. For instance, the presence of granular strings could be one possible explanation for observed changes, if it

was possible to assess that those changes occurred suddenly.

Finally, having the number and length of strings as a metric of collective motion and fragility allows us to take full advantage of the possibilities that are opened up by the simplicity of hard-sphere simulations: self-gravity can be included, external gravity can be varied, and their effect on the indicators of fragility of the granular material can be explored. It was found that external gravity changes collective behaviour: ensembles of particles exhibit more collective motion and, therefore, appear more fragile when held in place by lower external gravity. The fragility of planetary bodies is particularly important as it is potentially related to the onset of sudden fracture or failure events of the body.

Finally, having the number and length of strings as a metric of collective motion and fragility allows us to take full advantage of the possibilities that are opened up by the simplicity of hard sphere simulations: self-gravity can be included, external gravity can be varied, and their effect on the indicators of fragility of the granular material can be explored. It was found that external gravity changes collective behaviour: ensembles of particles exhibit more collective motion and, therefore, appear more fragile when held in place by lower external gravity. The fragility of planetary bodies is particularly important as it is potentially related to the onset of sudden fracture or failure events of the body. The simulations varying the inter-particle gravity of the system suggest that collective motion and thus, fragility, may depend closely on the balance between the gravitational potential energy and the kinetic energy of the system. This interesting discovery is highly relevant for small bodies and would be very interesting to consider in future studies.

Currently this work considers only a quasi-2d system. However, the advantage of the numerical code `pkdgrav` is that we can easily extend this to a fully 3d system. As the analysis indicates that collective behaviour is correctly captured in the simulations, string lengths and numbers may also be measured in 3d as metrics for fragility. This study is a first step that is necessary to ensure that the physics involved in the system we investigated is well computed and that gives us confidence that we can accomplish the next steps, which are to apply it directly to actual planetary science problems.

Using the numerical simulations it would be possible to investigate what happens when the small-particle additive concentration is increased above 10%, something which has never been tested experimentally. It could be investigated whether the scale of collective motion continues to increase or if there is a limiting small-particle additive concentration above which the scale of collective motion either decreases or remains constant. Numerical simulations would allow us to perform investigations that are difficult to access with experimental observations such as investigating collective motion within the bulk of a 3d granular system or investigating the fragility of bodies to deformations, e.g., due to tidal forces. The role of rotational versus translational motion in driving string formation is

also an interesting physics question, which could be addressed with the simulations but is outside of the scope of this current study. Additionally, the influence of boundary conditions, the tangential coefficient of friction and also cohesion on the formation of granular strings could be explored in future work.

Chapter 4

The AstEx Experiment: Design and Procedures

4.1 Summary of Chapter

The dynamics of granular materials are involved in planetary and small body evolution but appear to also be critical for the design and/or operations of landers, sampling devices and rovers. The AstEx experiment aims to develop a greater understanding of the mechanical response of granular material subject to external forces in varying gravitational environments.

AstEx, a parabolic flight experiment, was selected through the competitive European Space Agency (ESA) research student competition 'Fly your Thesis' in December 2008. The full experiment, entitled 'Simulating Asteroidal Regoliths: Implications for Geology and Sample Return', flew as part of ESA's 51st Microgravity Research Campaign in November 2009. The flight campaign was operated from Bordeaux in France by a company called Novespace.

The AstEx experiment uses a microgravity modified Taylor-Couette shear cell to investigate granular flow caused by shear forces under the conditions of parabolic flight microgravity. The aim of the experiment is to characterise the response of granular material to rotational shear forces in a microgravity environment. A particular emphasis has been put on investigating the steady state flow profiles, the mechanism of granular convection and the memory effects of sheared glass beads in the different gravitational regimes.

This chapter discusses the motivation behind the AstEx experiment, the technical design details, the experimental procedures and the data that were collected during the microgravity flight campaign. The data analysis pipeline will be presented in Chapter 5 and the results and interpretation will be presented in Chapter 6.

It must be noted that Dr. Ben Rozitis (currently a post-doctoral research fellow at The Open University, UK) was instrumental in getting the AstEx parabolic flight experiment selected to fly through the 'Fly your Thesis' programme. He, along with Thomas-Louis de Lophem (an engineer currently working for Electrabel, Belgium), also made significant contributions to the design of the AstEx experiment. As a result, many of the detailed descriptions of the experimental design presented in this chapter are based on documents which were compiled collaboratively by the three of us. The hardware was then constructed by Kevin Dewar and Damian Flack (both engineers in the PSSRI workshop at The Open University). The experimental procedures were planned by myself and the microgravity experiments were carried out by myself, Ben Rozitis and Thomas-Louis de Lophem.

4.2 Motivation for AstEx

As discussed extensively in Chapter 1, despite their very low surface gravities, asteroids are often covered by regolith, a layer of granular material, that can range from a fine powder (particles of a few microns in size) to a gravel-like structure of varying depths (particles of a few centimetres or metres). Therefore, understanding the physics of granular material is important for the interpretation of spacecraft observations (images, spectral observations, or topography) but is also critical for the design and operations of landers, sampling devices and rovers. The AstEx experiment was designed to study the mechanical response of granular material subject to shear forces in a microgravity environment using a Taylor-Couette shear cell.

Couette flow, a term named after the French physicist Maurice Couette, was first used in the field of fluid dynamics. It refers to the laminar flow (a streamlined flow in parallel layers within which there are no cross currents or eddies) of a fluid between two parallel plates, one of which is moving relative to the other. In this simple Couette geometry the two plates cannot extend infinitely in the flow direction, and so, in order to study shear-driven flows, Sir Geoffrey Taylor created a Couette shear cell using rotating co-axial cylinders. It was using this geometry that Taylor discovered the Taylor vortex flow (Taylor, 1923). Taylor vortices are formed when the angular velocity of the inner cylinder is increased above a certain threshold and the Couette flow becomes unstable. Since this discovery, the circular Couette shear cell, also known as the Taylor-Couette shear cell, has been used in countless experiments in fluid dynamics and, more recently, in studies of granular material.

Although a similar experimental set-up can be used to study both fluids and granular materials the two media react very differently to shear stresses. Neglecting possible edge effects and effects due to the curvature of the shear cell, the Couette (angular velocity) profile of a Newtonian fluid (a fluid for which there is a linear relationship between the stress and the strain) is a decreasing function

across the entire shear cell width (i.e., linearly decreasing with increasing r).

To demonstrate this Fig. 4.1 shows the theoretical Couette profile of a Newtonian fluid (solid line). Also shown in Fig. 4.1 is the Couette profile of granular matter consisting of spherical glass beads (grain diameter, d = 4 mm) from an experiment performed as part of this thesis (open circles with error bars). The fluid deforms uniformly whilst the granular material develops a shear band; a narrow zone of large relative particle motion bounded with essentially rigid regions. Almost all of the energy input into the granular system by the inner cylinder is dissipated by friction within this narrow region producing large velocity gradients. Shear bands mark areas of flow, material failure, and energy dissipation, and as such they are important in many geophysical processes.

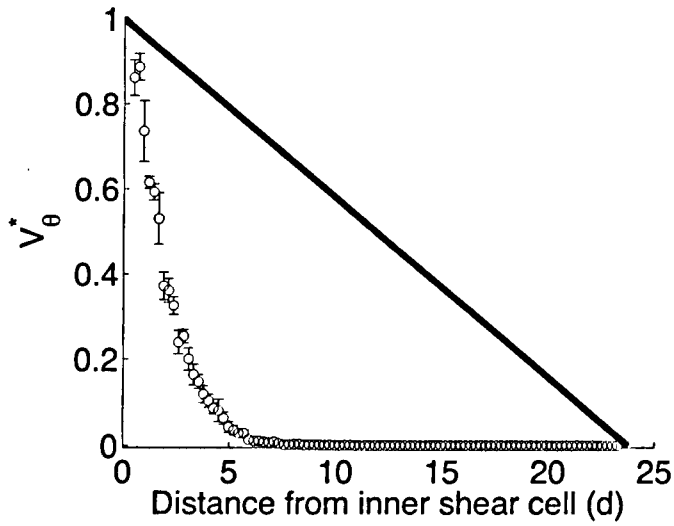

Figure 4.1: **Comparison of the Couette (angular velocity) profile of a fluid and a granular material** - The normalised angular velocity profile of a sheared granular material is shown (open circles with error bars) and compared to the theoretical angular velocity profile of a Newtonian fluid (solid line). $V^*_\theta = V_\theta/\omega$ where V_θ is the mean particile angular velocity and ω is the inner cylinder angular velocity. A region of local failure of the granular material near the shearing surface can be seen. This is known as a shear band.

The AstEx team chose to use the simplest Taylor-Couette geometry as shown in Fig. 4.2. There are two concentric cylinders; the outer cylinder has an inner radius of 195 mm and the inner cylinder has an outer radius of 100 mm. The outer cylinder is fixed and its inside surface is rough with a layer of particles, the outer surface of the inner cylinder is also rough but it is free to rotate, and the floor between the two cylinders is smooth and fixed in place. The gap between the two cylinders is filled with granular material (grain diameter, d = 3 or 4 mm) upon which the rotating inner cylinder applies shear stresses.

Various different configurations of the Taylor-Couette shear cell have been used to study the effect of shear stresses on granular materials experimentally. For example, Bocquet *et al.* (2001) shear a granular material in a Taylor-Couette cell with a rotating inner cylinder and stationary outer cylinder.

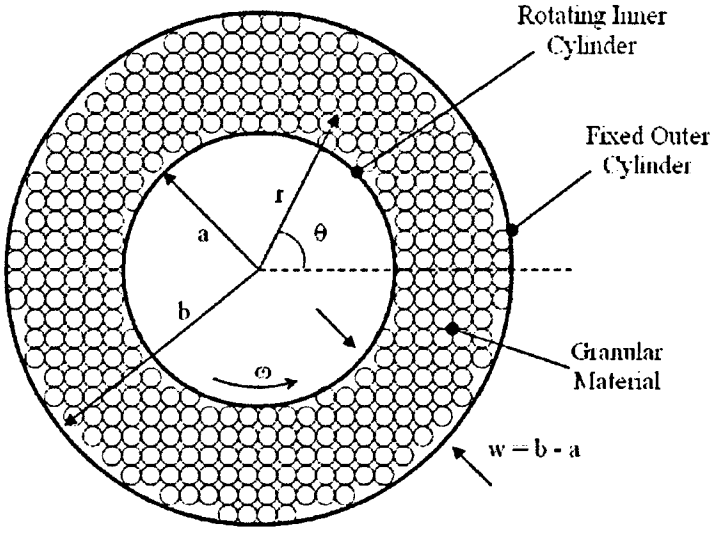

Figure 4.2: **The Taylor-Couette Geometry** - a = Inner Cylinder Radius, b = Outer Cylinder Radius, w = Width of Shear Region, r = Radial Distance, θ = Angular Distance, ω = Inner Cylinder Angular Velocity. Image from Toiya (2006).

The inner cylinder is connected to the motor via a spring that allows either stick-slip motion or steady shearing depending on the parameters. By performing force measurements they determined that the shear force acting on the moving cylinder is independent of shearing velocity. The dynamics of individual particles were also investigated by measuring the mean velocity of particles on the top-surface. They conclude that the normalised velocity profiles are independent of shearing velocity and of the type of motion of the inner cylinder (i.e., stick-slip or continuous sliding).

Khosropour *et al.* (1997) investigated the size segregation of a binary mixture of spherical glass particles in a Taylor-Couette geometry, where the cylinders are made of smooth glass and the flow is generated by the shearing motion of the inner cylinder. The trajectories of 1, 2, and 3 mm glass particles, placed at the bottom of the cell, were followed as they moved through a 1 mm medium. They observed that the larger particles rose to the top and remained on the surface. However, the small particles (those comprising the medium) exhibited convective-like motion rising at the outer radius and falling at the inner radius. Toiya (2006) has also seen evidence for granular convection in a Taylor-Couette experiment in which the bottom plate is attached to the rotating inner cylinder and the outer cylinder is fixed. In their experiments, when the filling height is large enough for the effect of the bottom plate to be negligible on the top surface, the velocity of particles on the top surface in the radial direction (V_r) has a dip near the centre of the shear band (Fig. 4.3 (a)). This indicates that a convection roll is possibly centered around the shear band. A diagram explaining why such a dip in radial motion implies convection may be occuring is given in Fig. 4.3 (b)-(c).

The most researched type of convective flows in granular matter are vibration-induced convective flows. Convective flows have been observed, for example, in many experiments performed by vibrating

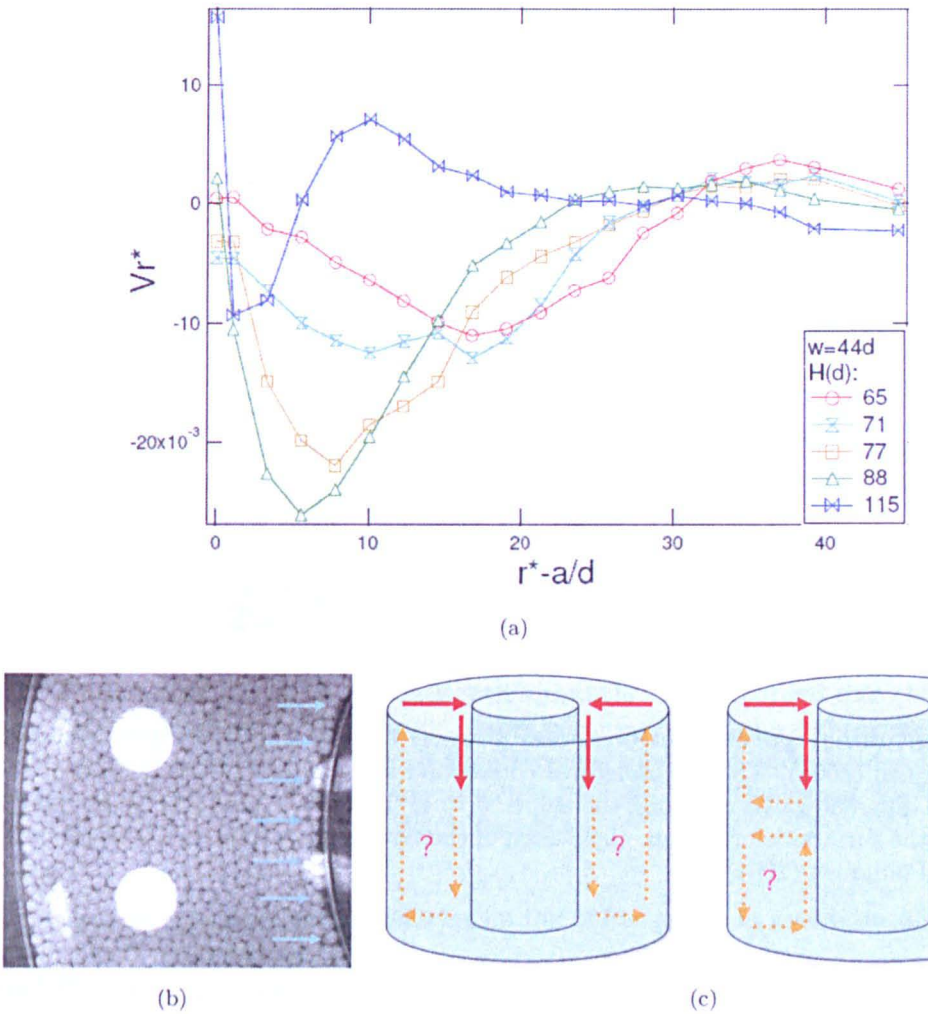

(a)

(b)

(c)

Figure 4.3: **Schematic to explain convection in a Taylor-Couette shear cell** - (a) Steady-state V_r^* for 1 mm particles from Toiya (2006). Negative values indicate that the radial velocity points toward the inner wall. Locations of minima move closer to the inner wall for greater filling height. $V_r^* = V_r/a$, and $r^* = r/d$, where d is a particle diameter. (b) A dip in the radial velocity profile implies that particles are moving towards the inner shearing cylinder as shown by the direction of the arrows in this image of the top surface of the AstEx shear cell. If there is a constant flux of particles towards the inner cylinder then these particles must also be moving down the inner cylinder wall as shown in the two schematics (c) of radial flow in a Taylor-Couette shear cell. The mean negative radial motion implies that convective flows are occuring. However, from imaging just the top surface it is not possible to know whether there is one large convective cell within the bulk or several smaller ones.

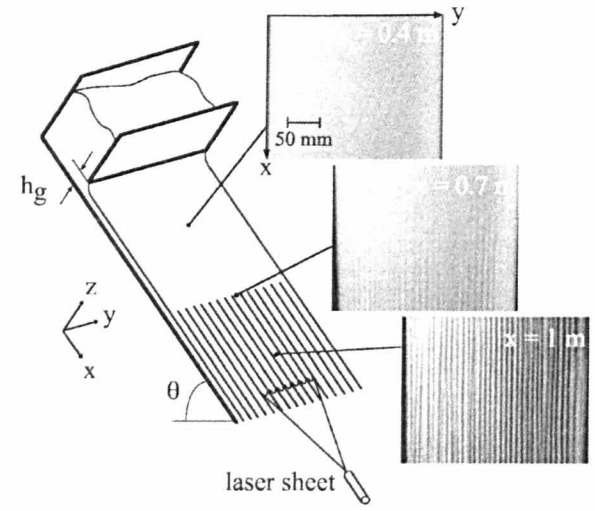

(a)

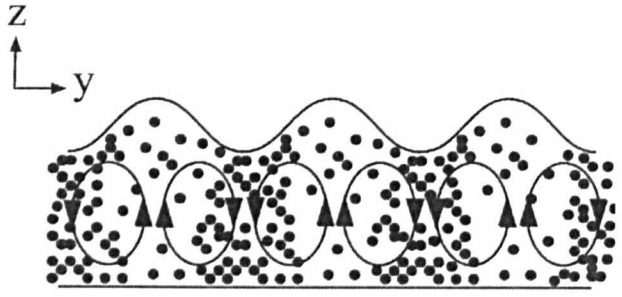

(b)

Figure 4.4: **Longitudinal Vortices in Granular Flows** - (a) Sketch of the experimental setup of Forterre & Pouliquen (2001). The three pictures correspond to top views of the free surface lit from the side at three different locations along the slope. $\theta = 41°$, $h_g = 13$ mm. The sheet laser light is used to measure the surface deformation. (b) Sketch of the flow in a cross section. Images both taken from Forterre & Pouliquen (2001).

granular material in a direction parallel to the external gravitational field i.e., vertical shaking (e.g., Eshuis *et al.*, 2010; Hsiau & Chen, 2000; Rodriguez-Linan & Nahmad-Molinari, 2006; Tai *et al.*, 2010). Convective flows have also been seen when the axis of vibration is parallel to the external gravitational field i.e., horizontal shaking (e.g., Liffman *et al.*, 1997; Raihane *et al.*, 2009; Saluena & Poschel, 2000; Tennakoon *et al.*, 1999). Forterre & Pouliquen (2001) have also found evidence for convection in rapid granular flows down rough inclined planes. Using the experiment shown in Fig. 4.4 (a) they found an instablity in the granular flow. From measurements of the surface velocities they have shown that this instability is associated with the formation of longitudinal vortices in the granular flow. The mechanism they propose is based on the density profile inversion: it can be seen in Fig. 4.4 (b) that the dense (thus heavy) part of the flow moves down (in the plane perpendicular to the flow direction) while the dilute (thus light) part moves up. However, they note that in a granular dissipative gas (such as they have in the rapid flow), the density profile actually results from a complex balance between gravity, collisions and dissipation, and its prediction is not straightforward.

Granular convection is a process often invoked by the community of small body scientists to interpret the surface geology of asteroids. Miyamoto *et al.* (2007) suggest that the arrangements of the gravels on Itokawa's surface are largely due to granular convective processes. It is suggested (Asphaug, 2007) that piles of aligned boulders are formed where convection meets a boundary layer, perhaps analogous to miniature mountain belts (Fig. 4.5). Miyamoto *et al.* (2007) have also proposed that apparent upstream sloping, or seas, on Itokawa could be caused by convective surfaces. However, since Itokawa has long lost any internal heat source capable of driving convection, the energy source would have to be a granular thermal input (Asphaug, 2007). As discussed in detail in Chapter 1, this energy could come from small impacts on the asteroid from micrometeorites.

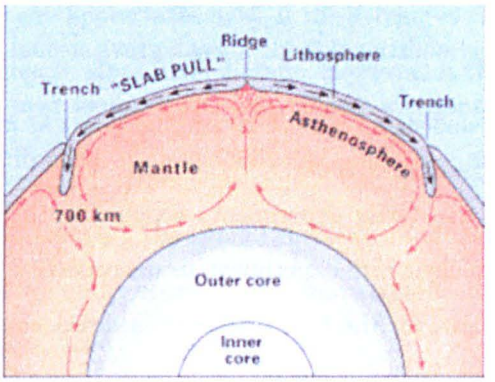

Figure 4.5: **Convection currents in the Earth's mantle** - It is theorized that convection currents within the Earth's mantle cause the creation of new oceanic crust at the mid-oceanic ridges. Oceanic crust is destroyed at areas where this crust type becomes subducted under lighter continental crust. This process also creates the deep oceanic trenches (Source: U.S. Geological Survey. Image taken from *http : //www.eoearth.org/article/Plate_tectonics*).

When discussing images of boulders sitting on top of fine grains in gravitationally stable orientations on Itokawa (see images in Chapter 1) Miyamoto *et al.* (2007) suggest that these boulders are stranded by vibration-induced convections. Similarly, Asphaug *et al.* (2001) discuss the possiblity that the large blocks crowding the regolith of Eros may have risen from below. It has been suggested that dynamic segregation, by the Brazil-nut effect (see Section 1.6.2), may be easier to achieve on asteroids than on planets. In a later article it is also stated that, "all other considerations aside, granular convective processing is favoured by microgravity"(Asphaug, 2007).

In a liquid or gas, natural convective flows are initiated due to temperature gradients within the medium. The temperature differences affect the density and subsequently the relative bouyancy of the fluid or gas. Bouyancy variations can also be introduced due to other material properties and, in an external gravitational field, this can lead to gravitational convection. Once the pressure gradient is removed, such as in the case when there is no external gravitational field, convective flows due to buoyancy can no longer occur. This has been demonstrated by many experiments designed to investigate convective flows in liquids and gases in a microgravity environment (e.g., Olson & Miller,

2009; Shevtsova *et al.*, 2010; Zhou *et al.*, 2002).

From all of the experimental results presented above it is clear that convection can occur in a granular material. However, in all of these experiments there is a buoyancy force because a pressure gradient occurs within the medium due to the Earth's gravititational field. It has not been possible to find any published research investigating convective granular flows in a microgravity environment, but intuitively we may expect that, as for liquids and gases, granular convection can not occur without buoyancy.

The statements related to granular convection on asteroids (Asphaug, 2007; Asphaug *et al.*, 2001; Miyamoto *et al.*, 2007) now seem a little surprising given our hypothesis that granular convection depends strongly on the external gravitational field: a weak gravitational acceleration, such as is found at the surface of small bodies, means a smaller pressure gradient near or on the surface which may reduce the efficiency of granular convection. As this has never been directly investigated experimentally this is one of the aims of the AstEx experiment. Examining the radial velocity profiles of the particles undergoing a constant shear rate experiment in microgravity (as already performed on the ground; Toiya, 2006) would allow, for the first time ever, a direct comparison of the mechanism of granular convection in a microgravity environment.

Performing a constant shear rate experiment with the Taylor-Couette shear cell in different gravitational environments allows us to investigate how the granular flows differ between the gravitational regimes and to investigate how convective flows change in the different gravity regimes. One further subject of interest that can be studied during a constant shear rate experiment is dilatency. The concept of dilatency (see Section 1.5.3) describes how a compacted granular material must expand in order to undergo shear. Experiments of sheared granular materials have never been performed at constant volume without exerting a variable pressure as, under the force of gravity, this is not physically possible due to this principle of dilatency. Removing the external gravity and fixing the volume of the granular material would allow, for the first time, shear experiments of granular material to be performed at constant volume without any confining pressure.

As just mentioned there are many interesting questions that can be answered by performing constant shear rate experiments. However, it is not only constant shear rate experiments that are of interest. Toiya (2006) investigated memory effects in a sheared granular material using a Taylor-Couette geometry where the bottom plate is attached to the rotating inner cylinder and the outer cylinder is fixed. Using this experimental set-up it has been shown that the flow of granular matter is strongly influenced by the network of direct contacts with neighbouring particles (Falk *et al.*, 2008; Toiya, 2006). This contact network, in turn, is shaped by how the material evolved with time. When uniform shear or compression is applied a stronger contact network in the direction of forc-

ing develops. When the shear direction is reversed, or the direction of compression is changed, the material rearranges until it forms a new contact network that can best support the new direction of compression or shear (Falk *et al.*, 2008). This is illustrated in the schematic in Fig. 4.6; the force chains aligned to cause jamming in one direction are not suited to jam under the reverse driving. Therefore, time is required to re-form a force chain network subsequent to reversal of shear direction. This is further emphasised in Fig. 4.7 which shows the results of investigations into particle velocity distributions in a Taylor-Couette shear cell during constant shear rate and shear reversal experiments. The six lines show the angular velocity measured in six concentric rings during the experiment just described. When sheared in the initial direction the system reaches steady state during which three of the six rings do not experience any appreciable flow. If the driving is discontinued and then reapplied the system reaches the same steady state immediately. However, if the driving is stopped and then applied in the reverse direction, a transient sets in during which flow is evident both in the regions that were flowing and in the previously jammed regions. Average flowing velocities in all regions are faster initially and drop off with roughly the same time-scale in all regions. The implication is that regions that normally do not move under steady shear, move significantly during reversal of the shear direction (Falk *et al.*, 2008; Toiya, 2006).

Studying the reversal of shear in a granular material in microgravity has the potential to shed light on different behaviours that are evident when granular material is sheared in different directions, such as the transient weakening found to occur on the ground. Additionally, the flow fields during the shear reversal experiments of Falk *et al.* (2008) are accompanied by compaction due to gravity. It is not clear how the force chains would break and reform in the absence of a preferred guiding direction such as gravity. If the same characteristic transient weakening of granular material during shear reversal is also observed in microgravity this could potentially be exploited to make a more power-efficient asteroid surface sampling mechanism.

The geology and dynamics of granular materials on the surfaces of asteoroids could also depend on the direction of shear that they have undergone. For instance, impact phenomena (Holsapple *et al.*, 2002; Paolicchi *et al.*, 2002), tidal forces from planetary encounters (Bottke & Melosh, 1996), and YORP spin up (Bottke *et al.*, 2002b) (see Section 1.2) could apply shear forces to the surface. Therefore, asteroid surface materials may not necessarily behave as one might expect.

In summary, there are many interesting questions that can be answered by performing experiments of granular material subject to shear forces in a microgravity environment using a Taylor-Couette shear cell. To try to address as many of these questions as possible the AstEx experiment has several key research objectives:

1. To investigate how a steady state granular flow induced by rotational shear forces in microgravity

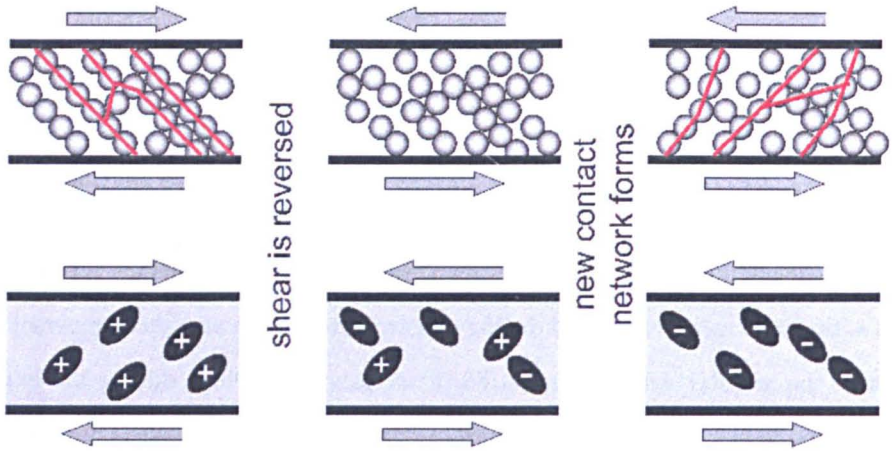

Figure 4.6: **Schematic of shear reversal experiments** - The breaking and re-forming of a contact network through shear reversal in dry granular matter in a Taylor-Couette geometry is illustrated schematically. The arrows indicate the relative movement of the cylinder walls and the red lines through the particles in the upper diagrams indicate the stress transmission. The positive and negative signs show the principal direction of the stress transmission. When shear is started opposite to the prior shear direction, transiently the material compacts and is easy to shear. Image from Falk *et al.* (2008).

differs from a steady state granular flow on Earth induced by rotational shear forces.

2. To investigate if granular convection occurs in our granular system on the ground and, if it does, to determine if the convection is enhanced or reduced in microgravity.

3. To investigate if hysteresis (memory effects) that leads to a transient weakening of the granular material occuring after shear reversal is enhanced or reduced in the microgravity environment.

4. To investigate how a granular material behaves when maintained at a constant volume without any confining pressure during shear (possible only in microgravity).

4.3 Creating a microgravity environment

In order to reduce the ambient gravitational acceleration during our experiments to levels close to those found at the surface of an asteroid we must find a way of achieving microgravity. Microgravity, the condition of relative near weightlessness, can only be achieved on Earth by putting an object in a state of free-fall. There are several possible ways to do this and many of these are discussed below. The first possibility would be to use a drop tower. The drop tower contains a free-standing chamber within a concrete shell (this prevents the transmission of wind-induced vibrations, which could otherwise result in the airtight drop capsule hitting the walls). The duration of free-fall depends on the height of the tower and the degree of evacuation (some facilities perform drops at very low pressures to remove aerodynamic drag, others do not attempt to create vacuum conditions). The

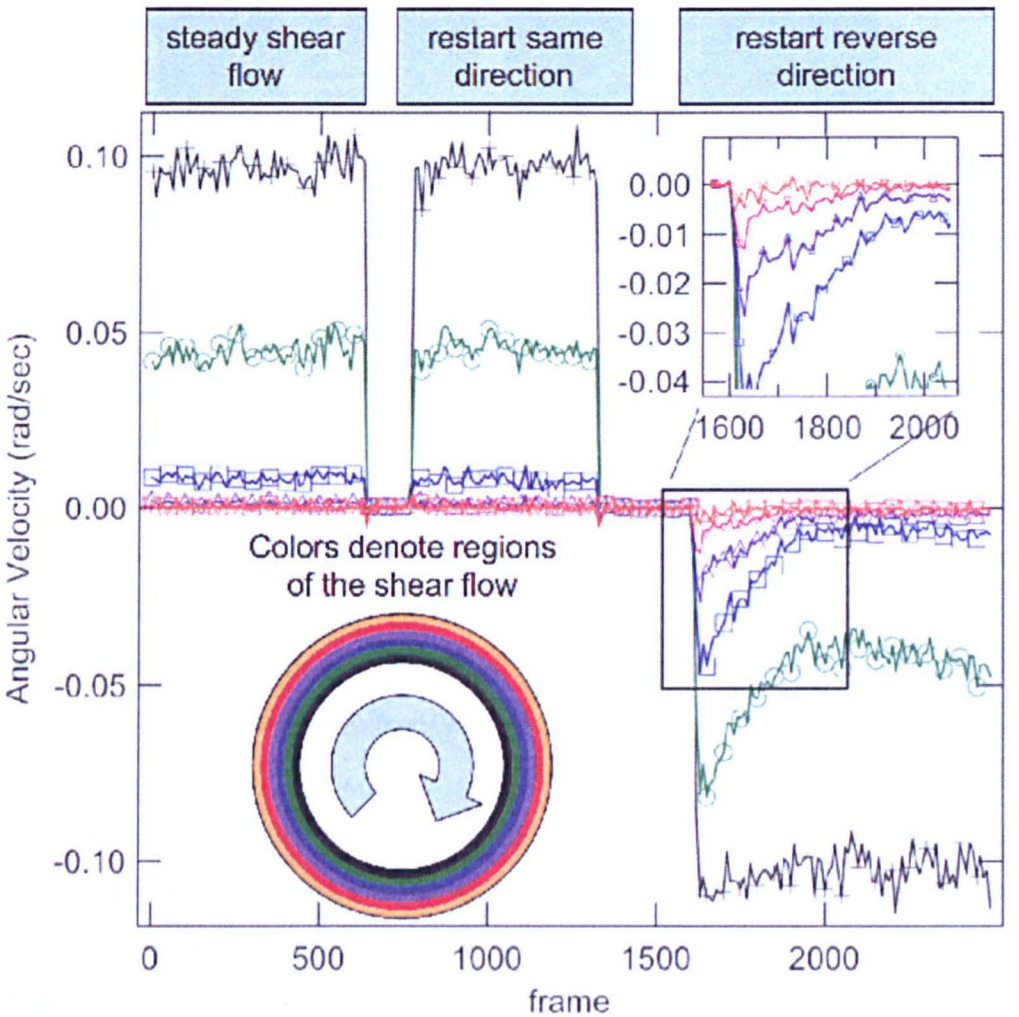

Figure 4.7: **Results of shear reversal experiments in 1 g** - Angular velocity as a function of time (in frames) measured in six concentric rings during granular flow in a Taylor-Couette cell. Driving stops and restarts in the same direction, and the steady state recovers instantaneously. Then the shear is reversed, and a transient flow regime precedes the establishment of steady state shear in the opposite direction. Each concentric ring is represented by a line on the plots of angular velocity above. Image from Falk *et al.* (2008).

Figure 4.8: **The Bremen Drop Tower Facility.** - (a) The ZARM Drop Tower in Bremen. Image from the ZARM Drop Tower Bremen General Information (2000). (b) Standard drop capsule (pressurizable cover is removed). Image from the ZARM Drop Tower User Manual (2011).

drop tower at the Centre of Applied Space Technology and Microgravity at the University of Bremen (Fig. 4.8 (a)), for example, has a 123-metre-high drop tube (actual drop distance is 110 m), which is pumped down to about 10 Pa ($\sim 10^{-4}$ atmospheres) prior to every free-fall experiment. This facility can provide 4.7 seconds of weightlessness with release of the drop capsule (Fig. 4.8 (b)) and this can be increased to 9 seconds with the use of a catapult.

Parabolic flights can also provide a microgravity environment. Such flights are normally operated using modified comercial aeroplanes. During each parabola of a parabolic flight there are three distinct phases: a ~20 second ~1.8 g injection phase as the plane accelerates upwards, a ~22 second microgravity phase as the plane passes through the top of the parabola (during this period the pilot carefully adjusts the thrust of the aircraft to compensate for the air drag so that there is no lift), and finally, a ~20 second ~1.8 g recovery phase as the plane pulls out of the parabola. Figure 4.9 shows a schematic explaining this process. During one flight there are several parabolas (31 with Novespace in Europe) and each flight campaign consists normally of several flights (3 with Novespace). This means that, with Novespace, there are 93 parabolas in one flight campaign giving approximately 30 minutes of (disconnected) microgravity in total.

A third way of achieving microgravity is using a sounding rocket[1]. Sounding rockets are divided into two parts: the payload and a rocket motor. After the launch, as the rocket motor consumes its fuel, it separates from the payload and falls back to Earth. The scientific payload, which must be

[1]The name sounding rocket comes from the nautical term "to sound"which means to take measurements (*http : //www.nasa.gov/missions/research/f_sounding.html*).

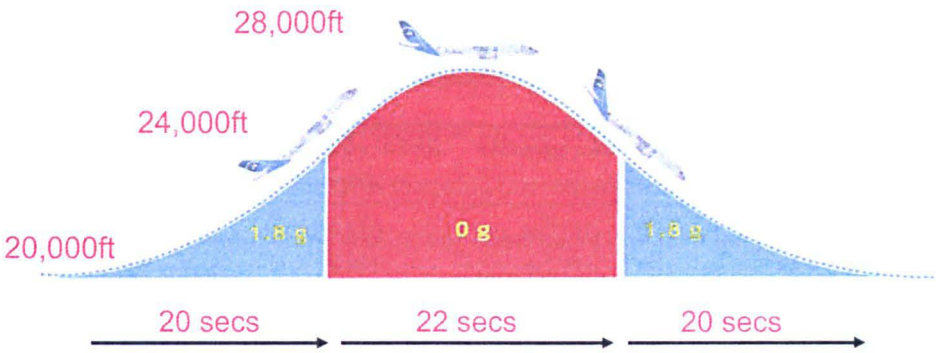

Figure 4.9: **The sequence of events during a parabolic flight** - Schematic explaining the three distinct phases during a parabola: a ~20 second ~1.8 g injection phase as the plane accelerations upwards, a ~22 second microgravity phase as the plane passes through the top of the parabola, and finally a ~20 second ~1.8 g recovery phase as the plane pulls out of the parabola. The altitude of the aircraft varies from ~6 to ~8.5 km. Image from CNES.

fully automated, continues on a parabolic trajectory into space and then comes back down to Earth with the help of a parachute. The scientific payloads are carried to altitudes of approximately 100 km and data is often collected and returned to Earth by telemetry links, which transfer the data from the payload directly to researchers on the ground.

Flying an experiment on the International Space Station (ISS) is another possible way of obtaining microgravity. The ISS is in a low-Earth orbit and provides a platform suitable for long-term microgravity experiments and microgravity experiments that require human researchers. If an experiment could be fully automated it could also be put into an unmanned orbital flight to achieve a very long period of microgravity.

Magnetic levitation, a technique in which magnetic fields are used to counteract gravity and suspend an object, can also be used to simulate microgravity. However, this is not a possible option for our experiment because, even if we were to levitate the AstEx shear cell, the individual grains would still feel the gravitational field.

Another way of simulating a microgravity environment is neutral buoyancy; a technique which is used extensively in astronaut training. A laboratory designed to perform such simulations consists of a large pool of water and tests are performed underwater on equipment (such as robots, satellites and spacesuits) specially designed to be neutrally bouyant. Neutral buoyancy is achieved when the buoyant force is equal to the force of gravity (i.e., the object has an equal tendency to float as it does sink). As the forces cancel out there is no net force and the result is similar to microgravity. Of course, when using neutral buoyancy there are clearly effects of drag from the water which would not be present in microgravity. Similarly to the problem for the magnetic levitation, if we wanted to perform our experiment in a neutral buoyancy laboratory we would need to make every particle in our experiment neutrally buoyant. Additionally, we do not want to have any influence of fluids on

Table 4.1: Comparison of the different ways of achieving microgravity. The information for this table was taken from the ZARM Drop Tower Bremen General Information (2000).

	Level of microgravity	Reduced gravity time	Manual access
Drop Towers	10^{-5} - 10^{-6} g	~10 secs	no
Parabolic Flight Aircraft	10^{-2} - 10^{-4} g	~20 secs	yes
Sounding Rockets	10^{-4} - 10^{-5} g	minutes	no
Unmanned orbital vehicles	10^{-5} g	weeks to months	no
Manned Space Station	10^{-3} - 10^{-5} g	hours to months	yes

our experiment. For both of these reasons it can be concluded that neutral buoyancy is not a feasible option for the AstEx experiment.

Table 4.1 compares the advantages and disadvantages of each of the different ways of achieving microgravity that could physically work for the AstEx experiment: drop towers, parabolic flight aircraft, sounding rockets, unmanned orbital vehicles and the ISS. As can be seen in the table, the microgravity time available and the quality of the microgravity vary greatly between methods.

In order to asses the best option for the AstEx experiment we need to have an idea of the timescales that will be required to perform the experiment. Figure 4.10 displays the characteristic timescales for a shear reversal experiment previously conducted on the ground (Losert & Kwon, 2001). After rotation of the inner cylinder is started at a rotation frequency of 0.02 Hz, a steady flowing state is reached within the first 0.4 seconds. When the motion of the cylinder is stopped and is restarted in the direction opposite to the prior shear direction, the steady flowing state is reached only after several seconds. A single complete shear reversal experiment takes ~20 seconds, which is similar to the microgravity time available during a single parabola of a parabolic flight.

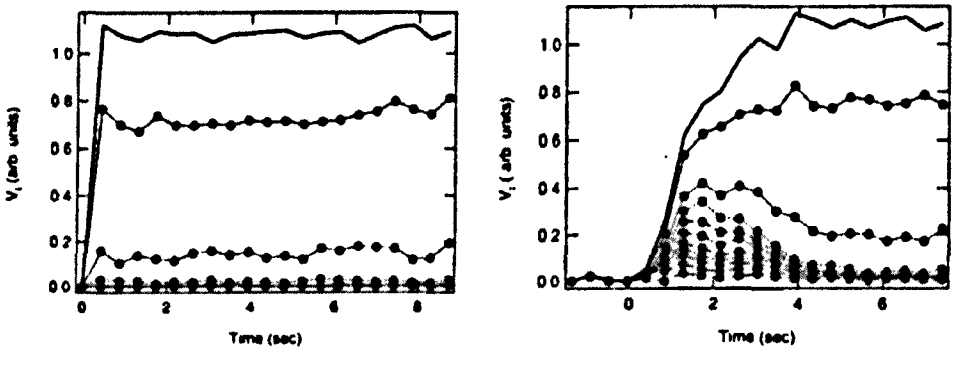

Figure 4.10: **Characteristic timescales of shear motion and shear reversal.** - Average particle velocity as a function of time at different distances from the inner cylinder. Inner cylinder motion is started at t=0s. Previous motion caused by the inner cylinder is shown on the left and motion caused by shear reversal is shown on the right. The frequency of inner cylinder rotation was 0.02 Hz. Image from Losert & Kwon (2001).

If the AstEx experiment could be fully automated it could fly on a sounding rocket. However, it

would be difficult within just one flight of a sounding rocket to perform the many experiments needed to ensure reproducibilty of the results. Therefore, assuming that the AstEx experiment requires a human researcher, and that the timescale required for the shear reversal experiments is approximately 20 seconds, we are left with the choice of performing our experiment in a parabolic flight aircraft or on the ISS. Finally, in order to minise the cost of the experiment, we decided a parabolic flight campaign was probably the most feasible way forward.

4.4 AstEx experimental hardware

Described in this section is the hardware developed for the AstEx experiment. This section is based upon two documents that were compiled collaboratively by the AstEx team. The first document is the Experiment Safety Data Package (ESDP), a report on all the technical aspects of the AstEx experiment rack: size, mass, nature of all the components, resistance to shocks, behaviour in zero-g, electrical requirements, etc. The second document is a technical report about the AstEx experiment prepared for the ESA Erasmus Archive[1].

4.4.1 The AstEx experimental rack

Figures 4.11 and 4.12 show how a Taylor-Couette shear cell is mounted inside the A300 Zero-G aircraft for testing in microgravity conditions. The experiment rack consists of two parts: a test compartment, and a laptop work station. The test compartment is where the experiments take place and it contains one removable shear cell at a time. Built into the test compartment is a motor powered by an inverter, an enclosed toothed belt pulley system, four illumination lights, and two high-speed cameras. Situated next to the test compartment is the laptop work station where two laptops are mounted to allow two experimenters to control the various components of the experimental hardware and to perform the experiments. The entire experiment rack is 1006 × 1250 × 750 mm in size, and has a total mass of ~170 kg.

4.4.2 The microgravity-modified shear cell

The flow of granular material due to shear forces is studied using Taylor-Couette geometry as described above in Section 4.2 and Fig. 4.2. Figure 4.13 is a photograph of a single shear cell. The shear cells are mounted on a polycarbonate base 650 mm long and 450 mm wide before being placed into position in the experiment rack. Only one shear cell can be attached to the experiment rack at one time. The outer cylinder of each shear cell is made from a cast Acrylic tube with a 400 mm outside diameter

[1]This document can be found here:
http://eea.spaceflight.esa.int/?pg=xprec&id=9139&t=2641532544&oss=rozitis

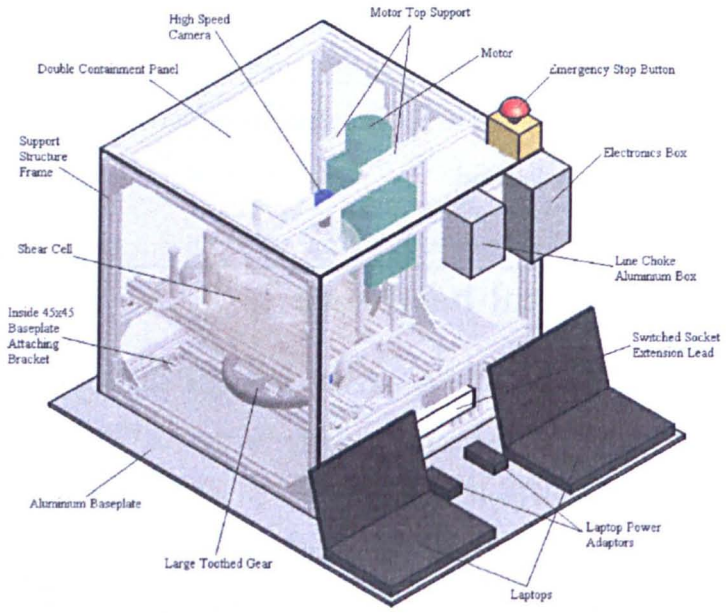

Figure 4.11: **Front view of the AstEx experimental rack** - Design drawings of the AstEx experimental rack (front view).

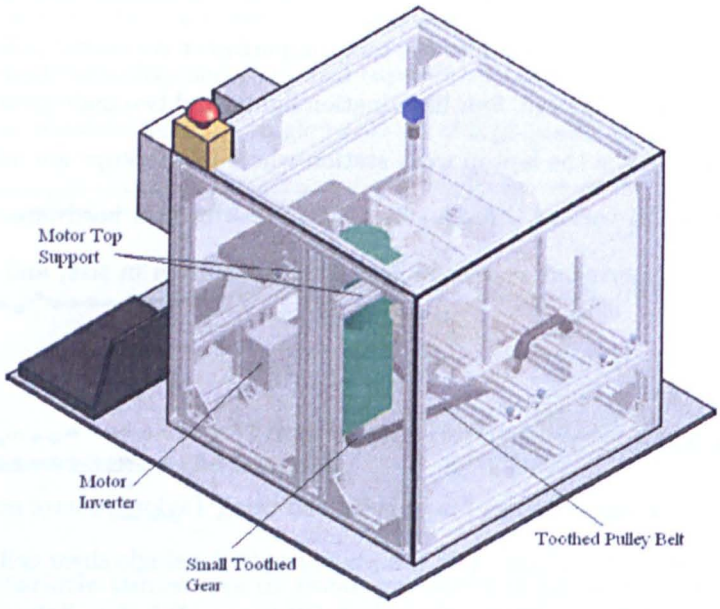

Figure 4.12: **Rear view of the AstEx experimental rack** - Design drawings of the AstEx experimental rack (back view).

and a 5 mm wall thickness and the inner cylinder is made from the same material but with a 200 mm outside diameter and a 3 mm wall thickness. This gives a gap size of 95 mm between the inner and outer cylinders, or ~32 bead diameters if 3 mm size beads are used. Both the inner and outer cylinders are 200 mm in height. When filled with beads to a height of 100 mm the whole unit (shear cell+base+beads) has a total mass of ~27.5 kg. The polycarbonate base features two handles used to carry and shake the shear cell. The outer wall of the inner cylinder is coated in a layer of beads to give a frictional surface. The inner surface of the outer cylinder is also coated in a layer of beads because this makes it closer to a possible real-world situation. This also avoids potential packing crystallisation from occuring - something which has been observed in other experiments that had a smooth outer wall (e.g., Wang *et al.*, 2008). The inner cylinder has a steel shaft running through the centre and is attached to the outer cylinder by two bearings contained inside a housing unit. This steel shaft attaches to the driving shaft and transmits the torque produced by the motor to the inner cylinder.

Figure 4.13: **An AstEx Shear Cell** - A photograph of the AstEx microgravity modified Taylor-Couette shear cell.

Figure 4.14 shows the internal workings of a shear cell. In a normal Taylor-Couette shear cell the granular material does not have a top constraint (e.g., Toiya, 2006). This allows the granular material to dilate and compact during shear experiments. However, without a top constraint in microgravity the granular material will just float away. To keep the granular material contained a movable and transparent pressure disk is used. It is loaded by 3 weak springs to apply a very small force using

sprung loaded roller balls (Fig. 4.15). A more detailed discussion of the pressure plate is provided in Section 4.4.4. One of the transparent pressure disks was designed so that it can also be fixed in place to allow experiments to be performed at constant volume. To maintain a granular seal the spaces between all moving parts are <0.5 mm to prevent a single glass bead from escaping.

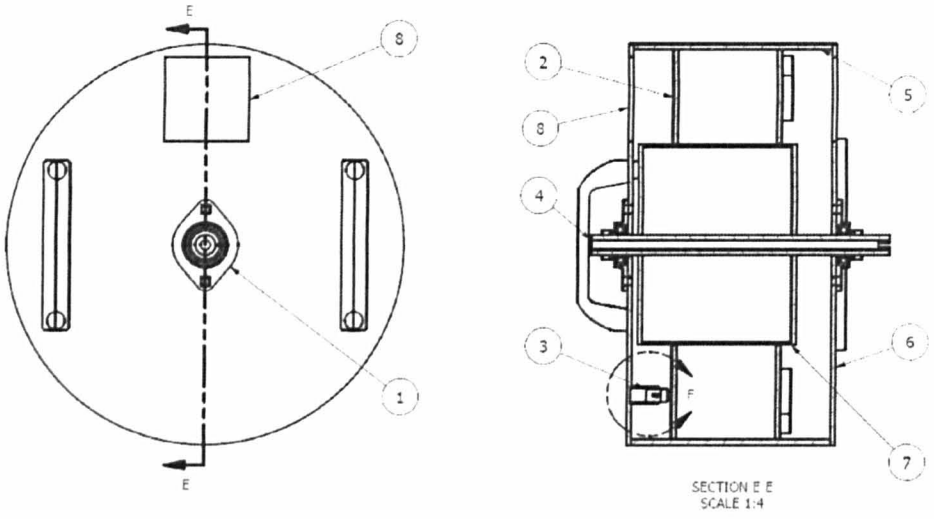

Figure 4.14: **Internal workings of a microgravity shear cell** - (1) Housing unit with bearing (2) Movable pressure disk (3) Pressure springs (4) Steel shaft (5) Fixed outer cylinder (6) Fixed bottom plate (7) Rotating inner cylinder (8) Camera viewport.

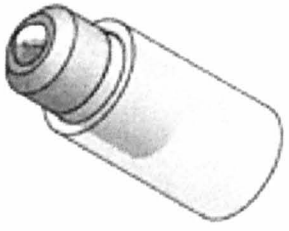

Figure 4.15: **The ball transfer unit** - The ball transfer unit used in the AstEx pressure plates.

Since the shear cells are self-contained units each shear cell contains glass beads of a certain size that cannot be easily exchanged. The granular material (glass beads) fills the shear cells to a height of 100 mm. The glass beads used in the AstEx experiment were soda lime glass beads with a density of 2.55 g cm^{-3}. In total three complete shear cells were built: one with 3 mm glass beads (~0.37 million beads), one with 4 mm glass beads (~0.16 million glass beads), and one constant volume shear cell containing 3 mm glass beads (~0.37 million beads). The shear cells were designed so that they could be easily exchanged between flights when the plane is on the ground. This allows all three shear cells to be flown during the parabolic flight campaign; one per flight.

4.4.3 Shear cell mounting

Figure 4.16 indicates how a shear cell is mounted inside the experiment rack. The shear cell itself is attached to the polycarbonate base via two aluminium securing bars. When a shear cell needs to be replaced the aluminium bars are undone, removed and then replaced again once the new shear cell is in position. The polycarbonate base, with a shear cell attached, is secured to the rack by four guide rods running through four holes in the polycarbonate base. Once in place there are two sliding locking bars to connect the two guide rods on each side of the shear cell. When these bars are locked the polycarbonate base is fixed securely in place. When the locking bars are undone the polycarbonate base is free to slide vertically up and down the guide rods.

During a parabola the polycarbonate base is always locked in place to allow experiments to be performed. It is unlocked during level flight to allow the experimenters to shake the shear cell between parabolas to reset the granular material contained inside the shear cell for the next experimental test (see the experimental procedures in Section 4.5 and Appendix A).

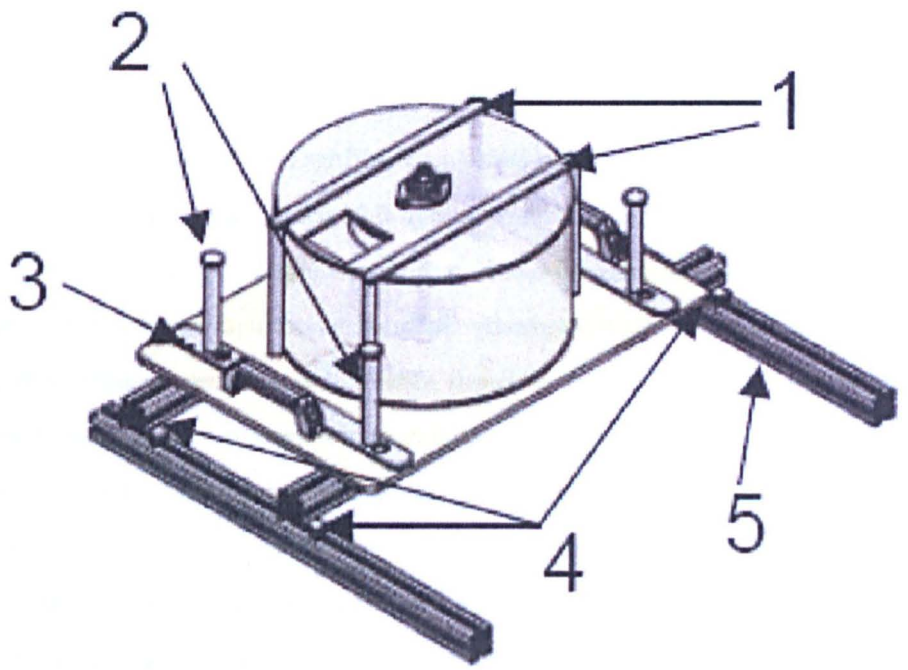

Figure 4.16: **Shear cell mounting** - (1) Shear cell securing bars (2) Guide rods (3) Sliding locking bars (4) Silent blocks (5) Support structure.

4.4.4 Counteracting imperfect microgravity

The microgravity environment on a parabolic flight is not perfect; there are small fluctuations which Novespace aim to maintain within the limits of 0 ± 0.05 g. This means that at times the experiment will experience small amounts of negative g. It is uncertain whether this negative g will reset the

grain contact network. To avoid the potential problematic effects of having negative gravity acting on the granular material the AstEx experiment was designed to ensure that all gravity fluctuations are positive. This is achieved by exerting a very low positive force on the top surface of the beads using the sprung loaded movable pressure disk described in Section 4.4.2.

The packing fraction for randomly packed spheres ranges from 0.555 (in the 0 g limit) to 0.645 (Onoda & Liniger, 1990). Assuming that, in 1 g, the beads initially fill the shear cell to a height of 100 mm with a packing fraction of ~0.6 then, if in microgravity the beads in the AstEx experiment dilate to a packing fraction of 0.555 the filling height would increase by 8.1 mm to 108.1 mm. If during the course of the experiments the beads then rearranged themselves to have the maximum random packing fraction (i.e., 0.645) the filling height would change to 93 mm. For simplicity, we assume that, theoretically, the filling height can vary between 100 ± 8.1 mm during the course of an experiment.

The mass of beads contained in the shear cell, assuming an initial packing fraction of 0.6 and a filling height of 100 mm is 13.47 kg. The force required to counteract the maximum amplitude of the gravity fluctuations (0.05 g) is 6.6 N. This force is distributed between 3 springs; each, therefore, exerts 2.2 N. A spring, which will provide a roughly constant force at all filling heights in the range 100 ± 8.1 mm, would be very long and have a very low spring constant. This is, unfortunately, not a feasible solution. The solution chosen was to assume the springs each provide a force of 2.2 N at the normal filling height (packing fraction = 0.6), a force of 0 N at the minimum filling height (packing fraction = 0.645) and a maximum force of 4.4 N at the maximum filling height (packing fraction = 0.555). This is reasonable as the negative gravity fluctuations occur during the microgravity phase when the particle packing fraction is at its lowest. Therefore, the pressure exerted is greatest in microgravity and this will counteract any effects of the negative gravity. Using these three forces at the three different filling heights and Hooke's Law[1] the required spring constant was calculated to be 0.272 N mm^{-1}.

Although not perfectly constant, the pressure plate with these weak springs (Fig. 4.14) should simulate the effect of very low positive gravity. During the microgravity phase of a parabola the particles in the experiment will experience an effective gravity fluctuating between 0 and 0.1 g depending on the particle packing fraction. This is equivalent to pressure variations of between 0 and 149 Pa assuming that the pressure is equally distributed over the entire area of the plate.

Aircraft vibrations may also reset the contact networks set up in the granular material. To get statistically valid results the experiment ideally needs to be free of aircraft vibrations and free of gravity jitters during the microgravity phases. To minimise these effects we attempt to isolate the shear cell from the aircraft vibrations. This is done by mounting silent blocks (a type of vibration

[1] Hooke's Law states that $F = k\delta x$, where k is the spring constant and δx is the displacement of the spring. δx is given by, $\delta x = x_o - x_l$, where x_o is the free length and x_l is the compressed length of the spring

isolator made of rubber) between the two strut profiles on which the shear cell is resting and the rest of the support structure frame (Fig. 4.16).

4.4.5 The mechanical system

The rotation rate for the inner cylinder of the shear cell was required to be very low i.e., <1 RPM. To provide the driving force a Watt Drive HU50C 64K4 inline helical geared motor is used. It is a three phase motor[1] and is controlled by a Moeller DF51-322-025 three phase inverter. The motor operates at 120 W and runs at 1330 RPM. However, the motor has an in-built gear system with a ratio of 123.14:1, giving an output speed of 10.8 RPM. To achieve the desired rotation speed for the experiment a toothed belt pulley system is used to achieve the final 10:1 reduction in rotation rate. The driving shaft of the pulley system connects to the shaft of the inner cylinder via a pin and groove slotting principle. The inner cylinder shaft then rotates the inner cylinder at the desired very slow speed of <1 RPM. The specific rotation speed is set by the inverter, and a load trip is programmed to protect the shear cell if the torque transmitted to the inner cylinder becomes too great.

4.4.6 Data collection

Two high-speed cameras (Matrix Vision Blue Fox 120aG) image the top and bottom glass bead layers of the shear cells. The cameras, which each have a resolution of 640 × 480 pixels, are mounted to the experiment rack in the test compartment and image the glass beads through camera viewports built into the shear cells (see Figs. 4.11–4.14). Four energy-saving reflector lamps are mounted next to the cameras (two for each camera) to illuminate the glass beads. For the particle tracking algorithm (see Chapter 5) to be accurate particles must move <1/10 d between consecutive frames (where d is the particle diameter). The fastest rotation rate used for the AstEx experiments is 0.1 rad s^{-1} which corresponds to a maximum speed of 10 mm s^{-1} at the inner shear cell. The smallest particles used in the AstEx experiment (3 mm diameter) will take a minimum of 0.03 seconds to move 1/10 d, therefore, a minimum frame rate of 33 fps is required for the particle tracking algorithm. It was decided to use a frame rate of 100 fps.

Two laptops are required for the AstEx experiment to collect and store data. One laptop controls the top camera and the second laptop controls the bottom camera and the motor. It was, of course, also important to ensure that the laptops do not have inbuilt freefall sensors!

It was intended to take 10,000 images with each camera during each experimental run. These 10,000 images were to be recorded into the random access memory of the laptop (one laptop per

[1] A three phase motor means the three circuit conductors carry three alternating currents (of the same frequency) which reach their instantaneous peak values at different times. One conductor is taken as the reference and the other two currents are delayed in time by one-third and two-thirds of one cycle of the electric current. This delay between phases has the effect of giving constant power transfer over each cycle of the current.

camera) during the experiment and then written to the laptop hard drive afterwards. For this to be succesful during the flight, the $\sim$ 6 GB of data had to be saved to the hard drive within the time between parabolas (i.e., in less than two minutes). Saving the data using the standard software provided with the cameras was not fast enough and so Dr. Ben Rozitis wrote a special AstEx data acquisition software to optimise the process of recording the data.

4.4.7 Health and safety requirements

Since the glass beads used in this experiment are small (3-4 mm) they are given the same precautions as a fluid onboard a parabolic flight and, therefore, require double containment. The shear cells themselves are self-contained units and act as a single layer of containment. The acrylic used to make the shear cells is a high resistance polymer that is used to make bullet-proof windows. Finite Element Analyses performed by Thomas-Louis de Lophem show that the shear cell itself is able to withstand up to 40 g when filled with 15 kg of beads (this is well above the estimated 9 g peak force that could be experienced during a crash landing[1]). In addition, to reinforce the structural strength still further, the shear cell is fitted with metallic U-shaped clamps and coated with an adhesive film. Therefore, even if the acrylic material was to fail, it would be prevented from shattering by the adhesive film. However, if in the very unlikely scenario that some fragments were ejected they would then be contained by the 5 mm thick external polycarbonate panels that form the double containment shell. These panels are also reinforced by an adhesive film.

Half of the top panel is able to slide open to give access to the shear cell in order to shake it and exchange it. This sliding access door has an interlock safety switch to automatically stop the motion of all moving parts of the experiment when the door is open. This ensures that no contact can be made with any moving parts at any time (despite the fact that the shear cell and polycarbonate base also serve as a physical barier to the moving parts).

The complete electrical system of the experiment is protected by a single, easily accessible emergency stop button. In the event of an emergency, actuating this button will cut off all 220 V AC power to the equipment. The electrical system is also protected by a differential circuit-breaker rated at 30 mA, and a fast-blow fuse rated at 6 A. Individual components of the experimental hardware are also protected by their own fuse but of lower values specific to their needs.

Finally, before loading the experiment into the aircraft it was also covered in foam padding to prevent any accidents from occuring during the parabolas.

[1] It is a Novespace requirement that the experiment be able to withstand the 9 g peak force that could be experienced during a crash landing.

4.4.8 Hardware modifications during flight campaign

All of the above details describe how the AstEx experiment was designed, prepared and built before going to Bordeaux for the two-week flight campaign. However, during the first week of the flight campaign (the preparation week) many further modifications were made to the AstEx experiment. These changes were made either upon request from the safety engineers (from ESA, Novespace or the Centre d'Essai en Vol [CEV]), or in order to improve the performance of the experiment.

4.4.8.1 Changes requested by safety engineers

During the preparation week the AstEx team were requested by the parabolic flight safety team to implement several changes. The changes requested were the following:

- Installation of extended handle bars to make the lifting and shaking of the shear cell easier. See before and after photos in Fig. 4.17 (a) and (b).
- Installation of additional motor grounding wires to provide *further* redundancy to the electrical system.
- Addition of protective plastic covers to the light switches as they were directly switching 240 V. See before and after photos in Fig. 4.17 (c) and (d).
- Addition of a removable strap around shear cell mounting and experiment rack to increase the number of attachment points from 5 to 6. Although 5 attachment points are more than sufficient for the normal operation during parabolic flight, it was felt that the complete rack did not have the sufficient safety margin during a crash landing i.e., when the peak forces are $\sim$9 g. This strap was added before take-off and landing but was removed once the aircraft had reached level flight to allow the experiments to be conducted. See before and after photos in Fig. 4.17 (e) and (f).
- Have a pair of gloves available that must be worn during lifting and shaking of the shear cell in order to protect the experimenters hands from being accidently cut from sharp edges, and to protect them from being burnt from the light bulbs

4.4.8.2 Changes to improve experiment performance

In the final month before the flight campaign several last minute design changes to the experiment were requested following the safety reviews conducted by Novespace, ESA, and the CEV. As a result, the experimental hardware was fully finished just a few days before the campaign started, leaving insufficient time for the AstEx team to properly test and debug the experiment in its fully integrated form.

Figure 4.17: **Before and after photos of the hardware changes requested during the parabolic fligth campaign** - (a) Original shear cell handle bars, (b) Extended shear cell handle bars, (c) Unprotected switches, (d) Switches after the addition of protective plastic covers, (e) Removable attachment strap removed (f) Removable attachement strap in place.

This testing and debugging phase therefore occurred during the preparation week of the parabolic flight campaign.

During testing it was quickly discovered that when the motor is running it can cause an image transfer error in the data connection between the high-speed cameras and the laptops. This was occurring for roughly a third of all images taken and this would have been an unacceptable loss of data for the intended parabolic flight experiments. By showing that the problem still occurred when the laptops and high-speed cameras were run from the laptop batteries only i.e., by separating the two power supplies, we were able to identify the source of the problem to be electromagnetic interference from the motor and its inverter. Similarly, the motor inverter data connection to one of the laptops was unstable and the communication repeatedly timed out. These problems did not manifest when the components of the experiment were tested individually but only when tested as a whole unit.

Unfortunately, the motor inverter was placed right next to the laptops and the USB data cables and could not be moved. The problem of electrical intereference was reduced by making three changes:

- The USB data cables were all coverered with aluminium foil to act as a shield.
- The USB data cables were moved as far away from the motor and inverter as possible.
- By finding the optimal laptop/high-speed camera/motor inverter connection combination.

After making these changes the problems occurred far less frequently but they did not disappear completely. If the experiment is to fly again the motor inverter should definitely be placed on the opposite side of the experiment rack and a special electromagnetic interference dampening device for the motor inverter should be installed. It would also be useful to coat the USB data cables in proper shielding tape.

As mentioned in Section 4.4.6, it was initially intended to take and save 10,000 images for each experimental run using the data acquisition software written by Ben Rozitis to optimise the process of recording the data. This was tested several times before the campaign and did work very well as long as the laptop hard drives were running fast and efficiently. To ensure the laptops were fast and efficient it became routine to defragment the laptop hard drives on a regular basis between testing and between experiments. However, on one occasion in the days leading up to the first flight, the defragmentation process had the opposite effect on one of the laptop hard drives: the speed at which the data was saved was reduced drastically. At this slower speed it would not have been possible to save all of the images to the hard drive between parabolas. The problem was resolved by partitioning the slow laptop hard drive into two separate disk drives and completely re-formatting one of them. When the data acquisition software was rerun from the freshly formatted partition it was running at full speed

again. It still remains unknown as to why the defragmentation process had such a counterintuitive effect.

4.5 AstEx experimental procedures

During the microgravity flight campaign there are three flights and in each flight there are 31 parabolas. As mentioned in Section 4.3 and shown in the schematic in Fig. 4.9, during each parabola there are three distinct phases: a $\sim$ 20 second $\sim$ 1.8 g injection phase, a $\sim$22 second microgravity phase, and a $\sim$ 20 second $\sim$ 1.8 g recovery phase. Between the end of one parabola and the start of the next there is a 2 minute 1 g rest period. This means the starts of the parabolas are 3 minutes apart. After each set of 5 parabolas it is standard procedure to take a longer 1 g rest of 4-8 minutes. The experimental procedures during a flight must be carefully designed for such an environment and then executed with scrupulous timing otherwise there is a risk of losing data. There are two different experimental modes used during the microgravity flight campaign:

- Mode 1 - The motor rotates the inner cylinder in the same direction for the full 20 seconds of microgravity.
- Mode 2 - The motor rotates the inner cylinder in one direction for the first 10 seconds of microgravity and then stops and reverses the direction for the remaining 10 seconds.

The first mode allows experiments to be performed investigating the steady state flow of granular materials under a constant shear rate. The second mode allows experiments to be performed investigating the flow of granular materials under a reversal of the shear direction. As we use the motor only to a fraction of its maximum operating power, and because it has a very large gearing ratio, the time taken for the motor to accelerate to the required speed or to reverse the direction of rotation is almost negligible.

Only one shear cell is flown per flight. The experiment is prepared during steady flight before the parabola sequence begins (see Appendix A). During each parabola the same sequence of events is followed. Approximately 5 seconds before the start of the injection phase of the parabola the experimenters start the high-speed cameras recording. During the $\sim$1.8 g injection phase the experimenters do nothing except monitor the experimental equipment for any malfunctions. As soon as the microgravity phase starts the experimenters start the motor. If the experiment is of type Mode 2 then halfway through the microgravity phase the direction of the motor rotation is reversed. During the $\sim$1.8 g recovery phase the motor is left running. Finally, when the 1 g rest phase starts the motor and high-speed cameras are stopped. During the 2 minute rest period the experimenters ensure all data

from the high-speed cameras are saved to the laptop hard drives, and the shear cell must be prepared for the next experiment. The shear cells are prepared by inspecting them for any damage or leaks, and shaking them by hand to reset the glass beads back to a reasonably consistent initial arrangement and to attempt to remove any contact networks and possible memory effects from the granular material. This procedure is repeated for each parabola; however, during the longer 4-8 minute rests the motor rotation speed was also adjusted. After the fourth parabola in each set of five the shear cell was not shaken in order to determine if the shaking did or did not influence the results (see Section 5.4.3). The experiments that were planned for each of the three parabolic flights are described in Tables 4.2–4.4.

4.6 Parabolic flight campaign

4.6.1 Problems encountered during the flights

4.6.1.1 Slow laptop hard drives due to aircraft vibrations

The first problem encountered during the first parabolic flight was that both laptops were saving the high-speed camera images to their hard drives much slower than on the ground. As a result the data were not being saved to the hard drives in the time periods between parabolas. To reduce the time spent saving the data the amount of data taken during one experiment was reduced by changing the camera frame rate from 100 fps to 60 fps. This is still much higher than the minimum camera frame rate needed to allow accurate particle tracking (see Section 4.4.6).

In addition, the length of time the cameras were taking images was also reduced during the flight i.e., the number of images taken per run was reduced from 10,000 to ~2,500. This meant that the camera was started a few seconds before the ~0 g phase and stopped a few seconds after the ~0 g phase. Unfortunately, due to the changes that had to be made to the camera settings no data were recorded for the top camera during five of the first ten parabolas of the first flight.

After the first flight landed the laptops returned to normal. It was determined, therefore, that aircraft vibrations were interfering with the hard drive write processes and making them much slower. Unfortunately there was no immediate fix for that problem so the camera frame rate was kept at 60 fps for the rest of the flight campaign and between 2,500 and 5,000 images were recorded for each parabola.

In the current configuration the laptops are mounted directly onto the experiment base plate. If the AstEx experiment is to fly again and a higher frame rate is necessary, a possible solution could be to mount the laptops on top of foam pads/mats to absorb and dampen the aircraft vibrations. An alternative solution would be to replace the laptop hard drives with expensive solid state hard drives as they have no mechanical moving parts and would, therefore, be completely immune to the aircraft

Table 4.2: Planned Experiments for Microgravity Flight 1: "Constant" Pressure, 4 mm Beads.

Parabola Number	1-4	5	6-9	10	11-14	15	16-19	20	21-24	25	26-29	30
Bead Size (mm)	4	4	4	4	4	4	4	4	4	4	4	4
Motor Rotation Rate (rad s^{-1})	0.025	0.025	0.025	0.025	0.05	0.05	0.05	0.05	0.1	0.1	0.1	0.1
Experimental Mode	1	1	2	2	1	1	2	2	1	1	2	2
Shake before parabola?	Y	N	Y	N	Y	N	Y	N	Y	N	Y	N

Table 4.3: Planned Experiments for Microgravity Flight 2: "Constant" Pressure, 3 mm Beads.

Parabola Number	1-4	5	6-9	10	11-14	15	16-19	20	21-24	25	26-29	30
Bead Size (mm)	3	3	3	3	3	3	3	3	3	3	3	3
Motor Rotation Rate (rad s^{-1})	0.025	0.025	0.025	0.025	0.05	0.05	0.05	0.05	0.1	0.1	0.1	0.1
Experimental Mode	1	1	2	2	1	1	2	2	1	1	2	2
Shake before parabola?	Y	N	Y	N	Y	N	Y	N	Y	N	Y	N

Table 4.4: Planned Experiments for Microgravity Flight 3: Constant Volume, 3 mm Beads.

Parabola Number	1-4	5	6-9	10	11-14	15	16-19	20	21-24	25	26-29	30
Bead Size (mm)	3	3	3	3	3	3	3	3	3	3	3	3
Motor Rotation Rate (rad s^{-1})	0.025	0.025	0.025	0.025	0.05	0.05	0.05	0.05	0.1	0.1	0.1	0.1
Experimental Mode	1	1	2	2	1	1	2	2	1	1	2	2
Shake before parabola?	Y	N	Y	N	Y	N	Y	N	Y	N	Y	N

vibrations.

4.6.1.2 Motor inverter connection timeouts

During the first flight the data connection from the motor inverter to one of the laptops timed out multiple times i.e., the data connection was interupted. Reinitialising the connection would have taken more time than was available between parabolas so the motor inverter data recording was suspended. This meant that for much of the first flight we do not have a record of the motor performance. The electrical time out was possibly caused by electromagnetic interference, or due to the laptop hard drive slow down (see above). During the second and third flights the data connection timed out only once, meaning that an almost complete record is available of the motor performance from those flights. As the motor data is not used in the experimental analysis the electrical time-outs did not cause any problems. However, should the motor data be deemed important the problem would be prevented in the future by minimising the electromagnetic interference and laptop aircraft vibration problems as already described above.

4.6.1.3 Stuck shear cell

As described in Section 4.5, it was standard practice for one of the experimenters to shake the shear cells between experiments to attempt to remove any contact networks and possible memory effects from the granular material. During the third flight it became increasingly difficult to shake the shear cell between parabolas 11 and 17. Then finally, during parabola 18, the shear cell became permanently stuck. Unfortunately, this means that the motor was not started during parabolas 18 and 19 whilst attempts were being made to free the shear cell. However, during one of these parabolas the high-speed cameras were still started providing useful data on how the beads behaved in imperfect microgravity conditions without any shearing force applied (see Chapter 5). Despite the shear cell being stuck several centimetres above its normal position the drive shaft was still able to rotate the inner cylinder. Experiments were, therefore, performed as normal for the remaining parabolas of the third flight experiments but without the shaking of the shear cell between experiments.

After the campaign had finished the experiment was transported back to the workshop at The Open University to free the stuck shear cell using a blow torch. Inspection of the shear cell drive shaft afterwards indicated that the two drive shafts had corroded and bonded together in the humid environment of the Novespace workshop. The corrosion occurred because the drive shafts were made out of mild steel which was a cheaper alternative to stainless steel. If the experiment is to fly again then the shear cell drive shafts should be remade out of stainless steal to prevent this problem from reoccurring.

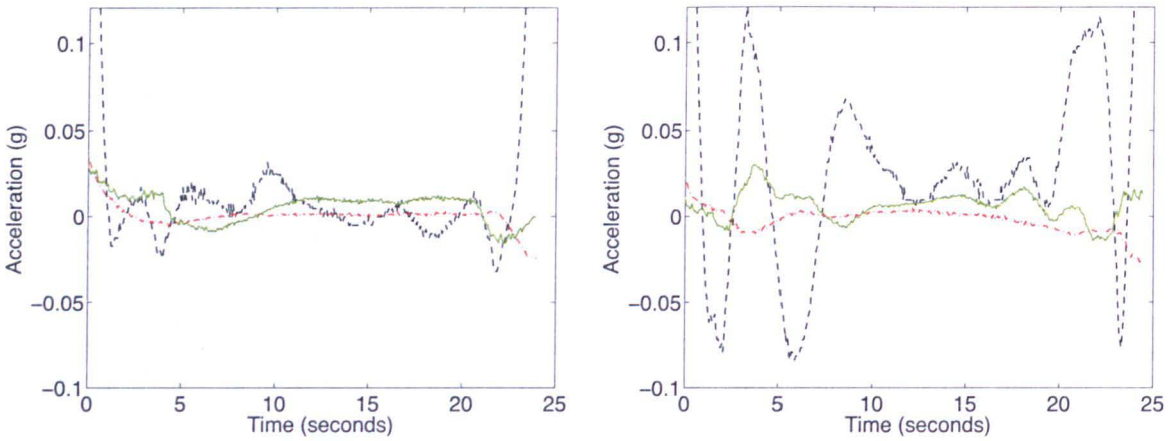

Figure 4.18: **The quality of microgravity** - Two examples of the gravity data during the microgravity phase of a parabola showing the acceleration in the z-direction (dashed black line), in the x-direction (dashed-dotted red line) and in the y-direction (solid green line). (a) An example of a good parabola when the gravity levels remain within ± 0.05 g (b) An example of a bad parabola when the gravity levels are, at times, much larger than ± 0.05 g.

4.6.1.4 Quality of the microgravity

One of the major issues during the parabolic flight campaign was the quality of the microgravity. Although the majority of the microgravity periods of the parabolas during the first two flights remained within the anticipated limits of ± 0.05 g the quality of the third flight was very poor. A combination of turbulence and large cumulonimbus clouds that had to be avoided meant that during the microgravity portion of the parabola there were often gravity fluctuations much larger than ± 0.05 g. In Fig. 4.18 the gravity data from two example parabolas are shown. Figure 4.18 (a) is an example of a good parabola, and Fig. 4.18 (b) is an example of a very poor parabola.

4.6.1.5 Quality of the hypergravity

Originally the AstEx experiment was not intended to take advantage of the $\sim$1.8 g period of the parabolas. However, for reasons that will be discussed in Section 4.6.2, in the third flight experiments were performed regularly during the second $\sim$1.8 g phase of the parabola. At the beginning of the second hypergravity phase there is a sharp change from microgravity to having a vertical acceleration of approximately $\sim$1.8 g. Next, the gravity level remains at approximately $\sim$1.8 g for 15-20 seconds and then finally there is a decrease in vertical acceleration back to the steady flight 1 g level. However, the gravity level sometimes has large fluctuations around $\sim$1.8 g and the transition from the vertical acceleration of $\sim$1.8 g to 1 g during this part of the parabola is not always smooth. In Fig. 4.19 the gravity data from two example parabolas are shown. Figure 4.19 (a) shows a parabola in which the vertical acceleration in second hypergravity phase remains relatively constant around $\sim$1.8 g and then

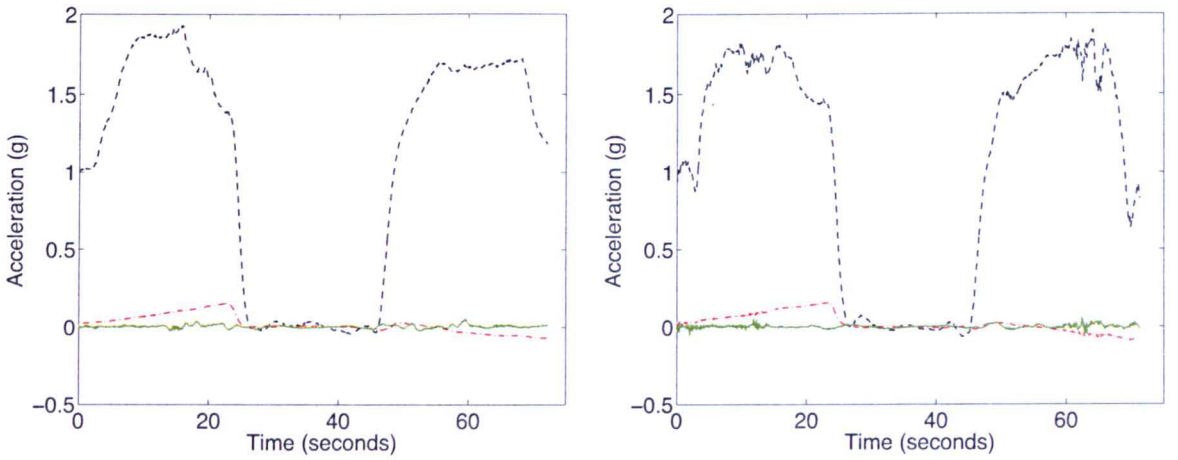

(a) (b)

Figure 4.19: **The quality of microgravity** - Two examples of the gravity data during a full parabola showing the acceleration in the z-direction (dashed black line), in the x-direction (dashed-dotted red line) and in the y-direction (solid green line). (a) The vertical acceleration in second hypergravity phase of this parabola remains relatively constant around $\sim$1.8 g and then there is a smooth transition from $\sim$1.8 g to 1 g. (b) The vertical acceleration in second hypergravity phase of this parabola has large fluctuations and then during the transition the vertical acceleration drops to $<$0.7 g before finally reaching 1 g.

there is a smooth transition from $\sim$1.8 g to 1 g. Figure 4.19 (b) shows a parabola in which the vertical acceleration in second hypergravity phase of this parabola has large fluctuations and then during the transition the vertical acceleration drops to $<$0.7 g before finally reaching 1 g.

4.6.2 Problems encountered between the flights

4.6.2.1 Jammed constant volume shear cell

After the second flight the pressure plate was to be replaced with the constant volume shear cell lid. However, the constant volume lid had been placed onto a spare shear cell during transport and it had become attached to this shear cell. The metal of the two parts had bonded and, even with lubricant, hot water, brute force, mallets and the help of half the staff of Novespace it was not possible to remove it. As a result we were, unfortunately, forced to abandon the constant volume experiment. It was decided to re-fly the 4 mm constant pressure shear cell with slightly altered procedures.

During the third flight the procedures for the microgravity phases were kept identical to the first two flights for reproducibility but the $\sim$1.8 g phases were also used. As described in Section 4.5, during the first two flights the motor continued to run during the second $\sim$1.8 g phase of each parabola but often the imaging stopped. During the third flight, in every parabola where shear reversal was not performed in microgravity, shear reversal was performed in the second $\sim$1.8 g phase of the parabola. These new procedures mean that shear reversal data is available in three different gravity regimes ($\sim$0 g, 1 g, and $\sim$1.8 g).

After transporting the experiment back to the workshop at The Open University it was found that the drive shaft was once again to blame for the bonded lid. As mentioned in Section 4.6.1.3, this design fault can easily be rectified if the experiment is to fly again by remaking the drive shaft out of stainless steel.

4.7 Collected data during flight campaign

Constant shear rate and shear reversal experiments were carried out in microgravity and 1 g with granular materials of two different particle sizes (3 mm and 4 mm diameter), and with three different shear rates (0.025, 0.05 and 0.1 rad s^{-1}). In some parabolas experiments were also conducted in the ~1.8 g regimes giving data for three gravity regimes (1 g, ~0 g and ~1.8 g). We additionally conducted a few experiments in which we did not shake the granular material prior to the parabola in order to determine if the shaking did or did not influence the results.

Two experiments were performed where the beads were imaged without the motor rotating during steady 1 g flight before the parabolas started. Two more experiments were performed where the beads were imaged during the period of microgravity also without the motor rotating. These experiments should give us an indication of the influence of the aircraft vibrations and fluctuating gravity levels on the movements of the beads. This is discussed further in Chapter 5.

On average images were taken at a rate of 60 fps on both cameras simultaneously and we were able to collect on average ~68 seconds of data per parabola.

4.7.1 Summary of data collected

A summary of the experiments performed and data collected during the parabolic flight campaign are given in Table 4.5. In some parabolas we were unable to collect data due to the issues outlines in Section 4.6.1. In Table 4.5 the parabolas during which we encountered problems have only been included if we got enough useful data from either or both cameras.

During the flight campaign some experiments were also performed between flights, on the ground, with the AstEx experiment in its final location in the plane. The details of all of these experiments and the data collected are given in Table 4.6. Due to the restricted time available, and the issues discussed in Section 4.6.1, experiments were not performed for both bead sizes at all rotational velocities.

Several months after the flight campaign further ground-based tests were perfomed in the laboratory at The Open University. Many experiments were performed (uniform shear and shear reversal) with both bead sizes and at all three inner cylinder rotational velocities. Unfortunately, when the data were analysed (using the methods described in Chapter 5) the particle dynamics were very different

Table 4.5: A summary of the experiments performed during the 3 parabolic flights. Column 5 is the number of parabolas during which we performed each experiment and were able to record useful data over the course of the ESA 51st Parabolic Flight Campaign (*one parabola was aborted during the 3rd flight). The other columns show the details of the different experiments performed throughout the campaign.

Particle size (mm)	Angular velocity (rad s^{-1})	~0 g phase (Uniform shear/ Shear reversal)	Recovery ~1.8 g phase (Uniform Shear/ Shear reversal)	No. of parabolas during which data collected
3	0.025	Uniform	Uniform	5
3	0.025	Reversal	Uniform	4
3	0.05	Uniform	Uniform	5
3	0.05	Reversal	Uniform	5
3	0.1	Uniform	Uniform	5
3	0.1	Reversal	Uniform	5
4	0.025	Uniform	Uniform	5
4	0.025	Reversal	Uniform	10
4	0.025	Uniform	Reversal	5
4	0.05	Uniform	Uniform	6
4	0.05	Reversal	Uniform	6
4	0.05	Uniform	Reversal	6
4	0.025	Uniform	Uniform	6
4	0.1	Reversal	Uniform	8
4	0.1	Uniform	Reversal	5
4	0	-	-	2
Total number of parabolas used out of a possible 92*				88

to the experiments performed during the flight campaign. Specifically, the particle velocities were found to be larger in the tests performed in the laboratory compared to the tests performed during the flight campaign. The exact cause for this difference is unknown but it may be due to the fact that, after the bonded components of the shear cells were separated, they were well lubricated before being put back together. Therefore, there may be less friction between the components of the shear cell which increases slightly the rotational velocity. Another possibility is that the glue used to attach the particles to the outer wall of the inner cylinder has, over time, rubbed off onto the particles in the shear cell and is now providing a cohesive force between the particles. Whatever the reason may be for the difference the result is that, although these laboratory experiments are useful for certain tests, only ground-based data collected during the flight campaign can be used to compare directly with the microgravity experiments.

4.8 Chapter conclusions

The AstEx parabolic flight experiment was selected through a highly competitive process to be part of ESA's 'Fly your Thesis' programme. The experiment, which investigates granular flow caused by

Table 4.6: A summary of the experiments performed in the plane but on the ground over the course of the ESA 51st Parabolic Flight Campaign.

Particle size (mm)	Angular velocity (rad s^{-1})	Type of experiment (Uniform shear/ Shear Reversal)	No. of experiments performed
3	0.025	Uniform	2
3	0.025	Reversal	2
3	0.05	Uniform	1
3	0.05	Reversal	2
3	0.1	Uniform	2
3	0.1	Reversal	2
4	0.025	Uniform	2
4	0.025	Reversal	3
4	0.05	Uniform	4
4	0.05	Reversal	3
4	0.1	Uniform	0
4	0.1	Reversal	0

shear forces in a Taylor-Couette shear cell, was designed by the AstEx team, built at the workshop at The Open University and then flew as part of ESA's 51st Microgravity Research Campaign in November 2009. Useful data was collected in a total of 88 parabolas (out of a possible 92) making the experiment a huge success, particularly for a student team who had previously had no experience of experiment design and development.

Designing, building and flying a parabolic flight experiment was a very different process, in many ways, from how the AstEx team had imagined. Throughout the entire process from selection to the post-flight treatment of the collected data, the AstEx team were constantly learning. The lessons we learned cover many different aspects, which include learning how to write successful proposals and sell our science, the hands on experience of designing and building an experiment which can produce valuable science yet satisfy incredibly strict health and safety requirements, being responsible for a budget, being responsible for our own public outreach[1], and having the ability to deal quickly and efficiently with problems in a stressful environment!

4.8.1 Lessons learned

Highlighted below are a few of the key lessons the AstEx team have learned which we feel are important to keep in mind for future flights and would also be useful information for future 'Fly your Thesis' teams.

1. The design and construction of a parabolic flight experiment is an iterative process right up until the day of the first flight

[1]See the website *http://www.open.ac.uk/pssri/astex/* designed, constructed, written and updated my myself.

There are three entities involved in running a parabolic flight campaign: Novespace, ESA, and the CEV. The first entity a team deals with after selection is Novespace. Teams are requested by Novespace to have the design finalised several months before the flight campaign. However, as the experiment is designed and built expect many changes to be requested (sometimes major) by Novespace. They have several safety reviews of the design and can come to examine the experiment in person. Each safety review and visit is likely to result in requested changes being made to your experiment until they are convinced it meets all the necessary safety requirements.

Next, once Novespace are satisfied with your experiment they will pass your design documents on to ESA. The ESA safety review, which takes place just a few weeks before the flight campaign, may again result in more changes being requested despite Novespace being satisfied.

Finally, upon arrival at Novespace in Bordeaux for the parabolic flight campaign, Novespace, ESA and the CEV will all examine the experimental hardware, test the electrical wiring, and request to have the operating procedures demonstrated. Again, at this stage, just a few days before the first flight, it is likely that further changes or additions to your experiment will be requested before getting the final approval to fly.

2. Expect the unexpected - especially when it comes to safety

A parabolic flight environment is potentially a very dangerous one. ESA, Novespace and the CEV have a responsibility to ensure that the experiment will not put yourself or any other passengers at risk at any time. Any risk, however minor, of damage to the plane or injury to passengers is unacceptable. Understandably this responsibility is taken very seriously and the experiments must meet all requirements. However, it is highly likely that, even if you think you have considered absolutely everything and put in place all the necessary safety precautions, you will still be asked to do more to improve the safety! By the time we flew, the AstEx experiment had 4 levels of containment for the glass beads, was capable of withstanding over 40 g of acceleration, and was almost completely bullet and bomb proof as well!

3. Be prepared for the paperwork

The majority of the time spent working on a parabolic flight experiment in between selection and flight is consumed with paperwork. The ESDP (Experiment Safety Data Package mentioned in Section 4.4) is a long document which must be continually updated, reviewed and modified. It contains very detailed design drawings, electrical diagrams, measurements and calculations. Do not under estimate the time it will take to complete this document to the required standards.

4. Plan carefully and ensure you have time for testing

As a result of the points 1-3 above, running out of time during the experiment preparation is very likely. It is very important to ensure there is enough time to test and debug the experiment before

flying. Unfortunately, this is something that the AstEx team were not able to do. As a result there were many issues that were not discovered until during the parabolic flight campaign.

If we were to do it all over again we would do everything possible to ensure we had a fully functional experiment a few weeks before the first flight. This would allow time for detailed testing of the hardware and would also provide test data so that the data analysis could also be tried and tested. When analysing the data it is possible that you will come across things that you would like to include in your experiments (i.e., additional measurements or slight changes to the set up). Allowing time to look at some test data before the flight will provide the opportunity to make such additions or changes.

4.8.2 Design changes for future flights

The AstEx experiment worked very well but it could still be improved. Based on our experiences during the parabolic flight campaign a list has been made of the design changes the AstEx team would like to implement before any future flights. The AstEx team would like to:

- Remake the mild steel shaft and mild steel fittings using stainless steel to avoid all problems with corrosion.
- Rearrange the components inside the experimental rack to try to minimise electromagnetic interference from the motor and inverter. We would also add a special electromagnetic interference dampening device for the motor inverter, and coat the USB data cables in proper shielding tape.
- Use solid-state hard drives to ensure no problems are caused by the aircraft vibrations when trying to save the data.
- Implement a method of measuring the torque, and thus the shear strength, during the experiments.
- Implement a method of measuring the height of the pressure plate, and thus the dilation of the granular material, during the experiments.
- Adjust the camera illumination lights so that their reflections off the pressure disks do not appear in the images.
- Add in small accelerometer to the experiment, which is synced with the cameras, to record the gravity variations.

Chapter 5

The AstEx Experiment: Data Analysis

5.1 Summary of Chapter

This chapter describes how the data obtained during the parabolic flight campaign (as described in Section 4.7.1) are processed through the AstEx data analysis pipeline. The data analysis pipeline starts with the analysis of images and continues through to calculations of particle velocities with many intermediary steps. A detailed uncertainty analysis is performed and then, finally, a study is presented which considers the effect of all factors that may influence the measured particle velocities and, thus, the final experimental results. Although some examples of processed data are given in this chapter the results are not discussed in detail until the following chapter. As a result, there are no detailed discussions of granular material dynamics in this chapter.

5.2 Determination of particle velocities

5.2.1 Particle tracking

The raw data from the AstEx experiment are images. On average ~4000 images were taken with both the top and the bottom cameras during each of the experiments. The first step in the data processing pipeline is to analyse these images, which involves detecting the particles in each image and then tracking the particles between consecutive frames.

In each image approximately 600 particles can be seen (Fig. 5.1). Almost every single one of these particles is identified and subsequently tracked between consecutive images using an adaptation of a

subpixel-accuracy particle detection and tracking algorithm (Crocker & Grier, 1996).

This particle tracking process is completed in several stages. First, a band pass filter is applied to smooth the image and subtract the background. Then, the individual particles must be identified. This is done using an algorithm that specifically searches for local brightness maxima. To aid particle detection, particle size (in pixels) must be specified. A pixel is then selected as a candidate particle if no other pixel within the radius of the particle is brighter.

Next, the accuracy of the particles' position is improved. To do this the weighted centroids of the pixels in the regions around the locally brightest pixels are calculated and the centroid locations are then adjusted accordingly. At this stage a precise list of particle coordinates in one image can be produced. In Fig. 5.2 these position coordinates are plotted over the original image to verify the accuracy of the detection.

The following step is to detect the particles in all of the images taken during an experimental run and, finally, to construct two-dimensional particle trajectories from the list of particle coordinates determined for each frame (i.e., at discrete times). The algorithm which performs this task outputs the original data sorted into a series of trajectories assuming that no particle moves more than one half of a particle diameter in between frames (the results of the tracking are better if particles move less than one tenth of a particle diameter in between frames). Each of the identified particle trajectories (sometimes referred to as particle tracks) is assigned a unique ID number and a list containing the coordinates of the particle trajectories at each discrete time is produced.

Finally, a test must be performed to determine if the particles have been tracked to sub-pixel accuracy. The test involves plotting a histogram of the fractional part of both x and y coordinates for all particle trajectories at each time. This test indicates whether there is any pixel biasing, i.e., if the centre of the particles are preferrentially located within certain regions of the pixels. In an ideal case, for large enough numbers of particles, these histograms should be flat showing that the particle positions are randomly distributed and that there is no bias in the results (Fig. 5.3 (a) and (b)). If this is the case then the centres of the particles are located with an accuracy of approximately 1/10 pixel. As is sometimes the case, the histograms do not appear flat (Fig. 5.3 (c) and (d)) and the parameters must be adjusted and the particle tracking process reinitiated (if sub-pixel accuracy is desired).

5.2.2 Calculating the pixel scale

The pixel scale was calculated using the check beads: these are beads which are glued to the top surface of the confining pressure plate. The real separations were measured, centre to centre, with vernier callipers. The measured distances, shown in Fig. 5.4, are for the 4 mm shear cell and have an estimated uncertainty of $\pm$ 0.2 mm. The check beads were then identified in the images and their

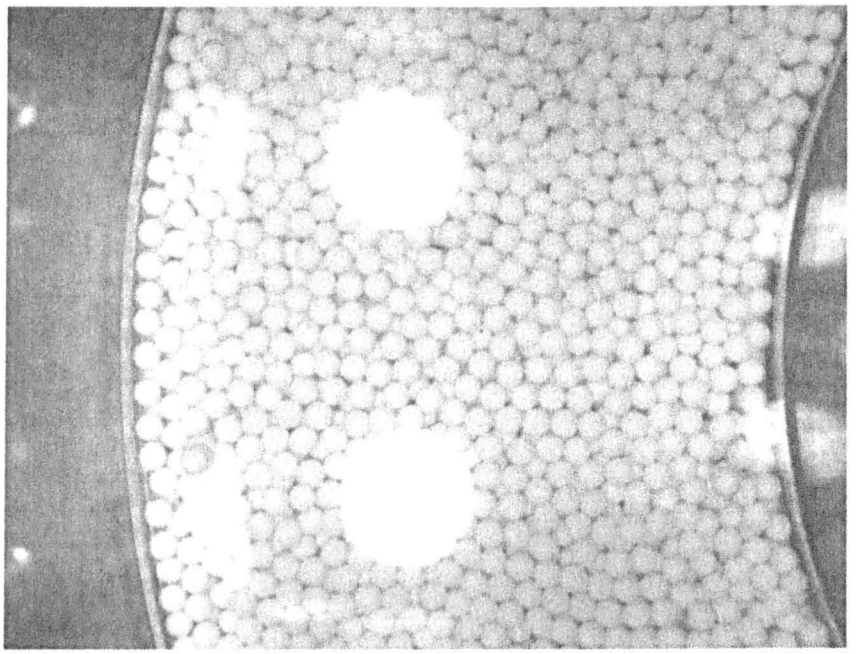

Figure 5.1: **AstEx example image** - An example image obtained of the top layer of beads during an experiment. Part of the inner cylinder wall is seen on the right and part of the outer cylinder wall is seen on the left. The two large bright white spots are the reflections of the lamps on the pressure plate. Further reflections can also be seen close to the outer cylinder and close to the inner cylinder.

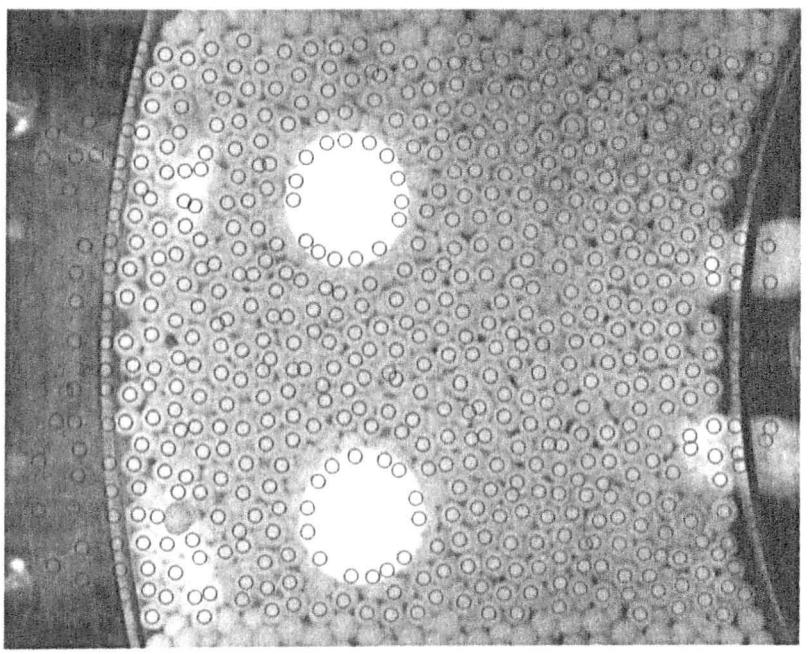

Figure 5.2: **AstEx example image showing detected particles** - Example of all the particles detected (blue circles) in one image (before any filtering). Many points are incorrectly identified as particles. Part of the inner cylinder wall is seen on the right and part of the outer cylinder wall is seen on the left.

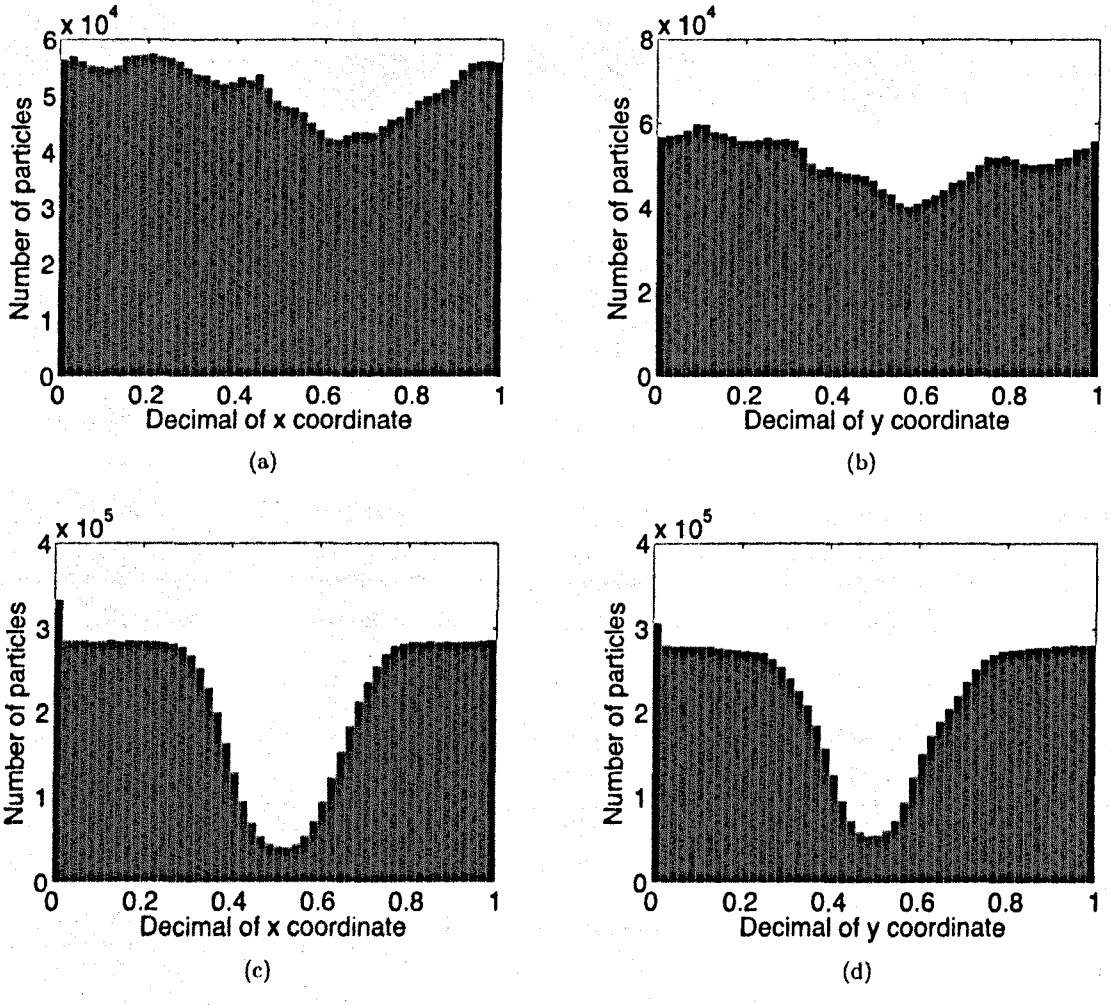

Figure 5.3: **Histograms demonstrating pixel biasing** - Histograms of the fractional part of particle coordinates for a set of data. (a) and (b) shown the x and y coordinates for data with no pixel biasing. (c) and (d) shown the x and y coordinates for data with pixel biasing.

centres were located (Fig. 5.5).

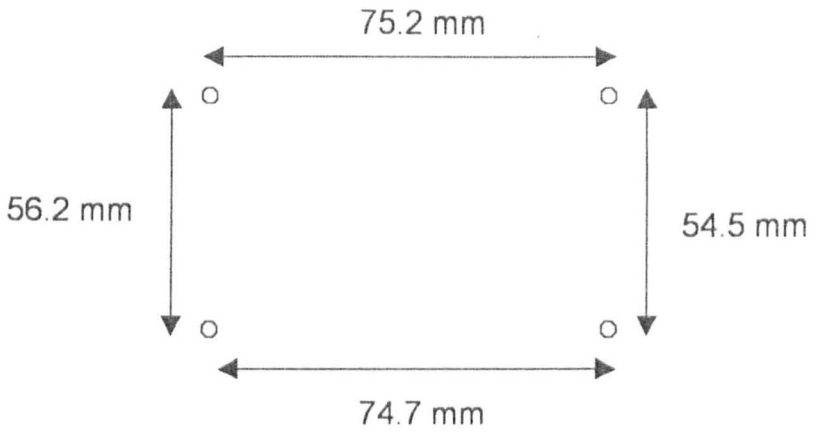

Figure 5.4: **The distances between check beads in mm** - The measured separation distances for the check beads on the 4 mm shear cell. The distances have an uncertainty of ± 0.2 mm.

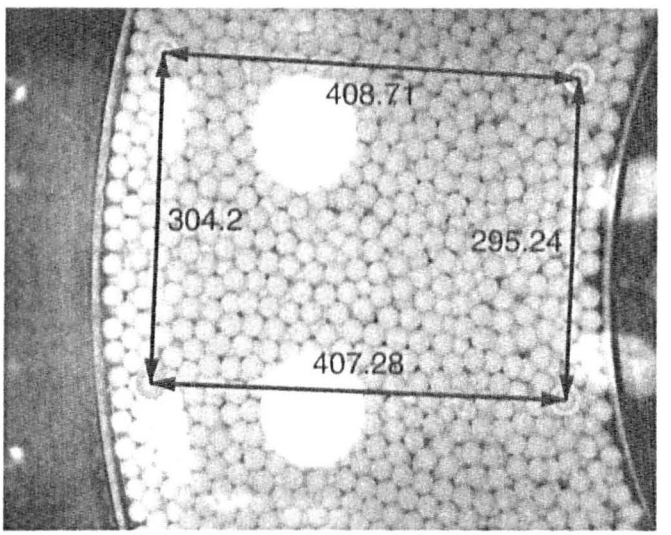

Figure 5.5: **The distances between check beads in pixels** - The check beads (identified by the particle tracking algorithm) in an image and the distances between them in pixels.

The pixel scale at the height of the check beads (i.e., on the surface of the pressure plate), found by comparing the inter-particle distances in pixels and mm, is 5.43 ± 0.02 pixels mm^{-1}.

The viewing geometry of the check beads in comparison to the top layer of beads within the shear cell is shown in Fig. 5.6. The pixel scale that has been calculated for the check beads on the surface of the pressure plate will not be the same as the pixel scale for the layer of beads below the pressure plate. The distance from the camera to the top of the pressure plate is 141 mm. The check beads on the surface are 4 mm in diameter and they sit at a depth of approximately 2 mm into the pressure plate (a

small hole was made to accommodate them). The pressure plate has a thickness of 5 mm. Therefore, assuming the pressure plate is resting on the top layer of beads contained below, the difference in height between the top of the check beads and the top of the beads below will be 7 mm. The distance to the camera from the check beads, R_1, is 139 mm and the distance from the top layer of beads below the pressure plate, R_2, is 146 mm. The pixel scale (PS) will decrease with distance from the camera according to $1/R$, where R is the distance to the camera. Therefore $PS_2 = PS_1(R_1/R_2)$. Assuming the pixel scale at the check beads (PS_2) is 5.43 $\pm$ 0.02 pixels mm^{-1} we can then determine that the pixel scale at the top layer of beads in the shear cell (PS_1) is 5.17 $\pm$ 0.02 pixels mm^{-1}.

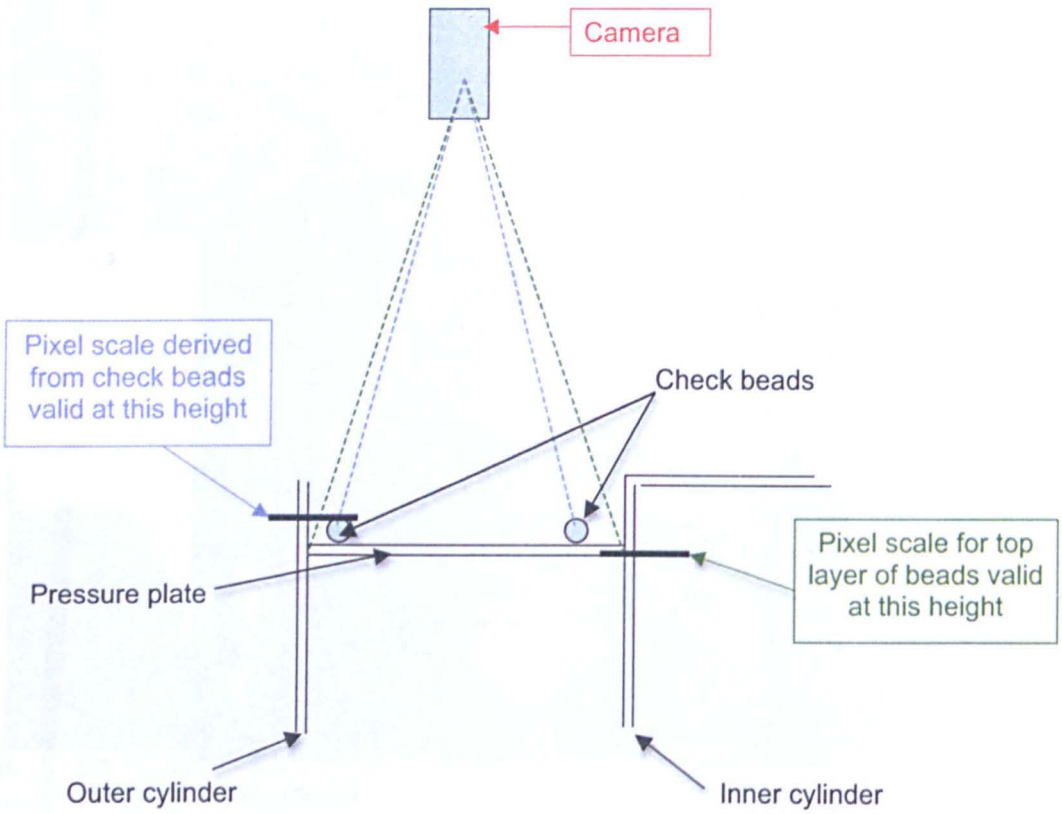

Figure 5.6: **The AstEx viewing geometry** - The viewing geometry of the check beads which are glued to the top of the confining pressure plate and the top layer of beads contained within the shear cell.

For the bottom camera, where there are no check beads, the pixel scale was calculated by choosing several particles in a line from within a crystallised region (the bottom surface was very crystallised). The distance between the centres of all of these particles can be combined with the known particle radius to calculate the pixel scale. In the few laboratory-based runs that were also performed with no pressure plate (see Section 5.4.1) the pixel scale on the top surface was calculated as accurately as possible using bead diameters.

5.2.3 Calculating the centre of the shear cells

Before any radial and angular displacements or velocities can be calculated the centre of the two dimensional disk must be known (i.e., the centre of the two concentric cylinders).

The first step was to take one image and identify, by hand, several points distributed around the walls of the two cylinders. Points were chosen on the inner wall of the outer cylinder and on the outer wall of the inner cylinder (Fig. 5.7). This then gives a series of points for the large cylinder inner edge as $(XL_1, YL_1), (XL_2, YL_2), ...(XL_n, YL_n)$, and for the small cylinder outer edge as $(XS_1, YS_1), (XS_2, YS_2), ...(XS_n, YS_n)$.

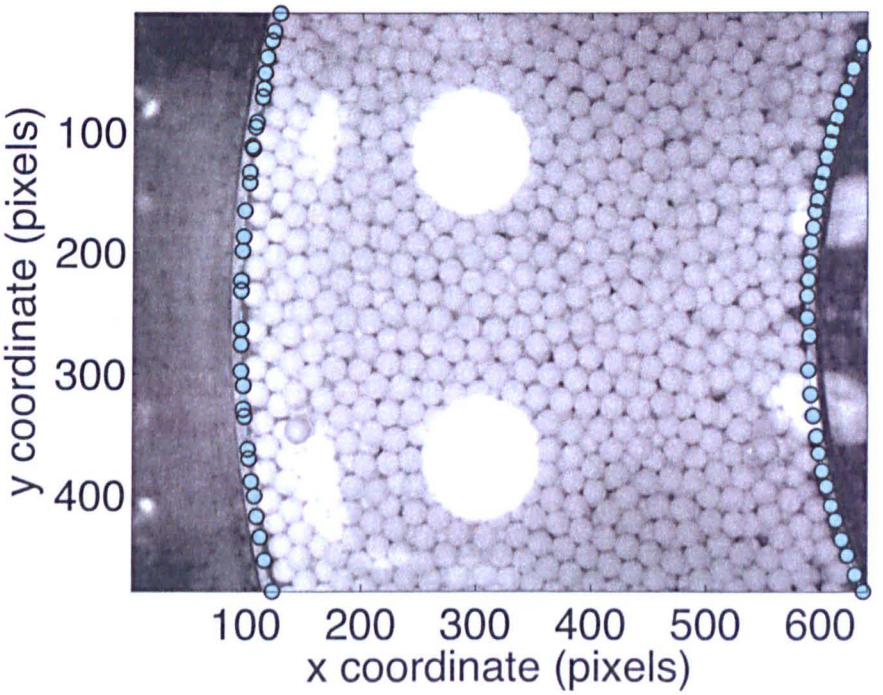

Figure 5.7: **Points used to calculate the centre of the shear cells** - The 38 points selected by hand on the inner wall of the outer cylinder (left) and the 32 points selected on the outer wall of the inner cylinder (right).

To calculate the centre points accurately it was necessary to minimise the difference between the known radii and the calculated radii for a given set of centre points. To do this the summed functions of A and B as shown below (Eqs. (5.1) and (5.2)) were minimised. The values of the two centre coordinates that correspond to the minimum values of A and B are thus the centre coordinates for the two cylinders.

$$A = \sum_{i=1}^{n} \left(RL - \sqrt{(XL_i - X_C)^2 + (YL_i - Y_C)^2} \right)^2 \tag{5.1}$$

$$B = \sum_{j=1}^{m} \left(RS - \sqrt{(XS_j - X_C)^2 + (YS_j - Y_C)^2} \right)^2 \tag{5.2}$$

Where RL = 195 mm × pixel scale and RS = 100 mm × pixel scale. (X_C, Y_C) are the coordinates of the centre position. As the circle centre coordinates and the circle radii are now known the full circle solutions can be plotted and compared to the original image to check for accuracy (Fig. 5.8). The coordinates found for the centres of the two cylinders are (in pixels):

- Outer cylinder: (1103.41, 253.63)
- Inner cylinder: (1103.61, 255.73)

This disagreement is 0.04 mm in the x-direction and 0.41 mm in the y-direction (this corresponds to within 1/8 of a 4 mm particle diameter or better in both cases). From this point onwards the mean of this centre position (1103.5, 254.7) is assumed for both cylinders for the normal set-up during the parabolic flight campaign.

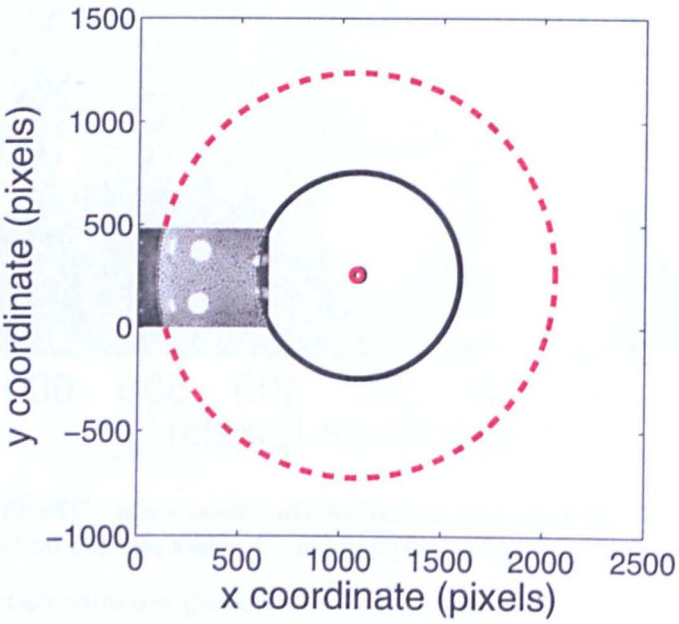

Figure 5.8: **The final circle solutions** - The circle solutions for the two cylinders, found via minimisation of the difference between the known radii and the calculated radii plotted over the original image. The solid black line and the dashed red line show the best fit circle solution for the inner and outer cylinders, respectively.

As mentioned in Chapter 4 there were two cameras: one to image the top surface and one to image the bottom surface. As also discussed in Section 4.7.1 some additional experiments were performed in the laboratory at The Open University several months after the parabolic flight campaign. In the laboratory tests the camera was not placed in exactly the same location as for the flight campaign tests. Therefore, for each of the different geometries (including when the shear cell became stuck at

Table 5.1: The pixel scale and centre of the shear cells for each of the 8 different types of experiment

Type of Experiment	Camera	Pixel Scale (pixels mm^{-1})	Center of the shear cells (pixels)
Flight campaign: normal set-up	Top	5.17	(1103.5, 254.7)
Flight campaign: normal set-up	Bottom	5.6	(-507.0, 209.7)
Flight campaign: end of Flight C	Top	5.5	(1150.4, 256.9)
Flight campaign: end of Flight C	Bottom	5.25	(-453.3, 210.0)
Laboratory based experiments: rerun of Flight A	Top	5.25	(1108.5, 260.1)
Laboratory based experiments: rerun of Flight B	Top	5.25	(1078.1, 250.3)
Laboratory based experiments: rerun of Flight A, no pressure plate	Top	5.25	(1108.5, 260.1)
Laboratory based experiments: rerun of Flight B,no pressure plate	Top	5.25	(1073.5, 245.4)

the end of Flight C) the pixel scale and the centre of the shear cells must both be calculated. A summary of the different geometries and the results of the pixel scale and locations of the centres of the shear cells are given in Table 5.1. Note that, although the data from the laboratory tests performed at The Open University are not used for comparison with the microgravity experiments, they are used for some tests such as to determine the influence of the pressure plate on the granular material (see Section 5.4.1).

5.2.4 Removing spurious particles

During the particle detection and tracking there are many points in the field of view which have been incorrectly classified as particles by the particle detection algorithm. These spurious particles, which can be seen in Fig. 5.2, are caused, for example, by reflections of the lamps on the pressure plate or by reflections of particles in the walls of the shear cell.

To remove such spurious particles they must first be identified. This is done by determining the intensities and sizes of the tracked particles. Normally the spurious particles lie outside the normal range. Figure 5.9 shows the particles in one image plotted as a function of their brightness. Figure 5.10 shows the same particles plotted as a function of particle size. The average brightness and particle size per particle trajectory are calculated and then, using the information obtained from the plots, a filtering criterion is applied to the data to remove the spurious data points from tracked-particle data. The spurious particles outside the shear cell i.e., with radii greater than that of the outer cylinder or less than that of the inner cylinder, are filtered out using the calculated radial coordinates of the shear cells as boundary conditions.

Figures 5.11 and 5.12 demonstrate a fully filtered image with no spurious particles. All spurious

particles have been removed by a combination of particle brightness filtering, particle size filtering and radial boundary filtering. As can be seen in Fig. 5.12, real particles are also sometimes lost in the filtering process. This, unfortunately, occurs in regions of high interest, such as near the inner, rotating cylinder on the top surface. A check, performed later in Section 5.4.2, demonstrates that losing these particles does not influence the measured particle dynamics.

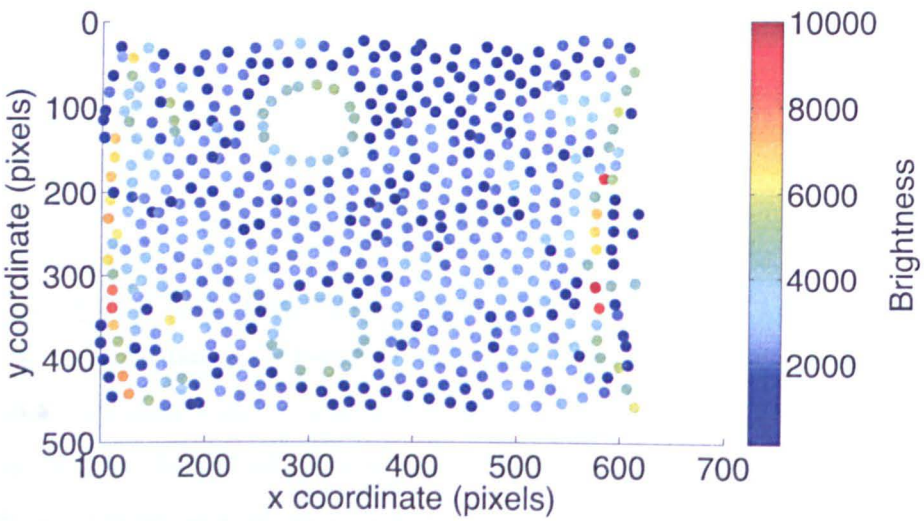

Figure 5.9: **Tracked particles plotted as a function of their brightness** - Particles detected in one frame are plotted in the location they were detected. The colour represents their brightness. Particles are not drawn to scale.

5.2.5 Particle lifetimes

Once the tracking has been performed and the spurious particles have been filtered out it is then possible to investigate the particle tracks. First, the particle lifetimes are considered (i.e., the length of the particle tracks) and then, in the next section, the locations of the first and last appearance of each particle are examined. To investigate the particle lifetimes, two example experiments were considered for both the top and bottom cameras. The first example is one which is likely to have the longest lasting particle tracks of any experiment i.e., an experiment with the 3 mm beads and the slowest motor rotation rate. The second example is likely to have the shortest particle tracks of any experiment i.e., an experiment with the 4 mm beads and the fastest motor rotation rate.

To analyse the mean track lengths as a function of distance from the moving inner cylinder the particles are separated, according to their radial position, into equal cylindrical rings (referred to as radial bins) reaching from the inner cylinder wall to the outer cylinder wall (Fig. 5.13). The mean particle track lengths in each of these radial bins, and for each of the four different types of run are given in Table 5.2. From these results we can draw several conclusions. First, as expected, the mean

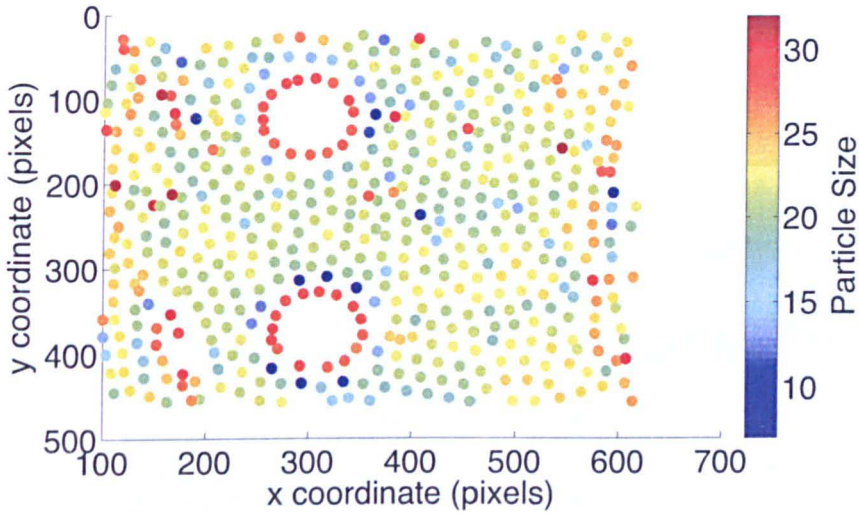

Figure 5.10: **Tracked particles plotted as a function of their size** - Particles detected in one frame are plotted in the location they were detected. The colour represents their detected size. Particles are not drawn to scale.

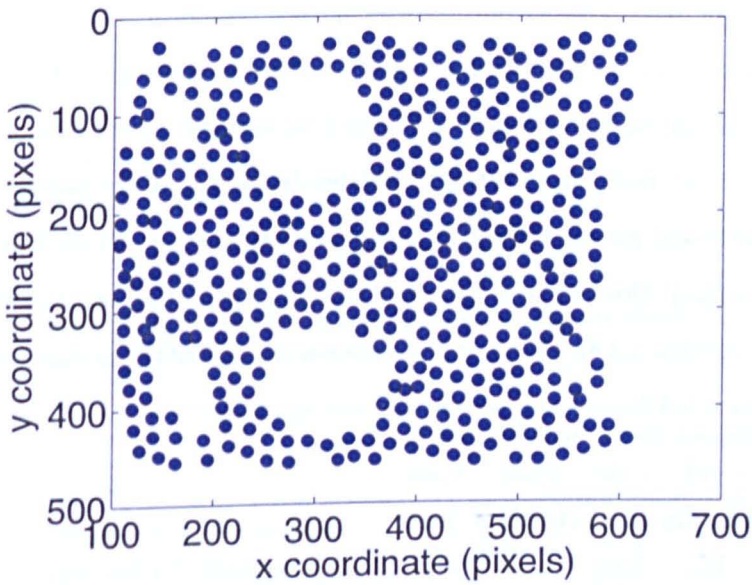

Figure 5.11: **Locations of particles that have survived the filtering** - Locations of particles detected in one frame after the filtering process. Particles have been filtered as a function of their radial position, size and brightness. No spurious particles remain. Particles are not drawn to scale.

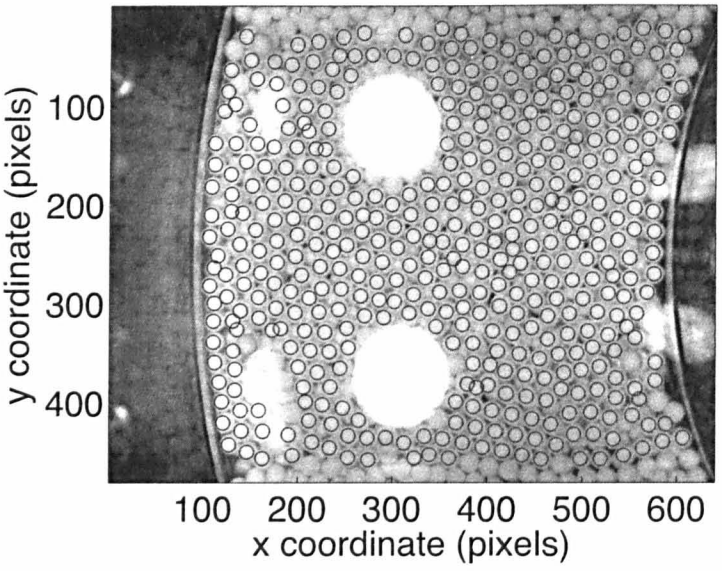

Figure 5.12: **Locations of particles that have survived the filtering plotted over the orginal image** - The locations of the particles from Fig. 5.11 plotted over the original image to demonstrate which particles have survived the filtering process. The locations of all particles initially detected, including spurious particles, can be seen in Fig. 5.2.

track lengths are shorter for the larger particles at the fastest angular velocity than for the smaller particles at the slowest angular velocity. The mean track lengths are also longer on the bottom surface than on the top surface for all experiments. This is mostly because there is less motion in general on the bottom surface but also because in the radial bins where there is the most motion (i.e., radial bin 1), there are no light reflections so the particles do not disappear and reappear. The tracks are, unsurprisingly, shortest in the inner radial bins where the particles move fastest. The shortest mean track length in any radial bin is only 191 frames (~3 seconds). This occurs, as expected, on the top surface, in the inner radial bin for the largest beads moving at the fastest angular velocity. Unfortunately, the short-lived particles occur in locations which are also the regions of interest (i.e., close to the shearing surface). However, as only sets of two consecutive frames are used to calculate the particle velocities (see Section 5.2.8), the short track lengths do not influence the measured velocities. This is verified in Section 5.4.2.

5.2.6 Particle births and deaths

To continue the investigations of the particle tracks, the first and last appearance of each particle are examined. The first instance a particle is detected in an experiment will be referred to as its "birth" and the last instance a particle is detected will be referred to as its "death". Or, in otherwords, a particles is "born" when it appears for the first time and "dies" when it disappears for the last time. Most particle births and deaths should be located at the edges of the field of view and around the

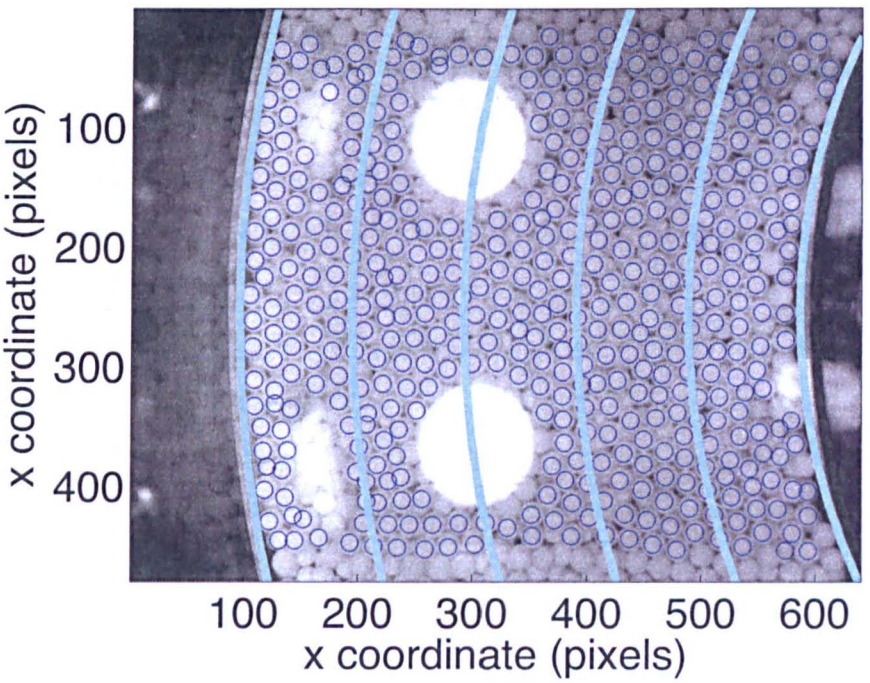

Figure 5.13: **Example image showing the radial bins used during the analysis** - One image with the boundaries of the five radial bins plotted over the top. The particles are split into these radial bins based on their radial position. Radial bin 1 is closest to the inner, rotating, cylinder (i.e., furthest to the right in this image).

Table 5.2: Mean particle track lengths in each of five radial bins are given for four different types of run. Bin 1 is the closest to the inner cylinder.

	Mean Particle Track Length (frames)				
	Bin 1	Bin 2	Bin 3	Bin 4	Bin 5
3 mm beads, 0.025 rad s^{-1}, Top surface	326	862	988	1024	982
3 mm beads, 0.025 rad s^{-1}, Bottom surface	464	869	1094	1118	1144
4 mm beads, 0.1 rad s^{-1}, Top surface	191	828	913	1057	991
4 mm beads, 0.1 rad s^{-1}, Bottom surface	206	952	1125	1078	671

light reflections.

First, taking a constant shear rate ground-based experiment with an inner cylinder angular velocity of 0.05 rad s^{-1} as an example, the locations of the particle births and deaths are plotted. Figure 5.14 shows the locations of the birth and death of all particles on the top surface (a) throughout an entire experiment (i.e., including the time before the motor is switched on and after the motor is switched off) and (b) during a 20 second period of motor rotation of the same experiment. Note that in the second plot there are many fewer particles. This is because those particles that are born before the 20 second period of motor rotation are not plotted. Likewise, those particles that die after the 20 second period of motor rotation are also not plotted.

There are more particle births in the top right of the image and more particle deaths in the bottom right of the image. It can, therefore, be concluded that the motor is rotating from large to small y (i.e., towards the bottom of the page as drawn in Fig. 5.14). As there are so few particles in the second image this demonstrates that most particles, especially in the middle of the field of view, have long lifetimes and, therefore, are born before the 20 second period of motor rotation and die after the 20 second period of motor rotation. This implies that there are only very few particle tracks affected by the light reflections.

To see exactly how many particles are being born and are dying near the light reflections or at the edges of the field of view, a 3d plot was produced showing the number of particle births and deaths at each location (Fig. 5.15). Figure 5.15 shows the number of births and deaths at each location on the top surface during a 20 second period of motor rotation. These figures show that the areas affected by the light reflections in the bulk are very well defined and are localised in just a few places. The same exercise is repeated for the bottom surface of the same ground-based experiment. Figure 5.16 shows the location of all births and deaths on the bottom surface (a) throughout an entire experiment and (b) during a 20 second period of motor rotation of the same experiment. Figure 5.17 shows the numbers of births and deaths at each location on the bottom surface during motor rotation. The highly localised nature of the births and deaths due to the light reflections is even more evident on the bottom surface.

From this analysis it can be concluded that the overall particle dynamics are unlikely to be influenced by the particles appearing and disappearing near the light reflections as there are many more particles completely unaffected by the light reflections than there are particles affected.

5.2.7 Smoothing the data

Using the particle positions in each frame, the average angular displacement and velocity of every particle can be computed. However, in order to extract meaningful information from the raw tracking

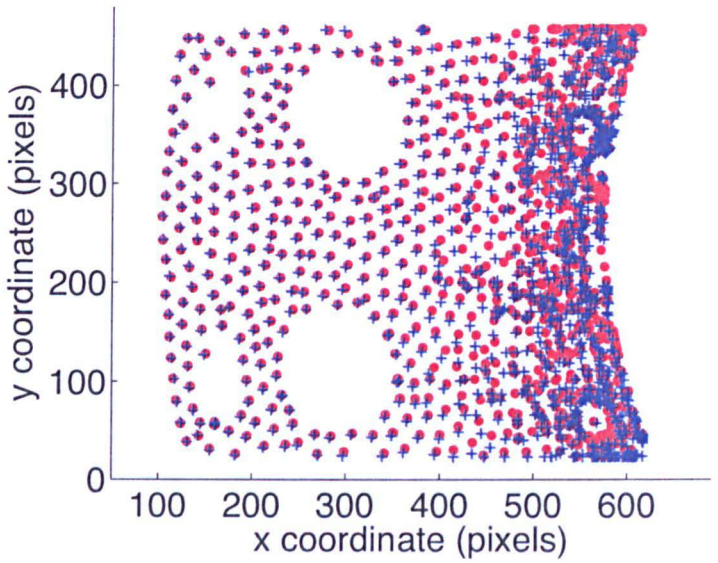

(a)

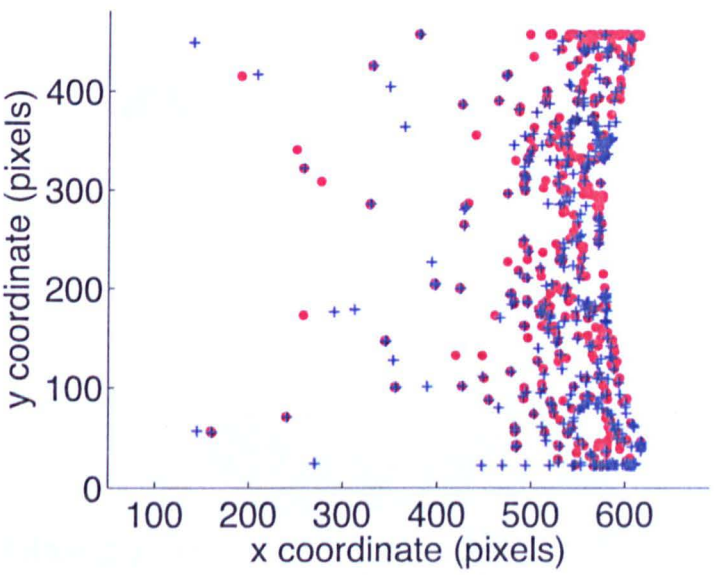

(b)

Figure 5.14: **The locations of particle births and deaths on the top surface** - The location of the first time a particle is detected (i.e., the location of its "birth") is represented by a red circle and the location of the last time a particle is detected (i.e., the location of its "death") is represented by a blue cross. Locations of all particle births and deaths are shown (a) throughout an entire experiment and (b) during a 20 second period of constant motor rotation at 0.05 rad s^{-1} on the ground.

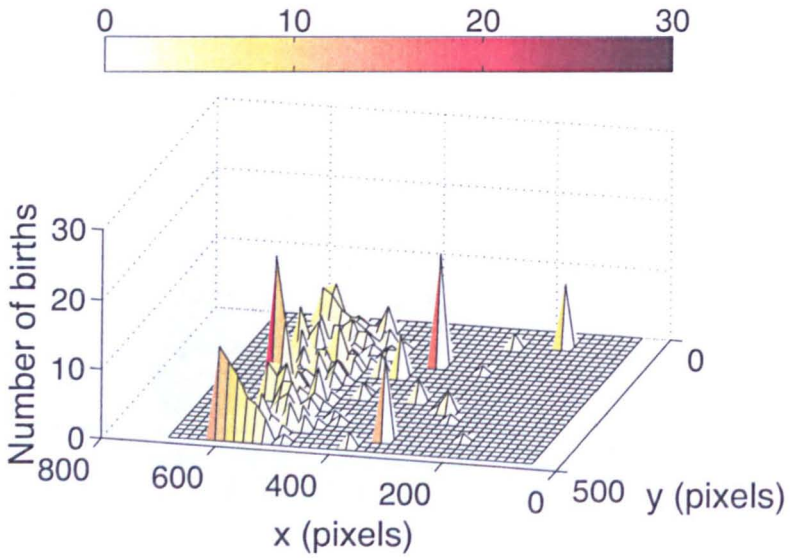

(a)

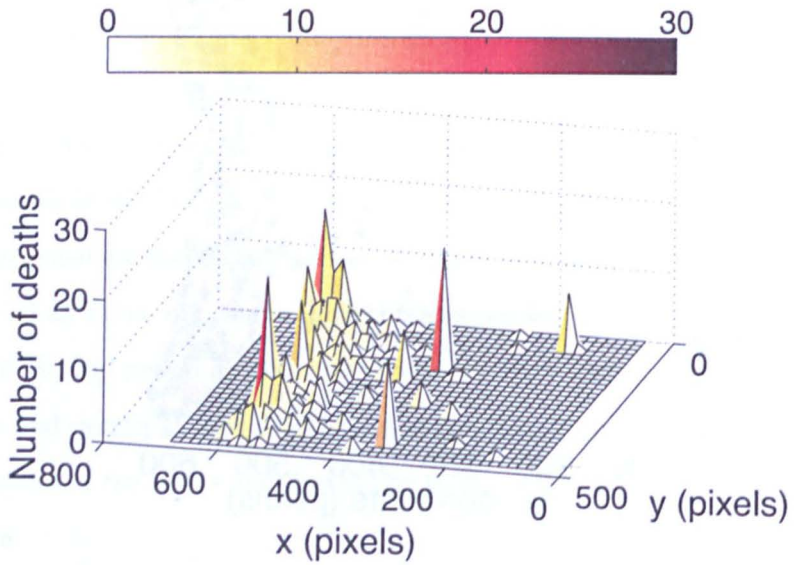

(b)

Figure 5.15: **Number of particle births and deaths on the top surface** - The number of particle births (a) and deaths (b) in each location on the top surface of a 20 second period of constant inner cylinder rotation at 0.05 rad s^{-1}. This experiment was performed on the ground.

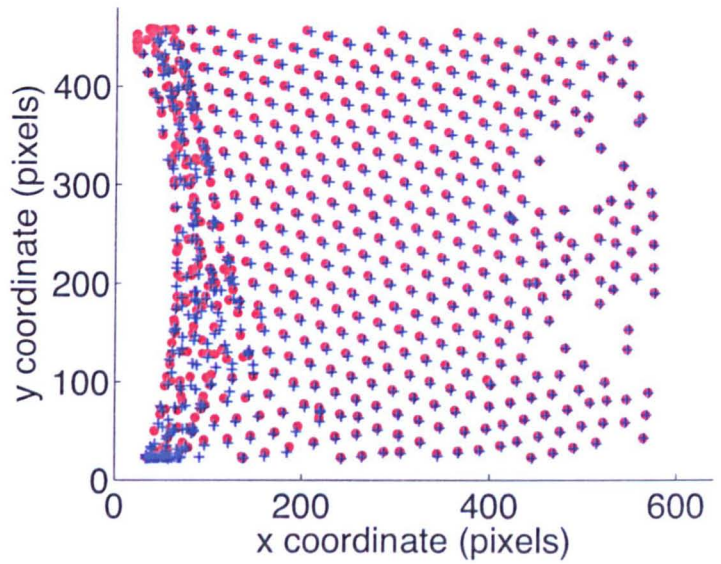

(a)

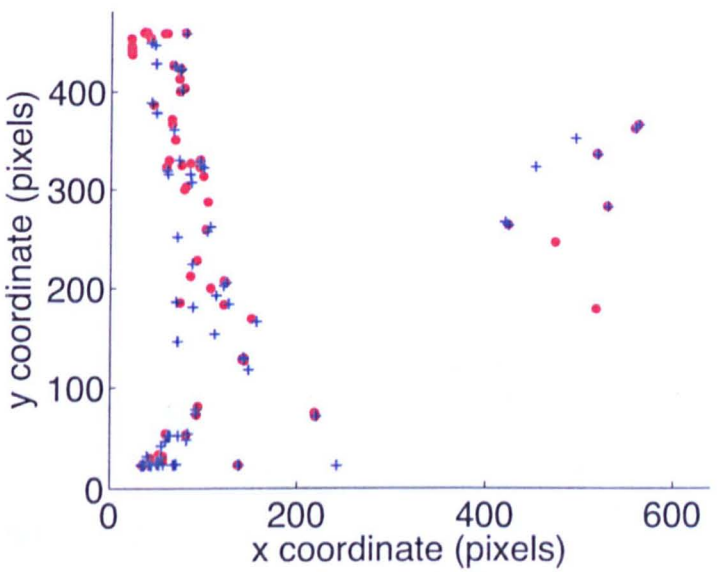

(b)

Figure 5.16: **The locations of particle births and deaths on the bottom surface** - The location of a particle birth is represented by a red circle and the location of a particle death is represented by a blue crosses. Locations of all particle births and deaths are shown (a) throughout an entire experiment and (b) during a 20 second period of constant motor rotation at 0.05 rad s^{-1} on the ground.

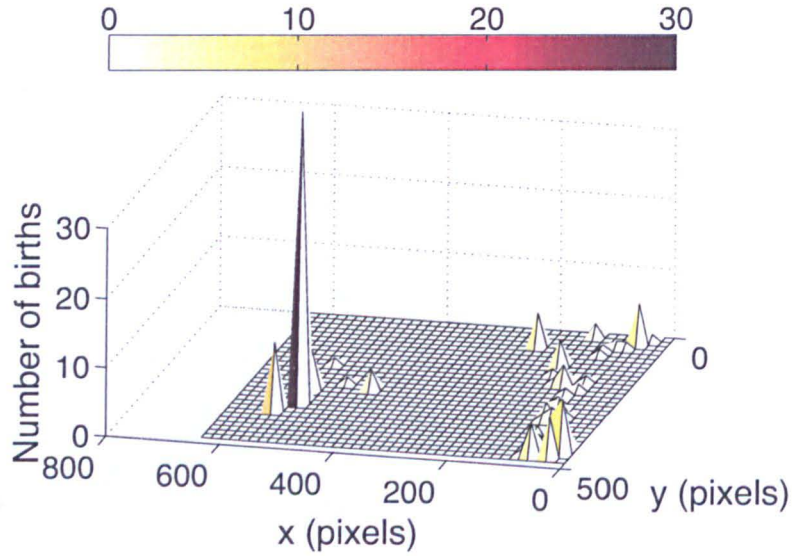

(a)

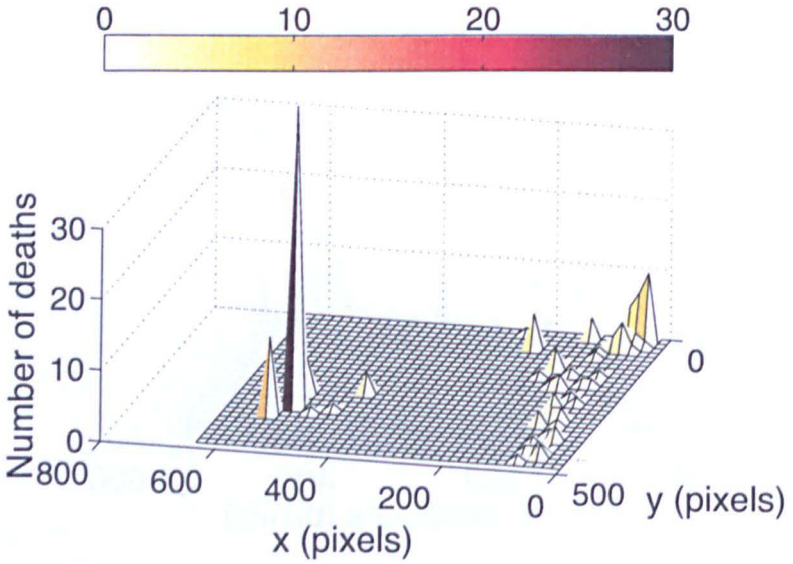

(b)

Figure 5.17: **Number of particle births and deaths on the bottom surface** - The number of particle births (a) and deaths (b) in each location on the bottom surface of a 20 second period of constant inner cylinder rotation at 0.05 rad s^{-1}. This experiment was performed on the ground.

data the positions of the particles must be smoothed over time. Without performing such smoothing the data would be dominated by noise. First, the particle positions (in Cartesian coordinates) are smoothed using a smoothing algorithm. The standard smoothing function available in Matlab employs a moving average filter. It was decided to employ a slightly more complex algorithm to perform a local regression weighted linear least squares fit. This algorithm, also known as a *loess* model (first proposed by Cleveland, 1979) separates the data into small subsets and then each subset is fit using a polynomial. The data in the subset are then weighted using least squares giving more weight to the points whose value are close to the value of the polynomial fit and less weight for those points whose values are far from the value of the polynomial fit. For the case of the AstEx data a second order polynomial is used. The size of the subsets of data are determined by the span of the smoothing algorithm: the wider the span, the more data that will be included in the subset.

The *loess* model is more computationally demanding than some other types of smoothing function (such as linear least squares regression), although, one of the main advantages of this method is that there is no need to specify a global function to fit a model to the data (as the data are fit in localised subsets). Another advantage of the *loess* model is that it prevents deviant points from distorting the smoothed points (Cleveland, 1979), something to which the standard moving average filter may be susceptible.

5.2.8 Calculating mean particle velocities

After the particle trajectories have been tracked, filtered and smoothed as described above, the instantaneous particle velocities are calculated in a process involving several steps. First, the smoothed positions for each particle (in Cartesian coordinates) are adjusted, using the coordinates at the centre of the cylinders as calculated in Section 5.2.3, so as the centre of the shear cells lies at position $(0, 0)$. The particle positions are then transformed from Cartesian coordinates to Polar coordinates.

Next, the angular and radial displacements, between every two consecutive frames, are determined for each particle. Finally, using the camera frame rate and the pixel scale determined in Section 5.2.2, the angular and radial displacements are converted into an instantaneous angular and radial velocity in units of rad s^{-1} and mm s^{-1}, respectively.

Once the instantaneous particle velocities have been calculated the particles are then separated, according to their radial position, into radial bins reaching from the inner cylinder wall to the outer cylinder wall (Fig. 5.13). Once the particles have been divided into radial bins the mean angular and radial particle velocities per bin can then calculated as a function of time during the experiment. The mean angular and radial particle velocities per radial bin will be referred to as $V_\theta(t)$ and $V_r(t)$, respectively.

The experiments were all controlled by hand and, therefore, the time at which the motor starts, relative to when the cameras start recording, varies between experiments. To be consistent during the analysis the *motor start time* was defined as the moment when $V_\theta(t)$ in the inner radial bin reaches $(1/5)\,\omega$ where ω is the inner cylinder angular velocity. In all experiments there is an initial acceleration of the particles after the motor is turned on. The mean particle velocity then takes 1-2 seconds to reach a steady state. Therefore, any steady state analysis discussed in the following sections and in Chapter 6 considers particle motion starting from 3 seconds after the *motor start time.* This moment is, henceforth, referred to as the *analysis start time.*

Unsurprisingly, $V_\theta(t)$ and $V_r(t)$ are highly dependent on both the span of the smoothing algorithm (Figs. 5.18 and 5.19) and the size (and number) of the radial bands (Figs. 5.20 and 5.21). It is, therefore, important to always ensure that the same degree of smoothing has been applied to the data and the same number of radial bins used when making direct comparisons between any two experiments. When choosing the degree of smoothing it is important to attempt to retain as much information as possible about the particle behaviour without allowing the data to be dominated by noise. In the majority of the analyses performed with the AstEx data the smoothing algorithm has been applied with a span of two seconds (between 120 and 196 frames depending on the camera frame rate).

One key feature that is evident in all of these plots of mean particle velocity as a function of time, but particularly in the plots of mean angular velocity (Figs. 5.18 and 5.20), is the presence of large-scale correlated fluctuations. There appears to be correlated motion from the inner to the outer radial bin. The source of these fluctuations, which are affecting all particles across the entire width of the shear cell, was originally unknown. After extensive research into all of the possible causes of such fluctuations, the conclusion was made that they are not caused by any hardware issues, nor are they introduced during the particle tracking or binning processes. The cause is real events occuring within the granular material, probably linked to force chain breaking and reforming. A full report on how this conclusion was made and all of the tests performed investigating the correlated and fluctuating particle velocities and associated issues can be found in Appendix B.

Considering the plots of mean radial velocity versus time (Figs. 5.19 and 5.21) it can be seen that the magnitude of the mean particle radial velocity is generally small (<1-2 mm s^{-1}) and that the mean radial velocity always fluctuates around zero. To determine if there is any bulk motion of particles in the positive or negative direction the radial velocities of particles must be binned over a longer period of time.

Figure 5.22 shows the mean particle radial velocity in the inner radial bin (of five) as a function of time for a ground-based experiment (0.05 rad s^{-1} inner cylinder angular velocity and 4 mm particles).

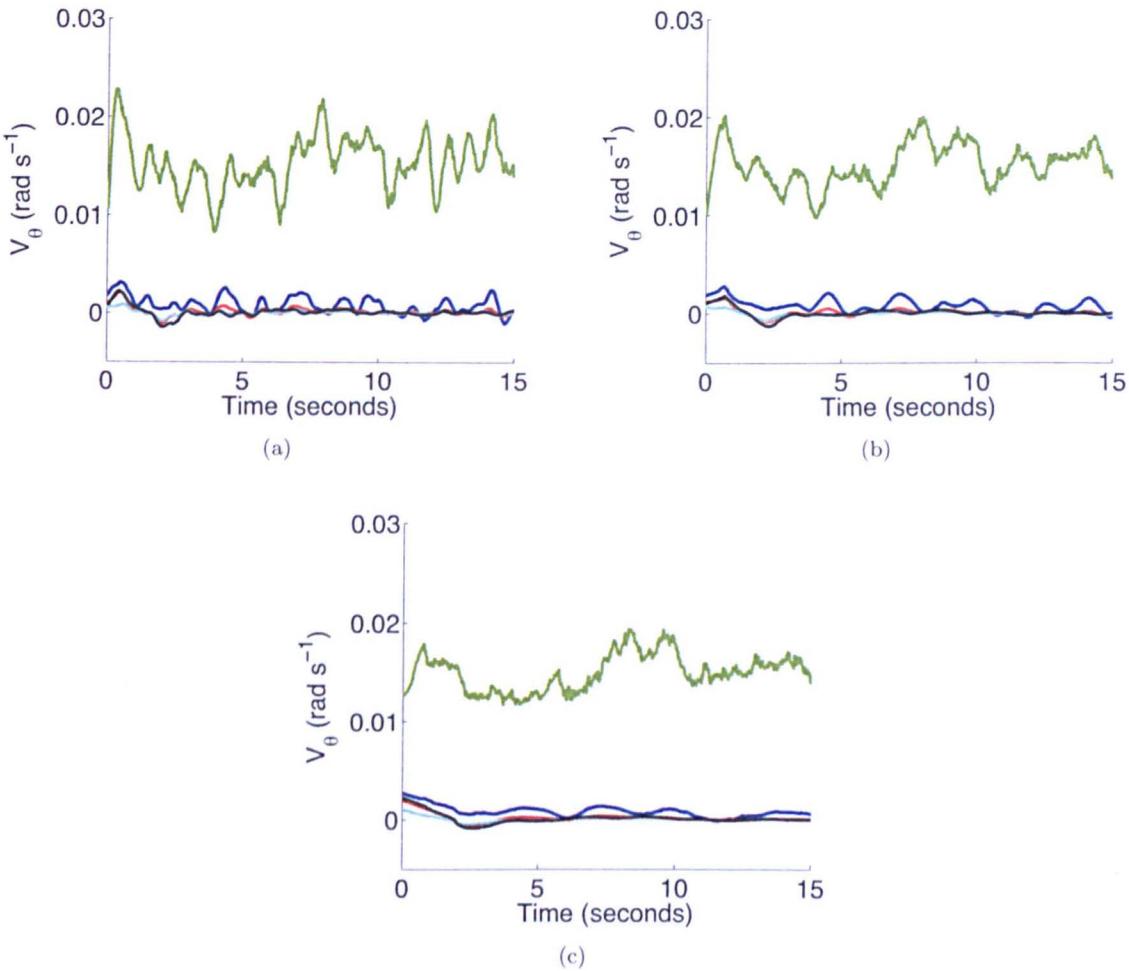

Figure 5.18: **Effect of smoothing on mean particle angular velocities** - The particles have been split into five radial bins and the mean V_θ for each radial bin is plotted as a function of time. In each of the three figures a different level of smoothing has been applied to the data before calculating the mean V_θ. A smoothing span of (a) one second (60 frames), (b) two seconds (120 frames) and (c) four seconds (240 frames) have been applied, respectively. The experiment used as an example here is a constant shear rate experiment performed in microgravity with 4 mm particles and an inner cylinder angular velocity of 0.05 rad s^{-1}. The respective radial bins, with bin 1 being the closest to the inner cylinder, are: bin 1 (green), bin 2 (blue), bin 3 (red), bin 4 (cyan), bin 5 (black).

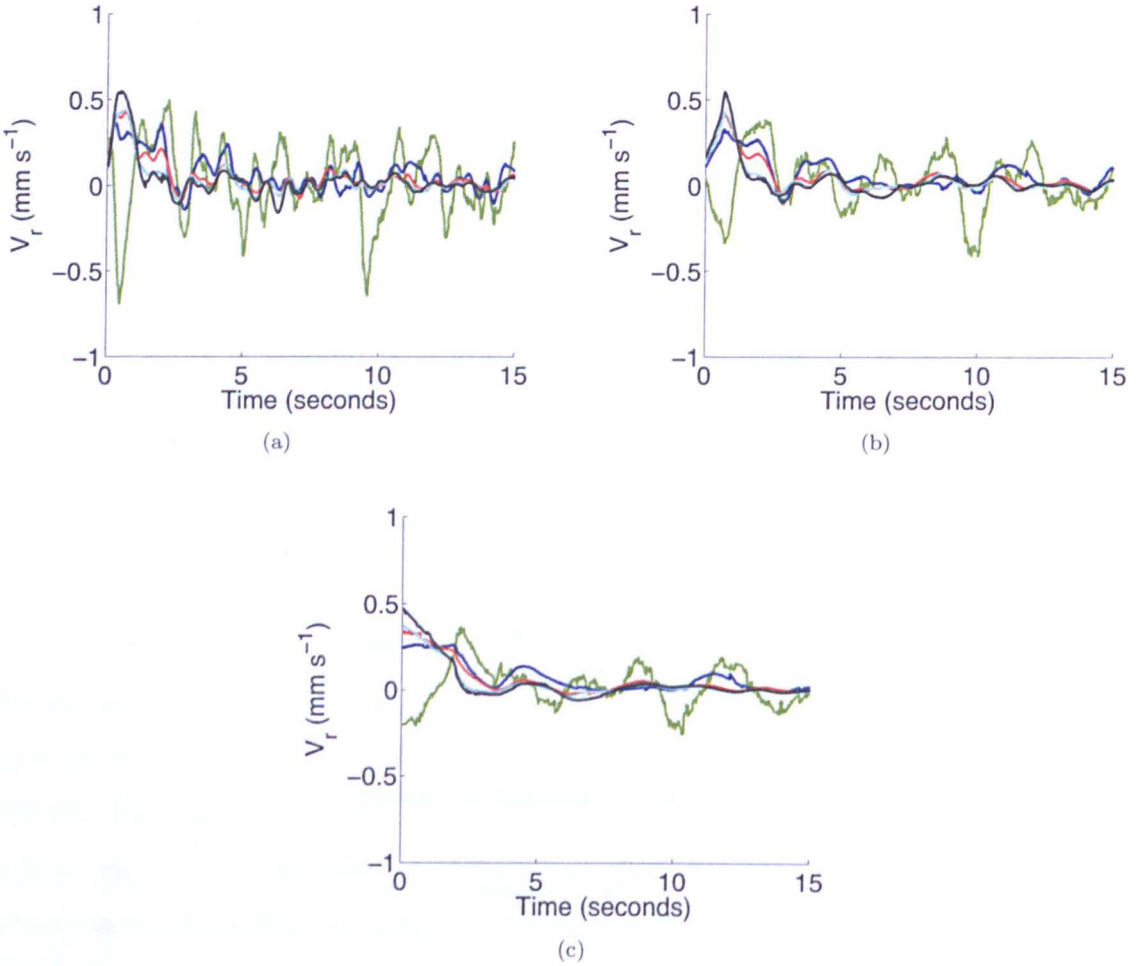

Figure 5.19: **Effect of smoothing on mean particle radial velocities** - The particles have been split into five radial bins and the mean V_r for each radial bin is plotted as a function of time. In each of the three figures a different level of smoothing has been applied to the data before calculating the mean V_r. A smoothing span of (a) one second (60 frames), (b) two seconds (120 frames) and (c) four seconds (240 frames) have been applied, respectively. The experiment used as an example here is a constant shear rate experiment performed in microgravity with 4 mm particles and an inner cylinder angular velocity of 0.05 rad s^{-1}. The respective radial bins, with bin 1 being the closest to the inner cylinder, are: bin 1 (green), bin 2 (blue), bin 3 (red), bin 4 (cyan), bin 5 (black).

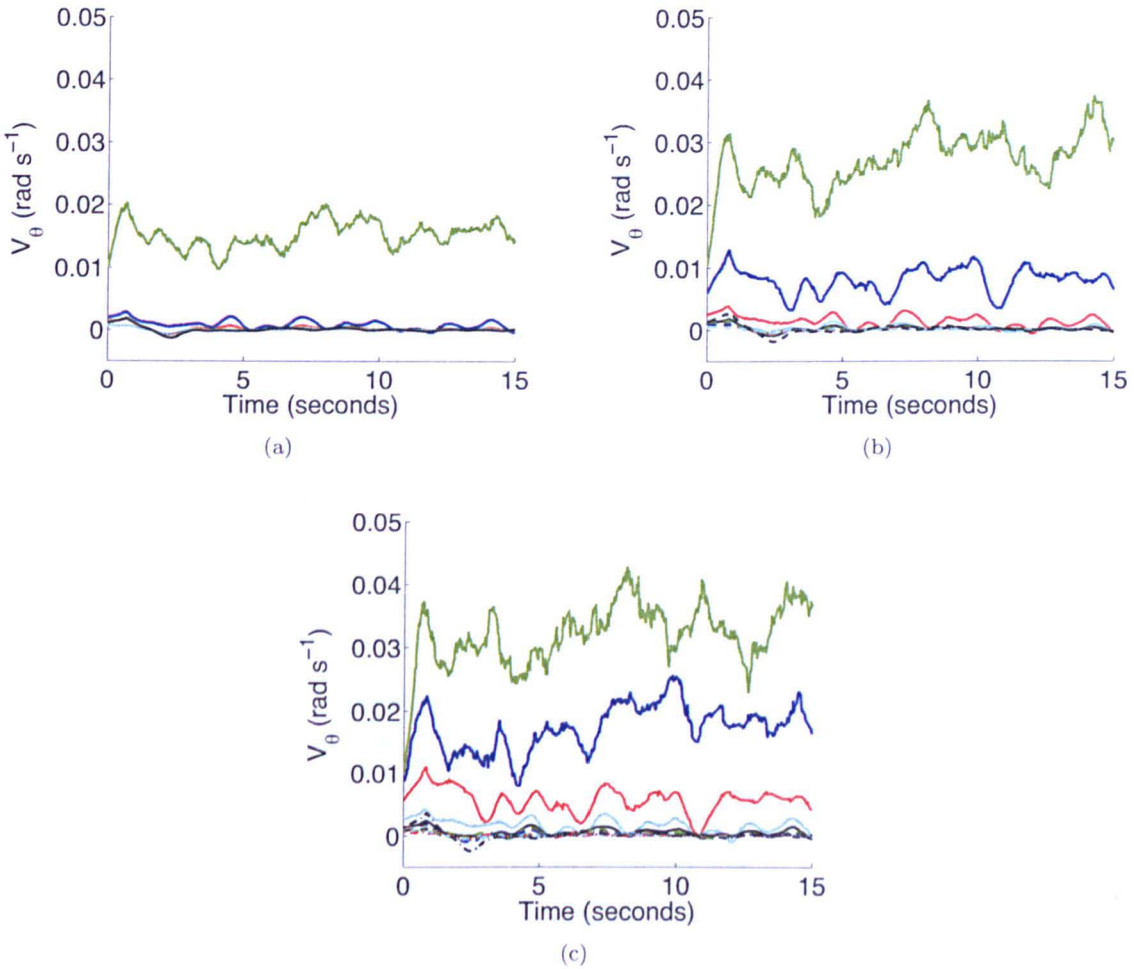

Figure 5.20: **Effect of decreasing radial bin width (and increasing radial bin number) on mean particle angular velocities** - The particles have been split into radial bins and the mean V_θ for each radial bin is plotted as a function of time. In the three plots the particles have been split into (a) five, (b) ten and (c) fifteen radial bins, respectively. The experiment used as an example here is a constant shear rate experiment performed in microgravity with 4 mm particles and an inner cylinder angular velocity of 0.05 rad s^{-1}. For each figure the span of the applied smoothing is 2 seconds (120 frames). The respective radial bins, with bin 1 being the closest to the inner cylinder, are: bin 1 (green), bin 2 (blue), bin 3 (red), bin 4 (cyan), bin 5 (black). Where appropriate, bins 6-10 use the same colours as bins 1-5 but with a dashed line and bins 11-15 use the same colours as bins 1-5 but with a dashed-dotted line.

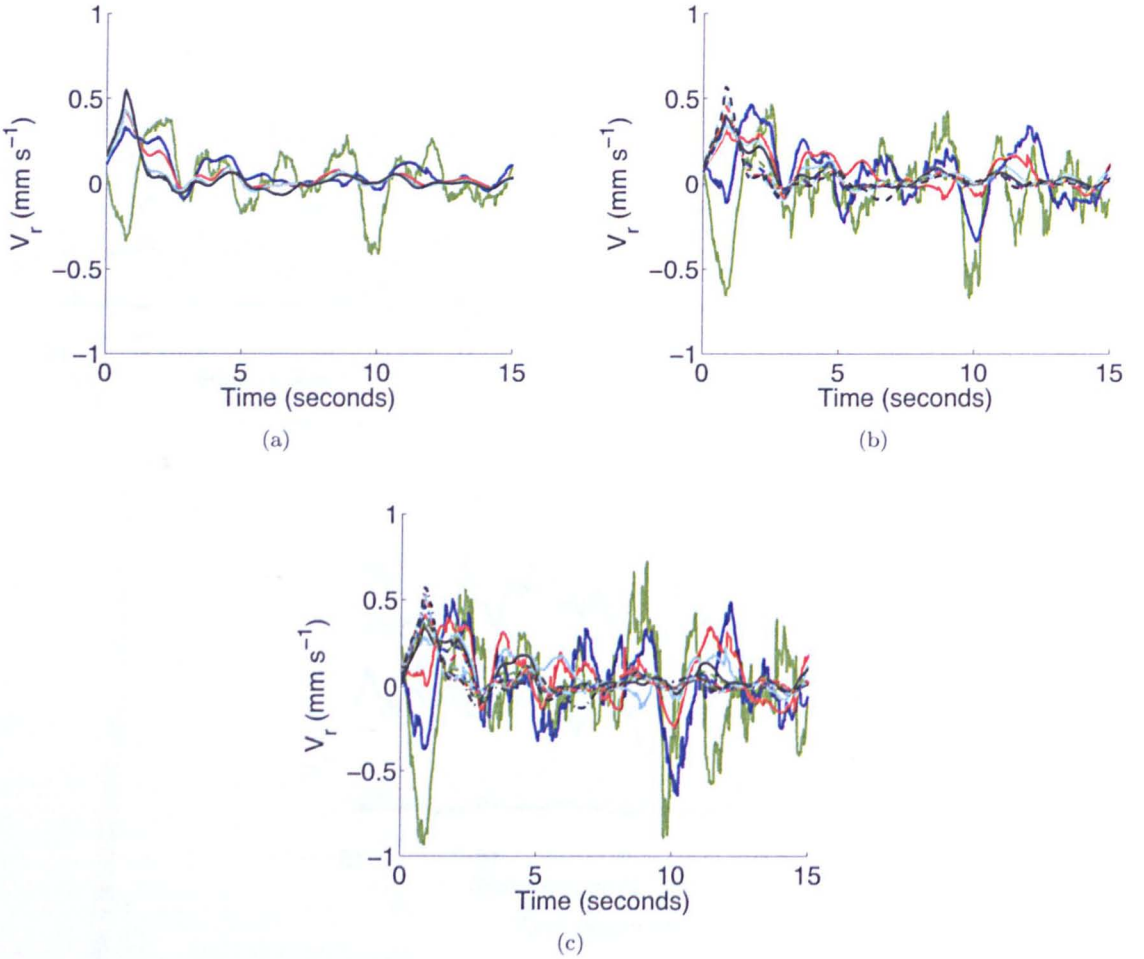

Figure 5.21: **Effect of decreasing radial bin width (and increasing radial bin number) on mean particle radial velocities** - The particles have been split into five radial bins and the mean V_r for each radial bin is plotted as a function of time. In the three plots the particles have been split into (a) five, (b) ten and (c) fifteen radial bins, respectively. The experiment used as an example here is a constant shear rate experiment performed in microgravity with 4 mm particles and an inner cylinder angular velocity of 0.05 rad s^{-1}. For each figure the span of the applied smoothing is 2 seconds (120 frames). The respective radial bins, with bin 1 being the closest to the inner cylinder, are: bin 1 (green), bin 2 (blue), bin 3 (red), bin 4 (cyan), bin 5 (black). Where appropriate, bins 6-10 use the same colours as bins 1-5 but with a dashed line and bins 11-15 use the same colours as bins 1-5 but with a dashed-dotted line.

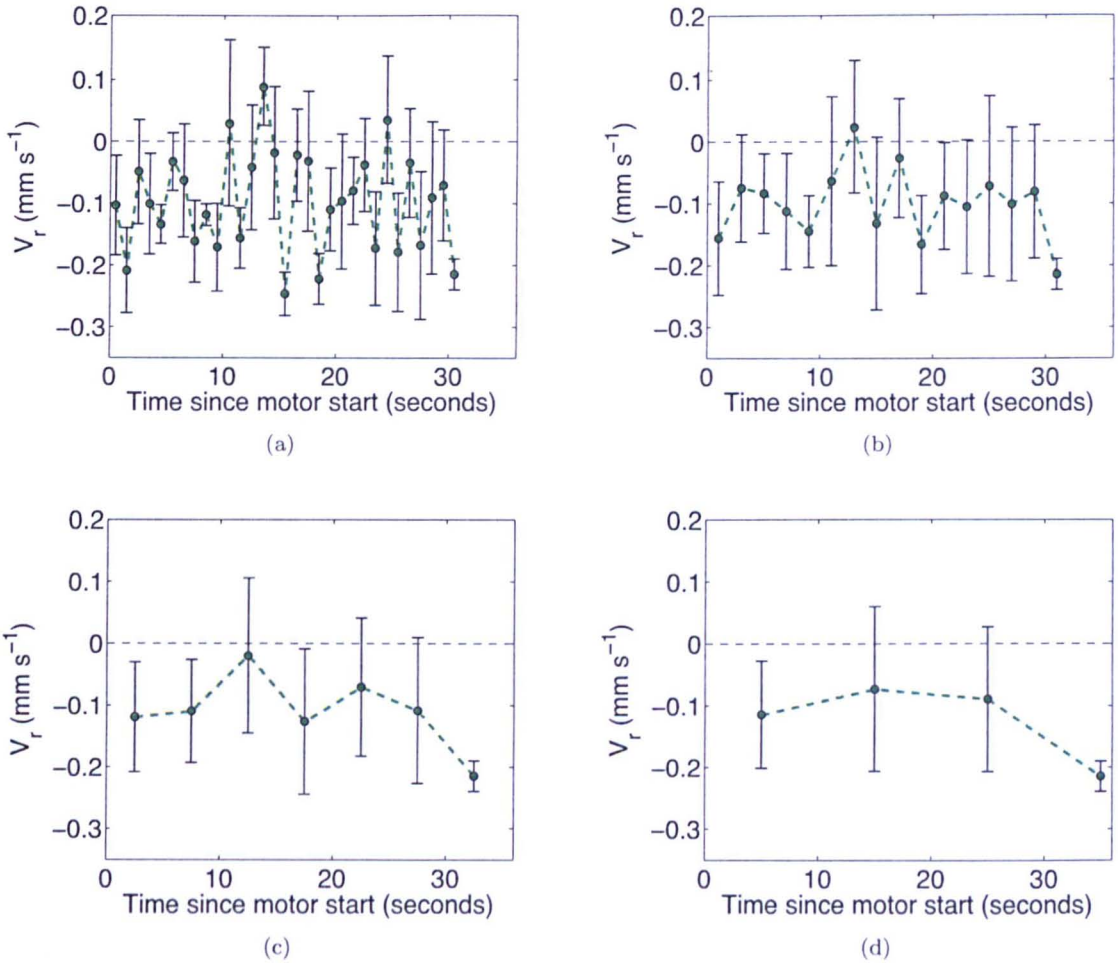

Figure 5.22: **Mean radial velocity averaged over different sizes of time bin** - The mean V_r of the inner radial bin (of five) as a function of time for the top surface in a ground-based experiment. The inner cylinder has an angular velocity of 0.05 rad s^{-1} and the particles are 4 mm in diameter. The mean particle radial velocity has been averaged over time periods of (a) 1 second, (b) 2 seconds, (c) 5 seconds and (d) 10 seconds, respectively. The mean V_r per time bin is plotted and the error bars represent the scatter of velocities (standard deviation) within the given time period.

The particle velocities have been averaged over different time periods. The mean particle radial velocity in the given time period and the scatter of velocities (standard deviation) within that time period are plotted. In this example it can be seen that, as the size of the time bin increases above 1 second, the net negative motion of the particles is easier to see. However, a time bin size of 10 seconds is too large for the AstEx data given the 22 second duration of the microgravity phase. Therefore, a time bin of 2 or 5 seconds will be used when examining the change of V_r over time.

In order to compare experiments at different inner cylinder rotational velocities and with different bead sizes, an attempt is made to normalise the results. The mean particle angular velocity, V_θ, will often be plotted in its normalised form,

$$V_\theta^* = \frac{V_\theta}{\omega} \tag{5.3}$$

where ω is the inner cylinder angular velocity. Similarly, the mean particle radial velocity, V_r, will often be plotted in its normalised form,

$$V_r^* = \frac{V_r}{(a\omega)} \tag{5.4}$$

where ω is again the inner cylinder angular velocity and a is the inner cylinder radius. To normalise also the rate of shear, the mean particle velocities are often plotted as a function of the inner cylinder displacement rather than against time. The inner cylinder displacement, in particle diameters, is given by $(a\omega t)/d$, where a is the radius of the inner cylinder, ω is, once again, the inner cylinder angular velocity, t is time and d is the particle diameter.

This provides a way of comparing different types of experiments with different particle sizes and at different shear rates. However, in the following sections the mean particle velocities will not always be plotted against inner cylinder displacement. This is because, for the AstEx experiment, the time at which events occur e.g., the transitions between the gravity regimes, is very important for some types of analysis. Therefore, the approach for representing the time will be chosen depending on the goal of the analysis.

5.2.9 Mean velocity profiles

To calculate the mean particle velocity profile (i.e., mean particle velocity as a function of distance from the inner shearing cylinder) the particles are first separated into radial bins. Next, the mean particle velocity in each of the radial bins is calculated over a period of fifteen seconds (i.e., from the *analysis start time* to the *analysis start time*+15 seconds). Fifteen seconds was chosen as this is a long enough period of time to obtain reasonable statistics and it also falls well inside the duration of microgravity during each parabola (~22 seconds)[1].

To calculate the mean angular velocity profiles one hundred radial bins were used. An example of an angular velocity profile for the top surface of the 4 mm beads on the ground at an inner cylinder rotational velocity of 0.05 rad s^{-1} is shown in Fig. 5.23. The normalised mean particle angular velocity, V_θ^* (see Eq. (5.3)), is plotted as a function of distance from the inner cylinder (i.e., distance from the shearing surface) in particle diameters.

The radial velocity profiles are calculated in the same manner as the angular velocity profiles. However, the radial bins used to represent the mean radial velocity profile need to be sufficiently large to capture the small-scale motion in the radial direction but also sufficiently small to ensure that important details are not being masked during the radial binning process. The mean radial velocity

[1]Tests were also performed taking two periods of 7.5 seconds instead of one 15 second period. The mean velocity profiles for the two shorter time periods are consistent to within error bars and also lie within the error bars of the mean velocity profile of the 15 second period.

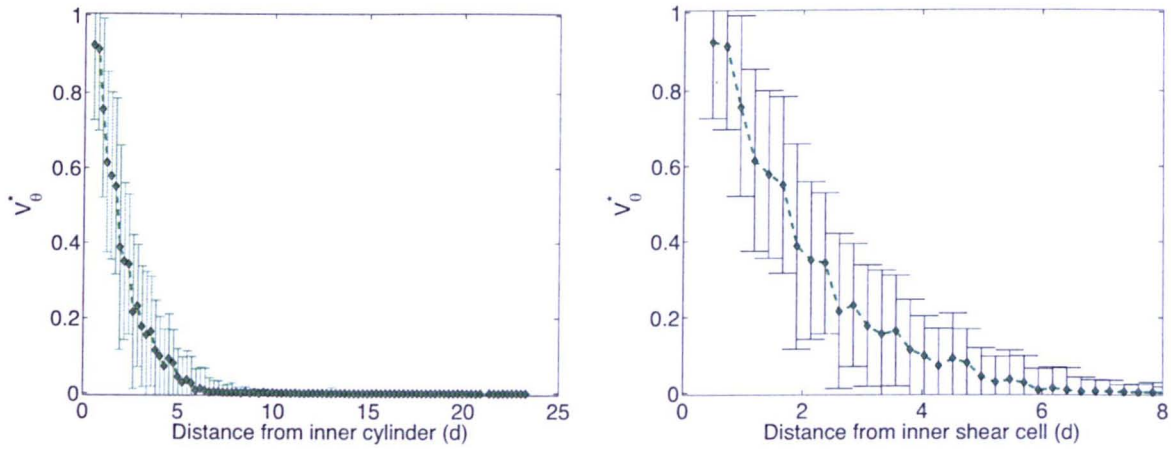

Figure 5.23: **Mean angular velocity profile example** - V^*_θ (see Eq. (5.3)) is plotted as a function of distance from the inner cylinder. The experiment is a constant shear rate experiment with an inner cylinder angular velocity of 0.05 rad s^{-1} on the ground: (a) Full angular velocity profile. (b) Angular velocity profile of the shear band (i.e., of the first 8 particle diameters). The error bars represent the standard deviation of V^*_θ over the fifteen second time period (this will be defined as the $S2$ scatter of V^*_θ in Section 5.3.2)

profile for one experiment is calculated using 5, 10, 20 and 30 radial bins and the results are shown in Fig. 5.24. In the these figures the normalised mean radial velocity, V^*_r (see Eq. (5.4)), is plotted as a function of distance from the inner cylinder. This exercise has demonstrated that some information is being overlooked when using 5 or 10 radial bins. Additionally, no more information is gained in having 30 radial bins instead of 20 radial bins. Therefore, it was decided that 20 radial bins was the most suitable choice and that this number of bins should be used from now on when comparing the mean radial velocity profiles.

5.3 Uncertainty analysis

In the AstEx experiment there is an uncertainty introduced to the data during the particle detection. This will be discussed in the first of the two sections dealing with the uncertainty analysis in the AstEx data. The second section will describe an analysis performed to understand the different contributions to the uncertainty of the mean velocity values coming from the scatter of particle velocities between particles, over time and, eventually, between different experiments of the same type.

5.3.1 Estimating the observational uncertainty

The observational uncertainty arises from the particle tracking which, if performed correctly, locates the centres of the particles with an accuracy of 1/10 of a pixel. In this section, by working through the steps involved to go from particle coordinates in Cartesian coordinates to angular and radial

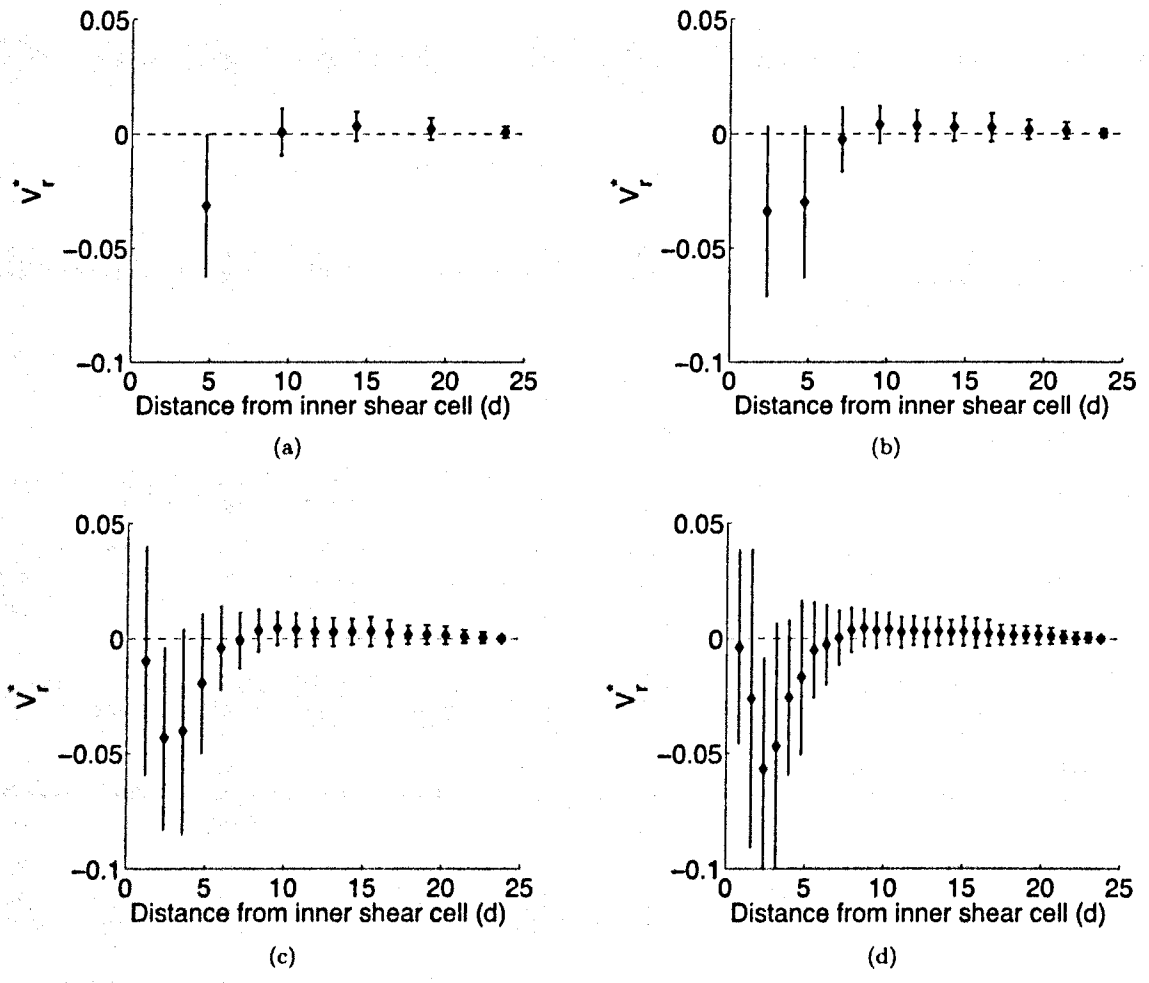

Figure 5.24: **Choosing the bin size for radial velocity profiles** - V_r^* (see Eq. (5.4) is plotted as a function of distance from the inner cylinder for one experiment using (a) 5, (b) 10, (c) 20 and (c) 30 radial bins. The error bars represent the standard deviation of V_r^* over the fiften second time period (this will be defined as the $S2$ scatter of V_r^* in Section 5.3.2). The experiment is ground-based with 4 mm beads and an inner cylinder angular velocity of 0.05 rad s^{-1}.

velocities, an estimate will be made of the uncertainties in the instantaneous and mean angular and radial velocities of the particles due to the uncertainty in the particle detection.

The first step after particle detection and tracking is to convert the Cartesian position coordinates of each particle (x, y) and associated uncertainties (δx, δy) to Polar coordinates. The r coordinate is given by,

$$r = \sqrt{x^2 + y^2} \tag{5.5}$$

and the θ coordinate is given by,

$$\theta = \tan^{-1}(y/x). \tag{5.6}$$

Assuming that δx is equal to δy then we can define an error in the position, δp, which will be,

$$\delta p = \sqrt{2}\delta x. \tag{5.7}$$

The r and θ coordinates will then have associated uncertainties of,

$$\delta r = \sqrt{2}\delta p \tag{5.8}$$

and

$$\delta\theta = \sqrt{2}\left(\frac{\delta p}{r}\right). \tag{5.9}$$

Then two consecutive radial positions of the particle (r_1 and r_2) are combined to give a radial displacement (S_r) between the two consecutive frames,

$$S_r = r_2 - r_1 \tag{5.10}$$

with

$$\delta S_r = 2\delta p. \tag{5.11}$$

Similarly, two consecutive angular positions (θ_1 and θ_2) are combined to give the angular displacement (S_θ) between the two consecutive frames,

$$S_\theta = \theta_2 - \theta_1 \tag{5.12}$$

with

$$\delta S_\theta = \frac{2}{r}\delta p. \tag{5.13}$$

Finally, the radial displacement (S_r) in pixels is then converted into an instantaneous radial velocity (V_r) in mm s^{-1} using the following equation,

$$V_r = \frac{fps}{PS}S_r \tag{5.14}$$

with

$$\delta V_r = \frac{2fps}{PS}\delta p \tag{5.15}$$

where PS is the value of the pixel scale and fps is the number of frames taken by the camera every second. Then the angular displacement (S_θ) is converted into an instantaneous angular velocity (V_θ) in rad s^{-1} using the following equation,

$$V_\theta = fpsS_\theta. \tag{5.16}$$

The angular velocity will, therefore, have an uncertainty given by,

$$\delta V_\theta = \frac{2fps}{r}\delta p. \tag{5.17}$$

It is then possible to estimate the minimum and maximum values of δV_θ and δV_r. As mentioned in Section 5.2.1, if the particle detection and tracking is performed correctly then the centres of the particles are located with an accuracy of $\sim 1/10$ pixel, therefore $\delta p = 1/10$ pixel, or for the case of the normal set-up when $PS = 5.17$ pixels mm^{-1}, we have $\delta p = 0.019$ mm. Assuming the camera frame rate is 60 fps (as was the case for most of the experiments) this gives, for the normal set-up, $\delta V_r = 0.45$ mm s^{-1}. Assuming the range of r in the field of view is 100 mm $< r <$ 195 mm, the range of δV_θ is then 0.011 rad s^{-1} $< \delta V_\theta <$ 0.023 rad s^{-1} with the largest uncertainty in δV_θ being the closest to the inner cylinder. Full calculations are given in Appendix C. Table 5.3 gives δV_r and the maximum δV_θ for each of the different experiment set-ups used for this thesis.

However, this uncertainty is the maximum possible error in the instantaneous velocity for one particle. It is not the uncertainty in the mean particle velocity over its lifetime. The maximum uncertainties in the mean angular and radial displacements of a particle over the lifetime of a particle track are,

$$\Delta S_r = 2\delta p \tag{5.18}$$

and,

$$\Delta S_\theta = \frac{2}{r}\delta p \tag{5.19}$$

respectively. This gives an uncertainty in the mean velocities over the particle's lifetime of,

$$\Delta V_r = \frac{\Delta S_r}{\overline{\Lambda}} \tag{5.20}$$

$$\Delta V_r = \frac{2}{\overline{\Lambda}}\delta p \tag{5.21}$$

and,

$$\Delta V_\theta = \frac{\Delta S_\theta}{\overline{\Lambda}} \tag{5.22}$$

$$\Delta V_\theta = \frac{2}{r\overline{\Lambda}}\delta p \tag{5.23}$$

where $\overline{\Lambda}$ is the mean track length of the particles. We can then estimate the maximum uncertainty in the mean velocity of a particle over its lifetime by making use of the mean particle lifetimes from Table 5.2. We will estimate the maximum values of ΔV_r and ΔV_θ in the inner radial bin for an experiment with the shortest possible particle tracks (i.e., the experiment given as an example in Table 5.2 with 4 mm beads and an inner cylinder angular velocity of 0.1 rad s^{-1}). For the inner radial bin of this experiment where $r \sim 110$ mm, $\overline{\Lambda} = 191$ frames. This is equivalent to 3.18 seconds. As stated above, $\delta p = 0.019$ mm for the case of the normal set-up. Therefore, the largest possible uncertainties in the mean particle velocities for the top surface of the normal set-up (i.e., for particles close to the inner cylinder in an experiment with the shortest particle tracks), are $\Delta V_r \sim 0.013$ mm s^{-1} and $\Delta V_\theta \sim 1.1 \times 10^{-4}$ rad s^{-1}. Given in Table 5.3 are the worst case ΔV_r and ΔV_θ for each of the different experiment set-ups used for this thesis.

Note, there are also two other uncertainties in the AstEx data: the uncertainty in the pixel scale (as described in Section 5.2.2), and the uncertainty in the centre of the two cylinders (as described in Section 5.2.3). The uncertainty in the pixel scale, which is on the order of $\pm$ 0.02 pixels mm^{-1}, is negligible.

If there is an uncertainty in the centre of the two cylinders (δX_c, δY_c) then this would influence the individual particle angular and radial velocities. If the error is in the y-direction then, for particles in approximately half of the field of view, V_θ would be slightly too large and, for particles in the other half of the field of view, V_θ would be slightly too small. However, in all of the AstEx analyses a mean V_θ is calculated in a radial bin. These radial bins encompas both halves of the field of view (i.e., the

Table 5.3: The observation errors in V_r and V_θ for all the different experiment set-ups. δV_r and δV_θ are the maximum possible uncertainties in the instantaneous radial and angular particle velocities, respectively. ΔV_r and ΔV_θ are the maximum possible uncertainties in the mean radial and angular particle velocities, respetively. In these calculations $\overline{\Lambda}$ is assumed to be 3.18 seconds on the top surface and 3.43 seconds on the bottom surface (see Table 5.2).

Type of Experiment	**Camera**	**Pixel Scale (pixels mm^{-1})**	**Camera frame rate (fps)**	δV_r **(mm s^{-1})**	**max** δV_θ **(rad s^{-1})**	**max** ΔV_r **(mm s^{-1})**	**max** ΔV_θ **(rad s^{-1})**
Flight campaign: normal set-up	Top	5.17	100	0.75	0.038	0.013	1.1×10^{-4}
Flight campaign: normal set-up	Bottom	5.6	100	0.64	0.035	0.011	1.0×10^{-4}
Flight campaign: normal set-up	Top	5.17	60	0.45	0.023	0.013	1.1×10^{-4}
Flight campaign: normal set-up	Bottom	5.6	60	0.38	0.021	0.011	1.0×10^{-4}
Flight campaign: end of Flight C	Top	5.5	60	0.40	0.021	0.011	1.0×10^{-4}
Flight campaign: end of Flight C	Bottom	5.25	60	0.44	0.023	0.013	1.1×10^{-4}
Laboratory based experiments	Top	5.25	62	0.45	0.024	0.013	1.1×10^{-4}

half with $y > 0$ and the half with $y < 0$) and, thus, include both particles with V_θ slightly too high and those with V_θ slightly too low. If δY_c is large then there may be a surplus of particles with V_θ too high or too low. However, assuming δY_c is small (it was found to be ~ 0.2 mm in Section 5.2.3), the net result is that the errors in V_θ cancel out. The same is true for the radial velocities if the error is in the y-direction.

If the uncertainty of the centre coordinates is in the x-direction, the angular and radial velocites of all particles will be affected and, as there is no symmetry, these effects will not cancel out. However, when calculating the centre coordinates, the x-coordinate (X_c) is very well constrained and δX_c is normally much smaller than δY_c (e.g., δX_c was found to be ~ 0.02 mm in Section 5.2.3). Given the small size of δX_c and the symmetry of any errors introduced by δY_c, we can assume that any uncertainties introduced by the centre of the two cylinders are negligible.

5.3.2 Definitions of scatter types

Each mean particle velocity (i.e., V_θ, V_r) calculated throughout the AstEx data pipeline presented above is calculated using many particle tracks, many frames and, eventually, also many experiments. In this section an analysis is performed to understand the different contributions to the uncertainty of the mean velocity values coming from the scatter of particle velocities between particles, over time and between different experiments of the same type.

As has been seen in Section 5.2.8, the first step in calculating the AstEx mean particle velocities (angular and radial) is to separate the particles into radial bins and calculate the mean particle velocity, as a function of time, for each of the radial bins. During this step of the analysis each measured mean instantaneous velocity (i.e., $V_\theta(t,r)$ or $V_r(t,r)$) will have an associated scatter. This scatter, which will now be referred to as $S1$, is the standard deviation of the particle velocities in each radial bin at any one moment in time. $S1$ represents the distribution of many individual particle velocities at any one moment in time within one radial bin. It is this scatter which is important when considering the significance of the mean instantaneous particle velocity as a function of time as it indicates how different the individual particle velocities in the radial band are from one another. If $S1$ is large at one instant in time this implies that, at that moment, there is a large spread of particle velocities within the radial band. If $S1$ is small this implies that there is a small spread of particle velocities within the radial band and so all particles are exhibiting similar behaviours.

Next, to find the velocity profiles, the mean particle velocities in each radial bin at each frame are binned together over a long period of time (normally 15 seconds). This gives a mean particle velocity for each radial bin as a function of distance from shearing surface over many frames (i.e., $V_\theta(r)$ or $V_r(r)$). The scatter associated with this mean particle velocity, which will now be referred to as $S2$,

is the standard deviation of the mean particle velocity over many frames. $S2$ represents the scatter in the mean particle velocity over time. Combining the value of the mean particle velocity (zero or non-zero) and the size of $S2$ allows a determination of whether bulk particle motion is occuring within the granular material. This will be further explained in Section 5.3.4 below.

Finally, the mean particle velocities calculated for each individual experiment need to be compared. To do this an overall mean particle velocity is calculated for each type of experiment. The scatter between the individual experimental results within each group give the final scatter which must be considered: scatter type $S3$. There will be two types of $S3$ referred to as $S3_a$ and $S3_b$. $S3_a$ is the standard deviation of mean particle velocities between experiments of the same type. $S3_b$ is the standard deviation of the mean $S2$ in mean particle velocity between experiments of the same type. This is explained in more detail in Section 5.3.5 below.

The three types of scatter ($S1$, $S2$ and $S3$) are summarised in Table 5.4 where a brief explanation is given as to what each one represents and what they can tell us about the experiment(s). In the following three sections the different scatters are presented for both the angular and radial velocities.

5.3.3 $S1$

First the mean angular velocities are considered. To understand if the extent of $S1$ is influenced by inner cylinder angular velocity, particle size, external gravitational acceleration or by the surface being imaged (i.e., top or bottom) one experiment of each type is chosen. The experiments with 4 mm particles are presented here. The experiments with 3 mm particles were also analysed in the same manner and the details can be found in the Supplementary Material.

Figures 5.25–5.26 show $S1$ of the normalised mean angular velocity ($V_\theta^*(t)$) of the inner radial bin (of five) in a selection of experiments. Figure 5.25 shows $S1$ and $V_\theta^*(t)$ for 4 mm particles on the top surface of the shear cell at three different rotational velocities and in both 1 g and microgravity. In all of these plots the data have not been smoothed so this is the scatter in the raw data. The angular velocities have been normalised (as described in Section 5.2.8) to allow a comparison between the relative magnitudes of the fluctuations. The normalised scatter in the unsmoothed data decreases with increasing angular velocity. This indicates that a large part of the scatter in the unsmoothed data may be due to experimental noise and not due to real particle motion (noise due to the scatter of real particle motion would probably vary with ω and thus appear the same size in each of the figures).

The next set of plots (Fig. 5.26) show $S1$ and $V_\theta^*(t)$ for the smoothed data of exactly the same experiments as shown in Fig. 5.25. The particle positions have been smoothed over 2 seconds to remove the experimental noise before the velocities and the subsequent mean velocities and $S1$ were calculated. As anticipated, the normalised scatter of the smooth data remains relatively constant (at

Table 5.4: Different types of scatter discussed in the uncertainty analysis and their implications.

Scatter type	Measures	Significance
$S1$	Standard deviation of the particle velocities in a radial bin at any one moment in time.	If large this indicates that there is a large distribution of particle velocities within the radial band at a given moment in time and so particles are exhibiting different behaviours. Plotting $S1$ as a function of time indicates if the distribution of particle velocities changes in time. => Are all particles behaving the same way? Are there any regime changes?
$S2$	Standard deviation of the mean particle velocity in a radial bin over many frames (equivalent to the RMS velocity)	If large this indicates that the mean particle velocity is fluctuating over time. => Is there persistent bulk motion? Are there lots of random velocity fluctuations?
$S3_a$	Standard deviation of mean particle velocities between experiments of the same type	If large this indicates that the mean particle velocities from the individual experiments of the same type are very different. => are the experiments reproducible on a macroscale?
$S3_b$	Standard deviation of the mean $S2$ scatter between experiments of the same type	If large this indicates that the distributions of particle velocities in the individual experiments of the same type are very different. => are the experiments reproducible on a microscale?

a value of ~ 0.3) as the angular velocity increases. This implies that the scatter in the smoothed data is real and not due to experimental noise. This confirms that the large scatter in the unsmoothed data is due to experimental noise and that most of this noise is successfully removed during the smoothing process.

The same exercise was then repeated looking at the mean normalised radial velocity ($V_r^*(t)$) of particles in the inner radial bin (of five). As for the angular velocities, the unsmoothed data is analysed first to determine the scatter in the raw data. Figure 5.27 shows $S1$ and $V_r^*(t)$ for the 4 mm particles on the top surface of the shear cell at three different rotational velocities and in both 1 g and microgravity. The mean and scatters are calculated using the unsmoothed data and the mean radial velocities have been normalised (as described in Section 5.2.8). The next set of figures (Fig. 5.28) show $S1$ and $V_r^*(t)$ for the smoothed data of exactly the same experiments. The particle positions have been smoothed over 2 seconds to remove the experimental noise before the velocities and the subsequent mean velocities and $S1$ were calculated.

Just as for the angular velocities, the normalised scatter in the unsmoothed data decreases with increasing angular velocity suggesting that a large part of the scatter is due to experimental noise. However, unlike for the angular velocity data, the extent of the normalised scatter in the smoothed data also decreases with angular velocity. The magnitude of the fluctuations of $V_r^*(t)$ also decrease with increasing angular velocity implying that perhaps the radial velocity (V_r) is not a linearly increasing function with inner cylinder angular velocity (ω).

The same analysis was performed for the bottom surface of the experiments and the trends, of constant $S1$ in $V_\theta^*(t)$ and decreasing $S1$ in $V_r^*(t)$ with increasing inner cylinder angular velocity, remain the same (Figs. 5.29 and 5.30). The same trends were found for the experiments with 3 mm particles, which were analysed in the same manner (see Supplementary Material).

For all experiments plotted in Figs. 5.26–5.30 the mean angular and mean radial velocities fluctuate in time but the extent of the scatter of particle velocities at any one moment in time remains relatively constant. This is demonstrated more clearly in the two plots in Fig. 5.31. These plots shows the mean $S1$ in V_θ^* and V_r^* for the different types of experiments. Again, it can be seen that the mean normalised $S1$ in V_θ^* for all experiments does not vary with inner cylinder angular velocity. However, the mean normalised $S1$ in V_r^* decreases with increasing inner cylinder angular velocity. Additionally, it can be seen that $S1$ is smaller for the 3 mm beads (represented by squares) than for the 4 mm beads (represented by circles). This may be because the motion of the smaller beads is inhibited by the presence of the pressure plate. This will be the subject of a discussion in Section 5.4.1.

The error bars in Fig. 5.31, which represent the scatter in the mean $S1$, are both quite small and of a very similar size for all the experiments. This implies that there are similar distributions of mean

$S1$ in all of the experiments and that these distributions are within a small range. In other words, there is a relatively small distribution of particle velocities within the experiments ($S1$ in V_θ^* is ~ 0.2 - 0.3, $S1$ in V_r^* is ~ 0.05 - 0.2) and this is a consistent trend over many experiments.

5.3.4 $S2$

To find the scatter in the mean particle velocity over time, i.e., $S2$, the distribution in the mean particle velocity as a function of distance from shearing surface over many frames must be determined. First the mean velocities, as a function of distance from the inner cylinder, in a 15 second period of constant shearing (i.e., V_θ vs r and V_r vs r) are considered (as described in Section 5.2.9). $S2$ in V_θ (V_r) is the standard deviation of the mean angular (radial) particle velocity over this 15 second time period.

If the value of the mean $V_\theta(r)$ or $V_r(r)$ is non-zero it can be assumed that there is a net motion of particles. A large $S2$ combined with a non-zero mean velocity would mean that there is a net motion of particles in one direction but that there are large variations in the mean particle velocity during the time period. This would imply, therefore, that there is *no bulk persistent motion.* However, if $S2$ in the mean velocity is small this implies that the particle velocities do not vary much over time during experiments. A small $S2$ combined with a non-zero mean velocity would imply that there is *persistent bulk motion* of particles.

If the mean velocity is zero, or close to zero, and $S2$ is small this implies there is very little particle motion occuring. If the mean velocity is zero, or close to zero, but $S2$ is large this implies that the individual particles have non-zero velocities but in different directions which give an overal mean velocity of zero. However, in this case there is no bulk motion of particles in a given direction.

$S2$ is, in fact, equivalent to the root mean square (RMS) of grain velocity fluctuations often used to calculate the granular temperature of a granular medium. The RMS velocity (V^{RMS}) is calculated using the following equation,

$$V^{RMS} = \sqrt{\frac{1}{N}\sum_{i=1}^{N}(V_i - \bar{V})} \tag{5.24}$$

where N is the number of particles, $\bar{V}$ is the mean particle velocity and V_i is the instantaneous particle velocity. This is exactly the same equation used to calculate the standard deviation of the mean velocity. As defined above, $S2$ is the standard deviation of the mean particle velocity over the 15 second time period i.e., the average RMS velocity over the 15 second time period. To remain self-consistent we will continue to use the terminology of $S2$, although, we note that $S2$ and RMS velocity (V^{RMS}) are interchangeable terms.

$S2$ in $V_\theta(r)$ has been calculated for every experiment performed during the flight campaign and

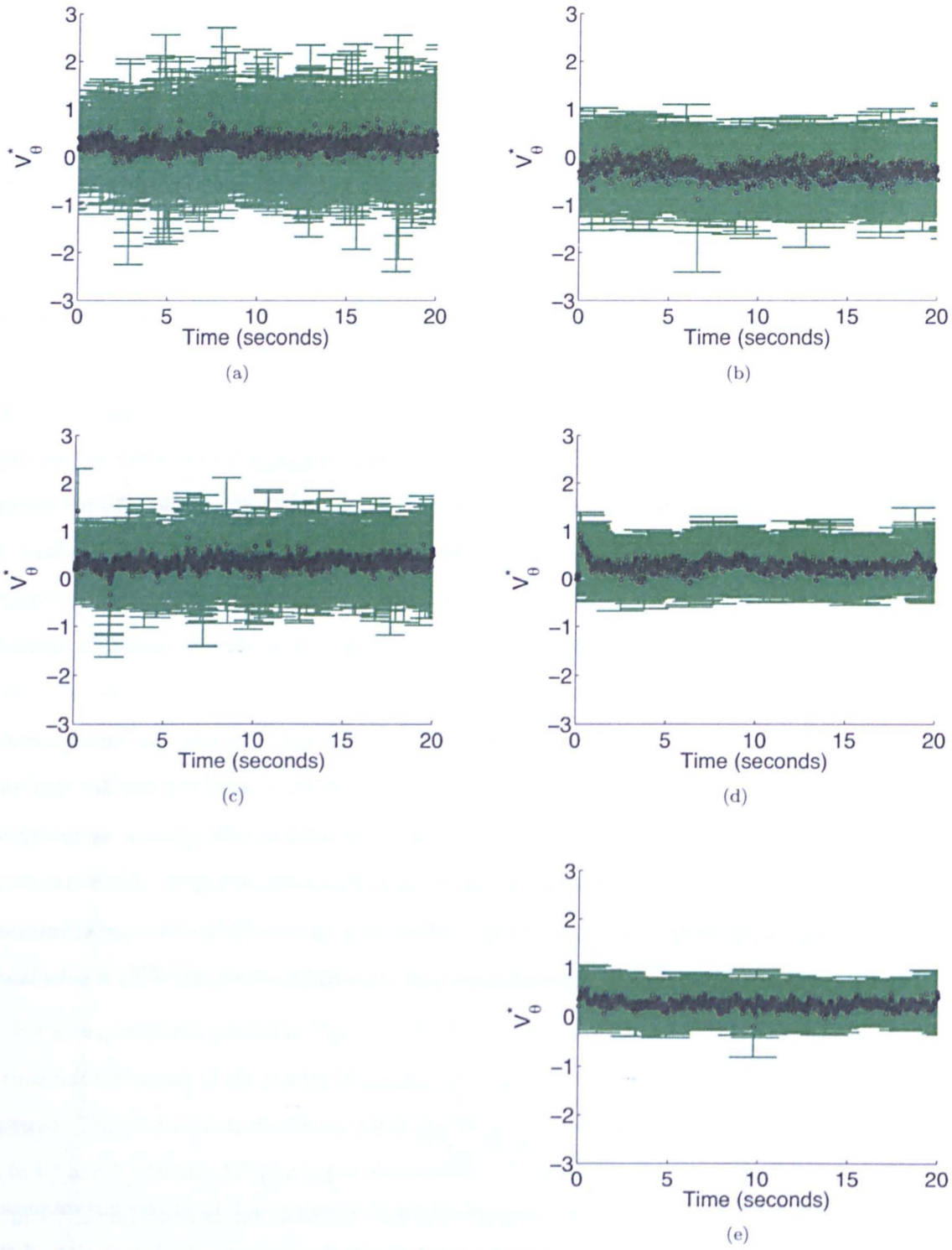

Figure 5.25: $S1$ **in** V_θ^* **for the inner radial bin of 4 mm beads on the top surface with no smoothing** - V_θ^* (defined in Eq. (5.3)) and $S1$ in the inner of five radial bins as a function of time in several experiments with 4 mm beads. V_θ^* and $S1$ are calculated using the raw, unsmoothed data: (a) 0.025 rad s^{-1} on the ground and (b) in microgravity, (c) 0.05 rad s^{-1} on the ground and (d) in microgravity and (e) 0.1 rad s^{-1} in microgravity. Note that there are no ground-based data available at 0.1 rad s^{-1}.

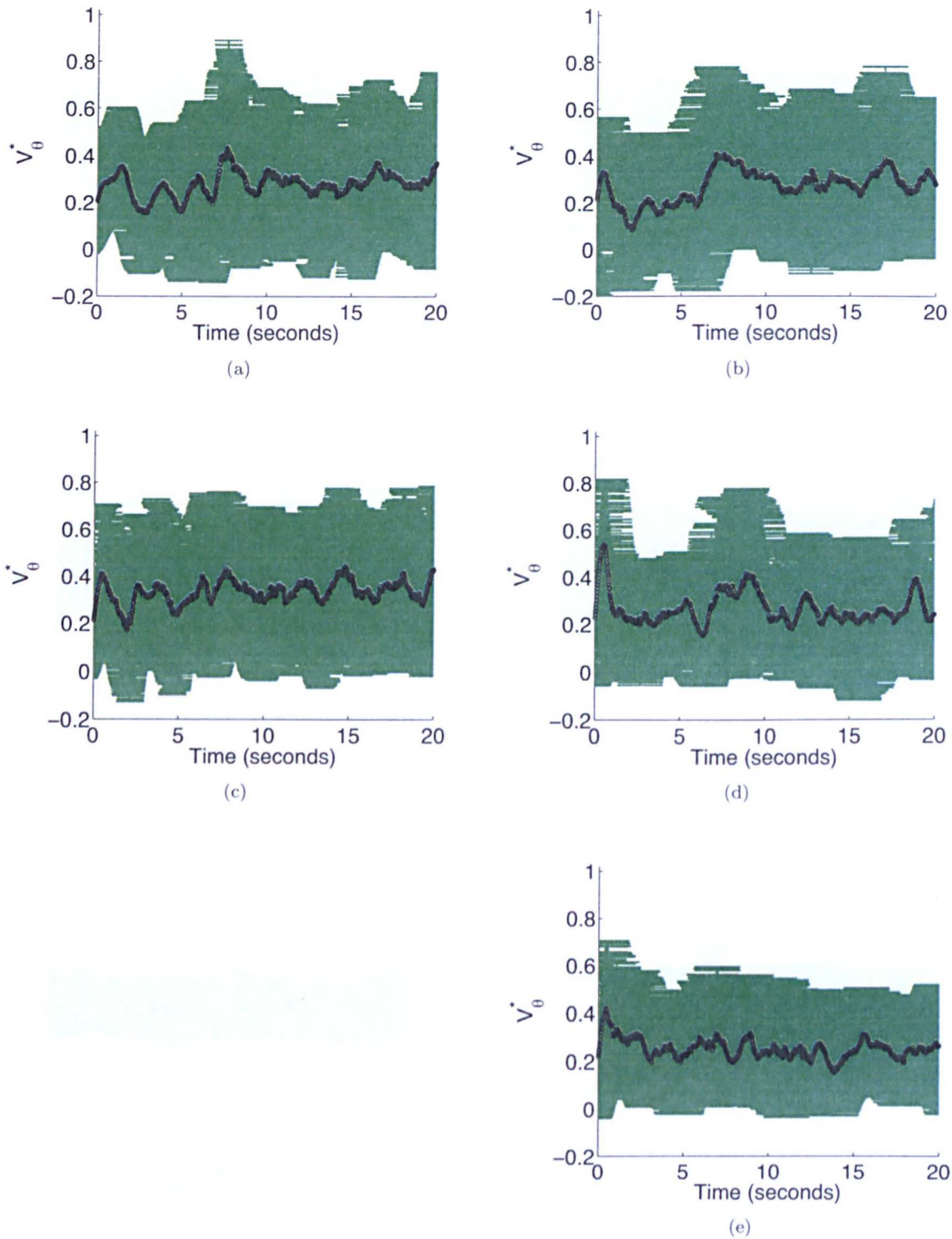

Figure 5.26: $S1$ **in** V_θ^* **for the inner radial bin of 4 mm beads on the top surface** - V_θ^* (defined in Eq. (5.3)) and $S1$ in the inner of five radial bins as a function of time in several experiments with 4 mm beads. V_θ^* and $S1$ are calculated using the smoothed data: (a) 0.025 rad s^{-1} on the ground and (b) in microgravity, (c) 0.05 rad s^{-1} on the ground and (d) in microgravity and (e) 0.1 rad s^{-1} in microgravity. Note that there are no ground-based data available at 0.1 rad s^{-1}.

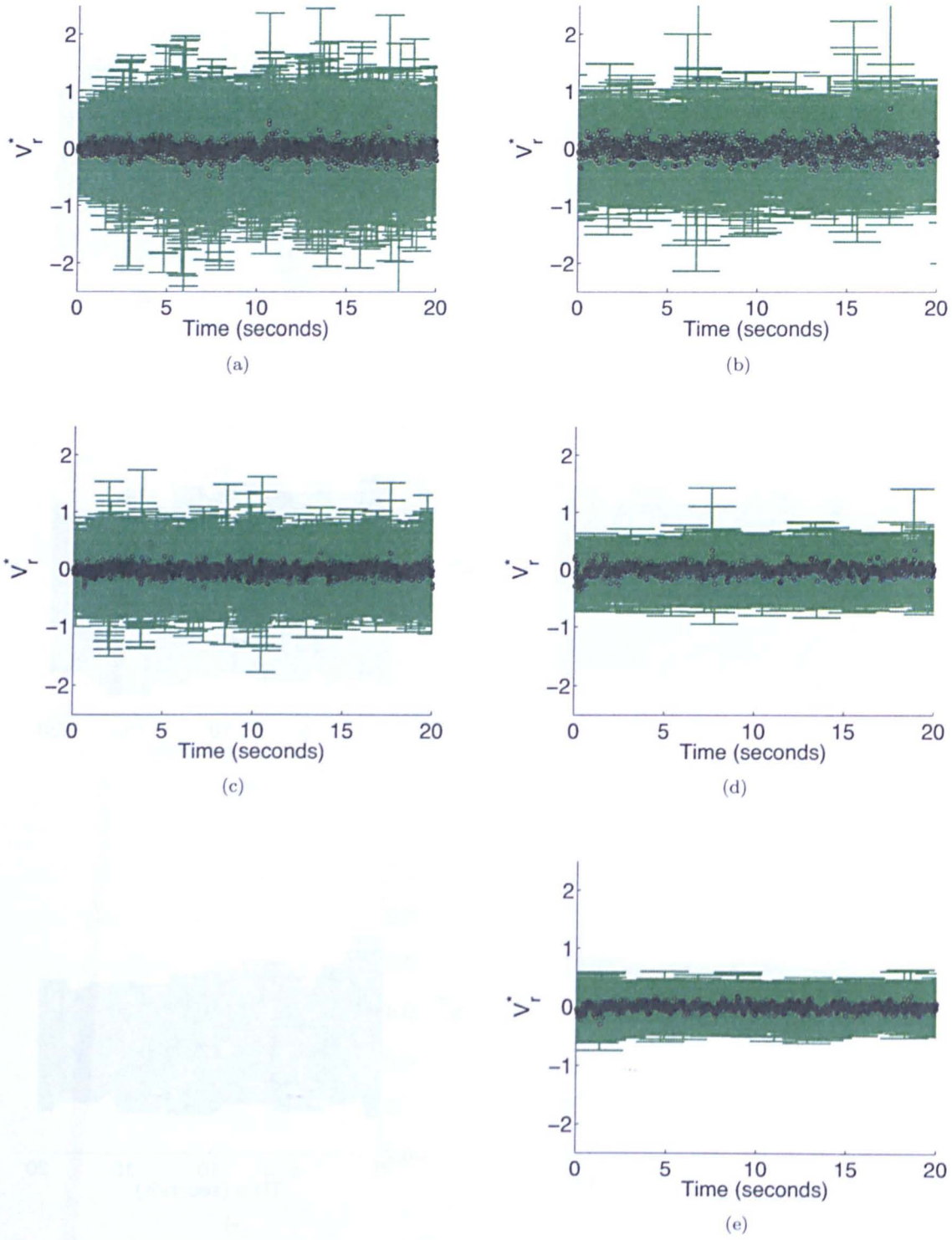

Figure 5.27: $S1$ **in** V_r^* **for the inner radial bin of 4 mm beads on the top surface with no smoothing** - V_r^* (defined in Eq. (5.4)) and $S1$ in the inner of five radial bins as a function of time in several experiments with 4 mm beads. V_r^* and $S1$ are calculated using the raw, unsmoothed data: (a) 0.025 rad s^{-1} on the ground and (b) in microgravity, (c) 0.05 rad s^{-1} on the ground and (d) in microgravity and (e) 0.1 rad s^{-1} in microgravity. Note that there are no ground-based data available at 0.1 rad s^{-1}.

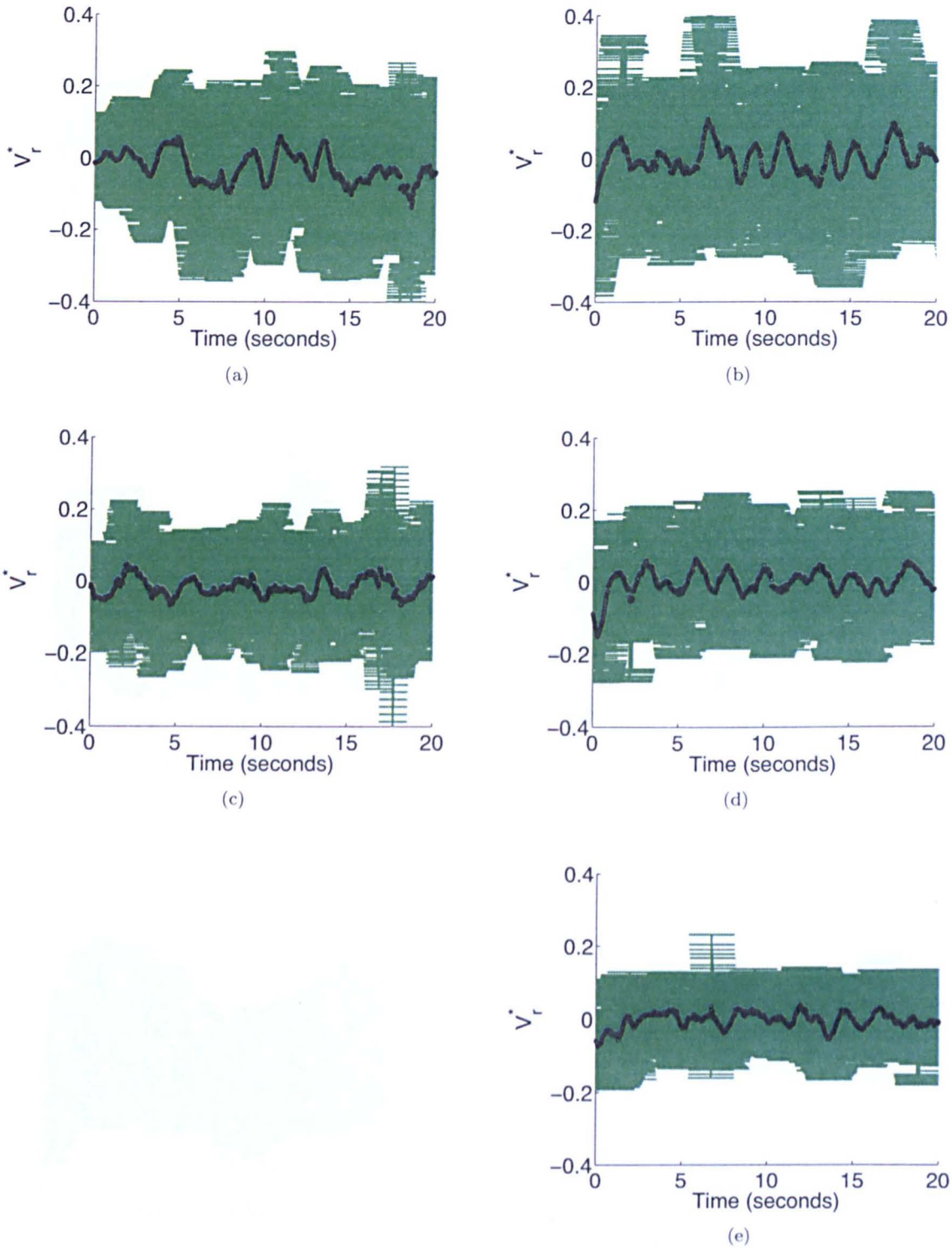

Figure 5.28: $S1$ **in V_r^* for the inner radial bin of 4 mm beads on the top surface** - V_r^* (defined in Eq. (5.4)) and $S1$ in the inner of five radial bins as a function of time in several experiments with 4 mm beads. V_r^* and $S1$ are calculated using the smoothed data: (a) 0.025 rad s^{-1} on the ground and (b) in microgravity, (c) 0.05 rad s^{-1} on the ground and (d) in microgravity and (e) 0.1 rad s^{-1} in microgravity. Note that there are no ground-based data available at 0.1 rad s^{-1}.

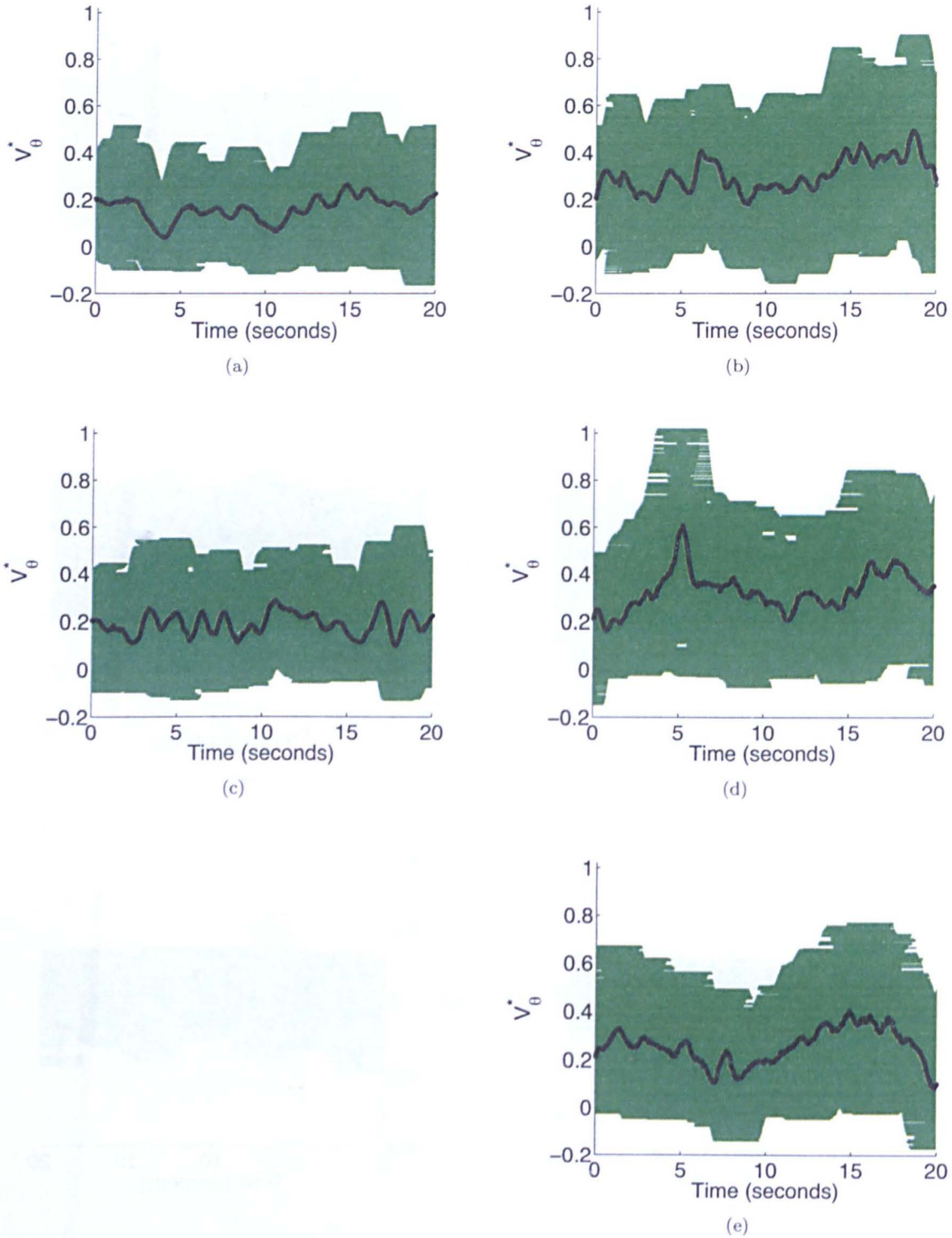

Figure 5.29: $S1$ **in** V_θ^* **for the inner radial bin of 4 mm beads on the bottom surface** - V_θ^* (defined in Eq. (5.3)) and $S1$ in the inner of five radial bins as a function of time in several experiments with 4 mm beads. V_θ^* and $S1$ are calculated using the smoothed data: (a) 0.025 rad s^{-1} on the ground and (b) in microgravity, (c) 0.05 rad s^{-1} on the ground and (d) in microgravity and (e) 0.1 rad s^{-1} in microgravity. Note that there are no ground-based data available at 0.1 rad s^{-1}.

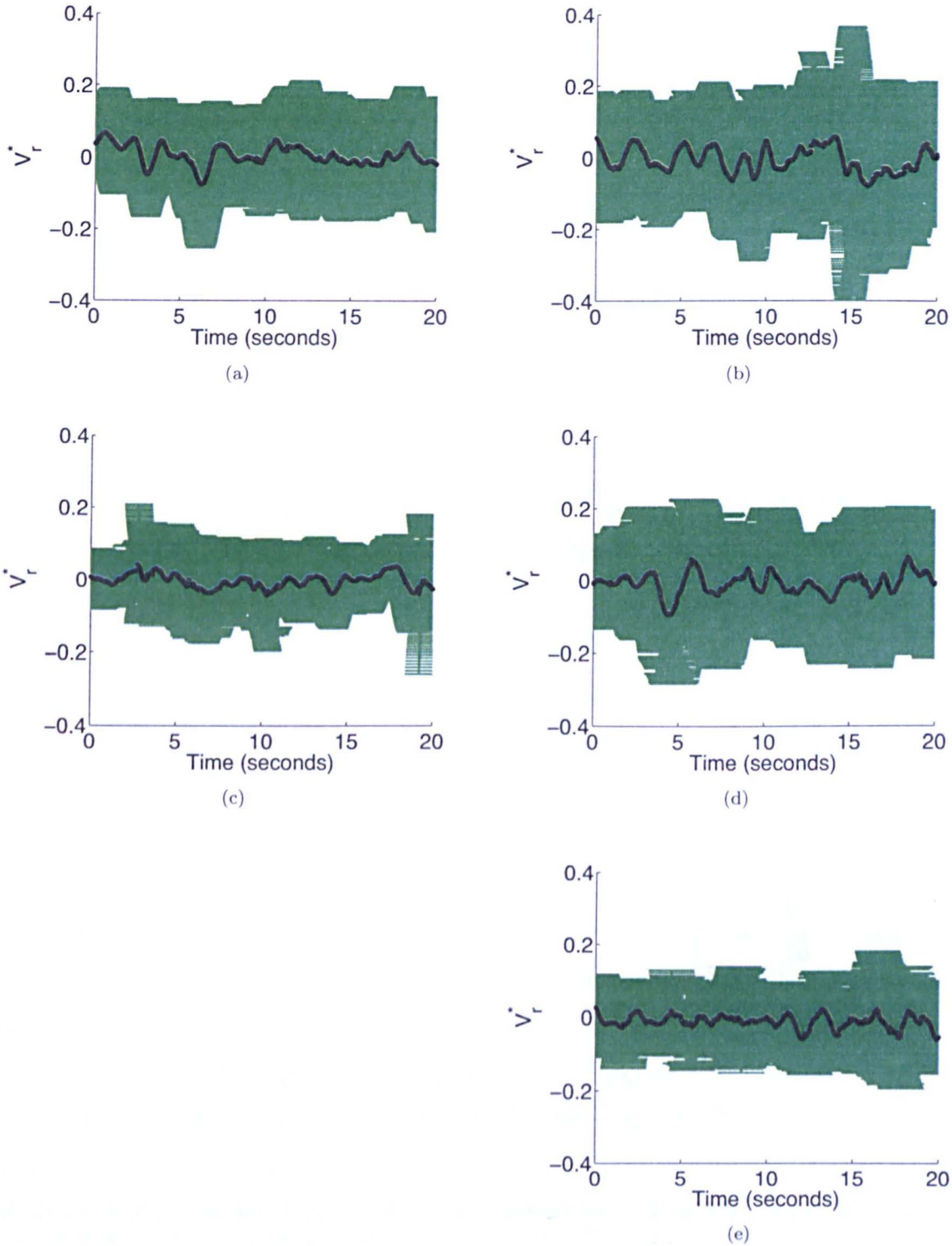

Figure 5.30: $S1$ **in** V_r^* **for the inner radial bin of 4 mm beads on the bottom surface** - V_r^* (defined in Eq. (5.4)) and $S1$ in the inner of five radial bins as a function of time in several experiments with 4 mm beads. V_r^* and $S1$ are calculated using the smoothed data: (a) 0.025 rad s^{-1} on the ground and (b) in microgravity, (c) 0.05 rad s^{-1} on the ground and (d) in microgravity and (e) 0.1 rad s^{-1} in microgravity. Note that there are no ground-based data available at 0.1 rad s^{-1}.

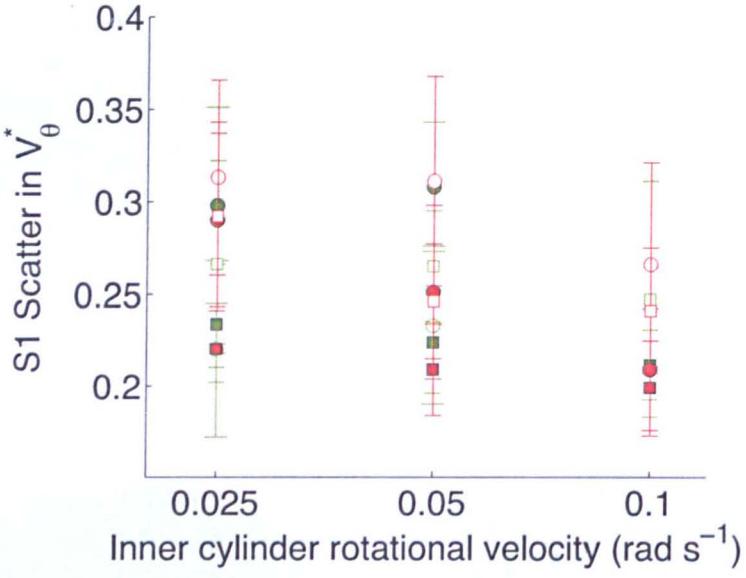

(a)

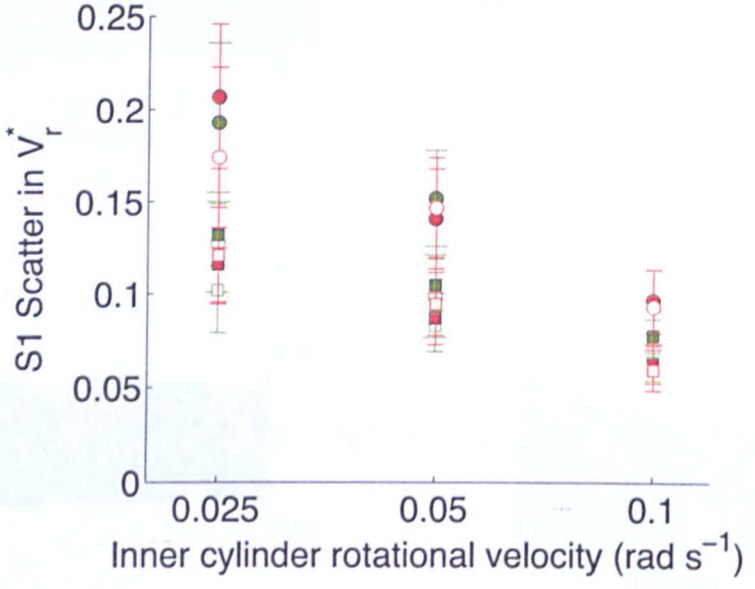

(b)

Figure 5.31: **Mean $S1$ for each experiment type** - The mean $S1$ in (a) V_θ^* and (b) V_r^* for the different types of experiments as a function of inner cylinder angular velocity. The error bars represent the scatter in the mean $S1$. The following code is used for the markers: ground-based experiments (green), microgravity experiment (red), 4 mm beads (circle), 3 mm beads (square). For each experiment, the scatter is shown for the top surface (filled marker) and for the bottom surface (open marker).

the full results are given in the Supplementary Material. Some examples are given in Figs. 5.32 and 5.33 below, which show the normalised mean angular velocity, V_θ^*, and $S2$ in V_θ^* for each of the (100) radial bins in several constant shear rate experiments at different inner cylinder rotational velocities.

There are some differences in the magnitudes and shapes of the angular velocity profiles between ground-based and microgravity experiments and between the top surface of the granular material and the lower surface. These differences will be the subject of an in-depth discussion in Chapter 6. Here the focus remains on $S2$ and the implications for interpreting the results.

From these figures we note that $S2$ in V_θ^* is largest at small distances from the inner cylinder where the motion is concentrated. However, the scatter is small enough, even at small distances from the inner cyliner, for the angular velocity profiles to be statistically significant. As V_θ^* is non-zero near the inner cylinder it can, therefore, be concluded that there is bulk motion of the particles in a preferential direction (as expected). Far from the inner cylinder the V_θ^* is close to zero and the scatter is very small. This implies that there is no particle motion at all in the angular direction. Similar trends in $S2$ are found both on the ground and in microgravity.

Next, the mean radial velocity, as a function of distance from the inner cylinder, in a 15 second period of constant shearing (i.e., V_r vs r) is considered. $S2$ in $V_r(r)$ has been calculated for every experiment performed during the flight campaign and the full results are given in the Supplementary Material. Some examples are given in Figs. 5.34 and 5.35, which show the normalised mean radial velocity and $S2$ for each of the twenty radial bins in several constant shear rate experiments at different inner cylinder rotational velocities. Again, the discussion regarding the differences between types of experiment is reserved for Chapter 6 and here the discussion remains centered on $S2$.

From these figures we note that $S2$ in V_r^* is very large close to the inner cylinder and, in some cases, far from the inner cylinder also. This scatter appears, in most cases, to be larger in microgravity than on the ground. This is probably due to the aircraft environment during the flight campaign (see discussion in Section 5.4). In the experiments where the V_r^* is close to zero and the scatter is large (such as the microgravity experiments in Fig. 5.34 and in the experiments of Fig. 5.35) this would imply that there is a large amount of random particle motion which results in a net radial velocity of zero. In the experiments where the V_r^* is non-zero and the scatter is large (such as the ground-based experiments in Fig. 5.34) this implies that there is a significant amount of random particle motion but there is also some net motion. As the scatter is large this net motion can not be conclusively defined as bulk motion in the individual experiments. However, if the same trends are present in several experiments of the same type then the conclusion can be drawn that there is a preferred direction of particle motion, which may be indicative of underlying bulk particle motion. $S3$ in the next section will compare experiments of the same type to detect potential trends.

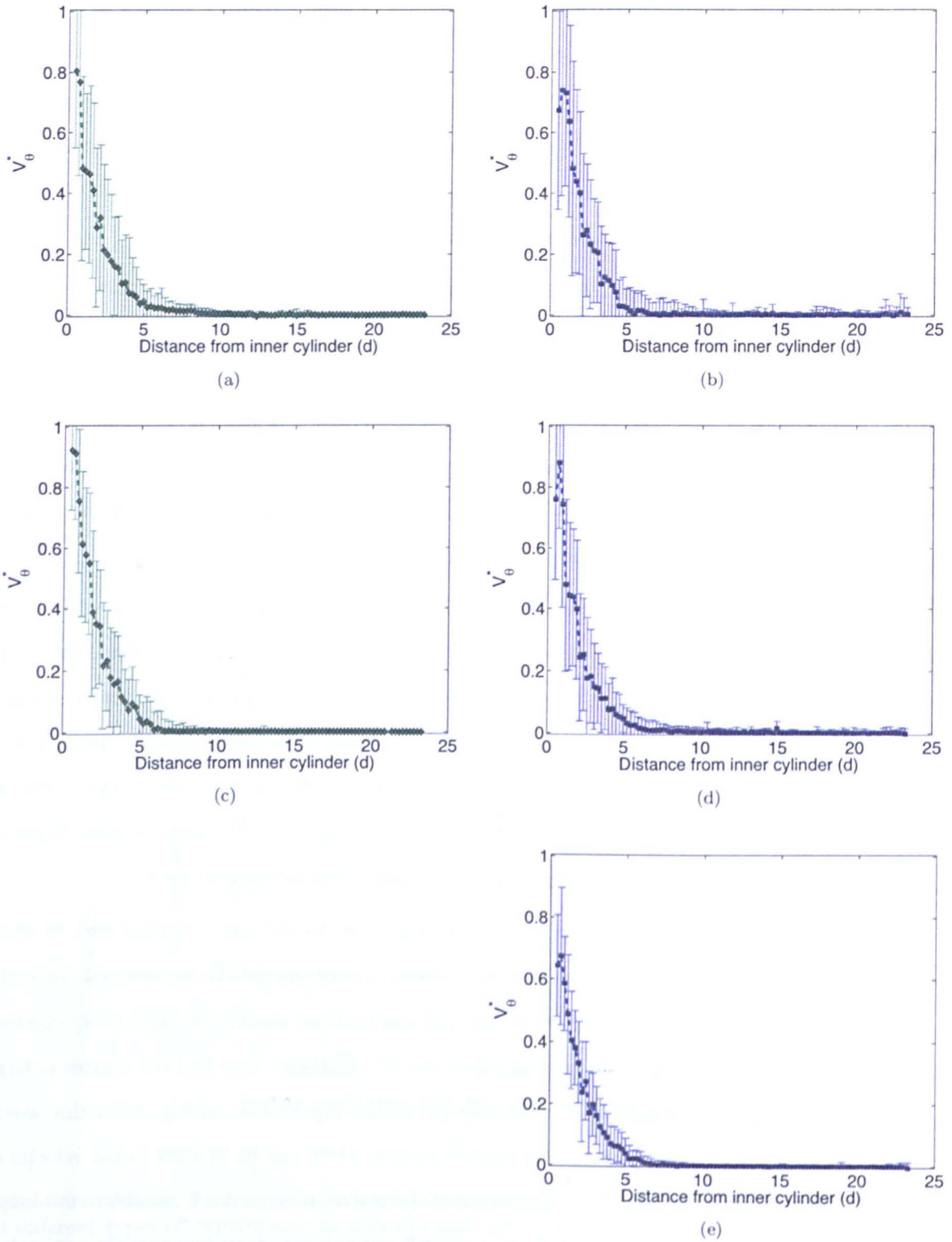

Figure 5.32: **Mean angular velocity profiles for the top surface of experiments with 4 mm beads** - V_θ^* is plotted as a function of distance from the inner cylinder. Each experiment is a constant shear rate experiment: (a) 0.025 rad s^{-1} on the ground and (b) in microgravity, (c) 0.05 rad s^{-1} on the ground and (d) in microgravity and (e) 0.1 rad s^{-1} in microgravity. Note that there are no ground-based data available at 0.1 rad s^{-1}. The error bars represent $S2$ i.e., the standard deviation of V_θ^* over the fiften second time period.

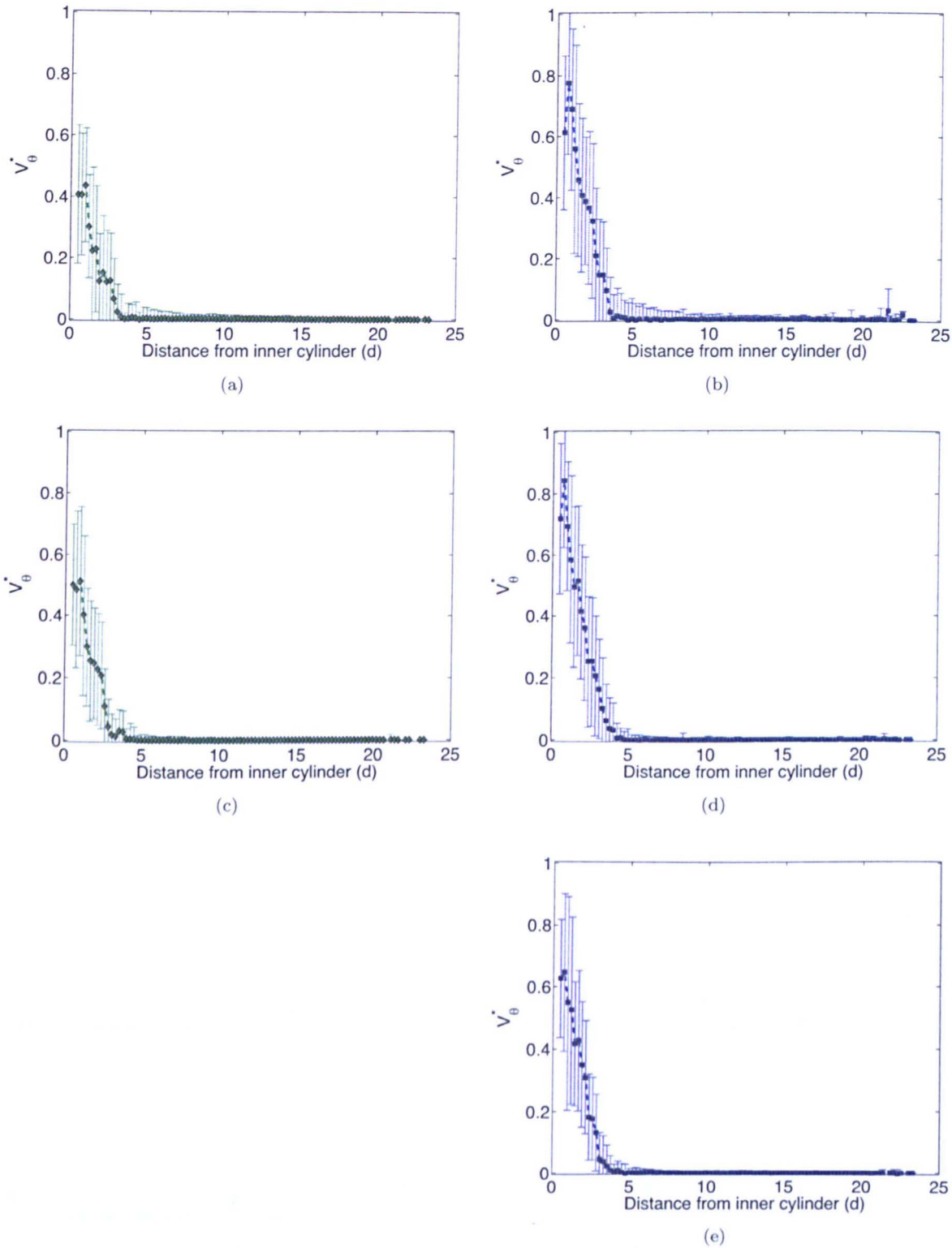

Figure 5.33: **Mean angular velocity profiles for the bottom surface of experiments with 4 mm beads** - V_θ^* is plotted as a function of distance from the inner cylinder. Each experiment is a constant shear rate experiment: (a) 0.025 rad s^{-1} on the ground and (b) in microgravity, (c) 0.05 rad s^{-1} on the ground and (d) in microgravity and (e) 0.1 rad s^{-1} in microgravity. Note that there are no ground-based data available at 0.1 rad s^{-1}. The error bars represent $S2$ i.e., the standard deviation of V_θ^* over the fiften second time period.

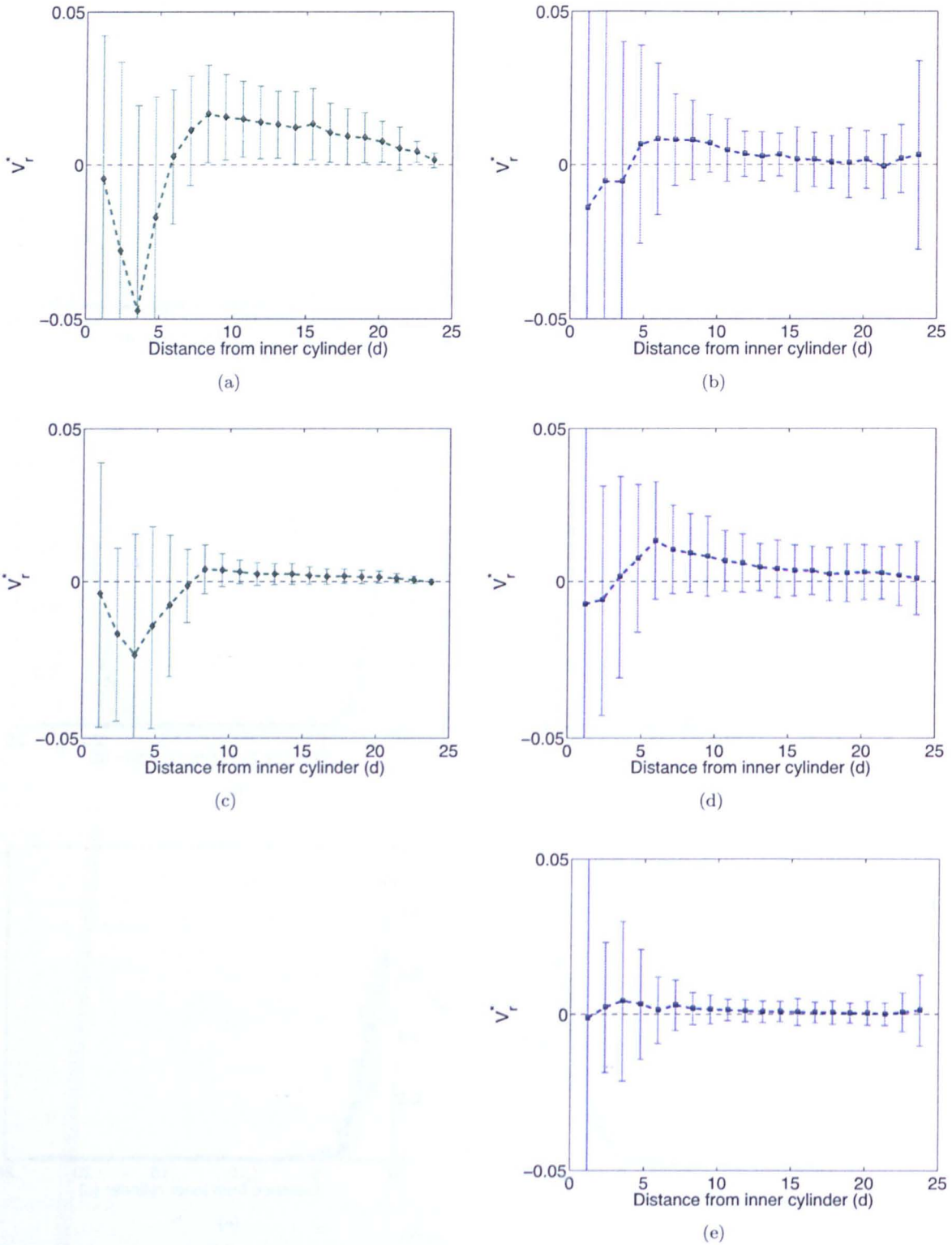

Figure 5.34: **Mean radial velocity profiles on the top surface of experiments with 4 mm beads** - V_r^* is plotted as a function of distance from the inner cylinder. Each experiment is a constant shear rate experiment: (a) 0.025 rad s^{-1} on the ground and (b) in microgravity, (c) 0.05 rad s^{-1} on the ground and (d) in microgravity and (e) 0.1 rad s^{-1} in microgravity. Note that there are no ground-based data available at 0.1 rad s^{-1}. The error bars represent $S2$ i.e., the standard deviation of V_r^* over the fifteen second time period.

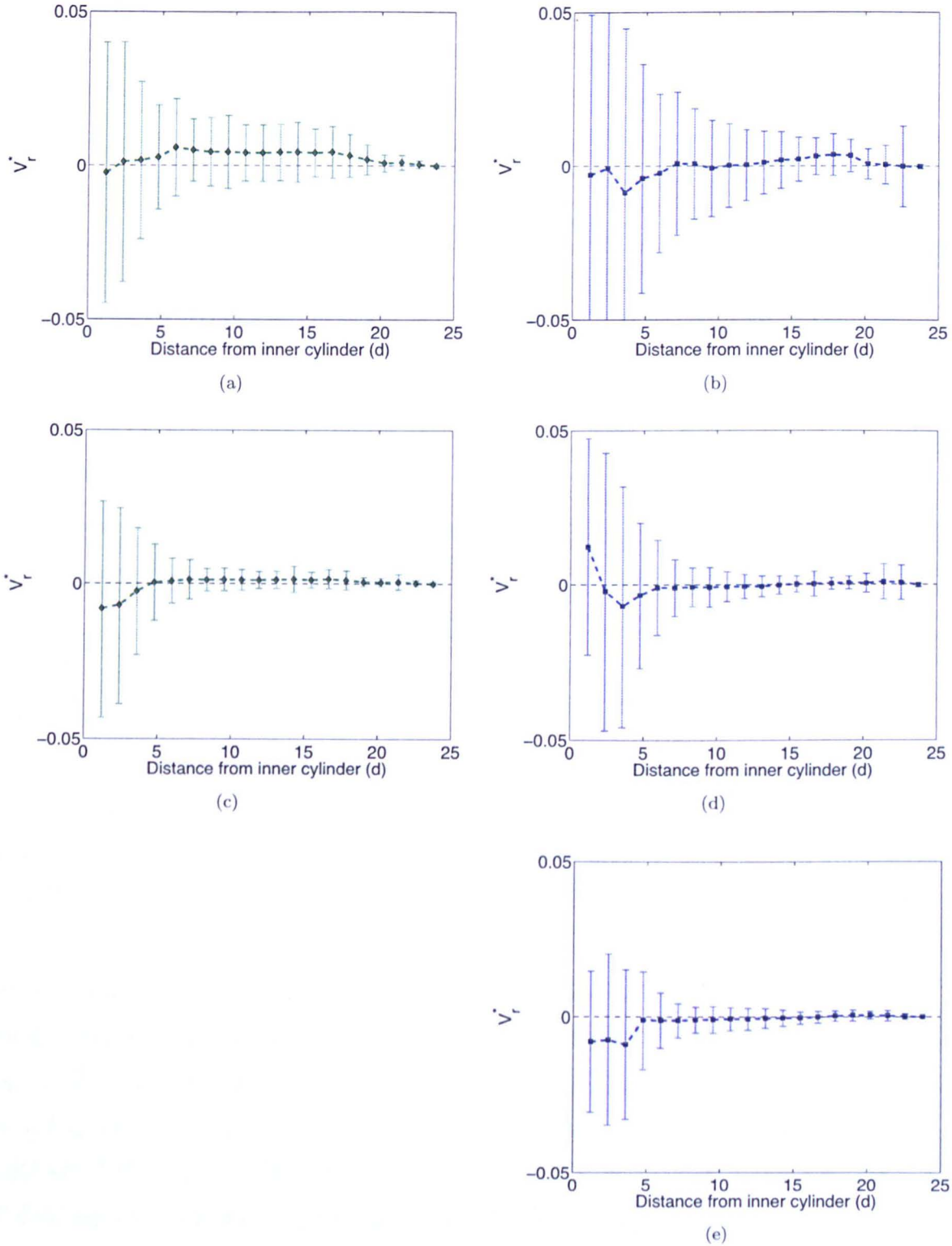

Figure 5.35: **Mean radial velocity profiles on the bottom surface of experiments with 4 mm beads** - V_r^* is plotted as a function of distance from the inner cylinder. Each experiment is a constant shear rate experiment: (a) 0.025 rad s^{-1} on the ground and (b) in microgravity, (c) 0.05 rad s^{-1} on the ground and (d) in microgravity and (e) 0.1 rad s^{-1} in microgravity. Note that there are no ground-based data available at 0.1 rad s^{-1}. The error bars represent $S2$ i.e., the standard deviation of V_r^* over the fifteen second time period.

5.3.5 $S3$

In this section a comparison is performed of the mean angular and radial velocities as a function of distance from the shearing surface between many experiments of the same type. The mean angular and radial velocities of several experiments in the same group will be referred to as, $\overline{V_\theta}$ and $\overline{V_r}$, respectively (with normalised versions $\overline{V_\theta^*} = \overline{V_\theta}/\omega$, and $\overline{V_r^*} = \overline{V_r}/(a\omega)$ where, as usual, a is the inner cylinder radius and ω is the inner cylinder angular velocity).

There will be two different types of $S3$. The first, which will be referred to as $S3_a$, compares the mean velocities between experiments of the same type. $S3_a$ is thus the standard deviation of the mean velocities (i.e., of $\overline{V_\theta}$ and $\overline{V_r}$). If $S3_a$ is small this implies that the mean values between experiments have consistently similar values and that, therefore, the experiment is reproducable on a macroscale. If $S3_a$ is large then the mean values will not be as meaningful.

The second type of $S3$, which will be referred to as $S3_b$, compares the $S2$ in the mean velocities between experiments of the same type (i.e., the $S2$ in V_θ and V_r for each experiment which are equivalent to the RMS velocity fluctuations in V_θ and V_r). $S3_b$ is, thus, the standard deviation of the mean $S2$ from the different experiments. If $S3_b$ is small this means that $S2$ is similar for all of the experiments within the group. This would imply that all of the experiments have a similar distribution of mean particle velocities over the duration of the experiment (i.e., the experiment is reproducable on a microscale). If $S3_b$ is large then this means that $S2$ is very different for all of the experiments within the group and, therefore, the distributions of mean particle velocities over the duration of the experiment are very different. An ideal set of experiments, which are fully reproducable, would have a very small $S3_a$ (i.e., reproducable on a macroscale) and also a very small $S3_b$ (i.e., reproducable on a microscale).

Below, the example is used of the 4 mm beads undergoing constant shearing with an inner cylinder angular velocity of 0.05 rad s^{-1}. The full results for all experiments are given in the Supplementary Material. Figure 5.36 (a) and (b) show $\overline{V_\theta^*}$ of the particles on the top surface of several experiments plotted as a function of distance from inner cylinder. Three curves are shown for groups of experiments that were performed on the ground, during Flight A and during Flight C, respectively. The error bars in these plots represent $S3_a$ (i.e., the standard deviation of $\overline{V_\theta^*}$ in each group of experiments). Considering these two figures it can been seen that, for each group of experiments, the error bars are, therefore, $S3_a$ are very small. This implies that the mean angular velocity profiles are very similar for all experiments performed under the same conditions.

Consider now Fig. 5.36 (c) and (d), which show the mean $S2$ of V_θ^* plotted as a function of distance from the inner cylinder for each of the three groups of experiments. The error bars represent $S3_b$ (i.e., the standard deviation of the mean $S2$ of V_θ^*). From these plots it can be seen that $S3_b$ is very similar

for all groups and, as the error bars in figures (c) and (d) are small there is a similar amount of $S2$ in all experiments within each group. This allows us to conclude that, *not only are the mean angular velocity profiles similar for each experiment group, but the distributions of individial particles' angular velocities are also similar for all experiments of the same group. This means that, for these sets of experiments, the angular velocity profiles are reproducable on a macroscale and microscale.*

However, it should be noted that during Flight C $S3_b$ is large close to the outer cylinder. As $\overline{V_\theta^*}$ is almost zero in this location (Fig. 5.36 (a)) this implies there is a large amount of random motion of the individual particles. This is probably caused by the aircraft environment and the strong fluctuations in the simulated gravity during this flight. This is discussed further in Section 5.4.

The same analysis performed looking at the bottom surface reveals similar results (Fig. 5.37). The differences in the angular velocity profiles between different types of experiments will be discussed later in Chapter 6.

The results of the radial velocity analysis using the beads on the top and bottom surfaces of the same experiments are shown in Figs. 5.38 and 5.39, respectively. $S3_a$ between experiments of the same groups is small (Fig. 5.38 (a)). This implies that the same trends are present in several experiments of the same type. $S3_b$ in V_r^* is much larger for the microgravity experiments (particularly for Flight C) than for the experiments performed on the ground (Fig. 5.38 (b)). This implies that there is a larger distribution of particle radial velocities in microgravity. As $\overline{V_r^*}$ is close to zero in this location (Fig. 5.38 (a)) this implies there is a large amount of random motion of the individual particles, again probably caused by the aircraft environment (e.g., varying simulated gravity), but with no overall net motion.

From these two figures the conclusion can be drawn that, in these experiments of the top surface, there are reproduceable trends within the experiment groups. In microgravity there is a wide and varying distribution of the individual particle velocities indicating a large amount of random particle motion. However, on the ground the distribution of particle velocities is smaller. *This smaller scatter, combined with the clear trend of having a preferred direction of particle motion, is indicative of underlying bulk particle radial motion on the ground.* These arguments will be invoked later during the discussion of granular convection in Chapter 6.

The same analysis has been performed looking at the radial velocity profiles on the bottom surface (Fig. 5.39). Again, as $S3_a$ between experiments of the same groups is small, this implies that the same trends are present in several experiments of the same type. $S3_b$ is smaller on the bottom surface meaning that there is less random motion on the bottom surface of the experiments than on the top surfaces. Also, the distributions of particle radial velocities between experiments of the same group are similar (because the size of the error bars in Fig. 5.39 (b) are small).

Comparing Fig. 5.38 (b) with Fig. 5.39 (b) we see that, for the experiments performed during Flight C, $S3_b$ is larger on the top surface than on the bottom surface very close to the inner cylinder and far from the inner cylinder (>6-7 d). Assuming gravity variations are the cause, this would imply that, at those distances, the particles on the top surface are much more sensitive to the gravity variations than at the same distances on the bottom surface. At intermediary distances i.e., ~2-6 d, the top and the bottom surfaces are both similarly affected by the gravity variations. The differences in the radial velocity profiles between different types of experiments will be discussed further in Chapter 6.

5.4 Factors influencing the measured particle velocities

As described in detail in Chapter 4, the AstEx experiment had to be modified for the microgravity environment. As a result of the modifications to the hardware and experimental set-up, there are a few factors that may influence the measured particle dynamics, namely the presence of the pressure plate and the light reflections. It was also part of the experimental procedures to shake the particles before each experiment was performed. The aim of the shaking was to attempt to remove any memory effects from the granular material, thus creating a reproducable initial configuration. As we have seen in Section 5.3.2, experiments of the same type have similar mean velocity profiles. However, the influence of shaking has not yet been directly investigated. Additionally, the flight environment with aircraft vibrations and gravity variations may also influence the particle dynamics. All such factors, which may influence the measured particle velocities and thus the final experimental results, are considered in this section. For the factors which are constant in time and may affect certain regions of the shear cell, i.e., due to the hardware, we examine their influence upon the velocity profiles. For the factors which may vary in time, such as the gravity fluctuations, we look at the velocity as a function of time.

5.4.1 The direct influence of the pressure plate

Experiments were performed on the ground with, and without, the pressure plate to determine if the pressure plate had any influence on the particle velocities. Figure 5.40 shows the normalised mean angular velocity profiles (i.e., $\overline{V_\theta^*(r)}$) of the 4 mm particles on the top surface of an experiment with the pressure plate and without the pressure plate. Mean angular velocity profiles are shown for three different inner cylinder angular velocities: 0.025 rad s^{-1}, 0.05 rad s^{-1} and 0.1 rad s^{-1}. The mean velocity profiles shown in this figure only extend up to 8 particle diameters from the shearing surface as further away there is very little motion and, therefore, no difference in the two profiles. The velocity profiles with and without the pressure plate are very similar, although, there are some irregularities in

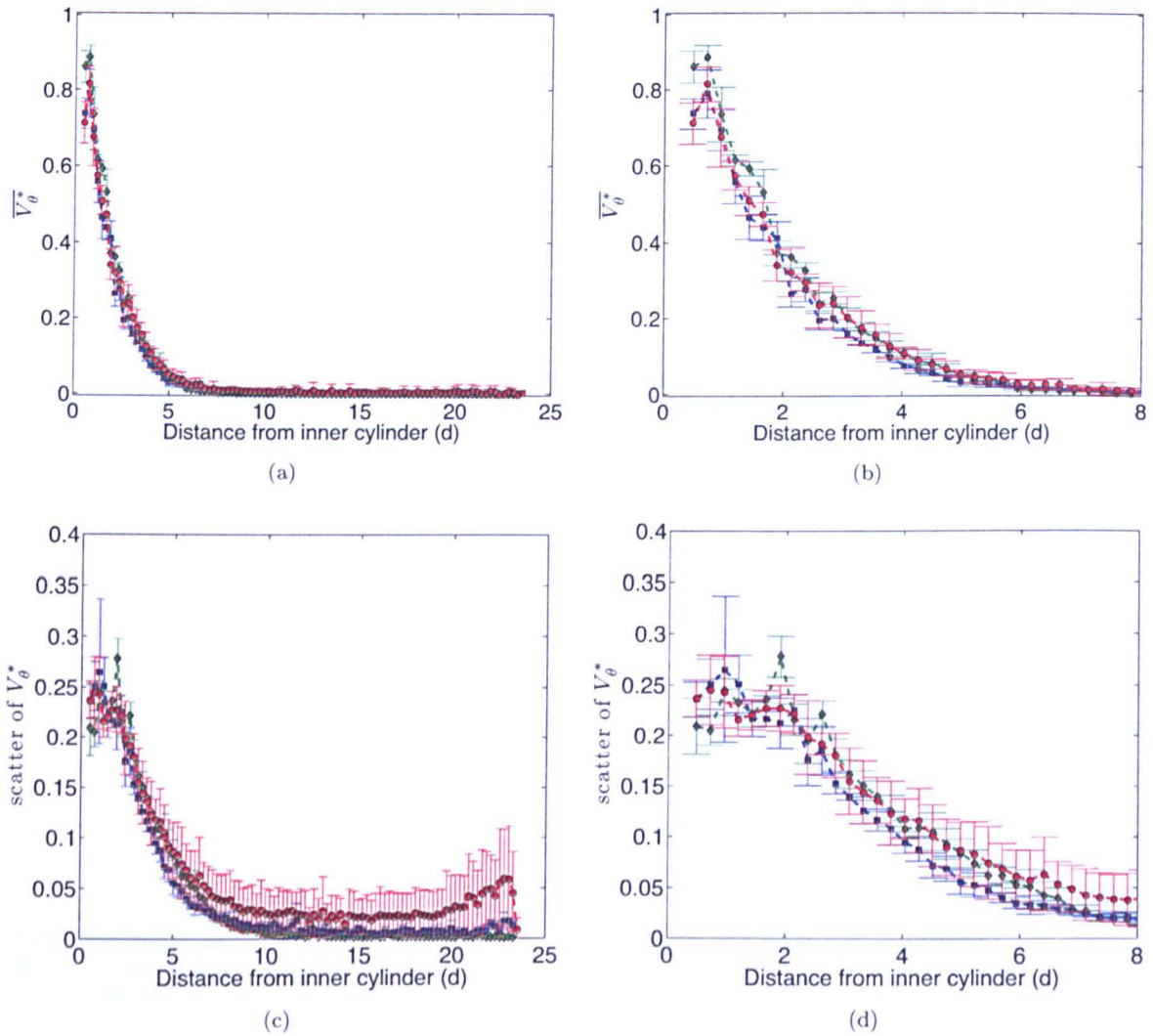

Figure 5.36: $S3$ **angular velocity analysis for 4 mm beads on top surface at 0.05 rad s^{-1}** - (a) $\overline{V_\theta^*}$ of each experiment group plotted as a function of distance from inner cylinder. The error bars represent $S3_a$ (i.e., the standard deviation of $\overline{V_\theta^*}$ for each group of experiments). (b) Same as (a) but zoomed in. (c) Mean $S2$ of V_θ^* (equivalent to V^{RMS}) plotted as a function of distance from the inner cylinder. The error bars represent $S3_b$ (i.e., the standard deviation of the mean $S2$ of V_θ^*). (d) Same as (c) but zoomed in. Green diamonds: 1 g, Blue squares: microgravity (Flight A), Red circles: microgravity (Flight C).

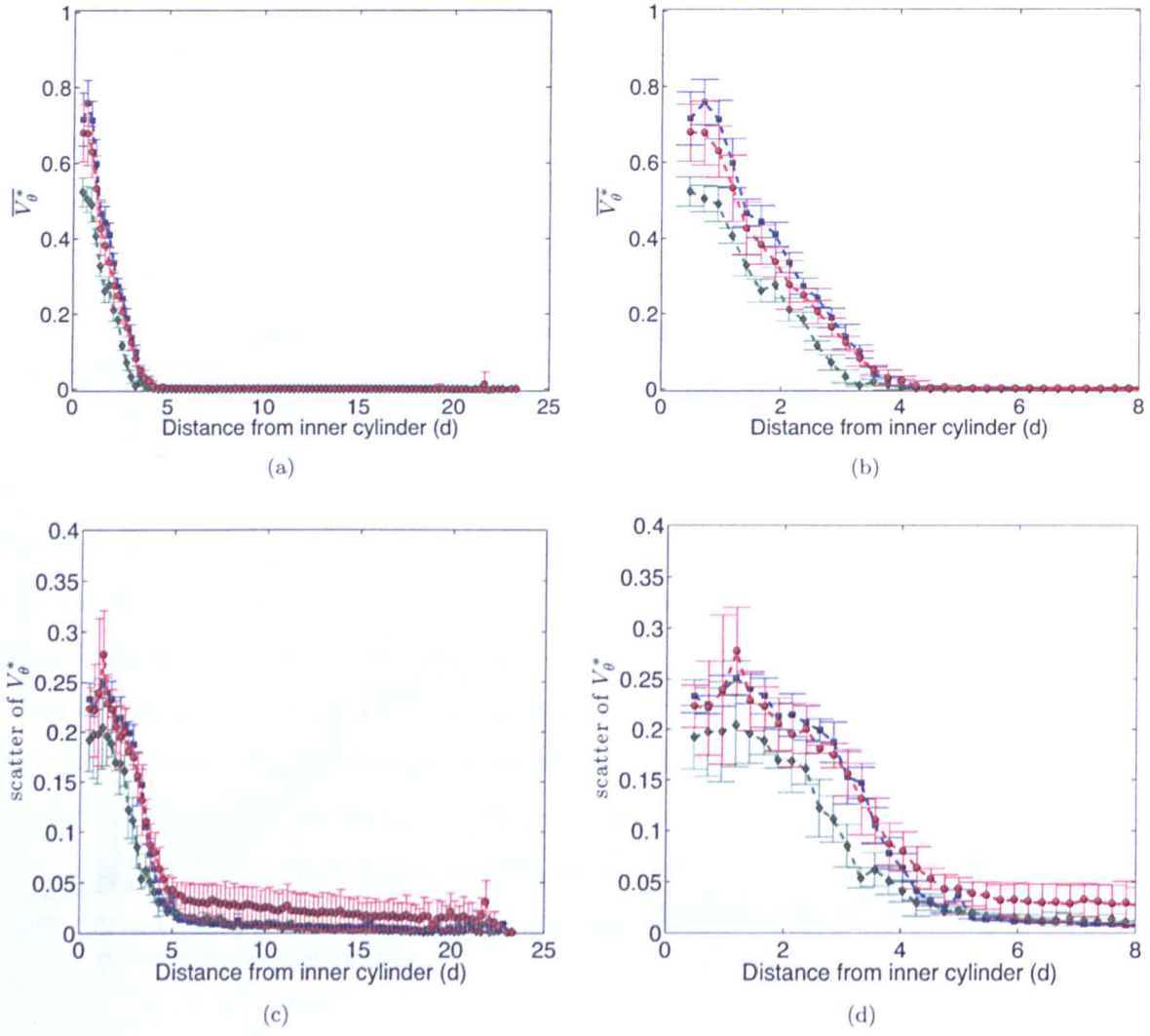

Figure 5.37: $S3$ **angular velocity analysis for 4 mm beads on bottom surface at 0.05 rad** $\mathbf{s}^{-1}$ - (a) $\overline{V_\theta^*}$ of each experiment group plotted as a function of distance from inner cylinder. The error bars represent $S3_a$ (i.e., the standard deviation of $\overline{V_\theta^*}$ for each group of experiments). (b) Same as (a) but zoomed in. (c) Mean $S2$ of V_θ^* (equivalent to V^{RMS}) plotted as a function of distance from the inner cylinder. The error bars represent $S3_b$ (i.e., the standard deviation of the mean $S2$ of V_θ^*). (d) Same as (c) but zoomed in. Green diamonds: 1 g, Blue squares: microgravity (Flight A), Red circles: microgravity (Flight C).

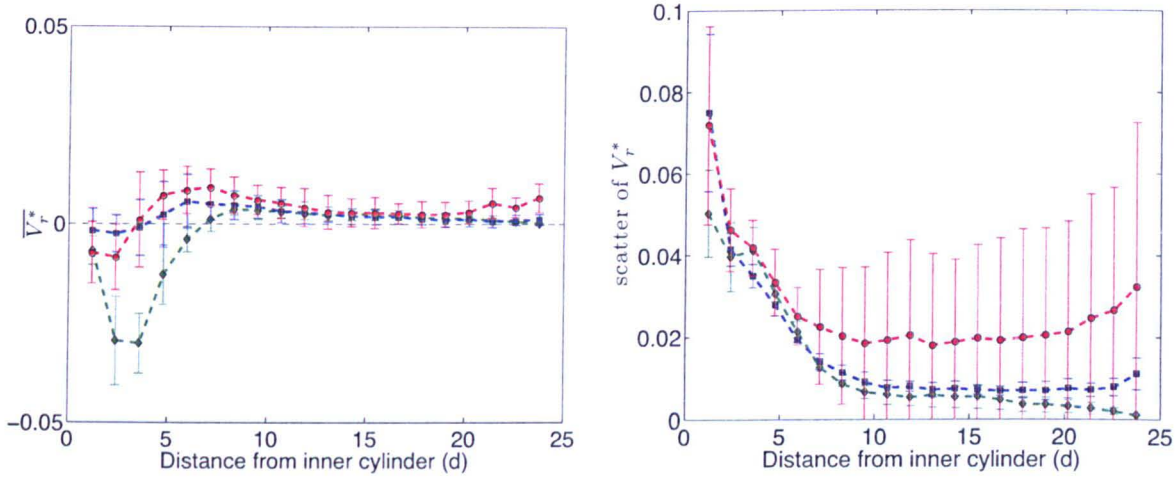

Figure 5.38: $S3$ **radial velocity analysis for 4 mm beads on top surface at 0.05 rad s^{-1}** - (a) $\overline{V_r^*}$ of each experiment group plotted as a function of distance from inner cylinder. The error bars represent $S3_a$ (i.e., the standard deviation of $\overline{V_r^*}$ for each group of experiments). (b) Mean $S2$ of V_r^* (equivalent to V^{RMS}) plotted as a function of distance from the inner cylinder. The error bars represent $S3_b$ (i.e., the standard deviation of the mean $S2$ of V_r^*). Green diamonds: 1 g, Blue squares: microgravity (Flight A), Red circles: microgravity (Flight C).

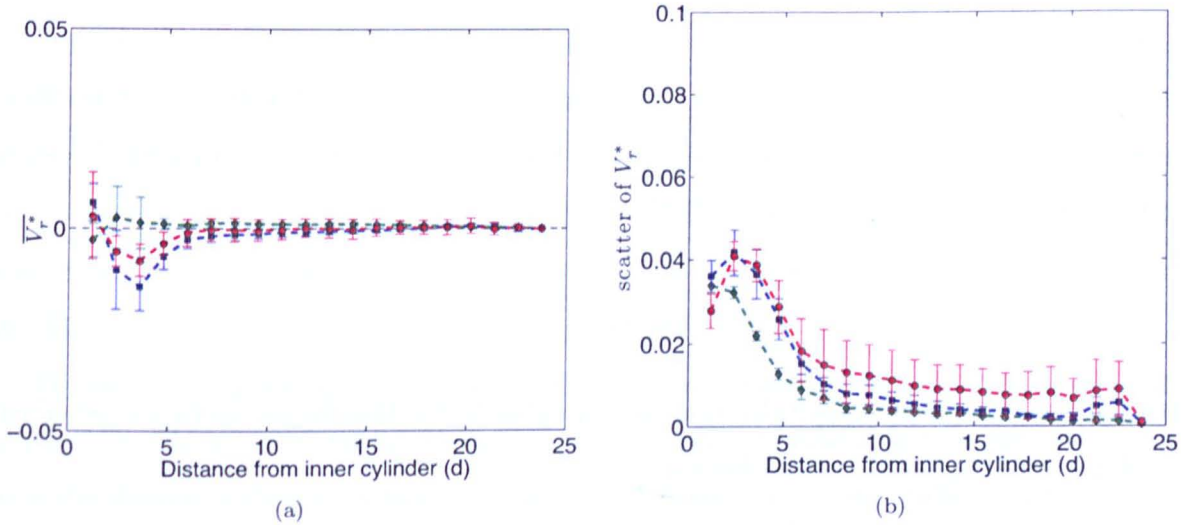

Figure 5.39: $S3$ **radial velocity analysis for 4 mm beads on bottom surface at 0.05 rad s^{-1}** - (a) $\overline{V_r^*}$ of each experiment group plotted as a function of distance from inner cylinder. The error bars represent $S3_a$ (i.e., the standard deviation of $\overline{V_r^*}$ for each group of experiments). (b) Mean $S2$ of V_r^* (equivalent to V^{RMS}) plotted as a function of distance from the inner cylinder. The error bars represent $S3_b$ (i.e., the standard deviation of the mean $S2$ of V_r^*). Green diamonds: 1 g, Blue squares: microgravity (Flight A), Red circles: microgravity (Flight C).

the velocity profiles with the pressure plate. These irregularities seem to occur at similar locations in all experiments and, therefore, may be caused by an inhomegenity in the pressure plate. Part of the pressure plate possibly exerts more pressure on the top layer of particles, or part of the pressure plate is perhaps rougher than the rest. The irregularities also become very slightly more pronounced as the angular velocity increases, which means that the pressure plate has a larger effect on the particles at larger rotation rates.

Figure 5.41 shows the normalised mean angular velocity profiles of the 3 mm particles on the top surface of an experiment with the pressure plate and without the pressure plate. This time the mean angular velocity profiles are shown for only two different inner cylinder angular velocities: 0.025 rad s^{-1} and 0.05 rad s^{-1}. Unfortunately, experiments were not performed with an inner cylinder angular velocity of 0.1 rad s^{-1}. Again the mean velocity profiles shown in this figure only extend up to 8 particle diameters from the shearing surface as further away there is very little motion and, therefore, no difference in the two profiles. Contrary to the 4 mm particle results, the pressure plate appears to have a very strong influence on the mean angular velocity profiles of the 3 mm particles. This may be because the filling heights are slightly different in the two shear cells; the mass of beads to be added to the shear cells was calculated assuming a random packing fraction of ~0.6 and a desired filling height of 100 mm. It is possible that the 3 mm particles have a lower packing fraction than the 4 mm beads and the filling height is, therefore, slightly higher. This would mean that the pressure plate is exerting a slightly larger pressure on the 3 mm beads.

However, the more likely explanation is that the rate at which the particles are decelerated by the pressure plate depends on their radius. Assuming we have one layer of mono-disperse particles (particle radius, r, and density, ρ), covering a given surface area, A_s, and with a 2d packing fraction, ϕ_{2d}, then the total number of particles in the layer, N_p, is given by,

$$N_p = \frac{A_s \phi_{2d}}{\pi r^2}. \tag{5.25}$$

If the total force exerted on the particles by the pressure plate is, F_N, then the normal force experienced by each particle (F_{Np}) on the surface layer is,

$$F_{Np} = \frac{F_N}{N_p} = \frac{\pi F_N r^2}{A_s \phi_{2d}}. \tag{5.26}$$

The frictional force experienced by each particle (F_{Sp}) is related to the normal force experienced by each particle via the following relation:

$$F_{Sp} = \mu_s F_{Np} \tag{5.27}$$

where μ_s is the coefficient of static friction. The resulting deceleration (a_p) of each particle in the surface layer due to the pressure plate is given by:

$$a_p = \frac{F_{Sp}}{M_p} = \frac{3\mu_s F_N}{4\phi_{2d}\rho r} \tag{5.28}$$

where the mass of each particle (M_p) is,

$$M_p = \frac{4\pi r^3 \rho}{3}. \tag{5.29}$$

Therefore, with constant total normal force, particle density, surface area and packing fraction, the deceleration of each particle varies inversely with r. This means that the smaller (3 mm) particles should be decelerated by the pressure plate more than larger (4 mm) particles, which is exactly what the experimental results are showing.

5.4.2 The influence of the light reflections

As has been seen in Section 5.2.4 (Fig. 5.12), as a result of the filtering that must be applied to remove spurious particles, sometimes real particles are lost. This, unfortunately, occurs in regions of high interest, such as near the inner cylinder on the top surface. As there are no reflections present when the pressure plate is removed the runs without the pressure plate permit some testing to be performed on how the filtering described in Section 5.2.4 affects the results.

First, the particle tracks are filtered based only on their radial position to remove spurious particles outside the shear cell. The particle tracks which survive can be seen in Fig. 5.42 (a). Next, the standard filtering criteria on the particle size and brightness (such as used to remove spurious particles when the pressure plate is present) is applied. The result is that many particle tracks near the outer and inner cylinders are lost (because particles in these locations are slightly higher and thus appear slightly larger). The particle tracks which survive can be seen in Fig. 5.42 (b).

The mean angular velocity profiles were calculated for both of these cases and the results are plotted in Fig. 5.43. The mean velocity profiles shown in this figure only extend up to 8 particle diameters from the shearing surface as further away there no difference in the two profiles. The profiles are essentially identical with a very small difference in magnitude very close to the inner cylinder and a small difference in the size of the scatter of particle velocities within the radial bins. However, it is safe to assume that the results are not influenced by the filtering, nor by the loss of some particles. This is because the averages are being taken over many particles and over many frames.

Another consequence of the light reflections is that, as discovered in Section 5.2.5, some particles have very short lifetimes. This occurs because particles regularly disappear for a short period of

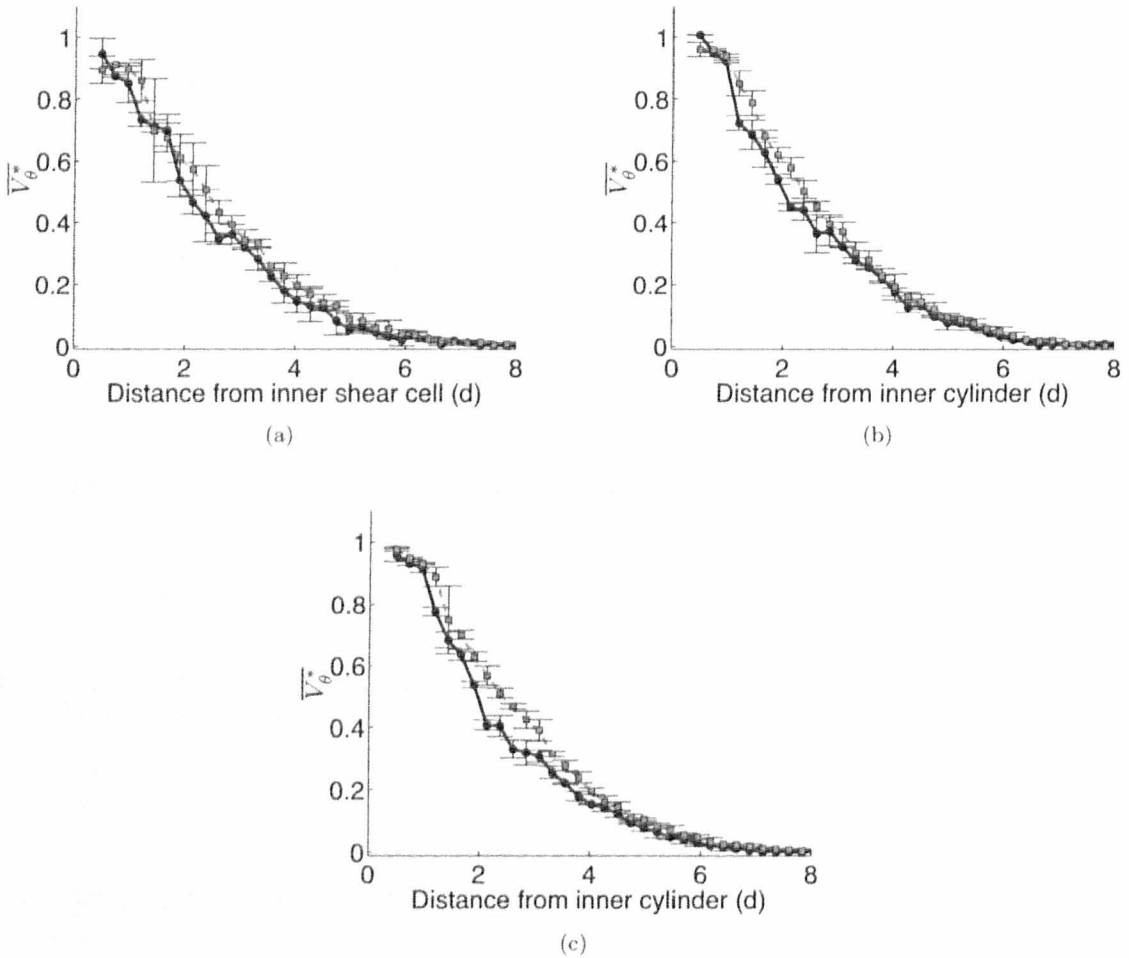

Figure 5.40: **The influence of the pressure plate on 4 mm bead angular velocity profiles** - $\overline{V_\theta^*}$ as a function of distance from the inner cylinder for the beads on the top surface of an experiment with 4 mm beads at an inner cylinder angular velocity of (a) 0.025 rad s^{-1}, (b) 0.05 rad s^{-1} and (c) 0.1 rad s^{-1}. Results obtained with the pressure plate (solid black line, solid circles) and without the pressure plate (dashed cyan line, cyan squares) are shown. The error bars represent the standard deviation of $\overline{V_\theta^*}$.

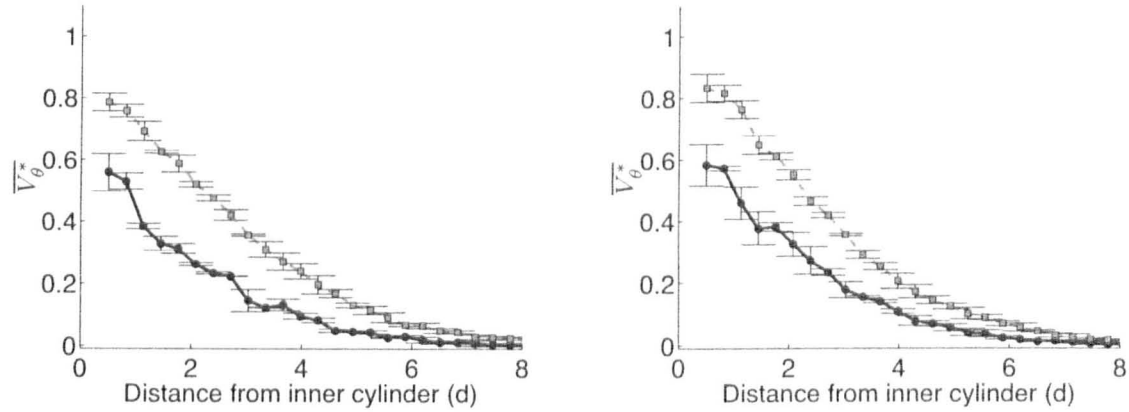

Figure 5.41: **The influence of the pressure plate on 3 mm bead angular velocity profiles** - $\overline{V_\theta^*}$ as a function of distance from the inner cylinder for the beads on the top surface of an experiment with 4 mm beads at an inner cylinder angular velocity of (a) 0.025 rad s^{-1} and (b) 0.05 rad s^{-1}. Results obtained with the pressure plate (solid black line, solid circles) and without the pressure plate (dashed cyan line, cyan squares) are shown. The error bars represent the standard deviation of $\overline{V_\theta^*}$.

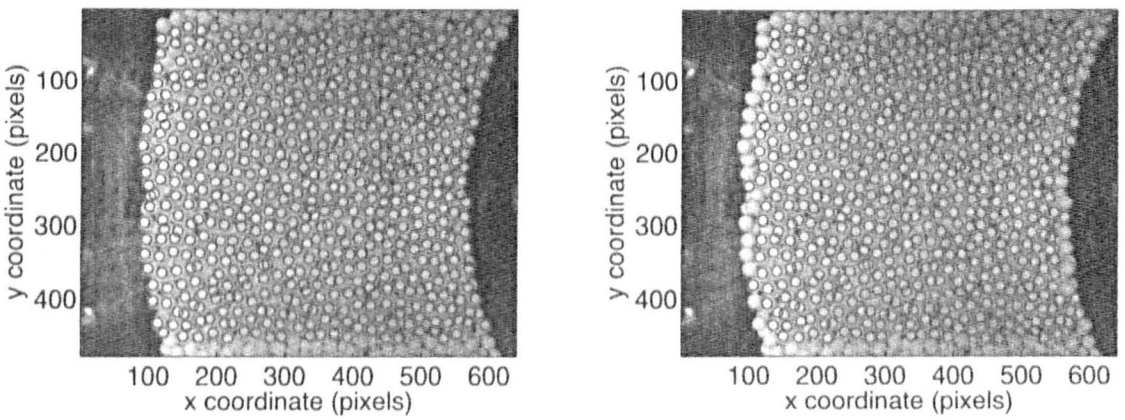

Figure 5.42: **Tracked particles with and without filtering** - An example image from a ground-based experiment with no pressure plate is shown. In (a), the particle tracks are filtered based only on their radial position to remove spurious particles outwith the shear cell. In (b), the standard filtering criteria on the particle size and brightness (such as used to remove spurious particles when the pressure plate is present) is applied. The locations of particles which survive are plotted on the image (blue circles).

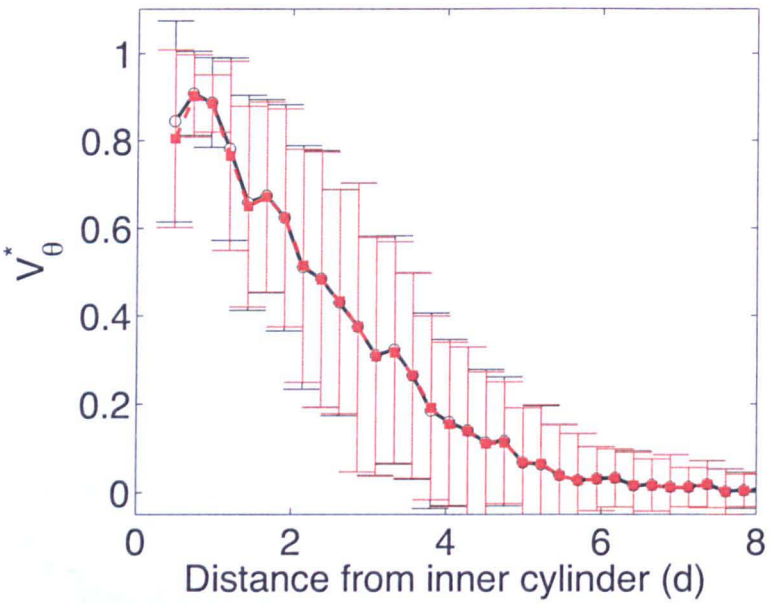

Figure 5.43: **Influence of filtering on mean particle angular velocity profiles** - V_θ^* as a function of distance from the inner cylinder for the beads on the top surface of an experiment with 4 mm beads, with no pressure plate and at an inner cylinder angular velocity of 0.025 rad s^{-1}. Shown is the mean V_θ^* calculated using all particle tracks (red squares) and the mean V_θ^* calculated using only the particles which survive the standard filtering criteria on the particle size and brightness (open circles). The error bars represent the standard deviation of the scatter of particle velocities within the radial bin (i.e., $S2$).

time (due primarily to the light reflections but also partly due to vertical particle motion). Upon reappearing they are assigned a new particle identity. Unfortunately these short-lived particles also often occur in locations which are also the regions of interest (i.e., close to the shearing surface).

To determine if track length influences the measured velocities, the particles in one experiment are separated into three groups based on their track length. Λ: $\Lambda < 3$ seconds (Group 1), $3 < \Lambda < 6$ seconds (Group 2) and $\Lambda > 6$ seconds (Group 3). There are always fewest particles in group two as generally the particles either exist for a very short time, or exist for a long time. The mean particle angular velocity profiles for each group are shown in Fig. 5.44. Looking at Fig. 5.44 (a), for the two groups with short particle lifetimes (white circles and red squares), particles with such a track length do not exist at every distance from the inner cylinder. This means that the short particle tracks are confined to certain regions of the shear cell (confirming the findings of Section 5.2.6 that only certain areas of the shear cell have a high frequency of particles appearing and disappearing). There are also some irregularities in the mean velocity profiles for the two groups with short particle lifetimes - particularly for group two. However, this is not surprising as the values per radial bin for these groups are the means of very few particles and so any unusually large or small particle displacements will strongly influence the mean value. Figure 5.44 (b) shows that all mean values for the three groups are consistent to within the error bars except for one point for group two (at $\sim$4.5 d from the inner

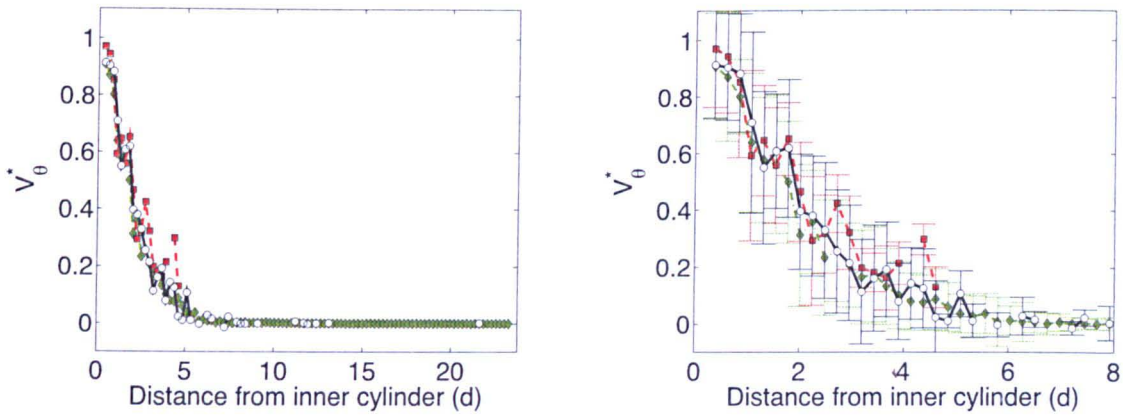

Figure 5.44: **Influence of particle track length on mean particle angular velocity profiles** - V_θ^* as a function of distance from the inner cylinder for the beads on the top surface of a ground-based experiment with 4 mm beads and at an inner cylinder angular velocity of 0.05 rad s^{-1}. The particles have been split into three groups based on their track lengths, Λ, and the mean velocity profile is calculated for each group. Black solid line with circle markers: $\Lambda < 3$ seconds. Red dashed line with square markers: $3 < \Lambda < 6$ seconds. Green dotted line with diamond markers: $\Lambda > 6$ seconds. (a) V_θ^* across the entire width of the shear cell. No error bars are shown to make it easier to see the mean values. (b) V_θ^* of the shear band (i.e., in the eight particle diameters closest to the shearing surface). The error bars represent the standard deviation of the scatter of particle velocities within the radial bin.

cylinder) which lies slightly above the one sigma limit for the mean velocity of group three. Therefore, we can conclude that, if there are enough particle tracks, the track length does not affect the measured dynamical properties. This is probably because, although the velocities are smoothed and binned as explained above, the instantaneous individual particle velocities are calculated using only sets of two consecutive frames (see Section 5.2.8).

5.4.3 The influence of shaking

During the flight campaign the standard experimental procedure was to shake the granular material before performing the experiment. However, some experiments were perfomed without shaking to allow a comparison to be performed between the shaken and unshaken experiments (see Section 4.5).

First the influence of shaking on the 4 mm beads is investigated. The runs with an inner cylinder angular velocity of 0.05 rad s^{-1} are taken as an example as this is the angular velocity for which there are most data available for these beads. The mean angular and radial velocity profiles of the 4 mm particles on the top surface that have been shaken and that have not been shaken are shown in Fig. 5.45. The influence of shaking is investigated for ground-based experiments (Fig. 5.45 (a) and (b)), for microgravity experiments from Flight A (Fig. 5.45 (c) and (d)) and for microgravity experiments from Flight C (Fig. 5.45 (e) and (f)). Figure 5.46 shows the results of the same experiments with 4 mm particles but for the bottom surface. There are many experiments in which the particles have

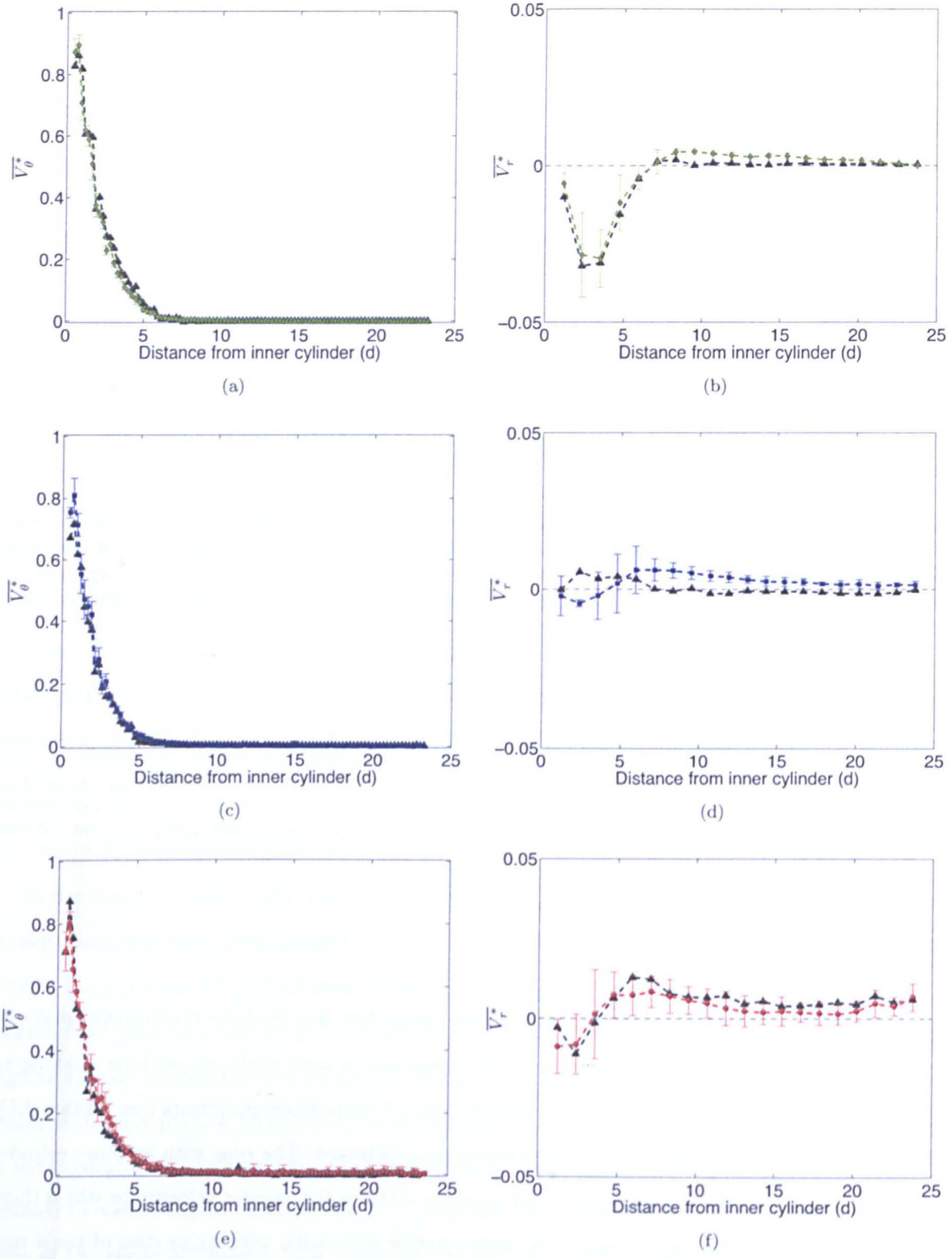

Figure 5.45: **The influence of shaking on the top surface of 4 mm beads** - The left plots show the mean angular velocity, $\overline{V_\theta^*}$, and the right plots the mean radial velocity, $\overline{V_r^*}$, both as a function of distance from the inner cylinder. The mean velocity profiles of particles are shown after shaking in 1 g (green diamonds in (a) and (b)), in microgravity during Flight A (blue squares in (c) and (d)) and in microgravity during Flight C (red circles in (e) and (f)). In each plot the black triangles represent the unshaken version of the same experiment. The error bars are the standard deviation of $\overline{V_\theta^*}$. The inner cylinder angular velocity in these examples is 0.05 rad s^{-1}.

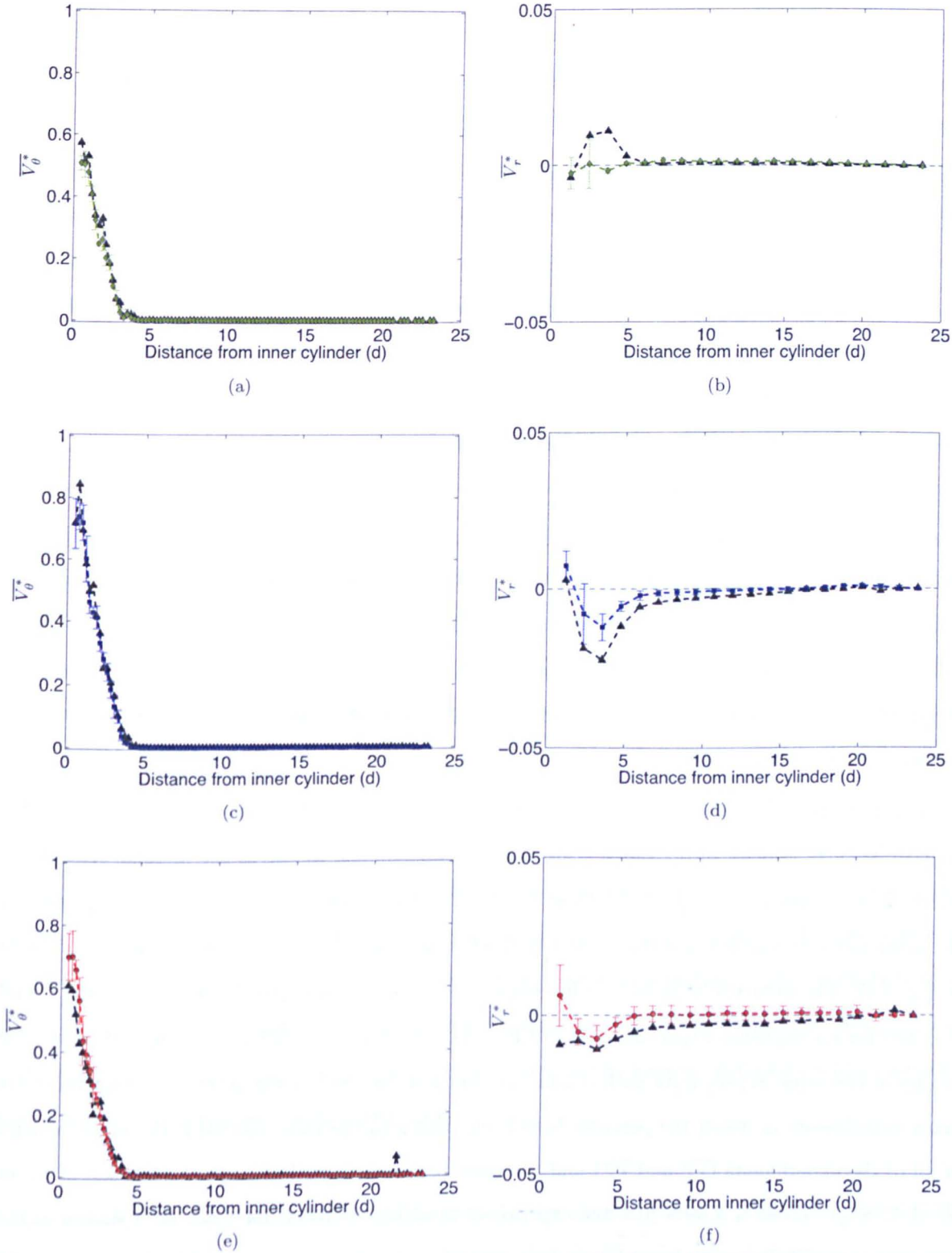

Figure 5.46: **The influence of shaking on the bottom surface of 4 mm beads** - The left plots show the mean angular velocity, $\overline{V_\theta^*}$, and the right plots the mean radial velocity, $\overline{V_r^*}$, both as a function of distance from the inner cylinder. The mean velocity profiles of particles are shown after shaking in 1 g (green diamonds in (a) and (b)), in microgravity during Flight A (blue squares in (c) and (d)) and in microgravity during Flight C (red circles in (e) and (f)). In each plot the black triangles represent the unshaken version of the same experiment. The error bars are the standard deviation of $\overline{V_\theta^*}$. The inner cylinder angular velocity in these examples is 0.05 rad s^{-1}.

been shaken so the value plotted is the mean velocity of all of the experiments ($\overline{V_\theta^*}$ and $\overline{V_r^*}$) and the error bars represent the standard deviation of $\overline{V_\theta^*}$ or $\overline{V_r^*}$ (i.e., $S3_a$). There is always just one experiment in which the beads have not been shaken so the error bars are not shown in these plots.

Figure 5.45 (left) shows the angular velocity profiles for the unshaken experiments lie almost entirely within the error bars of the mean angular velocity profiles of the shaken experiments. This means that on the top surface of the shear cell, the mean angular velocities of the 4 mm beads are not affected by the shaking of the granular material prior to the experiment. The radial velocity profiles (Fig. 5.45 [right]) for the unshaken experiments on the ground and in Flight C lie almost entirely within the error bars of the mean radial velocity profiles of the shaken experiments. However, for Flight A the radial velocity profile for the unshaken experiment does not lie within the error bars of the mean radial velocity profile of the shaken experiments.

The angular velocity profiles on the bottom surface of the same experiments are also largely unaffected by whether or not shaking has occured (Fig. 5.46). The only difference is a slightly decreased mean particle angular velocity near the inner cylinder for the unshaken experiment in Flight C. However, the radial velocity profiles of shaken and unshaken particles on the bottom surface display more variations. For each of the three experiment types shown on the right of Fig. 5.46 the non-shaken radial velocity profile close to the inner cylinder lies outwith the mean shaken radial velocity profile and has a larger magnitude.

Next the influence of shaking on the 3 mm beads is investigated. This time the runs with an inner cylinder angular velocity of 0.1 rad s^{-1} are taken as an example as this is the angular velocity for which there is most data available for these beads. The mean angular and radial velocity profiles of the 3 mm particles on the top surface that have been shaken and that have not been shaken are shown in Fig. 5.47. The influence of shaking is investigated for ground-based experiments (Fig. 5.47 (a) and (b)) and for microgravity experiments from Flight B (Fig. 5.47 (c) and (d)). Figure 5.48 shows the results of the same experiments with 3 mm particles but for the bottom surface. Again, there are many experiments in which the particles have been shaken so the value plotted is the mean velocity of all of the experiments ($\overline{V_\theta^*}$ and $\overline{V_r^*}$) and the error bars represent the standard deviation of $\overline{V_\theta^*}$ or $\overline{V_r^*}$ (i.e., $S3_a$). There is always just one experiment in which the beads have not been shaken so the error bars are not shown in these plots.

The mean angular velocity profiles of the 3 mm particles appear also to be largely unaffected by the shaking both on the top and the bottom surfaces (Figs. 5.47 and 5.48). The only exception is the bottom surface of the ground-based experiments: the two angular velocity profiles are quite different close to the inner cylinder with the unshaken profile being much larger in magnitude. Unfortunately data are not available for unshaken particles at the inner cylinder angular velocity of 0.025 rad s^{-1} and

0.05 rad s^{-1} so the same comparison cannot be made between shaken and unshaken 3 mm particles for these rotational velocities.

The radial velocity profiles of the 3 mm particles for the shaken and unshaken experiments (Figs. 5.47 and 5.48) are similar for both the top and bottom surfaces. Again, the two radial velocity profiles for the bottom surface of the ground-based experiment are slightly different. However, as the scale of radial motion is small and each curve shows the data from just one experiment this may not be significant.

Given the slight differences that have been observed between shaken and unshaken radial velocity profiles, particularly on the bottom surface of the experiments with 4 mm particles, it was decided to look more closely at the radial velocity profiles on the bottom surfaces of all experiments performed without shaking. Figure 5.49 shows the mean radial velocity profiles of the bottom surface for all remaining experiment types for which data exists for shaken and unshaken experiments. In general the shaken and unshaken granular material have very similar radial velocity profiles, although, there are some exceptions (Fig. 5.49 (b)). The differences for the microgravity experiments may be due to the variations in particle velocity caused by gravity fluctuations (see Section 5.4.5). However, the reason for the differences may simply be that each curve for the unshaken experiments shows the data from just one single experiment (hence the lack of error bars). As has been seen in Section 5.3.2 there are large distributions in the radial velocities of particles in each experiment. The net particle motion in the radial direction (if any) is, therefore, mostly due to random particle rearrangements which just happen to cause slightly different net motion between the experiments (except for the top surface of the ground-based experiments where there is evidence of possible bulk motion). There is likely to be a similar amount of random particle rearrangements affecting the mean angular velocities but the scale of the rearrangements, compared to the amount of motion in the angular direction, is much smaller and so the effect is much more difficult to notice.

In summary, as there are mostly no differences in the angular velocity profiles and only small differences in the radial velocity profiles it is decided that shaking the granular material using the method described in Chapter 4 does not influence the particle dynamics. It is probably the case, therefore, that all experiments performed during the flight campaign had a similar initial configuration, although, this is perhaps because all of the experiments also has a similar final configuration (which then provided the initial configuration for the following experiment). If the AstEx experiment is to fly again a better method of shaking the granular material may be required to fully re-set the system.

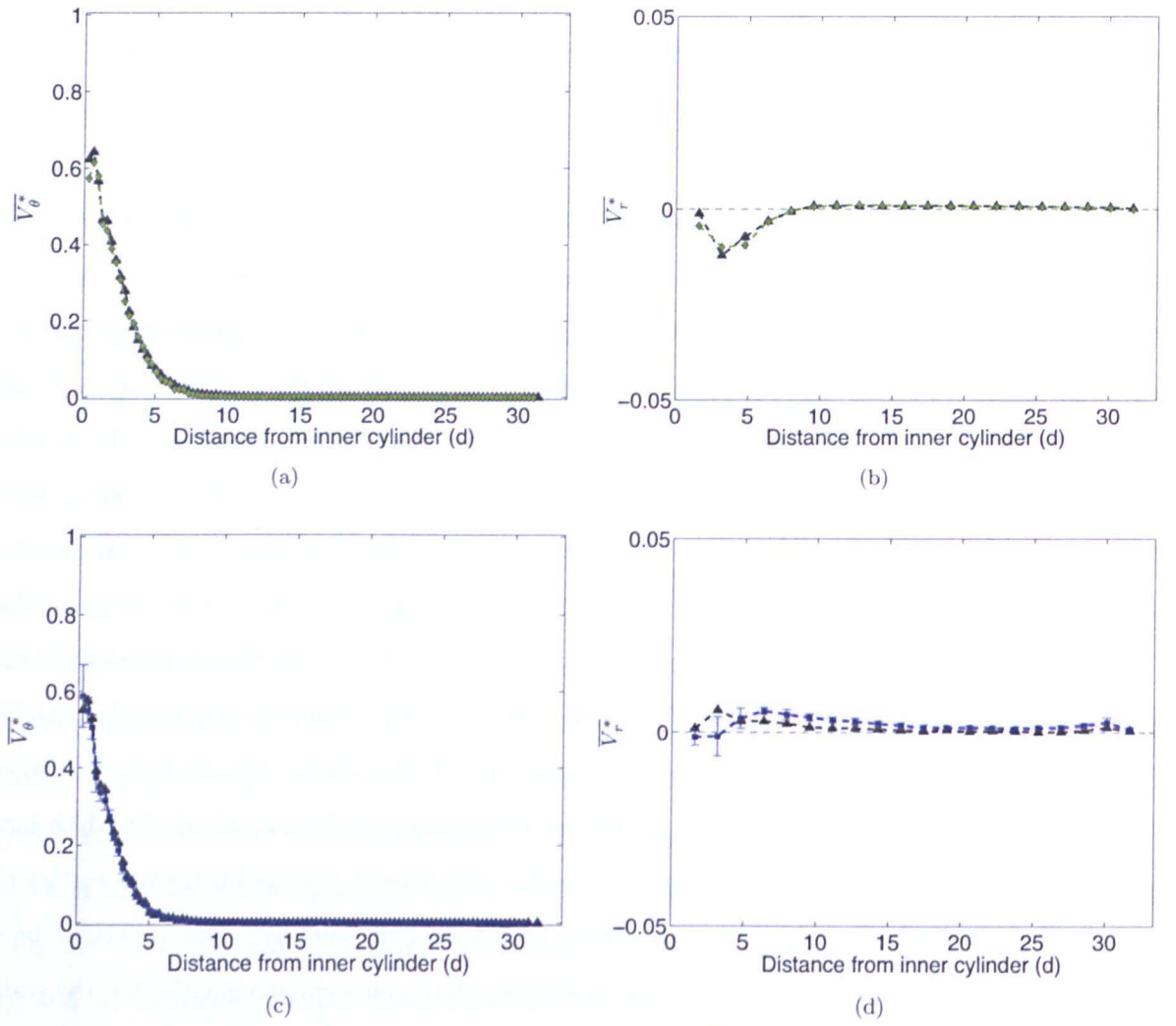

Figure 5.47: **The influence of shaking on the top surface of 3 mm beads** - The left plots show the mean angular velocity, $\overline{V_\theta^*}$, and the right plots the mean radial velocity, $\overline{V_r^*}$, both as a function of distance from the inner cylinder. The mean velocity profiles of particles are shown after shaking in 1 g (green diamonds in (a) and (b)) and in microgravity during Flight B (blue squares in (c) and (d)). In each plot the black triangles represent the unshaken version of the same experiment. The error bars are the standard deviation of $\overline{V_\theta^*}$. The inner cylinder angular velocity in these examples is 0.1 rad s^{-1}.

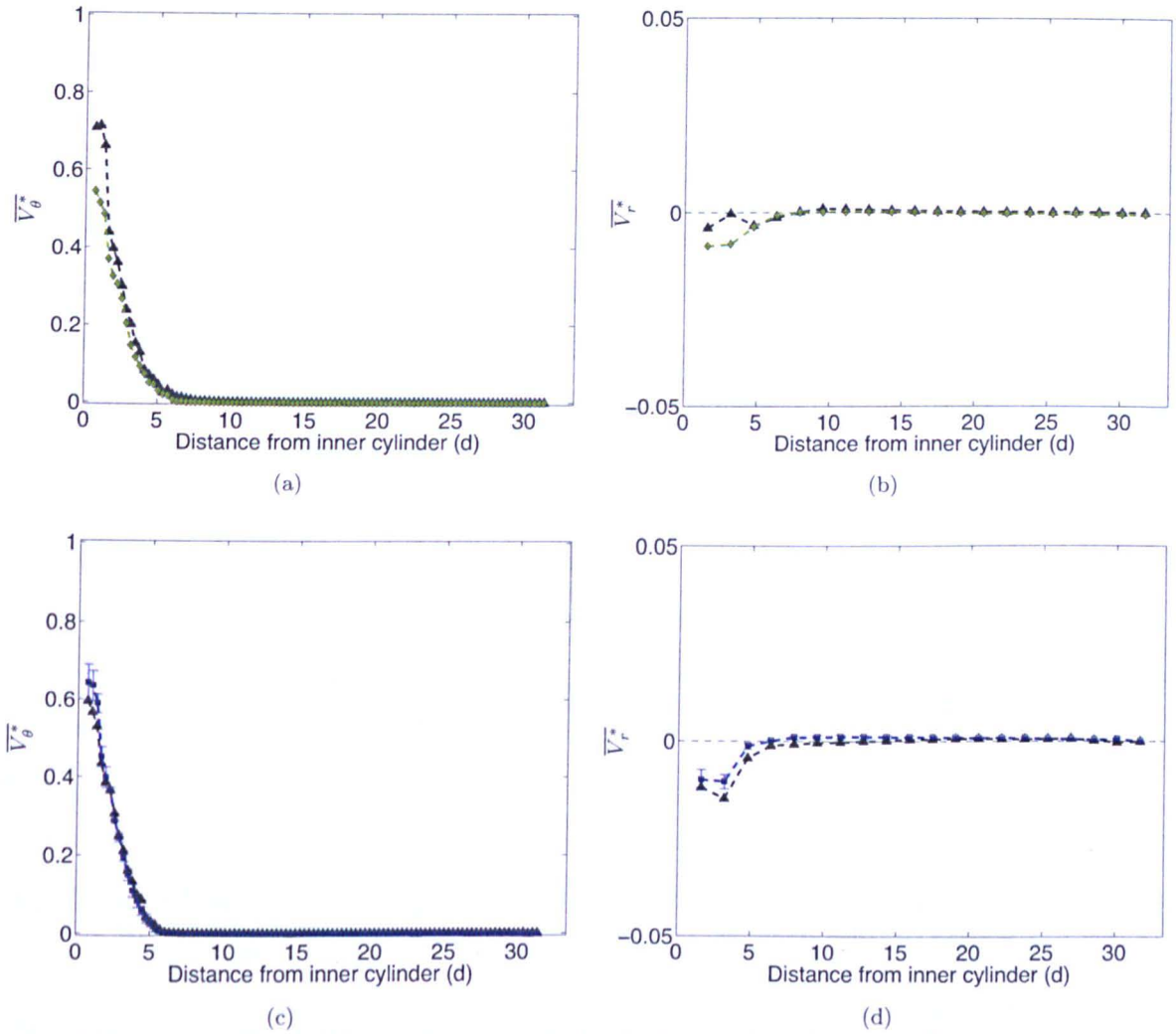

Figure 5.48: **The influence of shaking on the bottom surface of 3 mm beads** - The left plots show the mean angular velocity, $\overline{V_\theta^*}$, and the right plots the mean radial velocity, $\overline{V_r^*}$, both as a function of distance from the inner cylinder. The mean velocity profiles of particles are shown after shaking in 1 g (green diamonds in (a) and (b)) and in microgravity during Flight B (blue squares in (c) and (d)). In each plot the black triangles represent the unshaken version of the same experiment. The error bars are the standard deviation of $\overline{V_\theta^*}$. The inner cylinder angular velocity in these examples is 0.1 rad s^{-1}.

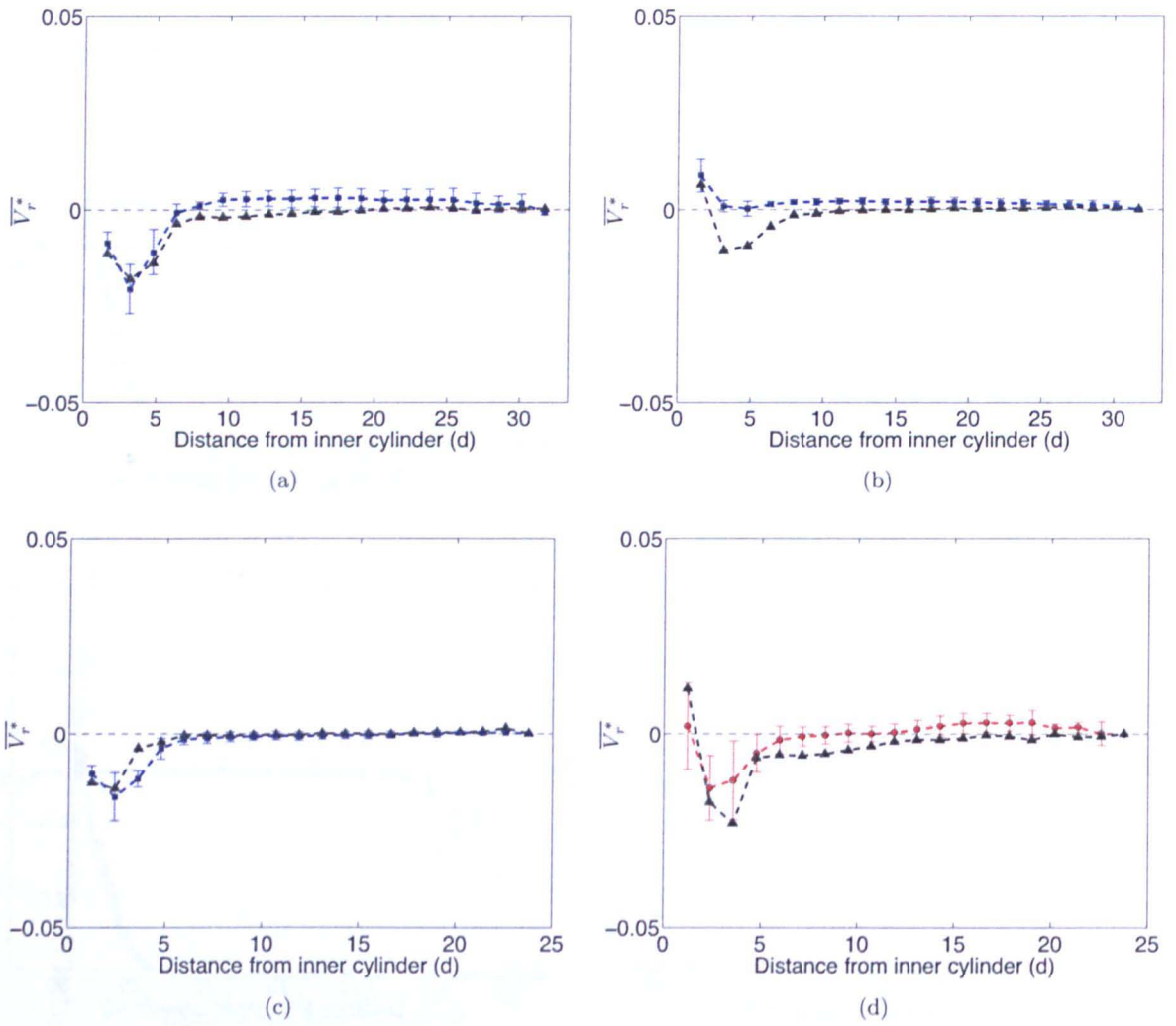

Figure 5.49: **The influence of shaking on the bottom surface radial velocity profiles** - The mean radial velocity, $\overline{V_r^*}$, as a function of distance from the inner cylinder for the bottom surface of four different types of experiment: (a) 3 mm particles in microgravity (Flight B) with an inner cylinder angular velocity of 0.025 rad s^{-1} with shaking (blue squares) and unshaken (black triangles); (b) 3 mm particles in microgravity (Flight B) with an inner cylinder angular velocity of 0.05 rad s^{-1} with shaking (blue squares) and unshaken (black triangles); (c) 4 mm particles in microgravity (Flight A) with an inner cylinder angular velocity of 0.1 rad s^{-1} with shaking (blue squares) and unshaken (black triangles); (d) 4 mm particles in microgravity (Flight C) with an inner cylinder angular velocity of 0.025 rad s^{-1} with shaking (red circles) and unshaken (black triangles). The error bars are the standard deviation of $\overline{V_r^*}$.

5.4.4 The influence of aircraft vibrations

In this section an experiment during steady flight (i.e., between parabolas), during which the cameras were switched on but the motor remained off, is investigated. Looking in high-resolution at any variations in angular and radial velocity over time should allow an estimation to be made of the influence of aircraft vibrations on the mean particle velocities. The variations in angular and radial velocities during steady flight are compared to the variations in angular and radial velocities of the particles on the ground with no motor rotation.

The mean angular and radial velocities of particles on the top and bottom surfaces, as a function of time, with no motor rotation are shown in Fig. 5.50 for ground-based data and in Fig. 5.51 for steady flight data. Also shown in these figures are the angular and radial velocity variations ($dV = V - meanV$) of the inner radial bin on the top surface and of the inner radial bin on the bottom surface as a function of time. In order to compare the different variations in angular and radial velocities on the top and bottom surfaces the angular velocity is converted from rad s^{-1} to mm s^{-1} using a radial distance in the middle of the inner radial bin (i.e., 110 mm).

On the ground, when there is no motor rotation there is very little motion (Fig. 5.50). The fluctuations around zero which can be seen may be a result of movement near the experiment (people, machines, etc.). They may also be caused by the particle detection and tracking algorithm. If this is the case it is possible that there are subtle changes in lighting which cause the centres of particles to be detected in slightly different locations between frames thus resulting in the detection of a small, but non-real velocity.

However, in Fig. 5.51 some larger fluctuations in V_θ and V_r are seen. These fluctuations, which are of approximately the same scale in V_θ and V_r (Fig. 5.51 (e) and (f)), are caused by the aircraft vibrations even though, as explained in Section 4.4.4, an attempt was made to isolate the shear cell from the external vibrations using silent blocks. The top surface is more sensitive to the aircraft vibrations with the largest velocity fluctations caused by the vibrations being $\sim 2 \times 10^{-4}$ rad s^{-1} in V_θ, and ~ 0.02 mm s^{-1} for in V_r.

5.4.5 The influence of gravity variations in microgravity

In this section the high-resolution variations in angular and radial velocity over time are compared to the flight data to determine if the fluctuations in gravitational acceleration influence the mean particle velocities. One experiment is considered where, during the parabola, the cameras were switched on but the motor remained off. The cameras were switched on before the microgravity phase began and continued taking images until after the microgravity phase had ended.

Figure 5.52 shows the mean angular and radial velocities of particles on the top and bottom

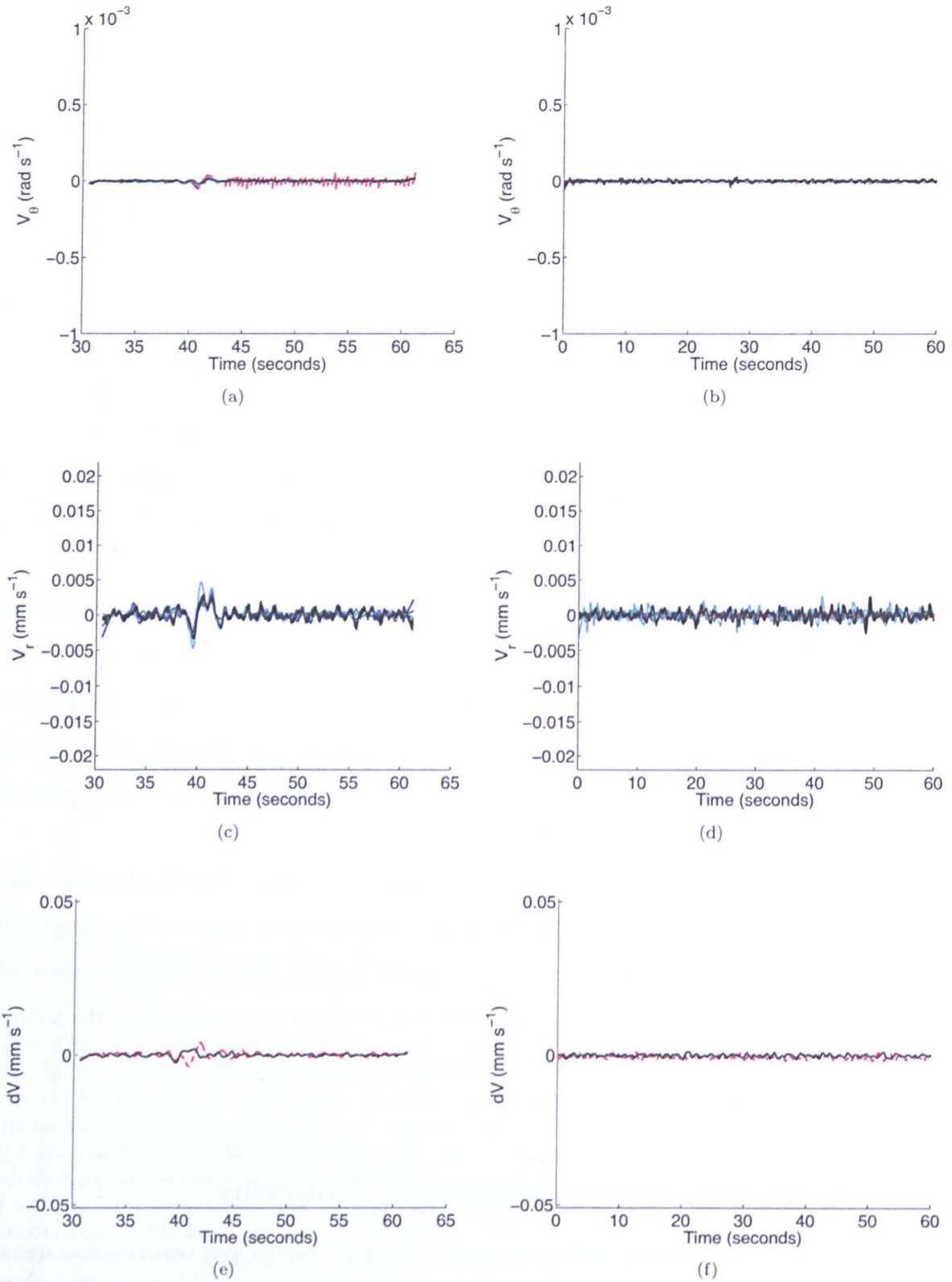

Figure 5.50: **Particle velocity fluctuations on the ground: no motor rotation** - (a) angular velocity of the particles on the top and (b) bottom surface divided into 5 radial bins; (c) radial velocity of the particles on the top and (d) bottom surface divided into 5 radial bins. The respective radial bins, with bin 1 being the closest to the inner cylinder, are: bin 1 (green), bin 2 (blue), bin 3 (red), bin 4 (cyan), bin 5 (black); (e) angular (red) and radial (black) velocity variations ($dV = V - meanV$) of the inner radial bin on the top surface and, (f) bottom surface.

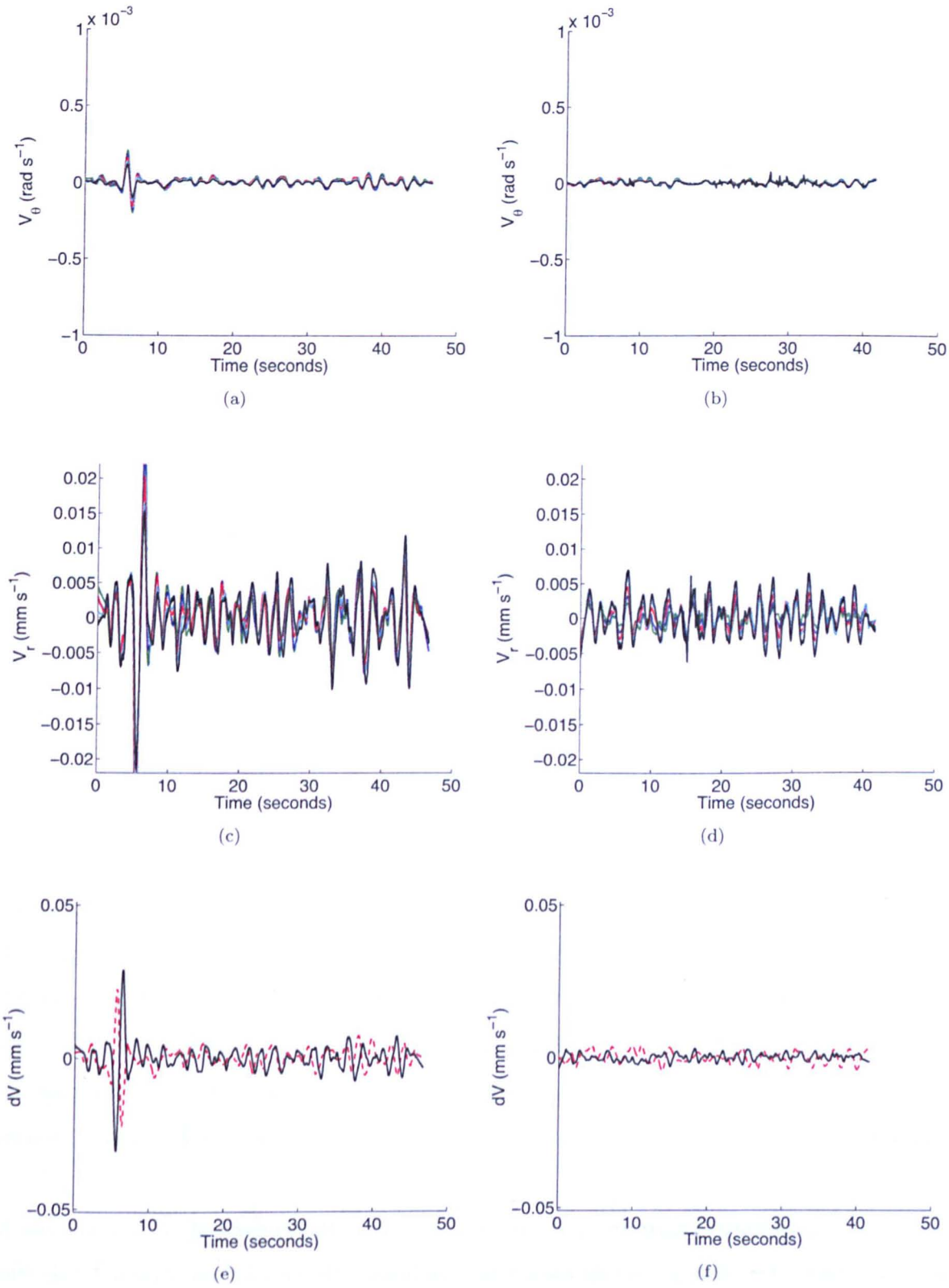

Figure 5.51: **Particle velocity fluctuations during steady flight: no motor rotation** - (a) angular velocity of the particles on the top and (b) bottom surface divided into 5 radial bins; (c) radial velocity of the particles on the top and (d) bottom surface divided into 5 radial bins. The respective radial bins, with bin 1 being the closest to the inner cylinder, are: bin 1 (green), bin 2 (blue), bin 3 (red), bin 4 (cyan), bin 5 (black); (e) angular (red) and radial (black) velocity variations ($dV = V - meanV$) of the inner radial bin on the top surface and, (f) bottom surface.

surfaces over time during this parabola as plotted in Fig. 5.50. For both the angular and the radial velocity there are periods where almost no velocity fluctuations can be seen on this scale. In between these two "calm" periods there is a section of time with large variations in the velocity. This section is the microgravity phase of the parabola. During the microgravity phase there are large deviations from the mean on the top surface at similar times for both V_θ and V_r. The bottom surface has smaller fluctuations in the radial and angular directions than the top surface. The largest velocity fluctations seen during this experiment are $\sim$0.01 rad s^{-1} in V_θ, and $\sim$2 mm s^{-1} in V_r. These are very large particle velocities compared to the regular motion when the motor is on and so we decided to look at the gravity fluctuations causing such velocities.

Figure 5.53 shows the variations in the acceleration (in x, y and z) during the microgravity phase of the parabola. The gradient of the accelerations in x, y and z is also shown. The z axis is vertical, x is in the axis of the aircraft and corresponds to a radial direction in our experiments and y is perpendicular to the axis of the aircraft and corresponds to the angular direction in our experiments. It can be seen that the quality of the microgravity is poor; the acceleration in the z-direction does not remain within the limits of $\pm$ 0.05 g. Unfortunately many of the parabolas, particularly during the 3rd flight (Flight C) had a poor quality of microgravity and this may influence the AstEx results. This gravity data for all parabolas in the flight campaign are given in the Supplementary Material.

5.5 Chapter conclusions

In this chapter the AstEx data pipeline has been presented. This pipeline begins with the image analysis (i.e., particle detection and tracking) then, through a series of intermediary steps, the particle velocities are determined as a function of time and as a function of distance from the shearing surface.

In the plots of particle velocity as a function of time, correlated large-scale fluctuations in the particle velocities were observed. It was found, via an in-depth investigation, that these fluctuations, which extend across the entire width of the shear cell, are probably caused by force chain breaking and reforming.

From an analysis of the scatter of particle velocities within the experiments at any moment in time it was found that, during constant shear rate experiments, the distribution of particle velocities remains relatively constant over time. In the same section (Section 5.3.2) a method was presented, with examples, to determine whether particles in an experiment are exhibiting bulk motion and also to determine whether a set of experiments are reproducable on a macroscale and a microscale. The methodology developed will be very useful in the following chapter when the AstEx results are presented and discussed.

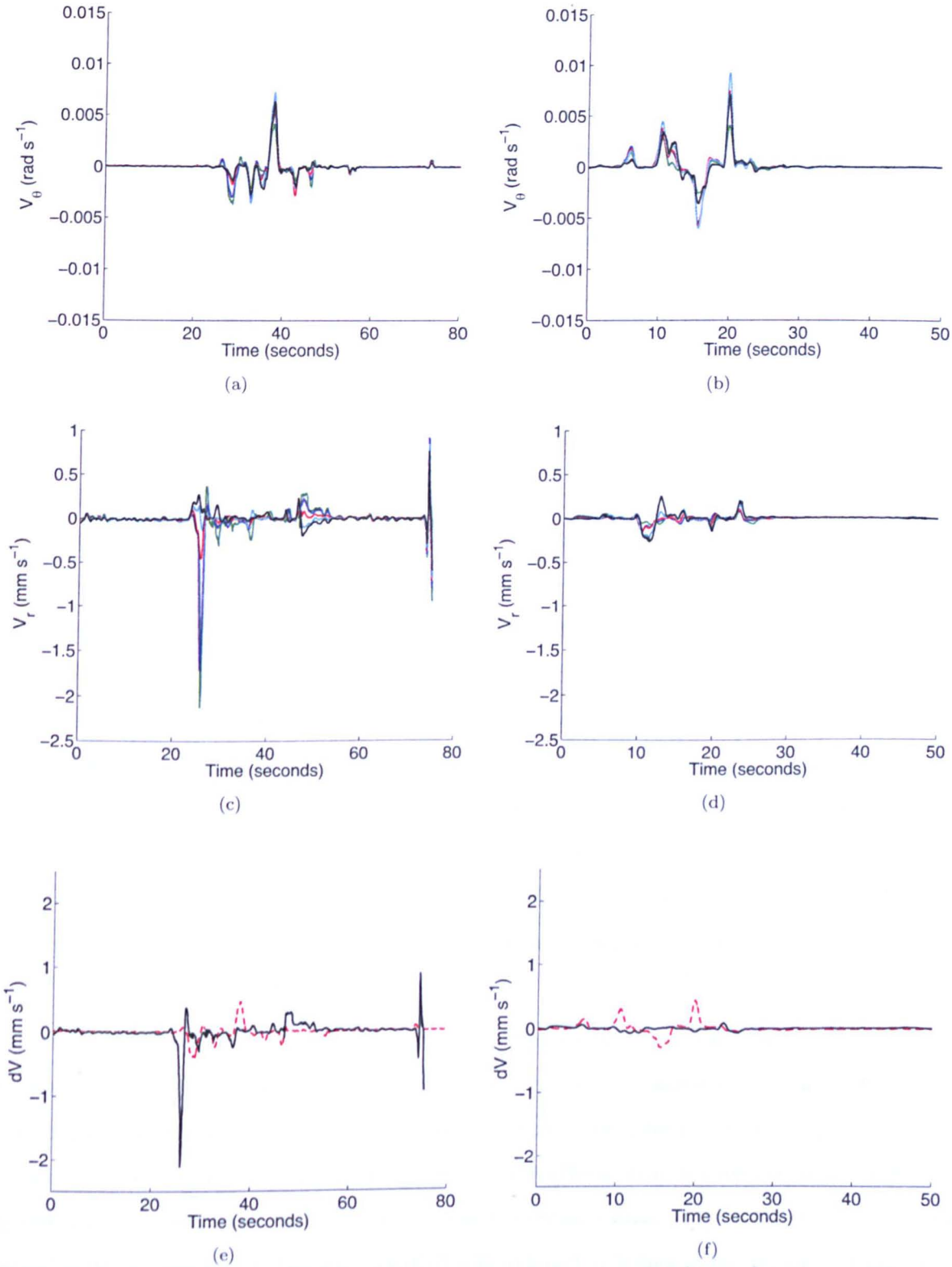

Figure 5.52: **Particle velocity fluctuations during Flight C, Parabola 0: no motor rotation** - (a) angular velocity of the particles on the top and (b) bottom surface divided into 5 radial bins; (c) radial velocity of the particles on the top and (d) bottom surface divided into 5 radial bins. The respective radial bins, with bin 1 being the closest to the inner cylinder, are: bin 1 (green), bin 2 (blue), bin 3 (red), bin 4 (cyan), bin 5 (black); (e) angular (red) and radial (black) velocity variations ($dV = V - meanV$) of the inner radial bin on the top surface and, (f) bottom surface.

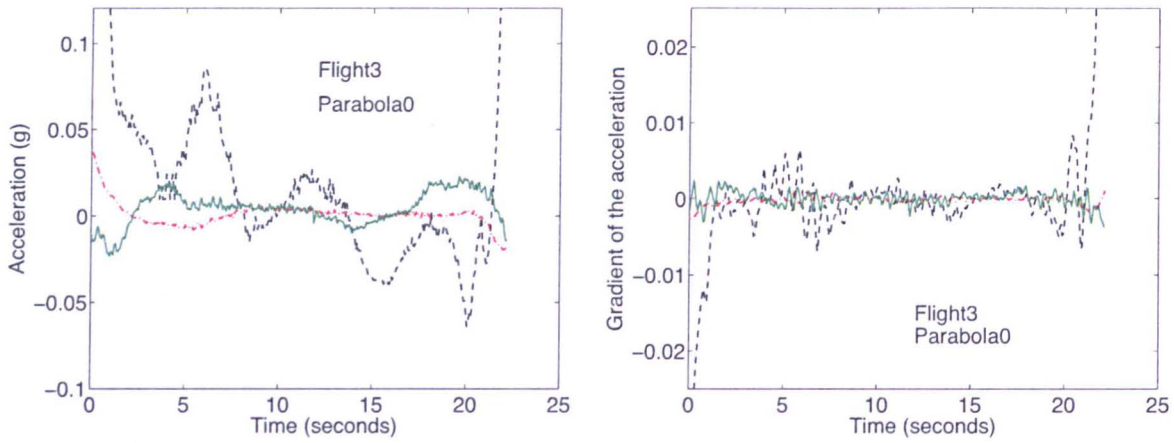

Figure 5.53: **Flight C, Parabola 0** - (a) The acceleration and, (b) the gradient of the acceleration during the microgravity part of the parabola in the z-direction (dashed black line), in the x-direction (dashed-dotted red line) and in the y-direction (solid green line).

An investigation was performed into all factors which may be influencing the particle dynamics in the AstEx experiment. The first factor considered was the pressure plate. It was found that the deceleration of the particles on the top surface of the shear cell, as a result of the pressure plate, varies inversely with the particle radius. As a consequence, the 4 mm particles are largely unaffected by the presence of the pressure plate, but, the 3 mm particles are strongly decelerated by the pressure plate. The light reflections on the pressure plate also cause some particles to have very short lifetimes and others to be excluded from the analysis altogether. It was concluded that the overall particle dynamics are unlikely to be influenced by short track lengths or by the particles excluded from the analysis. This is because only sets of two consecutive frames are used to calculate the particle velocities and also, there are many more particles completely unaffected by the light reflections than there are particles affected.

Shaking the granular material using the method described in Chapter 4 was found not to influence the particle dynamics. It is likely to be the case, therefore, that all experiments performed during the flight campaign had a similar initial configuration but this initial configuration was probably dependent on the experiment performed just previously. If the AstEx experiment is to fly again a better method of shaking the granular material may be required to fully re-set the granular material.

Finally, the aircraft vibrations were found to give particles very small velocities with an estimated maximum value of $\sim 2 \times 10^{-4}$ rad s^{-1} in V_θ, and ~ 0.02 mm s^{-1} for in V_r. The variations in the gravitational environment were found to influence the particles to a much greater extent causing short-term velocity fluctuations of approximately ~ 0.01 rad s^{-1} in V_θ, and ~ 2 mm s^{-1} in V_r in the worst case. Therefore, when interpreting the microgravity results attention must be paid to the variations in the simulated gravity during the parabolas in question. In addition, care should be

taken to differentiate between mean particle velocities caused by continuous particle motion and mean particle velocities caused by large and rapid particle displacements; gravity fluctuations are likely to be responsible for the latter. The method presented in Section 5.3.2 to detect persistent bulk particle motion will be very valuable in distinguising these two types of behaviour.

The AstEx data pipeline has been developed and tested. A method for comparing experiments has also been developed and we have an understanding of all of the factors influencing particle dynamics. Therefore, a direct and reliable comparison can now be made between the different types of experiment. This will be caried out in Chapter 6.

Chapter 6

The AstEx Experiment: Results and Interpretation

6.1 Summary of Chapter

In Chapter 5 the AstEx data pipeline was discussed. Additionally, a method was presented to determine whether particles in an experiment are exhibiting bulk motion and to determine whether a set of experiments are reproducable on a macroscale and a microscale. In addition, the following key conclusions were drawn:

- Correlated large-scale fluctuations in the particle velocities are observed that are probably caused by force chain breaking and reforming.
- The 4 mm particles are largely unaffected by the presence of the pressure plate but the 3 mm particles are strongly decelerated by the pressure plate.
- The light reflections on the pressure plate are unlikely to influence the overall particle dynamics.
- Shaking the granular material before an experiment does not change the particle dynamics.
- The aircraft vibrations do not influence the particle dynamics.
- The particle dynamics are influenced by the variations in the simulated gravity.

In this chapter the results from the AstEx microgravity experiment are presented and discussed. As outlined in Chapter 4, the AstEx experiment has several key research objectives:

1. To investigate how a steady state granular flow induced by rotational shear forces in microgravity differs from a steady state granular flow on Earth induced by rotational shear forces.

2. To investigate if granular convection occurs in our granular system on the ground and, if it does, to determine if the convection is enhanced or reduced in microgravity.

3. To investigate if hysteresis (memory effects) that leads to a transient weakening of the granular material occuring after shear reversal are enhanced or reduced in the microgravity environment.

4. To investigate how a granular material behaves when maintained at a constant volume without any confining pressure during shear (possible only in microgravity).

Unfortunately, due to the hardware problems outlined in Section 4.6.2, the experiments required to investigate the final objective could not be performed. The results and conclusions corresponding to the first three key objectives are presented below.

6.2 Steady state granular flow

Many previous ground-based experiments of granular shear with similar experimental set-ups have found that the angular velocity of particles decreases quickly over a few particle diameters away from the shearing wall and that the angular velocity profile, normalised by the shear rate, is independent of the shear rate (e.g., Behringer *et al.*, 1999; Bocquet *et al.*, 2001; Losert *et al.*, 2000; Mueth *et al.*, 2000). It has already been seen in Chapter 5 that the former of these two points is also true for the AstEx experiments performed on the ground and in microgravity. A shear band of several particle diameters in width is seen close to the inner shearing cylinder on the top and bottom surfaces of the AstEx experiment in both gravitational regimes (Figs. 5.23, 5.32, 5.33, 5.36 and 5.37).

In Section 5.3.2 the individual angular velocity profiles of many experiments were considered. In these experiments it was noted that $S2$ (see Table 5.4 and Section 5.3.2) in the mean normalised particle angular velocity of each experiment (V_θ^*, see Eq. (5.3)) is largest at small distances from the inner cylinder where the motion is concentrated. However, $S2$ is small enough, even at small distances from the inner cylinder, for the angular velocity profiles to be statistically significant. As V_θ^* is non-zero near the inner cylinder it can, therefore, be concluded that there is bulk motion of the particles in a preferential direction (as expected). Far from the inner cylinder V_θ^* is close to zero and $S2$ is very small. This implies that there is no particle motion at all in the angular direction. These trends in $S2$ are found in all angular velocity profiles both on the ground and in microgravity (see examples Section 5.3.2 and full results in the Supplementary Material). The only exception is that, during some microgravity constant shear rate experiments, $S2$ is slightly larger far from the inner cylinder due to the random particle motion caused by the fluctations in the simulated gravity.

In this section, which will investigate steady state granular flows, we will first test whether the normalised angular velocity profiles of constant shear rate ground-based AstEx experiments are in-

dependent of the shear rate. Next, we will test whether the normalised angular velocity profiles of constant shear rate experiments performed in microgravity are independent of shear rate. Finally, we will compare the angular velocity profiles of ground-based and microgravity experiments to determine whether the steady state granular flows in the two gravitational environments differ. This will be done by comparing experiments of the same type using the mean normalised particle angular velocities ($\overline{V_\theta^*}$) and the associated scatters ($S3_a$ and $S3_b$), as described in Section 5.3.2.

6.2.1 Steady state granular flow in 1 g

Considering first the shapes and widths of the angular velocity profiles from ground-based experiments, it can be seen that, on the top surface (Fig. 6.1 (a) and Fig. 6.2 (a)), the mean particle angular velocity ($\overline{V_\theta^*}$) decays exponentially with distance from the shearing surface and the shear band is approximately 6-7 particle diameters wide for all of the experiments. However, on the bottom surface (Fig. 6.1 (b) and Fig. 6.2 (b)) the shear band is much narrower (3-5 particle diameters wide) and, in the case of the 4 mm particles especially, the angular velocity profile is very steep. It is possible that the difference in the angular velocity profiles results from a difference in the packing fraction between the free top surface and the crystallised (i.e., hexagonally packed) bottom surface. Indeed, this same effect was found by Daniels & Behringer (2006) who reported that when a granular material is in the disordered state the shear band extends several particles, but while in the crystallised state, the shear is localised almost entirely to the first layer of particles. This hypothesis gains strength when stacked images of the top and bottom surfaces are considered in which several thousand images have been super-imposed (Fig. 6.3). The shear band near to the moving inner cylinder can be seen on the right of both images but it is much smaller in the crystallised granular material on the bottom surface than on the top surface.

Now, comparing the magnitudes of the angular velocity profiles of ground-based experiments for the 4 mm and 3 mm beads in Fig. 6.1 and Fig. 6.2, respectively, it can be seen that the maximum value of $\overline{V_\theta^*}$ on the top surface of experiments with the 3 mm beads is much smaller (0.5-0.6) than for the top surface of experiments with the 4 mm beads (0.7-0.9). This is because the motion of the smaller beads on the top surface is inhibited by the presence of the pressure plate (see discussion in Section 5.4.1). The relative sizes of the error bars means $S3_a$ (see Table 5.4 and Section 5.3.2) of $\overline{V_\theta^*}$ is also much smaller on the top surface of the 3 mm particles than on the top surface of the 4 mm particles. This indicates that the experiments looking at the top surface of 3 mm beads are more reproduceable than those looking at the top surface of the 4 mm beads. This is likely to be because the influence of the pressure plate makes the particle velocities more homogeneous.

It is also worth noting that the magnitudes of the angular velocity profiles of the 4 mm beads at

the bottom surface (Fig. 6.1 (b)) are much lower than at the top surface (Fig. 6.1 (a)). This may be linked to the crystallisation of the bottom surface but it is perhaps more likely to be because, in 1 g, the particle motion on the bottom surface is resticted due to the weight of the particles above (recall there are ~13.5 kg of beads in the shear cell). The same difference in magnitude of $\overline{V_\theta^*}$ on the top and bottom surfaces does not exist for the 3 mm beads because the motion of the top surface is also inhibited, albeit via a different mechanism.

Therefore, the mean normalised angular velocity profiles at different inner cylinder angular velocities (i.e., at different shear rates) are identical to within the error bars for both the 4 mm particles (Fig. 6.1), and the 3 mm particles (Fig. 6.2). This means that *the normalised angular velocity profiles of ground-based experiments are independent of the shear rate just as in previous experiments of granular shear in a Couette geometry* (see e.g., Behringer *et al.*, 1999; Bocquet *et al.*, 2001; Losert *et al.*, 2000; Mueth *et al.*, 2000).

6.2.2 Steady state granular flow in microgravity

The mean normalised angular velocity profiles for microgravity experiments at different inner cylinder angular velocities are shown for the 4 mm particles in Fig. 6.4, and for the 3 mm particles in Fig. 6.5. In these figures, and throughout this chapter, the data obtained during the different flights are treated as different experiment groups. This is because, during Flight C, the quality of the microgravity was very poor. Just as for the ground-based experiments, the normalised angular velocity profiles for microgravity experiments at different inner cylinder angular velocities are identical to within the error bars. This means that *the normalised angular velocity profiles of constant shear rate experiments performed in microgravity are independent of shear rate.*

The microgravity angular velocity profiles display the same trends as the ground-based experiments: on the top surface $\overline{V_\theta^*}$ decays exponentially with distance from the shearing surface and the shear band is approximately 6 particle diameters wide, on the bottom surface the shear band is narrower and, especially in the case of the 4 mm beads, the angular velocity profile is very steep. This would imply that the crystallisation continues to infuence the particle dynamics in microgravity.

Similar to the ground-based experiments, in microgravity the maximum value of $\overline{V_\theta^*}$ on the top surface of experiments is much smaller with the 3 mm beads than with the 4 mm beads (Fig. 6.4 (a) and Fig. 6.5 (a)). The pressure plate is, therefore, still affecting the 3 mm particles in microgravity. However, unlike on the ground, in microgravity there is not a large difference in the magnitudes of the angular velocity profiles of the 4 mm beads at the bottom surface compared to the top surface (Fig. 6.4 (b) and Fig. 6.5 (b)). This is because, in 1 g, the particle motion on the bottom surface is resticted due to the weight of the particles above, but in the microgravity environment, this weight is

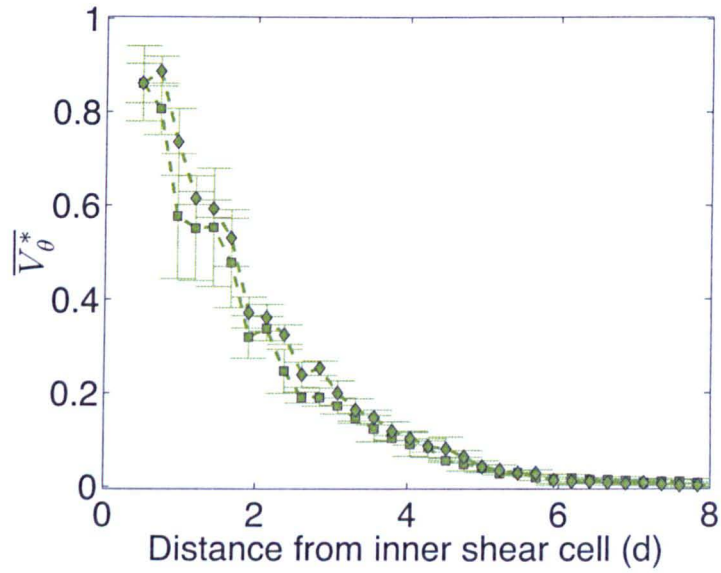

(a)

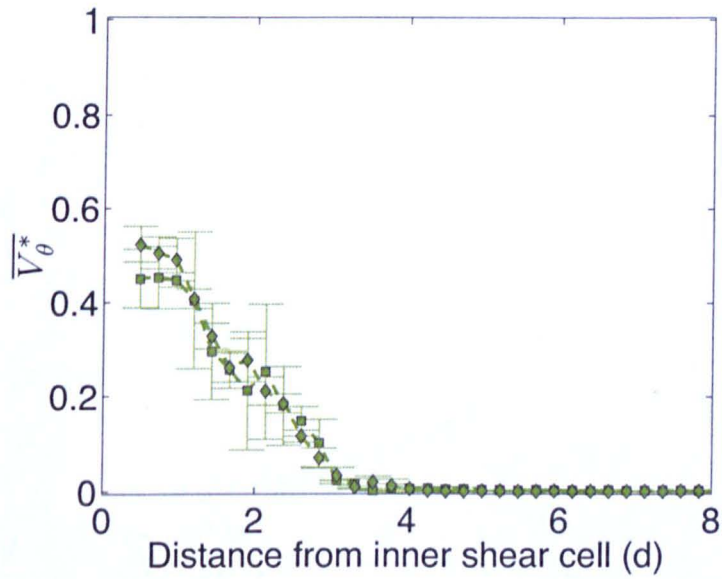

(b)

Figure 6.1: **Normalised angular velocity profiles for 4 mm beads in 1** g - $\overline{V_\theta^*}$ plotted as a function of distance from the inner cylinder for (a) the top surface and (b) the bottom surface of the ground-based experiments. Mean velocity profiles are shown for experiments with different inner cylinder angular velocities: 0.025 rad s^{-1} (diamonds) and 0.05 rad s^{-1} (squares). The error bars represent the standard deviation of $\overline{V_\theta^*}$ for each group of experiments (i.e., $S3_a$). The velocity profiles only extend up to 8 particle diameters from the shearing surface as further away there is very little motion.

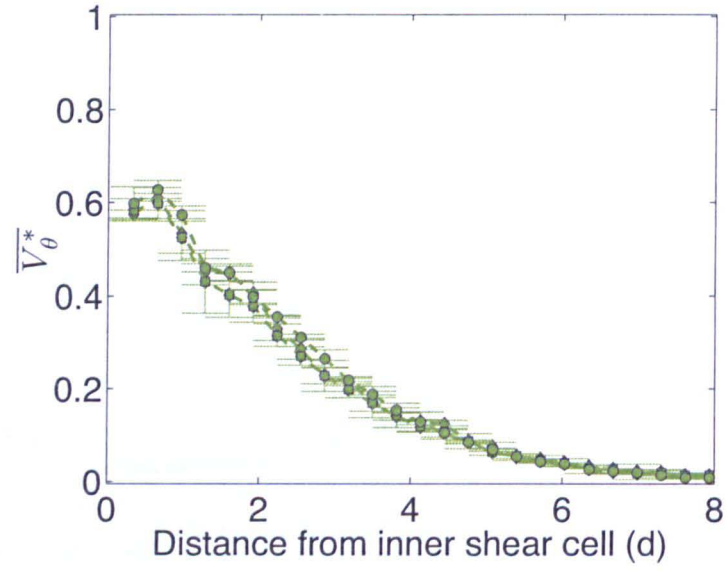

(a)

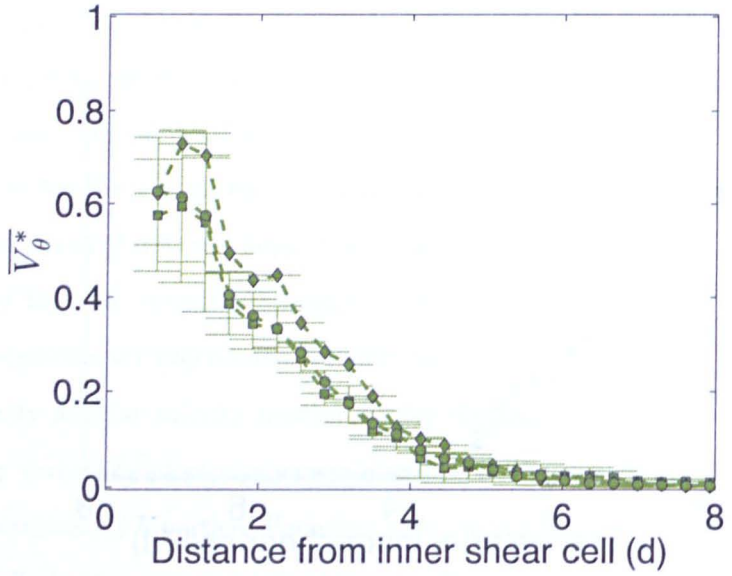

(b)

Figure 6.2: **Normalised angular velocity profiles for 3 mm beads in 1 g - $\overline{V_\theta^*}$** plotted as a function of distance from the inner cylinder for (a) the top surface and (b) the bottom surface of the ground-based experiments. Mean velocity profiles are shown for experiments with different inner cylinder angular velocities: 0.025 rad s^{-1} (diamonds), 0.05 rad s^{-1} (squares) and 0.1 rad s^{-1} (circles). The error bars represent the standard deviation of $\overline{V_\theta^*}$ for each group of experiments (i.e., $S3_a$). The velocity profiles only extend up to 8 particle diameters from the shearing surface as further away there is very little motion.

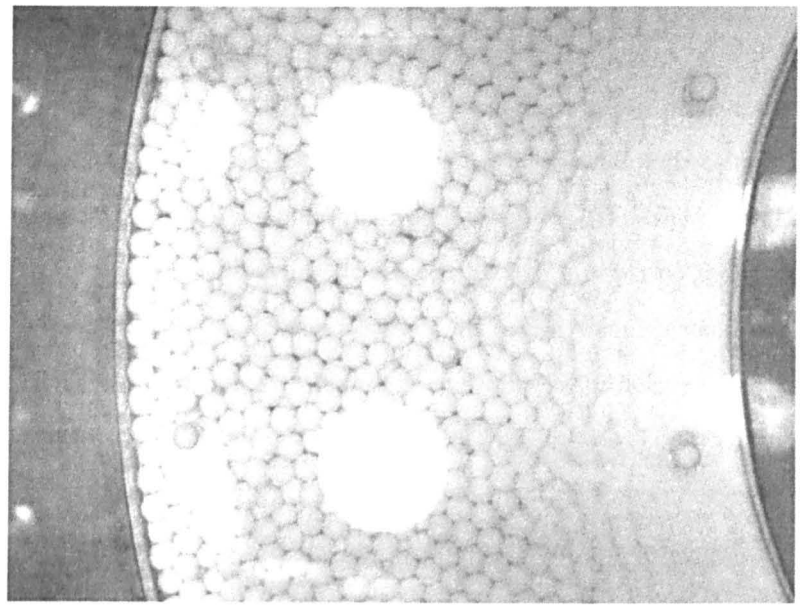

(a)

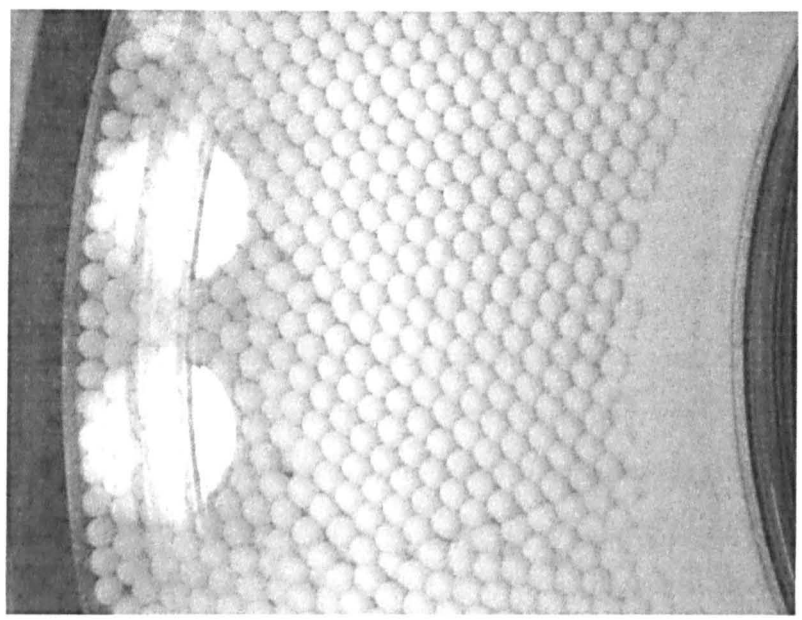

(b)

Figure 6.3: **Superposition of experimental images** - Stacked image made from >4000 frames taken of (a) the top surface, and (b) the bottom surface of the granular material. On the right, close to the inner cylinder, a shear band can be seen. This shear band is much larger in the disordered granular material of the top surface than in the crystallised granular material on the bottom surface.

removed and the particles on the bottom surface can move more freely.

Comparing the shape of the top surface angular velocity profiles of 4 mm beads obtained on the ground and in microgravity there is one noticeable difference: there is a reduced $\overline{V_\theta^*}$ very close to the inner cylinder in microgravity that does not occur on the ground (Fig. 6.4 (a) compared to Fig. 6.1 (a)). This dip can be explained by considering the shear cell set-up. The outer wall of the inner cylinder is coated with beads to make it rough. These beads are glued onto the wall of the inner cylinder but, due to the presence of the pressure plate, cannot extend above the height of the top layer of beads in the shear cell. Therefore, as the granular material dilates in the microgravity environment, the particles on the top surface nearest the inner cylinder will be in contact with the smooth surface of the inner cylinder rather than the rough surface of the glued-on beads. This will result in a reduced particle velocity very close to the inner cylinder in microgravity compared to the velocity on the ground. There is no similar dip observed on the top surface near the inner cylinder for the 3 mm particles (Fig. 6.5 (a)). This is probably because the particle velocities are already reduced by the pressure plate, but may also indicate that the glued-on beads extend slightly higher in the 3 mm bead shear cell.

6.2.3 Steady state granular flow in varying gravitational environments

It has been shown that the normalised angular velocity profiles of constant shear rate experiments performed both on the ground and during all microgravity flights are independent of shear rate. Therefore, we now combine all the data from all of the experiments of each type (i.e., experiments at all inner cylinder angular velocities with the same bead size, camera and gravitational environment) to perform a direct comparison between the two gravitational regimes. The data from each flight are again kept separate due to the varying quality of microgravity encountered during the different flights.

The mean normalised angular velocity profiles on the top surface are identical in both microgravity and on the ground for the 4 mm beads, except for the small difference in magnitude near the inner cylinder, which has been explained above (Fig. 6.6). As mentioned previously, the difference in the shape of the normalised angular velocity profiles on the bottom surface compared to the top surface is probably caused by the crystallisation (higher packing density) which is evident on the bottom surface in both gravitational regimes. In the case of the ground-based experiments, the difference in the magnitude of the normalised angular velocity profiles on the bottom surface compared to the top surface experiments, is probably due to the weight of the beads located above those at the bottom, restricting the motion of the bottom particles.

We have seen that, in the ground-based experiments, the pressure plate has a considerable influence on the top surface of the 3 mm beads (see Section 5.4.1). The decrease in the magnitude of the

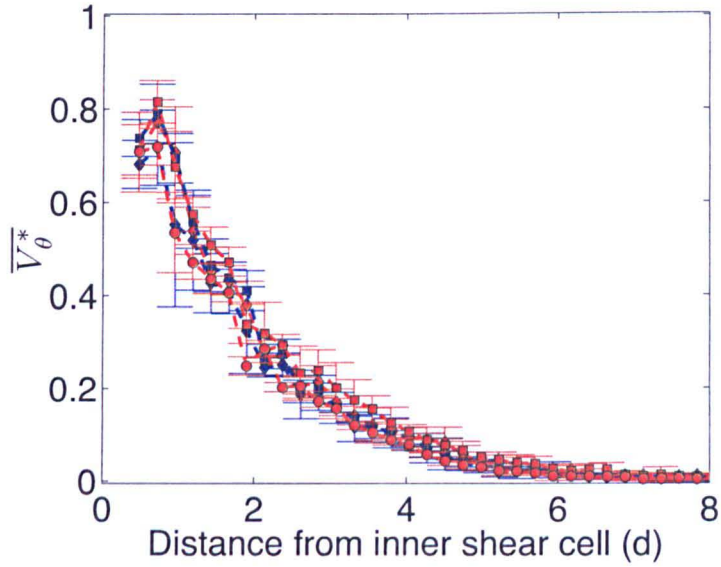

(a)

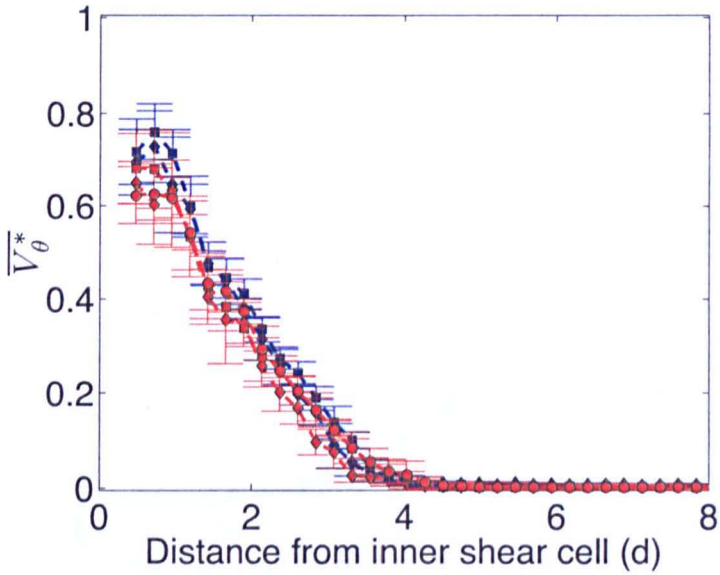

(b)

Figure 6.4: **Normalised angular velocity profiles for 4 mm beads in microgravity** - $\overline{V_\theta^*}$ plotted as a function of distance from the inner cylinder for (a) the top surface and (b) the bottom surface. Mean velocity profiles are shown for experiments during different flights: Flight A (blue) and Flight C (red), and with different inner cylinder angular velocities: 0.025 rad s^{-1} (diamonds), 0.05 rad s^{-1} (squares) and 0.1 rad s^{-1} (circles). The error bars represent the standard deviation of $\overline{V_\theta^*}$ for each group of experiments (i.e., $S3_a$). The velocity profiles only extend up to 8 particle diameters from the shearing surface as further away there is very little motion.

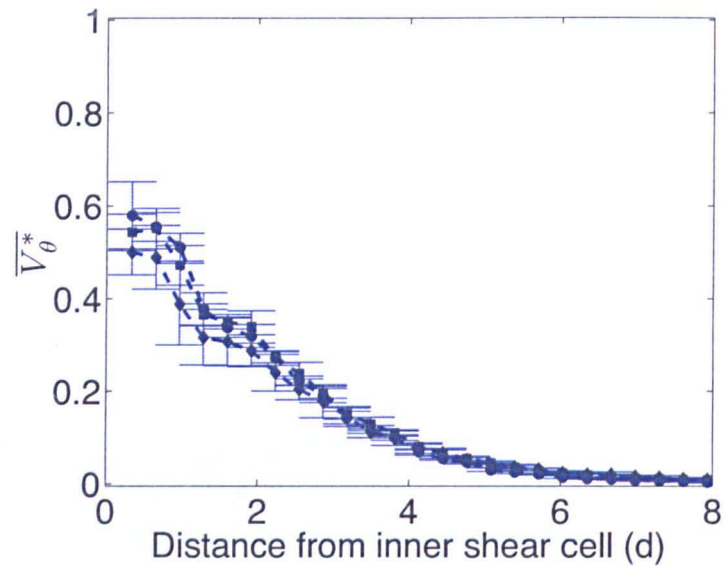

(a)

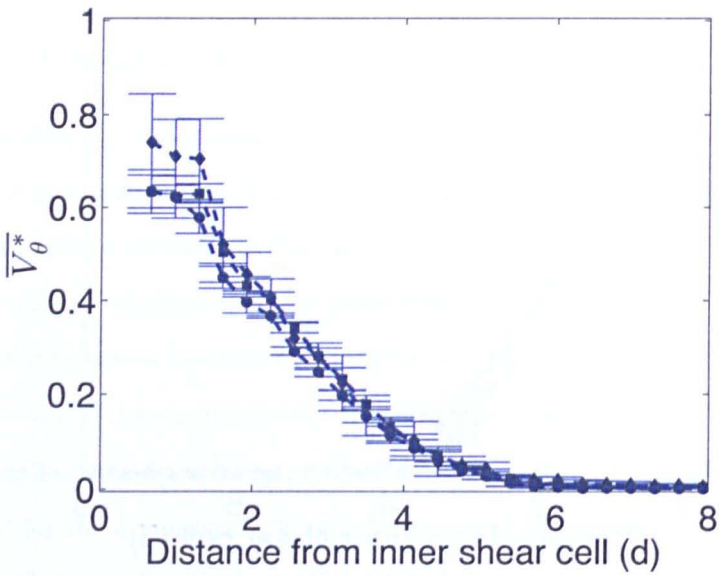

(b)

Figure 6.5: **Normalised angular velocity profiles for 3 mm beads in microgravity** - $\overline{V_\theta^*}$ plotted as a function of distance from the inner cylinder for (a) the top surface and (b) the bottom surface. Mean velocity profiles are shown for experiments with different inner cylinder angular velocities: 0.025 rad s^{-1} (diamonds), 0.05 rad s^{-1} (squares) and 0.1 rad s^{-1} (circles). All microgravity experiments were performed during Flight B. The error bars represent the standard deviation of $\overline{V_\theta^*}$ for each group of experiments (i.e., $S3_a$). The velocity profiles only extend up to 8 particle diameters from the shearing surface as further away there is very little motion.

normalised angular velocity profiles caused by the pressure plate is systematic as it affects all experiments of the same type in the same manner. However, the influence of the pressure plate does seem to be more important in microgravity experiments than in ground-based experiments (Fig. 6.7). This is probably because the 3 mm particle packing dilates in microgravity and, therefore, the particles are more likely to be in contact with the pressure plate than in ground-based experiments.

Again, as for the 4 mm beads, the shapes of the normalised velocity profiles with the 3 mm beads are different on the top and bottom surfaces in both microgravity and on the ground (due to the higher packing fraction which creates a narrower shear band). However, the magnitudes of all 3 mm particle velocity profiles are similar on both top and bottom surfaces (because the velocities of the 3 mm particles at the top surface are reduced by the pressure plate). The error bars of the normalised velocity profiles for all experiment groups on the ground and in microgravity (Figs. 6.6 and 6.7) are small, which means that there is a very small scatter in the mean angular velocities (i.e., a very small $S3_a$). This indicates that the angular velocity profiles of constant shear rate experiments are reproduceable on a macroscale.

The mean scatter of V_θ^* was defined as $S2$ in Section 5.3.2. However, we recall that this is exactly equivalent to the RMS velocity fluctuations. The RMS velocity fluctuations in a direction parallel to the mean flow (i.e., V_θ^{RMS}) decay as a function of distance from the shearing surface in a similar manner to the normalised angular velocity profiles (Figs. 6.8 and 6.9). Note that the RMS velocity fluctuations in a direction perpendicular to the mean flow (i.e., V_r^{RMS}) will be discussed later in Section 6.3.

On the ground the mean RMS velocity fluctuations are greater on the top (free) surface than on the bottom surface. In microgravity the mean RMS velocity fluctuations are of a similar magnitude on both surfaces for the 4 mm beads and are very slightly larger on the bottom surface compared to the top surface for the 3 mm beads. The error bars in the plots of the RMS velocity fluctuations for the 4 mm beads (Fig. 6.8) are small for the ground-based experiments indicating that there is a similar distribution of particle velocities in all ground-based experiments. These error bars are much larger for the microgravity experiments (especially for Flight C) indicating that there is a larger difference in the distribution of particle velocities between experiments of the same type i.e., there is more random particle motion. This is almost certainly due to the irregular and unsystematic variations in the simulated gravity during the microgravity phase of the parabolas. The error bars in the plots of the RMS velocity fluctuations for the 3 mm beads (Fig. 6.9) are quite small and similar in magnitude for the top and bottom surfaces of experiments in both gravitational regimes. This implies that every experiment of the same type with 3 mm beads has a similar distribution of particle velocities, again indicating that the pressure plate makes the particle velocities more homogeneous. Therefore, from

the above analysis we can conclude that, *the ground-based and microgravity experiments with the 3 mm beads are reproduceable on a microscale. However, due to the sensitivity of the 4 mm particles to the variations in the simulated gravity, the microgravity experiments with the 4 mm beads are not reproduceable on a microscale.*

In summary, from the experiments and analysis of steady state granular shear in varying gravity environments, we have learnt that:

- The angular velocity of particles decreases quickly over a few particle diameters away from the shearing wall for experiments performed both on the ground and in microgravity.
- The normalised angular velocity profiles of constant shear rate experiments performed both on the ground and in microgravity are independent of shear rate.
- The normalised angular velocity profiles of constant shear rate experiments performed both on the ground and in microgravity are almost identical (except for a few differences caused by the experiment set-up).
- A higher packing density of particles (such as at the bottom surface) reduces both the width of the shear band and the maximum angular velocity of the particles in experiments performed both on the ground and in microgravity.
- The mean RMS velocity fluctuations ($S2$) in a direction parallel to the mean flow are comparable for experiments performed both on the ground and in microgravity
- There are large differences in the distributions of particle velocities between experiments performed in microgravity (i.e., a large $S3_b$). This is due to random particle motion caused by the variations in simulated gravity.
- The random particle motion caused by gravity fluctuations does not affect the mean angular velocities averaged over a long time period.
- Taking all of the above into account we conclude that *the effect of constant shearing on a granular material in a direction perpendicular to the gravity field does not seem to be strongly influenced by gravity.*

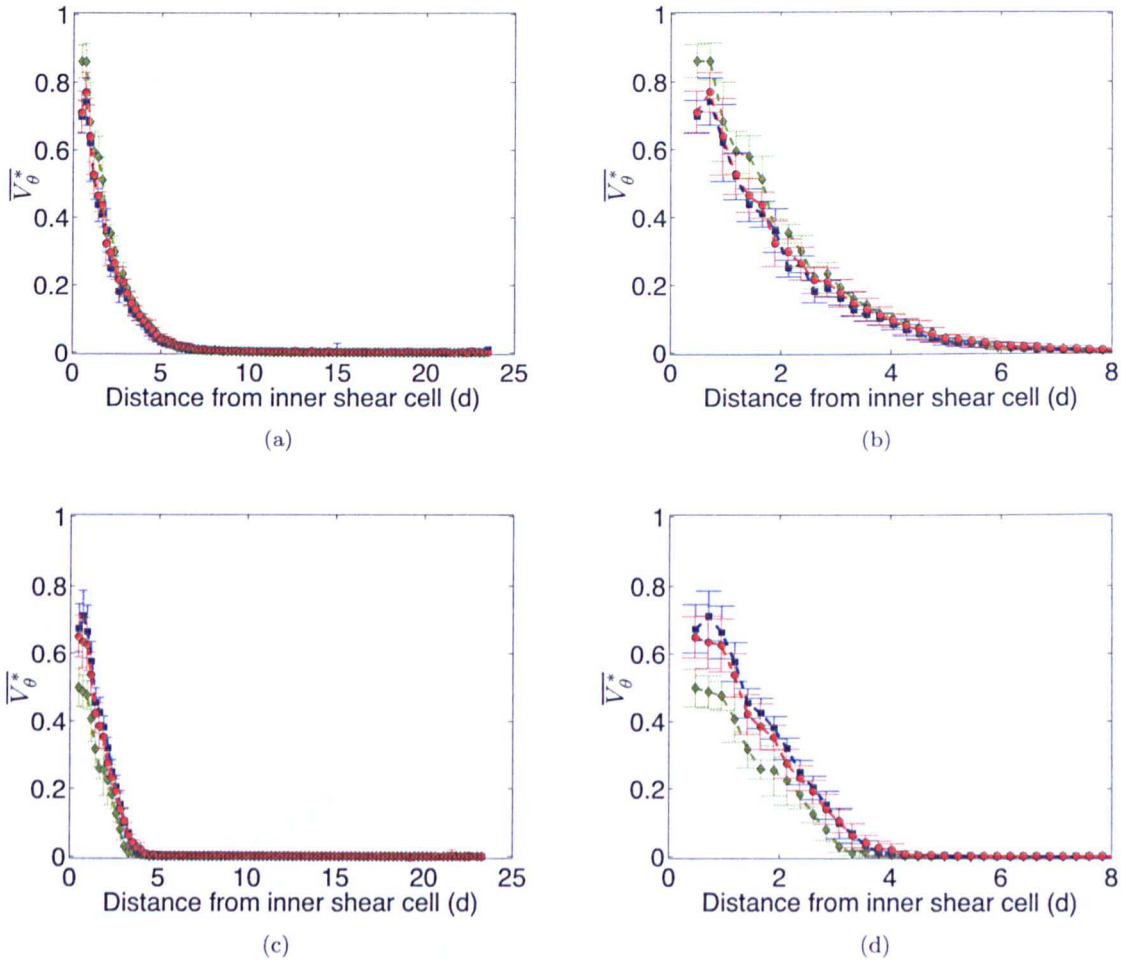

Figure 6.6: **Comparison of angular velocity profiles in 1 g and microgravity for the 4 mm beads** - $\overline{V_\theta^*}$ plotted as a function of distance from the inner cylinder on the top surface (upper plots) and on the bottom surface (lower plots). (a) and (c) show the entire width of the shear cell, (b) and (d) show a close up of the shear band. There are three types of experiment: ground-based (green diamonds), microgravity Flight A (blue squares) and microgravity Flight C (red circles). For each type, all experiments at all rotational velocities have been combined to produce the mean $\overline{V_\theta^*}$. The error bars represent the standard deviation of $\overline{V_\theta^*}$ for each group of experiments.

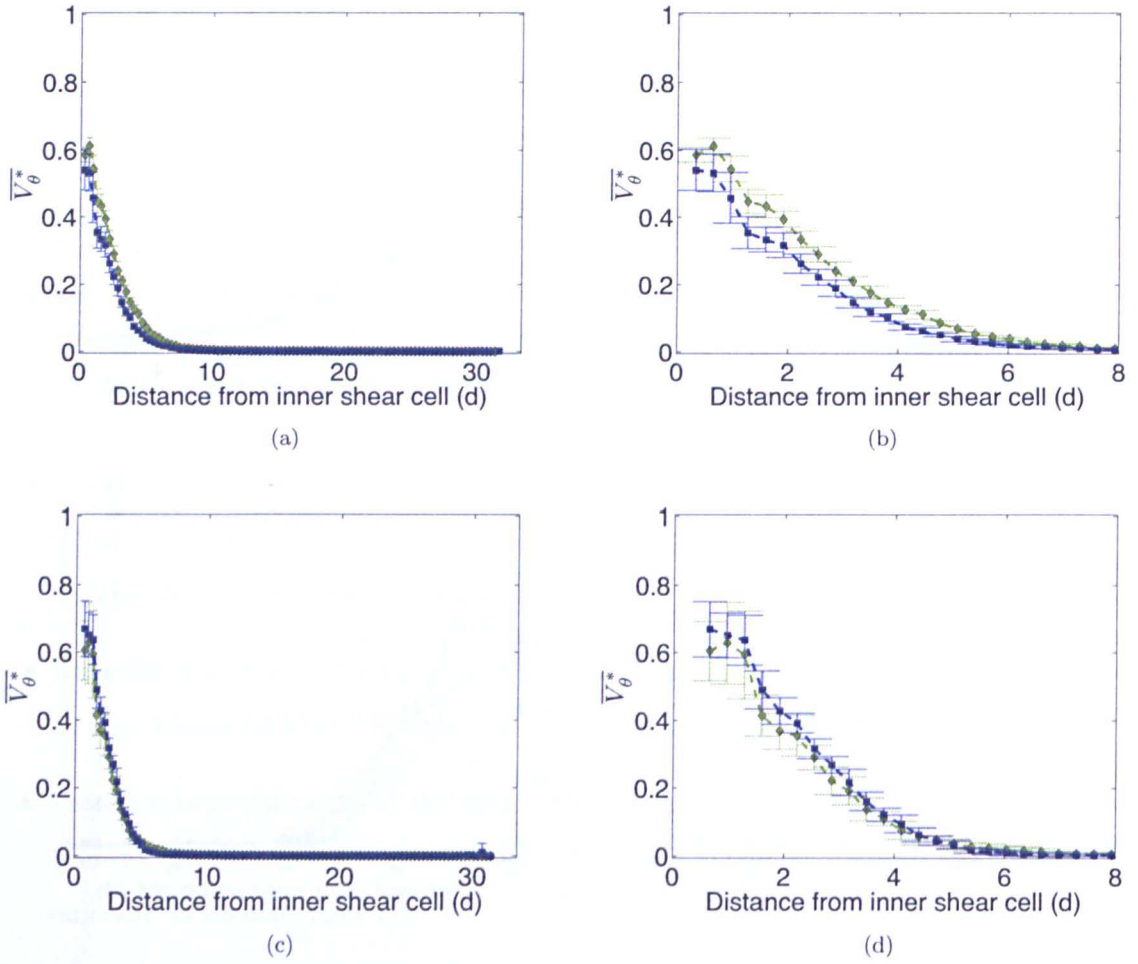

Figure 6.7: **Comparison of angular velocity profiles in 1 g and microgravity for the 3 mm beads** - $\overline{V_\theta^*}$ plotted as a function of distance from the inner cylinder on the top surface (upper plots) and on the bottom surface (lower plots). (a) and (c) show the entire width of the shear cell, (b) and (d) show a close up of the shear band. There are three types of experiment: ground-based (green diamonds), microgravity Flight A (blue squares) and microgravity Flight C (red circles). For each type, all experiments at all rotational velocities have been combined to produce the mean $\overline{V_\theta^*}$. The error bars represent the standard deviation of $\overline{V_\theta^*}$ for each group of experiments.

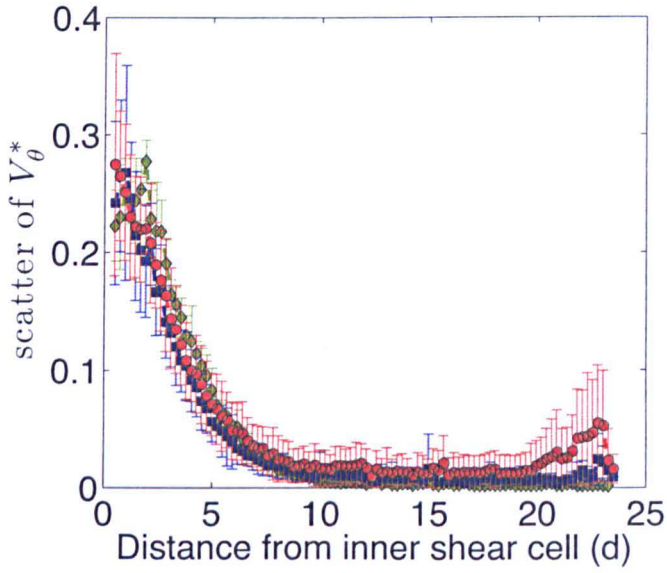

(a)

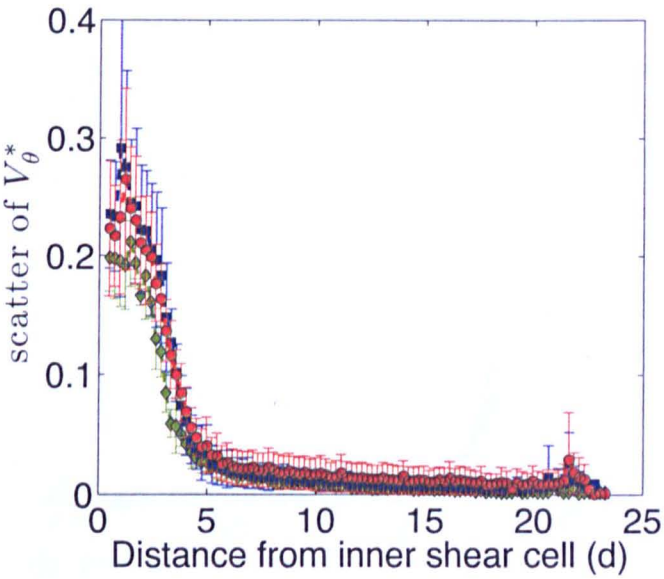

(b)

Figure 6.8: **Comparison of $S2$ of angular velocity profiles in 1 g and microgravity for 4 mm beads** - Mean $S2$ of V_θ^* (equivalent to the RMS velocity fluctuations; see Section 5.3.2) on (a) the top and (b) the bottom surface, for each type of experiment plotted as a function of distance from the inner cylinder. Results are shown for ground-based experiments (green diamonds), microgravity Flight A (blue squares) and microgravity Flight C (red circles).

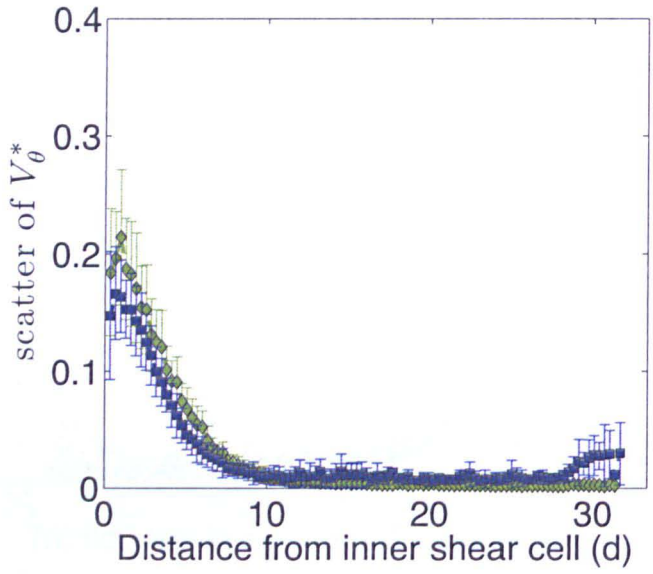

(a)

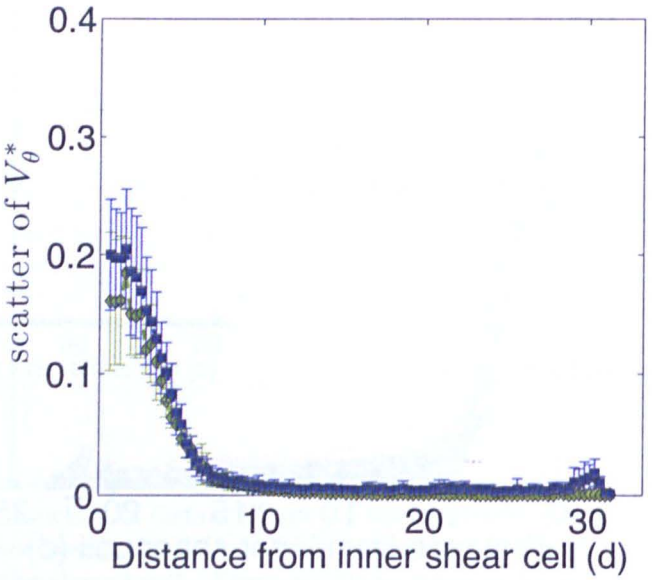

(b)

Figure 6.9: **Comparison of $S2$ of angular velocity profiles in 1 g and microgravity for 3 mm beads** - Mean $S2$ scatter of V_θ^* (equivalent to the RMS velocity fluctuations; see Section 5.3.2) on (a) the top and (b) the bottom surface, for each type of experiment plotted as a function of distance from the inner cylinder. Results are shown for ground-based experiments (green diamonds) and microgravity Flight B (blue squares).

6.3 Convective-like flows

Examining the radial velocity profiles of particles can indicate whether convective-like flows are occuring in the experiment. Specifically, if there is a dip in the radial velocity profile near the inner cylinder this indicates the possible presence of a convection roll in this region (see Section 4.2 and Fig. 4.3). As we have seen in Section 5.3.2, $S2$ in the radial velocities of the particles is large in almost all experiments (the individual radial velocity profiles for all experiments are provided in the Supplementary Material). In the experiments where V_r^* is close to zero and $S2$ is large this implies that there is a large amount of random particle motion that results in a net radial velocity of zero. In the experiments where the V_r^* is non-zero and $S2$ is large this implies that there is a significant amount of random particle motion but there is also some net motion. When $S2$ is large any net motion can not be conclusively defined as bulk motion in the individual experiments. However, if the same trends are present in several experiments of the same type then the conclusion can be drawn that there is a preferred direction of particle motion, which may be indicative of underlying bulk particle motion.

By comparing experiments of the same type using the mean particle radial velocities ($\overline{V_r^*}$) and the associated scatters ($S3_a$ and $S3_b$), as described in Section 5.3.2, we will first discuss if there is evidence for convective-like flows in the ground-based experiments. Then we will consider the mean radial velocity profiles and $S3$ scatters of the particles in the microgravity experiments. Finally, we will look at the mean radial motion of particles as a function of time to determine how persistent the radial motion is over time. For the experiments performed during a parabola we will also have a unique opportunity to directly compare the radial motion of particles in an experiment as the simulated gravity varies from $\sim$0 g to 1.8 g. This may allow a direct detection of regime changes between the varying gravitational environments.

The focus in this section will mostly be on the radial velocities of particles on the top (free) surface of the shear cell. However, the radial velocity profiles for the bottom surface will also be presented and discussed at the end of the section.

6.3.1 Radial particle motion in 1 g

Figure 6.10 shows the mean normalised radial velocity ($\overline{V_r^*}$), as a function of distance from the inner cylinder, for the 4 and 3 mm beads on the top surface of experiments on the ground with different inner cylinder angular velocities. The error bars in the radial velocity profiles show the scatter of mean radial velocities between experiments of the same type ($S3_a$). We can see that, although experiments of the same type are not identical (the size of the error bars is non-zero), there is a reproduceable trend in the shape of the radial velocity profiles. All of the ground-based experiments exhibit the

same characteristic large dip in the top surface radial velocity profile close to the inner cylinder. The dips in the radial velocity profiles occur between the inner cylinder and approximately 6-7 particle diameters distance from the inner cylinder. This, as we have seen in Section 6.2, is approximately the width of the shear band. Despite the small scale of the radial motion (only a few fractions of a millimeter per second), there is clearly a preferred direction of particle motion in this region of the top surface for all ground-based experiments. We can, therefore, conclude that within the shear band there is a continuous flux of particles towards the inner cylinder.

In the plots of Figure 6.10, although the dip is seen in all mean radial velocity profiles, the magnitude of the normalised radial velocity increases with decreasing inner cylinder angular velocity. This confirms that the mean particle radial velocity is not a linearly increasing function with inner cylinder angular velocity (as first suggested in Section 5.3.2), otherwise the dips would all be the same magnitude. It is not, therefore, possible to combine data from experiments at different inner cylinder angular velocities as we have done in the analyses of the particle angular velocities.

The magnitude of the dip in the radial velocity profiles is smaller for the 3 mm particles than for the 4 mm particles (Fig. 6.10). We have already seen that the angular motion on the top surface of experiments with the 3 mm beads is suppressed due to the presence of the pressure plate (Section 5.4.1), therefore, it is not surprising that the radial motion is also suppressed. Another feature, that is most evident in the radial velocity profiles with an inner cylinder angular velocity of 0.025 rad s^{-1}, is the small positive radial velocity extending from the end of the shear band (at 6-7 particle diameters) to the outer cylinder. Again, in this region, the error bars are small enough to imply that this is a consistent trend between many experiments. We can, therefore, conclude that outside of the shear band there is a continuous, flux of particles away from the inner cylinder. However, this motion is on a much smaller scale than the inwards radial motion within the shear band.

The mean scatter of the radial velocities in individual experiments was defined as $S2$ in Section 5.3.2 and is equivalent to the RMS velocity fluctuations in a direction perpendicular to the mean flow (i.e., V_r^{RMS}). As for the RMS velocity fluctuations in a direction parallel to the mean flow (see Section 6.2) the RMS velocity fluctuations in a direction perpendicular to the mean flow decay as a function of distance from the shearing surface (Fig. 6.11). The magnitude of V_r^{RMS} is smaller for the 3 mm beads than for the 4 mm beads. This is consistent with the angular velocity results and is because the pressure plate reduces particle motion. The error bars in the plots of the RMS velocity fluctuations are small indicating that there is a similar distribution of particle velocities in all ground-based experiments. However, it must be noted that the RMS velocity fluctuations are consistently larger in magnitude than the corresponding dip in the radial velocity profiles.

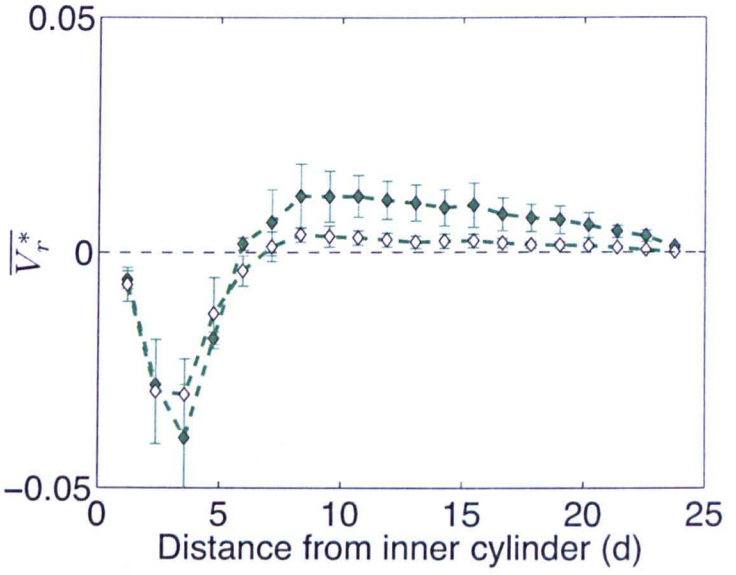

(a)

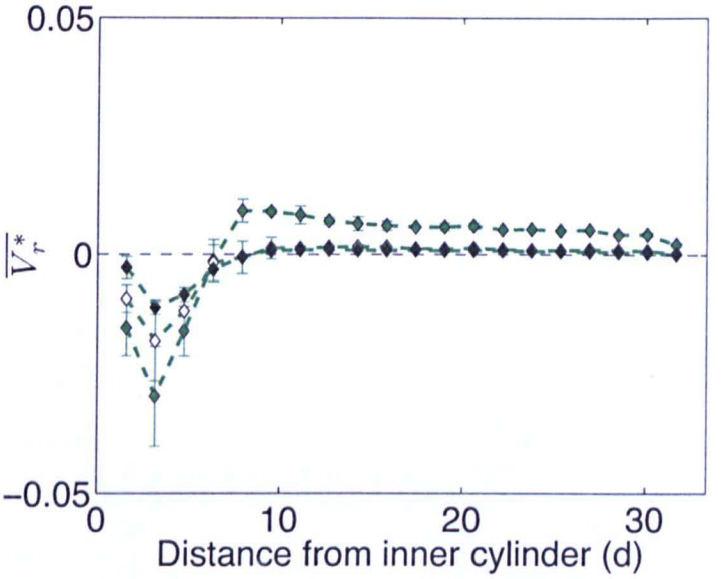

(b)

Figure 6.10: **Normalised radial velocity profiles in 1** g - $\overline{V_r^*}$ plotted as a function of distance from the inner cylinder on the top surface of ground-based experiments with (a) 4 mm and (b) 3 mm particles. Mean velocity profiles are shown for experiments with different inner cylinder angular velocities: 0.025 rad s^{-1} (solid colour markers), 0.05 rad s^{-1} (open markers) and 0.1 rad s^{-1} (black markers). The error bars represent the standard deviation of $\overline{V_r^*}$ for each group of experiments (i.e., $S3_a$).

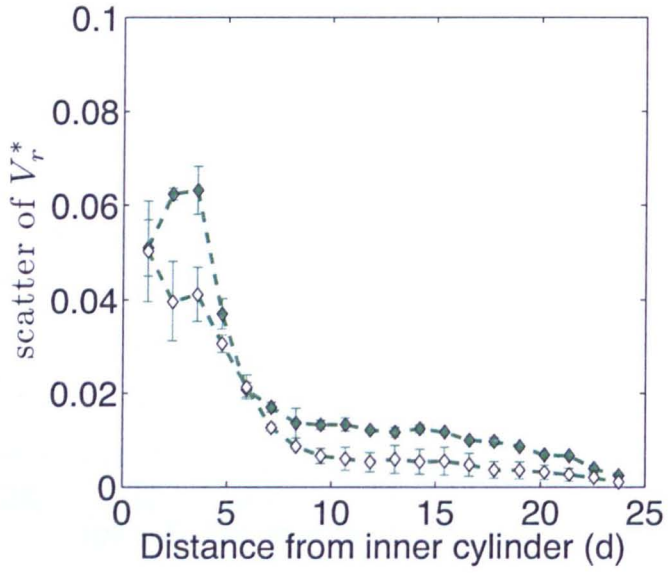

(a)

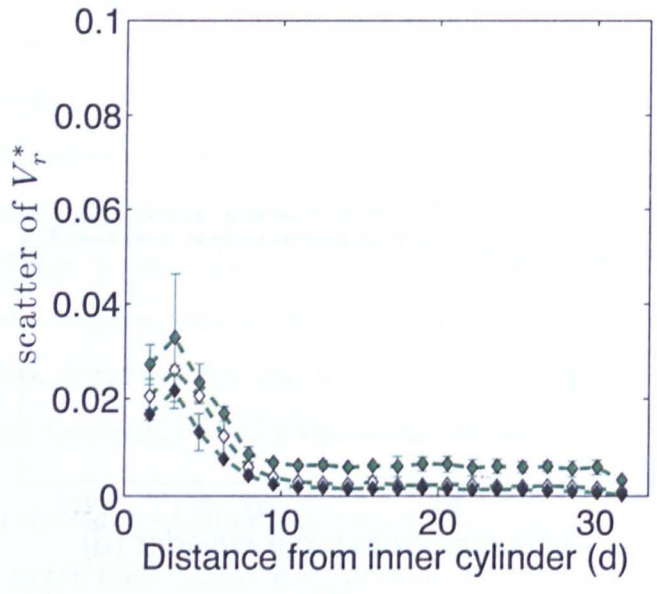

(b)

Figure 6.11: $S2$ **of radial velocity profiles in 1** g - The $S2$ scatter of V_r^* (i.e., RMS velocity fluctuations) plotted as a function of distance from the inner cylinder on the top surface of ground-based experiments with (a) 4 mm and (b) 3 mm particles. Mean results are shown for experiments with different inner cylinder angular velocities: 0.025 rad s^{-1} (solid colour markers), 0.05 rad s^{-1} (open markers) and 0.1 rad s^{-1} (black markers). The error bars represent the standard deviation of the mean $S2$ for each group of experiments (i.e., $S3_b$).

6.3.2 Radial particle motion in microgravity

Figure 6.12 shows the mean normalised radial velocity profiles for the 4 and 3 mm beads on the top surface of experiments in microgravity with different inner cylinder angular velocities. In these plots we can immediately see that there is no longer a characteristic dip in the radial velocity profiles near the inner cylinder as has been observed in the ground-based experiments.

Close to the inner cylinder the 4 mm beads appear to exhibit a slightly negative radial motion. However, looking carefully at Fig. 6.12 (a) we can see that the error bars are very large for the mean radial velocities very close to the inner cylinder (i.e., $S3_a$ is large). This indicates that there is a large distribution of mean particle radial velocities between the experiments and that this small amount of negative motion at the inner cylinder is possibly not a robust and reproducible behaviour. The extremely large value of the mean RMS velocity fluctuations in a direction perpendicular to the mean flow ($S2$) shown in Fig. 6.13 (a) confirms that there is a large amount of random particle motion in this region. In addition to the mean RMS velocity fluctuations being large near the inner cylinder, the error bars in Fig. 6.13 (a) are also very large near the inner cylinder (i.e., $S3_b$ is large). This indicates that, in this region of the shear cell during the microgravity experiments, there is a large difference in the RMS velocity fluctuations between different experiments. We can conclude, therefore, that, on the top surface of the 4 mm beads close to the inner cylinder, the particles are undergoing a lot of random agitation in the radial direction. This would imply that radial motion of particles in this region of the shear cell is very susceptible to the variations in the simulated gravity.

Close to the inner cylinder in the experiments with the 3 mm beads the scatter of mean radial velocities between experiments is much smaller (i.e., small error bars in Fig. 6.12 (b)), the width of the distributions of particle velocities within the experiments are smaller and more reproducible (i.e., smaller mean RMS velocity fluctuations and smaller error bars in Fig. 6.13 (b)). Again, this is probably because the motion of the 3 mm beads is suppressed due to the presence of the pressure plate (Section 5.4.1). This implies that the 3 mm particles are, therefore, less susceptible to the variations in the simulated gravity.

In the radial velocity profiles on the top surface of all of the microgravity experiments (Fig. 6.12) there appears to be a small positive radial velocity extending from a few particle diameters to the outer cylinder. In this region of the shear cell, the error bars of the mean radial velocity profiles are small enough (i.e., $S3_a$ is small) to imply that this is a consistent trend between many experiments. The mean RMS velocity fluctuations are also smaller further from the inner cylinder and for all experiment types, except those performed during the microgravity of Flight C, $S3_b$ is quite small at large distances from the inner cylinder (Fig. 6.13). This means that, in this region of the shear cell, the experiments are more reproduceable and there is less random agitation of the particles (except for during Flight

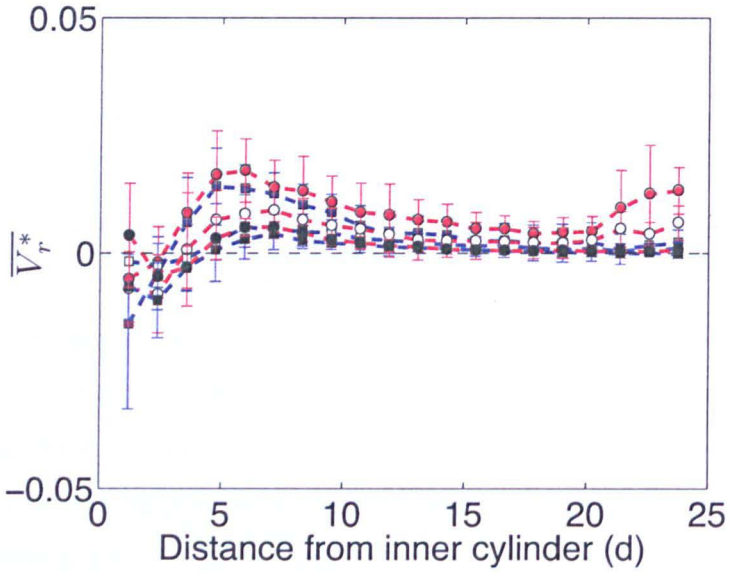

(a)

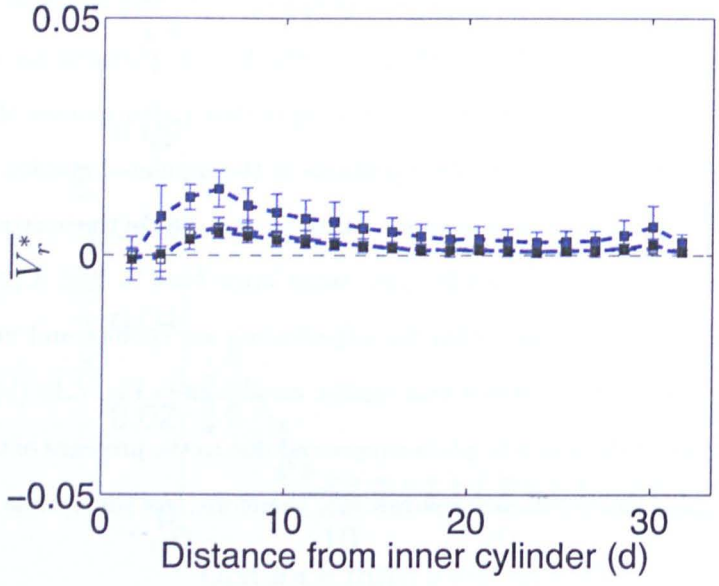

(b)

Figure 6.12: **Normalised radial velocity profiles in microgravity** - $\overline{V_r^*}$ plotted as a function of distance from the inner cylinder on the top surface of microgravity experiments (a) during Flight A (blue squares) and Flight C (red circles) with 4 mm particles and (b) during Flight B (blue squares) with 3 mm particles. Mean velocity profiles are shown for experiments with different inner cylinder angular velocities: 0.025 rad s^{-1} (solid colour markers), 0.05 rad s^{-1} (open markers) and 0.1 rad s^{-1} (black markers). The error bars represent the standard deviation of $\overline{V_r^*}$ for each group of experiments (i.e., $S3_a$).

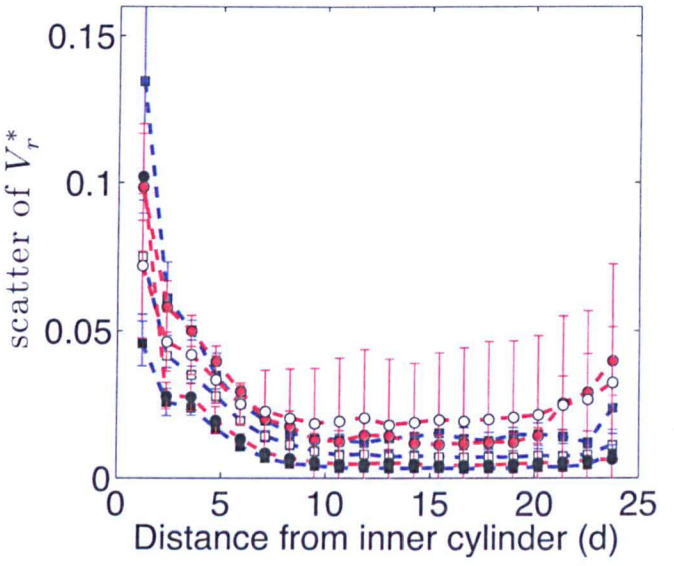

(a)

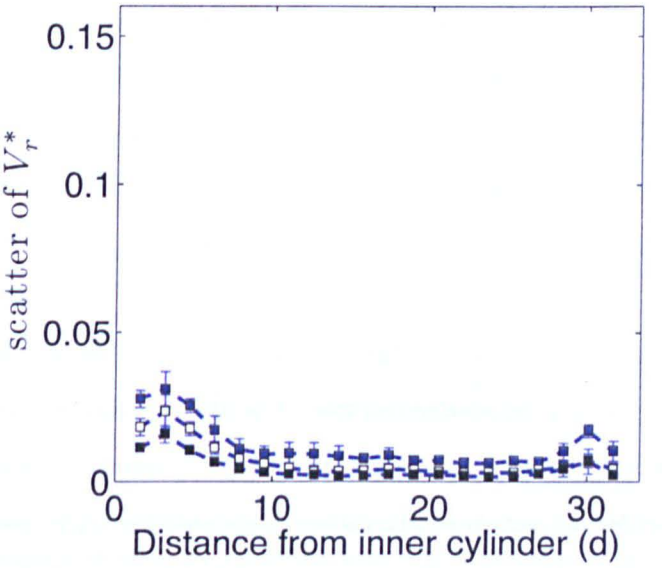

(b)

Figure 6.13: $S2$ **scatter of radial velocity profiles in microgravity** - The $S2$ scatter of V_r^* (i.e., RMS velocity fluctuations; see Section 5.3.2) plotted as a function of distance from the inner cylinder on the top surface of microgravity experiments (a) during Flight A (blue squares) and Flight C (red circles) with 4 mm particles and (b) during Flight B (blue squares) with 3 mm particles. Mean results are shown for experiments with different inner cylinder angular velocities: 0.025 rad s^{-1} (solid colour markers), 0.05 rad s^{-1} (open markers) and 0.1 rad s^{-1} (black markers). The error bars represent the standard deviation of the mean $S2$ for each group of experiments (i.e., $S3_b$).

C). We can, therefore, conclude that there is a very small, but continuous, flux of particles away from the inner cylinder in the microgravity experiments.

Additionally, the peak of this positive radial velocity seems to occur at approximately 6-7 particle diameters from the inner cylinder, which is the width of the shear band (Section 6.2). In other words, in microgravity the particles appear to have a maximum radial velocity close to the boundary between the shear band and the bulk of the granular material. The magnitude of the peak of the normalised radial velocity increases with decreasing inner cylinder angular velocity demonstrating, once again, that the mean particle radial velocity is probably not a linearly increasing function with inner cylinder angular velocity.

6.3.3 Comparing the radial velocities in varying gravitational environments

We have seen that there is no difference in the width of the shear band nor is there a difference in the magnitude of the angular velocities within the shear band (see Section 6.2) between the gravitational regimes of microgravity and 1 g. Interestingly, we see a clear change in the behaviour of the radial motion of particles in the shear band between the two gravitational regimes. The radial velocity profiles on the top surface of the ground-based experiments exhibit a large dip close to the inner cylinder which is indicative of convective-like motion. However, this dip is not present in the radial velocity profiles of microgravity experiments. This difference between the two gravitational regimes implies that the mechanisms driving the radial motion of particles in the two different gravity regimes may not be the same.

Figures 6.14 and 6.15 show the unnormalised radial velocity profiles on the top surfaces of the 4 mm beads and the 3 mm beads, respectively. From all of the experiments on the ground looking at the top surface we can conclude that, *within the shear band of constant shear rate experiments in 1 g there is a continuous flux of particles towards the inner cylinder. The peak of this inward radial motion occurs in the middle of the shear band. Outside of the shear band, there is a smaller, but still continuous, flux of particles away from the inner cylinder.*

From all of the experiments in microgravity looking at the top surface we can conclude that, *during constant shear rate experiments in microgravity there is a small, but continuous, flux of particles away from the inner cylinder starting at a distance of a few particle diameters and extending to the outer cylinder. The peak of this outer radial motion occurs close to the boundary of the shear band and the bulk of the granular material.*

The RMS velocity fluctuations in a direction perpendicular to the mean flow (Figs. 6.16 and 6.17) follow similar trends to the RMS velocity fluctuations discussed in Section 6.2: the mean RMS velocity

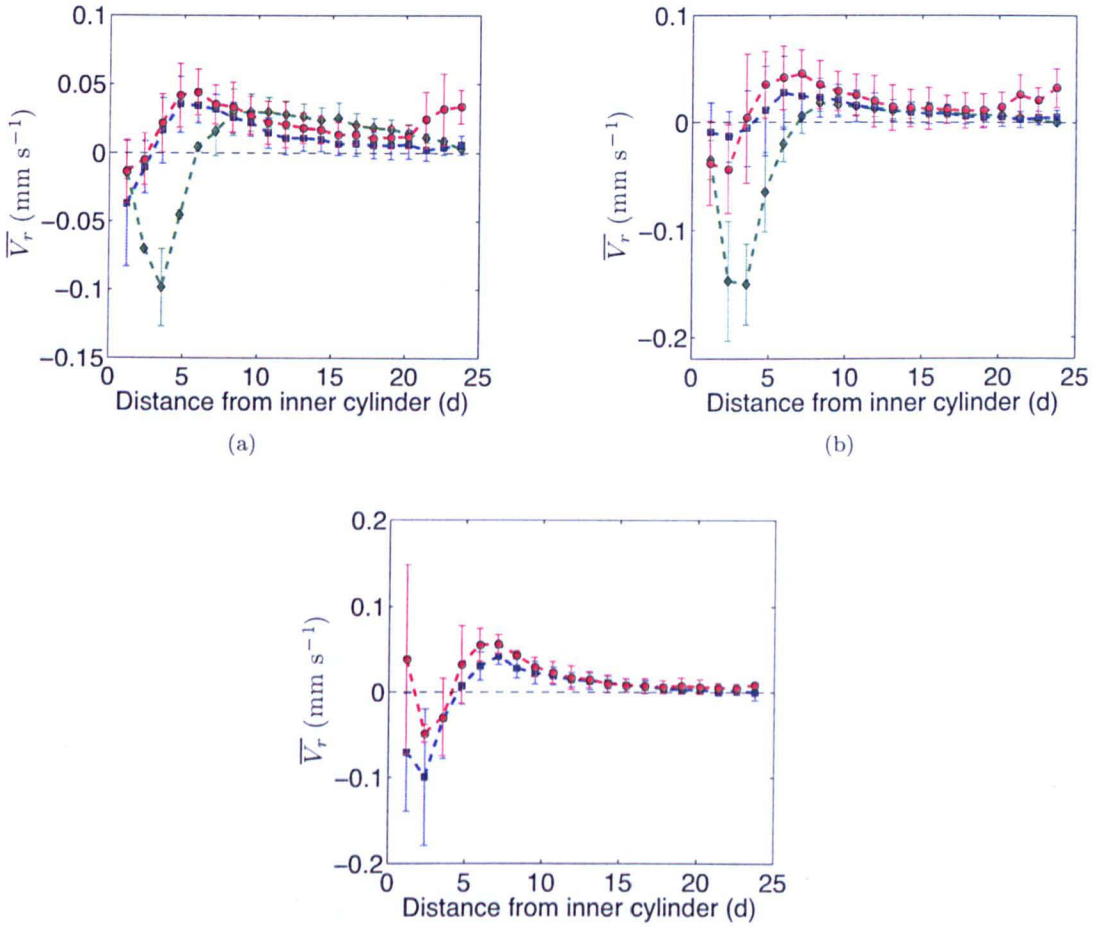

Figure 6.14: **Comparison of radial velocity profiles of the 4 mm beads in 1 g and microgravity** - $\overline{V_r}$ plotted as a function of distance from the inner cylinder for the top surface of experiments with an inner cylinder angular velocity of (a) 0.025 rad s^{-1} and (b) 0.05 rad s^{-1}. Results are shown for ground-based experiments (green diamonds), microgravity Flight A (blue squares) and microgravity Flight C (red circles). The error bars represent the standard deviation of $\overline{V_r}$ for each group of experiments (i.e., $S3_a$). See text for discussion on ground and microgravity differences.

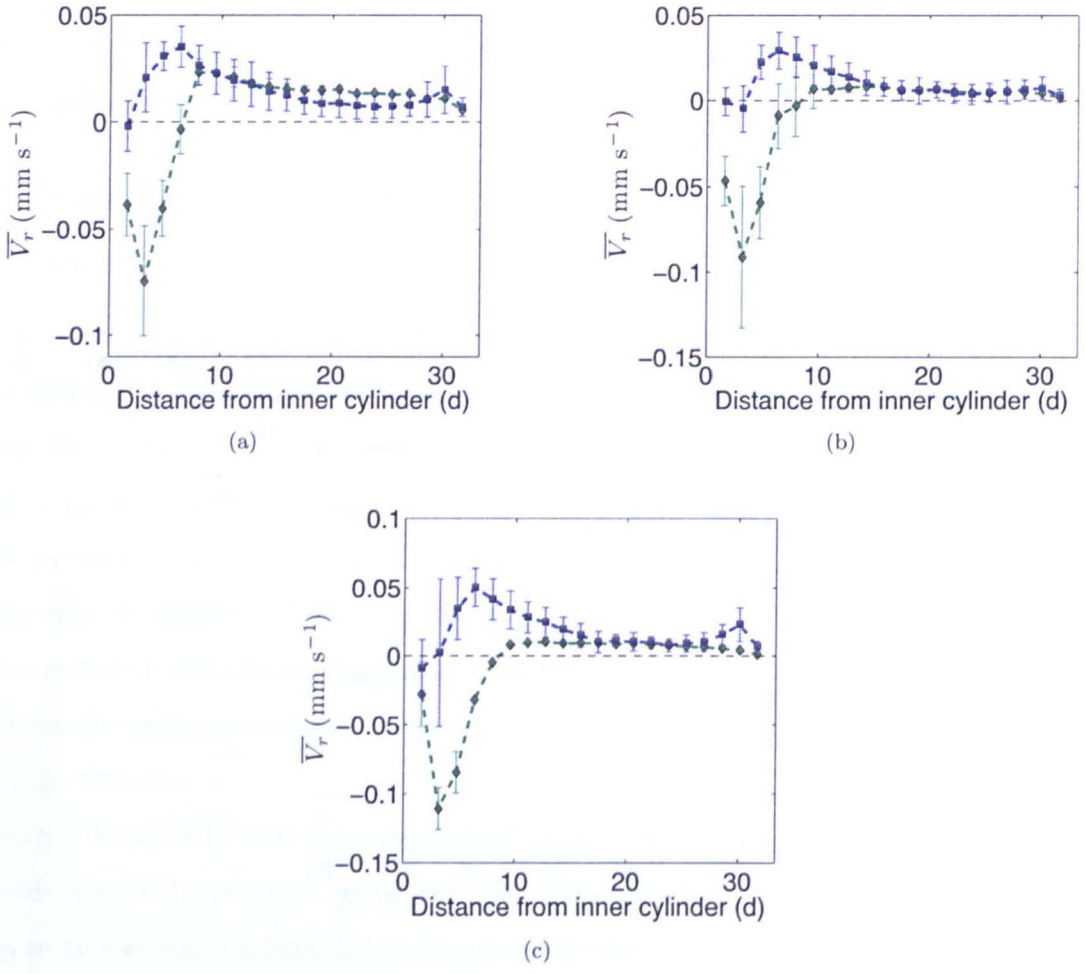

Figure 6.15: **Comparison of radial velocity profiles of the 3 mm beads in 1 g and microgravity** - $\overline{V_r}$ plotted as a function of distance from the inner cylinder for the top surface of experiments with an inner cylinder angular velocity of (a) 0.025 rad s^{-1}, (b) 0.05 rad s^{-1} and (c) 0.1 rad s^{-1}. Results are shown for ground-based experiments (green diamonds) and microgravity Flight B (blue squares). The error bars represent the standard deviation of $\overline{V_r}$ for each group of experiments (i.e., $S3_a$). See text for discussion on ground and microgravity differences.

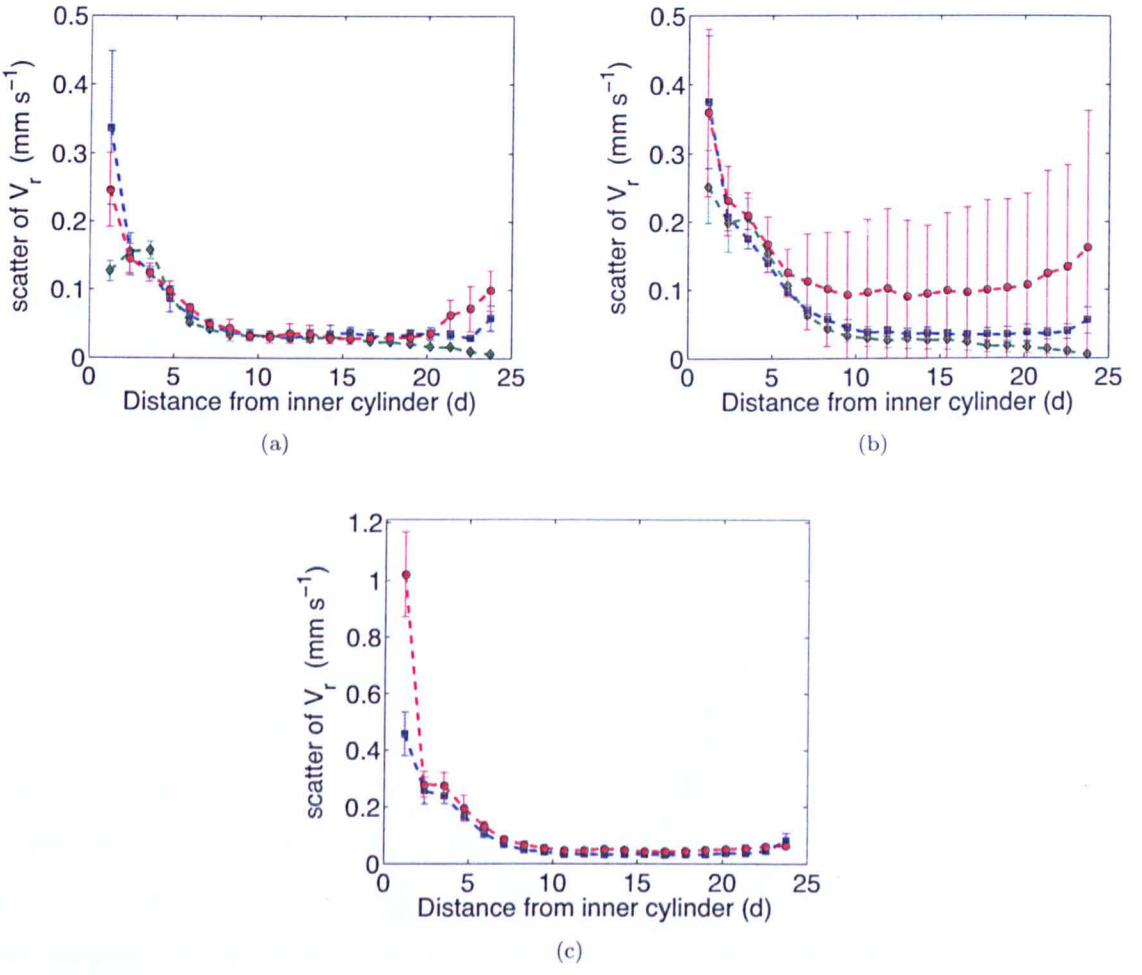

Figure 6.16: **Comparison of $S2$ of radial velocity profiles of the 4 mm beads on top surface** - $S2$ of V_r (i.e., RMS velocity fluctuations; see Section 5.3.2) plotted as a function of distance from the inner cylinder on the top surface of experiments with an inner cylinder angular velocity of (a) 0.025 rad s^{-1}, (b) 0.05 rad s^{-1} and (c) 0.1 rad s^{-1}. Results are shown for ground-based experiments (green diamonds), microgravity Flight A (blue squares) and microgravity Flight C (red circles). The error bars represent the standard deviation of the mean $S2$ for each group of experiments (i.e., $S3_b$).

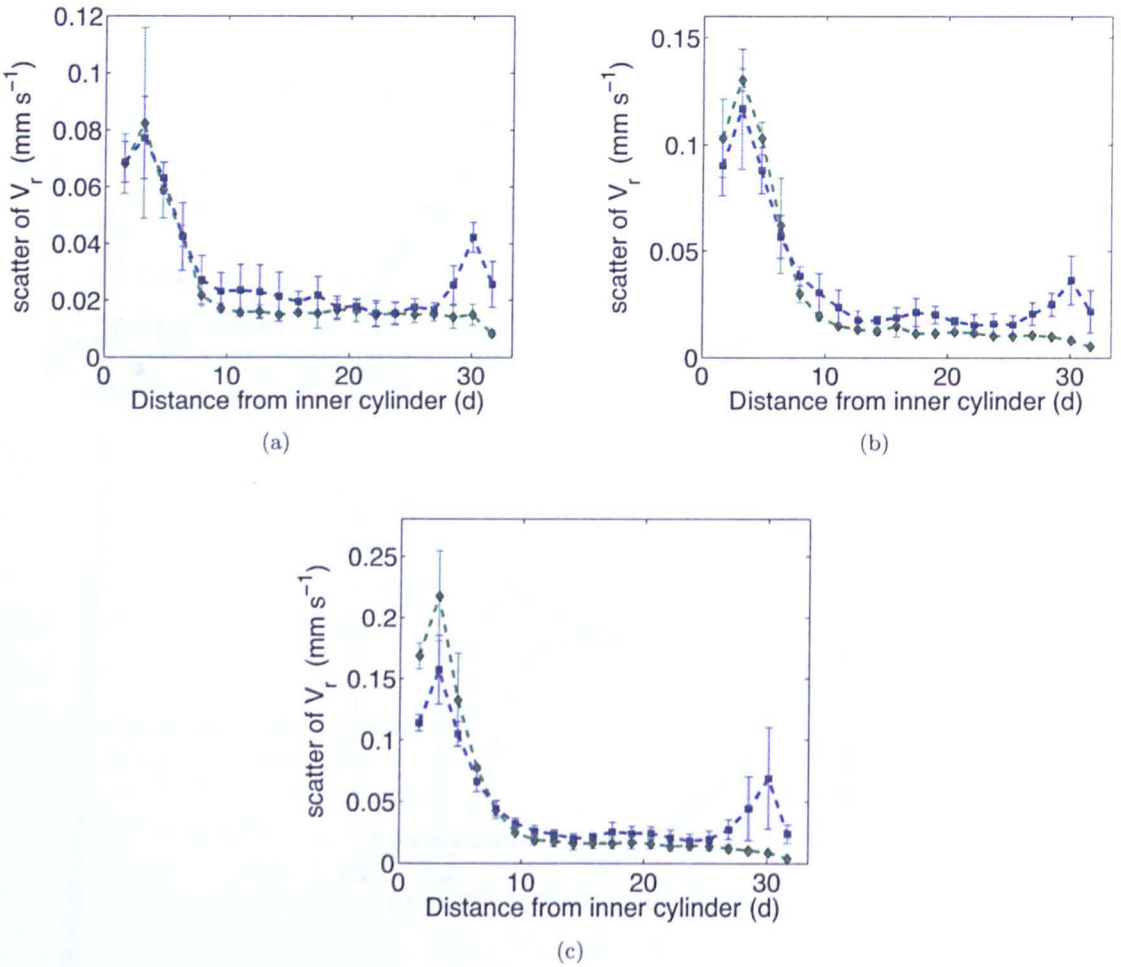

Figure 6.17: **Comparison of $S2$ of radial velocity profiles of the 3 mm beads on top surface** - $S2$ of V_r (i.e., RMS velocity fluctuations; see Section 5.3.2) plotted as a function of distance from the inner cylinder on the top surface of experiments with an inner cylinder angular velocity of (a) 0.025 rad s^{-1}, (b) 0.05 rad s^{-1} and (c) 0.1 rad s^{-1}. Results are shown for ground-based experiments (green diamonds) and microgravity Flight B (blue squares). The error bars represent the standard deviation of the mean $S2$ for each group of experiments (i.e., $S3_b$).

fluctuations decay as a function of distance from the shearing surface; for the 4 mm particles (Fig. 6.16) the mean RMS velocity fluctuations are smaller on the ground than in microgravity, although, for the 3 mm particles (Fig. 6.17) the mean RMS velocity fluctuations are of a similar magnitude on the ground and in microgravity. The magnitude of the mean RMS velocity fluctuations are also much greater for the 4 mm beads than for the 3 mm beads. This indicates that there is a larger amount of random agitation of the 4 mm particles in microgravity than of the 3 mm particles (consistent with what has been found previously in Section 6.2).

We have seen in Section 6.3.1 that there is a similar distribution of particle velocities in all ground-based experiments. Similarly, in Section 6.3.2 we have seen that there is a similar distribution of particle velocities in all microgravity experiments with 3 mm beads. However, for the microgravity experiments with 4 mm beads there is a larger difference in the distribution of particle velocities between experiments of the same type i.e., there is more random particle motion. This is almost certainly due to the irregular and unsystematic variations in the simulated gravity during the microgravity phase of the parabolas. The 3 mm beads are less sensitive to such variations due to the influence of the pressure plate.

We have compared radial velocity profiles between different experiments in two different gravity regimes and found significant differences. However, thanks to the gravitational environment available on a parabolic flight, we have a unique opportunity to confirm this difference by observing regime changes in the same experiment as the simulated gravitational field changes. Recall, from Chapter 4, that during each parabola of a parabolic flight there are three distinct phases: a $\sim$20 second $\sim$1.8 g injection phase as the plane accelerates upwards, a $\sim$22 second microgravity phase as the plane passes through the top of the parabola, and finally a $\sim$20 second $\sim$1.8 g recovery phase as the plane pulls out of the parabola. For all of the constant shear rate microgravity experiments performed during the flight campaign, the motor and cameras were switched on just after the transition from the first $\sim$1.8 g to the microgravity phase. For some experiments, the motor and camera were then left running throughout the rest of the parabola (i.e., through the microgravity period and through the $\sim$1.8 g recovery phase).

First we consider the variation of radial velocity as a function of time in the ground-based experiments. The inner radial bin (of five) was chosen for the analysis as it has a width of $\sim$6 particle diameters and, therefore, is approximately the size of the shear band (as we have seen above, we expect the inward radial motion in ground-based experiments to occur within the shear band). Figure 6.18 shows the mean radial velocity of the inner radial bin as a function of time throughout ground-based constant shear rate experiments at different inner cylinder rotational velocities. Each point represents the mean radial velocity of the particles in the radial bin during a period of 2 seconds. The error bars

represent the standard deviation of the mean radial velocity in the same time period.

In each of the six examples provided in Fig. 6.18 the radial velocity of the inner radial bin varies throughout time. However, despite the fluctuations, the mean values are clearly more negative than positive over the course of every experiment. This is consistent with the radial velocity profiles from above, which showed that, in the ground-based experiments, there is a net flux of particles towards the inner cylinder within the shear band.

Now we will consider how the mean radial velocity of the particles in the inner radial bin varies during a parabola. Due to the problems related to data acquisition during Flight A (see Section 4.6.1), the majority of parabolas for which the experiment was continued into the $\sim$1.8 g recovery phase occured during Flights B and C. However, as has been mentioned several times, Flight C had a poor quality of microgravity and, in addition, there were large gravity fluctuations during $\sim$1.8 g recovery phase. Therefore, the experiments presented here are the constant shear rate experiments performed during Flight B. Note that the plots of radial velocity as a function of time for all constant shear rate experiments performed during all of the flights are provided in the Supplementary Material.

Figures 6.19–6.21 show the mean radial velocities of the inner radial bin of particles, as a function of time, during constant shear rate experiments performed during a parabola. Five example experiments are provided at each of the three inner cylinder rotational velocities. In all of these plots the microgravity period lasts from 0 to $\sim$20 seconds after which there is a period of $\sim$1.8 g from $\sim$20 to $\sim$40 seconds. Finally, at $\gtrsim$40 seconds the gravitational acceleration returns to 1 g.

Again, just like for the ground-based experiments, there are fluctuations in the radial velocity over time. In the first 20 seconds of almost every single experiment the radial velocity fluctuates close to zero and often remains slightly more positive than negative. This is, once again, consistent with the radial velocity profiles from above which showed that within the shear band there is a small net positive flux of particles away from the inner cylinder.

If there truly is a change in the behaviour of particles in different gravitational regimes we should see a change in the radial velocities of the particles as the simulated gravity passes from microgravity to $\sim$1.8 g. This is exactly what is observed in almost every single experiment in Figs. 6.19–6.21. After approximately 20 seconds of constant shearing the particles, which were previously exhibiting small positive radial velocities, start suddenly to exhibit negative radial velocities. In many cases the magnitude of the negative radial velocities occuring in $\sim$1.8 g is much larger than the magnitude of the positive radial velocities occuring in microgravity.

From these results it is very clear that *there is a mechanism causing the inward motion of particles in the presence of an external gravitational field. This mechanism does not appear to be active during microgravity.* In the next section some ideas will be proposed that may explain this mechanism.

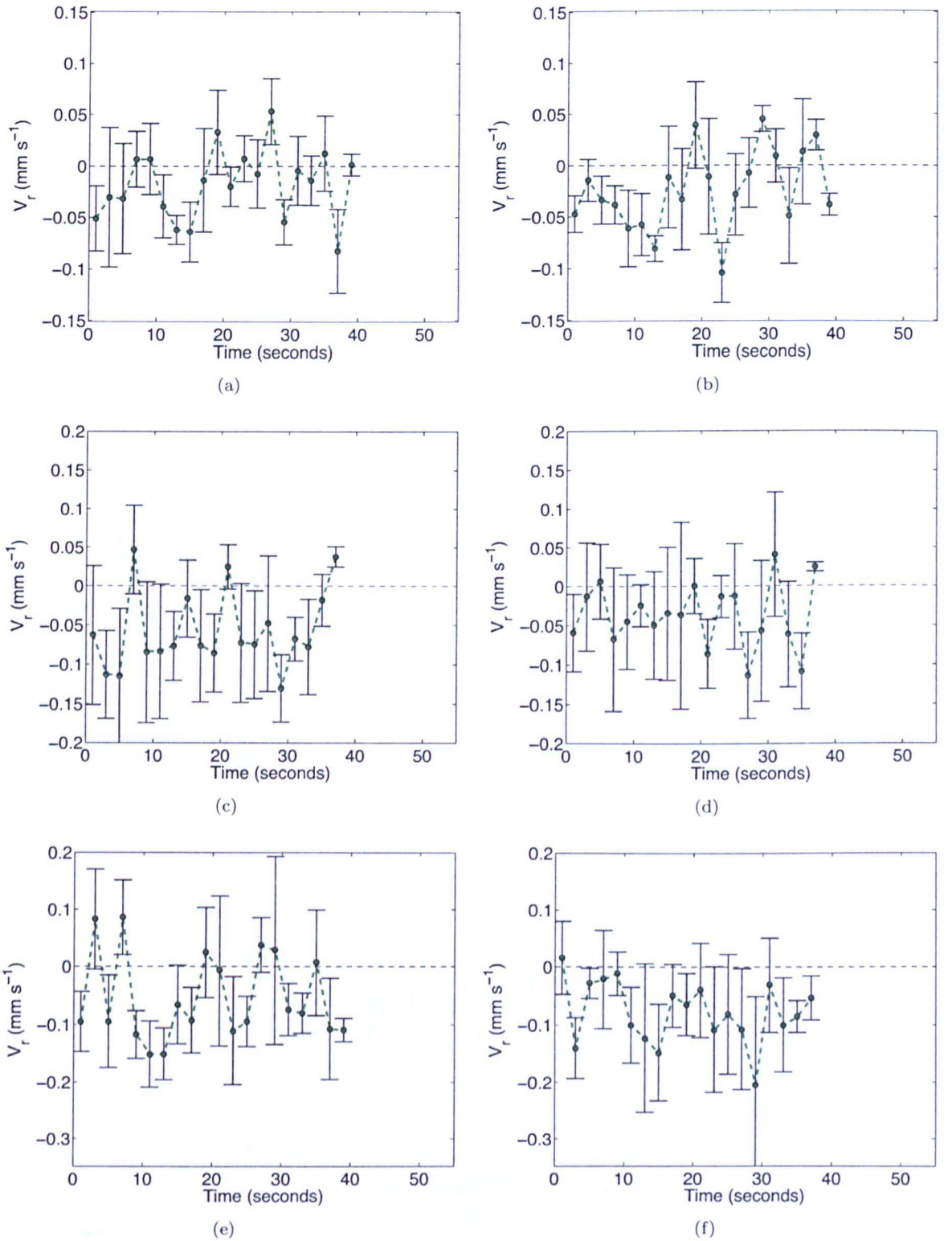

Figure 6.18: **Radial velocity of 3 mm particles as a function of time on the top surface in 1** g - V_r as a function of time for the inner radial bin (of five) during six constant shear rate experiments performed on the ground. Shown are results for experiments with an inner cylinder angular velocity of 0.025 rad s^{-1} (top), 0.05 rad s^{-1} (middle) and 0.1 rad s^{-1} (bottom). Each point represents the mean V_r of the particles in the radial bin during a period of 2 seconds. The error bars represent the standard deviation of V_r in the same time period.

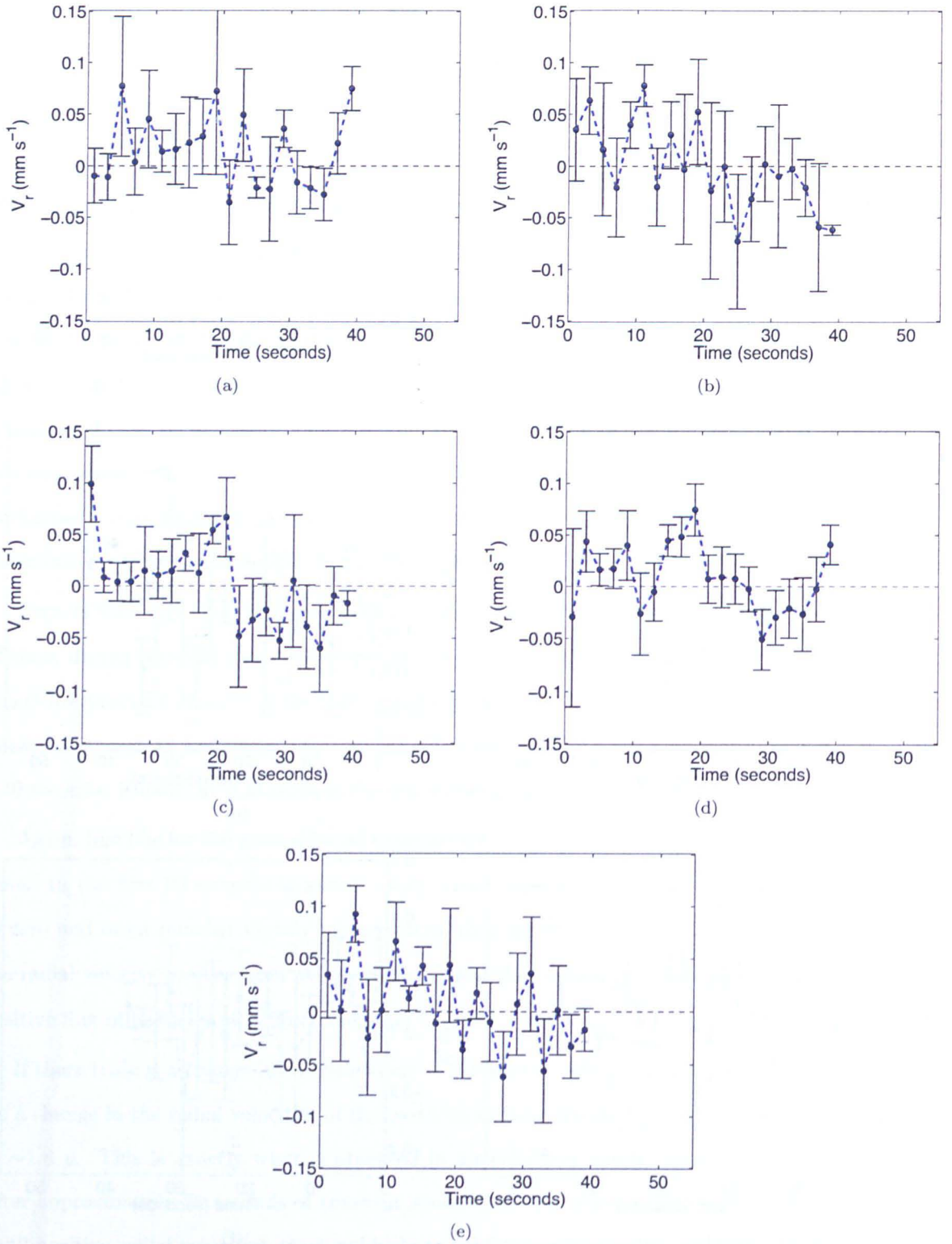

Figure 6.19: **Radial velocity of 3 mm particles as a function of time on the top surface during a parabola with an inner cylinder angular velocity of 0.025 rad s^{-1}** - V_r as a function of time for the inner radial bin (of five) during five constant shear rate experiments performed during parabolas of Flight B. Each point represents the mean V_r of the particles in the radial bin during a period of 2 seconds. The error bars represent the standard deviation of V_r in the same time period. The microgravity period lasts from 0 to ~20 seconds after which there is a period of 1.8 g from ~20 to ~40 seconds. Finally, at $\gtrsim$ 40 seconds the gravitational acceleration returns to 1 g.

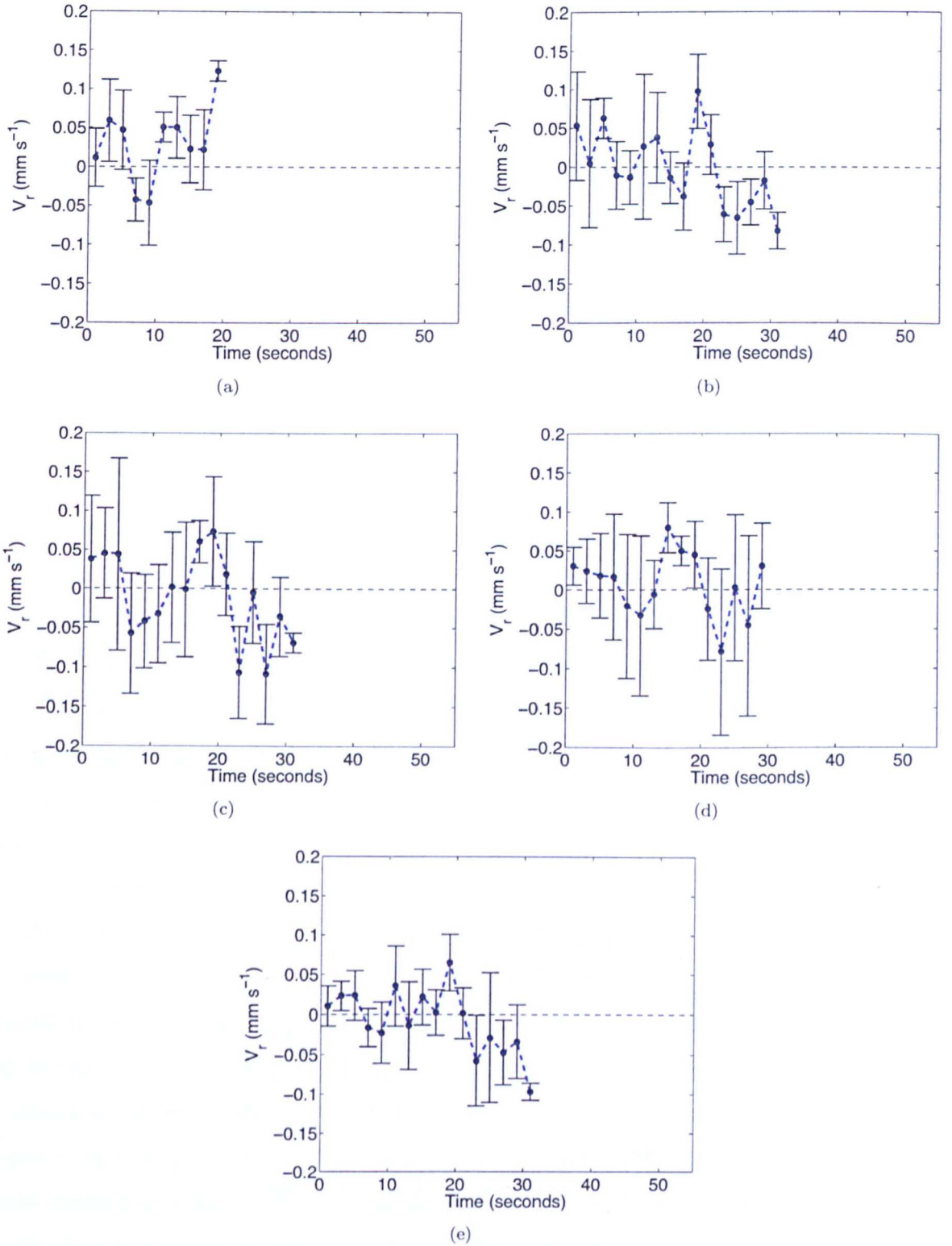

Figure 6.20: **Radial velocity of 3 mm particles as a function of time on the top surface during a parabola with an inner cylinder angular velocity of 0.05 rad s^{-1}** - V_r as a function of time for the inner radial bin (of five) during five constant shear rate experiments performed during parabolas of Flight B. Each point represents the mean V_r of the particles in the radial bin during a period of 2 seconds. The error bars represent the standard deviation of V_r in the same time period.The microgravity period lasts from 0 to ~20 seconds after which there is a period of 1.8 g from ~20 to ~40 seconds. Finally, at $\gtrsim$ 40 seconds the gravitational acceleration returns to 1 g.

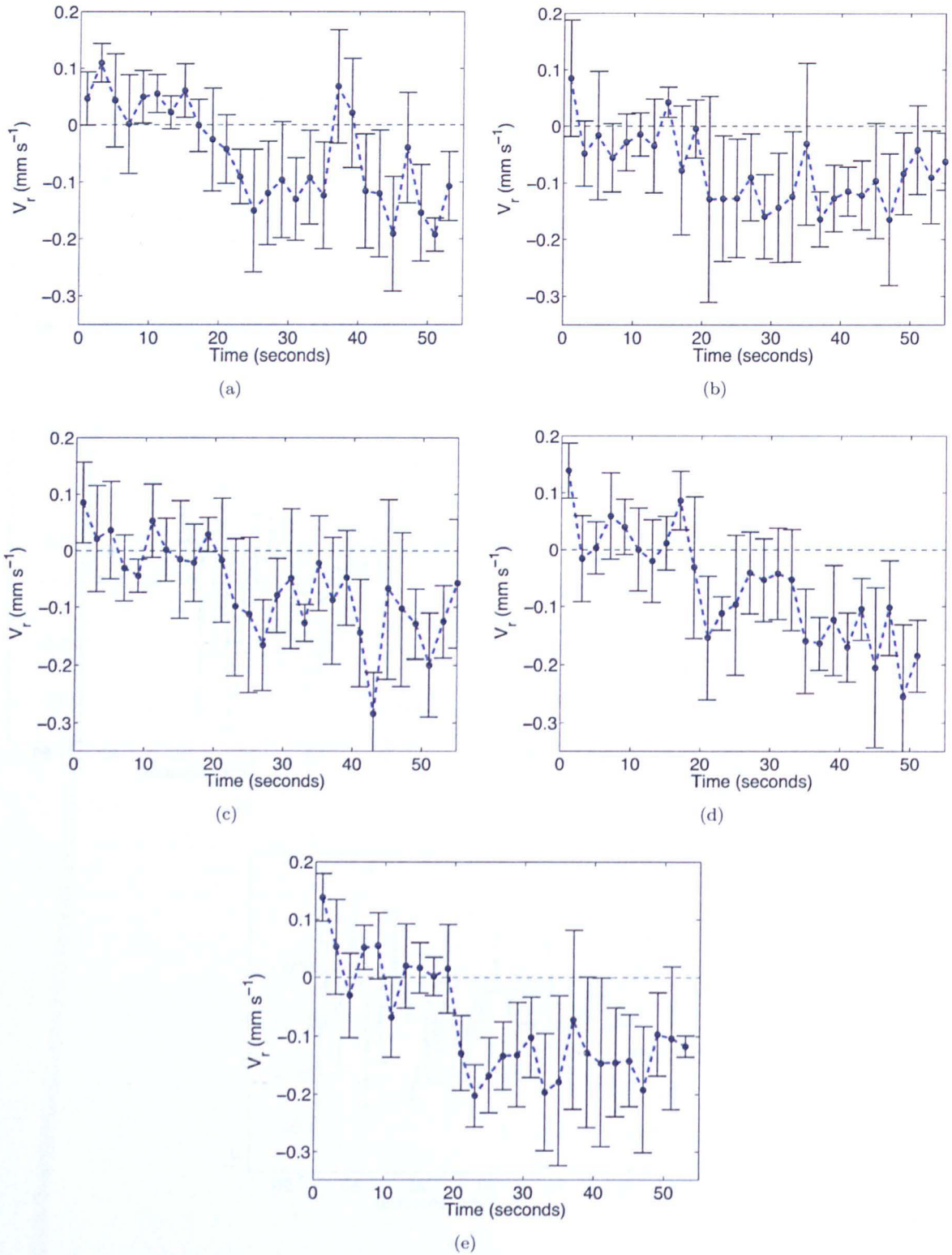

Figure 6.21: **Radial velocity of 3 mm particles as a function of time on the top surface during a parabola with an inner cylinder angular velocity of 0.1 rad s^{-1}** - V_r as a function of time for the inner radial bin (of five) during five constant shear rate experiments performed during parabolas of Flight B. Each point represents the mean V_r of the particles in the radial bin during a period of 2 seconds. The error bars represent the standard deviation of V_r in the same time period. The microgravity period lasts from 0 to ~20 seconds after which there is a period of 1.8 g from ~20 to ~40 seconds. Finally, at $\gtrsim$ 40 seconds the gravitational acceleration returns to 1 g.

6.3.4 Convective-like flows in varying gravitational environments

We have found that, within the shear band of constant shear rate experiments in 1 g, there is a continuous flux of particles towards the inner cylinder. The peak of this inward radial motion occurs in the middle of the shear band. Outside of the shear band, there is a smaller, but still continuous, flux of particles away from the inner cylinder. It has been explained that a net inward flux of particles near the inner cylinder is perhaps indicative of convective-like flows (see discussion above and in Section 4.2). From the results presented above looking at the radial velocity profiles on the top surface and the variation of the radial velocities as a function of time on the top surface, we have concluded that there is a mechanism causing the inward motion of particles in the presence of an external gravitational field and that this mechanism does not act during microgravity. Therefore, there is evidence for possible convective-like flows in ground-based experiments and in experiments performed in $\sim$1.8 g, but not in microgravity experiments.

We can perhaps understand the mechanism driving the convective-like motion of the granular material on the top surface by drawing some similarities with the instability mechanism proposed by Rajchenbach (1991) to explain internal convective motion in a cohesionless granular material submitted to vertical vibrations in the presence of an external gravitational field. Rajchenbach (1991) explains that the RMS velocity fluctuations of particles in a vibrated granular material increases with the decreasing bulk density of the granular material ($\rho(r)$). Invoking the principal of dilantency (i.e., a compacted granular materal must dilate before changing shape, in order to let individual particles move past their neighbours[1]) we can assume that the free surface of the vibrated granular material is the least dense region of the granular material. Also, as the vibrated granular material is compressible in nature, then $dp/d\rho > 0$, where p is the pressure[2]. Therefore, in such a vibrated granular material the pressure, density and RMS velocity fluctuations (V^{RMS}) of the grains depend on their depth (as measured from the free surface). At the free surface the pressure and density will be low but V^{RMS} will be high. The inverse will be true for the grains at the bottom surface. It is then suggested that, as there is an inhomogeneity of V^{RMS}, there is a net flux of particles from highly mobile, less dense regions to more dense regions with lower mobility (Rajchenbach, 1991). In this mechanism the analog of the temperature gradient, which acts on the Brownian diffusion, is the gradient of compactivity.

Consider, in a similar manner, the AstEx experiments performed on the ground. In the shear cell we have a granular material which will dilate as it is sheared. The grains on the top (free) surface will, therefore, be less densely packed than the grains in the bulk of the granular material. We have seen above (Figs. 6.8–6.9), that the RMS velocity fluctuations of the particles near the inner cylinder are

[1] See Section 4.2 for a more detailed discussion of dilatency.

[2] Note that the quantity $c = [dp/d\rho]^{1/2}$ is the velocity of compression waves in the dilated medium constituted of randomly agitated grains (Rajchenbach, 1991).

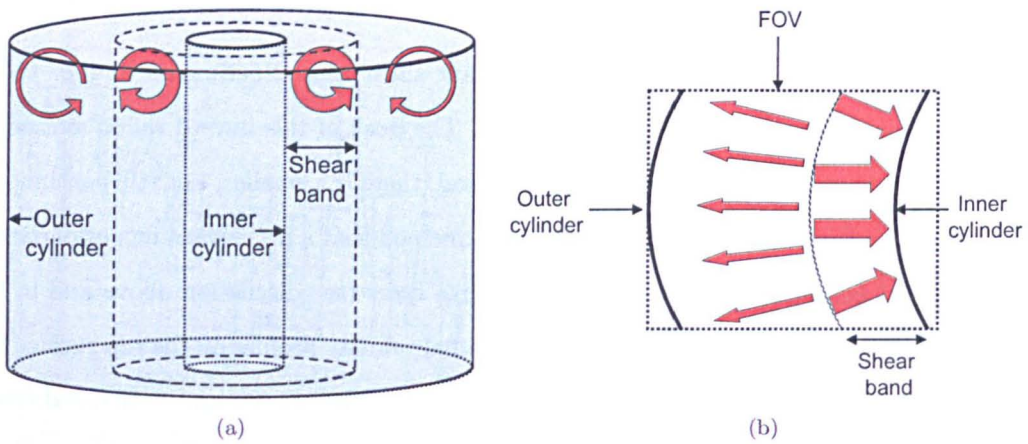

Figure 6.22: **Schematic diagram explaining the convective-like flows in the ground-based AstEx experiments** - Schematic of convective-like flows as viewed from (a) the side and, (b) above, in the field of view of the camera. The red arrows show the direction of particle motion (larger arrows imply a larger flux of particles). On the top surface there is a net inward flow of particles within the shear band and a smaller net outward flow of particles outwith the shear band.

greater on the top surface than on the bottom surface meaning that, in agreement with Rajchenbach (1991), the RMS velocity fluctuations decrease with increasing density and pressure. There is then an inhomogeneity in the RMS velocity fluctuations in the ground-based AstEx experiments. Following the logic presented above there will then be a net flux of particles from the highly mobile, less dense region of the free surface to the more dense regions with lower mobility in the bulk of the granular material. This explains why, in the ground-based experiments, the particles near the inner cylinder appear to be flowing from the top surface into the bulk of the granular material and establishing convective-like flows. The same mechanism will act on our experiment whenever shear is occuring in the presence of an external gravitational field because there will be a pressure and density gradient from the top (free) surface to the bottom surface.

If, as a result of such a mechanism, there is a convective-like flow of particles established within the shear band from the free surface near the inner cylinder into the bulk of the granular material, the particles must resurface some time later. This resurfacing will cause a small upwards flow of particles near the edge of the shear band. Then, upon reaching the surface, the particles will either move towards the inner cylinder, or towards the outer cylinder. This process may initiate a second, smaller convective flow towards the outside of the shear cell. This is illustrated in the schematic in Fig. 6.22 (a). The resulting motion on the top surface, as observed by the camera, would be an inward flux of particles within the shear band and a smaller outward flux of particles outwith the shear band. This is illustrated in the schematic in Fig. 6.22 (b). This may, therefore, explain why we have observed the smaller, but still continuous, flux of particles away from the inner cylinder outside of the shear band.

If this is the mechanism driving the convective-like flows, we can now understand why the inward

radial motion stops when the external gravitational field is removed. In the absence of an external gravitational field the granular material will dilate and the vertical pressure and density gradients will be removed. If the density becomes homogenous from the top to the bottom of the shear cell, the RMS velocity fluctuations should also become homogeneous from the top to the bottom of the shear cell. There no longer exists, therefore, a gradient of compactivity from the top to bottom of the shear cell. Therefore, in the absence of an external gravity field, there is no vertical inhomogeneity and, thus, no net flux of particles from the top surface into the bulk.

However, the granular material in the shear cell will still try to dilate under shear, even in microgravity. In this case, as there is no external gravitational field acting, the granular material can dilate horizontally, away from the shearing surface. This dilation may be responsible for the small, but continuous flux of particles away from the inner cylinder starting at a distance of a few particle diameters and extending to the outer cylinder during constant shear rate experiments in microgravity (see Section 6.3.2).

Interestingly, this dilation will probably create a density gradient from the inner to the outer cylinder with the lowest density region being found close to the inner cylinder. Then, if we have a density gradient in our system we will also have a gradient of compactivity and an inhomogeneity of the RMS velocity fluctuations. This time the gradient of the RMS velocity fluctuations is decreasing horizontally away from the shearing surface, rather than vertically from the free surface into the bulk of the material. This inhomogeneity may then cause a net flux of particles to move from the more mobile, less dense regions of the shear cell near the inner cylinder to the more dense regions with lower mobility close to the outer cylinder and this may, in turn, even cause a convective-like flow to be established from the inner to the outer cylinder.

As the experments we have performed in microgravity are very short (~20 seconds) it is not possible to determine whether the outward motion of particles in microgravity is a transient phase due to the initial dilation of the granular material, or whether, indeed, a convective-like flow has been established in the horizontal direction. It is also still not understood why the peak of the outer radial motion occurs close to the boundary of the shear band and the bulk of the granular material.

6.3.5 Radial motion of particles on the bottom surface

We will now consider the radial motion of the particles on the bottom surface of the shear cell in the varying gravitational regimes. Figure 6.23 shows the normalised radial velocity profiles for the 4 mm and the 3 mm particles on the bottom surface of ground-based experiments. These plots are shown on the same scale as the previous normalised velocity profiles on the top surface (Fig. 6.10). We can see immediately that, for both bead sizes, the scale of motion is much smaller on the bottom surface than

on the top surface. This is probably because the particle motion on the bottom surface is restricted by the weight of the particles situated above, but may also be partly a result of the crystallisation in the bottom surface, which makes it more difficult for particles to move and to rearrange.

The radial motion of the particles on the bottom surface in the ground-based experiments also appears to be random: sometimes the mean radial motion is inwards, and outwards. This implies that there is not a continuous flux of particles in a preferred direction on the bottom surface as we have seen on the top surface. This means that, if a convective cell does exist in the ground-based experiments, it does not extend all the way to the bottom of the shear cell. The small amounts of radial motion on the bottom surface are probably due to random particle rearrangements.

The individual plots of radial velocity as a function of time on the bottom surface of the ground-based constant shear rate experiments (see the Supplementary Material) show the mean radial velocities of the inner radial bin fluctuating above and below zero during constant shearing. This confirms that there is no continuous inward or outward movement of the particles.

Consider now the radial motion of particles in microgravity (Fig. 6.24). Immediately we can see that there appears to be some inward radial motion on the bottom surface during the microgravity phase. However, looking more closely at individual radial velocity profiles on the bottom surfaces in all experiments (see the Supplementary Material) we can see that in some experiments there is a net inward motion but in others there is a net outward motion of the particles. Often there also appears to be a small amount of outward motion immediately next to the inner cylinder (this can also be seen in Fig. 6.24 (a)). At slightly larger distances from the inner cylinder (~2-3 particle diameters), there appears to be some inward motion. Additionally, the RMS velocity fluctuations are, in general, very large for all the microgravity radial velocity profiles on the bottom surface (i.e., the error bars of the individual radial velocity profiles are large). This implies that there is a wide distribution of particle radial velocities during constant shearing in every experiment.

The individual plots of radial velocity as a function of time on the bottom surface of the microgravity constant shear rate experiments (see the Supplementary Material) show, just as in the ground-based experiments, mean radial velocities of the inner radial bin fluctuating above and below zero during constant shearing. Nonetheless, despite the extensive random motion which occurs, there does seem to be a slight preference for particles to exhibit a small net negative radial velocity. This net negative radial velocity often results from one or two large spikes in motion rather than a continuous flux of particles.

Considering closely the normalised radial velocity profiles in Fig. 6.24 we can see that, unlike for the normalised radial velocity profiles on the top surface, there does not seem to be any trend with increasing or decreasing inner cylinder angular velocity.

Recalling the gravitational conditions of the parabolic flight will perhaps help us to understand the origin of this radial motion. Before the microgravity phase begins there is a period of approximately 20 seconds when the simulated gravity is $\sim$1.8 g. During this hypergravity phase the particles in the shear cell will be pressed strongly towards the bottom of the shear cell. Then, when the transition to microgravity occurs the particles will start to move into a relaxed state. The vertical stress will be released but, because of the finite width of the shear cell, the horizontal stress will remain unreleased. The remaining horizontal stress causes a small horizontal flow because, in microgravity, the particles can slide past one another more easily (this horizontal motion cannot occur during 1 g or during the $\sim$1.8 g phase as the particles do not have space to move past one another). Note that this is the exact mechanism that has been proposed by Taguchi (1992) to explain elastically induced convection in vibrated granular materials. The difference is that, in a vibrated granular material, the transition from compressed material to material in free fall occurs every oscillation cycle (provided the acceleration amplitude of vibration is greater than gravity). In our system the parabola provides just one cycle from $\sim$1.8 g to microgravity and back to $\sim$1.8 g. However, during the parabolas with large gravity fluctuations it is possible that mini-cycles of the same effect could occur during the microgravity phase.

In the absence of the moving inner cylinder we would expect the horizontal stress to cause the particles to move away from the cylinder walls into the bulk of the granular material. Note that this is actually what we have witnessed, very close to the inner cylinder, in some experiments. However, in our experiment the material close to the inner shearing cylinder will be more dilate that the material further from the inner cylinder (again, due to Reynold's dilatency principle). It is possible that the less densely packed beads move more quickly into a relaxed state once the vertical stress is released (i.e., upon entering microgravity). This would mean that the packing density of the beads near the inner cylinder would decrease slightly more rapidly than the packing density of the beads further from the inner cylinder. If the beads near the inner cylinder decrease in packing density they will leave a small volume of space into which other particles can move. This space provides a preferential direction for the horizontal flow of particles further from the inner cylinder. The rate of motion of the particles towards the inner cylinder will depend on the time it takes for the packing of the beads near the inner cylinder to dilate and create the necessary space. This timescale probably depends on the configuration of particles, the inner cylinder rotation rate and on the quality of microgravity.

Another possible explanation for the more rapid dilation of the particle packing near the inner cylinder could be that, during the $\sim$1.8 g phase when the particles are pressed strongly towards the bottom of the shear cell, they rearrange slightly to form a more dense, lower energy, arrangement. However, the particles glued to the inner cylinder will not move. This means that there could be a larger vertical stress on the particles in contact with the glued-on particles. When the transition

from $\sim$1.8 g to microgravity occurs and the vertical stress is removed the particles near the inner cylinder may then move upwards more suddenly than the other particles in the shear cell thus dilating the material near the inner cylinder more rapidly and creating the necessary space for the horizontal motion of particles on the bottom surface.

These are just some possible explanations. Additional experiments (or numerical simulations) would be needed to confirm them or to determine other causes. However, whatever the mechanism acting on the bottom surface, it is not producing the same kind of continuous bulk flow of particles toward the inner cylinder as we have seen on the top surface in the presence of an external gravitational field.

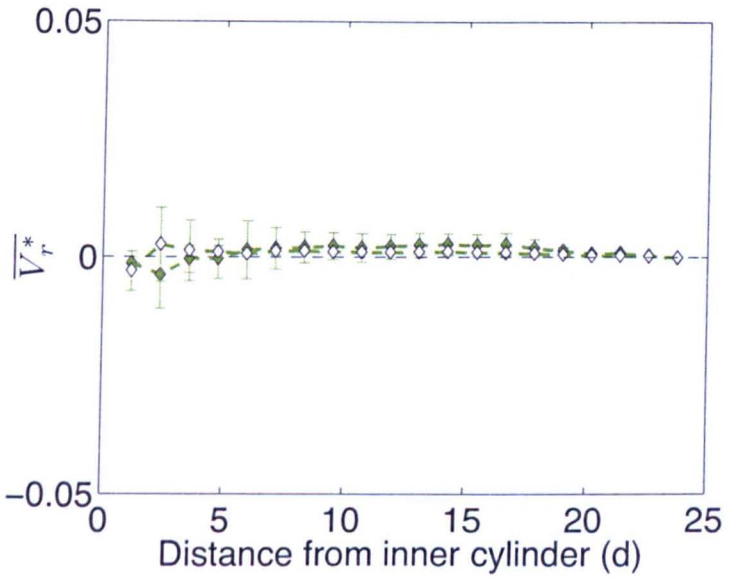

(a)

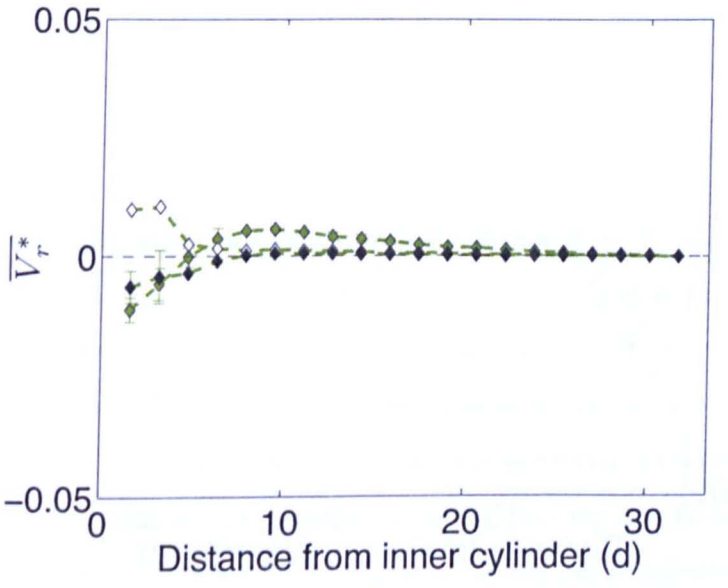

(b)

Figure 6.23: **Normalised radial velocity profiles on the bottom surface on the ground** - $\overline{V_r^*}$ plotted as a function of distance from the inner cylinder for the ground-based experments with (a) 4 mm particles and (b) 3 mm particles. Mean velocity profiles are shown for experiments with different inner cylinder angular velocities: 0.025 rad s^{-1} (solid colour markers), 0.05 rad s^{-1} (open markers) and 0.1 rad s^{-1} (black markers). The error bars represent the standard deviation of $\overline{V_r^*}$ for each group of experiments (i.e., $S3_a$).

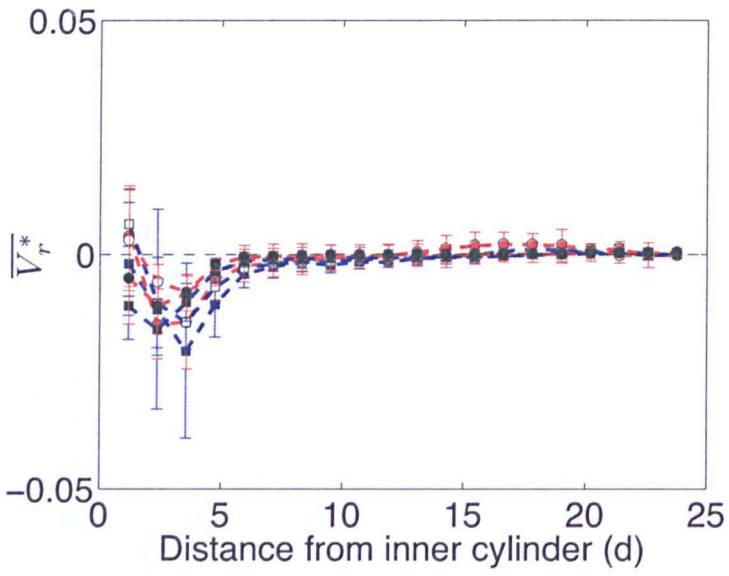

(a)

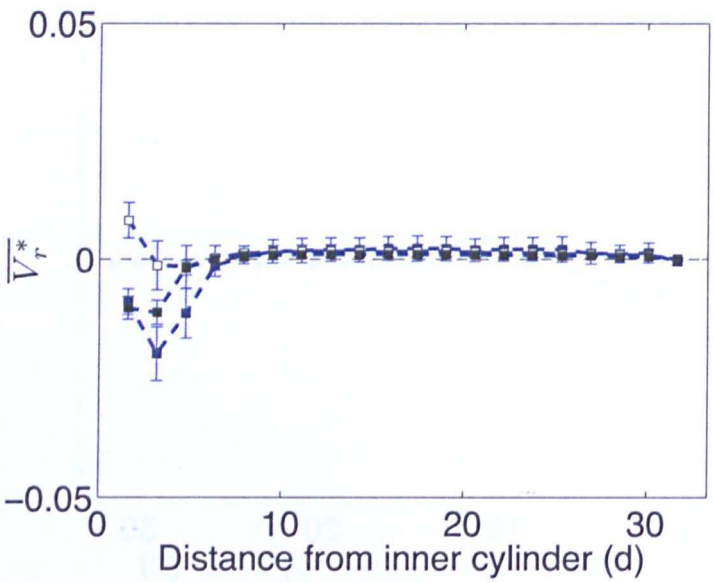

(b)

Figure 6.24: **Normalised radial velocity profiles on the bottom surface in microgravity** - $\overline{V_r^*}$ plotted as a function of distance from the inner cylinder for the microgravity experiments (a) during Flight A (blue squares) and Flight C (red circles) with 4 mm particles and (b) during Flight B (blue squares) with 3 mm particles. Mean velocity profiles are shown for experiments with different inner cylinder angular velocities: 0.025 rad s^{-1} (solid colour markers), 0.05 rad s^{-1} (open markers) and 0.1 rad s^{-1} (black markers). The error bars represent the standard deviation of $\overline{V_r^*}$ for each group of experiments (i.e., $S3_a$).

6.4 Hysteresis of granular material

As discussed in Section 4.2, the flow of granular matter has been shown in previous experiments to be strongly influenced by the network of direct contacts with neighbouring particles (Falk *et al.*, 2008; Toiya, 2006). This contact network, in turn, is shaped by how the material evolved with time. When uniform shear or compression is applied a stronger contact network in the direction of forcing develops. When the shear direction is reversed, or the direction of compression is changed, the material rearranges until it forms a new contact network that can best support the new direction of compression or shear (Falk *et al.*, 2008). This causes a temporary weakening of the granular material and, consequently, regions that normally do not move under steady shear, move significantly during reversal of the shear direction (Falk *et al.*, 2008; Toiya, 2006). This was illustrated in Fig. 4.6 (Section 4.2).

In this section we will first examine whether transient weakening is observed upon shear reversal in the AstEx experiments in 1 g. Then, we will examine whether transient weakening occurs in the absence of gravity. Finally, a technique for quantifying the extent of the transient weakening will be presented and a quantitative comparison will be made of the transient weakening between the gravitational regimes.

6.4.1 Detecting transient weakening after shear reversal

By considering plots of the normalised angular velocity as a function of inner cylinder displacement for each of the radial bins in a shear reversal experiment, we can examine the mean particle angular velocities before and after shear reversal. In Fig. 6.25 an example of a ground-based shear reversal experiment with 4 mm particles is given. The upper plots shows the shear reversal as viewed on the top surface while the lower plots shows the shear reversal as viewed on the bottom surface of the same experiment. The moment when shear reversal occurs is when the angular velocity of the inner (green) radial bin passes through zero. Shown for clarity are both the unnormalised and normalised plots. However, in subsequent analyses only the normalised plots will be considered. Similar plots for every shear reversal experiment performed during the flight campaign can be found in the Supplementary Material.

In the plots of the top surface it can be seen that, just after the point of shear reversal, there is a transient period during which the average flowing velocities in the previously flowing regions are faster. These increased velocities drop off with roughly the same timescale in all regions. However, on the bottom surface the shear reversal does not seem to temporarily increase the angular velocities of the particles.

This would imply that *transient weakening does occur in our experiment on the ground but only on the top (free) surface and not on the bottom surface where the granular material is crystallised and confined by the weight of the beads located above.*

6.4.2 Transient weakening in microgravity

Now we will investigate if transient weakening of the granular material occurs after shear reversal in the microgravity environment. Figure 6.26 shows plots of the normalised angular velocity as a function of inner cylinder displacement for the top surfaces of three example shear reversal experiments performed in microgravity at three different inner cylinder angular velocities. In each of these three plots there is a transient period during which the average flowing velocities in the previously flowing regions are faster. In addition, the regions which were not previously flowing move significantly during reversal of the shear direction. This behaviour is not confined to the regions near the inner cylinder. In fact, particle motion can be observed across the entire width of the shear cell. This is particularly evident in Fig. 6.26 (a).

Figure 6.27 shows the results of the same microgravity shear reversal experiments but this time looking at the bottom surface. Unlike in the ground-based experiment, in microgravity transient weakening is observed on the bottom surface. In the ground-based experiments the weight of beads located above those at the bottom prevents an increased velocity of the particles. However, in microgravity the particles on the bottom surface exhibit larger velocities just after shear reversal as this weight no longer exists.

This means that *transient weakening occurs in our experiment in microgravity on both the top and bottom surfaces. Additionally, shear reversal in microgravity has been seen to induce motion across the entire width of the shear cell, even in previously jammed regions.*

In the next section we will discuss how the extent of transient weakening can be quantified. This will then allow a direct comparison of the behaviour of the granular material under shear reversal in microgravity and on the ground.

6.4.3 Quantifying the hysteresis

Recall, from Section 5.2.8, the *motor start time* is defined as the moment when the mean angular velocity in the inner radial bin reaches (1/5) ω where ω is the inner cylinder angular velocity and the *analysis start time* is defined to be three seconds after the *motor start time.* Here the *shear reversal time* is defined as the moment when the mean angular velocity of the inner radial bin passes through 0 rad s^{-1}.

To quantify the degree of transient weakening occuring in the granular system after shear rever-

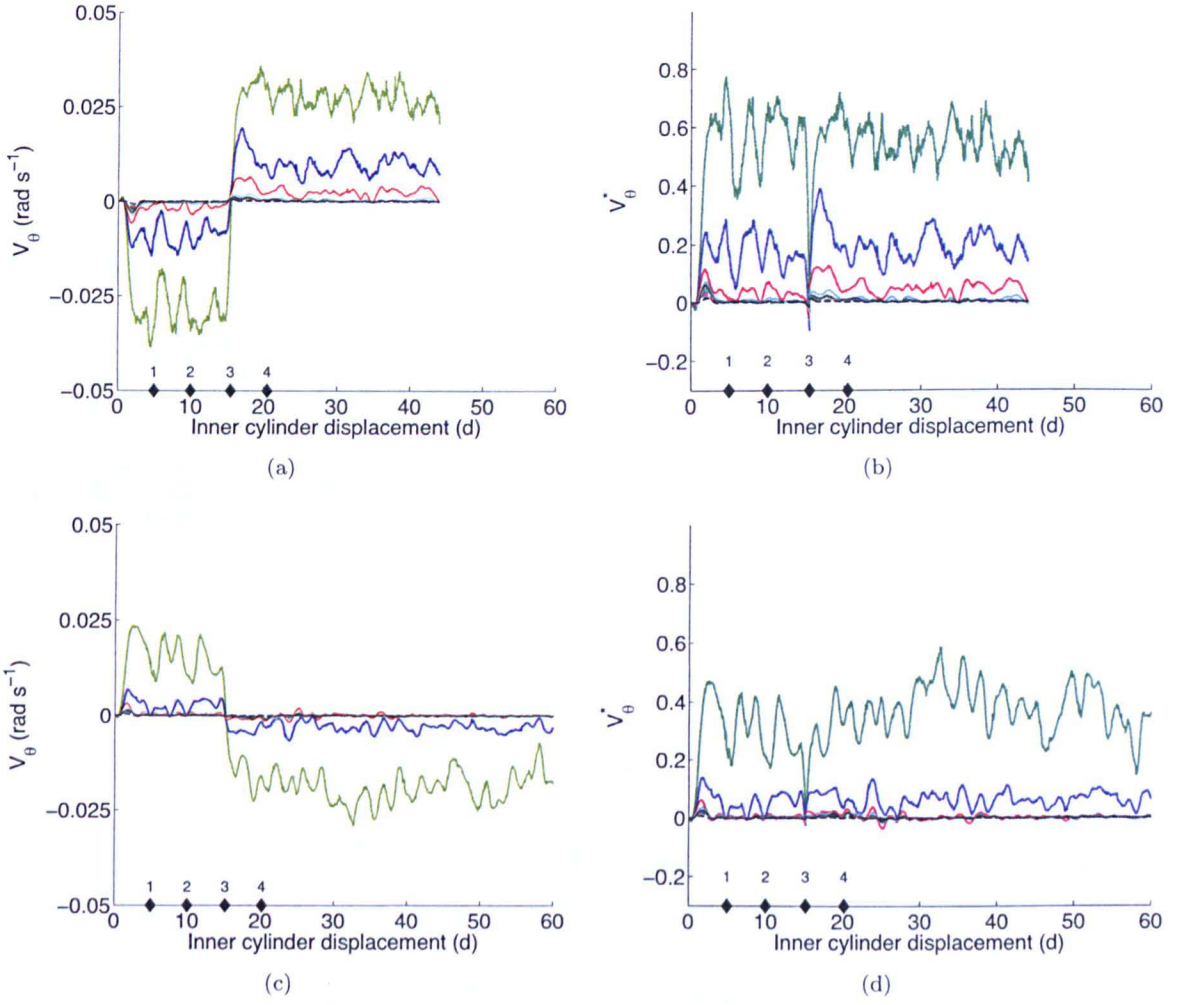

Figure 6.25: **Shear reversal experiment with 4 mm beads in 1 g - V_θ** (left) and V_θ^* (right) for each radial bin versus inner cylinder displacement in particle diameters for shear reversal experiments performed on the ground. (a), (b) Top surface and (c), (d) bottom surface with inner cylinder angular velocity of 0.05 rad s^{-1}. There are ten radial bins for each experiment. The order, from closest to the shearing surface to furthest away: solid green, solid blue, solid red, solid cyan, solid black, dashed green, dashed blue, dashed red, dashed cyan and dashed black. The numbered markers indicate (1) the *analysis start time*, (2) *analysis start time* plus the time required for the inner cylinder to rotate 5 d, (3) *shear reversal time* and (4) *shear reversal time* plus the time required for the inner cylinder to rotate 5 d. If the marker is white (not the case in these examples) this indicates that shear reversal occured before the inner cylinder has rotated 5 d.

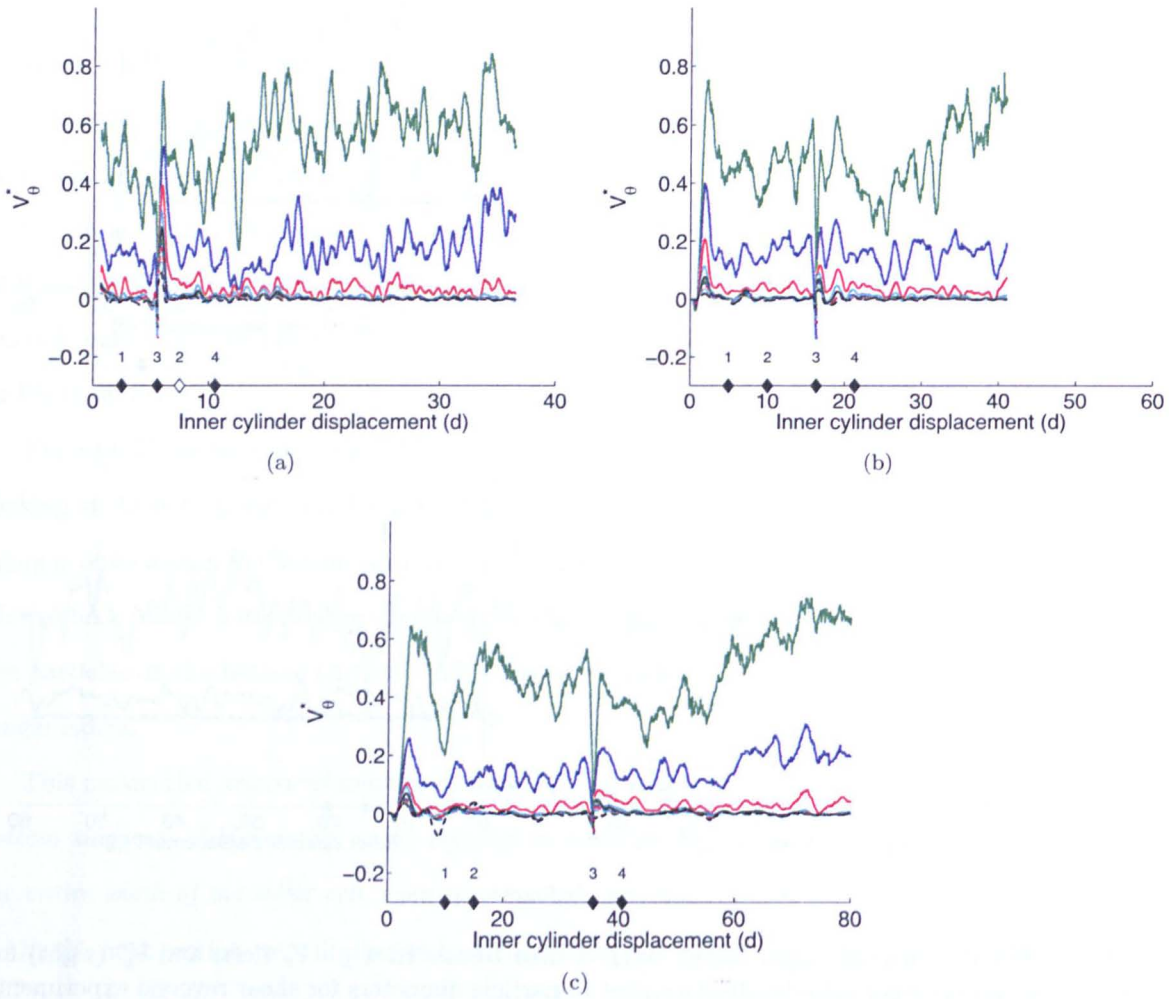

Figure 6.26: **Top surface during a shear reversal experiment with 4 mm beads in microgravity** - V^*_θ for each radial bin versus inner cylinder displacement in particle diameters for shear reversal experiments performed in microgravity. Results are shown for inner cylinder angular velocities of (a) 0.025 rad s^{-1}, (b) 0.05 rad s^{-1} and (c) 0.1 rad s^{-1}. There are ten radial bins for each experiment. The colour code and markers are the same as in Fig. 6.25.

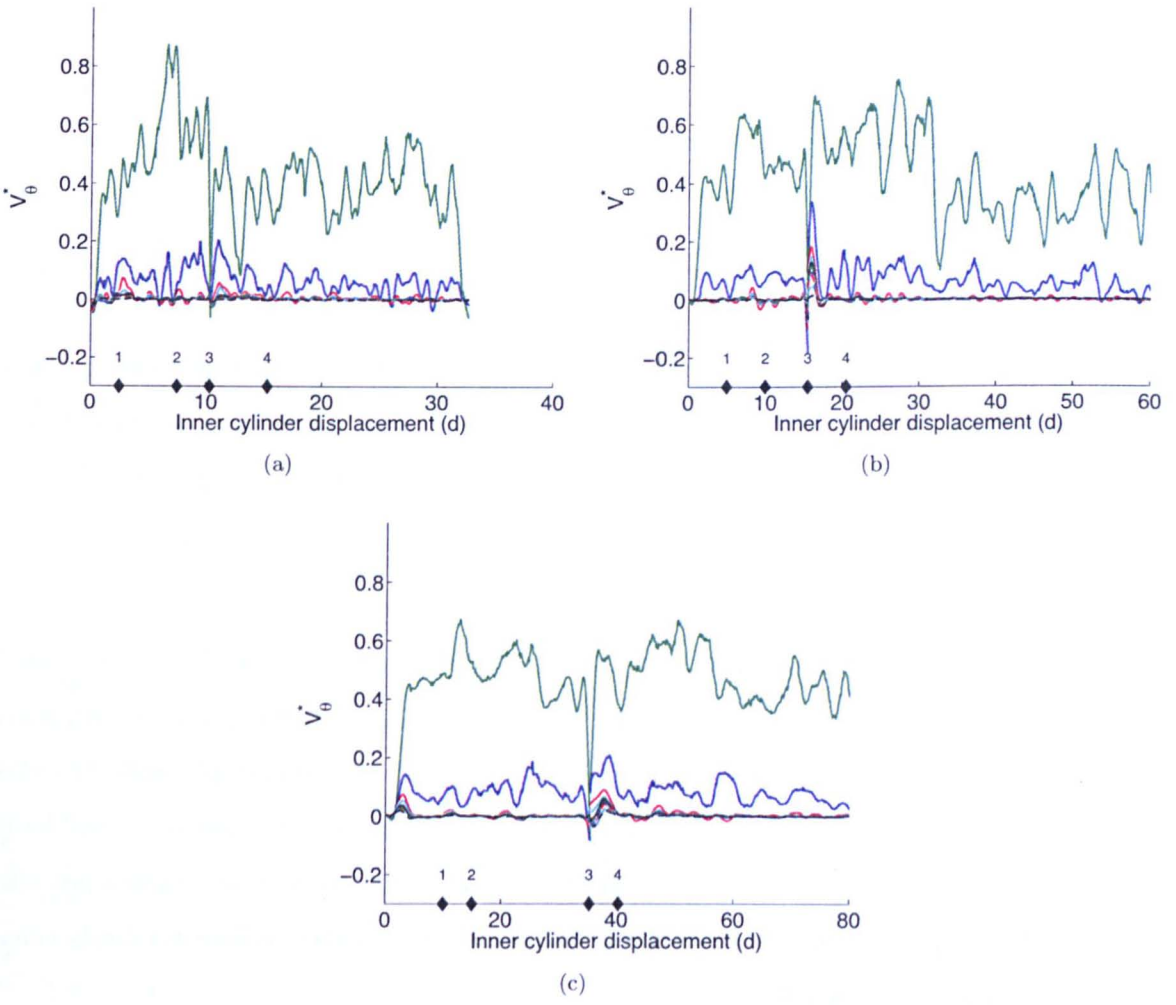

Figure 6.27: **Bottom surface during a shear reversal experiment with 4 mm beads in microgravity** - V_θ^* for each radial bin versus inner cylinder displacement in particle diameters for shear reversal experiments performed in microgravity. Results are shown for inner cylinder angular velocities of (a) 0.025 rad s^{-1}, (b) 0.05 rad s^{-1} and (c) 0.1 rad s^{-1}. There are ten radial bins for each experiment. The colour code and markers are the same as in Fig. 6.25.

sal we first calculate the mean angular displacement travelled by the particles undergoing constant shearing for a strain of five particle diameters i.e., during an inner cylinder displacement of 5 d[1]. This is calculated as a function of distance from the inner cylinder. To calculate the mean angular displacement travelled by the particles the location of each particle at both the *analysis start time* and after the time required for the inner cylinder to rotate 5 d are found (these two times are indicated in Figs. 6.25–6.26 by the markers 1 and 2, respectively). The displacement of a particle is then given by the absolute difference between the two angular coordinates. The particles are then separated into ten radial bins and the mean angular displacement of all particles within the radial bin is found ($S_\theta(r)$).

Next the mean angular displacement is calculated, in exactly the same manner, for the particles undergoing the same strain immediately after shear reversal i.e., starting from the shear reversal time and ending at the shear reversal time plus the time required for the inner cylinder to rotate 5 d (these two times are indicated in Figs. 6.25–6.26 by the markers 3 and 4, respectively).

Finally, the mean extra displacement, L_e, of particles during the transient state just after shear reversal is calculated, as a function of distance from the inner cylinder. This is given by the difference in the mean angular displacements travelled by the particles (for a strain of 5 d) just after shear reversal and during steady state shear. This is the same approach that was used to quantify the scale of the transient weaking in Toiya *et al.* (2004).

Figure 6.28 (a) shows the mean particle angular displacements for a strain of 5 d under constant shearing and immediately after shear reversal for an example ground-based experiment with 4 mm particles and an inner cylinder angular velocity of 0.05 rad s^{-1}. The extra displacement travelled by the particles just after shear reversal is shown in Fig. 6.28 (b). In the example ground-based experiment shown there is a mean extra displacement of $\sim 0.5\ d$ close to the inner cylinder just after shear reversal. Further from the inner cylinder, at a distance of $\gtrsim 7\ d$ there is no extra displacement of the particles after shear reversal.

An identical analysis is performed looking at the bottom surface of the same experiment (Fig. 6.29). In this example we can see that particles on the bottom surface near the inner cylinder have a negative extra displacement. This means that they move less distance just after shear reversal compared to during steady state shear. This agrees with our initial assessment based on the plots of angular velocity as a function of time that transient weakening does occur in our experiment on the ground, but only at the top (free) surface and not at the bottom surface where the granular material is crystallised and confined by the weight of the beads located above.

[1] A strain of 5 d is equivalent to an inner cylinder angular displacement of ~0.2 rad for the 4 mm beads and ~0.15 rad for the 3 mm beads.

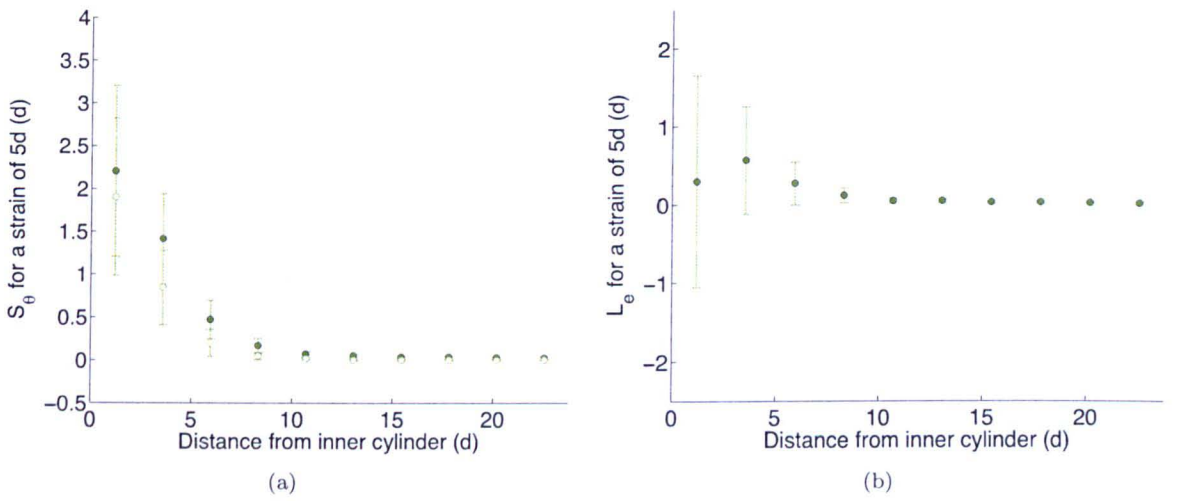

Figure 6.28: **Calculating the extra displacement of particles after shear reversal** - (a) The mean particle angular displacements ($S_\theta(r)$) on the top surface for a strain of 5 d under constant shearing (open markers) and immediately after shear reversal (solid markers) for an example ground-based experiment with 4 mm particles and an inner cylinder angular velocity of 0.05 rad s^{-1}. (b) The extra displacement ($L_e(r)$) of the particles just after shear reversal. The error bars in (a) represent the standard devation of the mean particle angular displacement (equivalent to $S2$). The uncertainties in the constant shearing mean displacement and the shear reversal mean displacement are combined in quadratic to give the error bars in (b).

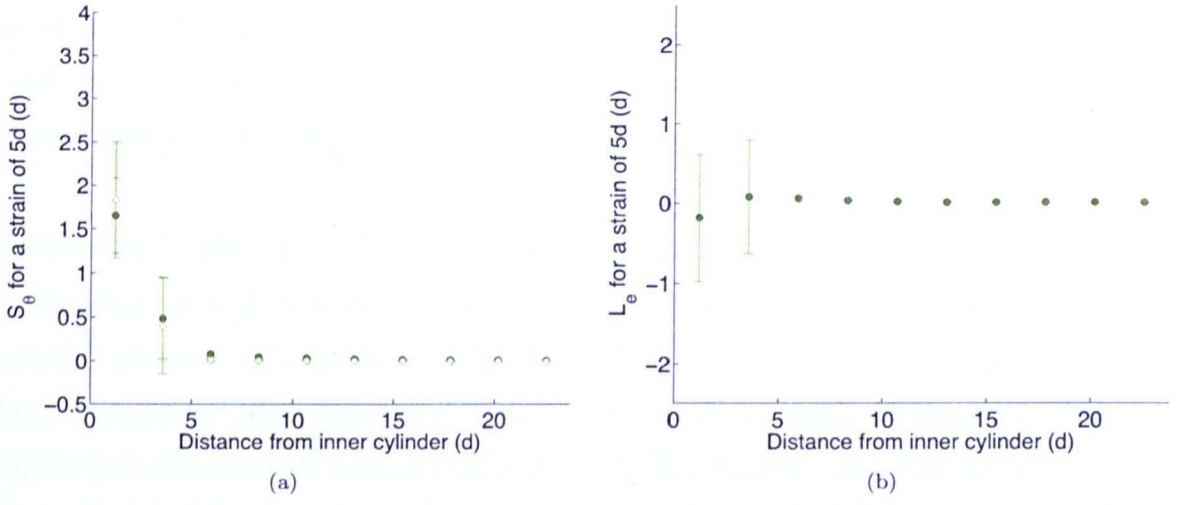

Figure 6.29: **Calculating the extra displacement of particles after shear reversal on the bottom surface** - (a) The mean particle angular displacements ($S_\theta(r)$) on the bottom surface for a strain of 5 d under constant shearing (open markers) and immediately after shear reversal (solid markers) for an example ground-based experiment with 4 mm particles and an inner cylinder angular velocity of 0.05 rad s^{-1}. (b) The extra displacement ($L_e(r)$) of the particles just after shear reversal. The error bars in (a) represent the standard devation of the mean particle angular displacement (equivalent to $S2$). The uncertainties in the constant shearing mean displacement and the shear reversal mean displacement are combined in quadratic to give the error bars in (b).

6.4.4 Hysteresis in varying gravitational environments

The mean angular displacement of particles undergoing a strain of five particle diameters is calculated for all experiments (constant shear rate and shear-reversal experiments in microgravity and on the ground) for which there are sufficient data. In other words, this is calculated for all experiments that neither end before the inner cylinder has moved 5 d, nor in which shear reversal, occurs before the inner cylinder has moved 5 d. The mean angular displacement of particles undergoing a strain of five particle diameters just after shear reversal is also calculated for all shear reversal experiments for which there are sufficient data.

The mean angular displacements under constant shear and after shear reversal are then calculated for each experiment type ($\overline{S_\theta(r)}$). This allows a calculation to be made of the mean extra displacement of particles after shear reversal ($\overline{L_e(r)}$) for each experiment type.

Consider first the extra displacement travelled by particles just after shear reversal for a strain of 5 d on the top surface (Figs. 6.30 and 6.31). Close to the shearing surface the reversal of the shear direction causes a larger extra displacement in 1 g than in microgravity. However, far from the shearing surface, there is a larger extra displacement of particles in microgravity compared to that in 1 g. In fact, in 1 g there is absolutely no movement in the regions far from the inner cylinder just after shear reversal. However, in microgravity we observe motion of the particles across the entire width of the shear cell just after shear reversal. This confirms our initial findings from Section 6.4.2.

This implies that *the spatial extent of the transient weakening is enhanced in the microgravity environment meaning that the transient shear band after reversal of shear direction is wider in microgravity than on the ground. However, close to the shearing surface the transient weakening may be reduced in the microgravity environment.*

Perhaps, due to compression of the granular material in the presence of an external gravitational field, a stronger contact network has formed in the ground-based experiments than in the microgravity experiments. The breaking of a stronger contact network may then cause an enhanced transient weakening compared to the weakening observed in the microgravity experiments. However, it would seem that, although the contact network may be weaker in microgravity, the influence of any change in the contact network may be felt by the granular material over much larger distances. The difference may also be enhanced by a weaker coupling between the granular material and the shear cells walls in microgravity than on the ground.

On the bottom surface of the shear cell (Figs. 6.32 and 6.33) the extra displacement travelled by the particles just after shear reversal for a strain of 5 d is smaller, at all distances from the inner cylinder, for the ground-based experiments compared to the microgravity experiments. Indeed, the extra displacement is often negative close to the inner cylinder for the ground-based results meaning

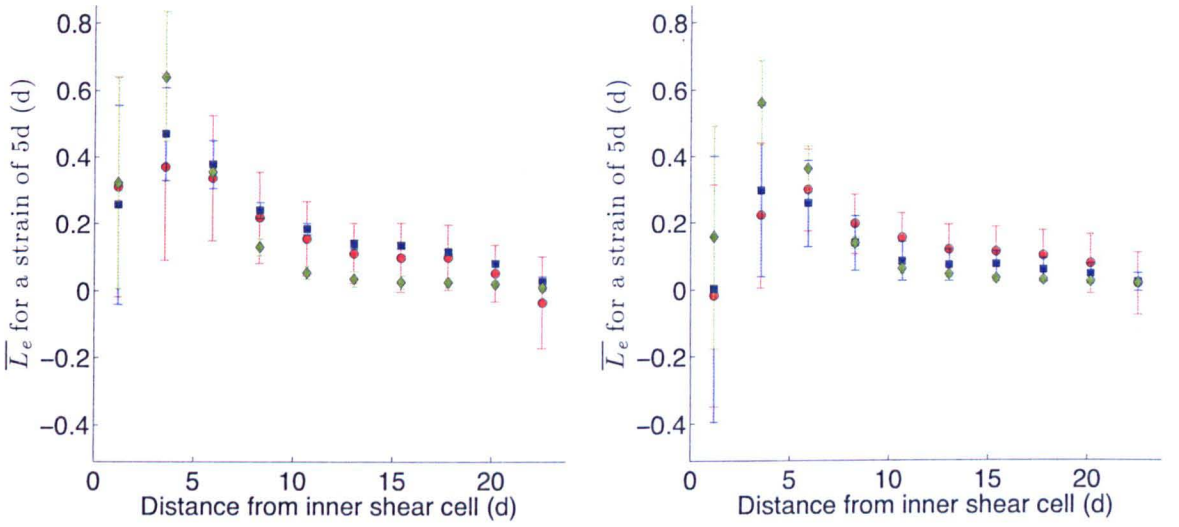

Figure 6.30: **Extra displacement of 4 mm particles on the top surface after shear reversal** - $\overline{L_e}$ as a function of distance from the inner cylinder with an inner cylinder angular velocity of (a) 0.025 rad s^{-1} and (b) 0.05 rad s^{-1}. $\overline{L_e(r)}$ is given for each experiment type: ground-based (green diamonds), microgravity Flight A (blue squares) and microgravity Flight C (red circle). The error bars represent the scatter of $L_e(r)$ between different experiments of the same type (equivalent to $S3_a$).

that the particles in this region move less distance just after shear reversal than during steady state shear. This is probably because, in 1 g, the weight of beads located above the bottom surface is strongly inhibiting the flow of granular material. However, this negative extra displacement is also observed in some of the microgravity experiments (Fig. 6.32 and Fig. 6.33 (b)). It is, therefore, possible that the cause is the crystallised packing of the granular material rather than the weight of the beads.

6.4.5 Transient weakening in hypergravity

Now we will investigate the extent of the transient weakening of the granular material just after shear reversal in the third gravitational environment: the ~1.8 g phase of the parabola. Figures 6.34 and 6.35 show plots of the normalised angular velocity as a function of inner cylinder displacement for the top and bottom surfaces, respectively. The results of three example shear reversal experiments performed in the hypergravity environment at three different inner cylinder angular velocities are shown. In each of the three plots of the top surface a period of transient weakening can be seen. This transient weakening becomes less obvious in the plots of the bottom surface. This is consistent with the 1 g results in which transient weakening was observed on the top surface and not on the bottom surface.

Unfortunately, there is no way of knowing exactly when the transitions from microgravity to hypergravity to 1 g occur[1]. It is, therefore, very difficult to accurately calculate the mean displacement

[1]We could perhaps consider using the plots of radial velocity as a function of time to determine when the regime

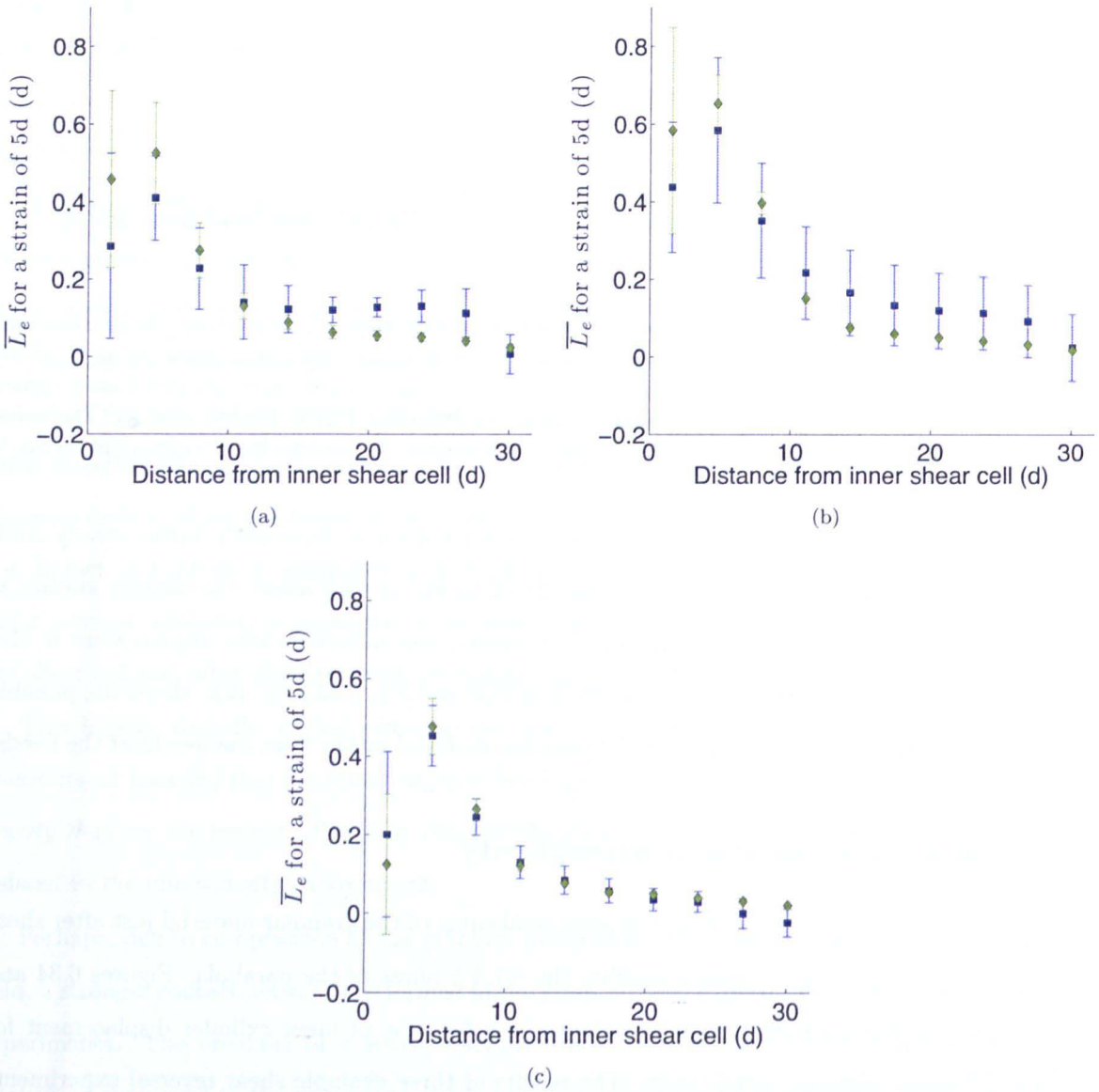

Figure 6.31: **Extra displacement of 3 mm particles on the top surface after shear reversal** - $\overline{L_e}$ as a function of distance from the inner cylinder with an inner cylinder angular velocity of (a) 0.025 rad s^{-1}, (b) 0.05 rad s^{-1} and (c) 0.1 rad s^{-1}. $\overline{L_e(r)}$ is given for each experiment type: ground-based (green diamonds) and microgravity Flight B (blue squares). The error bars represent the scatter of $L_e(r)$ different experiments of the same type (equivalent to $S3_a$).

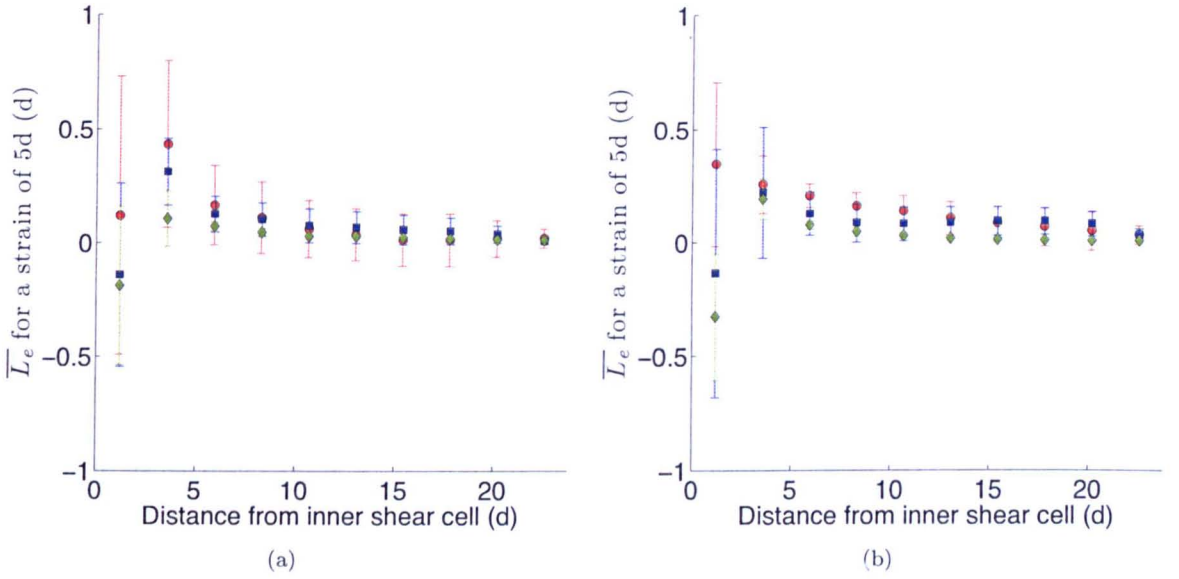

Figure 6.32: **Extra displacement of 4 mm particles on the bottom surface after shear reversal** - $\overline{L_e}$ as a function of distance from the inner cylinder with an inner cylinder angular velocity of (a) 0.025 rad s^{-1} and (b) 0.05 rad s^{-1}. $\overline{L_e(r)}$ is given for each experiment type: ground-based (green diamonds), microgravity Flight A (blue squares) and microgravity Flight C (red circle). The error bars represent the scatter of $L_e(r)$ between different experiments of the same type (equivalent to $S3_a$).

of particles during steady state shear for the ~1.8 g regime. However, we can calculate the mean displacement of particles just after shear reversal in ~1.8 g and compare this to the mean displacement of particles just after shear reversal in 1 g and in microgravity.

The results of this comparison can be seen in Fig. 6.36 for the top surface and in Fig. 6.37 for the bottom surface. The mean displacement of particles just after shear reversal in the ~1.8 g regime is very similar to the mean displacement of particles just after shear reversal is 1 g. By comparing the ~1.8 g and 1 g results to the microgravity results in Fig. 6.36, we can conclude that *when an external gravititational field is present, the particles on the top surface that are close to the inner cylinder move further for a given strain after shear reversal than when there is no external gravititational field present. However, far from the shearing surface, the particles on the top surface move further for a given strain after shear reversal when there is no external gravititational field present.*

Now, by comparing the ~1.8 g and 1 g results to the microgravity results in Fig. 6.37, we can conclude that *the particles on the bottom surface, at all distances from the shearing surface, move less for a given strain after shear reversal when an external gravitational field is present than when there is no external gravititational field present.*

change between microgravity and ~1.8 g occurs but this is not likely to be very accurate given the large fluctuations in such plots.

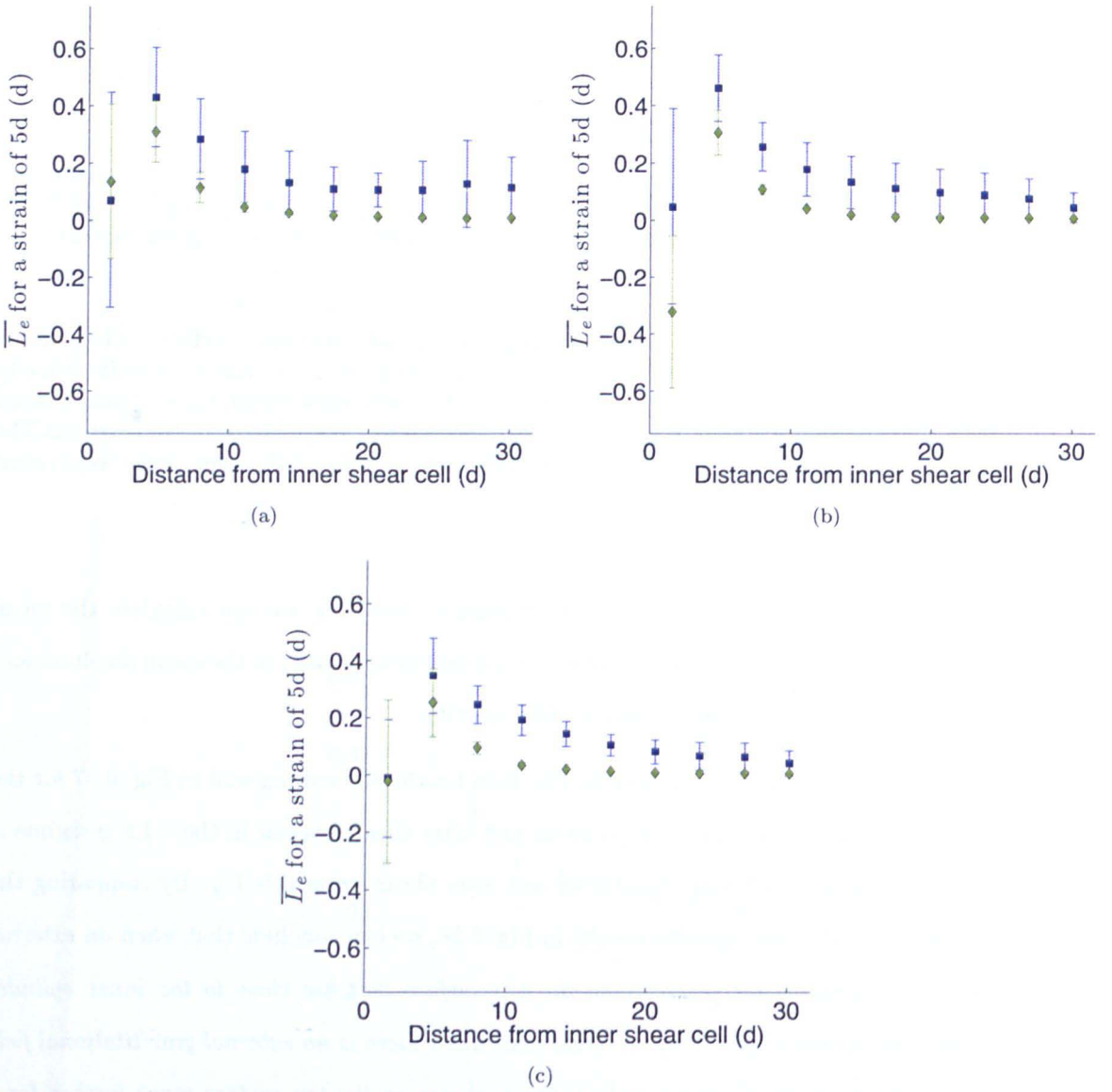

Figure 6.33: **Extra displacement of 3 mm particles on the bottom surface after shear reversal** - $\overline{L_e}$ as a function of distance from the inner cylinder with an inner cylinder angular velocity of (a) 0.025 rad s^{-1}, (b) 0.05 rad s^{-1} and (c) 0.1 rad s^{-1}. $\overline{L_e(r)}$ is given for each experiment type: ground-based (green diamonds) and microgravity Flight B (blue squares). The error bars represent the scatter of $L_e(r)$ different experiments of the same type (equivalent to $S3_a$).

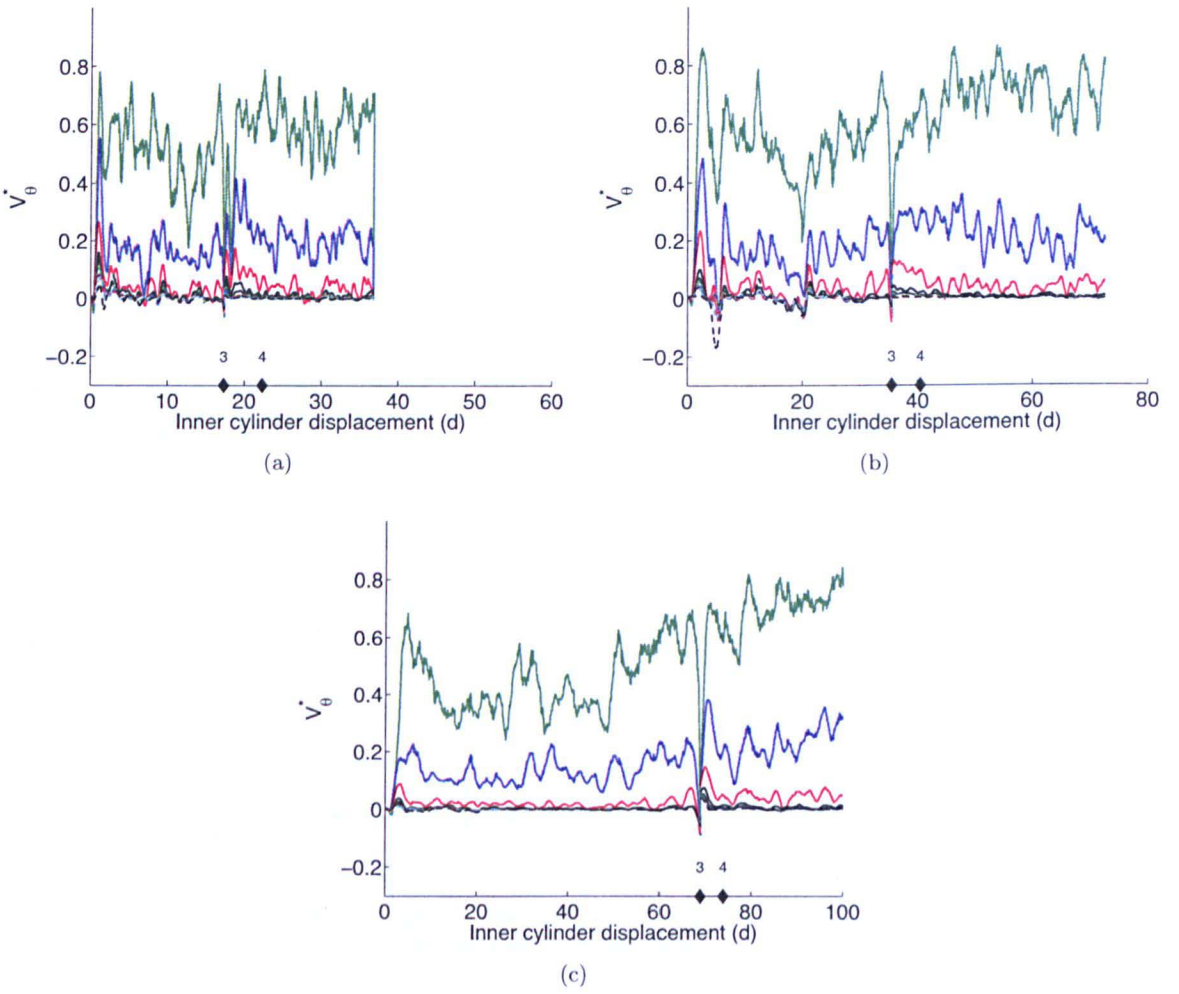

Figure 6.34: **Transient weakening of 4 mm beads on the top surface in hypergravity** - V_θ^* for each radial bin versus inner cylinder displacement in particle diameters during shear reversal experiments performed in hypergravity. (a) Top surface and (b) bottom surface with inner cylinder angular velocity of 0.025 rad s^{-1}. (c) Top surface and (d) bottom surface with inner cylinder angular velocity of 0.05 rad s^{-1}. There are ten radial bins for each experiment. The colour code and markers are the same as in Fig. 6.25.

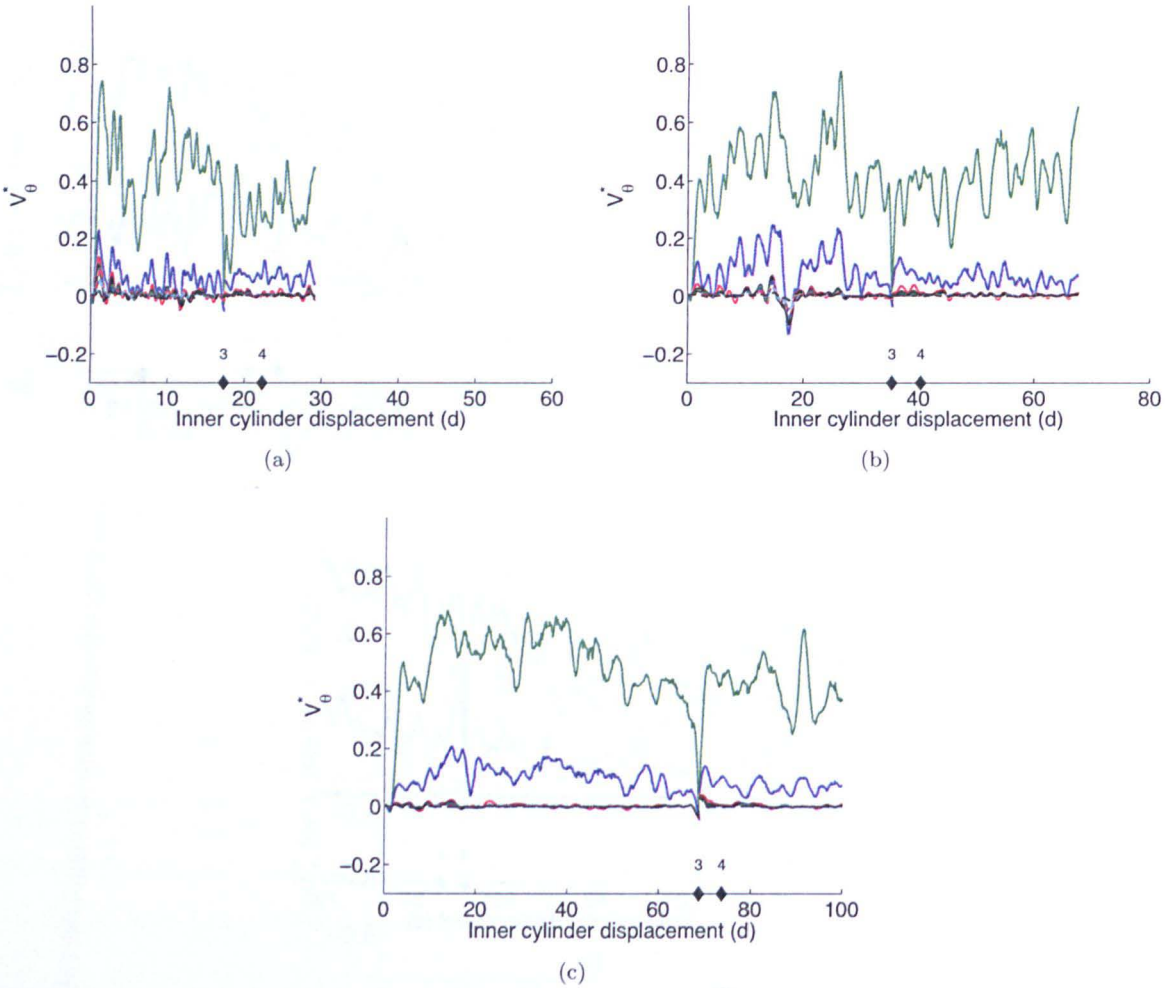

Figure 6.35: **Transient weakening of 4 mm beads on the bottom surface in hypergravity** - V_θ^* for each radial bin versus inner cylinder displacement in particle diameters during shear reversal experiments performed in hypergravity. (a) Top surface and (b) bottom surface with inner cylinder angular velocity of 0.025 rad s^{-1}. (c) Top surface and (d) bottom surface with inner cylinder angular velocity of 0.05 rad s^{-1}. There are ten radial bins for each experiment. The colour code and markers are the same as in Fig. 6.25.

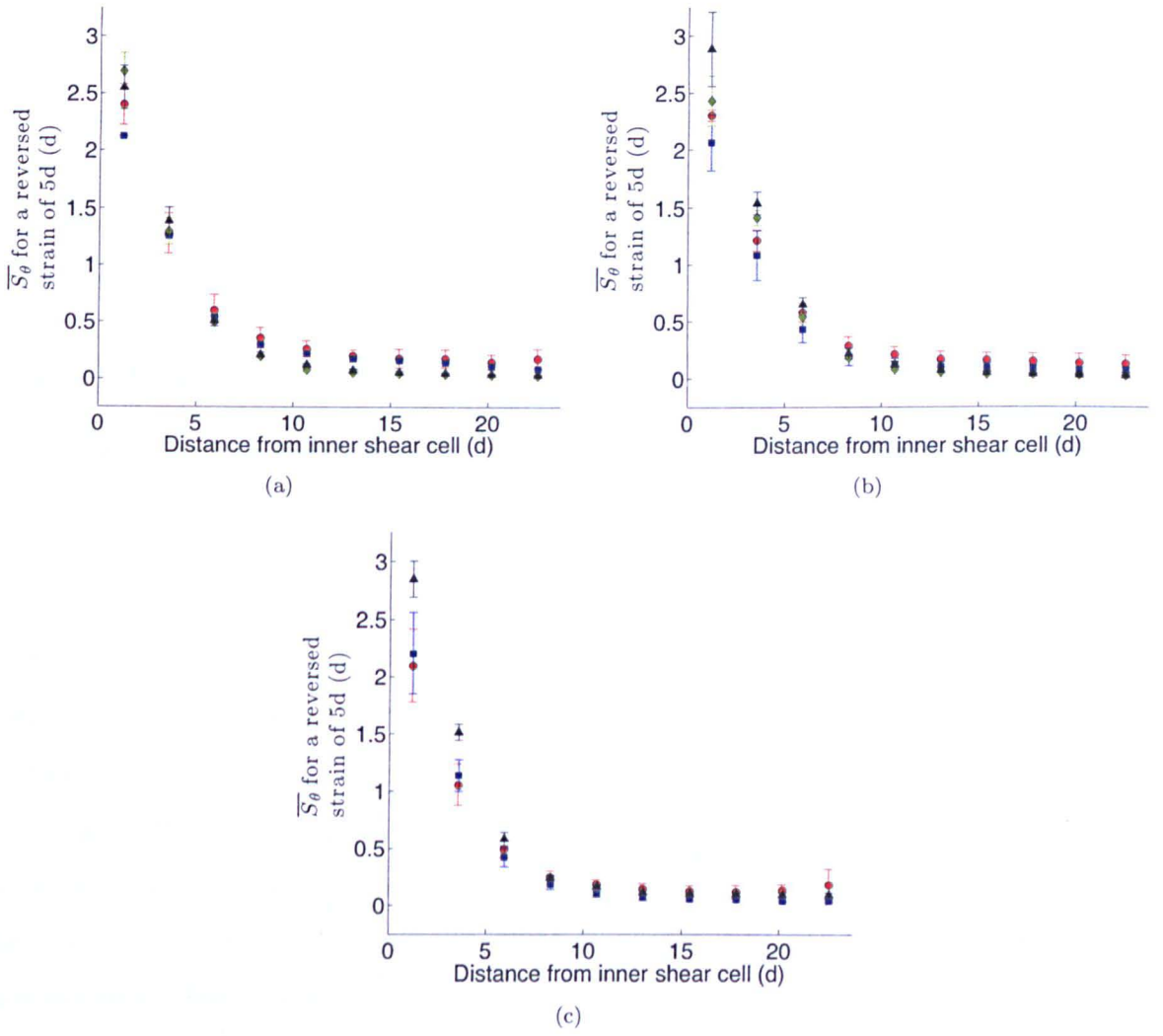

Figure 6.36: **Comparison of mean displacement on the top surface just after shear reversal in three gravity regimes** - Mean displacement of particles for a strain of 5 d just after shear reversal, as a function of distance from the inner cylinder. Results with inner cylinder angular velocities of (a) 0.025 rad s^{-1}, (b) 0.05 rad s^{-1} and (c) 0.1 rad s^{-1} are shown for four different types of experiment: ground-based (green diamonds), microgravity during Flight A (blue squares), microgravity during Flight C (red circles) and during the 1.8 g period of Flight C (black triangles).

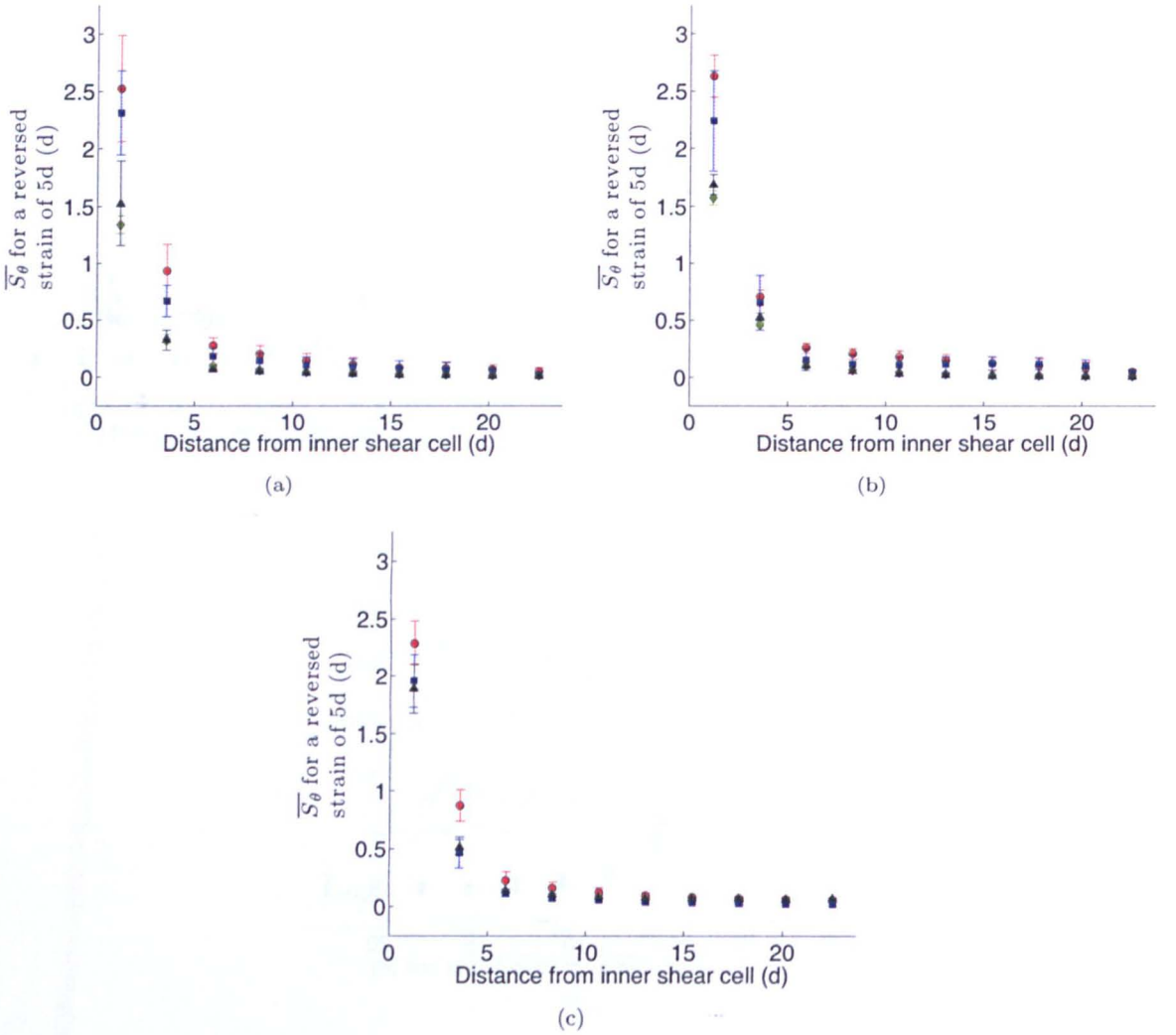

Figure 6.37: **Comparison of mean displacement on the bottom surface just after shear reversal in three gravity regimes** - Mean displacement of particles for a strain of 5 d just after shear reversal, as a function of distance from the inner cylinder. Results with inner cylinder angular velocities of (a) 0.025 rad s^{-1}, (b) 0.05 rad s^{-1} and (c) 0.1 rad s^{-1} are shown for four different types of experiment: ground-based (green diamonds), microgravity during Flight A (blue squares), microgravity during Flight C (red circles) and during the 1.8 g period of Flight C (black triangles).

6.5 AstEx Conclusions

6.5.1 Steady state flow in varying gravitational environments

From ground-based experiments of steady state granular shear we have found that, as in previous experiments (e.g., Behringer *et al.*, 1999; Bocquet *et al.*, 2001; Losert *et al.*, 2000; Mueth *et al.*, 2000), the angular velocity of particles decreases quickly over a few particle diameters away from the shearing wall for experiments performed on the ground and the angular velocity profiles in constant shear rate experiments performed on the ground, normalised by the shear rate, are independent of shear rate. However, from our experiments of steady state shear of a granular material in microgravity we have also shown that the same is true in the absence of an external gravitational field. In fact, in the AstEx experiment, the normalised angular velocity profiles in constant shear rate experiments performed both on the ground and in microgravity are almost identical (except for a few differences caused by the experiment set-up).

Comparisons of the steady state flow on the top (free) surface and on the crystallised bottom surface of the shear cell have confirmed the findings of Daniels & Behringer (2006) who discovered that when a granular material is in the disordered state, the shear band extends several particles. However, while in the crystallised state, the shear is localised almost entirely in the first layer of particles. The AstEx experiment has also shown that a higher packing density of particles reduces both the width of the shear band and the maximum angular velocity of the particles in experiments performed in microgravity.

The mean RMS velocity fluctuations in directions parallel to, and perpendicular to, the mean flow decay as a function of distance from the shearing surface. The mean RMS velocity fluctuations in a direction parallel to the mean flow are comparable for experiments performed both on the ground and in microgravity. The mean RMS velocity fluctuations in a direction perpendicular to the mean flow are smaller for the ground-based experiments than for the microgravity experiments. This difference, and the large differences found in the distributions of particle velocities between individual experiments performed in microgravity, are due to random particle motion caused by the variations in simulated gravity. However, the random particle motion caused by gravity fluctuations does not affect the mean angular velocities averaged over a long time period. Taking all of the above into account we conclude, therefore, that *the effect of constant shearing on a granular material in a direction perpendicular to the gravity field does not seem to be strongly influenced by gravity.*

However, we note that shear depends on many factors, for example, wall friction, the effective pressure forcing particles against the side boundaries, the velocity difference between the particles and the walls and the grain characteristics (e.g., Knight, 1997; Luding, 2008; Mair *et al.*, 2002).

There are many more experiments, or indeed numerical simulations, which could be performed to investigate the influence of these factors in varying gravitational environments. Given the densely packed nature of the granular material in the AstEx experiment the soft-sphere discrete element method implementation in `pkdgrav`, currently under developement, is likely to be the most suitable numerical method.

6.5.2 Convective-like flows in varying gravitational environments

The radial velocity profiles of the particles on the top surface of the experiments on the ground have shown that, *within the shear band of constant shear rate experiments in 1 g there is a continuous flux of particles towards the inner cylinder. The peak of this inward radial motion occurs in the middle of the shear band. Outside of the shear band, there is a smaller, but still continuous, flux of particles away from the inner cylinder.* Experiments in microgravity looking at the top surface of the particles have shown that, instead of having an inward radial motion, *during constant shear rate experiments in microgravity there is a small, but continuous flux of particles away from the inner cylinder starting at a distance of a few particle diameters and extending to the outer cylinder. The peak of this outer radial motion occurs close to the boundary of the shear band and the bulk of the granular material.*

We have examined how the mean particle radial velocities in a region close to the inner cylinder vary in time over the course of a parabola when the simulated gravity changes from microgravity to $\sim$1.8 g to 1 g. From these results it is very clear that *there is a mechanism causing the inward motion of particles on the top surface in the presence of an external gravitational field. This mechanism does not seem to be active in microgravity.*

It has been explained that a net inward flux of particles near the inner cylinder is perhaps indicative of convective-like flows in the granular material (see discussions in Section 6.3 and in Section 4.2). The AstEx results would indicate, therefore, that *convective-like flows are occuring in the presence of an external gravitational field but not in microgravity.* However, it was shown that in the presence of an external gravitational field there is no continuous bulk motion on the bottom surface of the shear cell during constant shear rate experiments. This means that, *if a convective cell exists in the granular material in the presence of an external gravitational field, it does not extend all the way to the bottom surface.*

A possible mechanism driving the convective-like flows has been suggested in Section 6.3.4 by drawing some similarities with the instability mechanism proposed by Rajchenbach (1991) to explain internal convective motion in a cohesionless granular material submitted to vertical vibrations in the presence of an external gravitational field. The grains on the top (free) surface of the experiment are less densely packed and have larger RMS velocity fluctuations than the grains in the bulk of

the granular material (as densely packed granular material dilates during shear). It was suggested that an inhomogeneity of the RMS velocity fluctuations exists, therefore, in the ground-based AstEx experiments and so there is a net flux of particles from the highly mobile, less dense region of the free surface to the more dense regions with lower mobility in the bulk of the granular material. This may explain why, in the ground-based experiments, the particles near the inner cylinder appear to be flowing from the top surface into the bulk of the granular material. The same mechanism will act in our experiment whenever there is an external gravitational field because, in the presence of an external gravitational field, there will be a pressure and density gradient from the top (free) surface to the bottom surface. Finally, the outward flux of particles that is observed outside of the shear band in the ground-based experiments can perhaps be explained by the presence of a second, smaller, convective roll acting in the opposite direction to the inner convective roll (see Section 6.3.4).

We suggest that, in the absence of an external gravitational field, the granular material will dilate and the vertical pressure and density gradients will be removed. Then, if the packing density becomes homogeneous from the top to the bottom of the shear cell, the RMS velocity fluctuations should also become homogeneous from the top to the bottom of the shear cell and there is no longer an inhomogeneity between the top surface and granular material inside the shear cell. This explains why, in the absence of a gravitational field, evidence of convective-like flows is not observed.

An explanation has also been proposed for the small, but continuous flux of particles away from the inner cylinder that has been observed during constant shear rate experiments in microgravity. This mechanism assumes that the granular material in the shear cell will still try to dilate under shear, even in microgravity. In this case, as there is no external gravitational field acting, the granular material can dilate horizontally, away from the shearing surface thus causing the observed outward motion of the particles.

However, it was noted that this horizontal dilation will probably create a density gradient from the inner to the outer cylinder with the lowest density region being found close to the inner cylinder. Then, if we have a density gradient in our system we will also have an inhomogeneity of the RMS velocity fluctuations, which may cause a net flux of particles to move from the more mobile, less dense regions of the shear cell near the inner cylinder to the more dense regions with lower mobility close to the outer cylinder and may even cause a convective-like flow to be established from the inner to the outer cylinder.

As the experiments we have performed in microgravity are very short (~20 seconds) it is not possible to determine whether the outward motion of particles is a transient phase due to the initial dilation of the granular material, or whether, indeed, a convective-like flow has been established in the horizontal direction. It is also still not understood why the peak of this outer radial motion occurs

close to the boundary of the shear band and the bulk of the granular material.

It was also found that *there there is a net, but not continuous, inward flux of particles on the bottom surface of the shear cell during constant shear rate experiments performed in microgravity.* A suggestion was made that this inward radial motion is linked to the vertical and horizontal stresses acting on the particles during the initial $\sim$1.8 g phase of the parabola and during the transition from $\sim$1.8 g to microgravity. More precisely, as the simulated gravity moves from $\sim$1.8 g to microgravity, the vertical stress on the particles will be released. However, because of the finite width of the shear cell, the horizontal stress will remain unreleased and may cause a small horizontal flow. The preferred direction of this flow would be towards the less dense regions of particles near the inner cylinder. This is just a possible suggestion. However, whatever the mechanism acting on the bottom surface, it is not producing the same kind of continuous bulk convective-like flow of particles toward the inner cylinder as we have seen on the top surface in the presence of an external gravitational field.

The mechanisms proposed in this chapter are just some possible explanations for the observed radial motion of particles. There are perhaps other mechanisms at play. Although granular convection in a Taylor-Couette shear cell has been observed several times experimentally (e.g., Khosropour *et al.* (1997), Toiya (2006)) there is no consensus on the mechanism driving such convection. However, several mechanisms, including those discussed in Section 6.3.4, have been proposed to explain the formation of convective flows in a vibrated granular material. For example, it has been suggested that convection in a granular material is directly linked to the interaction of grains with the container walls: reducing the friction of the wall, i.e., reducing the coupling between the particles and the walls, results in reduced convection (Knight *et al.*, 1993). The strong influence of the walls on convective flows has also been demonstrated in two-dimensional numerical simulations of a vibrated granular material by Gallas *et al.* (1992). Savage (1988) proposed that the vibrating base sends 'acoustic' waves upwards through the granular material which create the recirculating flows. These waves 'fluidise' the granular material but are in turn attenuated because of the dissipative nature of the collisions between the 'fluidised' particles. More recently Rodriguez-Linan & Nahmad-Molinari (2006) proposed that granular convection in such a system is driven by shearing internal forces. Nonetheless, as explained by Rodriguez-Linan & Nahmad-Molinari (2006), despite the fact that such granular convection in a vibrated granular material has been studied using particle velocimetry (Garcimartin *et al.*, 2002), magnetic resonance imaging (Nagel, 1992), positron emission tracking (Wildman *et al.*, 2001) and high-speed photometry methods (Garcimartin *et al.*, 2002; Philippe & Bideau, 2003), the underlying mechanism remains poorly understood.

Perhaps the AstEx results will already help the community of granular physicists to move one step closer to developing a more complete understanding of the convective processes occuring in the Taylor-

Couette shear cell. We could also consider performing more microgravity experiments to investigate the convective-like flows in more detail. For example, having faster inner cylinder rotation rates may increase the scale of the granular convection making observation of the radial particle motion easier. Alternatively, we could consider using tracer beads to track the bulk motion. However, it is unlikely that the ~22 seconds of microgravity during a parabola would be sufficient to observe large radial displacements even at higher inner cylinder angular velocities. If this were found to be the most suitable experiment for such an investigation then we should perhaps consider the option of sub-orbital flights, which provide approximately 5 minutes of microgravity time. However, these are not currently available.

Another option is, of course, to use our numerical model to simulate the dynamics of the granular material in our experiment over long periods of time. Three dimensional numerical simulations using the soft-sphere discrete element method implementation in `pkdgrav` would allow an investigation of, for example, the sensitivity of the convective processes to the elasticity and friction of particles and the walls, the inner cylinder rotational velocity and the varying gravity.

6.5.3 Hysteresis in varying gravitational environments

We have observed the occurence of hysteresis, in the form of transient weakening just after the reversal of shear direction, in three different gravitational regimes: 1 g, ~1.8 g and microgravity. By considering the mean extra displacement of particles just after shear reversal, i.e., the difference in the mean angular displacements travelled by the particles (for a strain of 5 d) just after shear reversal and during steady state shear, we have been able to quantify and compare the extent of the hysteresis in the different gravitational regimes.

We have observed that, close to the shearing surface, the reversal of the shear direction causes a larger extra displacement in 1 g than in microgravity. However, far from the shearing surface, there is a larger extra displacement of particles in microgravity compared to that in 1 g. This implies that *the spatial extent of the transient weakening is enhanced in the microgravity environment meaning that the transient shear band after reversal of shear direction is wider in microgravity than on the ground. However, close to the shearing surface the transient weakening may be reduced by the microgravity environment.*

From the experiments of shear reversal, looking at the bottom surface, we have observed that *the particles on the bottom surface at all distances from the shearing surface move less for a given strain after shear reversal when an external gravitational field is present than when there is no external gravititational field present.* In addition, the extra displacement on the bottom surface is often negative close to the inner cylinder for the ground-based results meaning that the particles in this region move

less distance just after shear reversal than during steady state shear. This negative extra displacement is also observed on the bottom surface in some of the microgravity experiments and, therefore, it is probable that the cause is the crystallised packing of the granular material rather than the weight of the beads located above the bottom surface.

By comparing the mean displacement of particles just after shear reversal in ~1.8 g, 1 g and microgravity we have found that *when an external gravititational field is present, the particles on the top surface that are close to the inner cylinder move further for a given strain after shear reversal than when there is no external gravititational field present. However, far from the shearing surface, the particles on the top surface move further for a given strain after shear reversal when there is no external gravititational field present.*

We have have also shown that, *the particles on the bottom surface at all distances from the shearing surface move less for a given strain after shear reversal when an external gravitational field is present than when there is no external gravititational field present.*

It was suggested that, perhaps, compression of a granular material in the presence of an external gravitational field increases the coupling of the granular material to the walls and creates a stronger contact network between the particles than in microgravity. *The breaking of a stronger contact network may then cause an enhanced transient weakening in the presence of an external gravitational field, with respect to the transient weakening that may occur in microgravity. However, it would seem that, although the contact network may be weaker in microgravity the influence of any change in the contact network i.e., during reversal of shear direction, is felt by the granular material over much larger distances.*

6.6 Implications of the AstEx results for asteroids

As mentioned in Section 4.2, granular convection is a process often invoked by the community of small body scientists to interpret the surface geology of asteroids. In fact, Asphaug (2007), state that, "all other considerations aside, granular convective processing is favoured by microgravity". However, the AstEx experiment has demonstrated that granular convection due to density and pressure gradients induced by an external gravitational field in a sheared granular material may actually be less efficient in microgravity. This conclusion was drawn as the convective-like flows which occur in our experiment in the presence of an external gravitational field do not occur during microgravity. Therefore, a weak gravitational acceleration, such as is found at the surface of small bodies, may reduce, rather than favour, the process of granular convection. This means that, in the presence of a weak gravitational field, any granular processes involving granular convection may require much longer timescales than

the same convective processes would require in the presence of a strong gravitational field.

On the other hand it must be noted that most of the discussions related to granular convection on asteroids (Asphaug, 2007; Asphaug *et al.*, 2001; Miyamoto *et al.*, 2007) seem to be focused around processes causing particle size segregation such as the Brazil-nut effect. However, as discussed in Chapter 1 it is not universally agreed that the Brazil-nut effect is caused by convection. The effect is believed by many to be due to mechanism of percolation or sieving: the shaking creates small gaps that are preferentially filled by small particles, the net effect being that the larger particles move upwards. We can imagine that particle segregation, driven by such a mechanism, may occur in the reduced-gravity environments found on asteroids.

It is important, therefore, that the correct terminology is used when discussing granular processes on planetary surfaces. Granular convection, for example, may lead to particle segregation but particle segregation does not always have to be caused by granular convection. Indeed, in Section 1.6.2 some examples are given of the occurence of particle segregation in a granular material which do not depend on convective-like flows. However, many of the other segregation mechanisms proposed (i.e., percolation or sieving) are gravity-driven so we may also expect such mechanisms to become less efficient as the external gravitational acceleration decreases. Indeed, recent numerical simulations of the Brazil-nut effect have shown that the velocity at which a large intruder in a granular material rises is reduced as the external gravity decreases (Tancredi *et al.*, 2011).

Space agencies are planning sample return missions to near-Earth asteroids to bring back to Earth a pristine sample of an asteroids surface e.g., Osiris-Rex and Hayabusa-2 (NASA and JAXA missions, respectively) which have already been selected for flight and MarcoPolo-R, a proposed mission led by ESA. These missions aim at investigating early Solar System processes by applying the vast array of laboratory analytical tools to the returned samples. Their scientific aims are, among others, to link meteorite classes to asteroid classes, and study components (such as interstellar grains, organics and volatiles) that do not survive the atmospheric entry or terrestrial contamination of meteorites. To ensure that the returned samples are unaltered there may be a requirement that the sample should be retrieved from a sufficient depth to ensure large surface temperature variations did not affect it. Also, sufficient sample mass must be returned to satisfy some of the ground-based laboratory analyses of rare components.

The AstEx experiment has shown that the effect of constant shearing on a granular material in a direction perpendicular to the gravity field does not seem to be strongly influenced by gravity. This means that shear bands can form on asteroid surfaces just as they do here on Earth. The AstEx experiment has demonstrated that transient weakening of granular material occurs during shear reversal in microgravity. This behaviour may, therefore, be exploited to make an asteroid

surface sampling mechanism. For example, to loosen the granular material on the surface of an asteroid a device could be used which reverses the direction of shear from time to time rather than using rotation in purely one direction. This may help to loosen and collect the required mass of regolith more rapidly or in a more power-efficient manner. Similarly, this method could be used to dig deeper into the regolith layer without consuming more power.

However, it must be noted that the transient weakening observed in the AstEx experiment in the different gravitational environments suggests that, perhaps, compression of a granular material in the presence of an external gravitational field creates a stronger contact network between the particles than in microgravity. The breaking of a stronger contact network may then cause an enhanced transient weakening in the presence of an external gravitational field, with respect to the transient weakening that may occur in microgravity. This means that, in the low-gravity environment of an asteroid surface, while transient weakening will still be experienced by the granular material close to the location of shear reversal, it may not weaken the material as much as if the shear reversal occured in the presence of a stronger gravitational field.

However, from the AstEx results, it would seem that, although the contact network may be weaker in microgravity the influence of any change in the contact network i.e., during reversal of shear direction, is felt by the granular material over much larger distances. In the AstEx experiment there was absolutely no motion at all at the outer edge of the shear cell during constant shearing in microgravity (except for the random motion due to the gravity fluctuations). However, just after shear reversal the particles at the very outer edge of the cylinder (i.e., at >30 particle diameters from the shearing surface) moved! This may have very important implications for our interpretation of asteroid surfaces. If, for instance, a rubble pile asteroid has undergone shear forces in one particular direction for some period of time e.g., due to tidal forces from planetary encounters (Bottke & Melosh, 1996) or YORP spin up (Bottke *et al.*, 2002b) (see Section 1.2), a very extended contact network may develop. Then, if an event was to occur which shears the surface in a different direction e.g., an impact (Holsapple *et al.*, 2002; Paolicchi *et al.*, 2002) the consequences could be incredibly long range.

Perhaps, then, a small event, e.g., a meteorite impact, on one side of a small rubble pile asteroid could destabilise regolith on the other side of the asteroid causing a granular flow. This would occur, not necessarily via seismic shaking, but via the long range transmission of forces through the contact network. This could mean that the asteroid surfaces are even more unstable than previously imagined. However, this also means that the consequences of, e.g., a meteorite impact, may be very different depending on the impact angle and location, and depending on the prior history of the asteroid surface.

The AstEx experiment has found some exciting results but, clearly, there is much more work still to be done. There still remain several important, but unanswered questions. Some examples of such

questions are given below.

- What is the mechanism driving convective-like flows in a Taylor-Couette shear cell filled with granular material?
- What is the minimum pressure/density gradient required to foster convection?
- We must also consider that, on an asteroid, granular flows are not necessarily confined to the surface. In that case, the lithostatic pressure gradient from the surface to the interior of an asteroid may provide the necessary pressure gradient[1]. What is the smallest asteroid for which the lithostatic pressure gradient is sufficient to foster convection?
- Can granular convection occur in the absence of a gravitational field if there is a gradient in the granular temperature?
- In the AstEx experiment the effect of shear reversal was felt across the entire shear cell. How extended can the force chain network be in microgravity? Over what distance can any changes in the force network be felt?
- Another important point that must be noted is that all of the above conclusions were found in an experiment in which confinement exists. What happens when there is no confinement?

Many of these questions cannot be answered by experiments. Luckily with `pkdgrav` we have the appropriate numerical tool.

[1] Ignoring the rotation of the body, a spherical asteroid with a constant bulk density of ρ has pressure P at a distance r from the center:

$$P(r) = \frac{2\pi}{3} G\rho^2 (R^2 - r^2) \tag{6.1}$$

where G and R are the gravitational constant and the radius of the body, respectively (e.g., Scheeres *et al.*, 2010).

Chapter 7

Conclusions

Granular materials (regolith) are extremely common at the surface of all solid planetary bodies. There is also evidence that this regolith is very complex and continues to be dynamically active. Therefore, the dynamics of granular materials are involved in many aspects of the evolution of solid bodies. Understanding the physics of this granular material is important for the interpretation of spacecraft observations (images, spectral observations, or topography) but is also critical for the design and operations of landers, sampling devices and rovers.

This thesis had two key components, both of which aim to increase our understanding of granular dynamics in varying gravitational conditions. The first component was dedicated to the validation of a numerical code to model the dynamics of granular material in varying gravitational environments such as on asteroids, Mars and the Moon. The second component focussed on the AstEx parabolic flight experiment with the aim of characterising the response of granular material to rotational shear forces in a microgravity environment.

More precisely, the first component focused on validating the hard-sphere discrete element method implementation in the parallel N-body code `pkdgrav` to simulate the dynamics of granular material. A key strength of this numerical tool is the capability to model granular material in varying gravitational environments. The granular dynamics modifications that were made during this thesis were reported in Chapter 2 and have been published (Richardson *et al.*, 2011). The modifications consist primarily of providing wall "primitives" to simulate the boundaries of the experimental apparatus. Certain primitives can also have translational or rotational motion, although to a limited extent. With this wide range of boundary conditions ("walls") we are able to represent the different geometries involved in experimental setups, but more generally provide the needed particle confinement and possible external forcings, such as induced vibrations, for small-scale investigations of regolith dynamics in varying gravitational environments (different surface slopes, etc.). Our approach is designed to be general and flexible: any number of walls can be combined in arbitrary ways to match the desired configuration without changing any code, whereas many existing methods are tailored for a specific

geometry.

Before we can simulate granular interactions on planetary bodies, the simulations must first be able to reproduce the dynamics of granular materials in more idealised conditions and match the results of existing laboratory experiments. As part of this thesis, several validation tests have been performed to demonstrate correct dynamic behaviour of the granular assembly as modelled with our numerical method. One simple validation test investigating granular flow in a tumbler was presented in Chapter 2 and were included in Richardson *et al.* (2011). The observed behaviour in our tumbler simulations shows that the code correctly models the transitions from global regimes with increasing tumbler rotational velocity. However, it was found that this numerical approach currently favours dilute or fluid flows over dense granular flows.

Next, as a stringent test of the numerical code the complex collective ordering and motion of granular material was investigated by direct comparison with laboratory experiments (see Chapter 3 and Murdoch *et al.*, 2012a). In these simulations a layer of granular material is vibrated between two plates. By performing a detailed comparison with experimental results it was demonstrated that the new adaptation of the parallel N-body hard-sphere code `pkdgrav` has the capability to model accurately the key features of the collective motion of a granular material (consisting of two different particle sizes) as a result of shaking. An in-depth discussion highlighting the difficulties involved in comparing experimental and simulation data directly was also included. These validation exercises have demonstrated that the hard-sphere implementation in `pkdgrav` is valid for modelling granular material in dilute regimes and is also capable of reproducing the dynamical behaviour of a specific dense system.

Previous studies have shown that collective motion is an indicator of fragility, which is particularly important to planetary bodies as it is potentially related to the onset of sudden fracture or failure events on the body. The sensitivity of our numerical simulations to variations in self-gravity and external gravity was also investigated in Chapter 3 and it was found that external gravity changes collective behaviour: ensembles of particles exhibit more collective motion and, therefore, appear more fragile when held in place by lower external gravity. The results, therefore indicate that decreasing the external gravitational acceleration makes the granular ensemble more fragile when subjected to local excitation amplitudes i.e., it is more prone to sudden, avalanche-like failure.

The second major component of this thesis, the AstEx parabolic flight experiment, flew in the ESA 51st Microgravity Research Campaign in November 2009 after being selected though ESA's highly competitive 'Fly your Thesis' progamme. The AstEx experiment, the first of its kind, investigated granular flow caused by shear forces in a microgravity modified Taylor-Couette shear cell. The experimental design, development and data analysis were all performed as part of this thesis. The full

experimental design was reported in Chapter 4 (and in Murdoch *et al.*, 2012b) and the data analysis pipeline was presented in Chapter 5. In Chapter 6 three detailed investigations were performed. The first investigation examined how steady state granular flows induced by rotational shear forces differ in microgravity and on Earth. The second investigation considered if granular convection occurs in our granular system on the ground and, if it does, to determine if the convection is enhanced or reduced in microgravity. The third and final investigation considered if hysteresis (memory effects), that leads to a transient weakening of the granular material after shear reversal, are enhanced or reduced in the microgravity environment.

Through the AstEx experiment, we found that the effect of constant shearing on a granular material in a direction perpendicular to the gravity field does not seem to be strongly influenced by gravity. Additionally, convective-like flows seem to occur in the AstEx experiment in the presence of an external gravitational field but not in microgravity (see Murdoch *et al.*, 2012d). The AstEx experiment has, therefore, demonstrated experimentally for the first time that granular convection is less efficient in microgravity. Therefore, a weak gravitational acceleration, such as the one found at the surface of small bodies, may reduce the process of granular convection. This means that, in the presence of a weak gravitational field, any granular processes involving granular convection may require much longer timescales than the same convective processes would require in the presence of a strong gravitational field. These results contradict previous hypotheses which suggest that "granular convective processing is favoured by microgravity" (Asphaug, 2007).

The AstEx experiment has also demonstrated, for the first time, that transient weakening of granular material occurs during shear reversal in microgravity (Murdoch *et al.*, 2012c). However, the transient weakening observed in the AstEx experiment in the different gravitational environments suggests that, perhaps, compression of a granular material in the presence of an external gravitational field creates a stronger contact network between the particles than in microgravity. The breaking of a stronger contact network may then cause an enhanced transient weakening in the presence of an external gravitational, with respect to the transient weakening that may occur in microgravity. This means that, in the low-gravity environment of an asteroid surface, while transient weakening will still be experienced by the granular material close to the location of shear reversal, it may not weaken the material as much as if the shear reversal occured in the presence of a stronger gravitational field.

However, from the AstEx results, it would seem that, although the contact network may be weaker in microgravity, the influence of any change in the contact network is felt by the granular material over much larger distances. This may have very important implications for our interpretation of asteroid surfaces. If, for instance, a rubble pile asteroid has undergone shear forces in one particular direction for some period of time e.g., due to tidal forces from planetary encounters (Bottke & Melosh, 1996)

or YORP spin up (Bottke *et al.*, 2002b), a very extended contact network may develop. Then, if an event was to occur which shears the surface in a different direction e.g., an impact (Holsapple *et al.*, 2002; Paolicchi *et al.*, 2002) the consequences could be incredibly long range. For example, perhaps an event, e.g., a micrometeorite impact, on one side of a small rubble pile asteroid could destabilise regolith on the other side of the asteroid causing a granular flow. This would occur, not necessarily via seismic shaking, but via the long range transmission of force through the contact network. This could mean that asteroid surfaces are even more unstable than previously imagined. However, this also means that the consequences of, e.g., a micrometeorite impact, may be very different depending on the impact angle and location, and depending on the prior history of the asteroid surface.

Chapter 8

Future perspectives

Granular dynamics are involved in a vast number of geological processes and as a result there are countless possible applications to which our numerical simulations could be applied. Landslides, for example, are not considered directly in this thesis, but are of major importance for the resurfacing of many planets, as illustrated by studies of Lajeunesse *et al.* (2010), Lucas *et al.* (2010), Lucas & Mangeney (2007) and Mangeney *et al.* (2007). We could also use our numerical simulations to investigate the scaling laws presented by Hatano (2007, 2008a,b, 2010). These scaling laws consider, for example, the properties of granular rheology near the jamming transition and the dynamical heterogeneity in a sheared granular material. Experimental and technological developments mean that impacts into granular materials can be performed in the laboratory at higher and higher impact velocities (e.g., Kadono *et al.*, 2010). These developments will provide new data for comparison with numerical simulations.

Great advances are being made in robotic planetary exploration and as a result there are many new and exciting space missions being planned to perform detailed investigations of rocky planetary bodies in our solar system. It is important to continue to increase our understanding of the different environments that will be encountered in planetary exploration to help in the design of any space mission (robotic or human), which will interact with the regolith-covered surface of planetary bodies.

All of the current and planned space missions to, for example, Mars, Mercury, Venus and small bodies will return high-resolution images to Earth. These images will provide scientists will more data of landslides, craters, dunes, gullies and many more geological features involving regolith in varying gravitational and environmental circumstances. The study of the physics of granular material will be vital to truly achieve the common scientific objective of all of these planetary science missions, which is to understand the geology of the bodies' surfaces.

Of particular interest is the current idea of a future human mission to a near-Earth asteroid; both

NASA and ESA are investigating the feasibility of such a mission. Before undertaking such a mission it is clear that a full understanding of the threats and dangers to the astronauts must be understood. Many of the risks associated with such a mission arise from the unknown environment, therefore, the greater an understanding we can develop of the asteroid surface and physical properties, the lower the risk involved in a human (or robotic) mission.

8.1 Future code development

The studies presented in Chapter 2 and Chapter 3 aim to evaluate one component of the overall approach, namely the hard-sphere discrete element method. It was demonstrated that the implementation in `pkdgrav` of this approach, which is valid for dilute regimes (e.g., planetary rings), is capable of reproducing the complex dynamical behaviour of a specific dense system as well. The next step will be to validate the implementation of the soft-sphere approach (Schwartz *et al.*, 2012) that is needed for the study of dense systems with many enduring particle-particle contacts.

The soft-sphere method accounts for enduring, multi-particle (>2 particle) contacts by tracking the dynamics of the contacts. In order to model short range interactions such as collisions and contacts between particles, soft-particle methods relate the interaction force between two discrete particles to the overlap of the particles that serves to represent the deformation at contact (Fig. 8.1). Different numerical codes use different force laws to model the interaction. One approach, and possibly the most simple, is to calculate the resulting force using the *linear spring dashpot model* in which the particle contact is viewed as a damped harmonic oscillator and the force model involves a linear repulsive and linear dissipative force (Luding, 2004). However, there are numerous force laws for normal (head-on) contacts that have been proposed in the literature (e.g., Brilliantov *et al.*, 1996; Kuwabara & Kono, 1987; Lee & Herrmann, 1993; Thornton, 1997; Walton & Braun, 1986) and the nature of the corresponding predictions can differ significantly even for simple two-body normal collisions (Shäfer *et al.*, 1996; Stevens & Hrenya, 2005). The effects of static friction and background friction can also be incorporated into soft-particle molecular dynamics and there are models which consider cohesion and thus possible plastic deformations at the point of contact (for a full discussion on these models see Luding, 1998, 2004).

The use of a soft-sphere simulation approach has several advantages. Since it is a force-based simulation, it is easy to augment the physics of interaction to include non-gravitational effects such as cohesion between touching grains (see Section 1.2.6 and Scheeres *et al.*, 2010) as well as exploring the effects of different grain strength and surface roughness models (Sánchez & Scheeres, 2011). As collisions are not predicted in advance, complicated particle and boundary geometries can be imple-

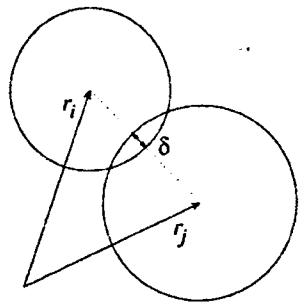

Figure 8.1: **Soft sphere model particle overlap** - Two particle contact with overlap δ. The interaction force depends on the overlap of the particles.

mented. Further, it is possible to simulate and track the transmission of forces through grains (e.g., Goldshtein *et al.*, 2002; Wada *et al.*, 2006).

However, the soft-sphere method also has two important disadvantages: it is difficult to accurately determine values for the numerous input parameters and it is relatively computationally intensive, which limits either the length of a simulation or the number of particles. Several soft-sphere codes take advantage of parallel processing capabilities to scale up the number of particles or length of the simulation (e.g., Cleary & Sawley, 2002; Kačianauskas *et al.*, 2010). Some soft-sphere methods also have the capability to include rotational degrees of freedom, inelastic collisions, and often complicated geometries (including polyhedra; e.g., Cleary & Sawley, 2002; Fraige *et al.*, 2008; Latham *et al.*, 2008; Szarf *et al.*, 2010).

As described in this thesis, in the hard-sphere method all particles are assumed to be perfectly rigid and, in between collisions, the particles move independently of one another. Collisions, which occur when the distance between two particles is equal to the sum of their radii, are treated as instantaneous point-contact events between rigid spheres. In the hard-sphere method the collisions are both binary and instantaneous, therefore, an event-driven algorithm can be employed to resolve collisions by anticipating trajectory crossing. This provides hard-sphere codes with a major time advantage in the resolution of a single collision; what requires dozens of time-steps for a soft-sphere code is resolved by hard-sphere codes in a single calculation (see Fig. 8.2 for a schematic explaining this). However, both methods have their respective strengths; the hard-sphere method permits longer time-steps in the dilute regime (see Section 1.5) and requires fewer material parameters, while the soft-sphere method enables more realistic treatment of friction, and is better suited to true parallelism (Schwartz *et al.*, 2011).

Eventually we would like to develop a hybrid method that includes both the hard-sphere and the soft-sphere approaches. For example, study of granular avalanches on asteroid surfaces could benefit from such hybridisation, since in an avalanche flow, the particles close to the top of falling particle layer, which undergo many collisions, exhibit fast, dilute flows, while particles at the bottom are in

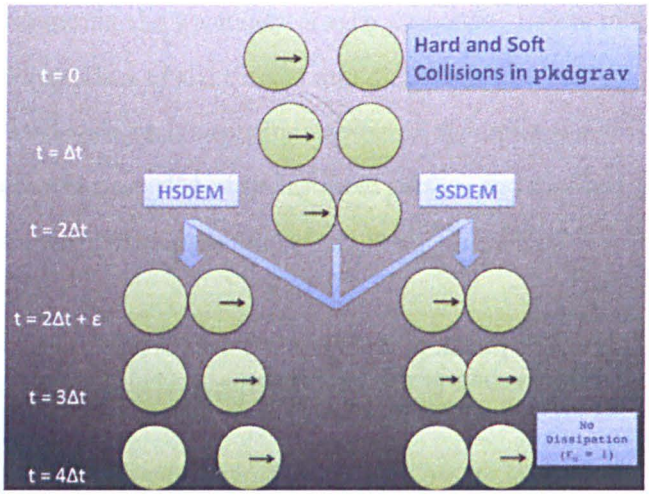

Figure 8.2: **Comparison of collisions in the hard- and soft-sphere methods** - In the hard-sphere method (HSDEM) particles are perfectly rigid and collisions are instantaneous. In the soft-sphere method (SSDEM) particles are allowed to overlap and the interaction force depends on the overlap of the particles. The hard-sphere method has, therefore, a major time advantage in the resolution of a single collision compared to the soft-sphere method. Image credit: S. Schwartz.

slow, dense flows, i.e., particles remain in contact with neighbours for long intervals. In the meantime, the code's ability to create arbitrary shapes through particle bonding, and to vary the external gravity, can still be exploited with the hard-sphere approach to investigate particle motions in dilute and/or highly energised environments. Taking again the example of a granular avalanche, the dilute layer could easily be studied with our hard-sphere approach, as Khakhar *et al.* (1997) did by separating the granular material in a rotating drum into a "rapid-flow region" and a fixed bed. We could also study the evolution of ejecta from impacts or the fluidisation of energised regolith on small-body surfaces, such as regolith motion resulting from the sudden impact of a small projectile on an asteroid's surface, as well as particle ring dynamics (e.g., Perrine *et al.*, 2011), tidal encounters (for which the encounter time is short or comparable to the dynamical time; e.g., Richardson *et al.*, 1998), and so on.

In addition to the implementation of the soft-sphere approach and eventually the hybrid method that switches between both approaches as needed, planned future code development includes adding support for rigid and semi-rigid particle aggregates (see Richardson *et al.*, 2009) that would allow study of more complex particle shapes in simulations of granular dynamics. We will also improve the degree of sophistication of the numerical code by adding new capabilities to model relevant processes such as wind flow. In addition, we would like to include cohesive forces and electrostatic forces into the code. Another planned development is to give particles a thermal expansion coefficient. This would allow the granular material to also respond to different thermal environments. We will also develop the code to be able to model the presence of liquids in between particles. Each new code development will be compared to laboratory experiments before being applied to planetary science applications.

8.2 Future research projects

Some ideas for future projects are discussed below.

8.2.1 Further AstEx experiments

The AstEx experiment worked very well considering it is the first experiment of this kind and produced some very interesting results. However, there are many more experiments that could be performed requiring minimal changes to the current set-up. We would nevertheless strive to implement the design changes listed in Section 4.8.2. Some future microgravity experiments that could be performed include experiments at constant volume as originally planned, or investigating the influence of polydispersity and of varying particle properties (i.e., density, friction). With the added torque sensor we would also have the possibility of considering more closely the influence of changing external gravity on the shear stress.

8.2.2 Numerical simulations of the AstEx experiment

To develop a better understanding of the mechanism driving convective-like flows in a Taylor-Couette shear cell filled with granular material we could perform numerical simulations using `pkdgrav`. As there is no time limit on the simulations, as long as we have access to free CPUs, we can investigate slow but long-term granular bulk flows. By performing simulations with varying external gravity we can investigate if there is a minimum pressure/density gradient required to foster granular convection. We may find that granular convection will always occur if a pressure gradient exists, but the timescales involved are strongly dependent on the external gravity.

8.2.3 Avalanches in varying gravitational conditions

Hofmeister *et al.* (2009) used the Bremen drop tower to test the flow of glass beads at reduced gravity levels of 0.01-0.3 g. A $4 \times 4 \times 15$ cm^3 box of material was housed in a centrifuge, such that terrestrial gravity vanished at drop, allowing 4.7 seconds of microgravity. Different morphologies are observed at the end of drop-tower flight; the horizontal extent of the avalanches decreases with decreasing gravity. As the final angle of repose should be independent of gravity this implies there are some cohesive forces acting on the granular material. We[1] have already performed several simulations with the hard-sphere code to model the case of an avalanche without cohesion (Fig. 8.3). In addition, I have already performed an extensive investigation into the influence of simulation parameters on the angle of repose. In the future we will model the avalanche with cohesive forces between the particles

[1]This work was done in collaboration with Kevin J. Walsh who is currently at the Southwest Research Institute, Boulder, Colorado, USA.

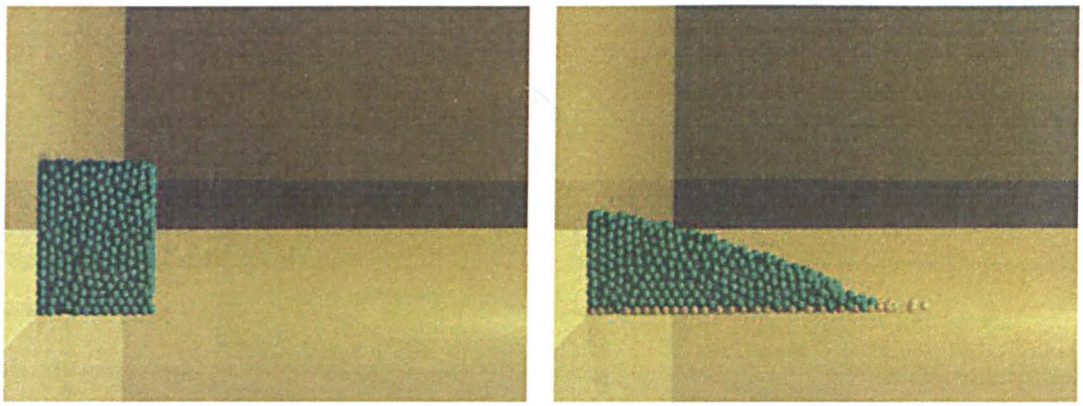

(a) (b)

Figure 8.3: **An example avalanche simulation** - (a) The intial particle locations; (b) the final particle locations after the avalanche. The residual gravity in this example is 0.1 g.

in order to help to explain the experimental results and to advance our understanding of the role of cohesion in granular flows in low gravity environments.

8.2.4 Compaction of asteroid regolith

As described in Chapter 1 asteroids experience both seismic shaking and large temperature variations. Also mentioned in Chapter 1 is the fact that granular materials experience compaction due to thermal cycling and gentle shaking. The final packing fraction of the compacted granular material is strongly dependent on the rate of thermal cycling or tapping. It would be very interesting to investigate how compact the regolith of an asteroid may be. This could be done experimentally, or with numerical simulations, using estimates of the thermal cycling rates and seismic shaking properties available in the literature. It would also be interesting to study if the rate of compaction changes with varying external gravity.

8.2.5 Ejecta and regolith formation

The debris ejected from an impact crater normally follow ballistic trajectories from their launch position within the final crater. Scaling laws for ejecta velocity profiles on airless bodies were first constructed experimentally by Housen *et al.* (1983). However, scaling laws predicting that small ($D < 70$ km) rocky asteroids should be barren (Housen, 1992), appear to be in contradiction with the presence of regolith on Itokawa (~0.3 km), Eros (~17 km) and all other asteroids visited by spacecraft. Another poorly constrained surface process involving granular material is the formation of secondary craters from the relatively low-velocity impacts of ejecta of a primary crater. As discussed by McEwen *et al.* (2005) it is still unclear whether small craters on Mars and the Moon are dominated by primary impacts or by secondary impacts of ejecta from much larger primary craters. Ivanov (2006) suggests

that if the currently observed meteoroid flux in the Earth-Moon system is approximately the same as in the last 100 Ma then most of the small (<200 m) craters, counted on the young (<100 Ma) lunar surface are primary, not secondary craters. Werner *et al.* (2009) argue that obvious secondary craters can be recognized and eliminated from the counts when making age determinations based on crater counts. However, they also acknowledge that there are sometimes ambiguous situations in which it is not possible to clearly distinguish primary from secondary craters and, therefore, crater counts become more difficult or are impossible. The possibility to identify secondary impact craters and to determine the conditions of their formation is fundamental to improve chronology of solid body surfaces by crater counting.

For high impact velocities large plastic deformation or phase changes of particles may occur and, therefore, our numerical code is not a suitable tool to model this process. Secondary craters, however, are produced via low-velocity impacts into granular material. As the impact velocities are normally lower than the material sound velocity (e.g., a few km s^{-1} for silicates) we can use our numerical tool to investigate the secondary crater formation process in the context of low-velocity impacts. This study would aid in the identification of secondary impact craters on planetary surfaces and contribute to the longstanding controversy about the relative abundances of small primary craters versus secondary craters on the Moon and other solid planetary bodies (Ivanov, 2006; McEwen *et al.*, 2005; Werner *et al.*, 2009).

8.2.6 Crater collapse

During the impact crater formation process the crater cavity passes through several stages arriving at an intermediate morphology called the transient crater. It is so-called because all gravity-dominated craters will undergo some subsequent gravitational collapse and modification immediately after excavation. In small craters the steepest part of the rim collapses into the crater bowl to produce a pool of broken rock in an otherwise unmodified transient crater. Large craters collapse more spectacularly, giving rise to central peaks, wall terraces, and internal rings in still larger craters. These are called "complex"craters (Melosh, 1989). The transition between simple and complex craters depends on $1/g$, suggesting that the collapse occurs when a strength threshold is exceeded. However, the effective strength during collapse is very low: only a few bars, and with little or no internal friction. This behaviour requires a mechanism for temporary strength reduction. Several models for this process, including acoustic fluidisation and shock weakening, have been considered by recent investigations. Acoustic fluidisation, involving vibration of granular material, appears to produce results in good agreement with observations (Melosh & Ivanov, 1999). Wünnemann & Ivanov (2003) have performed 2d hydrocode simulations of crater collapse demonstrating the depth-diameter dependence in

Figure 8.4: **Secondary craters** - THEMIS visible image of Mars showing clusters of irregular shallow craters, perhaps secondaries from a larger crater. The circular bowl-shaped craters (6 are easily seen; the largest is 2 km diameter) are likely primaries. Image taken from McEwen *et al.* (2005).

an acoustically fluidized target. Collins *et al.* (2002) have also used hydrocode simulations to investigate dynamic collapse of the Chicxulub crater. Recent field evidence for acoustic fluidisation in crater collapse (Yokoyama *et al.*, 2011) offers further support for the acoustic fluidisation model. However, a consensus about operating mechanisms during the collapse of impact craters has not been reached. Further study is therefore needed to fully understand softening mechanisms such as acoustic fluidisation. It is possible that to fully understand the process of gravitational collapse and the role played by acoustic fluidisation the particles should be treated distinctly and all collisions between particles should be resolved. We could, therefore, use our numerical method to test the acoustic fluidisation model (in 3d).

8.2.7 Crater degradation

After the initial gravitational collapse described in the previous section there are other processes that shape, modify and remove craters such as wind erosion and subsequent impact cratering due to micro-bombardment, which can destroy or cover up pre-existing craters (de Pater & Lissauer, 2001).

The crater degradation due to gravitational collapse and other modification processes means that the sharp rims of fresh craters become rounded while the interior slopes become shallower. Continued degradation causes a reduction in the height of the crater rim, and infilling produces a broad, flat crater floor at a higher elevation than the original cavity (Craddock *et al.*, 1997). It is, in principle, possible to estimate the age of a crater by determining the maximum slope of the inward crater rims. Qualitatively, the smaller the slope the more degradation has occurred and thus the older the age of the crater (Fig. 8.5). Using the recently released Lunar Reconnaissance Orbiter (LRO) data, Bouley & Baratoux (2011) have been able to study precisely the morphology of small craters ($D < 1$ km) and to observe the diversity of degradation features.

Evidence from Mars Global Surveyor has shown that there has been substantial modification of Martian craters by dust infilling in ancient cratered terrain (Hartmann *et al.*, 1999). We will study the long-term evolution of the crater morphology due to wind erosion, the main agent of crater degradation on planets such as Mars (or Venus). This is very important for the case of Mars, as there is approximately 3.5 Ga of history during which the erosion was limited to wind erosion (and impact erosion). There are many examples of crater degradation under such conditions and in various terrains (sedimentary rocks, massive volcanic rocks, cemented ash deposits, etc.). In particular, the impact craters on the flanks of large shield volcanoes experience very strong and regular catabatic winds every night (Spiga *et al.*, 2011). The wind velocity is well quantified, regular and understood to have been behaving in the same way for billions of years. This particular case, therefore, offers an excellent target for numerical modelling. We can use the known parameters to model the effect of

Figure 8.5: **Crater degradation** - Image of various stages of crater degradation and maximum rim slopes for a crater diameter of 200 m in the Mare Imbrium on the lunar surface. 30° is the slope of a fresh crater and 5° is the slope of an old crater. Image from Bouley & Baratoux (2011).

wind erosions on impact craters of various diameters and compare directly to observations.

Michel *et al.* (2009) estimated the age of asteroid Itokawa (at least ~75 Ma, and maybe as much as 1 Ga) by calculating the time needed to accumulate the observed craters on the asteroid's surface and also taking into account several processes, which can affect crater formation and crater erasure on such a low-gravity object. For instance, impact-induced seismic shaking, which causes the regolith to move, may erase small crater features and thus explain their paucity compared to predictions of dynamical models of projectile populations (e.g., Michel *et al.*, 2009; Richardson *et al.*, 2004). However, the predicted motion of regolith due to seismic shaking has never been explicitly demonstrated. Further work needs to be done investigating and quantifying this effect. The effects of seismic shaking on crater morphology are also interesting for larger bodies such as the Moon. We can perform numerical simulations to investigate directly the scaling laws relating the timescale of crater degradation to the ratio of shaking acceleration to gravitational acceleration. This research is vital to interpret the crater population on asteroids, and the impact cratering history of these bodies.

Another crater modification process we could investigate is the surface modification on small bodies (e.g., asteroids) due to tidal forces during close encounters with the Earth and other planets. It has been proposed that tidal stress on the surfaces of asteroids during planetary encounters is strong enough to disturb and expose unweathered surface grains and is the most likely dominant short-term asteroid resurfacing process (Marchi *et al.*, 2006; Richardson *et al.*, 1998). Recent research has reinforced this theory by demonstrating that asteroids that have had a close encounter with the Earth have fresher surfaces (Binzel *et al.*, 2010). However, the resurfacing predicted to occur during these

close encounters has never been modelled directly. We could investigate, using numerical simulations, the degree of resurfacing that can occur on an asteroid surface during a close planetary encounter.

8.2.8 Testing of asteroid surface sampling devices

As discussed in Chapter 1, the properties of regolith on the surface of asteroids vary greatly from one small body to the other. As we are unlikely to have any information about the surface properties before arriving at the asteroid it is important that the sampling mechanism can deal with a large range of possible surface properties and, in particular, a large range of particle sizes. Several kinds of sampling devices (e.g., cylindrical corers, brush wheels, etc.) can be constructed using the wall primitives available in our numerical method. The individual walls in the numerical simulation can be given rotational or translational motion to mimic the workings of the sampling mechanism. The efficiency of the devices (i.e., how much surface material is captured) could then be tested under different gravitational conditions and for different particle size distributions.

Appendix A

Checklist of procedures during flight

BEFORE 1ST PARABOLA

1. Turn on power
2. Switch on laptops
3. Remove securing strap
4. Start web camera software running
5. DriveSoft2 (Laptop 1 only):
   - 5.1 Add Inverter
   - 5.2 Click on 'All Parameters'
   - 5.3 Click on 'Upload'
   - 5.4 Start active monitoring
   - 5.5 Change motor speed if required
6. Cameras:
   - 6.1 Check settings are correct
   - 6.2 Start camera software
   - 6.3 Select the listed camera
   - 6.4 Take an initial image sequence
   - 6.5 Press any key to continue

AFTER ALL PARABOLAS

1. Turn motor off
2. Laptop 1: Close camera software
3. Close DriveSoft2 Monitor window
4. Laptop 1: Click on 'Offline'
5. Laptop 1: Close the DriveSoft2 software
6. Laptop 1: Stop web cam software
7. Laptop 1: Shut down
8. Laptop 2: Close camera software
9. Laptop 2: Stop web cam software
10. Laptop 2: Shut down
11. Turn off power to experiment
12. Add securing strap

Appendix B

Investigating the particle velocities

As mentioned in Section 5.2.8, all figures of mean particle velocity as a function of time, particularly those of mean particle angular velocity, exhibit large-scale correlated fluctuations. Examples of such fluctuations are shown in Fig. 5.18 and Fig. 5.20. These fluctuations are affecting all particles across the width of the shear cell but the source was unknown. This appendix explains the steps taken to investigate and understand the origins of these large-scale velocity fluctuations. These investigations are mostly focussed around the angular velocities of the particles as they permit the correlated fluctuations to be seen more clearly.

B.1 Investigating the source of the large-scale velocity fluctations

First, it was considered that perhaps an uneven camera frame rate could cause the fluctuations. This could be occuring as some cameras, when recording directly to disk in a windows environment, skip frames or take frames at uneven times. By verifying the camera statistics and checking the frame rate (as output during the experiments) it was determined that this was not occuring. Next, we considered if the fluctuations could be occuring due to a bias in the particle tracking. The variations occur simultaneaously across the entire width of the shear cell and this means that they cannot be due to any localised biasing. Large-scale pixel biasing was checked for and ruled out during the process of particle tracking (see Section 5.2.1). The source cannot be noise either as the fluctuations are too regular and are correlated between the different regions of the shear cell. The in-depth investigations of these fluctuations and conclusions are described below.

B.1.1 Method of binning

To be certain the fluctuations were not being introduced within the analysis an alternative method was developed to calculate the mean particle velocities. This alternative method first calculates the displacement vectors between every set of consecutive frames for each particle (in Cartesian coordinates). This coordinate system is then transformed into polar coordinates (again using the coordinates at the centre of the cylinders, as calculated in Section 5.2.3). The angular displacement, between two consecutive frames, are determined for each particle. The displacements over a defined time interval (e.g., 1 sec) are summed giving total angular displacement per particle, per time interval (i.e., one value per particle, per time interval). Then, as for the nominal method, once the particle displacements have been calculated the particles are then separated into radial bins and the mean particle angular velocity per bin is calculated, as a function of time, during the experiment (Fig. B.1). In this example of a constant shear rate experiment the imaging frame rate was 60 fps. The particle displacements are binned over a time interval of 1 second (i.e., 60 fps). Although much of the high resolution data is lost in comparison with the nominal method the large-scale correlated fluctations across the width of the shear band can still be seen. As we are interested in more high resolution data this method will not be used in future analyses. However, we have ruled out the method of velocity calculation as the source of the fluctuations.

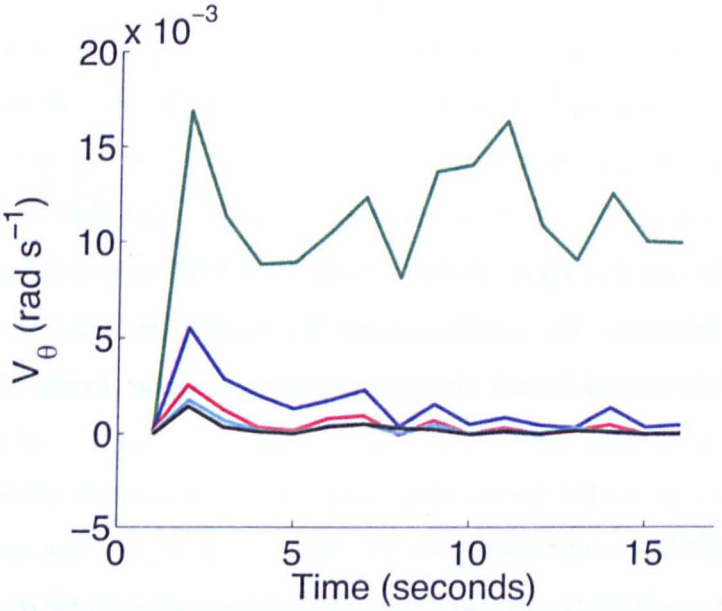

Figure B.1: **Mean particle velocities calculated with the alternative smoothing method.** - An alternative method is used to smooth and bin the data to determine if the fluctuations are being introduced within the analysis. In this method the high resolution data is lost but the large-scale correlated fluctations across the width of the shear band can still be seen. The experiment used as an example here is a constant shear rate experiment performed in microgravity with 4 mm particles and an inner cylinder angular velocity of 0.05 rad s^{-1}.

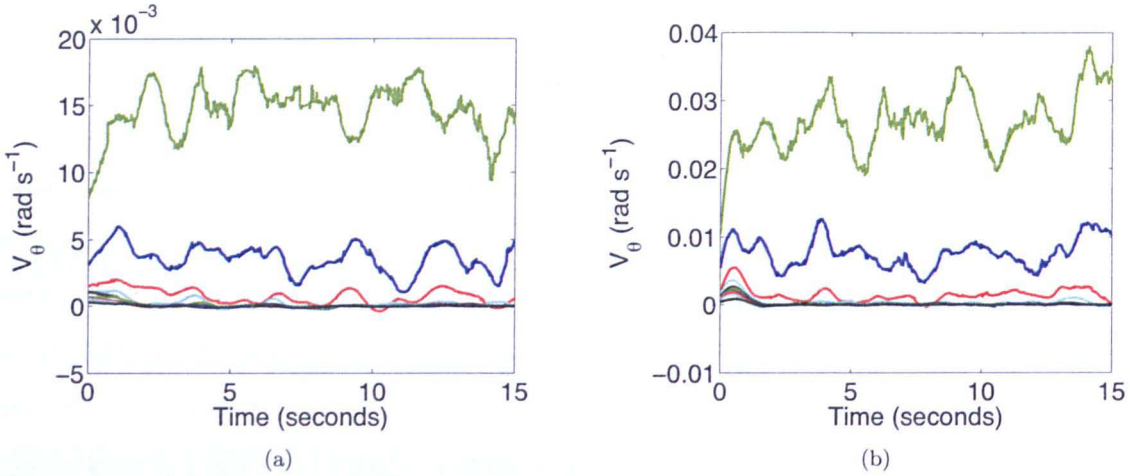

Figure B.2: **Mean particle velocities for ground-based experimental runs** - The mean velocities in two ground-based experiments with 4 mm particles undergoing a constant shear rate experiment are shown. In (a) the inner cylinder angular velocity is 0.025 rad s^{-1}, (b) the inner cylinder angular velocity is 0.05 rad s^{-1}. For both experiments the span of the applied smoothing is 2 seconds (120 frames) and the shear cell has been split into ten equal radial bins. The large-scale correlated fluctuations can be seen to also occur in the ground-based experiments.

B.1.2 Gravity variations

The next investigation aimed at determining if the gravity fluctuations were the cause of the large sale fluctuations. As described in Section 4.6.1 there were often large gravity fluctuations over the course of one parabola. If there is a shift, e.g., from positive to negative gravity, then the particles in the top layers will tend to force themselves upwards onto the pressure plate, momentarily increasing the friction and slowing them down. This effect would potentially apply to all radial zones at the same time and would affect the particle velocities proportionally, possibly producing correlated spikes and troughs as the microgravity environment changes. However, rather than try to correlate the microgravity fluctuations with the large-scale fluctuations, we decided to look at some ground-based constant shear rate experiments. The same correlated fluctuations are found in the ground-based results (Fig. B.2). The fluctuations cannot, therefore, be arising from the gravity variations over the course of a parabola.

B.1.3 Pressure plate

The velocity variations could be occuring simultaneously across the shear cell if the pressure exerted by the pressure plate changes. If, for example, the pressure plate is applying more than the average pressure (e.g., due to microgravity variations or particle packing rearrangements) then the surface layer beads may slow down due to more friction being exerted upon them. If on the other hand the pressure plate is applying less pressure than the average pressure then there is less friction allowing the beads to move more freely. So, if the pressure plate moves up and down, the pressure is varied

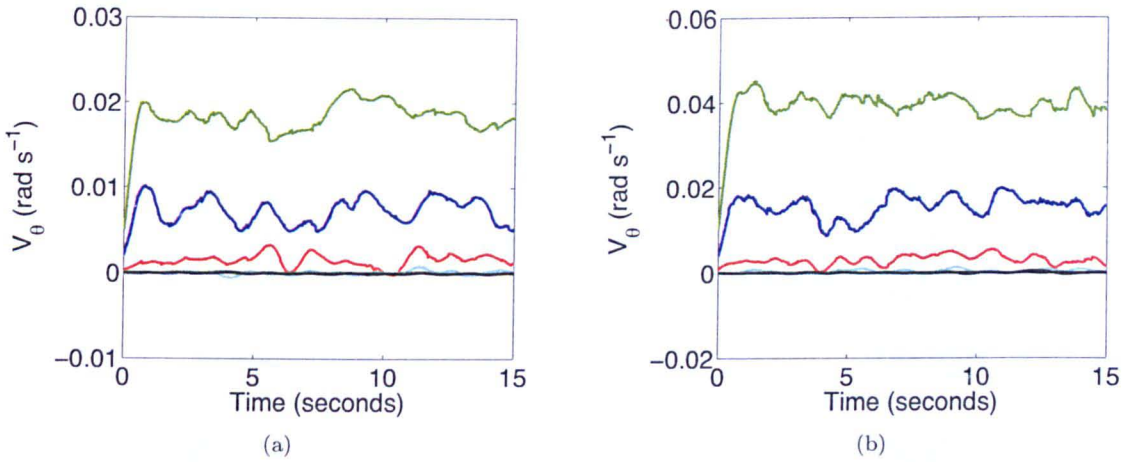

Figure B.3: **Mean particle velocities for experiments without the pressure plate** - The mean velocities in two ground-based experiments without the pressure plate in place are shown. In both experiments there are 4 mm particles undergoing a constant shear rate with a rotation rate of (a) 0.025 rad s^{-1} and (b) 0.05 rad s^{-1}. For both experiments the span of the applied smoothing is 2 seconds (120 frames) and the shear cell has been split into ten equal radial bins. The large-scale correlated fluctuations can be seen to also occur in the ground-based experiments with no pressure plate.

uniformly across the shear cell possibly causing the fluctuations to appear at the same time across it. This is not something that could be easily predicted or detected directly (we did not have a camera at the side to see if the pressure plate moves up and down or not). To determine whether the pressure plate may be causing these variations we performed tests without the pressure plate (Fig. B.3). In these two examples of experiments without the pressure plate the large-scale correlated fluctuations can still be seen. Therefore, we can conclude that the pressure plate is not the cause.

B.1.4 External vibrations

Next, we considered the possibility that there were external vibrations causing the correlated particle movement within the shear cell. These external vibrations could be caused by aircraft vibrations, vibrations from the experiment itself or simply vibrations caused by movement near the experiment (people, machines etc.). If there were any vibrations these would cause the particles and the camera to move independently of one another. By stacking together all of the images taken over the course of an experimental run any vibrational movement should be easily detected. Figures B.4 and B.5 show stacked images from the top camera and the bottom camera, respectively, in which several thousand images have been super-imposed. The shear band near to the moving inner cylinder can be seen but other than within this shear band there is no blurring in the images and thus no independent movement between the particles in the shear cell and the camera. Several different experimental runs were analysed like this (from the ground-based runs and the flight) and the images are consistenly clean.

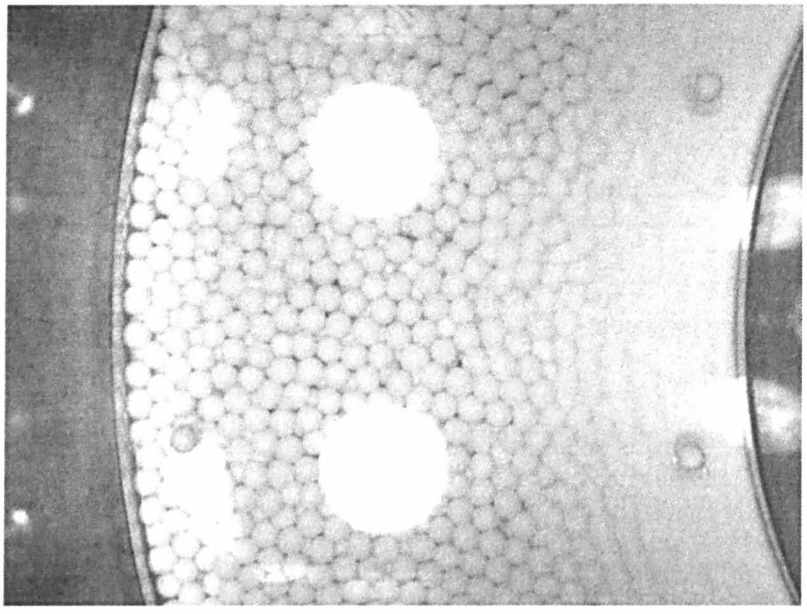

Figure B.4: **Superposition of experimental images taken using the top camera** - Stacked image made from > 4000 frames taken with the top camera looking down on the top surface of the shear cell.

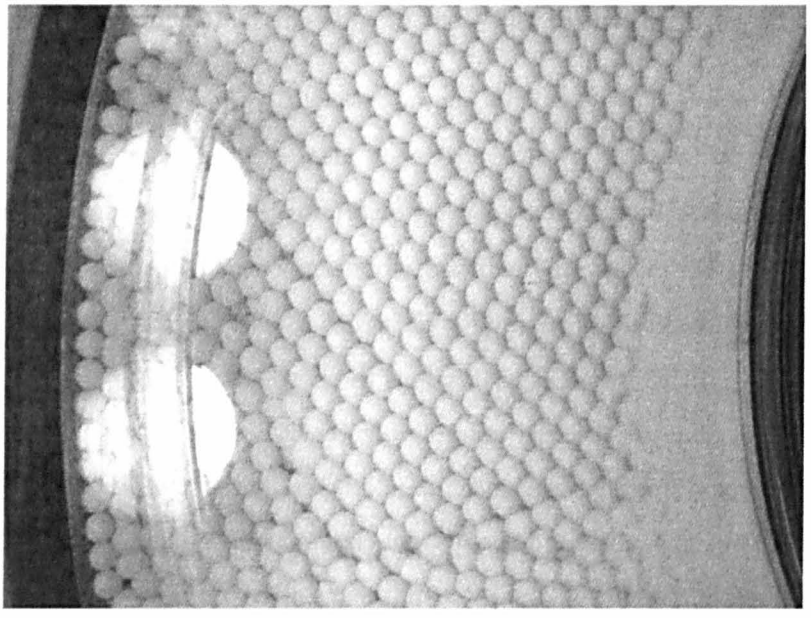

Figure B.5: **Superposition of experimental images taken using the bottom camera** - Stacked image made from > 4000 frames taken with the bottom camera looking up to the bottom surface of the shear cell.

B.1.5 Motor

As a final check we considered the possibility that the motor was not rotating at a constant rate and the variations in speed were being transmitted to the particles. As the motor is controlled by an inverter its rotation speed should be very accurately defined by the frequency at which the inverter is operating. The arrangement of the motor and inverter set-up was chosen to ensure that the output speed should be very constant. However, it is envisageable that some small variations in rotation rate could be caused by bad coupling between the motor and shear cell, or by poor coupling between the small and large gears of the pulley (the belt between the two gears is made of a rubber-like material which might flex).

There are 233 parameters output to file describing the behaviour of the motor over the course of one experimental run. However, there are only two parameters that show any real time response to what the motor is doing: the output frequency and the output current. When plotted versus time there is absolutely no change in the output frequency over the course of one experimental run (Fig. B.6). However, there is a small variation in the current consumed by the motor over several experimental runs (Fig. B.7). The output current varies by $\pm$ 0.01 A over the course of an experimental run which corresponds to a fluctuation of $< 2\%$ in the output current. However, it is important to note that the values of the current are only accurate to 0.01 A. The timescales of the variations are on the order of 1-2 seconds i.e., the output current increases or decreases away from the mean value for approx 1-2 seconds at a time. In principle these small changes in the current consumed could be an indication of changes in the motor speed. However, these fluctuations could also be an indication of the mechanical stress on the motors shaft; the more stress the greater the current required to maintain a constant rotation rate. Therefore, given the small variations, which are of the same order of magnitude as the accuracy of the data, and the different possible causes for the fluctuations it was decided that this was not a reliable method of detecting changes in the inner cylinder rotational velocity.

An alternative method was devised to try to measure more directly any variations in the inner cylinder rotation rate; stickers were placed on the top surface of the moving cylinder (Fig. B.8). The motor was turned on and the stickers were imaged as they rotated with the inner cylinder. The stickers were then tracked using the particle tracking algorithm giving x and y coordinates for the centres of all of the stickers for every frame. The nominal smoothing technique (as described in Section 5.2.7) was employed, with a smoothing span of 1 second (62 frames), to remove noise from the raw tracking data. In order to convert from Cartestian to Polar coordinates a best-fit geometric circle (formed by the locations of the centre points of the stickers over the course of the experiment) was calculated (Fig. B.9). The angular motion of the stickers could then be analysed.

First, the change in angular position (theta) over time was investigated for all of the stickers.

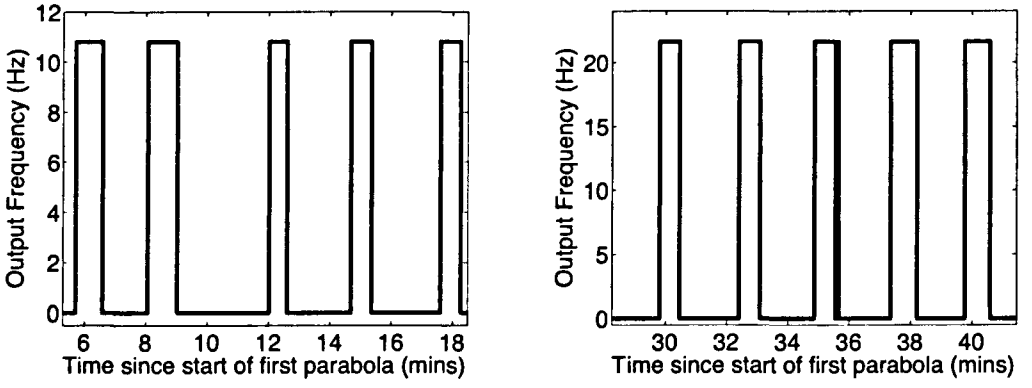

Figure B.6: **Variations of the motor output frequency during flight based experiments** - Both figures are for the 4 mm particles undergoing five experiments i.e., each 'spike' corresponds to one experimental run. In figure (a) the rotation rate is 0.025 rad s^{-1} and the output frequency remains constant at 10.8 Hz while the motor is on. In figure (b) the rotation rate is 0.05 rad s^{-1} and the output frequency remains constant at 21.8 Hz while the motor is on.

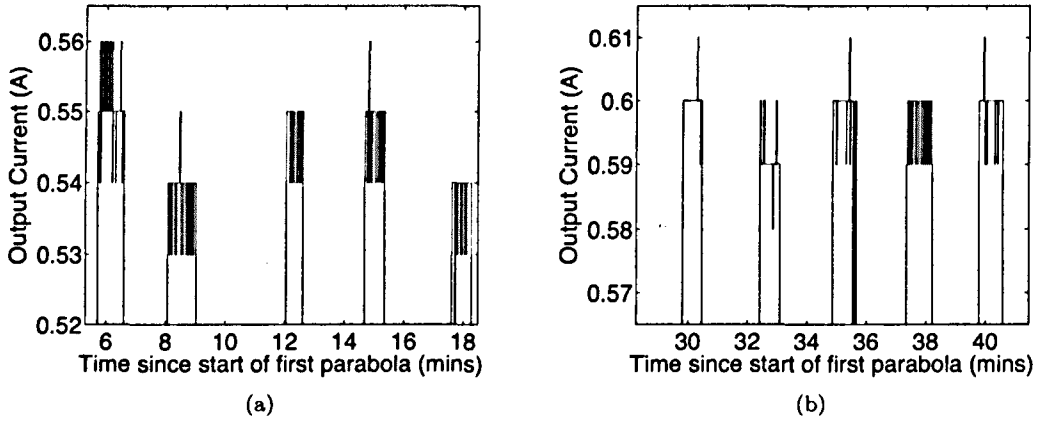

Figure B.7: **Variations of the motor current consumption during flight based experiments** - Both figures are for the 4 mm particles undergoing five experiments i.e., each 'spike' corresponds to one experimental run. In figure (a) the rotation rate is 0.025 rad s^{-1} and the mean current consumption is ~0.55 A. In figure (b) the rotation rate is 0.05 rad s^{-1} and the mean current consumption is ~0.6 A. The current measurements are accurate to 0.01 A and the fluctuations are of same magnitude. The timescales of the these variations are on the order of 1-2 seconds.

The angular positions of all stickers appear to change at a constant rate as would be expected for a constant rotation rate (Fig. B.10). However, when a more detailed investigation was performed of the rate of change of the angular position with time, i.e., the angular velocity, it was discovered that there were some variations. In Fig. B.11 it can be seen that these variations in angular velocity do not occur for all stickers at the same time so the change can not be attributed to a change in rotational velocity of the inner cylinder. Neither can the variations be attributed to an error in either the central coordinates of the circle used to transform the coordinates or due to a slightly strange viewing angle as the variations do not show a steady increase nor a steady decrease with x or y coordinates.

It was found that the variations in angular velocity are directly linked to the angular position of the stickers. In other words, for certain values of theta the angular velocity is greater and for others it is smaller. All stickers have the same changes at the same angular position (Fig. B.12), but not at the same time. Therefore, when the mean velocity of all of the stickers was plotted as a function of time, Fig. B.13, there are clear fluctuations. The rotational velocity of the inner cylinder in the example shown in Figs. B.10–B.13 was 0.1 rad s^{-1}. The mean angular velocity of the stickers after tracking, smoothing and conversion to polar coordinates was 0.099 ± 0.003 rad s^{-1}. However, the maximum amplitude of the fluctuations of angular velocity for the individual particles is much larger.

We can, therefore, conclude that the method of tracking and analysis does give reasonable results but it is very important to understand the cause of these small velocity fluctuations as these could, in principle, be the source of the large-scale correlated fluctuations witnessed in the mean angular velocities of the particles, or be the cause of other, undetected, inaccuracies.

Figure B.8: **Example image showing locations of stickers on moving cylinder** - These blue stickers were placed around the rim of the moving inner cylinder and were subsequently tracked to determine if there were fluctuations in the cylinder rotational velocity.

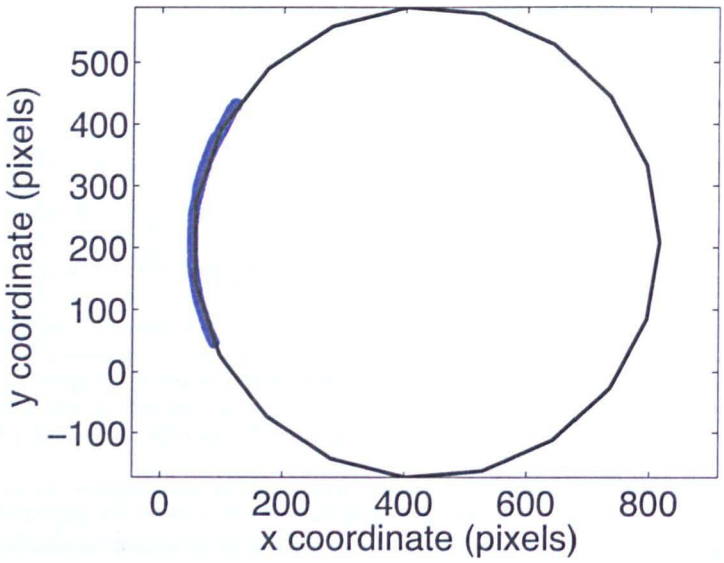

Figure B.9: **Best-fit circle from sticker centre coordinates.** - This best-fit geometric circle (formed by the locations of the centre points of the stickers over the course of the experiment) was calculated. The centre point was used to convert the sticker positions from cartestian to polar coordinates.

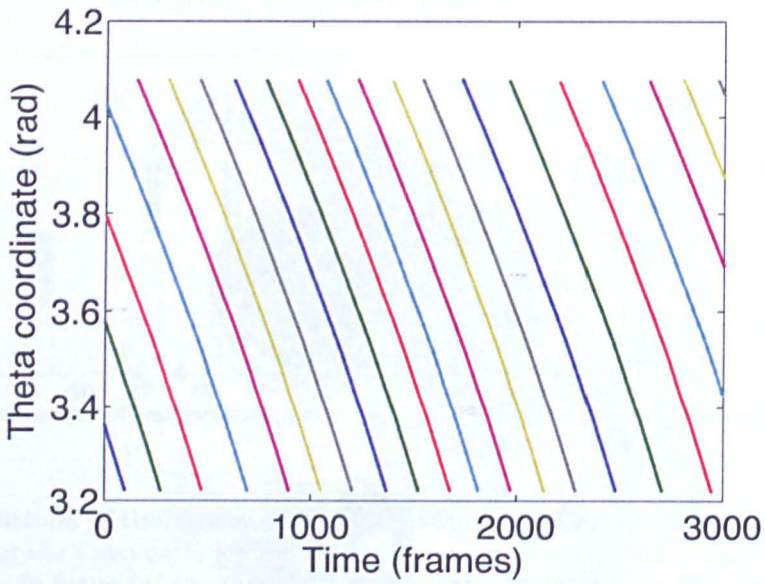

Figure B.10: **Angular position of stickers as a function of time** - The change in the angular position (theta) is plotted for several stickers against time. Each line represents a different sticker and the angular position appears to change at a constant rate as would be expected for a constant rotation rate.

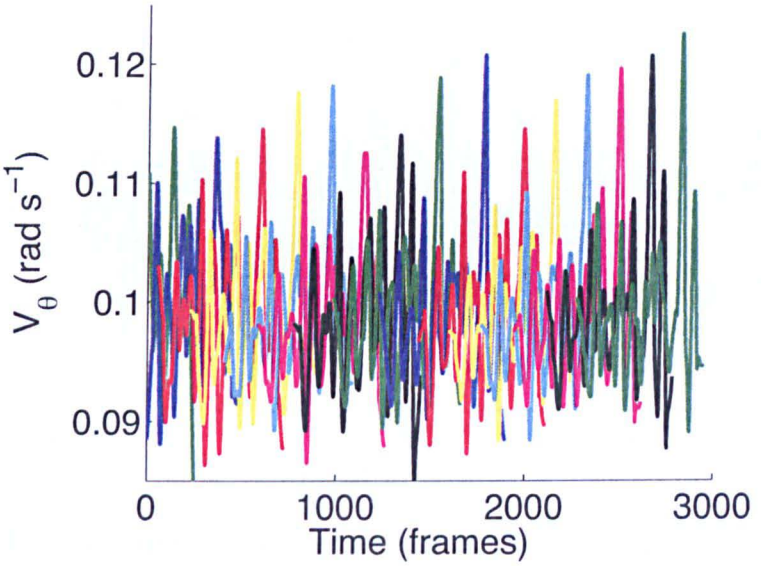

Figure B.11: **Angular velocity of stickers as function of time** - The angular velocities of several stickers are plotted against time. Each line represents a different sticker. There are large variations in angular velocity for all stickers but these do not occur for all stickers at the same time.

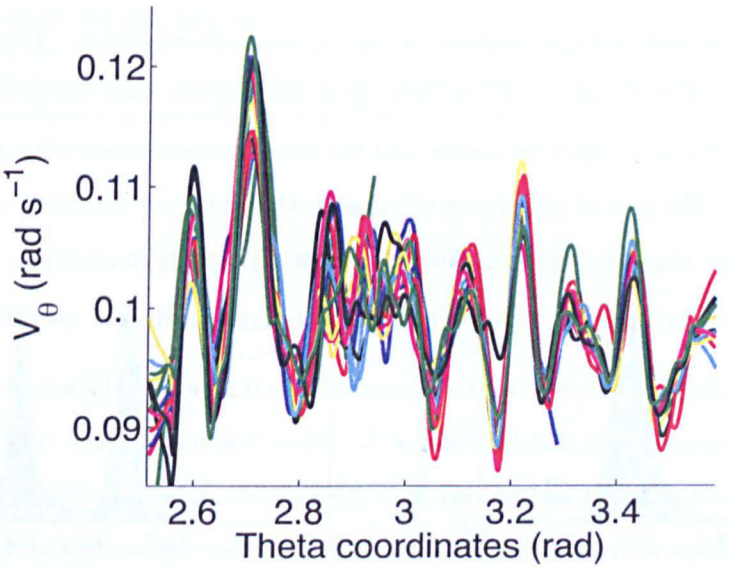

Figure B.12: **Mean angular velocity of stickers as a function of angular position** - The angular velocities of several stickers are plotted against angular position (theta). Each line represents a different sticker. There are large variations in angular velocity and these all seem to occur at the same angular positions.

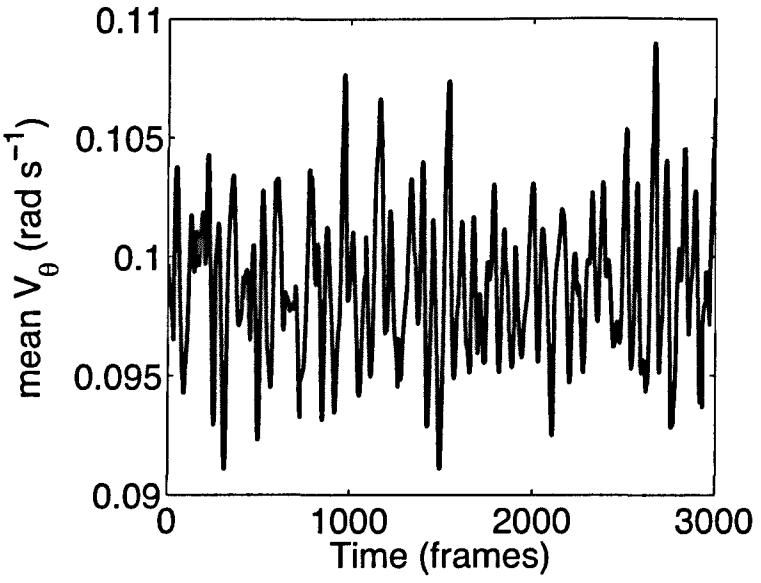

Figure B.13: **Variation of mean angular velocity of stickers with time** - The mean angular velocity for all of the stickers is plotted against time.

The above analysis was performed again but with no smoothing. This allows an investigation of the raw data at high resolution and a closer look at the effect of the smoothing algorithm. First, the individual particle angular velocities were plotted as a function of angular position. As there is no smoothing the angular velocity at each point is calculated using the angular position of a sticker in two consecutive frames as detected by the tracking algorithm. In Fig. B.14 the fluctuations of the sticker angular velocities with angular position are shown at high resolution. The first plot shows the variation of angular velocity for several stickers after the position data has been smoothed over 1 second. Each line represents a different sticker and the time between consecutive frames (i.e., data points) is 1/62 seconds. The second plot shows the unsmoothed angular velocity of each sticker. The values at each frame are connected with lines to allow the small-scale fluctuations to be seen more clearly. In the third plot the lines are removed and there is clearly a distinct quantisation occuring.

Although the mean angular velocity value is approximately 0.1 rad s^{-1} the actual values of angular velocity are clustered around 0.05 and 0.13 rad s^{-1}. These fluctuations and quantisation were an unexpected discovery and the next section discusses the possible causes. It would appear, from Fig. B.14, that smoothing helps to reduce the problem. This is further demonstrated in Fig. B.15 which shows the effect of smoothing on the distrubution of individual particle angular velocities. Before the data are smoothed the angular velocities are quantised around the same two distinct values seen in Fig. B.14. After the data have been smoothed the angular velocities have a guassian like profile, centred around the mean angular velocity. We can, therefore, conclude that smoothing helps to eliminate the problem of quantisation of small-scale fluctuations but we still do not understand the original cause.

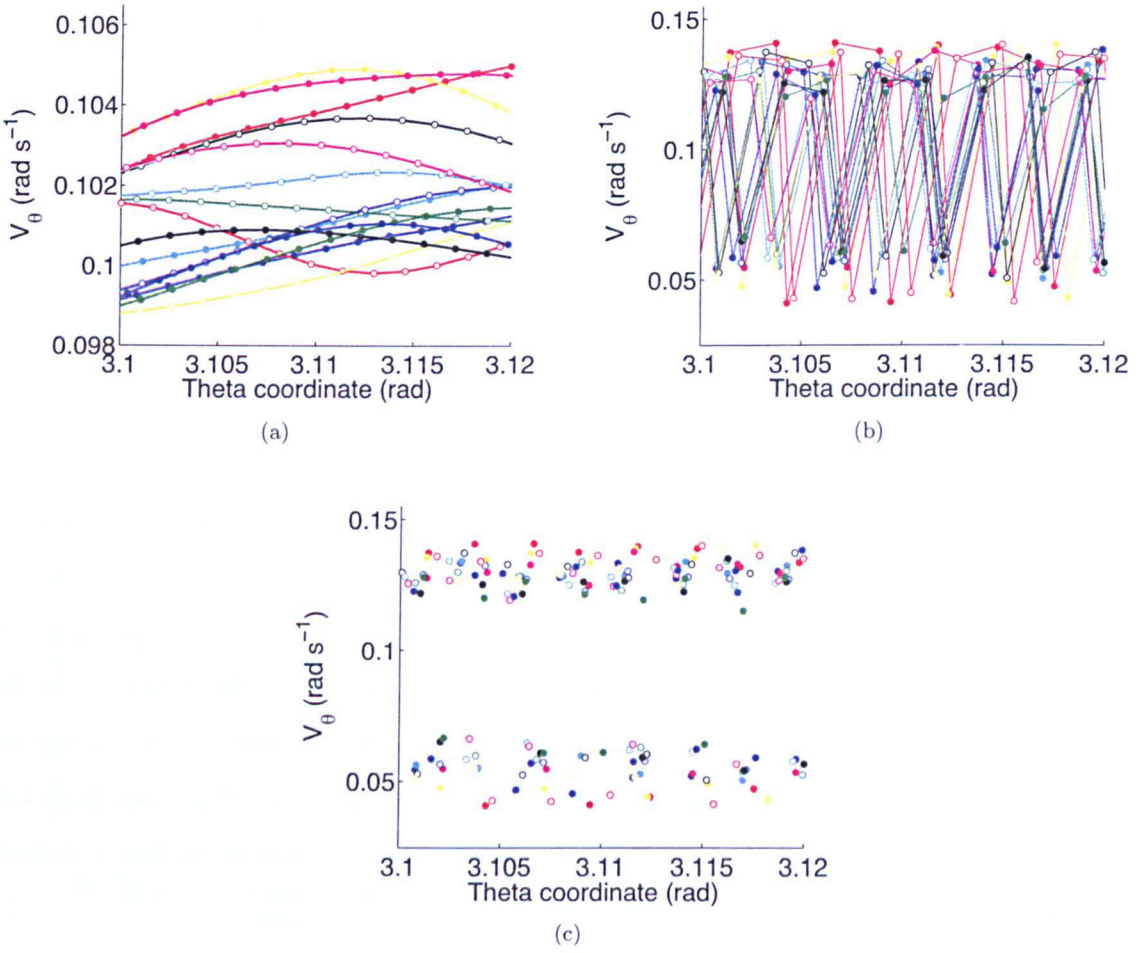

Figure B.14: **Small-scale fluctuations in the sticker angular velocities** - (a) Angular velocity calculated after having smoothed the position data (smoothing span of 1 second). Each line represents one sticker. (b) Unsmoothed angular velocity with lines drawn to see the jumps for each particle more clearly. (c) Unsmoothed angular velocity with lines removed to show quantisation more clearly.

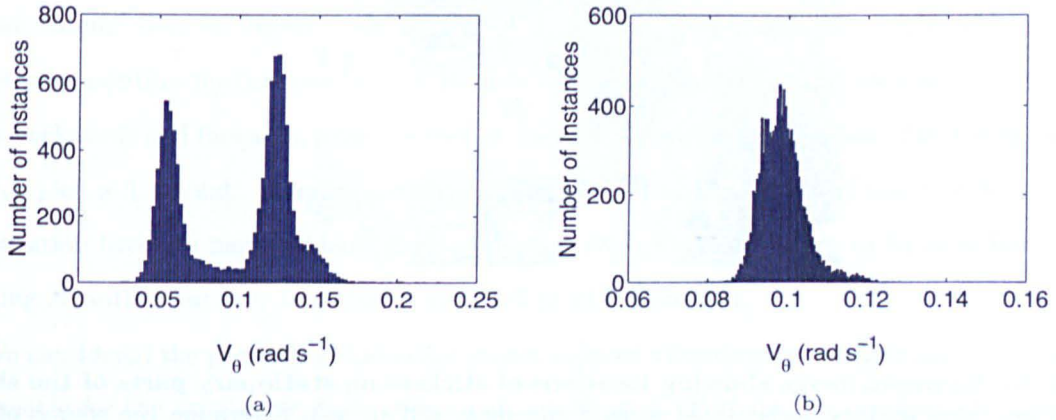

Figure B.15: **The effect of smoothing on the distribution of angular velocities** - The distribution of angular velocities, V_θ are shown with (a) no smoothing, and (b) smoothing with a span of 1 second (62 frames).

B.2 Investigating the source of the small-scale fluctuations and quantisation

As described above, the discovery of small-scale fluctuations and quantisation in the angular velocity of the sticker velocities when looking at high resolution was unexpected. In order to understand the possible consequences of the quantisation, the cause must first be understood. This section describes several different tests that were performed to find the origin of the small-scale fluctuations and quantisation.

B.2.1 Tracking stationary stickers

To determine the source of the small-scale fluctuations, stickers were placed on non-moving parts of the experiment. This way there could be no influence of moving parts and, as the stickers should have no motion at all, the cause of the small-scale fluctuations and quantisation should be easier to determine. The locations of the stationary stickers are shown in Fig. B.16. The stationary stickers were tracked in the same way as the moving stickers discussed in Section B.1.5. No smoothing was performed. As the particles were randomly placed on the equipment a central position cannot be easily defined. Therefore the Cartesian coordinate system is used for the analysis of these stationary particles and not the Polar coordinate system.

Figure B.16: **Example image showing locations of stickers on stationary parts of the shear cell** - These blue stickers were placed around the shear cell to help determine the source of the small-scale fluctuations and quantisation.

From the plot of unsmoothed x and y velocites (Fig. B.17) we can see large fluctuations. As the stickers are stationary this means that the difference in location between detected positions changes

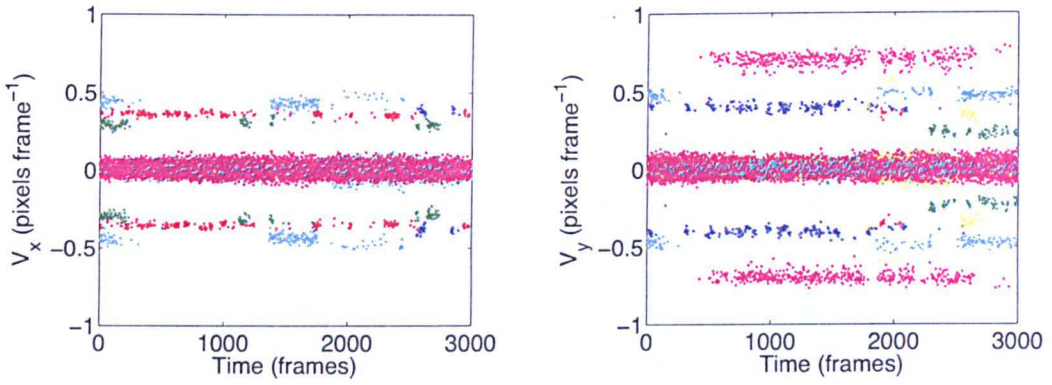

(a) (b)

Figure B.17: **Variation of x and y instantaneous velocities of the stickers with time** - (a) Unsmoothed V_x, (b) Unsmoothed V_y. Each colour represents a sticker.

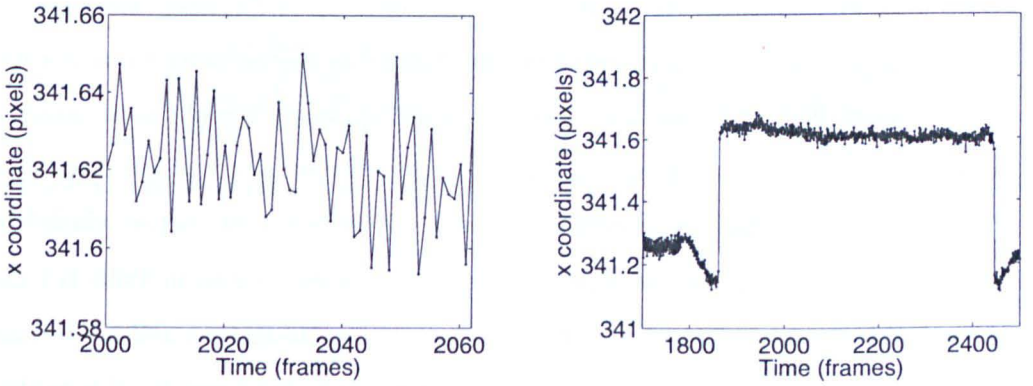

(a) (b)

Figure B.18: **Variation of x position with time for one sticker** - (a) Rapid fluctuations of x position of one sticker in a short time period (∼1 second). (b) Variation of x position of the same sticker over a longer time period (∼13 seconds).

from one frame to the next. The quantisation occurs at different times for different stickers, therefore, we can assume that an uneven camera frame rate is not a possible cause. Figure B.18 (a) shows a plot of x position fluctuations for one particle over short period in time showing how the centre shifts backwards and forwards, from one side of the actual position to the other. The timescale shown on this plot is 1 second. A longer timescale is considered in Fig. B.18 (b) and it is here that the quantisation becomes more evident. Small, subpixel level, fluctuations are to be expected from the tracking algorithm but very large jumps of $> 1/2$ pixel are unusual.

We considered the possibility that either motor induced vibrations or the lighting conditions were responsible for the small-scale fluctuations and quantisation. Perhaps, for example, the lights were flickering and this was altering the detected location of the particle centres between frames. Several tests were performed imaging and tracking the stationary stickers with several motor speeds and under various illumination conditions (several combinations of the lamps and also under natural

Table B.1: The motor and lighting conditions of a selection of tests performed with the stationary stickers. The mean x and y velocities calculated after the stickers have been tracked and the standard deviation in the mean velocities are reported.

Motor speed (rad s^{-1})	Lighting Conditions	Mean V_x (pixels s^{-1})	Mean V_y (pixels s^{-1})
0.1	All lamps on	-0.002 ± 5.9	0.004 ± 11.4
0.1	All lamps off	-0.020 ± 11.7	-0.005 ± 8.7
0.05	Lights on, over-exposed	0.003 ± 5.7	-0.009 ± 8.0
0.025	Lights on, over-exposed	0.005 ± 5.9	0.000 ± 12.0
0.0	All lamps on	0.005 ± 5.9	0.000 ± 6.3
0.0	Left lamps only	0.000 ± 6.2	0.001 ± 9.65
0.0	Right lamps only	0.000 ± 7.0	0.000 ± 6.3
0.0	All lamps off	0.000 ± 4.0	-0.001 ± 7.2
0.0	All lamps off	0.000 ± 7.3	0.000 ± 8.4

lighting provided by a large window in the ceiling of the laboratory). No difference was found in the size of the fluctuations for different motor speeds nor was there a difference when the motor was off completely. The scale of the fluctuations and quantisation did, however, become worse under some specific illumination conditions (e.g., when using natural lighting the amplitude of the fluctuations in position was sensitive to clouds passing in front of the sun). Nevertheless, no matter which lighting conditions were used, the quantisation and fluctations were still present. Given in Table B.1 are the conditions of a selection of tests performed, and the resulting x and y velocities, as well as the standard deviation in the velocities. The large standard deviation in the results is present in all runs showing that it is not being caused by the lighting conditions.

B.2.2 Tracking stationary particles

The next idea was that perhaps the quantisation originated because the stickers are flat and they, therefore, do not have the correct Gaussian profile for the centroiding algorithm (see Section 5.2.7). Using one of the ground-based runs performed previously, the positions of about 20 particles in the very middle of the shear cell were tracked and analysed while the motor was off. The locations of these particles are shown in Fig. B.19. Small-scale fluctuations (< 0.2 pixels) in the particle positions were still found but no quantisation was detected (Fig. B.20). As a result, it is possible that the small fluctuations are in fact due to pixelation and are inherent to the software. If this is the case, this is, therefore, unavoidable experimental noise that should even out over time. The quantisation probably arises due to the poor results of this particle tracking algorithm when tracking the flat stickers. To verify that this is really the case some simple simulations were performed. These are discussed in the next section.

Figure B.19: **Example image showing locations of mid place particles** - These particles, from a ground-based run, were chosen to investigate the fluctuations and quantisation in spherical particles.

Figure B.20: **Variation of position with time for one stationary particle** - (a) x coordinate, and (b) y coordinate, of a stationary mid-place particle plotted against time.

B.2.3 Simulations to investigate small-scale fluctuations and quantisation

To determine if pixelation is the cause of the small-scale fluctuations and quantisation some simple simulations were developed to model how an hypothetical particle is recorded by the camera and then tracked by the particle tracking algorithm. The first simple test was to generate test images of a number of small black "circles" (not perfect, but pixelated to be more realistic) randomly placed on a white background (Fig. B.21). In some simulations the particles remained stationary and in others the particles moved with a random, but constant, velocity. The sets of generated images were processed in an identical manner to the images of the stickers and particles discussed above. It was found that in the simulations of stationary particles, the output of the tracking and analysis is correct and the particle positions never change during the simulations. In the simulations of moving particles, as the particle velocities are constant, the tracked position coordinates should vary smoothly in time. However, there are small-fluctuations in the tracked position coordinates (Fig. B.22). So it would appear that the small fluctuations are, as predicted above, an inherent and unavoidable part of the software. On the otherhand, the cause for the quantisation is still unclear.

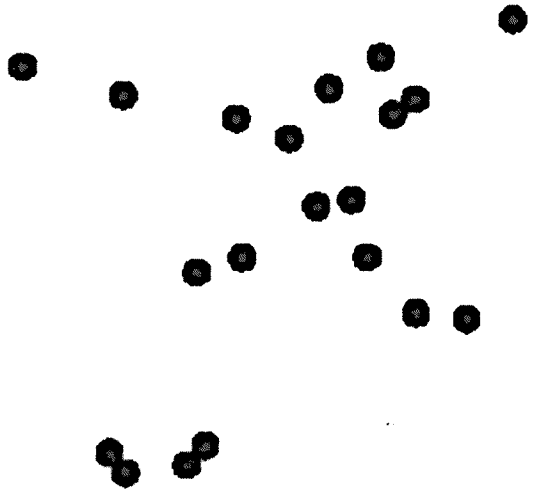

Figure B.21: **Generated Particles** - An example test image that was generated. There are a number of small black "circles" (not perfect, but pixelated to be more realistic) randomly placed on a white background.

It was considered that the problem of quantisation could be arising because the particle size and shape is changing slightly between frames. This could occur when particles move a very small (sub-pixel) distance between frames: the particle detection algorithm may detect the particle to be a slightly different size and shape thus potentially confusing the centroiding algorithm. To examine how the change in particle shape may affect the tracking algorithm a second second set of simulations were

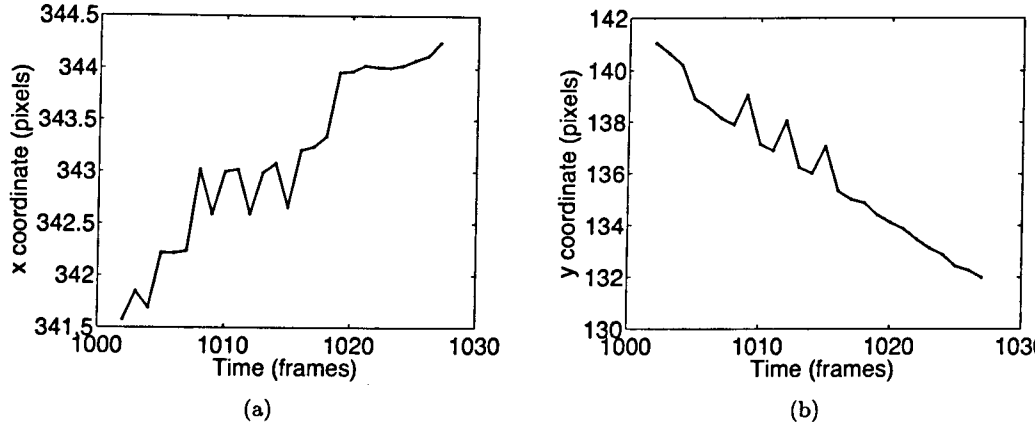

Figure B.22: **Variation of tracked position with time for one hypothetical particle** - (a) x coordinate, and (b) y coordinate, of a simulated particle plotted against time.

developed.

First, a large grid of squares is defined. Within each large square, a 10 × 10 grid of smaller squares is defined. We then use the analogy that each large square is equivalent to a pixel. A hypothetical "particle" is generated with a given centre point and radius. If the centre of a small square is inside the radius of the hypothetical particle, then the small square turns from white to black. If > 50% of the small squares within a large square are black then the large square (i.e., 'pixel') turns from white to black (see schematic in Fig. B.23).

The "particle" is given a two dimensional velocity and the position of the particle is propagated over several timesteps. The shape 'detected' at each timestep is recorded. Some example images from one simulation are shown in Fig. B.24. Note, the hypothetical particles are never circular as they are made using a grid of squares; the closest shape to circular we ever get is shown in the attached Fig. B.24 (a).

Figure B.25 shows the tracked x and y trajectories of one such simulated particle. The tracking algorithm detects the centre of the particle to be fluctuating, with occasional much larger jumps in position. In reality, the centre of the simulated particle moves at a constant velocity. However, in the plots of particle velocity (calculated using the particle position data from the tracking algorithm) as a function of time (Fig. B.26) there are very large fluctuations. The magnitude of the tracked particle velocity varies from almost 0 pixels/frame all the way up to 2.5-3 pixels/frame. There are also at least two, if not three, levels of fluctuations: those around 0.5, 1.75 and 2.75 pixels/frame for the x velocity and around 1, 1.75 and 3.25 pixels/frame for the y velocity.

In summary, the change of particle shape with time, or pixelation of particles, is likely to be where the quantisation is originating. The effect of pixelation became obvious when tracking the stickers because the effect is exaggerated in the cases where only a few test particles are available. Under

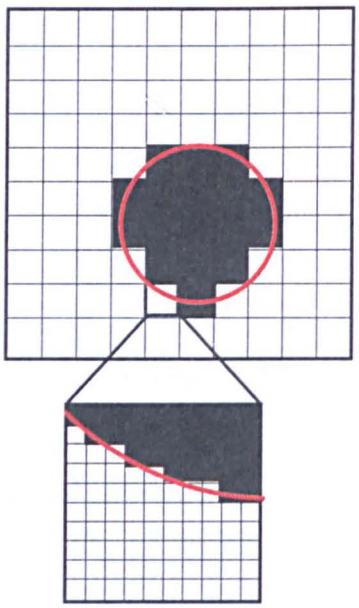

Figure B.23: **Schematic of the grid used to 'detect' particles** - A large grid of squares is defined. Within each large square, a 10×10 grid of smaller squares is defined. We then use the analogy that each large square is equivalent to a pixel. A hypothetical "particle" is generated with a given centre point and radius (see red circle). If the centre of a small square is inside the radius of the hypothetical particle, then the small square turns from white to black. If $> 50\%$ of the small squares within a large square are black then the large square (or pixel) turns from white to black.

these circumstances there are few position coordinates to work with when trying to choose the good parameters to avoid pixelation. The fact that the stickers and simulated particles are non-circular, completely flat images will only have increased the problem. When dealing with the real glass beads there are many more particles and they have much longer lifetimes so the parameters for the tracking algorithm can be adjusted much more accurately based on the large volume of position data available. The accuracy of the tracking will also be much improved due to the sub-pixel resolution we can obtain for truly spherical and not circular particles.

From these investigations we can conclude that the small-scale fluctuations are a normal, inherent and unavoidable part of the tracking software. The quantisation, however, arises due to poor choice of parameters and due to non-spherical particles: the algorithm cannot accurately detect the centres of particles which have non-gaussian profiles. As long as careful attention is paid to the choice of parametres, and real particles are used, the quantisation should not occur and the results of the particle tracking algorithm should be reliable. These effects are, therefore, unlikely to be causing the large-scale fluctuations in the mean particle velocities.

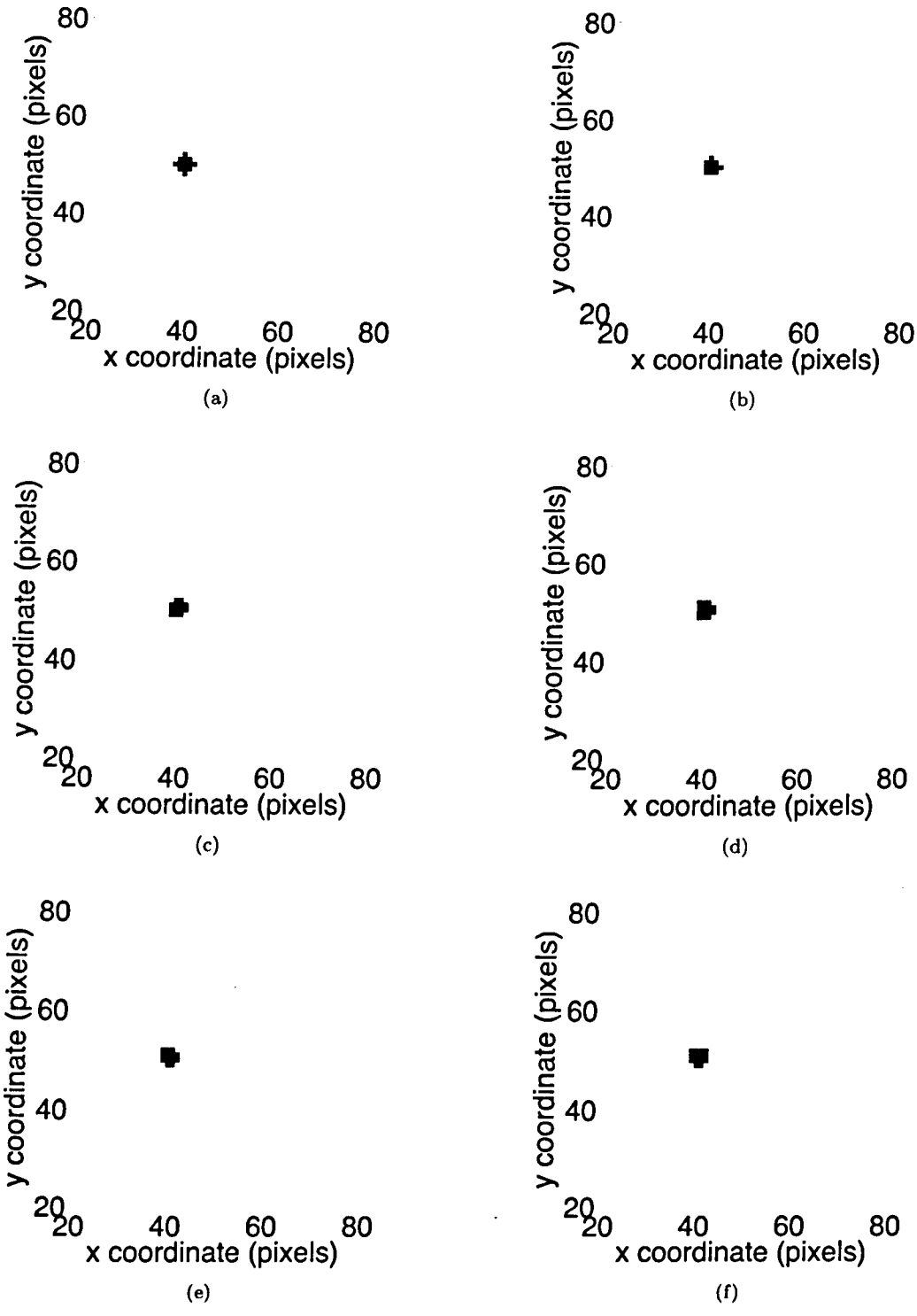

Figure B.24: **Simulated camera detection of particles** - The hypothetical "particle" generated and shown in Fig. B.23 is given a two dimensional velocity. The position of the particle is propagated over several timesteps. These plots show some example shapes of the 'detected' particle at each timestep.

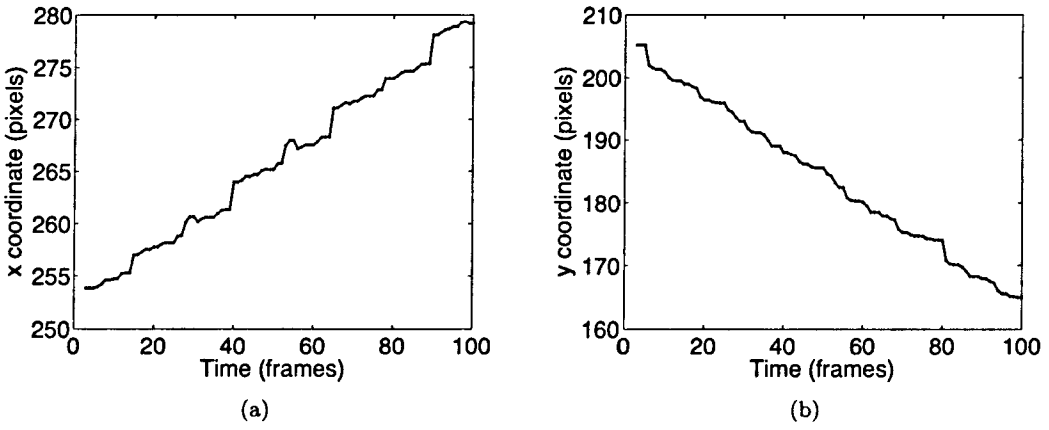

(a) (b)

Figure B.25: **Variation of tracked position with time for one hypothetical particle** - (a) x coordinate, and (b) y coordinate, of a simulated particle plotted against time.

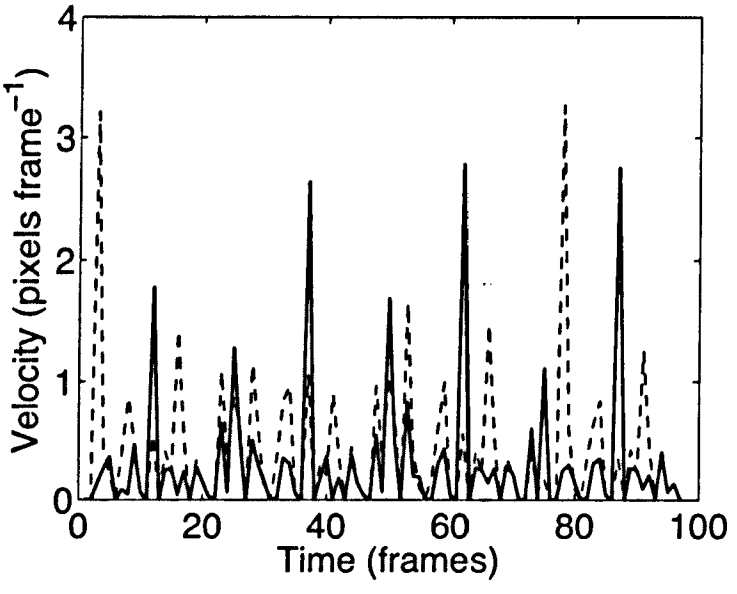

Figure B.26: **Variation of tracked velocity with time for one hypothetical particle** - The x velocity (solid line), and the y velocity (dashed line), of a simulated particle are plotted against time.

B.3 Force chain detection

As all of the possible artificial causes for the large-scale correlated fluctuations have been ruled-out they must, therefore, they must be real. It is likely that they are being caused by force chains within the granular material breaking and reforming across the width of the shear cell. If force chains are the cause it is possible that, from time to time, there is a bulk rearrangement of the granular material within the shear cell. To attempt to detect such a bulk rearrangement, one particle from the outermost radial bin (of five) was chosen. The outer radial bin was chosen as particles move less and, therefore, bulk rearrangements may be more obvious. The distances from this particle to all other particles in the shear cell were calculated. A histogram was then made showing the distribution of distances from this particle to all others (Fig. B.27). Throughout the experiment, while the motor is switched on, the distances from this particle to all other particles were recalculated and a histogram is made every 0.1 seconds representing the distribution of distances. If there is a large bulk rearrangement in the granular material then it is possible that there may be a sudden change in the shape of the distribution at a moment in time. A movie was made of the histograms to attempt to detect any such sudden changes in shape of the distribution. This exercise was repeated for every particle in the outer radial bin (of five radial bins) and the histogram movies were compared to determine if there was any evidence for sudden bulk rearrangement and, therefore, possible evidence for force chain breaking and reforming. Unfortunately, it was difficult to detect any dramatic changes in the distribution shapes by eye.

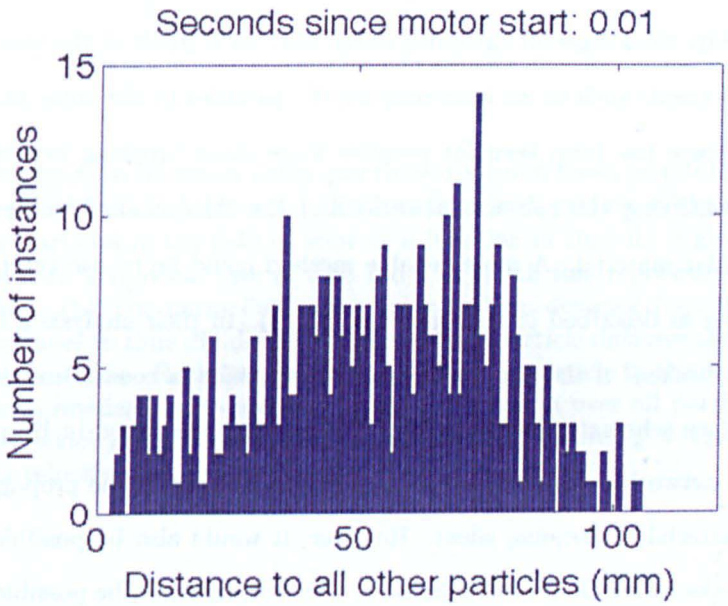

Figure B.27: **Interparticle distance distribution** - The distribution of distances from one particle in the outermost radial bin (of five) to all other particles in the field of view at one instant in time.

Next, the mean distance from each particle in the outer radial bin to all of the other particles in

the field of view was calculated as a function of time. Again, if there is a large bulk rearrangement in the granular material then it is possible that there may be a sudden change in the mean distance from each particle in the outer bin to all of the other particles. Figure B.28 (a) shows the mean distances from each particle in the outer of five radial bins to all of the other particles in the field of view as a function of time. The experiment in this example is a ground-based experiment with 4 mm beads with a rotation rate of 0.05 rad s^{-1}. It appears as though there are correlated fluctuations in the mean inter-particle distance throughout the radial bin. To verify this the normalised mean inter-particle distances (i.e., the mean inter-particle distance at each instance in time divided by the mean inter-particle distance throughout the 20 second period) are plotted as a function of time for each particle (Fig. B.28 (b)). A clear correlation is evident. Finally, in Fig. B.28 (c) the mean normalised inter-particle distance over all particles is plotted on the same plot as the normalised velocity, V_θ^* ($V_\theta^* = V_\theta/\omega$ where ω is the inner cylinder rotational velocity). Although the fluctuations in mean inter-particle distance and mean particle velocity do not overlap exactly it is possible to see how the two events may be linked. As mentioned in Chapter 1, force chains are a very complex and non-linear phenomenon and so, if the fluctuations are due to force chain breaking and reforming, it is not surprising that the correlation is not a simple one.

The same exercise was repeated for all particles in the inner radial bin (Fig. B.29). The first thing to note when comparing the results of the particles in the inner radial bin to those in the outer radial bin is that the mean inter-particle distance for each particle in the inner radial bin varies much more over the time of the experiment. This is not surprising as the particles in the inner radial bin are moving much more rapidly than those in the outer radial bin. As a result of the motion it is difficult to detect any correlated events such as we have seen for the particles in the outer radial bin.

Although some evidence has been seen for possible force chain breaking events, this is not an effective method of quantifying the contact networks and the force chain breaking and reforming events within the granular material. A more reliable method could be to use the time evolution of the broken-links network as described in Herrera *et al.* (2011). In their analysis a link between two particles is considered "broken" if the two particles that were once in contact move away from each other some time later (see schematic in Fig. B.30). The research described in Herrera *et al.* (2011) focusses on the broken network because they are primarily interested in the propagation of fracture events in a granular material undergoing shear. However, it would also be possible to consider the network of persistent links rather than broken links. It may not, however, be possible to perform such an analysis with the AstEx data as 3d particle coordinates are normally used. For the experiment analysed in Herrera *et al.* (2011) the particle positions are obtained in 3d using a laser sheet scanning approach (Slotterback *et al.*, 2008a).

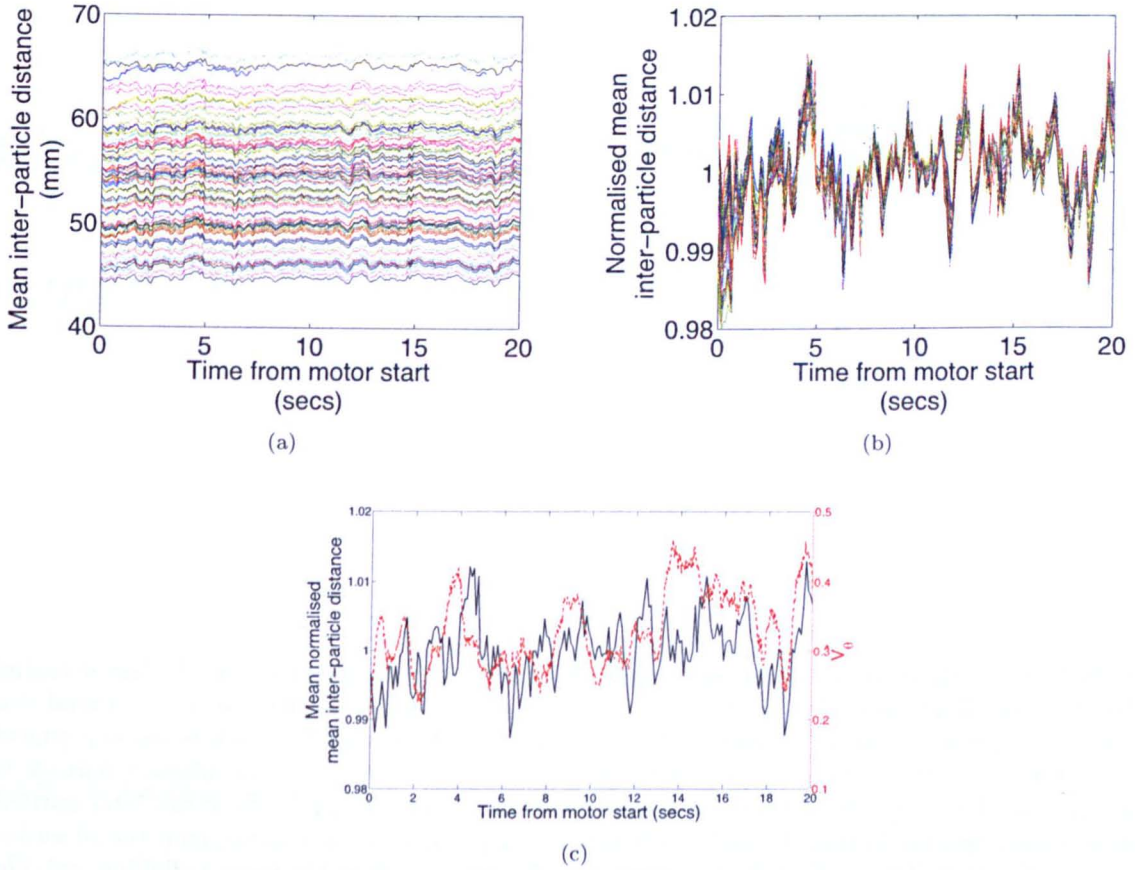

Figure B.28: **Investigation of mean inter-particle distance from particles in the outer radial bin to all other particles** - (a) The mean distance from each particle in the outer of five radial bins to all of the other particles in the field of view as a function of time for a ground-based experiment with 4 mm beads with a rotation rate of 0.05 rad s^{-1}. Each line represents a different particle in the outer radial bin. (b) The normalised mean inter-particle distance (i.e., the mean inter-particle distance at each instance in time divided by the mean inter-particle distance throughout the 20 second period) as a function of time. Each line represents a different particle in the outer radial bin. (c) The mean value of the normalised inter-particle distance, i.e., mean over all particles (black, solid line) and the normalised velocity of the inner of five radial bins, V_θ^*, where $V_\theta^* = V_\theta/\omega$ where ω is the inner cylinder rotational velocity (red, dashed line).

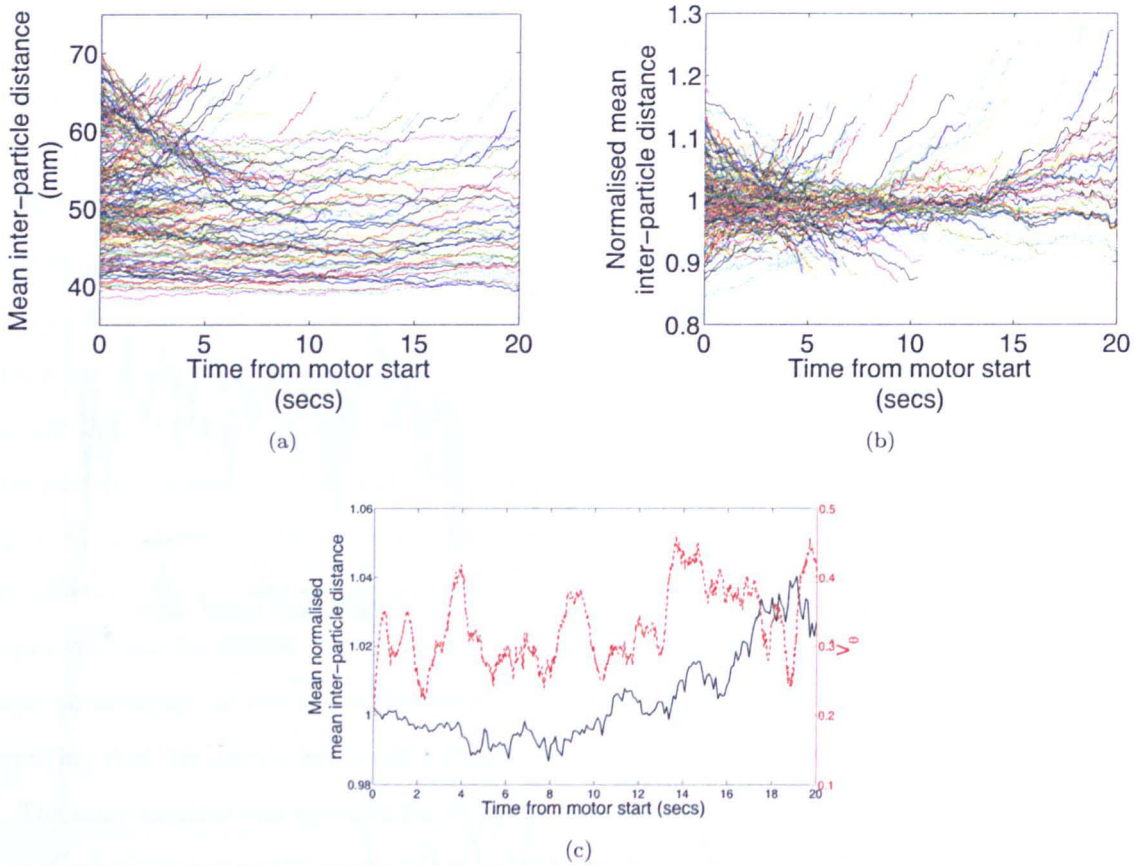

Figure B.29: **Investigation of mean inter-particle distance from particles in the inner radial bin to all other particles** - (a) The mean distance from each particle in the inner of five radial bins to all of the other particles in the field of view as a function of time for a ground-based experiment with 4 mm beads with a rotation rate of 0.05 rad s^{-1}. Each line represents a different particle in the inner radial bin. (b) The normalised mean inter-particle distance (i.e., the mean inter-particle distance at each instance in time divided by the mean inter-particle distance throughout the 20 second period) as a function of time. Each line represents a different particle in the inner radial bin. (c) The mean value of the normalised inter-particle distanc, i.e., mean over all particles (black, solid line) and the normalised velocity of the inner of five radial bins, V_θ^*, where $V_\theta^* = V_\theta/\omega$ where ω is the inner cylinder rotational velocity (red, dashed line).

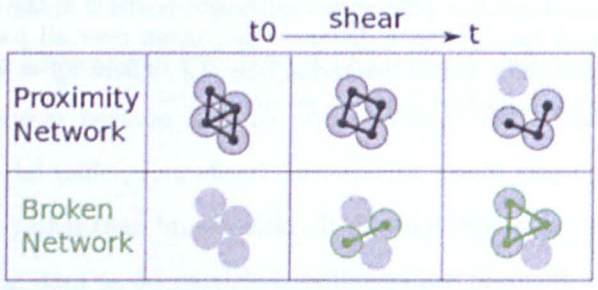

Figure B.30: **The broken-links network** - A schematic of the definition and growth of the broken-links network from Herrera *et al.* (2011)

Appendix C

Calculation of the observational error in V_r and V_θ

The r coordinate is given by,

$$r = \sqrt{x^2 + y^2}$$

and the θ coordinate is given by,

$$\theta = \tan^{-1}(y/x).$$

As r and θ are both functions of x and y we can use partial derivatives to propagate the uncertainties. For example, given $Z = f(a, b)$,

$$\delta Z = \sqrt{\left(\frac{\partial f}{\partial a}\delta a\right)^2 + \left(\frac{\partial f}{\partial b}\delta b\right)^2}$$

where δa is the uncertainty in a and δb is the uncertainty in b.

Therefore, the uncertainty in r is given by,

$$\delta r^2 = \left(\frac{\partial r}{\partial x}\delta x\right)^2 + \left(\frac{\partial r}{\partial y}\delta y\right)^2$$
$$\delta r^2 = \left(\frac{x}{\sqrt{x^2+y^2}}\right)^2 \delta x^2 + \left(\frac{y}{\sqrt{x^2+y^2}}\right)^2 \delta y^2$$
$$\delta r^2 = \left(\frac{x^2}{x^2+y^2}\right)\delta x^2 + \left(\frac{y^2}{x^2+y^2}\right)\delta y^2.$$

Assuming that δx is equal to δy then we can define an error in the position, δp, which will be equal to,

$$\delta p = \sqrt{\delta x^2 + \delta y^2}$$
$$\delta p = \sqrt{\delta x^2 + \delta x^2}$$
$$\delta p = \sqrt{2}\delta x.$$

Therefore,

$$\delta r^2 = \left(\frac{x^2}{x^2+y^2}\right)2\delta p^2 + \left(\frac{y^2}{x^2+y^2}\right)2\delta p^2$$
$$\delta r^2 = 2\left(\frac{x^2+y^2}{x^2+y^2}\right)\delta p^2$$
$$\delta r = \sqrt{2}\delta p.$$

The uncertainty in θ is given by,

$$\delta\theta^2 = \left(\frac{\partial\theta}{\partial x}\delta x\right)^2 + \left(\frac{\partial\theta}{\partial y}\delta y\right)^2$$
$$\delta\theta^2 = \left(\frac{-(y/x^2)}{(1+(y/x)^2)}\delta x\right)^2 + \left(\frac{(1/x)}{(1+(y/x)^2)}\delta y\right)^2$$
$$\delta\theta^2 = \left(\frac{(y^2/x^4)}{(1+(y/x)^2)^2}\delta x^2\right) + \left(\frac{(1/x^2)}{(1+(y/x)^2)^2}\delta y^2\right)$$

Again assuming that δx is equal to δy and, therefore, $\delta p = \sqrt{2}\delta x$,

$$\delta\theta^2 = \left(\frac{(y^2/x^4)}{(1+(y/x)^2)^2}2\delta p^2\right) + \left(\frac{(1/x^2)}{(1+(y/x)^2)^2}2\delta p^2\right)$$

$$\delta\theta^2 = \left(\frac{(1+(y/x)^2)}{(1+(y/x)^2)^2}\right)(1/x^2)2\delta p^2$$

$$\delta\theta^2 = \left(\frac{1}{(1+(y/x)^2)}\right)(1/x^2)2\delta p^2$$

$$\delta\theta^2 = \left(\frac{1}{(x^2+y^2)}\right)2\delta p^2$$

$$\delta\theta = \sqrt{2\left(\frac{1}{(x^2+y^2)}\right)}\delta p$$

$$\delta\theta = \sqrt{2}\left(\frac{\delta p}{r}\right).$$

Then two consecutive radial positions of the particle (r_1 and r_2) are combined to give a radial displacement (S_r) between the two consecutive frames,

$$S_r = r_2 - r_1$$

with

$$\delta S_r = \sqrt{2\delta r^2}$$

$$\delta S_r = \sqrt{4\delta p^2}$$

$$\delta S_r = 2\delta p.$$

Similarly, two consecutive angular positions (θ_1 and θ_2) are combined to give the angular displacement (S_θ) between the two consecutive frames,

$$S_\theta = \theta_2 - \theta_1$$

with

$$\delta S_\theta = \sqrt{2\delta\theta^2}$$

$$\delta S_\theta = \frac{2}{r}\delta p.$$

Finally, the radial displacement (S_r) in pixels is then converted into an instantaneous radial velocity (V_r) in mm s^{-1} using the following equation,

$$V_r = \frac{fps}{PS} S_r$$

with

$$\delta V_r = \frac{fps}{PS} \delta S_r$$
$$\delta V_r = \frac{2fps}{PS} \delta p$$

where PS is the value of the pixel scale and fps is the number of frames taken by the camera every second. Then the angular displacement (S_θ) is converted into an instantaneous angular velocity (V_θ) in rad s^{-1} using the following equation,

$$V_\theta = fps S_\theta.$$

The angular velocity will have an uncertainty given by,

$$\delta V_\theta = fps \delta S_\theta$$
$$\delta V_\theta = \frac{2fps}{r} \delta p.$$

References

ABE, S., MUKAI, T., HIRATA, N., BARNOUIN-JHA, O.S., CHENG, A.F., DEMURA, H., GASKELL, R.W., HASHIMOTO, T., HIRAOKA, K., HONDA, T., KUBOTA, T., MATSUOKA, M., MIZUNO, T., NAKAMURA, R., SCHEERES, D.J. & YOSHIKAWA, M. (2006). Mass and Local Topography Measurements of Itokawa by Hayabusa. *Science*, **312**, 1344–1347. 10, 19

ABELL, P.A., FERNANDEZ, Y.R., PRAVEC, P., FRENCH, L.M., FARNHAM, T.L., GAFFEY, M.J., HARDERSEN, P.S., KUSNIRAK, P., SAROUNOVA, L., SHEPPARD, S.S. & NARAYAN, G. (2005). Physical characteristics of Comet Nucleus C/2001 OG_{108} (LONEOS). *Icarus*, **179**, 174 – 194. 19

AICHELE, M., GEBREMICHAEL, Y., STARR, F.W., BASCHNAGEL, J. & GLOTZER, S.C. (2003). Polymer-specific effects of bulk relaxation and stringlike correlated motion in the dynamics of a supercooled polymer melt. *The Journal of Chemical Physics*, **119**, 5290–5304. 80, 104

ANTONY, S.J., HOYLE, W. & DING, Y., eds. (2004). *Granular materials: fundamentals and applications*. The Royal Society of Chemistry. 32

ASPHAUG, E. (2007). The Shifting Sands of Asteroids. *Science*, **316**, 993–994. 129, 130, 298, 299, 305

ASPHAUG, E. (2009). Growth and Evolution of Asteroids. *Annual Review of Earth and Planetary Sciences*, **37**, 413–448. 2, 4, 6, 7, 8, 12

ASPHAUG, E., MOORE, J.M., MORRISON, D., BENZ, W., NOLAN, M.C. & SULLIVAN, R.J. (1996). Mechanical and Geological Effects of Impact Cratering on Ida. *Icarus*, **120**, 158 – 184. 8

ASPHAUG, E., KING, P., SWIFT, M. & MERRIFIELD, M. (2001). Brazil nuts on Eros: Size-sorting of Asteroid Regolith. In *Lunar and Planetary Science Conference*, 1708. 27, 43, 129, 130, 299

ASPHAUG, E., RYAN, E.V. & ZUBER, M.T. (2002). Asteroid Interiors. In W.F. Bottke, A. Cellino, P. Paolicchi & R.P. Binzel, eds., *Asteroids III*, 463–484, University of Arizona Press. 7

BEHRINGER, R., HOWELL, D., KONDIC, L., TENNAKOON, S. & VEJE, C. (1999). Predictability and granular materials. *Physica D: Nonlinear Phenomena*, **133**, 1 – 17. 236, 238, 293

BELLEROSE, J., COOK, A., FANHESTOCK, E., MESTER, C., MURDOCH, N., OLDS, P., REDDY, V., ROZITIS, B., SCHINDLER, K. & YAMAGUCHI, T. (2008). DEx: Didymos Explorer - A low-cost mission to binary near Earth Asteroid Didymos. Tech. rep., NASA Ames S4P. 22

BELTON, M.J.S., CHAPMAN, C.R., THOMAS, P.C., DAVIES, M.E., GREENBERG, R., KLAASEN, K., BYRNES, D., D'AMARIO, L., SYNNOTT, S., JOHNSON, T.V., MCEWEN, A., MERLINE, W.J., DAVIS, D.R., PETIT, J.M., STORRS, A., VEVERKA, J. & ZELLNER, B. (1995). Bulk density of asteroid 243 Ida from the orbit of its satellite Dactyl. *Nature*, **374**, 785–788. 19

BENEDIX, G.K., MCFADDEN, L.A., MORROW, E.M. & FOMENKOVA, M.N. (1992). Bias correction factors for near-Earth asteroids. In A. W. Harris & E. Bowell, ed., *Asteroids, Comets, Meteors 1991*, 65–68. 17

BERARDI, C.R., BARROS, K., DOUGLAS, J.F. & LOSERT, W. (2010). Direct observation of stringlike collective motion in a two-dimensional driven granular fluid. *Phys. Rev. E*, **81**, 041301. 80, 83, 84, 87, 88, 90, 92, 94, 95, 98, 99, 104, 106

BINZEL, R.P., LUPISHKO, D.F., MARTINO, M.D., WHITELEY, R.J. & HAHN, G.J. (2002). Physical Properties of Near-Earth Objects. In W.F. Bottke, A. Cellino, P. Paolicchi & R.P. Binzel, eds., *Asteroids III*, 255–271, University of Arizona Press. 17

BINZEL, R.P., MORBIDELLI, A., MEROUANE, S., DEMEO, F.E., BIRLAN, M., VERNAZZA, P., THOMAS, C.A., RIVKIN, A.S., BUS, S.J. & TOKUNAGA, A.T. (2010). Earth encounters as the origin of fresh surfaces on near-Earth asteroids. *Nature*, **463**, 331–334. 29, 316

BLUM, J. & WURM, G. (2000). Experiments on Sticking, Restructuring, and Fragmentation of Preplanetary Dust Aggregates. *Icarus*, **143**, 138–146. 1

BLUM, J. & WURM, G. (2008). The Growth Mechanisms of Macroscopic Bodies in Protoplanetary Disks. *Annual Review of Astronomy and Astrophysics*, **46**, 21–56. 1

BOCQUET, L., LOSERT, W., SCHALK, D., LUBENSKY, T.C. & GOLLUB, J.P. (2001). Granular shear flow dynamics and forces: Experiment and continuum theory. *Phys. Rev. E*, **65**, 011307. 125, 236, 238, 293

BOTTKE, W.F. & MELOSH, H.J. (1996). Formation of asteroid satellites and doublet craters by planetary tidal forces. *Nature*, **381**, 51–53. 24, 28, 131, 300, 305

BOTTKE, W.F., RICHARDSON, D.C., MICHEL, P. & LOVE, S.G. (1999). 1620 Geographos and 433 Eros: Shaped by Planetary Tides? *Astrophysical Journal*, **117**, 1921–1928. 28

BOTTKE, W.F., MORBIDELLI, A., JEDICKE, R., PETIT, J.M., LEVISON, H.F., MICHEL, P. & METCALFE, T.S. (2002a). Debiased Orbital and Absolute Magnitude Distribution of the Near-Earth Objects. *Icarus*, **156**, 399 – 433. 15, 16

BOTTKE, W.F., VOKROUHLICKÝ, D., RUBINCAM, D.P. & BROZ, M. (2002b). The Effect of Yarkovsky Thermal Forces on the Dynamical Evolution of Asteroids and Meteoroids. In W.F. Bottke, A. Cellino, P. Paolicchi & R.P. Binzel, eds., *Asteroids III*, 395–408, University of Arizona Press. 27, 131, 300, 306

BOTTKE, W.F., VOKROUHLICKÝ, D., RUBINCAM, D.P. & NESVORNÝ, D. (2006). The Yarkovsky and Yorp Effects: Implications for Asteroid Dynamics. *Annual Review of Earth and Planetary Sciences*, **34**, 157–191. 27

BOULEY, S. & BARATOUX, D. (2011). Variation of small crater degradation on the Moon. In *Lunar and Planetary Science Conference*, 1388. 315, 316

BOWELL, E., HAPKE, B., DOMINGUE, D., LUMME, K., PELTONIEMI, J. & HARRIS, A.W. (1989). Application of photometric models to asteroids. In R. P. Binzel, T. Gehrels, & M. S. Matthews, ed., *Asteroids II*, 524-556. 15

BREU, A.P.J., ENSNER, H.M., KRUELLE, C.A. & REHBERG, I. (2003). Reversing the Brazil-Nut Effect: Competition between Percolation and Condensation. *Phys. Rev. Lett.*, **90**, 014302. 44

BRILLIANTOV, N.V., SPAHN, F., HERTZSCH, J.M. & POSCHEL, T. (1996). Model for collisions in granular gases. *Phys. Rev. E*, **53**, 5382–5392. 308

BRITT, D. & CONSOLMAGNO, G. (2000). The Porosity of Dark Meteorites and the Structure of Low-Albedo Asteroids. *Icarus*, **146**, 213 – 219. 19

BRITT, D.T., YEOMANS, D., HOUSEN, K. & CONSOLMAGNO, G. (2002). Asteroid Density, Porosity, and Structure. In W.F. Bottke, A. Cellino, P. Paolicchi & R.P. Binzel, eds., *Asteroids III*, 485–500. 19, 20, 21

BROWN, R.L. & RICHARDS, J.C. (1970). *Principles of Powder Mechanics*. Pergamon Press, Oxford. 39

BRUCKS, A., ARNDT, T., OTTINO, J. & LUEPTOW, R. (2007). Behavior of flowing granular materials under variable g. *Phys. Rev. E*, **75**, 032301-1–032301-4. 64, 68, 69

BURNS, J.A., LAMY, P.L. & SOTER, S. (1979). Radiation forces on small particles in the Solar System. *Icarus*, **40**, 1 – 48. 22

BUS, S., VILAS, F. & BARUCCI, M.A. (2002). Visible-Wavelength Spectroscopy of Asteroids. In W.F. Bottke, A. Cellino, P. Paolicchi & R.P. Binzel, eds., *Asteroids III*, 169–182, University of Arizona Press. 17

CAMPBELL, B.A. (1999). Surface formation rates and impact crater densities on Venus. *J. Geophys. Res.*, **104**, 21951–21955. 29

CAMPBELL, C.S. (1990). Rapid granular flows. *Annual Review of Fluid Mechanics*, **22**, 57–92. 34

CAMPBELL, C.S. (2002). Granular shear flows at the elastic limit. *Journal of Fluid Mechanics*, **465**, 261–291. 42, 89

CHAPMAN, C.R. (2004). Space weathering of asteroid surfaces. *Annual Review of Earth and Planetary Sciences*, **32**, 539–567. 9

CHAPMAN, C.R., MERLINE, W.J., THOMAS, P.C., JOSEPH, J., CHENG, A.F. & IZENBERG, N. (2002). Impact History of Eros: Craters and Boulders. *Icarus*, **155**, 104 – 118. 6

CHARNOZ, S., SALMON, J. & CRIDA, A. (2010). The recent formation of Saturn's moonlets from viscous spreading of the main rings. *Nature*, **465**, 752–754. 30

CHARNOZ, S., CRIDA, A., CASTILLO-ROGEZ, J.C., LAINEY, V., DONES, L., KARATEKIN, Ö., TOBIE, G., MATHIS, S., LE PONCIN-LAFITTE, C. & SALMON, J. (2011). Accretion of Saturn's mid-sized moons during the viscous spreading of young massive rings: Solving the paradox of silicate-poor rings versus silicate-rich moons. *Icarus*, **216**, 535–550. 30

CHENG, A.F., SANTO, A.G., HEERES, K.J., LANDSHOF, J.A., FARQUHAR, R.W., GOLD, R.E. & LEE, S.C. (1997). Near-Earth Asteroid Rendezvous: mission overview. *Journal of Geophysical Research*, **102**, 23695–23708. 3

CHENG, A.F., IZENBERG, N., CHAPMAN, C.R. & ZUBER, M.T. (2002). Ponded deposits on asteroid 433 Eros. *Meteoritics and Planetary Science*, **37**, 1095–1105. 8, 26

CHOWHAN, Z.T. (1995). Segregation of Particulate Solids Part I. *Pharm. Technol.*, **19**, 56. 43

CIAMARRA, M.P., NICODEMI, M. & CONIGLIO, A. (2007). Granular packs under vertical tapping: Structure evolution, grain motion, and dynamical heterogeneities. *Phys. Rev. E*, **75**, 021303. 42

CINTALA, M.J., HEAD, J.W. & VEVERKA, J. (1978). Characteristics of the cratering process on small satellites and asteroids. In *Lunar and Planetary Science Conference*, 3803–3830. 25, 26

CLEARY, P.W. & SAWLEY, M.L. (2002). DEM modelling of industrial granular flows: 3D case studies and the effect of particle shape on hopper discharge. *Applied Mathematical Modelling*, **26**, 89 – 111. 46, 309

CLEVELAND, W.S. (1979). Robust Locally Weighted Regression and Smoothing Scatterplots. *Journal of the American Statistical Association*, **74**, 829–836. 177

COLLINS, G.S., MELOSH, H.J., MORGAN, J.V. & WARNER, M.R. (2002). Hydrocode Simulations of Chicxulub Crater Collapse and Peak-Ring Formation. *Icarus*, **157**, 24 – 33. 315

COLWELL, J.E., GULBIS, A.A.S., HORÁNYI, M. & ROBERTSON, S. (2005). Dust transport in photoelectron layers and the formation of dust ponds on Eros. *Icarus*, **175**, 159 – 169. 22

COLWELL, J.E., BATISTE, S., HORÁNYI, M., ROBERTSON, S. & STURE, S. (2007). Lunar surface: Dust dynamics and regolith mechanics. *Rev. Geophys.*, **45**. 22

CORADINI, A., CAPACCIONI, F., ERARD, S., ARNOLD, G., DE SANCTIS, M.C., FILACCHIONE, G., TOSI, F., BARUCCI, M.A., CAPRIA, M.T., AMMANNITO, E., GRASSI, D., PICCIONI, G., GIUPPI, S., BELLUCCI, G., BENKHOFF, J., BIBRING, J.P., BLANCO, A., BLECKA, M., BOCKELEE-MORVAN, D., CARRARO, F., CARLSON, R., CARSENTY, U., CERRONI, P., COLANGELI, L., COMBES, M., COMBI, M., CROVISIER, J., DROSSART, P., ENCRENAZ, E.T., FEDERICO, C., FINK, U., FONTI, S., GIACOMINI, L., IP, W.H., JAUMANN, R., KUEHRT, E., LANGEVIN, Y., MAGNI, G., MCCORD, T., MENNELLA, V., MOTTOLA, S., NEUKUM, G., OROFINO, V., PALUMBO, P., SCHADE, U., SCHMITT, B., TAYLOR, F., TIPHENE, D. & TOZZI, G. (2011). The Surface Composition and Temperature of Asteroid 21 Lutetia As Observed by Rosetta/VIRTIS. *Science*, **334**, 492–. 11

COSTANTINO, D.J., SCHEIDEMANTEL, T.J., STONE, M.B., CONGER, C., KLEIN, K., LOHR, M., MODIG, Z. & SCHIFFER, P. (2008). Starting to Move through a Granular Medium. *Phys. Rev. Lett.*, **101**, 108001. 35

CRADDOCK, R.A., MAXWELL, T.A. & HOWARD, A.D. (1997). Crater morphometry and modification in the Sinus Sabaeus and Margaritifer Sinus regions of Mars. *J. Geophys. Res.*, **102**, 13321–13340. 315

CROCKER, J. & GRIER, D. (1996). Methods of Digital Video Microscopy for Colloidal Studies. *Journal of Colloid and Interface Science*, **179**, 298–310(13). 84, 160

DA CRUZ, F., EMAM, S., PROCHNOW, M., ROUX, J.N. & CHEVOIR, F. (2005). Rheophysics of dense granular materials: Discrete simulation of plane shear flows. *Phys. Rev. E*, **72**, 021309. 41

DAINTY, A., TOKSOZ, M., ANDERSON, K., PINES, P.J., NAKAMURA, Y. & LATHAM, G. (1974). Seismic Scattering and Shallow Structure of the Moon in Oceanus Procellarum. *Moon*, **9**, 11–29. 26

DANIELS, K.E. & BEHRINGER, R.P. (2006). Characterization of a freezing/melting transition in a vibrated and sheared granular medium. *Journal of Statistical Mechanics: Theory and Experiment*, **2006**, P07018. 237, 293

DE PATER, I. & LISSAUER, J. (2001). *Planetary Sciences*. Cambridge University Press, Cambridge. 315

DELANNAY, R., LOUGE, M., RICHARD, P., TABERLET, N. & VALANCE, A. (2007). Towards a theoretical picture of dense granular flows down inclines. *Nature Materials*, **6**, 99–108. 34, 75

DELBO, M. & MICHEL, P. (2011). Temperature History and Dynamical Evolution of (101955) 1999 RQ 36: A Potential Target for Sample Return from a Primitive Asteroid. *The Astrophysical Journal Letters*, **728**, L42. 14

DELBO, M., DELL'ORO, A., HARRIS, A.W., MOTTOLA, S. & MUELLER, M. (2007). Thermal inertia of near-Earth asteroids and implications for the magnitude of the Yarkovsky effect. *Icarus*, **190**, 236 – 249. 14, 15

DEMEO, F.E., BINZEL, R.P., SLIVAN, S.M. & BUS, S.J. (2009). An extension of the Bus asteroid taxonomy into the near-infrared. *Icarus*, **202**, 160–180. 17

DEMURA, H., KOBAYASHI, S., NEMOTO, E., MATSUMOTO, N., FURUYA, M., YUKISHITA, A., MURANAKA, N., MORITA, H., SHIRAKAWA, K., MARUYA, M., OHYAMA, H., UO, M., KUBOTA, T., HASHIMOTO, T., KAWAGUCHI, J., FUJIWARA, A., SAITO, J., SASAKI, S., MIYAMOTO, H. & HIRATA, N. (2006). Pole and global shape of 25143 Itokawa. *Science*, **312**, 1347–1349. 10, 11

DIVOUX, T., VASSILIEF, I., GAYVALLET, H. & GÉMINARD, J.C. (2009). Aging of a granular pile induced by thermal cycling. In M. Nakagawa & S. Luding, ed., *American Institute of Physics Conference Series*, vol. 1145 of *American Institute of Physics Conference Series*, 473–476. 42

DOMBARD, A.J. & FREED, A.M. (2002). Thermally induced lineations on the asteroid Eros: Evidence of orbit transfer. *Geophys. Res. Lett.*, **29**. 8

DOMBARD, A.J., BARNOUIN-JHA, O.S., THOMAS, P.C., PROCKTER, L.M. & CHENG, A.F. (2007). Can Boulders Supply Material for Ponds on the Asteroid 433 Eros? In *Lunar and Planetary Science Conference*, Lunar and Planetary Institute Science Conference Abstracts, 2221. 8, 27

DONATI, C., DOUGLAS, J.F., KOB, W., PLIMPTON, S.J., POOLE, P.H. & GLOTZER, S.C. (1998). Stringlike cooperative motion in a supercooled liquid. *Phys. Rev. Lett.*, **80**, 2338–2341. 80, 81, 104, 105

DUDOWICZ, J., FREED, K.F. & DOUGLAS, J.F. (2005). Direct computation of characteristic temperatures and relaxation times for glass-forming polymer liquids. *J. Chem. Phys.*, **123**, 111102. 81, 82

DURY, C.M. & RISTOW, G.H. (1999). Competition of mixing and segregation in rotating cylinders. *Physics of Fluids*, **11**, 1387–1394. 76

DURY, C.M., RISTOW, G.H., MOSS, J.L. & NAKAGAWA, M. (1998). Boundary effects on the angle of repose in rotating cylinders. *Phys. Rev. E*, **57**, 4491–4497. 76

ELASKAR, S., GODOY, L., GRAY, D. & STILES, J. (2000). A viscoplastic approach to model the flow of granular solids. *International Journal of Solids and Structures*, **38**, 2185–2214. 45

ESHUIS, P., VAN DER MEER, D., ALAM, M., VAN GERNER, H.J., VAN DER WEELE, K. & LOHSE, D. (2010). Onset of Convection in Strongly Shaken Granular Matter. *Phys. Rev. Lett.*, **104**, 038001. 128

FALK, M.L., TOIYA, M. & LOSERT, W. (2008). Shear transformation zone analysis of shear reversal during granular flow. *arXiv.org:0802.1752*. 130, 131, 132, 133, 277

FARINELLA, P. & DAVIS, D.R. (1992). Collision rates and impact velocities in the main asteroid belt. *Icarus*, **97**, 111 – 123. 26

FARINELLA, P. & VOKROUHLICKY, D. (1999). Semimajor Axis Mobility of Asteroidal Fragments. *Science*, **283**, 1507. 27

FORTERRE, Y. & POULIQUEN, O. (2001). Longitudinal Vortices in Granular Flows. *Phys. Rev. Lett.*, **86**, 5886–5889. 128

FORTERRE, Y. & POULIQUEN, O. (2008). Flows of Dense Granular Media. *Annual Review of Fluid Mechanics*, **40**, 1-24. 34, 40, 41

FRAIGE, F.Y., LANGSTON, P.A. & CHEN, G.Z. (2008). Distinct element modelling of cubic particle packing and flow. *Powder Technology*, **186**, 224 – 240. 46, 309

FRITSCH, C.C. & LANGOWSKI, J. (2010). Anomalous diffusion in the interphase cell nucleus: The effect of spatial correlations of chromatin. *The Journal of Chemical Physics*, **133**, 025101. 101

FUJIWARA, A. & ASADA, N. (1983). Impact fracture patterns on phobos ellipsoids. *Icarus*, **56**, 590 – 602. 8

FUJIWARA, A., KAWAGUCHI, J., YEOMANS, D.K., ABE, M., MUKAI, T., OKADA, T., SAITO, J., YANO, H., YOSHIKAWA, M., SCHEERES, D.J., BARNOUIN-JHA, O., CHENG, A.F., DEMURA, H., GASKELL, R.W., HIRATA, N., IKEDA, H., KOMINATO, T., MIYAMOTO, H., NAKAMURA, A.M., NAKAMURA, R., SASAKI, S. & UESUGI, K. (2006). The Rubble-Pile Asteroid Itokawa as Observed by Hayabusa. *Science*, **312**, 1330–1334. 6, 10, 11, 25

GALLAS, J.A.C., HERRMANN, H.J. & SOKOŁOWSKI, S. (1992). Convection cells in vibrating granular media. *Phys. Rev. Lett.*, **69**, 1371–1374. 296

GARCIMARTIN, A., MAZA, D., ILQUIMICHE, J.L. & ZURIGUEL, I. (2002). Convective motion in a vibrated granular layer. *Phys. Rev. E*, **65**, 031303. 296

GOERTZ, C.K. (1989). Dusty plasmas in the solar system. *Reviews of Geophysics*, **27**, 271–292. 22

GOLDHIRSCH, I. (2003). Rapid Granular Flows. *Annual Review of Fluid Mechanics*, **35**, 267–293. 34

GOLDREICH, P. & SARI, R. (2009). Tidal Evolution of Rubble Piles. *Astrophysical Journal*, **691**, 54–60. 47

GOLDSHTEIN, A., KAMENETSKY, V., POTAPOV, A., SHAPIRO, M., CAMPBELL, C. & DEGANI, D. (2002). Hydrodynamics of rapid granular flow of inelastic particles into vacuum. *Granular Matter*, **4**, 115–127, 10.1007/s10035-002-0111-9. 309

GRADIE, J. & TEDESCO, E. (1982). Compositional Structure of the Asteroid Belt. *Science*, **216**, 1405–1407. 19

GRAY, J. & HUTTER, K. (1997). Pattern formation in granular avalanches. *Continuum Mechanics and Thermodynamics*, **9**, 341–345, 10.1007/s001610050075. 35, 36

GRAY, J.M.N.T. & ANCEY, C. (2011). Multi-component particle-size segregation in shallow granular avalanches. *Journal of Fluid Mechanics*, **678**, 535–588. 46

GRAY, J.M.N.T. & CHUGUNOV, V.A. (2006). Particle-size segregation and diffusive remixing in shallow granular avalanches. *Journal of Fluid Mechanics*, **569**, 365–398. 44, 45

GRD MIDI (2004). On dense granular flows. *The European Physical Journal E: Soft Matter and Biological Physics*, **14**, 341–365, 10.1140/epje/i2003-10153-0. 39, 41

GUDHE, R., YALAMANCHILI, R. & MASSOUDI, M. (1994). Flow of granular materials down a vertical pipe. *International Journal of Non-Linear Mechanics*, **29**, 1 – 12. 32

GUI, N. & FAN, J. (2009). Numerical simulation of motion of rigid spherical particles in a rotating tumbler with an inner wavelike surface. *Powder Technology*, **192**, 234 – 241. 76

HALEKAS, J.S., DELORY, G.T., LIN, R.P., STUBBS, T.J. & FARRELL, W.M. (2009). Lunar surface charging during solar energetic particle events: Measurement and prediction. *J. Geophys. Res.*, **114**. 22

HARRIS, A.W. (1996). The Rotation Rates of Very Small Asteroids: Evidence for 'Rubble Pile' Structure. In *Lunar and Planetary Science Conference*, Lunar and Planetary Inst. Technical Report, 493. 16

HARRIS, A.W. (2005). The surface properties of small asteroids from thermal-infrared observations. *Proceedings of the International Astronomical Union*, **1**, 449–463. 14

HARTMANN, W.K., MALIN, M., MCEWEN, A., CARR, M., SODERBLOM, L., THOMAS, P., DANIELSON, E., JAMES, P. & VEVERKA, J. (1999). Evidence for recent volcanism on Mars from crater counts. *Nature*, **397**, 586–589. 25, 315

HATANO, T. (2007). Power-law friction in closely packed granular materials. *Phys. Rev. E*, **75**, 060301. 307

HATANO, T. (2008a). Power-law rheology and the dynamical heterogeneity in a sheared granular material. *ArXiv e-prints*. 307

HATANO, T. (2008b). Scaling Properties of Granular Rheology near the Jamming Transition. *Journal of the Physical Society of Japan*, **77**, 123002. 307

HATANO, T. (2010). Critical Scaling of Granular Rheology. *Progress of Theoretical Physics Supplement*, **184**, 143–152. 307

HEISSELMANN, D., BLUM, J., FRASER, H. & WOLLING, K. (2009). Microgravity experiments on the collisional behavior of saturnian ring particles. *Icarus*, **206**, 424-430. 68

HERRERA, M., MCCARTHY, S., SLOTTERBACK, S., CEPHAS, E., LOSERT, W. & GIRVAN, M. (2011). Path to fracture in granular flows: Dynamics of contact networks. *Phys. Rev. E*, **83**, 061303. 342, 344

HICKS, M., BURATTI, B., JR., R.N. & RABINOWITZ, D. (2000). Physical observations of 1996 PW and 1997 SE5: Extinct Comets or D-Type Asteroids? *Icarus*, **143**, 354 – 359. 19

HOFMEISTER, P.G., BLUM, J. & HEISSELMANN, D. (2009). The Flow Of Granular Matter Under Reduced-Gravity Conditions. In *American Institute of Physics Conference Series*, vol. 1145, 71–74. 311

HOLSAPPLE, K. (2001). Equilibrium Configurations of Solid Cohesionless Bodies. *Icarus*, **154**, 432 – 448. 16, 45

HOLSAPPLE, K., GIBLIN, I., HOUSEN, K., NAKAMURA, A. & RYAN, E. (2002). Asteroid Impacts: Laboratory Experiments and Scaling Laws. In W.F. Bottke, A. Cellino, P. Paolicchi & R.P. Binzel, eds., *Asteroids III*, 443–462, University of Arizona Press. 25, 131, 300, 306

HOLSAPPLE, K.A. (2004). Equilibrium figures of spinning bodies with self-gravity. *Icarus*, **172**, 272 – 303. 16, 45

HOLSAPPLE, K.A. (2007). Spin limits of Solar System bodies: From the small fast-rotators to 2003 EL61. *Icarus*, **187**, 500 – 509. 17, 18

HOLSAPPLE, K.A. & MICHEL, P. (2006). Tidal disruptions: A continuum theory for solid bodies. *Icarus*, **183**, 331–348. 45

HOLSAPPLE, K.A. & MICHEL, P. (2008). Tidal disruptions: II. A continuum theory for solid bodies with strength, with applications to the Solar System. *Icarus*, **193**, 283 – 301. 18, 45

HONG, D. & MCLENNAN, J. (1992). Molecular dynamics simulations of hard sphere granular particles. *Physica A: Statistical Mechanics and its Applications*, **187**, 159 – 171. 46

HOPKINS, P., FORTINI, A., ARCHER, A.J. & SCHMIDT, M. (2010). The van Hove distribution function for Brownian hard spheres: Dynamical test particle theory and computer simulations for bulk dynamics. *Journal of Chemical Physics*, **133**, 224505. 104

HOUSEN, K.R. (1992). Crater Ejecta Velocities for Impacts on Rocky Bodies. In *Lunar and Planetary Science Conference*, Lunar and Planetary Institute Science Conference Abstracts, 555. 312

HOUSEN, K.R., SCHMIDT, R.M. & HOLSAPPLE, K.A. (1983). Crater ejecta scaling laws - Fundamental forms based on dimensional analysis. *J. Geophys. Res.*, **88**, 2485–2499. 312

HSIAU, S.S. & CHEN, C.H. (2000). Granular convection cells in a vertical shaker. *Powder Technology*, **111**, 210 – 217. 128

HSIEH, H.H. & JEWITT, D. (2006). A Population of Comets in the Main Asteroid Belt. *Science*, **312**, 561–563. 2

HUGHES, A.L., COLWELL, J.E. & DEWOLFE, A.W. (2008). Electrostatic dust transport on Eros: 3-D simulations of pond formation. *Icarus*, **195**, 630 – 648. 22

HUILIN, L., YUNHUA, Z., DING, J., GIDASPOW, D. & WEI, L. (2007). Investigation of mixing/segregation of mixture particles in gas-solid fluidized beds. *Chemical Engineering Science*, **62**, 301 – 317. 46

IORDANOFF, I. & KHONSARI, M.M. (2004). Granular Lubrication: Toward an Understanding of the Transition Between Kinetic and Quasi-Fluid Regime. *Journal of Tribology*, **126**, 137–145. 41

IVANOV, B. (2006). Earth/Moon impact rate comparison: Searching constraints for lunar secondary/primary cratering proportion. *Icarus*, **183**, 504 – 507. 312, 313

IVANOV, B.A. (2001). Mars/Moon Cratering Rate Ratio Estimates. *Space Science Reviews*, **96**, 87–104. 25

JAEGER, H.M., NAGEL, S.R. & BEHRINGER, R.P. (1996). Granular solids, liquids, and gases. *Rev. Mod. Phys.*, **68**, 1259–1273. 32, 37, 39, 43

JANSEN (1895). Versuche uber Getreidedruck in Silozellen. *Z. Verein Deutsch. Ing.*, **39**. 37

JASTER, A. (1999). Computer simulations of the two-dimensional melting transition using hard disks. *Phys. Rev. E*, **59**, 2594–2602. 92

JEWITT, D. & LUU, J. (1993). Discovery of the candidate Kuiper belt object 1992 QB1. *Nature*, **362**, 730–732. 2

JOP, P., FORTERRE, Y. & POULIQUEN, O. (2006). A constitutive law for dense granular flows. *Nature*, **441**, 727–730. 41, 42

JUTZI, M., BENZ, W. & MICHEL, P. (2008). Numerical simulations of impacts involving porous bodies: I. Implementing sub-resolution porosity in a 3D SPH hydrocode. *Icarus*, **198**, 242 – 255. 20

KAASALAINEN, M., DURECH, J., WARNER, B.D., KRUGLY, Y.N. & GAFTONYUK, N.M. (2007). Acceleration of the rotation of asteroid 1862 Apollo by radiation torques. *Nature*, **446**, 420–422. 14

KAČIANAUSKAS, R., MAKNICKAS, A., KAČENIAUSKAS, A., MARKAUSKAS, D. & BALEVIČIUS, R. (2010). Parallel discrete element simulation of poly-dispersed granular material. *Advances in Engineering Software*, **41**, 52 – 63. 309

KADONO, T., SAKAIYA, T., HIRONAKA, Y., OTANI, K., SANO, T., FUJIWARA, T., MOCHIYAMA, T., KUROSAWA, K., SUGITA, S., SEKINE, Y., NISHIKANBARA, W., MATSUI, T., OHNO, S., SHIROSHITA, A., MIYANISHI, K., OZAKI, N., KODAMA, R., NAKAMURA, A.M., ARAKAWA, M., FUJIOKA, S. & SHIGEMORI, K. (2010). Impact experiments with a new technique for acceleration of projectiles to velocities higher than Earth's escape velocity of 11.2 km/s. *J. Geophys. Res.*, **115**. 307

KAWASAKI, K. (1986). *Monte Carlo calculation of the flow of granular materials*. Ph.D. thesis, California Institute of Technology. 46

KAYE, B.H. (1997). *Powder mixing, Volume 10*. Chapman and Hall, London. 39

KHAKHAR, D.V., MCCARTHY, J.J. & OTTINO, J.M. (1997). Radial segregation of granular mixtures in rotating cylinders. *Physics of Fluids*, **9**, 3600–3614. 76, 310

KHOSROPOUR, R., ZIRINSKY, J., PAK, H.K. & BEHRINGER, R.P. (1997). Convection and size segregation in a Couette flow of granular material. *Phys. Rev. E*, **56**, 4467–4473. 126, 296

KNIGHT, J.B. (1997). External boundaries and internal shear bands in granular convection. *Phys. Rev. E*, **55**, 6016–6023. 293

KNIGHT, J.B., JAEGER, H.M. & NAGEL, S.R. (1993). Vibration-induced size separation in granular media: The convection connection. *Phys. Rev. Lett.*, **70**, 3728–3731. 43, 44, 45, 296

KNIGHT, J.B., FANDRICH, C.G., LAU, C.N., JAEGER, H.M. & NAGEL, S.R. (1995). Density relaxation in a vibrated granular material. *Phys. Rev. E*, **51**, 3957–3963. 42

KOSINSKI, P. & HOFFMANN, A.C. (2009). Extension of the hard-sphere particle-wall collision model to account for particle deposition. *Phys. Rev. E*, **79**, 061302. 46

KRIM, J. & BEHRINGER, R. (2009). Friction, force chains, and falling fruit. *Physics Today*, **62**, 66–67. 37

KUWABARA, G. & KONO, K. (1987). Restitution Coefficient in a Collision between Two Spheres. *Japanese Journal of Applied Physics*, **26**, 1230–1233. 308

LAJEUNESSE, E., MALVERTI, L. & CHARRU, F. (2010). Bed load transport in turbulent flow at the grain scale: Experiments and modeling. *J. Geophys. Res.*, **115**. 307

LATHAM, J.P., MUNJIZA, A., GARCIA, X., XIANG, J. & GUISES, R. (2008). Three-dimensional particle shape acquisition and use of shape library for DEM and FEM/DEM simulation. *Minerals Engineering*, **21**, 797 – 805. 46, 309

LEBOFSKY, L.A., SYKES, M.V., TEDESCO, E.F., VEEDER, G.J., MATSON, D.L., BROWN, R.H., GRADIE, J.C., FEIERBERG, M.A. & RUDY, R.J. (1986). A refined 'standard' thermal model for asteroids based on observations of 1 Ceres and 2 Pallas. *Icarus*, **68**, 239–251. 13

LEE, J. & HERRMANN, H.J. (1993). Angle of repose and angle of marginal stability: molecular dynamics of granular particles. *Journal of Physics A: Mathematical and General*, **26**, 373. 308

LEE, P. (1995). Electrostatic Levitation of Fines on Asteroids. *Meteoritics*, **30**, 535. 22

LEE, P. (1996). Dust Levitation on Asteroids. *Icarus*, **124**, 181–194. 8, 26

LEINHARDT, Z.M. & RICHARDSON, D.C. (2005). Planetesimals to Protoplanets. I. Effect of Fragmentation on Terrestrial Planet Formation. *Astrophysical Journal*, **625**, 427–440. 50

LEINHARDT, Z.M., RICHARDSON, D.C. & QUINN, T. (2000). Direct N-body Simulations of Rubble Pile Collisions. *Icarus*, **146**, 133–151. 50

LIFFMAN, K., METCALFE, G. & CLEARY, P. (1997). Granular Convection and Transport due to Horizontal Shaking. *Phys. Rev. Lett.*, **79**, 4574–4576. 128

LIU, A.J. & NAGEL, S.R. (1998). Nonlinear dynamics: Jamming is not just cool any more. *Nature*, **396**, 21–22. 81

LODDERS, K. & FEGLEY JR., B. (1998). *The Planetary Scientist's Companion*. Oxford University Press, New York. 29

LOSERT, W. & KWON, G. (2001). Transient and Steady-State Dynamics of Granular Shear Flows. *Advances in Complex Systems*, **4**, 369–377. 136

LOSERT, W., BOCQUET, L., LUBENSKY, T.C. & GOLLUB, J.P. (2000). Particle Dynamics in Sheared Granular Matter. *Phys. Rev. Lett.*, **85**, 1428–1431. 38, 236, 238, 293

LOWRY, S.C., FITZSIMMONS, A., PRAVEC, P., VOKROUHLICKY, D., BOEHNHARDT, H., TAYLOR, P.A., MARGOT, J.L., GALAD, A., IRWIN, M., IRWIN, J. & KUSNIRAK, P. (2007). Direct Detection of the Asteroidal YORP Effect. *Science*, **316**, 272–274. 14

LUCAS, A. & MANGENEY, A. (2007). Mobility and topographic effects for large Valles Marineris landslides on Mars. *AGU Fall Meeting Abstracts*, A1090. 307

LUCAS, A., MANGENEY, A. & MHGE, D. (2010). Granular Flow Dynamics on Earth, Moon, and Mars from analytical, numerical and field analysis. *AGU Fall Meeting Abstracts*, A730. 307

LUDING, S. (1998). Collisions and Contacts between two particles. *Physics of dry granular Media*. 308

LUDING, S. (2004). Molecular Dynamics Simulations of Granular Materials. *The Physics of Granular Materials*. 75, 308

LUDING, S. (2008). The effect of friction on wide shear bands. *Particulate Science and Technology*, **26**, 33–42. 293

LUPISHKO, D.F. & DI MARTINO, M. (1998). Physical properties of near-Earth asteroids. *Planetary and Space Science*, **46**, 47–74. 19

MAIR, K., FRYE, K.M. & MARONE, C. (2002). Influence of grain characteristics on the friction of granular shear zones. *J. Geophys. Res.*, **107**. 293

MAKSE, H.A., JOHNSON, D.L. & SCHWARTZ, L.M. (2000). Packing of Compressible Granular Materials. *Phys. Rev. Lett.*, **84**, 4160–4163. 39, 75

MANGENEY, A., BOUCHUT, F., THOMAS, N., VILOTTE, J.P. & BRISTEAU, M.O. (2007). Numerical modeling of self-channeling granular flows and of their levee-channel deposits. *J. Geophys. Res.*, **112**. 307

MARCHI, S., MAGRIN, S., NESVORNÝ, D., PAOLICCHI, P. & LAZZARIN, M. (2006). A spectral slope versus perihelion distance correlation for planet-crossing asteroids. *MNRAS*, **368**, L39–L42. 29, 316

MARCHI, S., MASSIRONI, M., CREMONESE, G., MARTELLATO, E., GIACOMINI, L. & PROCKTER, L. (2011). The effects of the target material properties and layering on the crater chronology: The case of Raditladi and Rachmaninoff basins on Mercury. *Planetary and Space Science*, **59**, 1968–1980. 29

MARGOT, J.L., NOLAN, M.C., BENNER, L.A.M., OSTRO, S.J., JURGENS, R.F., GIORGINI, J.D., SLADE, M.A. & CAMPBELL, D.B. (2002). Binary Asteroids in the Near-Earth Object Population. *Science*, **296**, 1445–1448. 22

MASSEY, R. (2011). Planetary science comes to Nantes. *Astronomy and Geophysics*, **52**, 6.27–6.30. 12, 30

MCCARTHY, J.J. (2009). Turning the corner in segregation. *Powder Technology*, **192**, 137 – 142. 35

MCCARTHY, J.J. & OTTINO, J.M. (1998). Particle dynamics simulation: a hybrid technique applied to granular mixing. *Powder Technology*, **97**, 91 – 99. 76

MCCARTHY, J.J., SHINBROT, T., METCALFE, G., WOLF, J.E. & OTTINO, J.M. (1996). Mixing of granular materials in slowly rotated containers. *AIChE Journal*, **42**, 3351–3363. 76

MCCARTHY, J.J., KHAKHAR, D.V. & OTTINO, J.M. (2000). Computational studies of granular mixing. *Powder Technology*, **109**, 72 – 82. 76

MCEWEN, A.S., PREBLICH, B.S., TURTLE, E.P., ARTEMIEVA, N.A., GOLOMBEK, M.P., HURST, M., KIRK, R.L., BURR, D.M. & CHRISTENSEN, P.R. (2005). The rayed crater Zunil and interpretations of small impact craters on Mars. *Icarus*, **176**, 351 – 381. 312, 313, 314

MEHTA, A.J. (2007). *Granular Physics*. Cambridge University Press, New York. 45, 75

MELOSH, H.J. (1989). *Impact cratering: A geologic process*. Oxford Monographs on Geology and Geophysics. 313

MELOSH, H.J. & IVANOV, B.A. (1999). Impact Crater Collapse. *Annual Review of Earth and Planetary Sciences*, **27**, 385–415. 313

MELOSH, H.J. & SCHENK, P. (1993). Split comets and the origin of crater chains on Ganymede and Callisto. *Nature*, **365**, 731–733. 28

MELOSH, H.J. & WHITAKER, E.A. (1993). Lunar crater chains. *Nature*, **365**, 713–713. 28

MICHEL, P. (2011). Physical Properties of NEOs that Inform Mitigation. In *IAA Planetary Defense Conference*. 16, 17, 20

MICHEL, P. & DELBO, M. (2010). Orbital and thermal evolutions of four potential targets for a sample return space mission to a primitive near-Earth asteroid. *Icarus*, **209**, 520 – 534. 14

MICHEL, P., BENZ, W., TANGA, P. & RICHARDSON, D.C. (2001). Collisions and Gravitational Reaccumulation: Forming Asteroid Families and Satellites. *Science*, **294**, 1696–1700. 3, 20, 50

MICHEL, P., BENZ, W. & RICHARDSON, D.C. (2003). Disruption of fragmented parent bodies as the origin of asteroid families. *Nature*, **421**, 608–611. 50

MICHEL, P., O'BRIEN, D.P., ABE, S. & HIRATA, N. (2009). Itokawa's cratering record as observed by Hayabusa: Implications for its age and collisional history. *Icarus*, **200**, 503–513. 6, 25, 316

MIKA, J.T. & POOLMAN, B. (2011). Macromolecule diffusion and confinement in prokaryotic cells. *Current Opinion in Biotechnology*, **22**, 117 – 126. 101

MIYAMOTO, H., YANO, H., SCHEERES, D.J., ABE, S., BARNOUIN-JHA, O., CHENG, A.F., DEMURA, H., GASKELL, R.W., HIRATA, N., ISHIGURO, M., MICHIKAMI, T., NAKAMURA, A.M., NAKAMURA, R., SAITO, J. & SASAKI, S. (2007). Regolith Migration and Sorting on Asteroid Itokawa. *Science*, **316**, 1011–1014. 10, 26, 82, 119, 129, 130, 299

MONETTI, R., HURD, A. & KENKRE, V.M. (2001). Simulations for dynamics of granular mixtures in a rotating drum. *Granular Matter*, **3**, 113–116, 10.1007/s100350000078. 76

MOTHE-DINIZ, T., CARVANO, J.M. & LAZZARO, D. (2003). Distribution of taxonomic classes in the main belt of asteroids. *Icarus*, **162**, 10 - 21. 19

MUELLER, M. (2007). *Surface Properties of Asteroids from Mid-Infrared Observations and Thermophysical Modeling*. Ph.D. thesis, Freie Universitat Berlin. 13, 14

MUETH, D.M., DEBREGEAS, G.F., KARCZMAR, G.S., ENG, P.J., NAGEL, S.R. & JAEGER, H.M. (2000). Signatures of granular microstructure in dense shear flows. *Nature*, **406**, 385–389. 39, 236, 238, 293

MURDOCH, N., MICHEL, P., RICHARDSON, D.C., NORDSTROM, K., BERARDI, C.R., GREEN, S.F. & LOSERT, W. (2012a). Numerical simulations of granular dynamics II. Particle dynamics in a shaken granular material. *Icarus*, **219**, 231–335. 80, 304

MURDOCH, N., ROZITIS, B., GREEN, S.F., DE LOPHEM, T., MICHEL, P. & LOSERT, W. (2012b). A microgravity-modified taylor couette shear cell. *In preparation*. 305

MURDOCH, N., ROZITIS, B., GREEN, S.F., MICHEL, P., DE LOPHEM, T. & LOSERT, W. (2012c). AstEx Microgravity Experiment: Simulating Asteroid Regoliths. *In preparation*. 305

MURDOCH, N., ROZITIS, B., GREEN, S.F., MICHEL, P., DE LOPHEM, T. & LOSERT, W. (2012d). Granular Convection in Varying Gravitational Environments. *In preparation*. 305

NAGEL, S.R. (1992). Instabilities in a sandpile. *Rev. Mod. Phys.*, **64**, 321–325. 296

NEWMARK, N. (1965). Effects of earthquakes on dams and embankments. *Geotechnique*, **15**, 139–160. 82

NICHOL, K., ZANIN, A., BASTIEN, R., WANDERSMAN, E. & VAN HECKE, M. (2010). Flow-Induced Agitations Create a Granular Fluid. *Phys. Rev. Lett.*, **104**, 078302. 35

OGAWA, S., UMEMURA, A. & OSHIMA, N. (1980). On the equations of fully fluidized granular materials. *Zeitschrift fur Angewandte Mathematik und Physik (ZAMP)*, **31**, 483–493, 10.1007/BF01590859. 38

OLAFSEN, J. & URBACH, J. (2005). Two-dimensional melting far from equilibrium in a granular monolayer. *Physical review letters*, **95**. 94

OLSON, S. & MILLER, F. (2009). Experimental comparison of opposed and concurrent flame spread in a forced convective microgravity environment. *Proceedings of the Combustion Institute*, **32**, 2445 - 2452. 129

ONODA, G.Y. & LINIGER, E.G. (1990). Random loose packings of uniform spheres and the dilatancy onset. *Phys. Rev. Lett.*, **64**, 2727–2730. 142

OSTRO, S.J., MARGOT, J.L., BENNER, L.A.M., GIORGINI, J.D., SCHEERES, D.J., FAHNESTOCK, E.G., BROSCHART, S.B., BELLEROSE, J., NOLAN, M.C., MAGRI, C., PRAVEC, P., SCHEIRICH, P., ROSE, R., JURGENS, R.F., DE JONG, E.M. & SUZUKI, S. (2006). Radar Imaging of Binary Near-Earth Asteroid (66391) 1999 KW4. *Science*, **314**, 1276–1280. 29, 48

PAOLICCHI, P., BURNS, J.A. & WEIDENSCHILLING, S.J. (2002). Side Effects of Collisions: Spin Rate Changes, Tumbling Rotation States, and Binary Asteroids. In W.F. Bottke, A. Cellino, P. Paolicchi & R.P. Binzel, eds., *Asteroids III*, 517–526, University of Arizona Press. 131, 300, 306

PERKO, H.A., NELSON, J.D. & SADEH, W.Z. (2001). Surface Cleanliness Effect on Lunar Soil Shear Strength. *Journal of Geotechnical and Geoenvironmental Engineering*, **127**, 371–383. 24

PERRINE, R.P., RICHARDSON, D.C. & SCHEERES, D.J. (2011). A numerical model of cohesion in planetary rings. *Icarus*, **212**, 719 - 735. 310

PHILIPPE, P. & BIDEAU, D. (2003). Granular Medium under Vertical Tapping: Change of Compaction and Convection Dynamics around the Liftoff Threshold. *Phys. Rev. Lett.*, **91**, 104302. 296

POHLMAN, N.A., SEVERSON, B.L., OTTINO, J.M. & LUEPTOW, R.M. (2006). Surface roughness effects in granular matter: Influence on angle of repose and the absence of segregation. *Phys. Rev. E*, **73**, 031304. 76

POSCHEL, T. & BUCHHOLTZ, V. (1995). Complex flow of granular material in a rotating cylinder. *Chaos, Solitons and Fractals*, **5**, 1901 - 1905, 1907–1912, structure Formation in Continuous Dynamical Systems. 76

POULIQUEN, O. (2010). Granular Flows. In *Numerical Modeling of Asteroids as Granular Systems*. 40

POULIQUEN, O., CASSAR, C., JOP, P., FORTERRE, Y. & NICOLAS, M. (2006). Flow of dense granular material: towards simple constitutive laws. *Journal of Statistical Mechanics: Theory and Experiment*, **2006**, P07020. 39, 41, 42

PRAVEC, P., VOKROUHLICKÝ, D., POLISHOOK, D., SCHEERES, D.J., HARRIS, A.W., GALÁD, A., VADUVESCU, O., POZO, F., BARR, A., LONGA, P., VACHIER, F., COLAS, F., PRAY, D.P., POLLOCK, J., REICHART, D., IVARSEN, K., HAISLIP, J., LACLUYZE, A., KUŠNIRÁK, P., HENYCH, T., MARCHIS, F., MACOMBER, B., JACOBSON, S.A., KRUGLY, Y.N., SERGEEV, A.V. & LEROY, A. (2010). Formation of asteroid pairs by rotational fission. *Nature*, **466**, 1085–1088. 24

PRESS, W.H., TEUKOLSKY, S., VETTERLING, W.T. & FLANNERY, B.P. (2007). *Numerical Recipes: The Art of Scientific Computing*. Cambridge University Press, New York, 3rd edn. 53

PROCKTER, L., THOMAS, P., ROBINSON, M., JOSEPH, J., MILNE, A., BUSSEY, B., VEVERKA, J. & CHENG, A. (2002). Surface Expressions of Structural Features on Eros. *Icarus*, **155**, 75 - 93. 8

RADJAI, F. & RICHEFEU, V. (2009). Contact dynamics as a nonsmooth discrete element method. *Mechanics of Materials*, **41**, 715 - 728. 47

RADJAI, F. & ROUX, S. (2004). Contact dynamics study of 2D granular media: Critical states and relevant internal variables. In H. Hinrichsen & D.E. Wolf, eds., *The Physics of Granular Media*, 165–186, Wiley-Vch, Berlin. 39

RAIHANE, A., BONNEFOY, O., GELET, J.L., CHAIX, J.M. & THOMAS, G. (2009). Experimental study of a 3D dry granular medium submitted to horizontal shaking. *Powder Technology*, **190**, 252–257. 128

RAJCHENBACH, J. (1991). Dilatant Process for Convective Motion in a Sand Heap. *EPL (Europhysics Letters)*, **16**, 149. 269, 270, 294

RAMPINO, M.R. & VOLK, T. (1996). Multiple impact event in the paleozoic: Collision with a string of comets or asteroids? *Geophysical Research Letters*, **23**, 49–52. 28

RAPAPORT, D.C. (2002). Simulational studies of axial granular segregation in a rotating cylinder. *Phys. Rev. E*, **65**, 061306. 76

REIS, P.M., INGALE, R.A. & SHATTUCK, M.D. (2006). Crystallization of a Quasi-Two-Dimensional Granular Fluid. *Phys. Rev. Lett.*, **96**, 258001. 92

REYNOLDS, O. (1885). On the dilatancy of media composed of rigid particles in contact with experimental illustrations. *Philos. Mag. Ser.*, **5**, 469 - 481. 39

RICHARD, P., NICODEMI, M., DELANNAY, R., RIBIERE, P. & BIDEAU, D. (2005). Slow relaxation and compaction of granular systems. *Nature Materials*, **4**, 121–128. 32

RICHARDSON, D.C. & WALSH, K.J. (2006). Binary Minor Planets. *Annual Review of Earth and Planetary Sciences*, **34**, 47–81. 50

RICHARDSON, D.C., BOTTKE, W.F. & LOVE, S.G. (1998). Tidal Distortion and Disruption of Earth-Crossing Asteroids. *Icarus*, **134**, 47–76. 28, 29, 310, 316

RICHARDSON, D.C., QUINN, T., STADEL, J. & LAKE, G. (2000). Direct Large-Scale N-Body Simulations of Planetesimal Dynamics. *Icarus*, **143**, 45 – 59. 48, 49, 50, 52

RICHARDSON, D.C., LEINHARDT, Z.M., MELOSH, H.J., BOTTKE, W.F. & ASPHAUG, E. (2002). Gravitational Aggregates: Evidence and Evolution. In *Asteroids III*, 501–515. 47

RICHARDSON, D.C., MICHEL, P., WALSH, K.J. & FLYNN., K.W. (2009). Numerical simulations of asteroids modelled as gravitational aggregates with cohesion. *Planetary and Space Science*, **57**, 183–192. 49, 52, 53, 54, 56, 310

RICHARDSON, D.C., WALSH, K.J., MURDOCH, N. & MICHEL, P. (2011). Numerical simulations of granular dynamics: I. Hard-sphere discrete element method and tests. *Icarus*, **212**, 427–437. 51, 53, 57, 303, 304

RICHARDSON, J.E., MELOSH, H.J. & GREENBERG, R. (2004). Impact-Induced Seismic Activity on Asteroid 433 Eros: A Surface Modification Process. *Science*, **306**, 1526–1529. 6, 25, 79, 115, 316

RICHARDSON, J.E., JR., MELOSH, H.J., GREENBERG, R.J. & O'BRIEN, D.P. (2005). The global effects of impact-induced seismic activity on fractured asteroid surface morphology. *Icarus*, **179**, 325 – 349. 9, 26, 79, 82, 83, 115

RIGGLEMAN, R.A., YOSHIMOTO, K., DOUGLAS, J.F. & DE PABLO, J.J. (2006). Influence of Confinement on the Fragility of Antiplasticized and Pure Polymer Films. *Phys. Rev. Lett.*, **97**, 045502. 80, 81

ROBINSON, M.S., THOMAS, P.C., VEVERKA, J., MURCHIE, S. & CARCICH, B. (2001). The nature of ponded deposits on Eros. *Nature*, **413**, 396–400. 8

ROBINSON, M.S., THOMAS, P.C., VEVERKA, J., MURCHIE, S.L. & WILCOX, B.B. (2002). The geology of 433 Eros. *Meteoritics and Planetary Science*, **37**, 1651–1684. 6, 8, 9, 26

RODRIGUEZ-LINAN, G.M. & NAHMAD-MOLINARI, Y. (2006). Granular convection driven by shearing inertial forces. *Phys. Rev. E*, **73**, 011302. 128, 296

ROSATO, A., STRANDBURG, K.J., PRINZ, F. & SWENDSEN, R.H. (1987). Why the Brazil nuts are on top: Size segregation of particulate matter by shaking. *Phys. Rev. Lett.*, **58**, 1038–1040. 43

ROSATO, A.D., RATNASWAMY, V., HORNTROP, D.J., DYBENKO, O. & KONDIC, L. (2009). Density Relaxation of Granular Matter through Monte Carlo Simulations. *AIP Conference Proceedings*, **1145**, 481–484. 46

ROZITIS, B. (2011). *Characterisation of Near-Earth asteroids for a sample return mission*. Ph.D. thesis, The Open University. 14, 27, 28

ROZITIS, B. & GREEN, S.F. (2011). Directional characteristics of thermal-infrared beaming from atmosphereless planetary surfaces - a new thermophysical model. *MNRAS*, **415**, 2042–2062. 13, 14

RUBINCAM, D.P. (2000). Radiative Spin-up and Spin-down of Small Asteroids. *Icarus*, **148**, 2–11. 27

RUSSELL, C., CAPACCIONI, F., CORADINI, A., DE SANCTIS, M., FELDMAN, W., JAUMANN, R., KELLER, H., MCCORD, T., MCFADDEN, L., MOTTOLA, S., PIETERS, C., PRETTYMAN, T., RAYMOND, C., SYKES, M., SMITH, D. & ZUBER, M. (2007). Dawn Mission to Vesta and Ceres. *Earth, Moon, and Planets*, **101**, 65–91, 10.1007/s11038-007-9151-9. 3

RUSSELL, C., RAYMOND, C., MASE, R., RAYMAN, M., POLANSKEY, C., JOY, S., JAUMANNN, R., MCSWEEN, H., SYKES, M., MCFADDEN, L., LI, J., TRICARICO, P., KONOPLIV, A., ASMAR, S., ZUBER, M., SMITH, D., ROATSCH, T., CORADINI, A., MASTODEMOS, N., KELLER, H., NATHUES, A., DESANCTIS, M., PIETERS, C., PRETTYMAN, T., YINGST, R. & SCHENK, P. (2011). Exploring the smallest terrestrial planet: Dawn at Vesta Exploring the smallest terrestrial planet. In *EPSC-DPS Joint Meeting*, 97. 12

SAHL, S., LEUTENEGGER, M., HILBERT, M. & EGGELING, S.H.C. (2010). Fast molecular tracking maps nanoscale dynamics of plasma membrane lipids. *PNAS*, **107**, 6829–6834. 101

SAITO, J., MIYAMOTO, H., NAKAMURA, R., ISHIGURO, M., MICHIKAMI, T., NAKAMURA, A.M., DEMURA, H., SASAKI, S., HIRATA, N., HONDA, C., YAMAMOTO, A., YOKOTA, Y., FUSE, T., YOSHIDA, F., THOLEN, D.J., GASKELL, R.W., HASHIMOTO, T., KUBOTA, T., HIGUCHI, Y., NAKAMURA, T., SMITH, P., HIRAOKA, K., HONDA, T., KOBAYASHI, S., FURUYA, M., MATSUMOTO, N., NEMOTO, E., YUKISHITA, A., KITAZATO, K., DERMAWAN, B., SOGAME, A., TERAZONO, J., SHINOHARA, C. & AKIYAMA, H. (2006). Detailed Images of Asteroid 25143 Itokawa from Hayabusa. *Science*, **312**, 1341–1344. 11, 25

SALUENA, C. & POSCHEL, T. (2000). Convection in horizontally shaken granular material. *The European Physical Journal E: Soft Matter and Biological Physics*, **1**, 55–59, 10.1007/s101890050006. 128

SÁNCHEZ, P. & SCHEERES, D.J. (2011). Simulating Asteroid Rubble Piles with A Self-gravitating Soft-sphere Distinct Element Method Model. *Astrophysical Journal*, **727**, 120. 47, 308

SANCHEZ, P., SCHEERES, D.J. & SWIFT, M. (2010). Impact driven size sorting in self-gravitating granular aggregates. *Lunar Planet. Sci. 41.*. 47

SAVAGE, S.B. (1988). Streaming motions in a bed of vibrationally fluidized dry granular material. *Journal of Fluid Mechanics*, **194**, 457–478. 296

SCHEERES, D., HARTZELL, C., SANCHEZ, P. & SWIFT, M. (2010). Scaling forces to asteroid surfaces: The role of cohesion. *Icarus*, **210**, 968–984. 20, 22, 23, 24, 31, 33, 301, 308

SCHEERES, D.J. (2007). Rotational fission of contact binary asteroids. *Icarus*, **189**, 370–385. 24

SCHENK, P.M., ASPHAUG, E., MCKINNON, W.B., MELOSH, H.J. & WEISSMAN, P.R. (1996). Cometary Nuclei and Tidal Disruption: The Geologic Record of Crater Chains on Callisto and Ganymede. *Icarus*, **121**, 249–274. 28

SCHOFIELD, A. & WROTH, P. (1967). *Critical State Soil Mechanics*. McGraw-Hill, London. 39

SCHROTER, M., GOLDMAN, D.I. & SWINNEY, H.L. (2005). Stationary state volume fluctuations in a granular medium. *Phys. Rev. E*, **71**, 030301. 32

SCHWARTZ, S., RICHARDSON, D., MICHEL, P. & WALSH, K. (2011). Modeling the granular surface and interior of small bodies using the Soft-Sphere Discrete Element Method: implementation in the N-body code pkdgrav and tests. In *EPSC-DPS Joint Meeting*, vol. 1240. 309

SCHWARTZ, S., RICHARDSON, D. & MICHEL, P. (2012). An implementation of a Soft-Sphere Discrete Element Mechanics routine into a high-performance parallel tree code. *Submitted to Physical Review E*. 308

SHÄFER, J., DIPPEL, S. & WOLF, D.E. (1996). Force Schemes in Simulations of Granular Materials. *Journal de Physique I*, **6**, 5–20. 308

SHARMA, I., JENKINS, J. & BURNS, J. (2006). Tidal encounters of ellipsoidal granular asteroids with planets. *Icarus*, **183**. 45

SHARMA, I., JENKINS, J. & BURNS, J. (2009). Dynamical passage to approximate equilibrium shapes for spinning, gravitating rubble asteroids. *Icarus*, **200**, 304–322. 45

SHEVTSOVA, V., GAPONENKO, Y., MELNIKOV, D., RYZHKOV, I. & MIALDUN, A. (2010). Study of thermoconvective flows induced by vibrations in reduced gravity. *Acta Astronautica*, **66**, 166 – 173. 130

SHINBROT, T. & MUZZIO, F.J. (1998). Reverse Buoyancy in Shaken Granular Beds. *Phys. Rev. Lett.*, **81**, 4365–4368. 44

SICKAFOOSE, A.A., COLWELL, J.E., HORÁNYI, M. & ROBERTSON, S. (2000). Photoelectric Charging of Dust Particles in Vacuum. *Phys. Rev. Lett.*, **84**, 6034–6037. 22

SIERKS, H., LAMY, P., BARBIERI, C., KOSCHNY, D., RICKMAN, H., RODRIGO, R., A'HEARN, M.F., ANGRILLI, F., BARUCCI, M.A., BERTAUX, J.L., BERTINI, I., BESSE, S., CARRY, B., CREMONESE, G., DA DEPPO, V., DAVIDSSON, B., DEBEI, S., DE CECCO, M., DE LEON, J., FERRI, F., FORNASIER, S., FULLE, M., HVIID, S.F., GASKELL, R.W., GROUSSIN, O., GUTIERREZ, P., IP, W., JORDA, L., KAASALAINEN, M., KELLER, H.U., KNOLLENBERG, J., KRAMM, R., KÜHRT, E., KÜPPERS, M., LARA, L., LAZZARIN, M., LEYRAT, C., MORENO, J.J.L., MAGRIN, S., MARCHI, S., MARZARI, F., MASSIRONI, M., MICHALIK, H., MOISSL, R., NALETTO, G., PREUSKER, F., SABAU, L., SABOLO, W., SCHOLTEN, F., SNODGRASS, C., THOMAS, N., TUBIANA, C., VERNAZZA, P., VINCENT, J.B., WENZEL, K.P., ANDERT, T., PÄTZOLD, M. & WEISS, B.P. (2011). Images of Asteroid 21 Lutetia: A Remnant Planetesimal from the Early Solar System. *Science*, **334**, 487–. 11, 12, 19

SINGER, K., MCKINNON, W.B., SCHENK, P.M. & MOORE, J.M. (2009). Large Landslides on Iapetus: Implications for Crater and Ridge Modification. In *AAS/Division for Planetary Sciences Meeting Abstracts*, vol. 41 of *AAS/Division for Planetary Sciences Meeting Abstracts*. 30, 31

SLOTTERBACK, S., TOIYA, M., GOFF, L., DOUGLAS, J.F. & LOSERT, W. (2008a). Correlation between Particle Motion and Voronoi-Cell-Shape Fluctuations during the Compaction of Granular Matter. *Phys. Rev. Lett.*, **101**, 258001. 342

SLOTTERBACK, S., TOIYA, M., GOFF, L., DOUGLAS, J.F. & LOSERT, W. (2008b). Particle motion during the compaction of granular matter. *arXiv.org:0802.0485*. 42

SPIGA, A., FORGET, F., MADELEINE, J., MONTABONE, L., LEWIS, S.R. & MILLOUR, E. (2011). The impact of martian mesoscale winds on surface temperature and on the determination of thermal inertia. *Icarus*, **212**, 504–519. 315

STADEL, J.G. (2001). *Cosmological N-body simulations and their analysis*. Ph.D. thesis, University of Washington. 48, 49, 52

STARON, L. (2011). Continuum modeling of granular systems. In *Ecole CNRS - Systemes Autogravitants Granulaires*. 32, 33

STEVENS, A. & HRENYA, C. (2005). Comparison of soft-sphere models to measurements of collision properties during normal impacts. *Powder Technology*, **154**, 99 – 109. 308

STEVENSON, J.D. & WOLYNES, P.G. (2010). A universal origin for secondary relaxations in supercooled liquids and structural glasses. *Nat. Phys.*, **6**, 62–68. 81

SZARF, K., COMBE, G. & VILLARD, P. (2010). Polygons vs. clumps of discs: A numerical study of the influence of grain shape on the mechanical behaviour of granular materials. *Powder Technology*, **In Press, Corrected Proof**, –. 46, 309

TABERLET, N., RICHARD, P. & JOHN HINCH, E. (2006). *S* shape of a granular pile in a rotating drum. *Phys. Rev. E*, **73**, 050301. 72, 76

TAGUCHI, Y. (1992). New origin of a convective motion: Elastically induced convection in granular materials. *Phys. Rev. Lett.*, **69**, 1367–1370. 273

TAI, C., HSIAU, S. & KRUELLE, C. (2010). Density segregation in a vertically vibrated granular bed. *Powder Technology*, **204**, 255 – 262. 128

TANCREDI, G., MACIEL, A., HEREDIA, L., RICHERI, P. & NESMACHNOW, S. (2011). Granular physics in low-gravity environments using DEM. *ArXiv e-prints*. 299

TANGA, P., WEIDENSCHILLING, S.J., MICHEL, P. & RICHARDSON, D.C. (2004). Gravitational instability and clustering in a disk of planetesimals. *Astrophysical Journal*, **427**, 1105–1115. 50

TAYLOR, G.I. (1923). Stability of a Viscous Liquid Contained between Two Rotating Cylinders. *Royal Society of London Philosophical Transactions Series A*, **223**, 289–343. 124

TAYLOR, P.A., MARGOT, J.L., VOKROUHLICKY, D., SCHEERES, D.J., PRAVEC, P., LOWRY, S.C., FITZSIMMONS, A., NOLAN, M.C., OSTRO, S.J., BENNER, L.A.M., GIORGINI, J.D. & MAGRI, C. (2007). Spin Rate of Asteroid (54509) 2000 PH5 Increasing Due to the YORP Effect. *Science*, **316**, 274–277. 14

TENNAKOON, S.G.K., KONDIC, L. & BEHRINGER, R.P. (1999). Onset of flow in a horizontally vibrated granular bed: Convection by horizontal shearing. *EPL (Europhysics Letters)*, **45**, 470. 128

THOMAS, P., VEVERKA, J., BLOOM, A. & DUXBURY, T. (1979). Grooves on Phobos: Their Distribution, Morphology and Possible Origin. *J. Geophys. Res.*, **84**, 8457–8477. 11, 29

THOMAS, P.C. & ROBINSON, M.S. (2005). Seismic resurfacing by a single impact on the asteroid 433 Eros. *Nature*, **436**, 366–369. 26

THOMAS, P.C., JOSEPH, J., CARCICH, B., VEVERKA, J., CLARK, B.E., BELL, J.F., BYRD, A.W., CHOMKO, R., ROBINSON, M., MURCHIE, S., PROCKTER, L., CHENG, A., IZENBERG, N., MALIN, M., CHAPMAN, C., MCFADDEN, L.A., KIRK, R., GAFFEY, M. & LUCEY, P.G. (2002). Eros: Shape, Topography, and Slope Processes. *Icarus*, **155**, 18–37. 9

THORNTON, C. (1997). Coefficient of Restitution for Collinear Collisions of Elastic-Perfectly Plastic Spheres. *Journal of Applied Mechanics*, **64**, 383–386. 308

TOIYA, M. (2006). *Onset of Granular Flows by Local and Global Forcing*. Ph.D. thesis, University of Maryland. 126, 127, 130, 131, 139, 277, 296

TOIYA, M., STAMBAUGH, J. & LOSERT, W. (2004). Transient and Oscillatory Granular Shear Flow. *Phys. Rev. Lett.*, **93**, 088001. 38, 42, 282

VEVERKA, J., THOMAS, P., HARCH, A., CLARK, B., BELL, I., J. F., CARCICH, B., JOSEPH, J., CHAPMAN, C., MERLINE, W., ROBINSON, M., MALIN, M., MCFADDEN, L.A., MURCHIE, S., HAWKINS, I., S. E., FARQUHAR, R., IZENBERG, N. & CHENG, A. (1997). NEAR's Flyby of 253 Mathilde: Images of a C Asteroid. *Science*, **278**, 2109–2114. 19

VEVERKA, J., ROBINSON, M., THOMAS, P., MURCHIE, S., BELL, I., J. F., IZENBERG, N., CHAPMAN, C., HARCH, A., BELL, M., CARCICH, B., CHENG, A., CLARK, B., DOMINGUE, D., DUNHAM, D., FARQUHAR, R., GAFFEY, M.J., HAWKINS, E., JOSEPH, J., KIRK, R., LI, H., LUCEY, P., MALIN, M., MARTIN, P., MCFADDEN, L., MERLINE, W.J., MILLER, J.K., OWEN, J., W. M., PETERSON, C., PROCKTER, L., WARREN, J., WELLNITZ, D., WILLIAMS, B.G. & YEOMANS, D.K. (2000). NEAR at Eros: Imaging and Spectral Results. *Science*, **289**, 2088–2097. 6

VEVERKA, J., FARQUHAR, B., ROBINSON, M., THOMAS, P., MURCHIE, S., HARCH, A., ANTREASIAN, P.G., CHESLEY, S.R., MILLER, J.K., OWEN, W.M., WILLIAMS, B.G., YEOMANS, D., DUNHAM, D., HEYLER, G., HOLDRIDGE, M., NELSON, R.L., WHITTENBURG, K.E., RAY, J.C., CARCICH, B., CHENG, A., CHAPMAN, C., BELL, J.F., BELL, M., BUSSEY, B., CLARK, B., DOMINGUE, D., GAFFEY, M.J., HAWKINS, E., IZENBERG, N., JOSEPH, J., KIRK, R., LUCEY, P., MALIN, M., MCFADDEN, L., MERLINE, W.J., PETERSON, C., PROCKTER, L., WARREN, J. & WELLNITZ, D. (2001a). The landing of the NEAR-Shoemaker spacecraft on asteroid 433 Eros. *Nature*, **413**, 390–393. 9

VEVERKA, J., THOMAS, P.C., ROBINSON, M., MURCHIE, S., CHAPMAN, C., BELL, M., HARCH, A., MERLINE, W.J., BELL, J.F., BUSSEY, B., CARCICH, B., CHENG, A., CLARK, B., DOMINGUE, D., DUNHAM, D., FARQUHAR, R., GAFFEY, M.J., HAWKINS, E., IZENBERG, N., JOSEPH, J., KIRK, R., LI, H., LUCEY, P., MALIN, M., MCFADDEN, L., MILLER, J.K., OWEN, W.M., PETERSON, C., PROCKTER, L., WARREN, J., WELLNITZ, D., WILLIAMS, B.G. & YEOMANS, D.K. (2001b). Imaging of Small-Scale Features on 433 Eros from NEAR: Evidence for a Complex Regolith. *Science*, **292**, 484–488. 6, 8, 25

WADA, K., SENSHU, H., YAMAMOTO, S. & MARSUI, T. (2003). A Numerical Simulation Of Impacts Into Granular Materials By Distinct Element Method. In *Lunar and Planetary Science Conference*. 26

WADA, K., SENSHU, H. & MARSUI, T. (2005). A Numerical Simulation Of Impact Cratering On Adhesive Granular Materials. In *Lunar and Planetary Science Conference*. 26

WADA, K., SENSHU, H. & MATSUI, T. (2006). Numerical simulation of impact cratering on granular material. *Icarus*, **180**, 528 – 545. 46, 47, 309

WALSH, K.J. & RICHARDSON, D.C. (2006). Binary near-Earth asteroid formation: Rubble pile model of tidal disruptions. *Icarus*, **180**, 201 – 216. 28, 50

WALSH, K.J. & RICHARDSON, D.C. (2008). A steady-state model of NEA binaries formed by tidal disruption of gravitational aggregates. *Icarus*, **193**, 553–566. 28, 50

WALSH, K.J., RICHARDSON, D.C. & MICHEL, P. (2008). Rotational breakup as the origin of small binary asteroids. *Nature*, **454**, 188–191. 24, 27, 29, 47, 48, 50

WALSH, K.J., MORBIDELLI, A., RAYMOND, S.N., O'BRIEN, D.P. & MANDELL, A.M. (2011). A low mass for Mars from Jupiter's early gas-driven migration. *Nature*, **475**, 206–209. 1, 19

WALTON, O.R. & BRAUN, R.L. (1986). Viscosity, granular-temperature, and stress calculations for shearing assemblies of inelastic, frictional disks. *Journal of Rheology*, **30**, 949–980. 308

WANG, P., SONG, C., BRISCOE, C. & MAKSE, H.A. (2008). Particle dynamics and effective temperature of jammed granular matter in a slowly sheared three-dimensional couette cell. *Phys. Rev. E*, **77**, 061309. 139

WEEKS, E.R., CROCKER, J.C., LEVITT, A.C., SCHOFIELD, A. & WEITZ, D.A. (2000). Three-Dimensional Direct Imaging of Structural Relaxation Near the Colloidal Glass Transition. *Science*, **287**, 627–631. 81, 101

WEISS, B.P., ELKINS-TANTON, L.T., BARUCCI, M.A., SIERKS, H., SNODGRASS, C., VINCENT, J.B., MARCHI, S., WEISSMAN, P.R., PATZOLD, M., RICHTER, I., FULCHIGNONI, M., BINZEL, R.P. & SCHULZ, R. (2011). Possible evidence for partial differentiation of asteroid Lutetia from Rosetta. *Planetary and Space Science*, –. 11

WENTWORTH, C.K. (1922). A Scale of Grade and Class Terms for Clastic Sediments. *The Journal of Geology*, **30**, pp. 377–392. 32, 33

WERNER, S.C., IVANOV, B.A. & NEUKUM, G. (2009). Theoretical analysis of secondary cratering on Mars and an image-based study on the Cerberus Plains. *Icarus*, **200**, 406 – 417. 313

WHIPPLE, E.C. (1981). Potentials of surfaces in space. *Reports on Progress in Physics*, **44**, 1197. 22

WHITELEY, R.J. (2001). *A compositional and dynamical survey of the near-Earth asteroids*. Ph.D. thesis, University of Hawai'i at Manoa. 19

WILCOX, B.B., ROBINSON, M.S., THOMAS, P.C. & HAWKE, B.R. (2005). Constraints on the depth and variability of the lunar regolith. *Meteoritics and Planetary Science*, **40**, 695. 29

WILDMAN, R.D., HUNTLEY, J.M. & PARKER, D.J. (2001). Convection in Highly Fluidized Three-Dimensional Granular Beds. *Phys. Rev. Lett.*, **86**, 3304–3307. 296

WILLIAMS, J. (1976). The segregation of particulate materials. A review. *Powder Technology*, **15**, 245 – 251. 43

WOOD, D.M. (1990). *Soil Behavior and Critical State Soil Mechanics*. Cambridge University Press, Cambridge. 39

WÜNNEMANN, K. & IVANOV, B.A. (2003). Numerical modelling of the impact crater depth-diameter dependence in an acoustically fluidized target. *Planetary and Space Science*, **51**, 831 – 845. 313

WURM, G. & BLUM, J. (1998). Experiments on Preplanetary Dust Aggregation. *Icarus*, **132**, 125–136. 1

XU, H., REEVES, A. & LOUGE, M. (2004). Measurement errors in the mean and fluctuation velocities of spherical grains from a computer analysis of digital images. *Rev. Sci. Instrum*, **75**. 97, 101

YANO, H., KUBOTA, T., MIYAMOTO, H., OKADA, T., SCHEERES, D., TAKAGI, Y., YOSHIDA, K., ABE, M., ABE, S., BARNOUIN-JHA, O., FUJIWARA, A., HASEGAWA, S., HASHIMOTO, T., ISHIGURO, M., KATO, M., KAWAGUCHI, J., MUKAI, T., SAITO, J., SASAKI, S. & YOSHIKAWA, M. (2006). Touchdown of the Hayabusa Spacecraft at the Muses Sea on Itokawa. *Science*, **312**, 1350–1353. 10

YEOMANS, D.K., BARRIOT, J.P., DUNHAM, D.W., FARQUHAR, R.W., GIORGINI, J.D., HELFRICH, C.E., KONOPLIV, A.S., MCADAMS, J.V., MILLER, J.K., OWEN, W.M., SCHEERES, D.J., SYNNOTT, S.P. & WILLIAMS, B.G. (1997). Estimating the Mass of Asteroid 253 Mathilde from Tracking Data During the NEAR Flyby. *Science*, **278**, 2106–2109. 19

YEOMANS, D.K., ANTREASIAN, P.G., BARRIOT, J.P., CHESLEY, S.R., DUNHAM, D.W., FARQUHAR, R.W., GIORGINI, J.D., HELFRICH, C.E., KONOPLIV, A.S., MCADAMS, J.V., MILLER, J.K., OWEN, W.M., SCHEERES, D.J., THOMAS, P.C., VEVERKA, J. & WILLIAMS, B.G. (2000). Radio Science Results During the NEAR-Shoemaker Spacecraft Rendezvous with Eros. *Science*, **289**, 2085–2088. 6, 19

YOKOYAMA, E., TRINDADE, R., LANA, C., SOUZA FILHO, C., BARATOUX, D., MARANGONI, Y. & TOHVER, E. (2011). Magnetic fabric of Araguainha peak-ring structure (Central Brazil): implications for deformation mechanisms and central uplift formation. *submitted to Journal of Geophysical Research*. 315

ZHANG, H., SROLOVITZ, D.J., DOUGLAS, J.F. & WARREN, J.A. (2006). Characterization of atomic motion governing grain boundary migration. *Phys. Rev. B*, **74**, 115404. 81, 82

ZHANG, H., SROLOVITZ, D.J., DOUGLAS, J.F. & WARREN, J.A. (2009). Grain boundaries exhibit the dynamics of glass-forming liquids. *Proceedings of the National Academy of Sciences*, **106**, 7735–7740. 80, 104

ZHOU, B., LIU, Q., HU, L., YAO, Y. & HU, W. (2002). Space experiments of thermocapillary convection in two-liquid layers. *Science in China Series E: Technological Sciences*, **45**, 552–560, 10.1360/02ye9063. 130

ZHU, H., ZHOU, Z., YANG, R. & YU, A. (2007). Discrete particle simulation of particulate systems: Theoretical developments. *Chem. Engin. Sci.*, **62**, 3378–3396. 76

ZUBER, M.T., SMITH, D.E., CHENG, A.F., GARVIN, J.B., AHARONSON, O., COLE, T.D., DUNN, P.J., GUO, Y., LEMOINE, F.G., NEUMANN, G.A., ROWLANDS, D.D. & TORRENCE, M.H. (2000). The Shape of 433 Eros from the NEAR-Shoemaker Laser Rangefinder. *Science*, **289**, 2097–2101. 6, 7